Conference Proceedings of the Society for Experimental Mechanics Series

Jay Carroll · Samantha Daly *Editors*

Fracture, Fatigue, Failure, and Damage Evolution, Volume 5

Proceedings of the 2014 Annual Conference on Experimental and Applied Mechanics

SEM

Springer

Conference Proceedings of the Society for Experimental Mechanics Series

Series Editor

Tom Proulx
Society for Experimental Mechanics, Inc.,
Bethel, CT, USA

For further volumes:
http://www.springer.com/series/8922

Jay Carroll • Samantha Daly
Editors

Fracture, Fatigue, Failure, and Damage Evolution, Volume 5

Proceedings of the 2014 Annual Conference on Experimental and Applied Mechanics

Springer

Editors
Jay Carroll
Sandia National Laboratories
Albuquerque, NM, USA

Samantha Daly
University of Michigan
Ann Arbor, MI, USA

ISSN 2191-5644 ISSN 2191-5652 (electronic)
ISBN 978-3-319-06976-0 ISBN 978-3-319-06977-7 (eBook)
DOI 10.1007/978-3-319-06977-7
Springer Cham Heidelberg New York Dordrecht London

Library of Congress Control Number: 2014944551

Printed on acid-free paper

Springer is part of Springer Science+Business Media (www.springer.com)

Preface

Fracture, Fatigue, Failure and Damage Evolution, Volume 5: Proceedings of the 2014 Annual Conference on Experimental and Applied Mechanics represents one of eight volumes of technical papers presented at the 2014 SEM Annual Conference & Exposition on Experimental and Applied Mechanics organized by the Society for Experimental Mechanics and held in Greenville, SC, June 2–5, 2014. The complete Proceedings also includes volumes on: *Dynamic Behavior of Materials*; *Challenges in Mechanics of Time-Dependent Materials*; *Advancement of Optical Methods in Experimental Mechanics*; *Mechanics of Biological Systems and Materials*; *MEMS and Nanotechnology*; *Experimental Mechanics of Composite, Hybrid, and Multifunctional Materials*; *Experimental and Applied Mechanics*.

Each collection presents early findings from experimental and computational investigations on an important area within Experimental Mechanics, Fracture and Fatigue being one of these areas.

Fatigue and fracture are two of the most critical considerations in engineering design. Understanding and characterizing fatigue and fracture has remained as one of the primary focus areas of experimental mechanics for several decades. Advances in experimental techniques, such as digital image correlation, acoustic emissions, and electron microscopy, have allowed for deeper study of phenomena related to fatigue and fracture. This volume contains the results of investigations of several aspects of fatigue and fracture such as microstructural effects, the behavior of interfaces, the behavior of different and/or complex materials such as composites, and environmental and loading effects. The collection of experimental mechanics research included here represents another step toward solving the long-term challenges associated with fatigue and fracture.

Albuquerque, NM, USA — Jay D. Carroll
Ann Arbor, MI, USA — Samantha H. Daly

Contents

Chapter 1
Simulation of Arbitrary Mixed-Mode Crack Growth Using an Energy-Based Approach

B.R. Davis, P.A. Wawrzynek, and A.R. Ingraffea

Abstract A finite-element-based simulation technique is being developed to predict 3-D, arbitrary, non-planar evolution of mixed-mode crack growth. The approach combines a geometrically explicit crack front re-meshing scheme, and an energy-based growth formulation to predict extension magnitudes along the crack front. The technique also leverages a new 3-D mixed-mode energy release rate decomposition using the virtual crack extension (VCE) method. The energy-based crack growth formulation, previously implemented for planar crack growth, is extended to non-planar growth situations by employing a basis-function approach to describe crack front extensions. Rather than determining point-by-point extensions, calculating a governing function alleviates numerical influences on the crack growth predictions. The simulation technique seeks to mitigate computationally biased crack growth, as found in prescribed and mesh dependent methods, for example.

Keywords Crack growth • Energy release rate • Mixed-mode • Virtual crack extension • Finite-element analysis

1.1 Introduction

Many finite-element-based techniques have been developed to simulate 3-D arbitrary crack growth in structural components. Crack growth problems become inherently more difficult when complex loadings induce mixed-mode behavior. The resulting crack front evolution could become curved and tortuous. Utilizing a fracture mechanics approach to predict such complicated crack shape advances requires three main components: (1) crack representation, (2) fracture parameter calculations, and (3) crack extension application.

Currently, the prominent techniques for simulating 3-D, mixed-mode, arbitrary crack growth include the extended finite element method (XFEM) [1–3], cohesive zone elements [4, 5], and explicit crack front re-meshing schemes [6–9]. Each approach has been well developed throughout the literature, but as articulated in [10], suffer from some form of computational bias or require input on the expected crack evolution. For example, cohesive zone element approaches predict crack paths that are governed by the element locations, shapes, sizes and orientations. In some cases, finite element meshes are designed to adhere to the expected growth pattern, contradicting the notion of arbitrary crack evolution by linking a numerical artifact (the finite element mesh) with a physical phenomenon (crack growth). Alternatively, XFEM and re-meshing schemes often rely on user-prescribed growth increments to advance the front.

The unique crack growth simulation technique developed in [10] utilizes a new energy-based formulation that allows for the direct calculation of point-by-point crack front extensions. The formulation is derived from an energy expansion that depends on the first order variation of the energy release rate. The variation of energy release rate, made readily available via the virtual crack extension (VCE) method, acts as an influence function relating changes in energy from load increments to changes in geometry along the crack front. This term provides a mechanics-based approach to extract explicit crack extensions, avoiding the need to supply user-prescribed magnitudes of advance. The technique also employs a geometrically explicit crack representation that is continually updated through re-meshing schemes. As a result, mesh biased growth

B.R. Davis (✉) • P.A. Wawrzynek • A.R. Ingraffea
School of Civil and Environmental Engineering, Cornell University, 638 Rhodes Hall, Ithaca, NY 14853, USA
e-mail: brd46@cornell.edu

J. Carroll and S. Daly (eds.), *Fracture, Fatigue, Failure, and Damage Evolution, Volume 5: Proceedings of the 2014 Annual Conference on Experimental and Applied Mechanics*, Conference Proceedings of the Society for Experimental Mechanics Series,
DOI 10.1007/978-3-319-06977-7_1,

is reduced, allowing for the crack front to evolve arbitrarily. This form of crack representation is not a limitation of the technique, but deemed more practical for development purposes. The energy-based formulation can certainly be used with XFEM crack representations, for example.

The implementation of the simulation technique described in [10] is limited to mode I, planar crack growth conditions. It is the objective of the current work to extend the technique to simulate mixed-mode and non-planar, 3-D crack front evolution. To generalize the approach, an updated toolset is required. The commercial FRANC3D fracture analysis software [11] is used to represent and re-mesh the evolving non-planar crack front geometries. A new 3-D, mixed-mode VCE implementation (submitted and under review for publication) is developed to calculate the necessary energy release rates along the crack front. Finally, in conjunction with a trajectory criterion, a new basis-function approach to calculate extensions along an arbitrary front is constructed. The basis-function approach seeks to address sensitivity challenges associated with using a local, point-by-point approach for non-planar growth predictions. The focus of this proceeding will demonstrate the current status of the toolset development.

The next section will provide background and a description of the new 3-D, mixed-mode VCE implementation. Note that the full formulation and derivation of the mixed-mode VCE method will be available in an upcoming publication. Two examples are presented to verify the VCE mixed-mode energy release rate calculations. The following section will introduce the crack growth formulation, and its augmentation with the new basis-function methodology.

1.2 The Mixed-Mode Virtual Crack Extension Method

The VCE method for calculating energy release rates (also known as the stiffness derivative method) was first introduced by Dixon and Pook [12], and Watwood [13], and further developed by Hellen [14] and Parks [15]. Early VCE calculations utilized finite perturbations of meshes to approximate the required stiffness derivatives. This finite difference approach often introduced geometric approximation and numerical truncation errors. Using variational principle theories, a direct integral approach simplified the VCE method and improved accuracy and efficiency by eliminating the need for finite perturbations [16, 17]. The advent of the variational approach also allowed for the calculation of higher-order derivatives of energy release rate, the salient feature of the current method. Hwang et al. [18] generalized the variational formulations for planar 3-D cracks. A symmetric/anti-symmetric approach to decompose energy release rates, first demonstrated for a 2-D VCE method by Ishikawa [19] and later extended to 3-D equivalent domain J-integrals by [20–22], is used in the new 3-D VCE implementation.

1.2.1 Virtual Crack Extension Formulation

Following the formulation from [18], the VCE method is derived from the expression for the potential energy, Π, of a finite element system:

$$\Pi = \frac{1}{2} u^T K u - u^T f, \tag{1.1}$$

where u, K, and f are the displacement vector, the stiffness matrix, and the applied force vector, respectively.

The energy release rate, G, at crack-front position i is defined as the negative variation of the potential energy with respect to a virtual, incremental, crack-front extension, δa, in the normal direction of the front at that position:

$$G_i \equiv -\frac{\delta \Pi}{\delta A_i} = -\frac{\delta \Pi}{\delta a_i \ell_i}. \tag{1.2}$$

In the 3-D sense, the virtual extension has an associated area, δA_i, comprised of a virtual extension, δa_i, and an effective width, ℓ_i. Applying the variation to the finite element expression for potential energy leads to the following form of the energy release rate:

$$G_i = -\frac{1}{\ell_i} \left(\frac{1}{2} u^T \frac{\delta K}{\delta a_i} u - u^T \frac{\delta f}{\delta a_i} \right). \tag{1.3}$$

For simplicity in the current implementation, it is assumed that applied forces, f, are not influenced by the virtual incremental extension, and therefore the variational force term, $\frac{\delta f}{\delta a_i}$, is zero. The simplification reduces Eq. 1.3 to:

$$G_i = -\frac{1}{\ell_i}\left(\frac{1}{2}u^T\frac{\delta K}{\delta a_i}u\right). \tag{1.4}$$

Note, if the virtual extensions alter the nature of the applied load (e.g. with crack-face pressures, thermal, and body-force loadings), the effect must be accounted for with the variational force term, $\frac{\delta f}{\delta a_i}$, and included throughout the formulation.

The expression for the first-order variation of the energy release rate with respect to incremental crack extension, δa_j, follows from Eq. 1.4:

$$\frac{\delta G_i}{\delta a_j} = -\frac{1}{\ell_i}\left(u^T\frac{\delta K}{\delta a_i}\frac{\delta u}{\delta a_j} + \frac{1}{2}u^T\frac{\delta^2 K}{\delta a_i \delta a_j}u\right). \tag{1.5}$$

Note that Eqs. 1.4 and 1.5 represent the total global formulations of the VCE expressions for the energy release rate and rate of energy release rate. The integration and calculations are performed in a global coordinate system.

1.2.2 3-D Mixed-Mode Virtual Crack Extension Formulation

From Eq. 1.4, the energy release rate is composed of the stiffness derivative and nodal displacements. The stiffness derivative is fracture-mode invariant, leaving the displacements near the crack front to be decomposed into mode I, II, and III components. Using a local crack front coordinate system for each position along the front and the symmetric/anti-symmetric field decomposition found in [20], the local displacement modal contributions are determined such that:

$$u = u_I + u_{II} + u_{III}. \tag{1.6}$$

The decomposed displacements from Eq. 1.6 are substituted into Eq. 1.4, yielding the following expression for total energy release rate at position i:

$$G_i = -\frac{1}{\ell_i}\left[\frac{1}{2}(u_I + u_{II} + u_{III})^T\frac{\delta K}{\delta a_i}_L(u_I + u_{II} + u_{III})\right]. \tag{1.7}$$

Note that the stiffness derivative is also calculated in the local crack-front coordinate system to maintain consistency, and is denoted by subscript L. Expanding Eq. 1.7 leads to the separation of the decomposed energy release rate modes:

$$G_i = -\frac{1}{\ell_i}\left[\begin{array}{l}\left(\frac{1}{2}{u_I}^T\frac{\delta K}{\delta a_i}_L u_I\right) + \left(\frac{1}{2}{u_{II}}^T\frac{\delta K}{\delta a_i}_L u_{II}\right) + \left(\frac{1}{2}{u_{III}}^T\frac{\delta K}{\delta a_i}_L u_{III}\right)\\ + \left({u_I}^T\frac{\delta K}{\delta a_i}_L u_{II}\right) + \left({u_{II}}^T\frac{\delta K}{\delta a_i}_L u_{III}\right) + \left(\frac{1}{2}{u_{III}}^T\frac{\delta K}{\delta a_i}_L u_I\right)\end{array}\right]. \tag{1.8}$$

Extending from Ishikawa's 2-D VCE mode decomposition [19], the mode I and II energy release rates are as follows:

$$G_{Ii} = -\frac{1}{\ell_i}\left(\frac{1}{2}{u_I}^T\frac{\delta K}{\delta a_i}_L u_I\right), \tag{1.9}$$

$$G_{IIi} = -\frac{1}{\ell_i}\left(\frac{1}{2}{u_{II}}^T\frac{\delta K}{\delta a_i}_L u_{II}\right). \tag{1.10}$$

The unique contribution of the current implementation is the inclusion of the mode III energy release rate distribution along the crack front. The remaining terms in Eq. 1.8, excluding Eqs. 1.9 and 1.10, comprise a pure mode III component, $\frac{1}{2}{u_{III}}^T \frac{\delta K}{\delta a_i}_L u_{III}$, and three modal-interaction coupling terms. Understanding the influence of the coupling-mode terms is critical in determining their respective contributions to the 3-D mixed-mode energy release rates. Consider the following coupling mode terms from Eq. 1.8:

$$G_{I/II_i} = -\frac{1}{\ell_i}\left({u_I}^T \frac{\delta K}{\delta a_i}_L u_{II}\right), \tag{1.11}$$

$$G_{II/III_i} = -\frac{1}{\ell_i}\left({u_{II}}^T \frac{\delta K}{\delta a_i}_L u_{III}\right), \tag{1.12}$$

$$G_{III/I_i} = -\frac{1}{\ell_i}\left({u_{III}}^T \frac{\delta K}{\delta a_i}_L u_I\right). \tag{1.13}$$

Using symmetric and anti-symmetric arguments, it can be shown and verified numerically that calculating the coupling terms in Eqs. 1.11 and 1.13 about a symmetric domain lead to a cancellation effect. The result is $G_{I/IIi} = G_{III/Ii} = 0$. However, Eq. 1.12 has an additive effect that results in $G_{II/IIIi} \neq 0$. The only contributing non-zero components to $G_{II/IIIi}$ are out-of-plane shear. Therefore, any addition to the total energy release rate from $G_{II/IIIi}$ must be a factor of the out-of-plane mode III energy release rate:

$$G_{III_i} = -\frac{1}{\ell_i}\left(\frac{1}{2}{u_{III}}^T \frac{\delta K}{\delta a_i}_L u_{III}\right) + G_{II/III_i}. \tag{1.14}$$

With the individual mixed-mode terms determined and the modal-interaction coupling terms accounted for, the VCE total energy release is successfully decomposed, satisfying the following summation:

$$G_i = G_{I_i} + G_{II_i} + G_{III_i}. \tag{1.15}$$

1.2.3 Numerical Examples

In this section two verification analyses are presented to demonstrate the accuracy of the new, 3-D, mixed-mode energy release rate implementation using the VCE method. The mixed-mode VCE results are compared with analytical and M-integral methods. Each model and crack front geometry is meshed using the FRANC3D software.

The first problem considered a 45°-inclined circular crack centrally embedded within a rectangular isotropic body, as shown in Fig. 1.1. The model geometry was appropriately sized to approximate crack behavior within an infinite body. Analytical expressions for the mixed-mode I/II/III stress intensity factors for an inclined penny crack under remote tension [23] are used as a reference solution.

The second numerical example is a half-penny-shaped surface crack in an isotropic cylindrical specimen [24, 25]. Figure 1.2 shows the global geometry and loading conditions that induce mode II/III behavior along the crack front. The local, in-plane geometry of the crack front is depicted in Fig. 1.2. The VCE energy release rate results are compared with M-integral calculations using the FRANC3D software.

Figures 1.3 and 1.4 display the mixed-mode and total energy release rate distributions calculated by the VCE implementation for each example. The results compare extremely well with the reference solutions. The average percent differences between the VCE and reference results are 0.11 % and 0.23 % for the inclined circular crack and the surface-cracked cylinder, respectively.

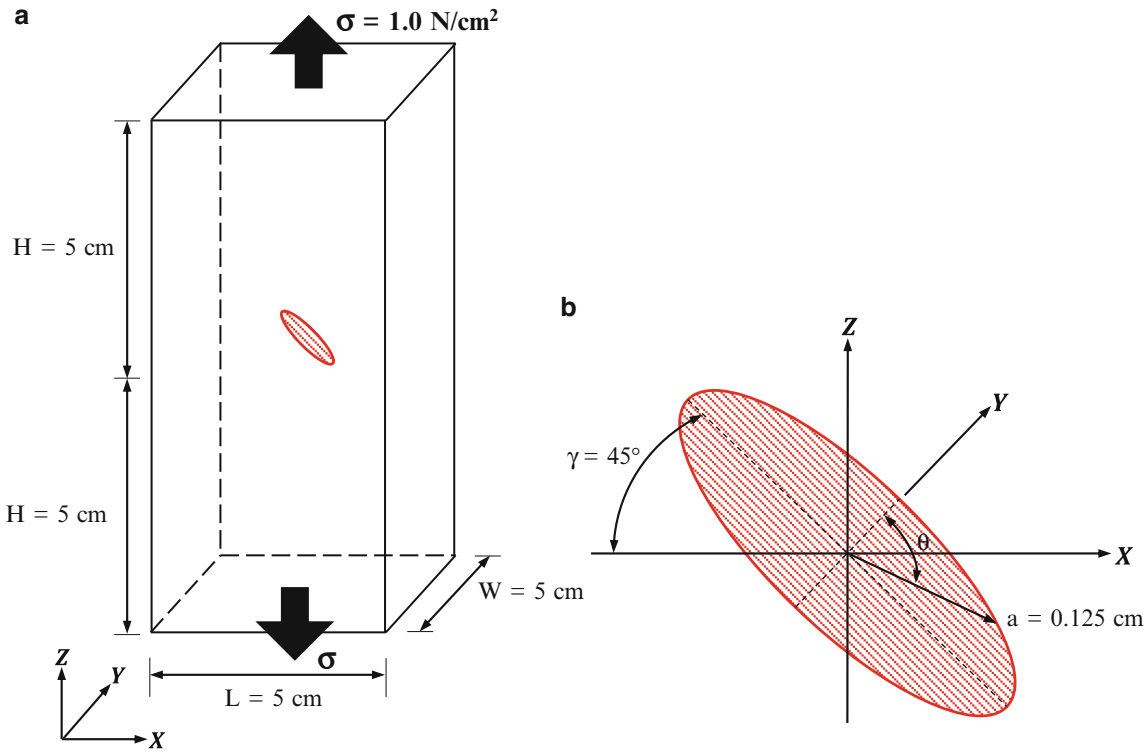

Fig. 1.1 Embedded inclined penny crack: (**a**) global geometry and loading conditions and (**b**) local crack-front geometry

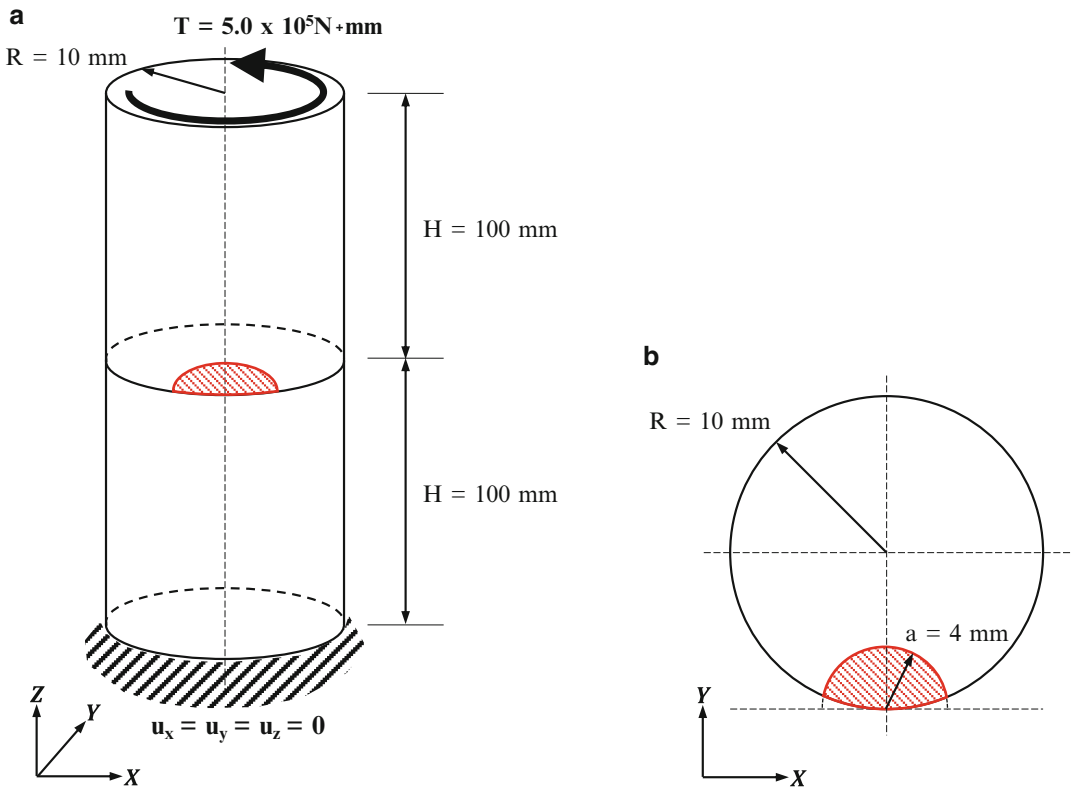

Fig. 1.2 Geometry and loading conditions for the penny-shaped surface crack in a cylindrical specimen: (**a**) global geometry and (**b**) local crack-plane geometry

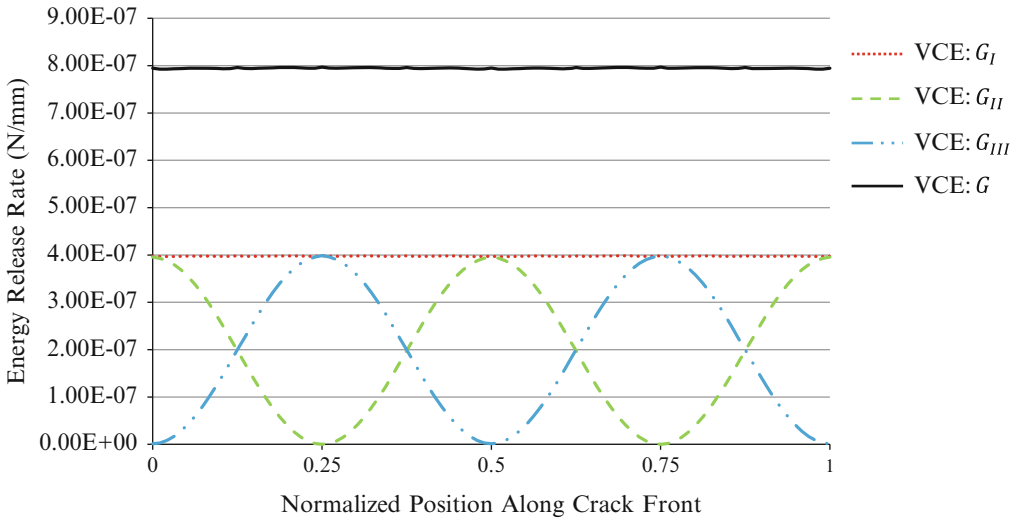

Fig. 1.3 Mixed-mode and total energy release rate distributions calculated by the VCE method for the inclined penny-crack specimen

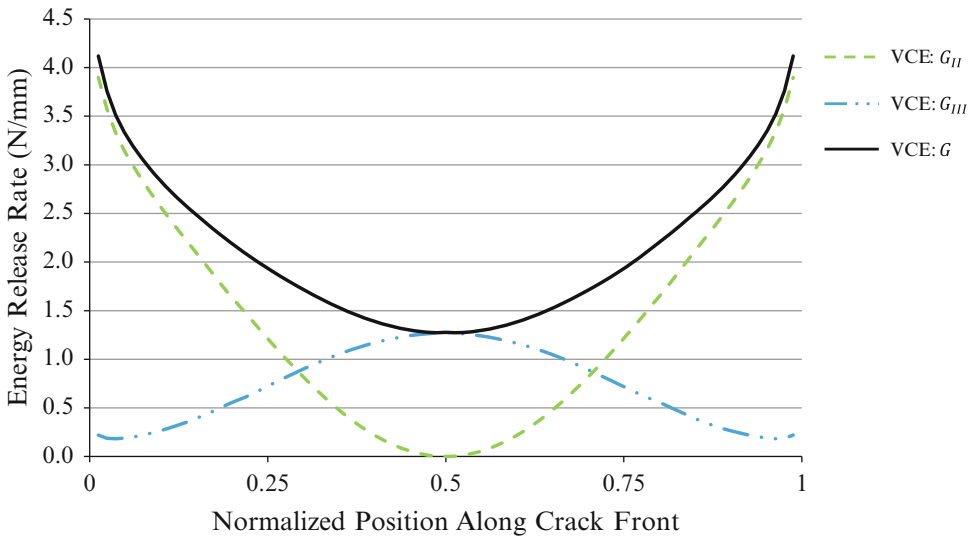

Fig. 1.4 Mixed-mode and total energy release rate distributions calculated by the VCE method for the surface-cracked cylindrical specimen

1.3 Crack Growth Formulation

The prediction of mixed-mode, non-planar crack front extensions requires two features. The first is a crack trajectory or kinking approach to determine the angle of advance for a position along the front. The second is a crack growth formulation to calculate the magnitudes of advances.

1.3.1 Crack Trajectory Criterion

For this work, a maximum critical energy release rate criterion is employed to obtain the extension angles [26]. For each position on the front, a series of virtual extensions that sweep radially along the local crack front normal are applied and energy release rates calculated. From this distribution the angle associated with the maximum energy release rate is chosen as the local position's extension angle. Certainly, other mixed-mode trajectory and kinking criteria can be used, such as maximum tensile stress and maximum shear stress.

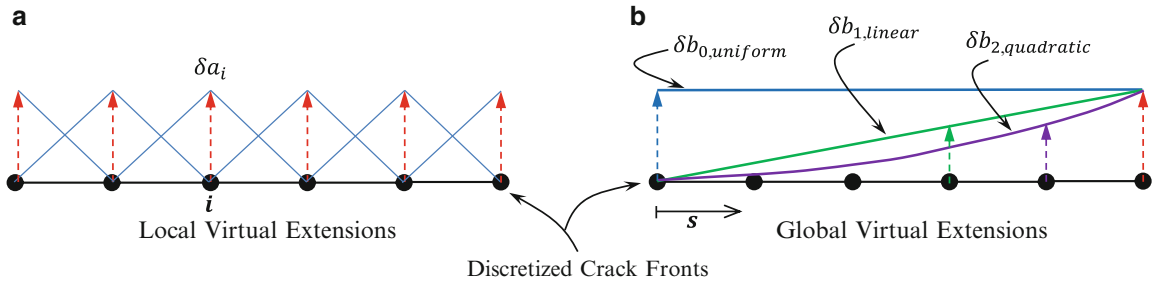

Fig. 1.5 Comparison between (**a**) local, point-by-point virtual crack extensions at position i, and (**b**) global basis-function virtual extensions along crack front length s

1.3.2 Basis-Function Growth Approach

The salient feature of this work is the modification of the crack growth formulation introduced in [10] to handle mixed-mode, non-planar growth situations. The planar growth formulation utilizes a balance equation extended from the first-order expansion of the energy release rate:

$$G_{ic} = G_i^0 + \frac{\delta G_i}{\delta P} \odot \Delta P_i + \frac{\delta G_i}{\delta a_j} \Delta a_j, \tag{1.16}$$

where G_{ic} is a critical energy release rate characterizing the material's resistance to crack growth; G_i^0 is the initial energy release rate prior to load increment ΔP_i; $\frac{\delta G_i}{\delta P} \odot \Delta P_i$ represents the energy contribution due to the applied load increment; $\frac{\delta G_i}{\delta a_j} \Delta a_j$ represents the energy contribution due to crack shape change. The $\frac{\delta G_i}{\delta a_j}$ term is the aforementioned rate of energy release rate parameter obtained through the VCE method that acts as an influence function relating energy changes to crack shape changes. By comparing energy contributions at an initial load level and after an applied load increment, Eq. 1.16 can be rearranged to directly obtain Δa_j, the point-by-point crack front extensions. Note that the critical energy release rate used for material toughness can be substituted with a mixed-mode fracture criterion or effective critical value and is not limited to a single toughness parameter.

Two major issues were encountered when attempting to apply the formulation for planar cracks described in [10] to non-planar growth situations. First, numerical sensitivities associated with the VCE calculations and the complicated front geometries were observed. These nominally insignificant undulations in energy release rate distributions along the front transpire through the growth formulation to create inconsistencies in the calculated crack front extension. These inconsistencies can accumulate and render the crack growth predictions nonsensical. Another concern is the accuracy of the VCE rate of energy release rate calculation. The suspect term within Eq. 1.5 is the variation of nodal displacements, $\frac{\delta u}{\delta a_j}$. The term, essentially, is obtained by applying a local virtual point perturbation at each position along the crack front and then obtaining a finite element solution. Similar to applying a nodal force in a standard finite element model, the local virtual point perturbation creates a region of high distortion near the perturbation.

To assuage both sources of error a new approach is applied to the VCE method. Rather than using local, point-by-point virtual extensions, δa_j, to calculate the rate of energy release rate, a basis-function approach is used. A set of linearly independent functions distributed along the crack front, δb_j, is used as virtual extensions. The expression for the rate of energy release rate now becomes:

$$\frac{\delta G_i}{\delta b_j} = -\frac{1}{\ell_i} \left(u^T \frac{\delta K}{\delta a_i} \frac{\delta u}{\delta b_j} + \frac{1}{2} u^T \frac{\delta^2 K}{\delta a_i \delta b_j} u \right). \tag{1.17}$$

The necessary calculations for each term are executed in a similar fashion to the standard local VCE approach. However, the second order virtual extensions are now globally applied across the crack front. Figure 1.5 shows a schematic demonstrating the difference between the local, point-by-point approach, and an example global, basis-function approach comprised of uniform, linear, and quadratic functions.

The augmented rate of energy release rate expression alters Eq. 1.16 so that the formulation calculates the coefficients of the basis functions that, when combined, represent a function for the predicted extensions along the crack front. The predicted extensions are then applied at the determined angle in the same manner described in the planar crack growth scheme.

The basis-function technique provides insulation against numerical noise by restricting the extension along the front to be smooth and continuous. The function characterizing the predicted growth mitigates the influence of the minor fluctuations in the energy release rate distributions on the individual front extensions. Additionally, by distributing the virtual extensions along the entire front, the point perturbation issue in the variation of nodal displacements is alleviated. This is analogous to applying a distributed force, i.e. a pressure, instead of nodal forces to avoid distortion in finite element results.

At this point no non-planar crack front evolution has been predicted using the basis-function approach. However, preliminary simulations have used the basis-function methodology to predict planar crack growth in a double cantilever beam specimen with applied displacement increments. The simulated uniform growth of the straight crack front compares well with analytical calculations and the local approach results from [10]. The predicted crack lengths have a relative difference of less than 1 %.

1.4 Conclusions

The presented work develops the toolset required for a new simulation technique to predict arbitrary mixed-mode crack growth. The technique relies on an explicit geometric representation of the crack through the meshing tools of FRANC3D. Fracture mechanics parameters of interest are calculated by a new 3-D mixed-mode VCE method. Finally, the energy-based crack growth formulation of [10] is modified through a novel basis-function approach to determine non-planar crack front extensions.

The development and implementation of the toolset is ongoing. Preliminary results show promise for mixed-mode and non-planar growth simulations. The VCE implementation is being extended to calculate energy release rates for anisotropic material systems, such as delaminations in composite laminates. The basis-function approach continues to be tested, and is being integrated within an incremental iterative crack growth simulation scheme for non-planar growth simulations.

Acknowledgements This work was funded by the NASA University Institutes Project under Grant NCC3-989, and the Cornell University Ross-Tetelman Fellowship in Civil and Environmental Engineering.

References

1. Areias PMA, Belytschko T (2005) Analysis of three-dimensional crack initiation and propagation using the extended finite element method. Int J Numer Methods Eng 63:760–788
2. Huang R, Sukumar N, Prévost J-H (2003) Modeling quasi-static crack growth with the extended finite element method. Part II: Numerical applications. Int J Solids Struct 40:7539–7552
3. Sukumar N, Chopp DL (2008) Three-dimensional non-planar crack growth by a coupled extended finite element and fast marching method. Int J Numer Methods Eng 76:727–748
4. Roy YA, Dodds RH (2001) Simulation of ductile crack growth in thin aluminum panels using 3-D surface cohesive elements. Int J Fract 110:21–45
5. Khoei AR, Moslemi H, Sharifi M (2012) Three-dimensional cohesive fracture modeling of non-planar crack growth using adaptive FE technique. Int J Solids Struct 49:2334–2348
6. Carter BJ, Wawrzynek PA, Ingraffea AR (2000) Automated 3-D crack growth simulation. Int J Numer Methods Eng 47:229–253
7. Moslemi H, Khoei AR (2009) 3D adaptive finite element modeling of non-planar curved crack growth using the weighted superconvergent patch recovery method. Eng Fract Mech 76:1703–1728
8. Gürses E, Miehe C (2009) A computational framework of three-dimensional configurational-force-driven brittle crack propagation. Comput Methods Appl Mech Eng 198:1413–1428
9. Maligno AR, Rajaratnam S, Leen SB, Williams EJ (2010) A three-dimensional (3D) numerical study of fatigue crack growth using remeshing techniques. Eng Fract Mech 77:94–111
10. Davis BR, Wawrzynek PA, Ingraffea AR (2014) 3-D simulation of arbitrary crack growth using an energy-based formulation—Part I: Planar growth. Eng Fract Mech 115:204–220
11. FRANC3D 6.0.5. Fracture Analysis Consultants, Inc., Ithaca, NY, USA (2013) www.francanalysis.com
12. Dixon J, Pook L (1969) Stress intensity factors calculated generally by the finite element technique. Nature 224:166–167
13. Watwood VB Jr (1969) The finite element method for prediction of crack behavior. Nucl Eng Des 11:323–332
14. Hellen TK (1975) On the method of virtual crack extensions. Int J Numer Methods Eng 9:187–207
15. Parks DM (1974) A stiffness derivative finite element technique for determination of crack tip stress intensity factors. Int J Fract 10:487–502
16. Haber RB, Koh HM (1985) Explicit expressions for energy release rates using virtual crack extensions. Int J Numer Methods Eng 21:301–315
17. Lin SC, Abel JF (1988) Variational approach for a new direct-integration form of the virtual crack extension method. Int J Fract 38:217–235
18. Hwang CG, Wawrzynek PA, Ingraffea AR (2001) On the virtual crack extension method for calculating the derivatives of energy release rates for a 3D planar crack of arbitrary shape under mode-I loading. Eng Fract Mech 68:925–947

19. Ishikawa H (1980) A finite element analysis of stress intensity factors for combined tensile and shear loading by only a virtual crack extension. Int J Fract 16:243–246
20. Nikishkov GP, Atluri SN (1987) Calculation of fracture mechanics parameters for an arbitrary three-dimensional crack, by the "equivalent domain integral" method. Int J Numer Methods Eng 24:1801–1821
21. Shivakumar KN, Raju IS (1992) An equivalent domain integral method for three-dimensional mixed-mode fracture problems. Engineering 42:935–959
22. Huber O, Nickel J, Kuhn G (1993) On the decomposition of the J-integral for 3D crack problems. Int J Fract 64:339–348
23. Kassir MK, Sih GC (1974) Three-dimensional crack problems, Mech. Fract. II. Noordhoff International Publishing, Leyden
24. Levan A, Royer J (1993) Part-circular surface cracks in round bars under tension, bending and twisting. Int J Fract 61:71–99
25. Ismail AE, Ariffin AK, Abdullah S, Ghazali MJ (2012) Stress intensity factors under combined tension and torsion loadings. Indian J Eng Mater Sci 19:5–16
26. Hussain MA, Pu SL, Underwood J (1974) Strain energy release rate for a crack under combined mode I and mode II. In: Fracture analysis. American Society for Testing and Materials, ASTM STP 560. pp 2–28

Chapter 2
Experimental and Predicted Crack Paths for Al-2024-T351 Under Mixed-Mode I/II Fatigue

E.E. Miller, M.A. Sutton, X. Deng, H. Watts, A.P. Reynolds, X. Ke, and H.W. Schreier

Abstract The aerospace industry has experience with a range of structural failures, oftentimes due to fatigue cracks in aircraft fuselage components that are exposed to relatively high stress levels during cyclic loading effects that lead to fatigue crack initiation at material defects and near stress concentrations. These aircraft components are under complex stress states. In this study, mixed mode I/II fatigue experiments and simulations are performed for an Arcan fixture and a 6.35 mm thick Al-2024-T351 specimen, a popular aerospace alloy. Experiments were performed for Arcan loading angles that gave rise to a range of Mode I/II crack tip conditions from $0 \leq \Delta KII/\Delta KI \leq \infty$. Measurements include the crack paths, loading cycles, and maximum and minimum loads for each loading angle. Simulations were performed using three-dimensional finite element analysis (3D-FEA) with 10-noded tetrahedral elements via the custom in-house FEA code, CRACK3D. While modeling the entire fixture-specimen geometry, a modified version of the virtual crack closure technique (VCCT) with automatic crack tip re-meshing and a maximum circumferential stress criterion was used to predict the direction of crack growth. Results indicate excellent agreement between experiments and simulations for the measured crack paths during the first several millimeters of crack extension.

Keywords Mixed mode • Fatigue • Arcan • Crack path • Modeling

2.1 Introduction

The aerospace industry has experience with a range of structural failures, oftentimes due to fatigue cracks in aircraft fuselage components that are exposed to relatively high stress levels during cyclic loading effects incurred during repeated take-off and landing events that lead to fatigue crack initiation at material defects and near stress concentrations. Numerous event over the last 30 years have been recorded where fatigue cracks in the fuselage have propagated to critical areas resulting the cabin opening up mid-flight and causing cabin depressurization along with numerous injuries and, in one case, death [1–3].

In fact, fatigue cracks are expected to form in the fuselage of modern airplanes due to repeated (a) pressurization and decompression of the cabin during every flight and (b) loading effects during take-off and landing. Thus, the propagation of cracks into critical joints continues to be an area of concern, especially since such propagation under complex stress states is not completely understood. Although procedures are currently in place to inspect and repair fatigue cracks, the ability to better predict how far a crack will propagate and in which direction it would grow when subjected to various loading conditions could save millions of dollars in premature inspection and repair, while also identifying the severity of an existing flaw in an aero-structure.

E.E. Miller (✉) • M.A. Sutton • X. Deng • H. Watts • A.P. Reynolds
Department of Mechanical Engineering, University of South Carolina, 300 Main St., Columbia, SC 29208, USA
e-mail: eileen.e.miller@boeing.com

X. Ke • H.W. Schreier
Correlated Solutions, Inc., 121 Dutchman Blvd, Columbia, SC 29063, USA

J. Carroll and S. Daly (eds.), *Fracture, Fatigue, Failure, and Damage Evolution, Volume 5: Proceedings of the 2014 Annual Conference on Experimental and Applied Mechanics*, Conference Proceedings of the Society for Experimental Mechanics Series,
DOI 10.1007/978-3-319-06977-7_2,

Crack propagation under Mode I loading is reasonably well understood [4]. Using a maximum circumferential stress (MCS) criterion, the predicted and actual crack trajectories during fatigue loading are perpendicular to the local $\sigma_{\theta\theta\ max}$ direction where $\sigma_{\theta\theta\ max}$ is the maximum circumferential stress ahead of the crack tip [5]. This direction nominally coincides with the loading direction when local conditions are not influenced by stress concentrations, material defections/inclusions, or other factors.

Now consider the case where a crack is under mixed-mode loading, that is, under any combination of two or more loading types. For the combination of Mode I and Mode II loading conditions, methods for obtaining a mixed-mode I/II stress state experimentally when applying uniaxial tensile loading include (a) use of kinked cracks, (b) use of cracks propagating away from a hole, and (c) use of an Arcan fixture [6–15]. Independent mixed mode loading studies by both Zhang et al. [21] and Lopez-Crespo et al. [22] have used an Arcan fixture to statically load an existing crack for conditions in which an empirical solution for the stress intensity factor (SIF) exits [23]. While their experimental results were consistent with the empirical solution, the empirical solution has limitations, mainly being that the model can only be used for determining the kinking angle for the initial crack propagation event.

Gaylon et al. [6] performed fatigue tests using the Arcan fixture. In this study, the authors determined the crack growth trajectory for various degrees of mixed-mode I/II loading. The measured crack trajectories suggest that for all combinations of Mode I/II loading, the fatigue cracks propagate in a manner that was locally dominated by K_I, while no crack propagation occurred for the pure Mode II loading case. However, there was such large scatter in the experimental data that it is difficult to definitively identify the trends. One cause of the inconsistency in the results was determined to be the three pin loading configuration used by the authors. It was suggested that future studies use only one pin for fixing the Arcan fixture to the test stand [7]; the use of a single pin is consistent with the work of Amstutz, Boone and others at the University of South Carolina [8, 9, 10].

Chao et al. [8] used the Arcan fixture with the one-pin configuration to study fatigue crack propagation under various mixed-mode loading conditions. Crack trajectories were compared to stable tearing results obtained under mixed-mode monotonic loading conditions. It was observed that cracks under fatigue loading propagate in a local Mode I direction for all loading cases including pure Mode II, unlike Gaylon's results. In Chao's studies, the amount of crack growth in fatigue for $\Phi = 75°$ and 90° was quite small, indicating that the crack surfaces interfered after a small amount of crack extension and impeded further crack growth. For stable tearing, after Mode II loading becomes dominant, cracks in aluminum alloys tended to propagate in the local shear direction; that is, approximately parallel to the direction of the pre-crack. This transition from Mode I dominated crack growth to Mode II dominated crack growth under stable tearing conditions is consistent with results obtained by Amstutz et al. [9, 10]. In Amstutz's work, the authors used the Arcan fixture to study mixed Mode I/II stable tearing crack growth. The results show that for most loading cases, where $K_{II}/K_{I,} < 1$, the crack propagates under local Mode I conditions. However, as K_I approaches zero and K_{II}/K_I reaches a critical value ($\Phi = 75°$ and 90° for Al 2024-T351), the crack begins to grow in Mode II. While this study included crack propagation, stable tearing occurs outside of the linear elastic range, and results suggest that the Mode II component has different effects in the linear elastic range than it does under elastic-plastic conditions.

Boljanovic [11] performed finite element analysis to model the results of Gaylon et al. The crack trajectories were simulated using MSC [12] a step-by-step method while applying the maximum circumferential stress (MCS) criterion to predict crack trajectory. Results of Boljanovic's work agree with Gaylon's experimental crack paths. However, the SIFs were not obtained at each step using the local crack tip field data, but were determined analytically after the simulation was performed since the step-by-step method of crack path prediction is quite time consuming. It is unclear if the analytical solution for the SIFs accounted for curvilinear crack paths.

The objective of the current study is to (a) perform experiments and measure the crack path and (b) perform simulations and predict the fatigue crack path in an aerospace aluminum alloy undergoing applied, far-field mixed-mode I/II conditions. The Arcan fixture will be utilized to achieve far-field mixed-mode I/II conditions in 6.35 mm thick Al-2024-T351 specimens. Crack paths, cycle count, and maximum and minimum loads will be measured during experiments, with loading ranging from $0 \leq K_{II}/K_I \leq \infty$. Simulations will then be performed using 3D-FEA. Crack trajectories will be predicted using virtual crack closure techniques (VCCT) and a MCS criterion. Local re-meshing will be used to extend the crack. The whole fixture and specimen will be modeled using 10-noded tetrahedral elements. Predicted crack paths will be compared to the results obtained experimentally, and the results will be discussed.

2.2 Experimental Work

2.2.1 Fixture and Specimen

The Arcan was used to achieve mixed-mode I/II loading for discrete values of K_{II}/K_I in the range $0 \leq K_{II}/K_I \leq \infty$. With loading angle Φ defined as shown in Fig. 2.1, the $\Phi = 0°$ pin holes correspond to nominally Mode I crack conditions and the $\Phi = 90°$ pin holes represent nominally Mode II crack loading conditions. As shown in Fig. 2.1, each butterfly-shaped specimen is 224.28 mm tall, 275.30 mm wide at the top and bottom of the specimen and 6.35 mm thick. Each specimen is manufactured from Al-2024-T351 to form an LT orientation crack configuration (crack is along the transverse direction (T) and perpendicular to the rolling direction (L) in the aluminum specimen) [13] with Young's modulus $= 7.11 \times 10^{10}$ Pa and Poisson's ratio $= 0.33$. A jeweler's saw blade, size 0/6, was used to create an initial through-thickness edge notch 6.35 mm long in the width direction on the left side of the specimen in the vertical center. The front and back surfaces of the specimens were sanded with 600 grit sand paper before final sanding with 800 grit sandpaper to remove small surface defects. Metal polish was used to create a mirror finish on the surfaces for visually tracking crack tip progression during the experiment.

2.2.2 Set Up

A 50 kip (227 kN) servo-hydraulic Material Test System (MTS) controlled by TestStar II software was used to apply tensile loads to the Arcan fixture and specimen. Figure 2.2 shows the set up without the microscope objectives. The backing plate (not visible in Fig. 2.2) is attached to the top and bottom pieces of the Arcan fixture and is oriented at 45°.

During testing, the crack tip was tracked using the microscope objective and the slide apparatus. The objective is attached to the dual slide apparatus shown in Fig. 2.3. The apparatus consists of (a) a single, horizontally mounted manual screw driven slide manufactured by Velmex with a digital caliper to provide a metric positional measurement, (b) a second vertically-oriented Velmex slide with digital caliper that was mounted to the horizontal slide. The microscope objective was then connected to the vertical slide. Both vertical and horizontal slides operate independently, allowing for horizontal and vertical measurements of the crack tip position during the fatigue process.

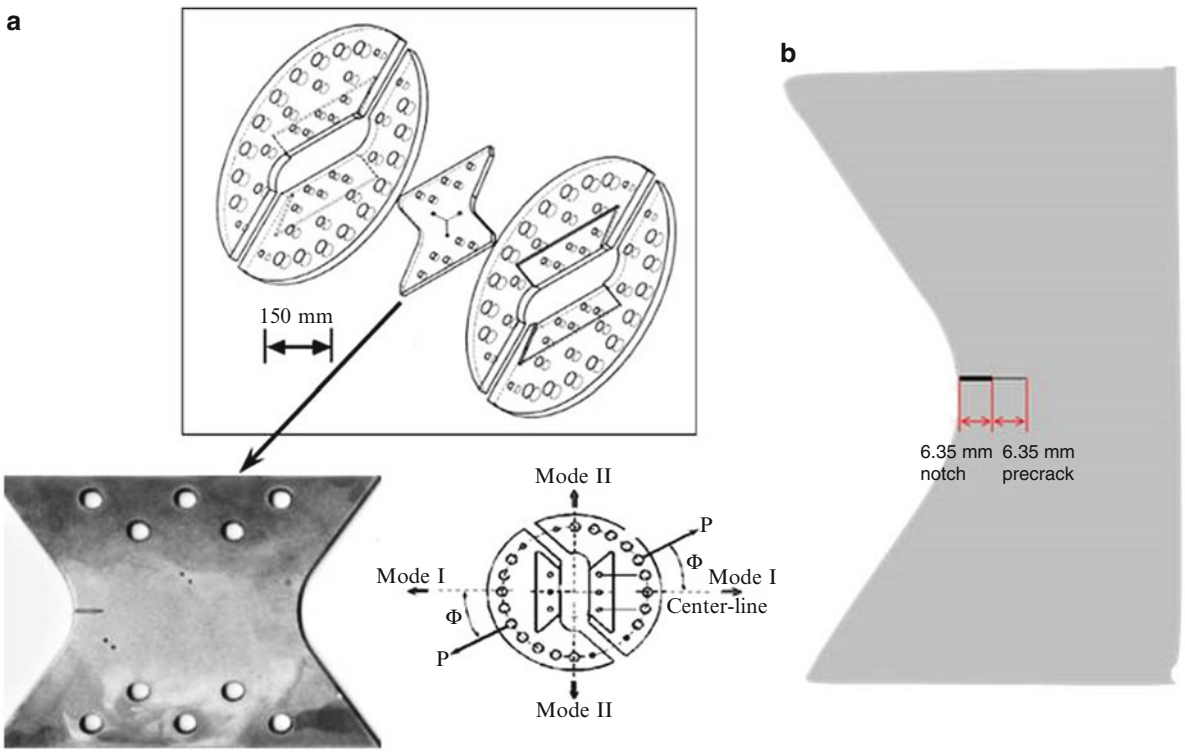

Fig. 2.1 (**a**) Mixed mode I/II Arcan test fixture and butterfly shaped test specimen. Angle $\Phi = 0°$ corresponds to far-field tension and $\Phi = 90°$ is far-field shear (**b**) diagram of notch and pre-crack

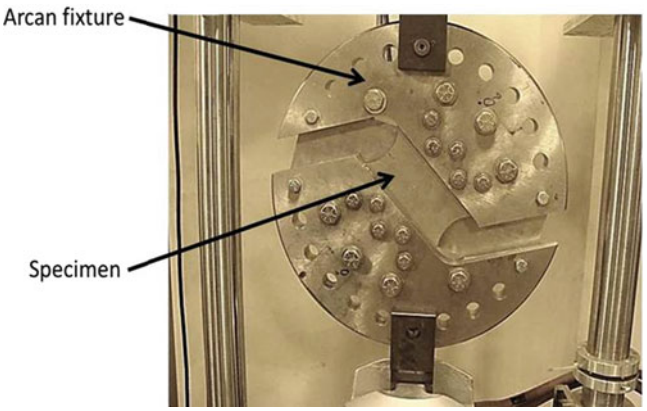

Fig. 2.2 Image of experimental set up

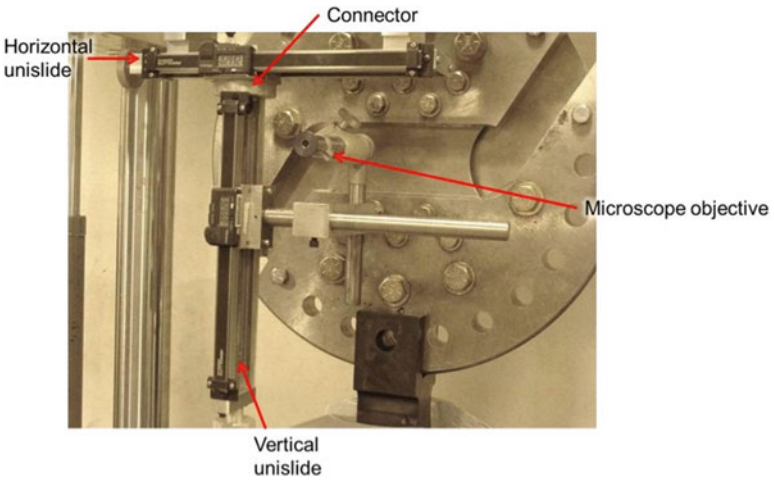

Fig. 2.3 Two degree-of-freedom slide apparatus

2.2.3 Load Prediction

Load shedding was performed to avoid the risk of initiating stable tearing or formation of a large plastic zone at the crack tip. Given that the empirical solution for the stress intensity factor was only valid for static loading and the traditional method of load prediction was going to be quite crude, a modified approach was taken. The goal of the modified approach was to keep ΔK constant in order to avoid excessive plasticity in the crack tip region, crack slanting, or crack tearing. Since the method for estimating the SIF was quite crude, and did not account for the various loading angles and resulting K_I and K_{II} values, it was determined that following Paris' Law for the material was a more accurate method of crack growth control for ΔK_{eq} which is defined as follows [14];

$$\Delta K_{eq} = \gamma \Delta K_I + (1-\gamma)\sqrt{(\Delta K_I)^2 + \gamma_1(\Delta K_{II})^2 + \gamma_2(\Delta K_{III})^2} \tag{2.1}$$

where γ, γ_1, and γ_2 are parameters to be defined. Using ΔK_{eq} and assuming that there is no crack closure effect, the crack growth rate can be determined using Paris' Law. That is, the authors opted to maintain the same crack growth rate throughout the experiment.

From the previous test data, it was determined that a crack growth rate of $\approx 6 \times 10^{-5}$ mm/cycle was a safe rate to run the experiments and maintain nominally linear elastic conditions. A loading ratio R = 0.4 was chosen for the experiment. This crack growth rate was maintained by allowing the crack to grow until the rate increased to $\approx 8 \times 10^{-5}$ mm/cycle. The load was then dropped by approximately 5 %, resulting in a crack growth rate of $\approx 4 \times 10^{-5}$ mm/cycle. This process was repeated to maintain an average crack growth rate of $\approx 6 \times 10^{-5}$ mm/cycle and therefore maintain a constant average ΔK_{eq} during the experiment.

2.2.4 Procedure

Initially, the specimen is oriented to be in the Mode I configuration. The specimens were fatigue pre-cracked an additional 6.35 mm for a total crack length of 12.7 mm. Fatigue loading was applied in force control at 10 Hz. Then the fixture was rotated in the test stand to the appropriate loading angle. A total of six experiments were performed at loading angles $\Phi = 15°$, 30°, 45°, 60°, 75°, and 90°, with $\Phi = 90°$ degrees being nominally Mode II crack loading. For the loading cases $\Phi = 15°$, 30°, and 45°, the one degree of freedom slide apparatus was used for tracking the crack tip. The two degree of freedom slide apparatus was built and used to track the crack tip for $\Phi = 60°$, 75°, and 90°. Again, fatigue loading at 10 Hz was applied in force control. The crack tip position was measured approximately every 5,000–20,000 cycles.

2.3 Theoretical Work

2.3.1 Approach

CRACK3D is a three-dimensional finite element code first developed by the University of South Carolina and later jointly by the University of South Carolina and Correlated Solutions, Inc. It is capable of simulating elastic-plastic stable tearing crack extension and linear-elastic fatigue crack propagation, both with curved crack fronts and curvilinear crack paths for mixed-mode conditions. Two methods of crack growth simulations are available: nodal release and local re-meshing. In the case that the crack path is to be predicted, local re-meshing is used to extend the crack [15, 19, 20]. For the case of fatigue crack propagation, there are three steps to crack growth predictions: (1) will the crack grow? (2) in what direction will it grow? (3) how far will it extend for a certain number of loading cycles or how many loading cycles will be required to extend the crack by a certain amount?

For determining if the crack will propagate, $\Delta K > \Delta K_{TH}$ must be true. CRACK3D can be used to evaluate ΔK, which can be used to check if $\Delta K > \Delta K_{TH}$ is satisfied. Once this crack growth criterion is met, CRACK3D can be used to simulate the crack growth process and predict (a) the direction of crack growth and (b) the variations of stress intensity factors with the amount of crack growth, which can be used to predict the number of loading cycles as a function of the amount of crack growth. In CRACK3D the determination of stress intensity factors is done using the method of three-dimensional virtual crack closure technique (3D-VCCT) [5, 15, 16, 19, 20], which is based on the approach of the strain energy release rate [17]. Once the SIFs for the maximum applied load are predicted using the VCCT, the direction in which the crack will propagate is predicted using Maximum Circumferential Stress Criterion [5]. A fatigue crack growth rate model, such as the Paris' Law, is used to determine how many cycles it will take for the crack to grow the amount of crack extension chosen by the user [18].

To apply the VCCT in crack growth simulations using the local re-meshing option (instead of the nodal release option), the local mesh immediately ahead and behind the crack front must be properly structured, so that the local mesh immediately behind the crack front can be viewed as being shifted by one element size from the local mesh immediately ahead of the crack front. Therefore, once crack growth is determined to occur along a certain direction with a certain increment, the new mesh around the new crack front is generated such that there is a structured mesh (within a local re-meshing zone around the new crack front) with equal number of elements behind the crack front and ahead of the crack front [15, 19, 20].

2.3.2 Geometry, Mesh Generation and Boundary Conditions

The Arcan fixture and specimen were modeled as shown in Fig. 2.4. For simplicity, this fixture-specimen connection is approximated by a continuous bond at the fixture-specimen boundary. To this end, the bolts are not modeled and the fixture and specimen are treated as three solid regions with different thicknesses. An idealized through-thickness edge notch and pre-crack exactly 12.7 mm long was modeled as the initial crack in the exact geometric vertical center of the specimen and is perfectly horizontal into the width of the specimen. The volumes were then meshed with 10 noded tetrahedral elements.

For each loading angle, Φ, a set of lines (one on the top fixture and the other on the bottom fixture) corresponding to the center of the pins were created on the surface of the fixture model in the through-thickness direction. The boundary conditions were such that the displacement of the bottom line was set to zero in the x and y directions (u_x, and $u_y = 0$) and only the z displacement specified was of the center point on the bottom line ($u_z = 0$). The displacement of the corresponding

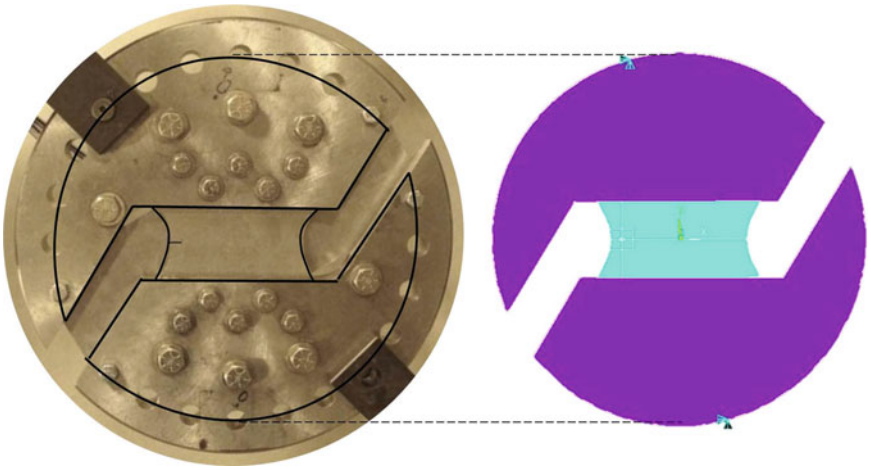

Fig. 2.4 Diagram of a picture of actual Arcan fixture and specimen (*left*) and image of finite element model geometry (*right*)

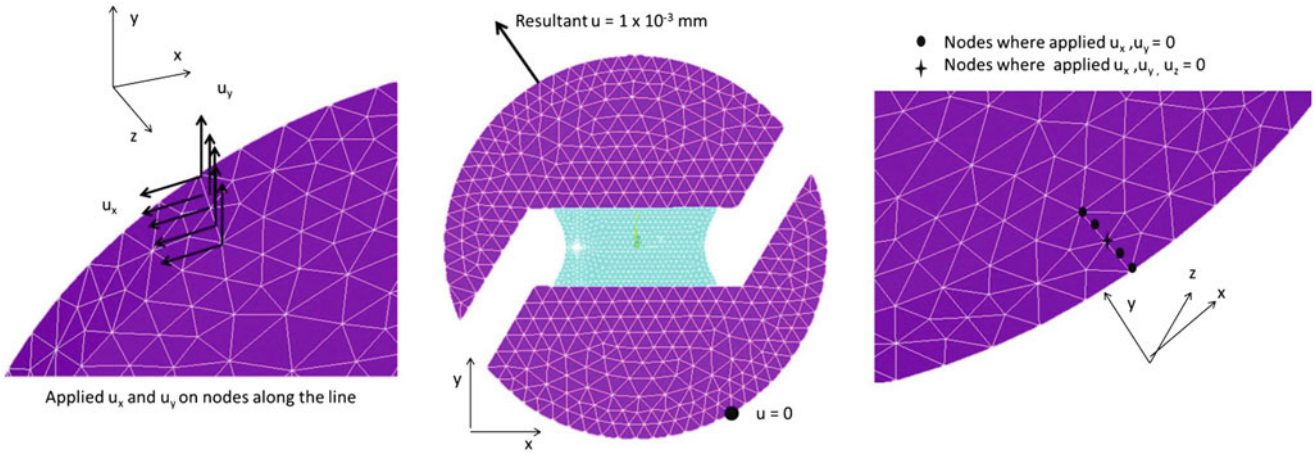

Fig. 2.5 Boundary conditions at $\Phi = 30°$

top line had a magnitude of 1×10^{-3} mm along the direction of loading, Φ, as shown in Fig. 3.7, which was decomposed into x and y components (Fig. 2.5).

2.4 Results

For loading cases 15°, 30°, 45°, and 60°, fatigue crack propagation occurred, and for loading cases 75° and 90°, no crack propagation occurred. The experimental and predicted crack paths are plotted in Fig. 2.6.

The ΔK_I and ΔK_{II} for each loading cases $\Phi = 15°, 30°, 45°$, and 60° are plotted along the crack length a in Figs. 2.7–2.10 respectively.

2.5 Discussion

Prior to discussing the results for the Arcan fatigue studies, it is important to note that benchmark studies have been performed, and it has been verified that CRACK3D is able to accurately predict the crack path for elastic plastic stable tearing using the Arcan fixture to achieve mixed-mode loading conditions using local re-meshing [9, 10, 15, 19, 20]. The direction of crack extension for stable tearing is predicted with a different criteria, crack opening displacement [9, 10, 15, 19, 20], while as discussed here, VCCT and MCS criterion are used in predicting the direction of fatigue crack propagation.

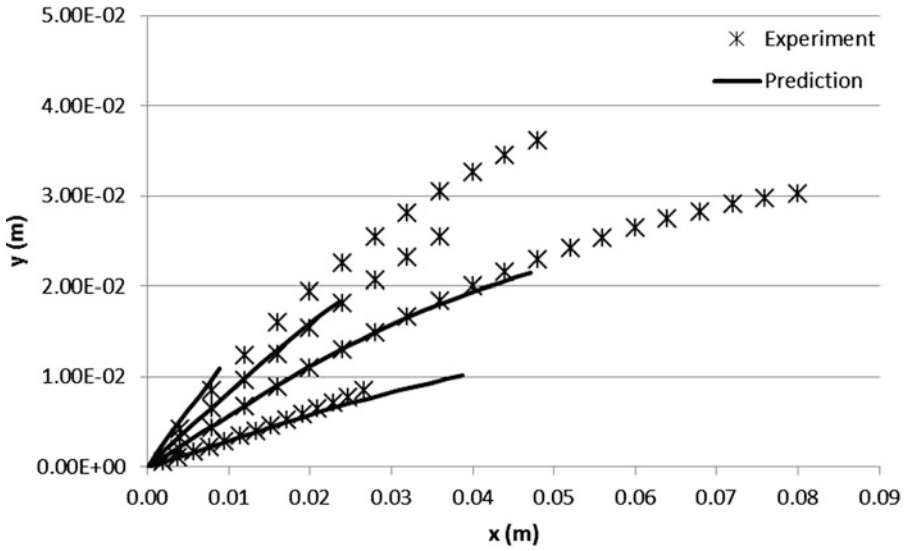

Fig. 2.6 Experimental and predicted crack paths

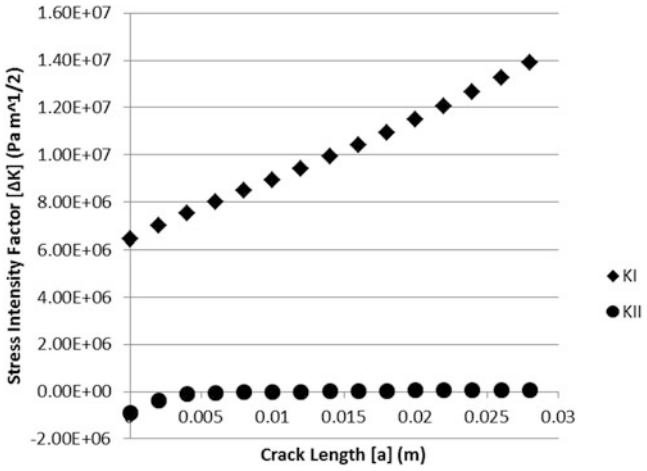

Fig. 2.7 Plot of ΔKI and ΔKII along the crack path for the 15°

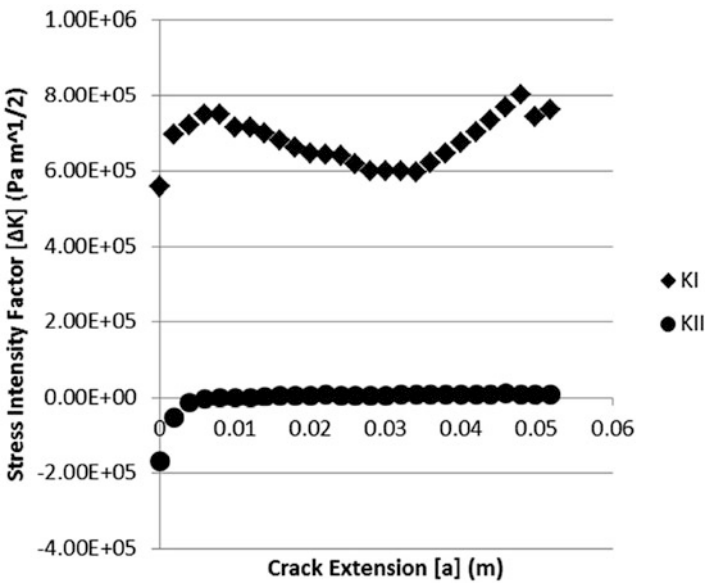

Fig. 2.8 Plot of ΔKI and ΔKII along the crack path for the 30°

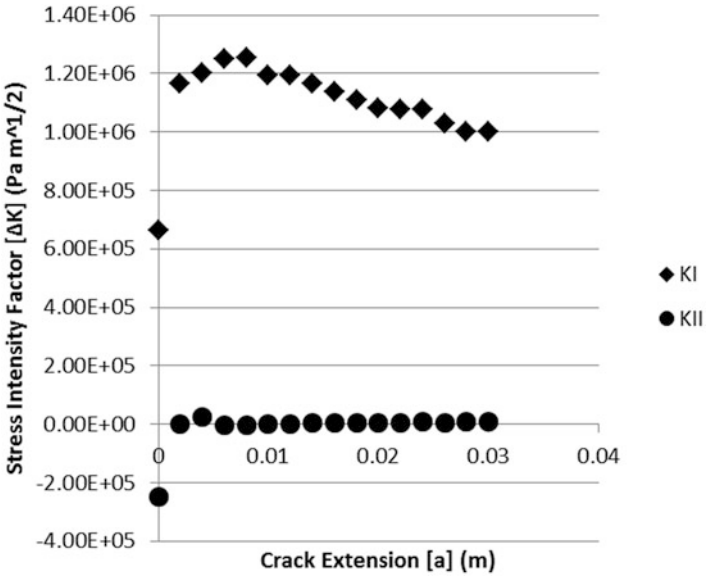

Fig. 2.9 Plot of ΔKI and ΔKII along the crack path for the 45°

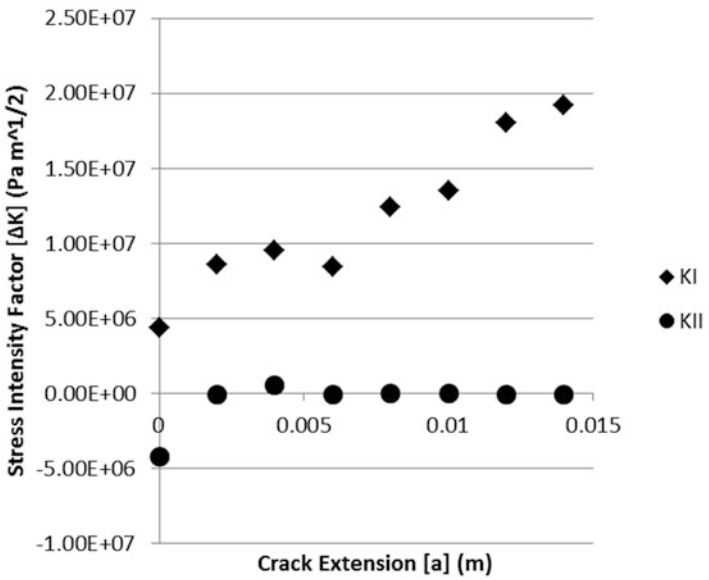

Fig. 2.10 Plot of ΔKI and ΔKII along the crack path for the 60°

First, as shown in Fig. 2.6, there is excellent agreement between the measured and predicted crack growth paths. It is worth noting that, for each simulation, at a certain point CRACK3D was unable to re-mesh the volume according to the re-meshing criteria provided in the code. Thus, the program was terminated at this point. Though the precise reason for the inability to continue propagating the fatigue crack is not fully understood, it must be stated that there is no theoretical reason why there should be an issue in the ability to predict the direction of crack propagation for longer amounts of crack extension using MCS criterion. Since other fatigue studies were performed with CRACK3D where the crack grew all the way across a different specimen geometry, the most likely reason for the limited amount of crack extension is that CRACK3D could not arrange elements in an acceptable manner inside the size of the re-meshing region for this specimen geometry to "match" the surrounding, un-meshed region.

Secondly, as shown in Figs. 2.7–2.10, the simulation data shows that the crack growth process is occurring under nominally Mode I conditions, with $\Delta K_{II} = 0$, confirming that the fatigue crack tended to propagate under locally tensile conditions. For small loading angles, the crack growth direction is approximately perpendicular to the loading direction. However, as loading angle increases, the crack deviates from the perpendicular direction, implying that the local Mode I direction is no longer perpendicular to the loading angle. In fact, the curvilinear trend of the crack path which begins around x = 0.03 m is the result of the influence of the loading process via the Arcan fixture on the stress field in the specimen.

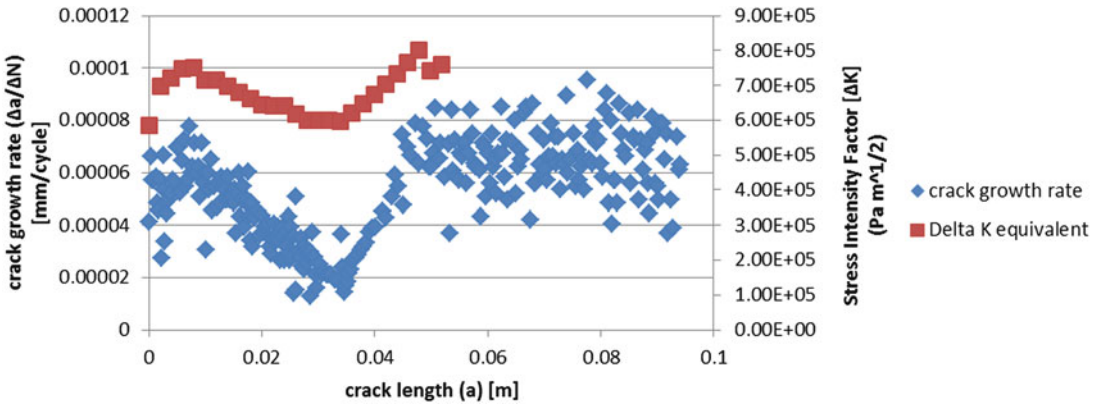

Fig. 2.11 Plot of ΔKeq and da/dN along crack length for 30° loading case

Thirdly, we were unable to observe crack growth for $\Phi = 75°$ and $\Phi = 90°$. There are two plausible reasons why the crack did not grow in these cases. Firstly, other studies have shown that the stress distribution for the Arcan fixture is not uniform, with the largest gradients occurring in the 75° orientation [6]. The relatively short initial notch and initial pre-crack used in the experiment may have positioned the crack tip in an area of negative or low stress. This may have put the crack into compression or kept ΔK_{eq} below ΔK_{TH}, the threshold value required to initiate crack growth in the material. Preliminary FEA by the author was consistent with this observation. Another possibility for both $\Phi = 75°$ and 90° is that the Mode II component of the far field loading is larger than the Mode I component. In such cases, there may not be sufficient Mode I loading to open the crack tip and overcome friction and local plastic deformation along the contacting crack surfaces to allow the fatigue crack to propagate.

Fourthly, in regards to the efficiency and effectiveness of this modified method for controlling the change in SIF during the experiment, this modified method is based on the premise that, according to Paris' Law, da/dN and ΔK_{eq} are proportional. Thus, trends in the measured crack growth rate and the computed ΔK_{eq} at the crack tip should be consistent throughout the crack growth process. Figure 2.11 shows a direct comparison of the scaled ΔK_{eq} and the discrete crack growth rate recorded during the experiment, $\Delta a/\Delta N$, as a function of crack length, a.

2.6 Conclusions

Fatigue crack growth experiments have been performed successfully on an edge-cracked Arcan specimen manufactured from 2024-T351 aluminum and subjected to far-field mixed mode I/II loading with loading angles $\Phi = 15°$, 30°, 45°, and 60°. Results show that (a) crack extension occurs along different curvilinear paths for each loading angle, extending from the original crack tip towards the upper Arcan grip, (b) initial kinking angle of the fatigue crack indicates that the local Mode I direction deviates the direction perpendicular to the loading angle as the Mode II component of loading increases, (d) the load shedding process used to maintain crack growth rates in a specific range that was used for $\Phi = 30°$, 45°, and 60° is consistent with controlling ΔK_{eq}, as shown through direct comparison of experimental crack growth rates and predicted ΔK_{eq} values at points along the measured crack paths, and (d) further study is required for loading angles $\Phi = 75°$ and 90° where fatigue crack growth was not observed experimentally.

Simulations of the fatigue crack growth process for the Arcan fixture-specimen combination have been performed using a custom-finite element code for fracture analysis, CRACK3D. In this code, VCCT is used to quantify the local stress intensity factors and the MCSC is used to determine the direction of current crack extension. Results from the simulations show that (a) CRACK3D is an effective simulation platform for fatigue crack growth in many cases, (b) the re-meshing algorithms in CRACK3D are not readily adaptable for crack growth near material junctures where there are significant differences in element size; the ability to handle such cases is currently being developed, but not yet available, (c) direct comparison of the experimental results and predictions indicate that the measured and CRACK3D predicted crack paths using local re-meshing to maintain accuracy in the local fields are in excellent agreement over the range of crack growth where the simulations were convergent, (d) predictions using an idealized notch and pre-crack yield little error between the predicted and experimental crack paths, and (e) indicate that the direction of crack propagation corresponds to the direction which maximizes Mode I and minimized Mode II, which is consistent with results from previous studies [6, 8].

References

1. National Transportation Safety Board (1988) Aloha Airlines, Flight 243, Boeing 737-200, N73711
2. Southwest Checks Fleet after Hole forces Landing: Hole in fuselage causes pressure-loss scare on Boeing 737, Associated Press, 14 July 2009. [online] Available: http://www.nbcnews.com/id/31902513/ns/travel-news/t/southwest-checks-fleet-after-hole-forces-landing/#.U5HoABDm-QA [Accessed June 2013].
3. L. Stark, M. Hosford and M. S. James, Southwest Air Emergency: Inspection Program Missed Crack in Plane, 3 April 2011. [Online]. Available: http://abcnews.go.com/US/southwest-air-emergency-inspection-program-missedcracks- plane/story?id=13286094#.UbtcfpXD_IU. [Accessed June 2013].
4. Ewalds HL, Wanhill RJ (1984) Fracture mechanics. Edward Arnold Ltd, London
5. Erdogan F, Sih GC (1963) On the crack extension in plates under plane loading and transverse shear. J Basic Eng 85(4):519–527
6. Fawaz SA (2009) Personal Conversation
7. Greer JM, Galyon Dorman SE, Hammond MJ (2011) Some comments on the Arcan mixed-mode (I/II) test specimen. Eng Fract Mech 78: 2088–2094
8. Liu S, Chao YJ, Gaddam RR (2004) Fracture type transition under mixed mode I/II quasi-static and fatigue loading conditions. In Society for Experimental Mechanics
9. Amstutz BE, Sutton MA, Dawicke DS (1995) Experimental study of mixed mode I/II stable crack growth in thin 2024-T3 aluminum. Fatigue and Fracture, ASTM STP 1256, vol. 26. pp 256–273
10. Amstutz BE, Sutton MA, Dawicke DS, Boone ML (1997) Effects of mixed mode I/II loading and grain orientation on crack initiation and stable tearing in 2024-T3 aluminum. ASTM STP 1296, vol. 27. pp 105–125
11. Boljanovic S, Maksimovic S (2011) Analysis of the crack growth propagation process under mixed-mode loading. Eng Fract Mech 78: 1565–1576
12. MSC Software [Online]. Available: www.mscsoftware.com/product/msc-nastran
13. ASTM International [Online]. Available: http://www.astm.org/Standards/E399.htm
14. Richard HA, Buchholz FG, Kullmer G, Schöllmann M (2003) 2D- and 3D-mixed mode fracture criteria. Key Eng Mater 251–252:251–260
15. Deng X, Ke X, Sutton MA, Miller EE, Schreier HW (2012) 3D VCCT with locally structured re-meshing for evaluation mixed-mode stress intensity factors in crack growth simulations along curved crack paths. In: Presentation at the Society of Engineering Science 49th annual technical meeting, Georgia Tech, GA, USA, 10–12 Oct 2012
16. Okada H, Kawai H, Araki K (2008) A virtual crack closure-integral method (VCCM) to compute the energy release rates and stress intensity factors based on quadratic tetrahedral finite elements. Eng Fract Mech 75:4466–4485
17. Ewalds HL, Wanhill RJ (1984) Fracture mechanics. Edward Arnold Ltd, London
18. Paris P, Erdogan F (1963) A critical analysis of crack propagation laws. J Basic Eng 85:528–534
19. Deng X, Ke X, Sutton MA, Miller EE, Schreier HW (2012) Locally structured re-meshing to enable accurate determination of stress intensity factors using 3D VCCT for crack growth simulations with curved crack paths. In: Presentation at the international symposium on solid mechanics in honor of Professor Xing Zhang, Beijing University of Aeronautics and Astronautics, China, 3 Nov 2012
20. Den X, Ke X, Sutton MA, Miller EE, Schreier HW (2013) FEM for 3D SIF determination for fatigue crack growth simulations with curved crack fronts and paths. In: To be presented at the ASME 2013 international mechanical engineering congress & exposition, San Diego, CA, USA, 15–21 Nov 2013
21. Zhang R, He L (2012) Measurement of mixed-mode stress intensity factors using digital image correlation. Opt Lasers Eng 50:1001–1007
22. Lopez-Crespo P, Sherenlikht A, Patterson EA, Yates JR, Withers PJ (2008) The stress intensity of mixed mode cracks determined by digital image correlation. J Strain Anal 43:769–780
23. Murakami Y (1987) Stress intensity factors handbook, vol 1. Pergamon Press, Oxford

Chapter 3
On Numerical Evaluation of Mixed Mode Crack Propagation Coupling Mechanical and Thermal Loads in Wood Material

Hassen Riahi, Rostand Moutou Pitti, Frédéric Dubois, and Eric Fournely

Abstract The mixed-mode crack growth coupling mechanical and thermal loads in wood material is investigated in this numerical work. The analytical formulation the crack driving force, namely the energy release rate, is introduced by T-integral that takes into account mixed mode fracture, thermal process in orthotropic material and pressure applied on the crack lips. This new formulation is based on Nother's theorem and the definition of the strain energy density according to Lagrangian's and Eulerian's configurations. Moreover, this analytical formulation is implemented in finite element software Cast3m. First of all, several numerical examples, dealing with isotropic material, are provided to illustrate the accuracy of the FEM model. Then, the crack resistance of a timber CTS (Compact Tension Specimen) is investigated to show the efficiency of the proposed approach in the case of orthotropic material.

Keywords Wood fracture • Mixed mode • Thermal fields • Path independent integral • Finite element method

3.1 Introduction

Due to the advantages provided by its mechanical behaviour particularly under extreme loading conditions such as fire and seismic events, in addition to its aesthetic and environmental effects, timber is commonly employed in building and civil engineering structures. Hence, the accurate knowledge of its mechanical properties seems to be essential. Although the considerable efforts devoted in this field of scientific research, the physics related to the real behaviour of timber material is still misunderstood. Timber is considered as orthotropic material having three planes of symmetry, which usually results in complex forms of the governing equation (e.g. stress-strain relationship). Moreover, due to its natural origin, timber contains an array of defects such as knots which locally modify its mechanical properties, and hence, timber is rather a heterogeneous material. As well known, timber elements exhibit micro-cracks which can propagate due to fatigue, overload or creep loading and cause failure of the structure. In addition, timber is a hygroscopic material whose mechanical behaviour is very sensitive to climatic changes such as temperature and moisture variations which contribute to a redistribution of stresses in the material that can be followed by degradation. For example, drying process accelerate the crack growth, while wetting process induce the delay of the crack propagation. To predict the crack growth process many numerical methods were developed to characterize the mechanical fields in the neighbourhood of the crack. Among them, the background of energy methods come from invariant integrals which enables to evaluate the crack driving forces such as the crack growth rate and the stress intensity factors. The most popular is the J-integral proposed by Rice [1] based on the assessment of the strain energy density and Noether's theorem [2]. This method is inefficient when dealing with mixed mode crack growth problems because it is necessary to separate the displacement field into a symmetric and antisymetric parts. To circumvent this difficulty, Chen and Shield [3] have developed the M-integral which enables us to get separated fracture modes based on a bilinear form of the strain energy density introducing virtual mechanical fields. Unfortunately, these tools are still

H. Riahi • R. Moutou Pitti (✉) • E. Fournely
Clermont Université, Université Blaise Pascal, Institut Pascal, BP 20206, F-63000 Clermont-Ferrand, France

CNRS, UMR 6602, Institut Pascal, F-63171 Aubiere, France
e-mail: hassen.riahi@etudiant.univ-bpclermont.fr; rostand.moutou_pitti@univ-bpclermont.fr

F. Dubois
Heterogeneous Material research Group, Université de Limoges, Egletons, France

J. Carroll and S. Daly (eds.), *Fracture, Fatigue, Failure, and Damage Evolution, Volume 5: Proceedings of the 2014 Annual Conference on Experimental and Applied Mechanics*, Conference Proceedings of the Society for Experimental Mechanics Series,
DOI 10.1007/978-3-319-06977-7_3,

mathematically limited to simple loading and boundaries conditions. In this work a new formulation of the A-integral is propose based on the analytical work developed by Moutou Pitti et al. [4]. This formulation takes into account the effects of thermal load, induced by temperature variation, and complexes boundaries conditions, such as contact between crack lips during crack growth process.

This paper is organized into three sections. In the first one, the mathematical formulation of the invariant integrals T and A is presented, completed by the derivation of the mixed mode stress intensity factors. In the second section, the accuracy of the numerical model is assessed based on examples dealing with elastic isotropic material. The third section is dedicated to study the efficiency of the proposed approach in the case of anisotropic material, where crack growth analysis on wood Compact Tension Specimen is performed.

3.2 Analytical Formulation of the Invariant Integrals T and A

First of all, let us recall the mathematical formulation of T-integral. Let Ω be a cracked body and Γ a path which surrounds the crack tip oriented by the normal $\overrightarrow{n}$ of component n_j, as shown in Fig. 3.1a.

The T-integral is given by:

$$T = \int_{\Gamma} \frac{1}{2}\left[\sigma^{v}_{ij,k}\, u_i - \sigma^{u}_{ij}\, v_{i,k}\right] n_j \, d\Gamma + \int_{\Gamma} \frac{1}{2}\left[\gamma \Delta T_{,j}\,(v_k - \psi_k) - \gamma \Delta T\left(v_{k,j} - \psi_{k,j}\right)\right] n_j \, d\Gamma + \int_{L} \frac{1}{2}\left[p\, v_{1,1} - q\, v_{2,1}\right] dx_1 \tag{3.1}$$

The first integral is the classical term of the T-integral which represent the effect of mechanical loads applied far from the crack, where σ^{u}_{ij} and σ^{v}_{ij} are stress tensor components deduced from the real displacement field u and the virtual displacement field v, respectively. The second integral represents the effect of thermal load induced by temperature variation ΔT, with ψ is a virtual displacement field as defined by Bui et al. [5] and γ is a real coefficient function of material parameters. The third integral represents the effect of pressures p and q applied perpendicularly to the crack lips, where $L = OA_1 + OB_1$ is the integration path.

Experience have shown that integration through curvilinear path induce some inaccuracy on numerical results. To overcome this problem, the curvilinear path is transformed into surface domain by introducing a vector field $\overrightarrow{\theta}$ [6] as shown in Fig. 3.1b. This mapping function is continuously differentiable and takes these values: $\overrightarrow{\theta} = (1, 0)$ inside the ring V, and: $\overrightarrow{\theta} = (0, 0)$ outside it. Hence, the use of the Gauss-Ostrogradsky's theorem enables us to obtain the A-integral given by:

$$A = \int_{\Omega} \frac{1}{2}\left[\sigma^{v}_{ij,k}\, u_i - \sigma^{u}_{ij}\, v_{i,k}\right] \theta_{k,j} \, dS + \int_{\Omega} \frac{1}{2}\left[\gamma \Delta T_{,j}\,(v_k - \psi_k) - \gamma \Delta T\left(v_{k,j} - \psi_{k,j}\right)\right] \theta_{k,j} \, dS + \int_{L} \frac{1}{2} F_i\, v_{i,j}\, \theta_j \, dx_1 \tag{3.2}$$

where $F_1 = p$ and $F_2 = q$ on the upper lip and $F_1 = -p$ and $F_2 = -q$ on the lower lip.

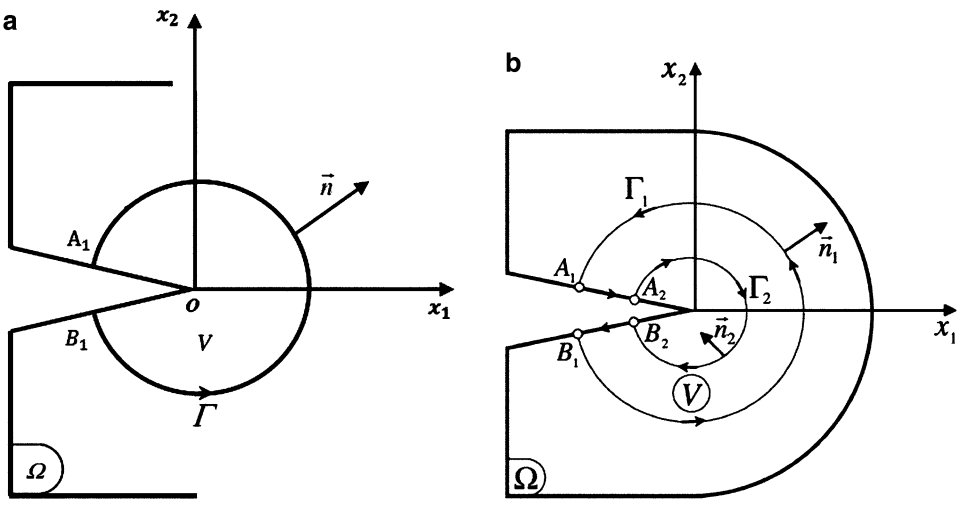

Fig. 3.1 (**a**) Curvilinear domain integral, (**b**) surface domain integral

Note that, Eq. 3.2 represent the energy release rate. The mixed mode separation can be obtained by performing two distinct computations of the real stress intensity factors K_I^u and K_{II}^u for particular values of virtual stress intensity factors K_I^v and K_{II}^v, such as:

$$K_I^u = 8\frac{A\left(K_I^v = 1, K_{II}^v = 0\right)}{C_1}; \quad K_{II}^u = 8\frac{A\left(K_I^v = 0, K_{II}^v = 1\right)}{C_2} \tag{3.3}$$

where C_1 and C_2 denote the elastic compliances in opening and shear modes, respectively.

3.3 Numerical Implementation

The analytical formulation of A-integral was implemented in the finite elements software Cast3m [7]. In order to illustrate the accuracy of the numerical results it has been decided to deal at first with isotropic material having a Young's Modulus $E = 20000\ daN/mm^2$, Poisson's coefficient $\nu = 0.3$ and linear expansion coefficient's $\alpha = 5\ 10^{-6}\ °C^{-1}$. The first problem deal with rectangular plate ($2b = 400\ mm$, $2h = 1200\ mm$) with a central crack ($2a = 200\ mm$) under tension $\sigma = 1 daN/mm^2$ applied on the lips (see Fig. 3.2a). The aim of this problem is to validate the third integral in Eq. 3.2 representing the effect mechanical loads applied on the crack lips. Due to the symmetry only a half of the plate is modeled. Figure 3.2b, c illustrate the finite element mesh and the deformation of the plate due to the applied load, respectively. Moreover, in order to have good accuracy on the computation of the mechanical fields, a refined mesh is adopted in the neighborhood of the crack tip.

Due to these loading and boundaries conditions, only opening fracture mode predominates, as confirmed by the deformation of the plate depicted in Fig. 3.2c. In this context, Fig. 3.2d illustrates the evolution of the stress intensity factor K_I versus the integration crown. Note that, the crown number 1 is the nearest one to the crack tip. As can be seen, the convergence of the quantity K_I is well achieved, since its value is stabilized from the third integration crown. Moreover, the finite element estimate of K_I (blue line) is in good agreement with the reference solution (red dashed line [8]) since the error does not exceed 1 %. Note that, the numerical computation is performed under plan strain assumption.

The second problem deal with rectangular plate ($2L = 800\ mm$, $2W = 200\ mm$) with edge crack ($a = 100\ mm$) subjected to linear temperature field $\Delta T = 2T_0\frac{x}{W}$, where $x \in \left[\frac{-W}{2}, \frac{W}{2}\right]$ and $T_0 = 100\ °C$. The geometry of the plate is depicted in Fig. 3.1a. The main objective now is to validate the formulation of the second integral in Eq. 3.2 which represents the effect of thermal load. Figure 3.3b, c illustrate the finite element mesh and the deformation of the plate due to the applied temperature field. The finite element analysis performed under the assumption of plane strain condition and the plate movement in vertical direction at the bottom and top edges is restricted. We are interested to the estimate of the opening mode stress intensity factor K_I. Figure 3.3d illustrates the evolution of the stress intensity factor K_I against the integration crown. As can be seen, the convergence is well achieved from the second integration crown. Moreover, the figure shows good agreement

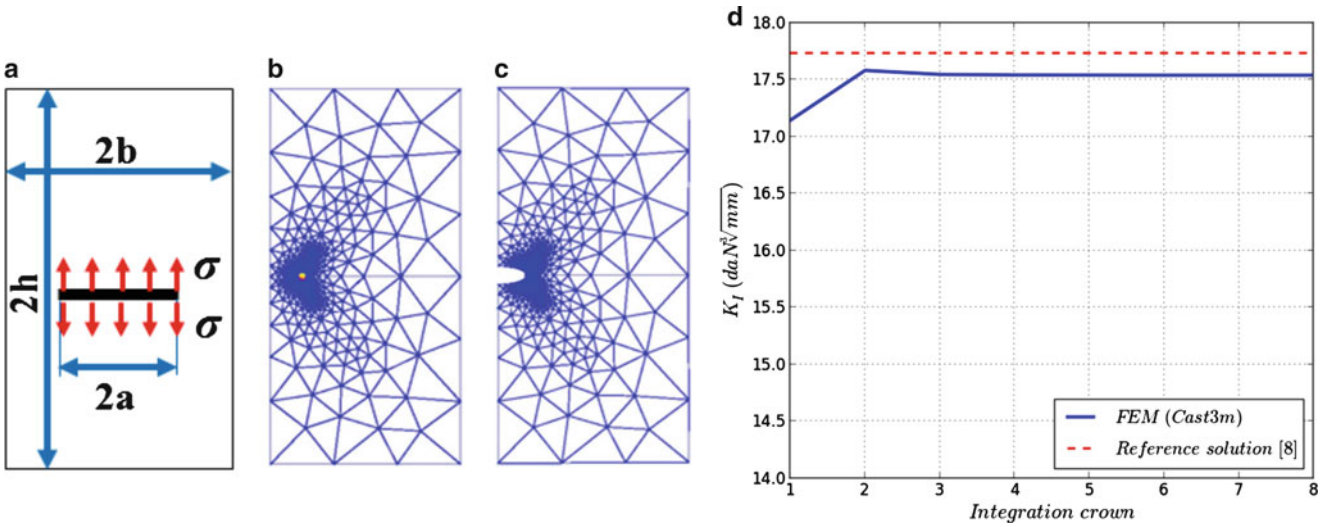

Fig. 3.2 (**a**) Geometry of a rectangular plate with central crack, (**b**) FE mesh, (**c**) deformation shape, (**d**) path independence of the opening mode stress intensity factor

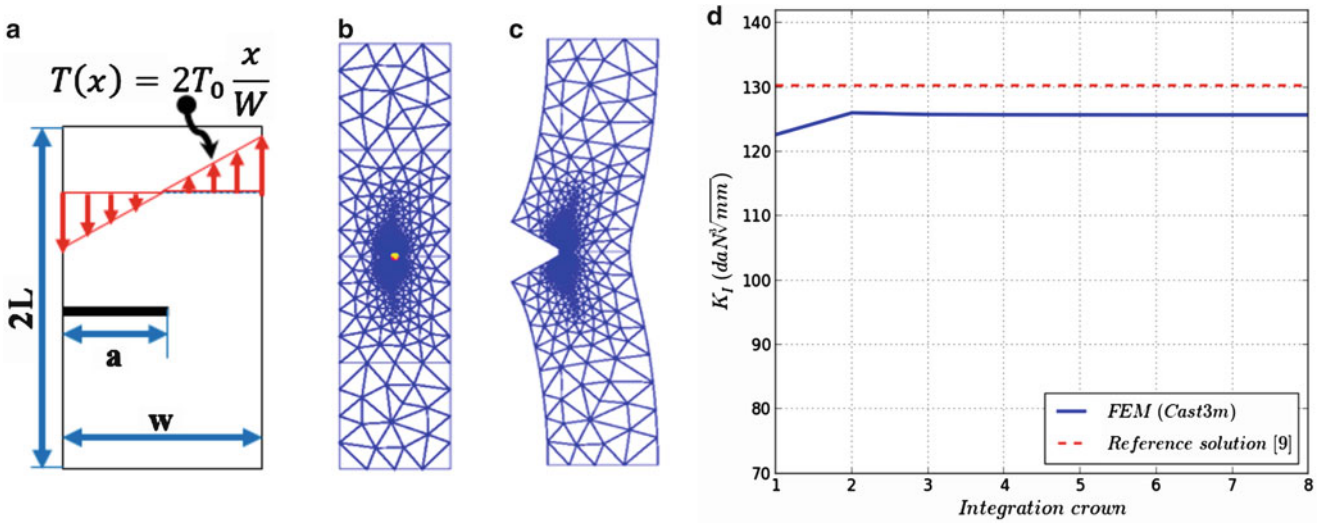

Fig. 3.3 (**a**) Geometry of a rectangular plate with edge crack, (**b**) FE mesh, (**c**) deformation shape, (**d**) path independence of the opening mode stress intensity factor

between the finite element results and the reference solution taken from the literature [9], since the error does not exceed 3.4 %. Again, the accuracy and the efficiency of the numerical implementation of the A-integral are approved.

3.4 Application to Wood Material

Now we are interested to orthotropic material. Thus, we employ a timber CTS (Compact Tension Specimen) of side of 50 *mm*. The crack length is 25 *mm*. The external load is an unitary loading applied to a steel contour as depicted in Fig. 3.4a. The points A_i and B_i, $i = \{1, \ldots, 7\}$ represent the location of holes where unspecified forces can be applied with angle β directed according to the crack in trigonometrical direction. For example, the pure opening mode (mode I) is obtained by applying opposite forces in A_1 and B_1 with $\beta = 0°$, while a loading with $\beta = 90°$ applied in A_7 and B_7 correspond to the case of pure shear mode (mode II). Intermediary positions represent different mixed mode configurations.

In order to study the fracture strength of wood material, a finite element model is developed in the software Cast3m. Unfortunately, it is difficult to found analytic solution for this problem. Thus, the accuracy of the finite elements implementation is evaluated through the study of the convergence of the numerical results with respect to the number of crowns around the crack tip taken in the calculation of the crack driving forces. The number of crowns represent the surface of the integration ring V used in the definition of the A-integral (see Fig. 3.1b). We note that, the numerical analysis is performed under plan stress conditions and based on the finite element mesh depicted in Fig. 3.1b. The timber CTS specimen is made on pine spruce having the following elastic mechanical properties: longitudinal modulus $E_1 = 1500\ MPa$, transverse modulus $E_2 = 600\ MPa$, shear modulus $G_{12} = 700\ MPa$, and Poisson's coefficient $\nu_{12} = 0.5$.

Figure 3.5a, b illustrate the evolution of stress intensity factors K_I and K_{II} with respect to the number of crowns and for different loading orientations β, respectively. As can be seen the convergence of the quantities K_I and K_{II} is well achieved with increasing the crown sizes. Good accuracy is observed for all loading orientations when the integration path is greater than the third crown size. Hence, the independence of the A-integral to the integration path is verified. We have also shown that the singularity of the mechanical fields induce inaccuracy on the numerical results. This disturbance is clearly observed when the integration process is based on the first crown, the nearest one to the crack tip.

3.5 Conclusion

The Knowledge of crack driving forces such as energy release rate and stress intensity factors is very important in the assessment of the reliability of flawed structures. A new formulation of the A-integral is proposed, which allow to take into account the effect of thermal load induced by temperature variation, in addition to mechanical load applied on crack lips.

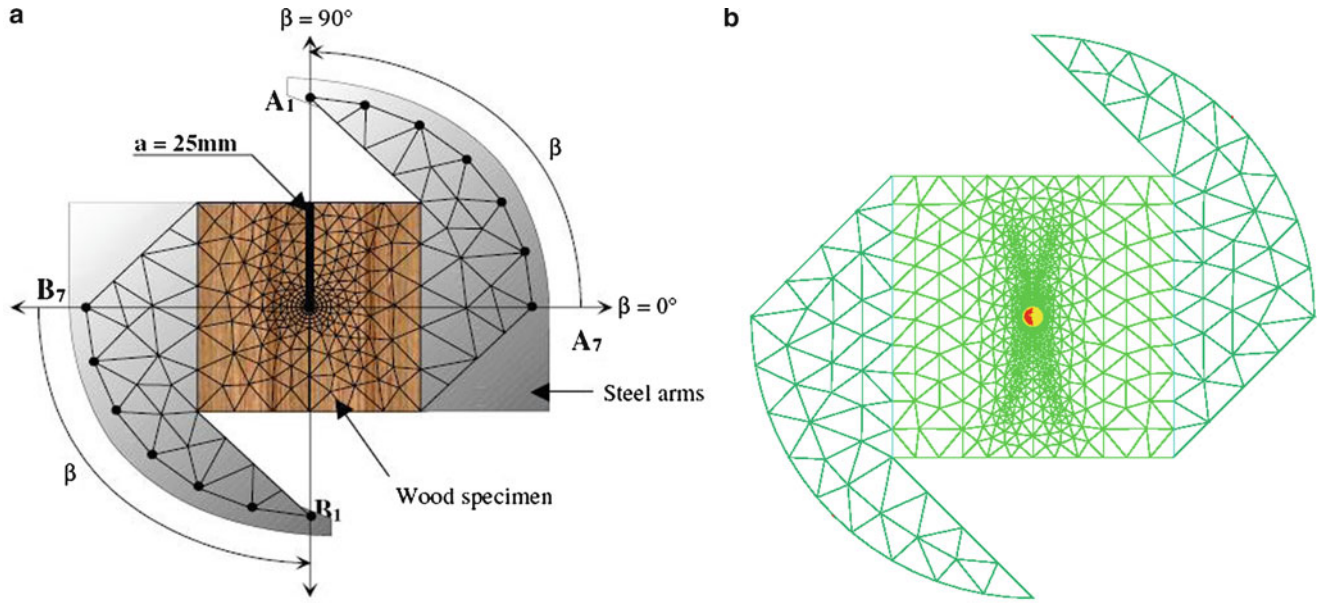

Fig. 3.4 (**a**) Geometry of a CT specimen, (**b**) FE mesh

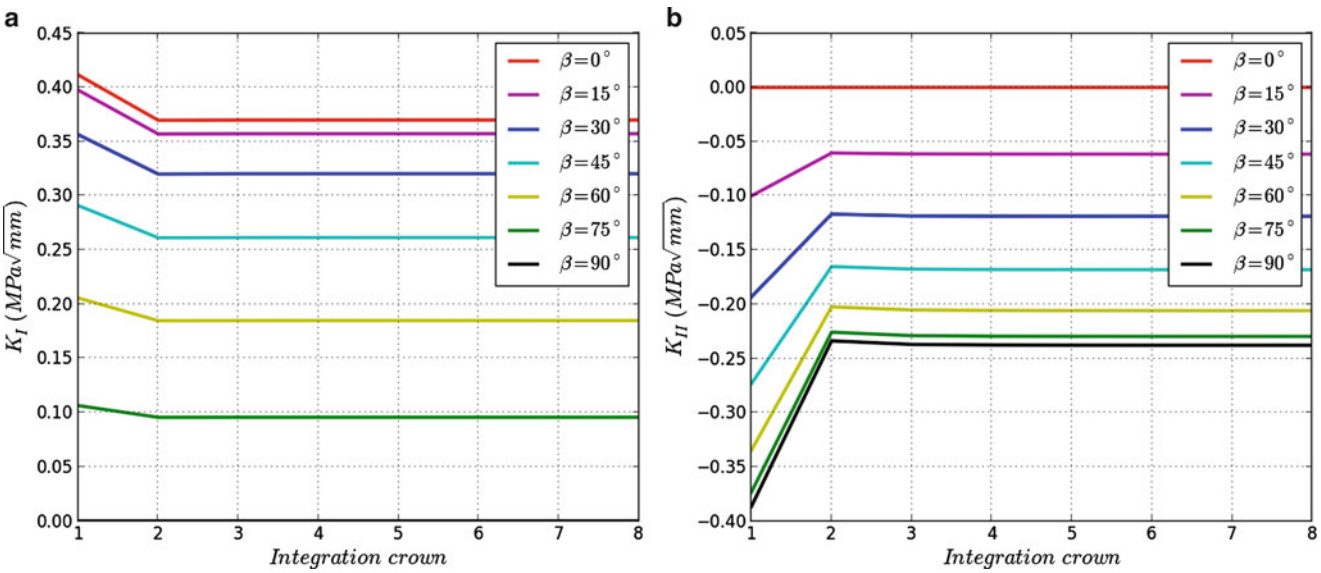

Fig. 3.5 Path independence verification of the stress intensity factors (**a**) K_I, (**b**) K_{II}

The efficiency of the numerical implementation, in finite element software, is assessed through many problems dealing with isotropic and orthotropic materials. A good accuracy is observed on the estimates of the stress intensity factor since the relative error does not exceed 3.4 %. Moreover, the convergence is well achieved since the values of the stress intensity factors are stabilized when the surface of the ring used in the integration is greater than the third crown of elements around the crack tip.

In this paper, the analysis is achieved under the assumption of elastic material. However, timber material has a viscoelastic behavior which can be easily implemented in finite element software using spectral decomposition method of the creep tensor. This will be the subject of undergoing researches, in addition to the development of the A-integral in order to take into account the effect of moisture variation. Also, we hope to investigate the effect of uncertainties in the material and load parameters on the reliability of wood structure subjected to crack growth, by using stochastic computation methods.

Acknowledgments The authors wish to strongly acknowledge the National Agency of Research (ANR) for its financial support of this work through the project CLIMBOIS N° ANR-13-JS09-0003-01 labeled by ViaMeca.

References

1. Rice JR (1968) A path independent integral and the approximate analysis of strain concentrations by notches and cracks. J Appl Mech 35: 379–386
2. Noether E (1918) Invariant variations problem. Transport Theory Stat Phys 1:183–207
3. Chen FMK, Shield RT (1977) Conservation laws in elasticity of the J-Integral. J Appl Math Phys 28:1–22
4. Moutou Pitti R, Dubois F, Petit C (2010) Generalization of T and A integrals to time-dependent materials: analytical formulations. Int J Fract 161:187–198
5. Bui HD, Proix JM (1985) Découplage des modes mixtes de rupture en thermoélasticité linéaire par des intégrales indépendantes du contour. Acte du Troisième Colloque Tendances Actuelles en Calcul de Structure, Bastia. pp 631–643
6. Destuynder P, Djaoua M, Lescure S (1983) Some remarks on elastic fracture mechanics. J Méc Théor Appl 2:113–135
7. Charvet-Quemin F, Combescure A, Ebersol L, Charras Th, Millard A. Méthode de calcul du taux de restitution de l'énergie en élastique et en non linéaire matériau. Report DEMT; 1986. p. 86/438
8. Rooke DP, Cartwright DJ (1976) Compendium of stress intensity factors. HMSO, London
9. Wilson WK, Yu IW (1979) The use of the J integral in thermal stress crack problems. Int J Fract 15:377–387

Chapter 4
Curvilinear Fatigue Crack Growth Under Out-of-Phase Loading Conditions

Xiaomin Deng, Xiaodan Ke, Michael A. Sutton, Haywood S. Watts, and Hubert W. Schreier

Abstract Methods for predictive modeling and simulation of crack branching and curvilinear crack paths under cyclic out-of-phase loading conditions have been developed and implemented in a custom finite element code CRACK3D. 3D mixed-mode stress intensity factors (SIFs) for fatigue crack growth simulations with curved crack paths and curved crack fronts are determined using the 3D virtual crack closure technique (3D VCCT) and a locally structured re-meshing approach in which the local region immediately surrounding a moving crack front is automatically re-meshed with a structured mesh pattern to facilitate the 3D VCCT and maintain its accuracy. The prediction of the crack growth direction is achieved using the maximum circumferential stress criterion. Fatigue crack growth events under out-of-phase loading conditions in cruciform aluminum specimens with a central hole and an edge crack at the hole are simulated. Simulation predictions of crack branching angles and the curvilinear paths of the branched cracks agree well with experimental measurements.

Keywords Fatigue crack growth • Out-of-phase • Mixed mode • Curved crack path • Local remeshing

4.1 Introduction

Fatigue crack growth in metals has been studied mostly under in-phase loading conditions, in which all loadings have the same cyclic time dependence. However, fatigue crack growth in critical structures often occur under out-of-phase loading conditions, such as under biaxial loading conditions in which two sets of biaxial cyclic loads have the same frequency but with a phase difference. Studies of fatigue crack growth under out-of-phase loading conditions have been limited in the literature. Most available studies have been focused on experimental investigations under biaxial loading conditions.

As shown in Fig. 4.1, there are two common specimens for fatigue crack growth tests under multi-axial and out-of-phase loading conditions (e.g. [1]): (a) cruciform specimen with biaxial normal loading, and (b) thin-walled tube specimen with axial tension and torsion loading. In particular, the cruciform specimen has been the most common specimen in the literature [2–8].

For the cruciform specimen, as shown in Fig. 4.1, the cyclic biaxial loading can be expressed in terms of the applied nominal stresses in the vertical direction (along y) and horizontal direction (along x), respectively:

$$\begin{aligned} S_x &= \sigma_{xm} + \sigma_{xa} \sin \omega t \\ S_y &= \sigma_{ym} + \sigma_{ya} \sin (\omega t + \phi) \end{aligned} \tag{4.1}$$

where σ_{xm} and σ_{ym} are the mean values, σ_{xa} and σ_{ya} are the amplitudes, ω is the frequency, t is time and ϕ is the phase angle (phase difference). When $\phi = 0$ the loading is *in-phase* and when $\phi \neq 0$ the loading is *out-of-phase*. Often $\phi = \pi = 180°$ is

X. Deng (✉) • M.A. Sutton • H.S. Watts
Department of Mechanical Engineering, University of South Carolina, Columbia, SC 29208, USA
e-mail: deng@cec.sc.edu

X. Ke • H.W. Schreier
Correlated Solutions, Inc., 121 Dutchman Blvd., Columbia, SC 29063, USA

J. Carroll and S. Daly (eds.), *Fracture, Fatigue, Failure, and Damage Evolution, Volume 5: Proceedings of the 2014 Annual Conference on Experimental and Applied Mechanics*, Conference Proceedings of the Society for Experimental Mechanics Series,
DOI 10.1007/978-3-319-06977-7_4,

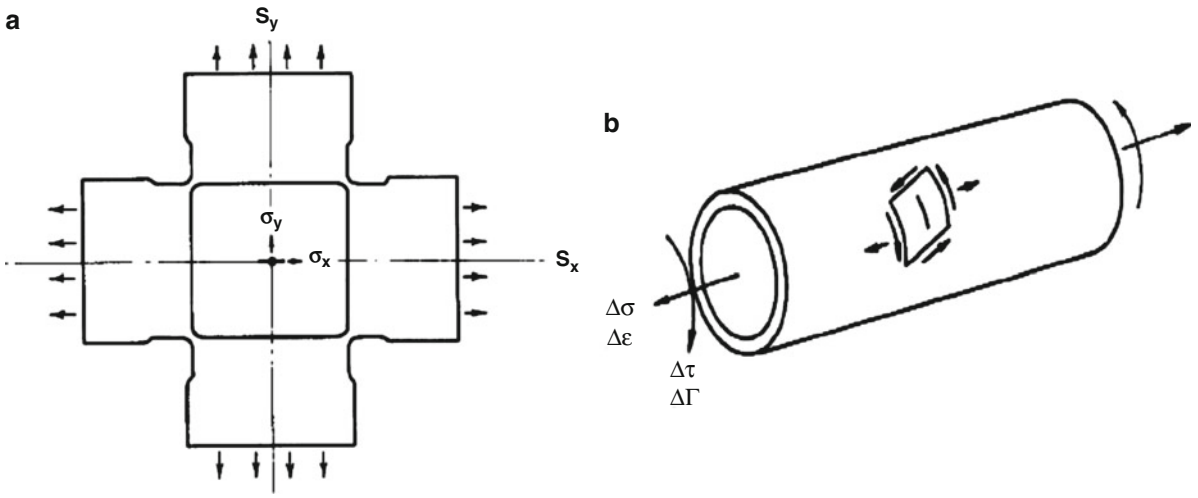

Fig. 4.1 Two common specimens [1] for fatigue crack growth tests under multi-axial and out-of-phase loading conditions: (**a**) cruciform specimen and (**b**) thin-walled tube specimen

used for out-of-phase loading. In general, two stress ratios (which are the R ratio if they are the same) can be defined for the cyclic loads:

$$R_x = S_{x\,\min}/S_{x\,\max} = (\sigma_{xm} - \sigma_{xa}) / (\sigma_{xm} + \sigma_{xa})$$
$$R_y = S_{y\,\min}/S_{y\,\max} = \left(\sigma_{ym} - \sigma_{ya}\right) / \left(\sigma_{ym} + \sigma_{ya}\right) \tag{4.2}$$

The ratio (the load biaxiality) between the two amplitudes of biaxial loading is often defined as:

$$\lambda = S_{y\,\max}/S_{x\,\max} = \left(\sigma_{ym} + \sigma_{ya}\right) / (\sigma_{xm} + \sigma_{xa}) \tag{4.3}$$

Under linearly elastic conditions, the effects of biaxial and out-of-phase loading on fatigue crack growth has been investigated in the literature in terms of the effects of λ and ϕ on (a) the crack path and (b) the fatigue crack growth rate. However, there is little theoretical development for crack path and life predictions under out-of-phase loading conditions and the findings from experimental studies are sometimes inconsistent and contradictory.

Beaver [1] provided a review of the literature up to early 1980s, with focus on the effect of biaxial loading under in-phase and out-of-phase loading conditions, which concluded that nearly all fatigue and fracture properties of metals are significantly affected by biaxial loading and that out-of phase loading decreases the fatigue strength.

Kitagawa et al. [2] studied fatigue crack growth under biaxial tensile load conditions for a structural sheet steel. They found that crack growth rate is affected by a cyclic tensile load applied in the direction of crack growth which decreases as the said load increases; that the rate increases if the biaxial loads are increasingly out of phase; and that the threshold stress intensity range is a function of load biaxiality, phase difference and stress ratio.

Qian et al. [3] carried out mixed-mode fatigue crack growth tests in stainless-steel cruciform specimens in which a center initial crack oriented at 45° was loaded biaxially. When the loadings were in-phase, the crack was deflected with the initial crack growth angles less than 50° and when they were out-of-phase, it was branched with the initial crack growth angles larger than 50°. In all cases, the deflected or branched cracks propagated in Mode I.

Shaniavski et al. [4] studied fractographic peculiarities of fatigue crack growth in cruciform specimens of D16T aluminum alloy under out-of-phase biaxial tension and tension-compression. In the range of biaxial load ratios λ from -0.5 to $+0.5$ and an R-ratio of 0.3, fatigue striation formation took place in which the striation spacing and the crack growth rate increase as the phase difference ϕ increases from 0 to 180°.

Rozumek et al. [5] conducted fatigue crack growth experiments under out-of-phase cyclic loading in cruciform specimens made of 18G2A steel with and without a stress concentrator in the form of a central hole. The authors analyzed these tests numerically and evaluated the crack growth rate behavior.

Sunder and Ilchenko [6] developed an easy to use digitally controlled biaxial test system for cruciform specimens under in-phase and out-of-phase loading conditions. They studied fatigue crack growth in cruciform specimens under constant amplitude and a load spectrum superposed with biaxial quasi-static load simulating internal cabin pressure. It is observed

that fatigue crack growth rates are noticeably sensitive to load biaxiality under both constant amplitude and spectrum loading. Characteristic stress intensity for constant amplitude in-phase and out-of-phase loading was computed accounting for instantaneous biaxiality at the peak and valley of axial loading component. The authors found that the effect of biaxiality at intermediate axial load levels may be negligible.

Shanyavskiy [7] carried out fatigue crack growth experiments on cruciform specimens in the range of thickness 1.2–10 mm of Al-based alloys, loaded under constant and variable amplitudes of uniaxial and biaxial loads, including sequences of various overloads, for various phase angles. To represent the effects of λ and ϕ as well as the effects of R and ω on the crack growth rate, an equivalent stress intensity factor $K_e = K_I F(\lambda, R, \phi, \omega)$ was proposed and determined by the investigator.

Lee and Taylor [8] performed fatigue crack growth tests on cruciform specimens of aluminum alloy 1100-H14 and 7075-T651 under in-phase (IP) and 180° out-of-phase (OP) loading of stress ratio 0.1. The specimens contain a horizontal (0°) or an inclined (45°) center notch crack. The authors studied the effects of λ and ϕ on crack path, crack growth rate and fatigue life. Among other things, the authors found that (a) at a given K, a lower σ_{ya} induced a longer fatigue life under IP and OP loading, and the fatigue life was longer under IP loading, (b) the fatigue crack path profile was influenced by K, phase angle (0° or 180°), and initial center notch (0° or 45°); and (c) the fatigue crack growth rate was lower and the fatigue life longer for a greater K under IP loading, whereas it changed little with change in K under OP loading.

Of the studies cited above, only references [3] and [8] presented results on the effects of λ and ϕ on crack growth path. In particular, the cruciform specimens considered in reference [3] have an initial crack with a 45° orientation. Under out-of-phase loading, the authors of reference [3] found that two branch cracks were created at the two tips of the initial crack, which were not observed in corresponding experiments with in-phase loading.

In the current study, fatigue crack growth under out-of-phase loading conditions has been investigated by considering two sets of stress intensity factors resulting from two sets of sinusoidal cyclic loads with a phase angle difference. A crack path and life prediction theory has been developed for fatigue crack growth under out-of-phase loading conditions using an equivalent stress intensity factor range ΔK_{eq}. For the case with a phase angle difference of 180°, this theory has been implemented in a custom finite element code CRACK3D and validated experimentally. In this theory, a criterion for crack branching and crack path prediction has been developed based on the well-known *maximum circumferential stress criterion* [9], and life prediction in the form of a (crack length) vs. N (number of loading cycles) is performed by using the Mode I baseline fatigue crack growth rate data in the form of da/dN vs. ΔK_{eq}. Due to the lack of experimental data, the crack path and life prediction theory for out-of-phase loading cases when the phase angle difference is not 180° has not been validated.

4.2 Theoretical Development

As noted earlier, there has been very little theoretical development reported in the literature that provides theories for crack path prediction (including possible crack branching at an existing crack tip due to out-of-phase loading) and for life prediction (in the form of a vs. N curves) for fatigue crack growth under out-of-phase loading conditions. To provide a consistent basis for crack path and life predictions under out-of-phase loading conditions, an attempt has been made to develop a set of theoretical hypotheses based on principles from mechanics and mathematics and to validate these hypotheses experimentally.

Consider the general case of fatigue crack growth under out-of-phase cyclic loading conditions, with loading component set #1 (the in-phase loading component) and loading component set #2 (the out-of-phase loading component). The two loading sets can be expressed by Eq. 4.1 but with x changed to 1 and y changed to 2. In general, the two sets of loading do not need to be along two orthogonal directions, say x and y. That is, they do not necessarily create a biaxial loading situation (although they do in fatigue crack growth tests on cruciform specimens loaded biaxially). Similarly, two cyclic stress ratios (which are the R ratio if they are equal) can be defined for the cyclic loads and expressed by Eq. 4.2, and the loading ratio (which is the loading biaxiality in the case of biaxial loading) between the amplitudes of the two loading sets can be expressed by Eq. 4.3, both with x changed to 1 and y changed to 2.

Under linearly elastic conditions, it can be shown that the Mode I and Mode II stress intensity factors (SIF) due to the two sets of loading can be expressed as:

$$\begin{aligned} K_{I1} &= 0.5K_{I1\max}\left[(1+R_1)+(1-R_1)\sin\omega t\right], \\ K_{II1} &= 0.5K_{II1\max}\left[(1+R_1)+(1-R_1)\sin\omega t\right], \\ K_{I2} &= 0.5K_{I2\max}\left[(1+R_2)+(1-R_2)\sin(\omega t+\phi)\right], \\ K_{II2} &= 0.5K_{II2\max}\left[(1+R_2)+(1-R_2)\sin(\omega t+\phi)\right]. \end{aligned} \tag{4.4}$$

In the above, K_{I1max} and K_{II1max} are the maximum values of K_I and K_{II}, respectively, due to set #1 loading, and K_{I2max} and K_{II2max} are the maximum values of K_I and K_{II}, respectively, due to set #2 loading. *If needed, similar expressions for Mode III SIFs can also be written, which are omitted here for the sake of brevity.*

In the theory presented below, consistent with the Paris Law for the rate of fatigue crack growth, the amount of SIF values exceeding their minimums will be used as the driving forces. That is, we take the view that fatigue damage is caused by the oscillatory range between the minimum and maximum SIF values. As such, we deduct the minimum values of the SIFs from the expressions in Eq. 4.4 and define the following SIF range variations with time:

$$\begin{aligned}
\Delta K_{I1} &= 0.5\,(1-R_1)\,K_{I1\,\max}\,[1+\sin\omega t]\,,\\
\Delta K_{II1} &= 0.5\,(1-R_1)\,K_{II1\,\max}\,[1+\sin\omega t]\,,\\
\Delta K_{I2} &= 0.5\,(1-R_2)\,K_{I2\,\max}\,[1+\sin(\omega t+\phi)]\,,\\
\Delta K_{II2} &= 0.5\,(1-R_2)\,K_{II2\,\max}\,[1+\sin(\omega t+\phi)]\,.
\end{aligned} \tag{4.5}$$

If needed, similar expressions for Mode III can also be written. The individual Mode I and Mode II SIF ranges in Eq. 4.8 due to the two sets of loading can be added to obtain the total Mode I and Mode II SIF ranges:

$$\Delta K_I = \Delta K_{I1} + \Delta K_{I2}, \quad \Delta K_{II} = \Delta K_{II1} + \Delta K_{II2} \tag{4.6}$$

A certain equivalent stress intensity factor range ΔK_{eq} can now be defined. For example, based on the relationship between the strain energy release rate and SIFs, ΔK_{eq} can be defined as follows through its squared value:

$$\Delta K_{eq}^2 = \Delta K_I^2 + \Delta K_{II}^2 + (1+\upsilon)\,\Delta K_{III}^2 \tag{4.7}$$

where υ is the Poisson's ratio. In many out-of-phase loading situations (e.g. cruciform specimens under biaxial out-of-phase loads), K_{III} is zero and can be omitted from Eq. 4.7. It is noted that ΔK_{eq}^2 is a function of ωt.

To develop a theory for the prediction of the in-plane crack growth direction under out-of-phase loading conditions, we propose three hypotheses based on observations of experimental results in the literature. These hypotheses can be further refined as more experimental data become available and new analytical studies are carried out.

Hypothesis 1 The initial crack growth direction is controlled by the maximum values of ΔK_{eq}^2 reached as a function of ωt during a complete loading cycle. In general, there may be several maximum values. If there is one dominant maximum value and others are relatively small, then there will be one crack growth direction (i.e., there is no branching at the initial crack tips). If there are several dominant maximum values, then there will be several crack growth directions (i.e., there will be branching at the initial crack tips). The branch with the most dominant maximum value will grow faster than those with the less dominant maximum values.

Hypothesis 2 Each initial crack growth direction is determined by the ratio of ΔK_I and ΔK_{II} at the value of ωt when ΔK_{eq}^2 becomes a maximum, in the form of the Maximum Circumferential Stress Criterion [9], given by

$$\tan\left(\frac{\theta_c}{2}\right) = \pm\frac{1}{4}\left(\frac{\Delta K_I}{|\Delta K_{II}|} - \sqrt{\left(\frac{\Delta K_I}{\Delta K_{II}}\right)^2 + 8}\right) \tag{4.8}$$

where θ_c is the crack growth direction angle, "+" is for $\Delta K_{II} > 0$ and "−" is for $\Delta K_{II} < 0$. it is noted that the kinking angle is relative to the local tangential direction of the crack path at the current crack tip in a counterclockwise manner.

Hypothesis 3 After crack growth from the initial crack tips, the direction of crack growth at each crack tip will be controlled by one dominant maximum value of ΔK_{eq}^2 reached as a function of ωt during a complete loading cycle. This direction is determined by the ratio of ΔK_I and ΔK_{II} at the value of ωt when ΔK_{eq}^2 reaches the maximum, in the form of the Maximum Circumferential Stress Criterion [9], as given in Eq. 4.8.

To develop a theory for life prediction under out-of-phase loading conditions, we propose a fourth hypothesis. This hypothesis can be further refined as more experimental data become available and new analytical studies are carried out.

Hypothesis 4 The a (crack length) vs. N (number of loading cycles) curve for each crack (or a branch crack in the case of crack branching) under out-of-phase loading conditions is controlled by the maximum value of ΔK_{eq} reached as a function of ωt during a complete loading cycle and by the baseline fatigue crack growth rate data da/dN as a function of ΔK_{eq} under Mode I and in-phase loading conditions.

4.3 Validation Experiments

Experimental data in the literature for fatigue crack growth under out-of-phase loading conditions are unfortunately not complete to the extent that they can enable comparisons of predicted and measured crack path and fatigue life. As such, new validation experiments have been performed by AFRL with the participation of a master's degree graduate student, Haywood S. Watts, from the University of South Carolina (USC). These joint AFRL-USC fatigue crack growth experiments under out-of-phase loading conditions were conducted on a special type of cruciform specimens under biaxial out-of-phase loading conditions. Due to space limitation, the description below is very brief but details of the experiments can be found in [10].

The overall shape of the cruciform specimen is similar to the one shown in Fig. 4.1 but it contains a central hole. A horizontal or inclined notch is cut on the left side of the hole. Then a fatigue pre-crack is made at the tip of the notch with the same orientation. Figure 4.2 shows the hole with an inclined notch as well as the fatigue pre-crack (the inclination or notch angle with respect to the left-ward x-axis is denoted by ϕ, which is nominally 45° but the actual value is different in the specimens). Fatigue crack growth experiments were performed on specimens made of aluminum alloy 7075-T6 or 2024-T351. Specimens made of 2024-T351 have a horizontal notch while those made of 7075-T6 have an inclined notch.

4.4 Finite Element Model and Results of Validation Simulation

A finite element model has been developed for one of the experiments performed jointly by AFRL and USC. This case involves fatigue crack growth in a specimen made of aluminum alloy 7075-T6 loaded biaxially with a 180° phase angle, a biaxiality loading ratio of 1 and R ratios of $R_1 = R_2 = 0.5$. The specimen has an initial notch length of 1.10 mm, a fatigue pre-crack length of 2.14 mm, and a notch angle of 43.5°.

Two finite element meshes have been created for the model with the initial crack. The two meshes are similar except in the crack region. In the coarse mesh, there are two elements both along the length of the crack and along the crack front (i.e. through the specimen thickness), and in the fine mesh, there are four elements both along the length of the crack and along the crack front. Away from the crack region, only one element is used through the specimen thickness in both meshes. Figure 4.3 shows a global 3D view of the fine mesh, and Fig. 4.4 shows a local 3D view of the fine mesh in the crack region.

Finite element simulations of the fatigue behavior of the specimen under biaxial out-of-phase loading conditions have been carried out using the in-house finite element code CRACK3D. During simulation, when crack growth is predicted along a certain direction, a local region around the crack front is automatically selected based on user input in which automatic local re-meshing will be performed by the code. Immediately around the predicted new crack front, a structured mesh will be created to enable the use of the 3D Virtual Crack Closure Technique (3D VCCT) for efficient and accurate determination of energy release rates and stress intensity factors along the crack front. In the rest of the local region, unstructured re-meshing will be performed with graded element sizes to bridge between the small elements immediately around the new crack front and usually larger elements in rest of the specimen surrounding the local region.

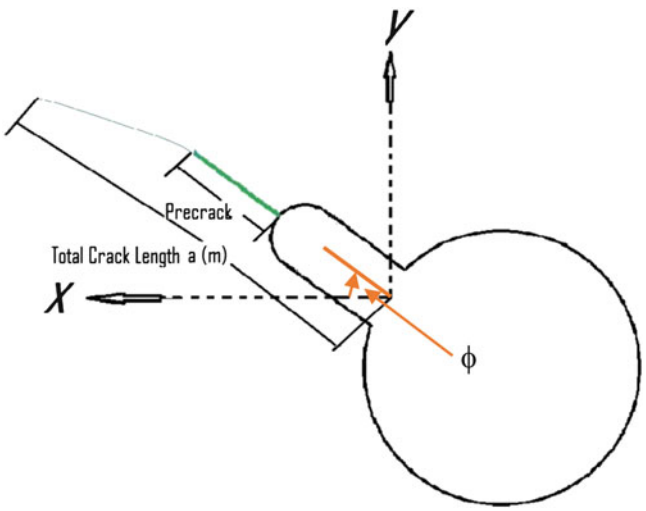

Fig. 4.2 A schematic of the hole in the cruciform specimen, showing the notch, the fatigue pre-crack and the notch angle

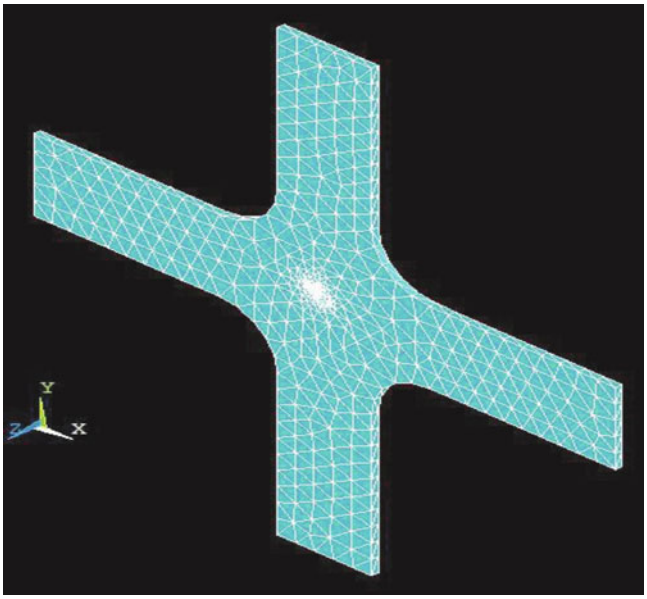

Fig. 4.3 A global 3D view of a finite element model of the cruciform specimen with a fine mesh

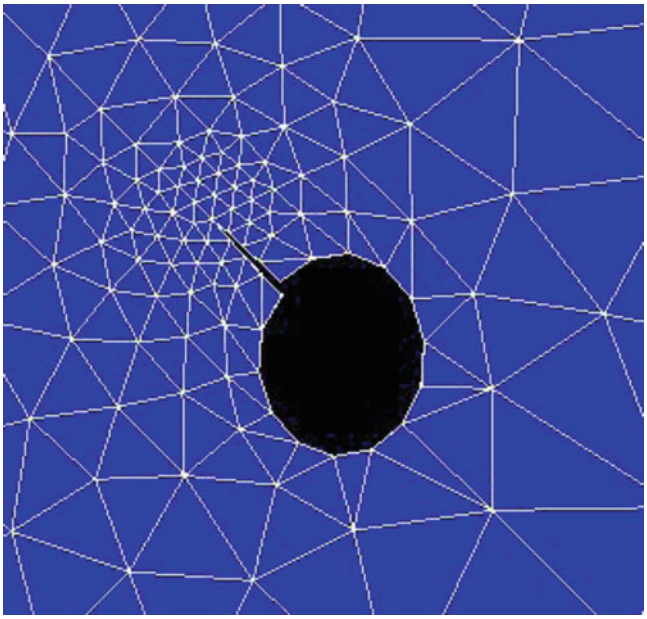

Fig. 4.4 A local frontal view of the finer mesh in the crack region

For the case of fatigue crack growth in the specimen made of aluminum alloy 7075-T6 loaded biaxially with a 180° phase angle, a biaxiality loading ratio of 1 and R ratios of $R_1 = R_2 = 0.5$, two branch cracks are predicted at the initial crack tip according to Hypotheses 1 and 2 using SIF values from CRACK3D solutions. The predicted branch crack directions agree very well with experimental measurements (see reference [11] for details). Then, after two short branch cracks are inserted at the initial crack tip, then CRACK3D simulates the growth of the two branch cracks under biaxial out-of-phase loading conditions according to Hypothesis 3. The predicted crack paths for the two branch cracks are compared with the measured crack paths in Fig. 4.5, which shows good agreement. Life predictions in the form of a (crack length) vs. N (loading cycle) for both of the branch cracks are also made according to Hypothesis 4 and are compared with experimental measurements with reasonably good agreement (details can be found in reference [11]).

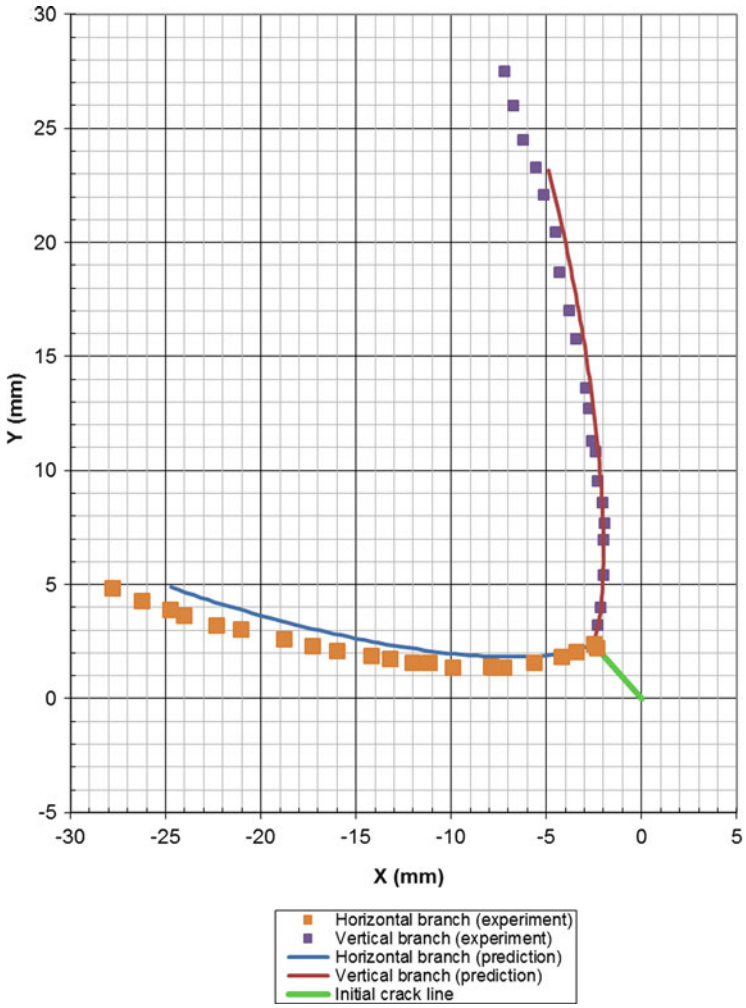

Fig. 4.5 Predicted branch crack paths and comparison with measured crack paths

4.5 Conclusions

Methods for predictive modeling and simulation of crack branching and curvilinear crack paths under cyclic out-of-phase loading conditions have been developed and implemented in a custom finite element code CRACK3D. In the theoretical development of this study, four hypotheses have been made for the predictions of branch cracks, their orientation angles, their growth paths, and their lives in the form of a (crack length) vs. N (loading cycle) curves. Fatigue crack growth events under out-of-phase loading conditions in cruciform aluminum specimens with a central hole and an edge crack at the hole are simulated. Simulation predictions of crack branching angles and the curvilinear paths of the branched cracks agree well with experimental measurements. Simulation predictions of a vs. N curves also compare reasonably well with measurements.

Acknowledgment The authors gratefully acknowledge the financial support provided by an AFRL SBIR project (Contract#: FA8650-10-C-3001). They would also like to express their gratitude to AFRL engineers Mr. Robert Reuter and Mr. Jim Harter for their support and helpful discussions.

References

1. Beaver PW (1985) Biaxial fatigue and fracture of metals: a review. Metals Forum 8(1):14–29
2. Kitagawa H, Yuuki R, Tohgo K (1979) A fracture mechanics approach to high-cycle fatigue crack growth under in-plane biaxial loads. Fatig Eng Mater Struct 2:195–206
3. Qian C-F, Wang M-O, Wu B-J, Dai S-H, Li JCM (1996) Mixed-mode fatigue crack growth in stainless steels under biaxial loading. J Eng Mater Tech 118:349–355

4. Shaniavski AA, Orlov EF, Grigoriev VM (1997) Fatigue crack growth in D16T Al-alloy sheet subjected to biaxial out-of-phase loading. Fatig Frac Eng Mater Struct 20(7):975–983
5. Rozumek D, Lachowicz CT, Macha E (2010) Analytical and numerical evaluation of stress intensity factor along crack paths in the cruciform specimens under out-of-phase cyclic loading. Eng Fract Mech 77:1808–1821
6. Sunder R, Ilchenko BV (2011) Fatigue crack growth under flight spectrum loading with superposed biaxial loading due to fuselage cabin pressure. Int J Fatig 33:1101–1110
7. Shanyavskiy A (2011) Fatigue cracking simulation based on crack closure effects in Al-based sheet materials subjected to biaxial cyclic loads. Eng Fract Mech 78:1516–1528
8. Lee EU, Taylor RE (2011) Fatigue behavior of aluminum alloys under biaxial loading. Eng Fract Mech 78:1555–1564
9. Erdogan F, Sih GC (1963) On the crack extension in plates under plane loading and transverse shear. ASME J Basic Eng 85:519–527
10. Watts HS (2013) Investigation of fatigue crack propagation in aluminum due to mixed mode biaxial loading. Final technical report, Department of Mechanical Engineering, University of South Carolina, Columbia, SC, May 2013
11. Deng X, Schreier HW (2013) High performance computer tool for predictions of fatigue crack growth and stable crack extension in aircraft structures. Final report for AFRL SBIR Project FA8650-10-C-3001, December 2013

Chapter 5
Fracture Surface Transition for Notched Bars in Torsion

Alan T. Zehnder and Natasha Zella

Abstract Under torsional loading a circular rod of a brittle material fails along a spiral fracture surface. By notching the rod deeply enough the fracture will be constrained to a nominally flat, but localy faceted fracture surface. This faceted surface consists of a sequence of 45 degree surfaces linked to each other. Using notched PMMA rods under torsional loading, the notch depth at which the surface transitions from spiral to nominally flat is mapped out experimentally. The results show that for a notch depth/radius >20 % the surface is nominally flat. For notch depths/radius <10 % the surface is spiral.

Keywords Mode III • Torsion • Mixed-mode • PMMA • Crack path

5.1 Introduction

The ability to predict fracture surface evolution and stability in three dimensions and under mixed-mode loading remains a challenging and compelling problem in mechanics. Some of the challenges come from the mechanics of the problem, e.g. the choice of local and/or global criteria for extent and direction of crack growth, linking up of microcracks growing on different surfaces, and friction across the surfaces. Other challenges arise from the complexity of implementing computational procedures for fracture surface evolution, such as remeshing of complex and evolving fracture surfaces [1], phase field methods [2], cohesive zone methods [3], atomistic [4], peridynamics [5] and other particle-like approaches.

The present work focuses on the fracture of circumferentially notched, circular PMMA rods loaded in torsion. Our working hypothesis is that although the fracture is nominally brittle, ultimately resulting in local Mode-I fracture surfaces, as the notch depth is increased, the fracture surface will transition from being a spiral to a macroscopically flat surface. The goal of this work is to experimentally map out that transition and to provide detailed information about the fracture surfaces and internal cracks that develop during failure. These results provide a challenging problem to models and approaches to simulation of mixed-mode fracture surface evolution.

The extension of cracks under monotonic and cyclic Mode-III and Mode I/Mode III loading has a long history of study beginning with Sommer [6] who performed an experiment in which flat, circular, internal cracks in a glass were loaded with internal pressure and an externally applied torsional load producing a mixed Mode I/Mode III load. As the cracks extended the torsional stresses and hence K_{III} increased. This causes the fracture surface to break up into what Sommer called "lances", which are narrow fingers where the crack twists as it grows. These twisted regions link up to produce a non-planar fracture surface with a "sawtooth" or "factory roof" profile as the surface is traversed in the circumferential direction.

Knauss [7] loaded a straight crack in a sheet of Solithane 113 in anti-plane shear to produce almost pure Mode-III loading along the crack front. It was observed that spiral shaped microcracks, oriented at 45° to the main crack front initiated. In this orientation, the microcracks are under tensile, or Mode I loading, consistent with the theory that in the absence of material or fracture toughness anisotropy, elastic cracks will grow in a local Mode I manner.

A.T. Zehnder (✉)
Field of Theoretical and Applied Mechanics, Cornell University, Ithaca, NY 14853, USA
e-mail: atz2@cornell.edu

N. Zella
College of Engineering, Cornell University, Ithaca, NY 14853, USA

J. Carroll and S. Daly (eds.), *Fracture, Fatigue, Failure, and Damage Evolution, Volume 5: Proceedings of the 2014 Annual Conference on Experimental and Applied Mechanics*, Conference Proceedings of the Society for Experimental Mechanics Series,
DOI 10.1007/978-3-319-06977-7_5,

Similar behavior was found by Tschegg [8] in a study of mixed Mode I/Mode III fatigue crack growth in 4,340 steel. At the lowest cyclic stress intensity factors, where the fracture behavior is nominally brittle, it was observed that the crack grew along a series of planes oriented at 45° to the initial crack front. These planes link up to form a macroscopically flat fracture surface containing numerous facets running radially and oriented at 45° to the overall fracture plane producing the factory roof fracture profile. Similar fracture patterns are observed in ceramics [9] and [10]. At higher loads, where greater levels of crack tip plasticity occur Tschegg [8] observes that the fracture transitions to a surface that is macroscopically flat and no longer has the factory roof profile. These cracks grew in a self-similar manner with the local failure plane coinciding with the plane of maximum shear stress rather than the planes of maximum normal stress seen in brittle fracture. The transition from tensile to shear fracture has also been observed under monotonic loading. Working with circumferentially cracked rods of PMMA and 7,075 Al samples Liu et al. [11] observed that the PMMA rods always exhibited brittle failure with the factory roof type surface. The 7,075 rods transitioned from brittle to ductile fracture as the ratio of K_I to K_{III} decreased.

Post-fracture images of Liu et al.'s PMMA samples demonstrate another transition. Although fracture remains brittle the overall fracture surface is spiral (similar to that of a stick of chalk broken by twisting) for $K_I/K_{III} < 1.6$ and is macroscopically flat (although with the factory roof profile) for $K_I/K_{III} > 2.6$. These observations were for a notch depth to diameter of $(b-a)/b = 0.08$. The exact transition point is not determined nor is the impact of different notch depths explored. In studies of failure criteria under tension and shear Berto et al. [12, 13] tested PMMA rods with U and V shaped notches and varying notch root radii. They observe that at a fixed notch depth the fracture surface transitions from spiral to flat as the notch root radius decreases. Note that Hull [14] provides a thorough review of crack surface evolution in the presence of Mode-III. For a thorough review of Mode I/Mode III fracture see [11].

Taking the results of refs [13] and [12] together it is observed that the overall fracture surface in cracked or notched rids that fail in a brittle manner can transition from a spiral to a flat but faceted surface as the level of tension to torsion increases and as the notch becomes sharper, concentrating load at the notch root. In the present work we further explore this transition by mapping out the spiral and flat fracture regimes for circumferentially notched PMMA rods with varying notch depth. The notches are approximately square with corner radii of less than 0.1 mm, sharp enough that, the fracture load is insensitive to notch radius [12]. Future work will explore the effects of varying tension/torsion ratio as well as notch depth ratio.

5.2 Experimental Method

5.2.1 Samples and Loading

The test samples, see Fig. 5.1, are 203 mm long circumferentially notched, circular, PMMA rods, with diameter $2b = 25.4$ mm and notch depths, $b-a$, ranging from 1.27 to 5.08 mm. Circumferential notches were cut in the samples using a steel cutting tool ground to a width of approximately 1 mm. The cutting speed was kept low to prevent melting of the PMMA during cutting.

Tests were performed by monotonically loading the samples to failure in pure torsion in a servo-hydraulic axial-torsional testing system. The axial load was controlled at zero while the samples were twisted in rotation control. Hydraulic collet grips hold the samples in the axial-torsional servo-hydraulic testing machine. The distance between the grips is approximately 152 mm.

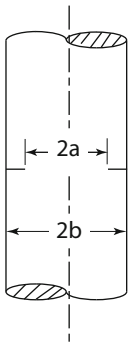

Fig. 5.1 Test specimens are circular rods with diameter, $2b = 25.4$ mm, length of 203 mm and varying notch depth. The samples are loaded with torque, T

5.2.2 Nominal Stress Intensity Factors

Although the sample contains a square notch, not a sharp crack, results will be presented in terms of the nominal stress intensity factors, K_{III} computed assuming a sharp crack of the same depth as the notch [15],

$$\begin{aligned} K_{III} &= \frac{2T}{\pi a^3}\sqrt{\pi(b-a)}\sqrt{\frac{a}{b}}F_3\left(\frac{a}{b}\right), \\ F_3 &= \frac{3}{8}\left[1+0.5\left(\frac{a}{b}\right)+0.375\left(\frac{a}{b}\right)^2+0.313\left(\frac{a}{b}\right)^3+0.273\left(\frac{a}{b}\right)^4+0.208\left(\frac{a}{b}\right)^5\right], \end{aligned} \tag{5.1}$$

where T is the torque, b the radius, and a is the radius of the uncracked region.

5.3 Results

Torsional fracture experiments were performed on samples with notch depths systematically varied from 0 to 0.4 of the radius and the fracture. As the notch depth was increased it is observed that the fracture transitions from an overall spiral surface to a mixed spiral and flat surface to a nominally flat surface. Examples of each of the three types of surfaces are given in Fig. 5.2. The spiral surface is the surface you would obtain by twisting a piece of chalk to failure. The spiral-flat surfaces are a mix of the spiral surface with a region of nominally flat fracture. The flat fracture surface is anything but flat at the small scale. As in other studies of Mode-III fracture the surface consists of a sawtooth surface consisting of linked facets at approximately 45° to the axis of the rod. Multiple microfractures emanate from the main fracture surface into the interior of the rod as can be seen in Fig. 5.2.

Figure 5.3 plots the fracture surface type versus the normalized notch depth. For the shallowest notches, $(b-a)/a \leq 0.1$ the fracture surfaces are always spiral or spiral/flat. For deep notches, $(b-a)/b \geq 0.3$ the surface is always nominally flat. In the transition zone $0.1 < (b-a)/a < 0.3$ the surfaces are a mix of spiral/flat and flat with predominantly flat surfaces for notches with $(b-a)/a > 0.2$. Computing the nominal stress intensity factor for all experiments, see Fig. 5.4, it is seen that the nominal fracture toughness K_{III} is 3.5–4.5 MPa$\sqrt{m}$ and does not vary with notch depth.

To develop a better understanding of the fracture surfaces as well as of the structure of the interior cracks micro-CT scans were performed on several samples. And example, showing mating fracture surfaces for a nominally flat surface sample is shown in Fig. 5.5. The figure shows that multiple facets develop from the initial crack front. These facets are spaced 2–4 mm apart. As the crack grows towards the center of the sample, the facets merge and coarsen.

5.4 Summary and Future Work

Notched rods of PMMA were tested in torsion to fracture. As the notch depth increases, the overall fracture surface transitions from a spiral fracture to a nominally flat, but locally faceted surface. The transition occurs between 0.1 to 0.3 notch depth to radius fraction. Future work will map out the fracture surfaces for varying notch ratios of tension to torsion as well as varying notch depth, resulting in an experimentally obtained phase map in the space of notch depth and $K_I : K_{III}$. Results of the work will be presented as a challenge for testing the ability of computational models to predict these complex and evolving fracture surfaces.

Acknowledgements This work was supported by a grant from Cornell's Engineering Learning Initiatives. This work was enabled by use of the Cornell University Biotechnology Resource Center (BRC).

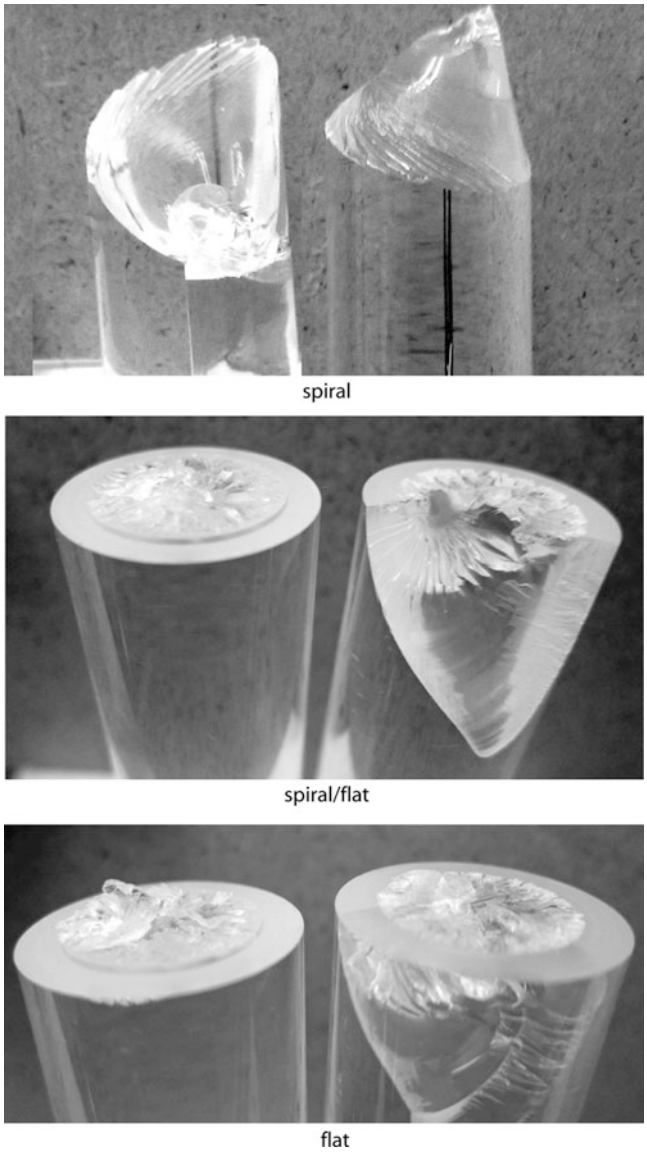

Fig. 5.2 Examples of spiral, spiral/flat and nominally flat fracture surfaces

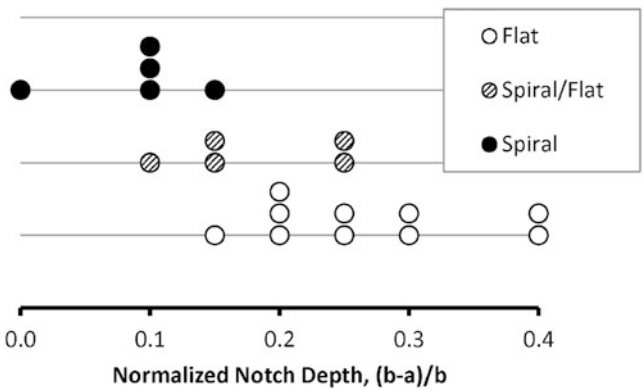

Fig. 5.3 Transition of fracture surface from spiral to flat as notch depth increases. Each experiment is coded as having either a spiral, spiral/flat or flat surface. The vertical scale is arbitrary and serves simply to separate the data points

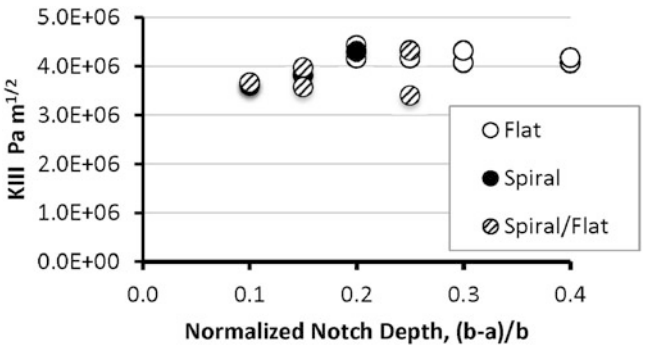

Fig. 5.4 Nominal K_{III} values at fracture. Fracture surface is coded as in Fig. 5.3

Fig. 5.5 Mating fracture surfaces for a sample with nominally flat fracture. Fracture surfaces are imaged using computed tomography (GE eXplore CT-120) at 25 μm voxel size

References

1. Carter BJ, Wawrzynek PA, Ingraffea AR (2000) Automated 3-D crack growth simulation. Int J Numer Methods Eng 47(1–3):229–253
2. Hakim V, Karma A (2009) Laws of crack motion and phase-field models of fracture. J Mech Phys Solids 57(2):342–368
3. Park K, Paulino GH, Celes W, Espinha R (2012) Adaptive mesh refinement and coarsening for cohesive zone modeling of dynamic fracture. Int J Numer Methods Eng 92(1):1–35
4. Coffman VR, Sethna JP, Heber G, Liu M, Ingraffea A, Bailey NP, Barker EI (2008) A comparison of finite element and atomistic modelling of fracture. Model Simul Mater Sci Eng 16(6):065008 (15 pp)
5. Youn DH, Bobaru F (2010) Studies of dynamic crack propagation and crack branching with peridynamics. Int J Fract 162(1–2):229–244
6. Sommer E (1969) Formation of fracture 'lances' in glass. Eng Fract Mech 1(3):539–546
7. Knauss W (1970) An observation of crack propagation in anti-plane shear. Int J Fract 6(2):183–187
8. Tschegg EK (1983) Mode III and mode I fatigue crack propagation behavior under torsional loading. J Mater Sci 18(6):1604–1614
9. Tschegg EK, Suresh S (1988) Mode III fracture of 4340 steel: effects of tempering temperature and fracture surface interference. Metallurgical Trans A 19(12):3035–3044
10. Suresh S, Tschegg EK (1987) Combined mode I-mode III fracture of fatigue-precracked alumina. J Am Ceramic Soc 70(10):726–733
11. Liu S, Chao YJ, Zhu X (2004) Tensile-shear transition in mixed mode i/iii fracture. Int J Solids Struct 41(22–23):6147–6172
12. Berto F, Cendon DA, Lazzarin P, Elices M (2013) Fracture behaviour of notched round bars made of PMMA subjected to torsion at -60C. Eng Fract Mech 102:271–287
13. Berto F, Elices M, Lazzarin P, Zappalorto M (2012) Fracture behaviour of notched round bars made of PMMA subjected to torsion at room temperature. Eng Fract Mech 90:143–160
14. Hull D (1993) Tilting cracks: the evolution of fracture surface topology in brittle solids. Int J Fract 62(2):119–138
15. Tada H, Paris P, Irwin G (2000) Stress analysis of cracks handbook, 3rd edn. ASME Press, New York

Chapter 6
Mixed Mode Evaluation of Different Grinding Depths in FRPC Repairs

T.S. Chawla and M.N. Cavalli

Abstract Variations in repair parameters and techniques have a significant influence on the mechanical properties of repaired fiberglass reinforced composite materials. A common method to repair damaged fiberglass wind turbine blades is to conduct hand layup repairs after grinding out the damaged portion. In one sided repair, the ply to which the damage extends depth wise is usually ground off completely and repairs are conducted on the top surface of the next ply. The scope of this work was to observe the effect on repair fracture toughness values when repairs are conducted with this top ply ground off partially. Mixed mode I–mode II testing was carried out on repaired fiberglass composite materials to determine the crack initiation fracture toughness values of two kinds of repairs; one with the top ply intact and other with the top ply partially ground off. The results from this testing were compared to those obtained from mode I testing conducted on similar repairs.

Keywords Glass-fiber composites • Composite repairs • Mixed-mode testing • Fracture toughness • Out-of-autoclave

6.1 Introduction

Continuous efforts are being made to improve the quality of repairs conducted on both engineering and advanced fiber reinforced composite parts and structures. The target is to restore the composite part to its initial structural integrity with minimal degradation in mechanical and cosmetic properties. Since fiber reinforced composites are subjected to different modes of loading while in service, it is pertinent that they be tested under various loading conditions. Delamination of repairs may be caused by a combination of loading modes. One such commonly tested mixed mode loading comprises examining effects of combined mode I and mode II loads. Initially, the Standard Test Method for Mixed Mode I–Mode II Interlaminar Fracture Toughness of Unidirectional Fiber Reinforced Polymer Matrix Composites (ASTM D 6671/D 6671M – 06) [1] was developed for evaluating the interlaminar fracture toughness of unidirectional fiber reinforced polymer matrix composites under mixed mode I–mode II loading. Though this method describes in details the mixed-mode bending (MMB) test as applicable to use with unidirectional carbon fiber tape laminates [2–5] with brittle and tough single-phase polymer matrices, it has also been extensively used to test the toughness of both glass fiber reinforced composites and materials bonded with adhesive joints [6–12].

For the presented work, mixed mode I–mode II testing was carried out to investigate fracture toughness of glass fiber reinforced polymer composite repairs conducted with variation in repair methods. This was in continuation of earlier work [13] involving mechanical characterization of vinyl ester resins with varying compositions. The previous work was carried out to improve the strength of repairs conducted on glass fiber reinforced polyester wind turbine blades. During characterization with mode I loading it was found that the fracture toughness of the repairs increased significantly when the top ply of the repair surface was ground off partially. This led to further investigation to see if similar effects due to variation in grinding depths could be seen under mixed mode loading.

T.S. Chawla (✉)
Plastics Engineering Technology, Engineering Technology Department, Western Washington University, Bellingham, WA 98225-9086, USA
e-mail: Tanveer.Chawla@wwu.edu

M.N. Cavalli
Department of Mechanical Engineering, University of North Dakota, 243 Centennial Drive, Stop 8359, Grand Forks, ND 58202-8359, USA
e-mail: matthewcavalli@mail.und.nodak.edu

J. Carroll and S. Daly (eds.), *Fracture, Fatigue, Failure, and Damage Evolution, Volume 5: Proceedings of the 2014 Annual Conference on Experimental and Applied Mechanics*, Conference Proceedings of the Society for Experimental Mechanics Series,
DOI 10.1007/978-3-319-06977-7_6,

6.2 Specimen Preparation

The specimens for mixed mode testing (Fig. 6.1) were made in accordance with ASTM D 6671/D 6671M – 06. The lower adherend (parent laminate) represented a fiber glass reinforced polyester composite and the upper adherend (repair laminate) simulated the flat part of a one-sided scarf repair. The lay-up and materials used for the upper and lower adherends are given in Table 6.1. Commercially available resins were used for parent laminate resin infusion as well as for hand layup repairs. The listed number of plies was chosen in order to have specimens with h 5 mm (Fig. 6.1). The lower adherends (parent laminates) were manufactured using vacuum assisted resin transfer/infusion molding (VARTM/VARIM) (Fig. 6.2.) and were cured at room temperature for 24 h. They were further post-cured in an oven at 60 °C for 24 h and then at 95 °C for 3 h to ensure that they had the same degree of cure. In order to study the effect of variation in grinding depth on the mixed-mode fracture toughness of the repairs, complete top plies in one set of four parent laminates and partial top plies in the other set of four parent laminates were ground off. The variation in top ply grinding depths is shown in Fig. 6.3. Then the simulated

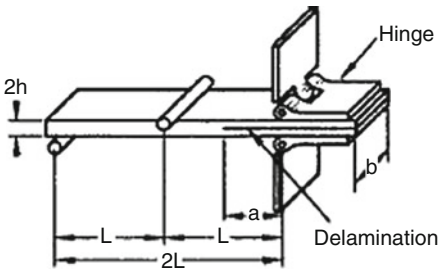

Fig. 6.1 Mixed mode specimen [1]

Table 6.1 Specimen Lay-up and post curing details

Lay-up	Part	Details
5 × Unidirectional plies (0°, glass fiber)	Repaired Laminate:	Curing:
1 × Chopped strand mat	Hand Lay-up	24 h at room temperature
	Polyester and Vinyl Ester repair resins	Post curing:
	(**Upper adherend**)	16 h at 40 °C
Insert (Crack Initiator)	Polymer film	Thickness ≤ 13 μm
5 × Unidirectional plies (0°, glass fiber)	Parent Laminate:	Curing:
	VARTM	24 h at room temperature
	Polyester infusion resin	Post curing:
	(**Lower adherend**)	24 h at 60 °C
		3 h at 95 °C

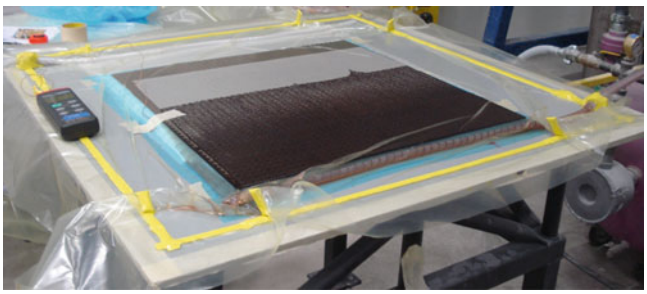

Fig. 6.2 VARTM set-up (during infusion)

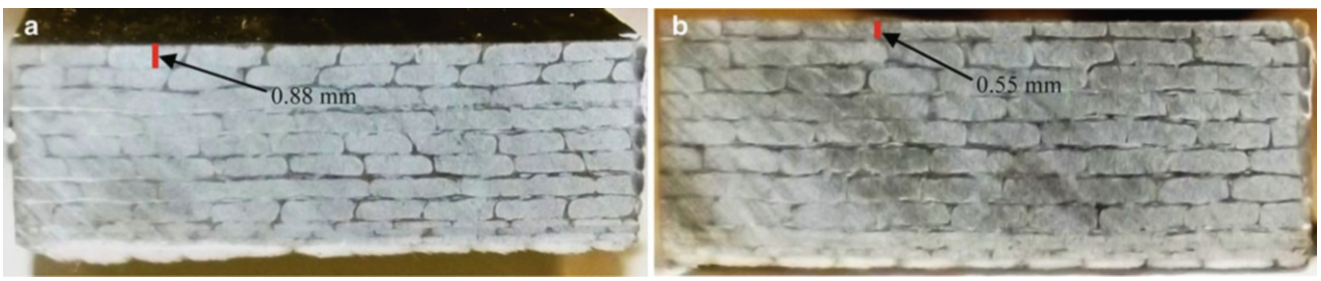

Fig. 6.3 Repair surface top ply grinding depth variation. (**a**) Complete top ply ground off. (**b**) Partial top ply ground off

repairs were carried out on these ground parent laminates to create the upper adherends by using the hand layup technique. Two laminates in each set were repaired using a polyester repair resin. The remaining four laminates (two from each set) were repaired using a vinyl ester repair resin. Polymer inserts (thickness < 13 μm) were used to create pre-cracks of 25 mm in each specimen at the resin inlet during repair. The repairs were allowed to cure at room temperature for 24 h. Then, post-curing was carried out on them along with the parent adherends for 16 h in the oven at 40 °C.

The repaired plates were sectioned into 25 mm wide and 250 mm long specimens with premium grade carbide toothed saw. Plexus MA300 (methacrylate adhesive) was used to bond piano hinges to the specimens after light sanding at the region of application of adhesive. The delaminated section of the specimen was 75 mm in length and the hinges were applied so as to have the load line at a distance of 25 mm from the pre-crack tip. The edges of the specimens were coated with a water-based white typewriter fluid and thin lines were marked every 1 mm for a distance of 30 mm from the end point of the pre-crack. Along the load line a speckled pattern was created on the specimen. The mm markings were done in order to make it easier to monitor crack propagation. The speckled pattern was created on each specimen in order for Vic-2D Correlation Software to be able to correlate the pictures obtained to calculate the stroke displacement that occurred during each test.

6.3 Testing and Calculations

Specimens consisting of parent plates manufactured with an infusion grade polyester resin and glass fibers and repaired with polyester and vinyl ester repair resins were tested under mixed-mode mode I–mode II loading. The length of the lever arm, *c* (Fig. 6.4), of the mixed mode I–mode II testing apparatus was varied for each of the mode mixtures ($G_{II}/G = 0.2$, 0.5 and 0.8) before testing. The length L (Fig. 6.1) was kept constant at 50 mm.

Two levels of grinding of the top ply of the parent plate were evaluated. Three specimens were tested at each mixed mode ratio for all cases. Specimens were mounted on the mixed mode I–mode II (ASTM D 6671/D 6671M – 06) test fixture and testing was carried out on the Shimadzu AG-IS Universal Testing Machine under displacement control at a crosshead rate of 0.5 mm/min. Loads were recorded using TRAPEZIUM 2 control software linked to the universal testing machine and images of the loaded samples were captured with a Retiga 1300 camera using the Vic-Snap software. These images were analyzed for stroke displacements using Vic-2D Digital Image Correlation Software. Figure 6.5 shows the experimental set-up for the testing carried out.

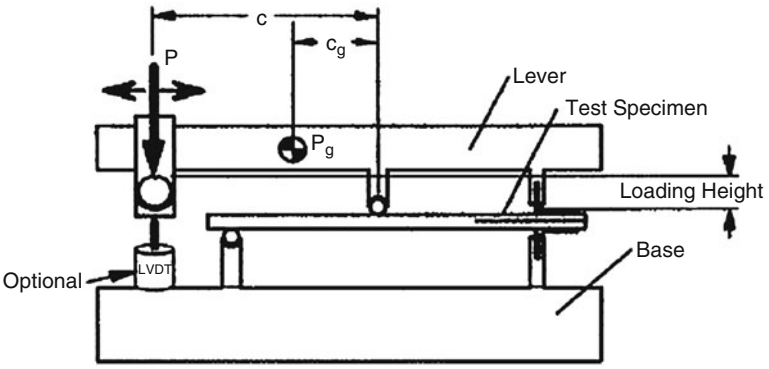

Fig. 6.4 Test fixture and parameters of mixed-mode test [1]

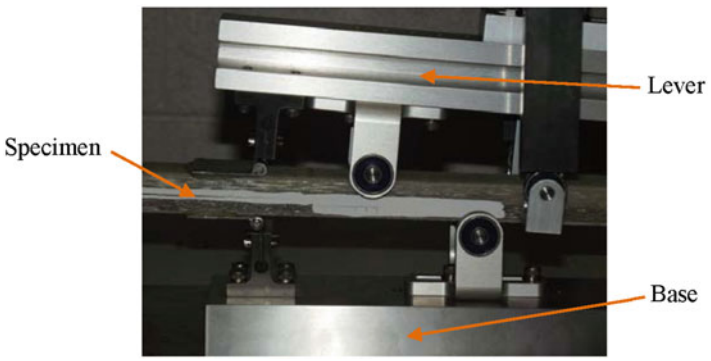

Fig. 6.5 Experimental set-up for mixed mode testing

On conclusion of all testing, calculations were carried out using the equations given in ASTM D 6671/D 6671M – 06 [1] and values of flexural modulus, mode I and mode II components of strain energy release rate and the combined mixed mode strain energy release rate were obtained.

6.4 Results and Discussion

In mode I testing of double cantilever beam (DCB) specimens [13] it was seen that difference in grinding depth of the top surface of the parent plate while preparing it for repairs does affect the fracture toughness values of the repairs. As in the case of mixed mode specimens, the lower adherends of the DCB specimens depicted parent fiber glass reinforced polyester (infusion grade) composites whereas the upper adherends represented hand layup repairs carried out with vinyl ester repair resins on them. In all of the specimens with the top plies partially ground off, the fracture toughness values calculated at a crack length of about 105 mm were much higher than those obtained from specimens made with same repair resins but with their top plies ground off completely. When the top plies are ground off completely, the resulting exposed surface on which the repairs are carried out comprises mainly infusion resin. Whereas, when the top plies are ground off partially, the resulting surface has a mixture of exposed fibers and the infusion resin. These exposed fibers bond with the repair resin and this results in pronounced fiber bridging while the specimens are being tested, thus leading to high fracture toughness values. Figure 6.6 depicts a comparison of the normalized mode I fracture toughness values obtained from DCB specimens repaired with top parent plies completely ground off (Plot (i), Fig. 6.6) to those with the top parent plies partially ground off (Plot (ii), Fig. 6.6). Similar results were obtained from DCB specimens prepared with two other vinyl ester repair resins with different additives. One resin had core shell rubber particles in it whereas the other had a lesser amount of styrene than that in the repair resin of which the results are shown below. The exact compositions are not known due to proprietary reasons.

For the mixed mode testing also, one set of plates was repaired with the top unidirectional glass-fiber ply completely ground off, thus exposing a surface comprising mainly of cured resin. The top unidirectional glass-fiber ply of the other set was partially ground off to expose a surface comprising of a mixture of glass fibers and cured resin. Delamination fracture toughness values, calculated from the critical loads obtained from testing, were plotted as a function of mode mixtures for the different resins and grinding levels. It was not possible to plot the delamination propagation fracture toughness values as the crack growth was very fast in mixed-mode testing.

A typical mixed mode I–mode II delamination fracture toughness contour is shown in Fig. 6.7 for the repair carried out using the polyester repair resin after grinding off the top ply of the parent plate completely. The delamination fracture toughness values increase with an increase in the percentage of mode II loading from 20 to 80 % as expected. The scatter in the toughness values does not bear a linear relation with the increase in mode II percentage. As shown in the plot, the mixed mode fracture toughness values obtained at different mode II ratios can be generally fitted by an exponential curve. Similar trend was found by Benzeggagh and Kenane [6] and further corroborated by other researchers like Dharamawan et al. [10].

Similar fracture toughness contours are shown in Figs. 6.8–6.10 for the polyester repair resin with partial top ply ground off, the vinyl ester repair resin with complete top ply ground off and vinyl ester repair resin with partial top ply ground off, respectively.

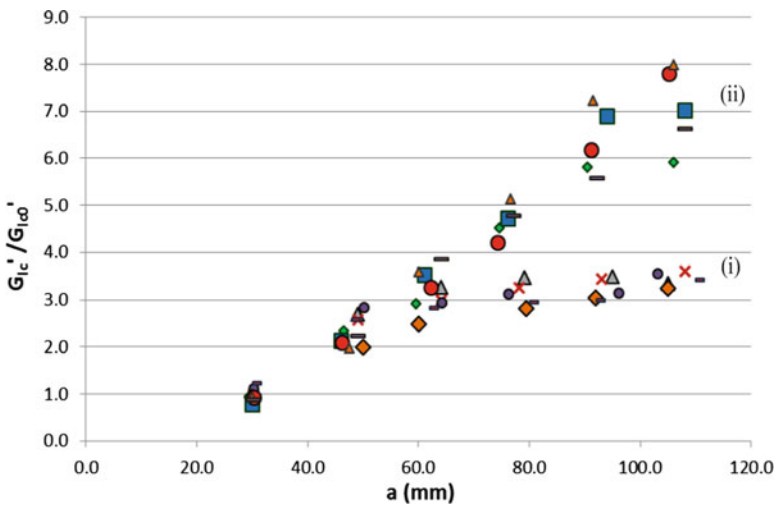

Fig. 6.6 Comparison of mode I fracture toughness values of DCB specimens with (*i*) whole top ply ground off and (*ii*) partial top ply ground off

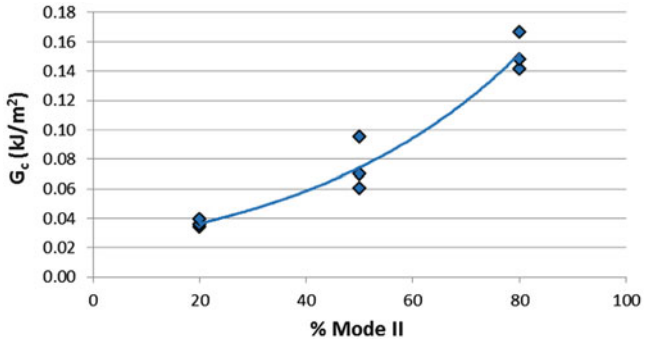

Fig. 6.7 Delamination mixed mode I-mode II fracture toughness values for repairs with whole top ply ground off

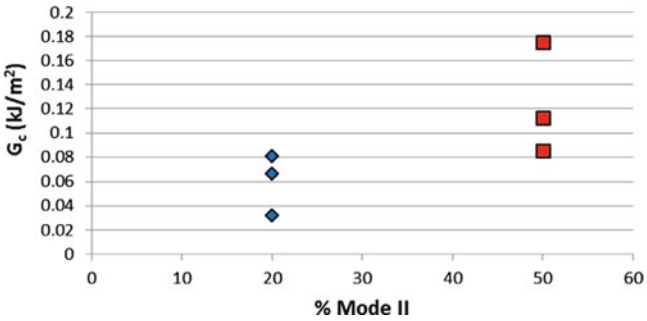

Fig. 6.8 Delamination fracture toughness values for polyester repair resin with partial top ply of parent plate ground off

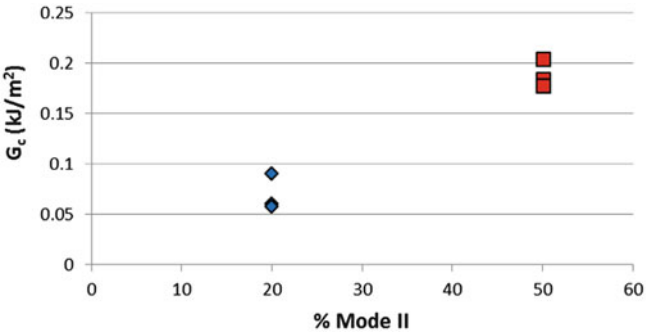

Fig. 6.9 Delamination fracture toughness values for vinyl ester repair resin with whole top ply of parent plate ground off

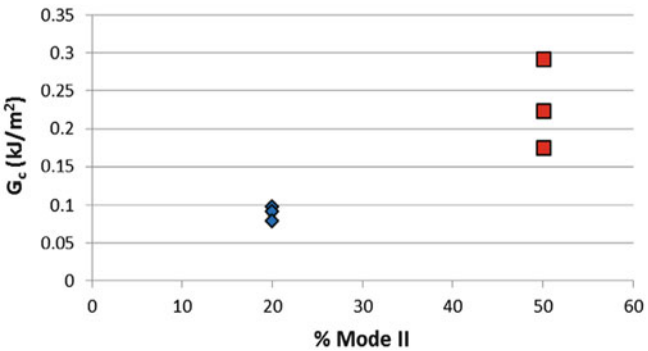

Fig. 6.10 Delamination fracture toughness values for vinyl ester repair resin with partial top ply of parent plate ground off

In all of these three cases (Figs. 6.8, 6.9, and 6.10) the methacrylate adhesive used to bond the hinges to the composite specimens was not able to bear the high shear loads at mode mixity ratio $G_{II}/G = 0.8$ and the hinges came off the specimens before crack initiation. The values of delamination fracture toughness for the mode mixity ratio $G_{II}/G = 0.8$ for these specimens were not recorded. The loads at which the hinges came off were of the order of 1.55 ± 0.15 kN. A smaller thickness of each adherend approximately 2–3 mm may be required for the hinges to be able to bear the high mode II loads. The length L can also be increased in future tests.

Results from the mixed mode G_{II}/G_c ratios of 0.2 and 0.5 (Figs. 6.11 and 6.12) show that specimens repaired with the vinyl ester repair resin exhibit higher delamination fracture toughness values in mixed mode I–mode II testing as compared

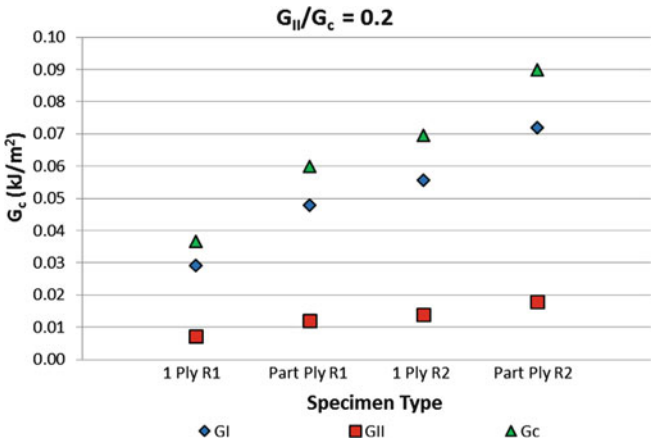

Fig. 6.11 Fracture toughness values for polyester repair resin (R1) and vinyl ester repair resin (R2) at different grinding levels under mode II 20 % loads (1 Ply—Complete top ply ground off, Part Ply—Partial top ply ground off)

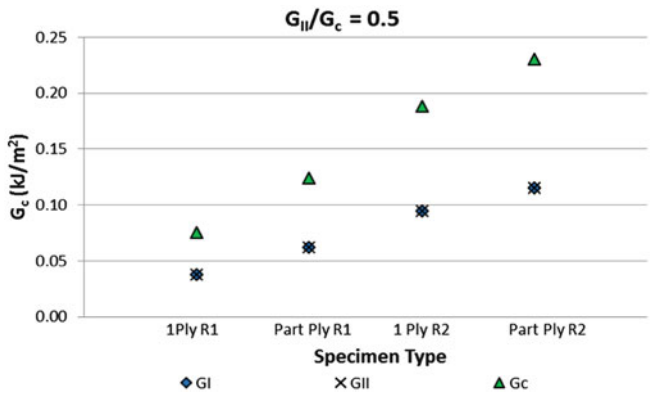

Fig. 6.12 Fracture toughness values for polyester repair resin (R1) and vinyl ester repair resin (R2) at different grinding levels under mode II 50 % loads (1 Ply—Complete top ply ground off, Part Ply—Partial top ply ground off)

to those repaired with the polyester repair resin. In case of both repair resins, specimens repaired with partial top plies of the parent plates ground off have better fracture toughness values than the repairs with the complete top plies of the parent plates ground off.

Images of the fractured surfaces of specimens tested under various mixed mode ratios are shown in Fig. 6.13. The specimens that were repaired with polyester resin and tested with mixed mode ratio $G_{II}/G = 0.2$, do not show significant signs of fiber bridging or effects of mode II loading (Fig. 6.13). In the case of specimens repaired with polyester repair resin and tested with mixed mode ratio $G_{II}/G = 0.5$, there are some signs of plastic deformation of the repair resin (depicted by white regions) under shear loads (Fig. 6.13). For mode II 80 % loads the specimens repaired with polyester repair resin have more pronounced signs of fiber bridging as well as deformation of the repair resin due to shear loads.

The fractured surfaces of all specimens repaired with vinyl ester repair resin show marked regions of fiber bridging and shear deformation (Fig. 6.13, f, h) of the repair resin under mode II loads. This is reflected in the higher fracture toughness values obtained for the vinyl ester repair resin. In mode I testing the fibers in the bridging zone are mainly acted upon by tensile forces and they slow down crack growth. But in the case of high shear loads they break easily, thus letting cracks propagate fast at the bonded interface. Thus even though fiber bridging was present in some cases, propagation fracture toughness values could not be attained for mixed mode I–mode II testing.

6.5 Conclusions

Fracture toughness values of vinyl ester repair resin were evaluated against those for polyester repair resin and it was found that repairs carried out with the former are better than those conducted with the latter repair resin. Furthermore, repairs done after grinding off the top ply of the parent composite part partially provide higher mixed mode I–mode II fracture toughness values as compared to those conducted after grinding off one complete top ply.

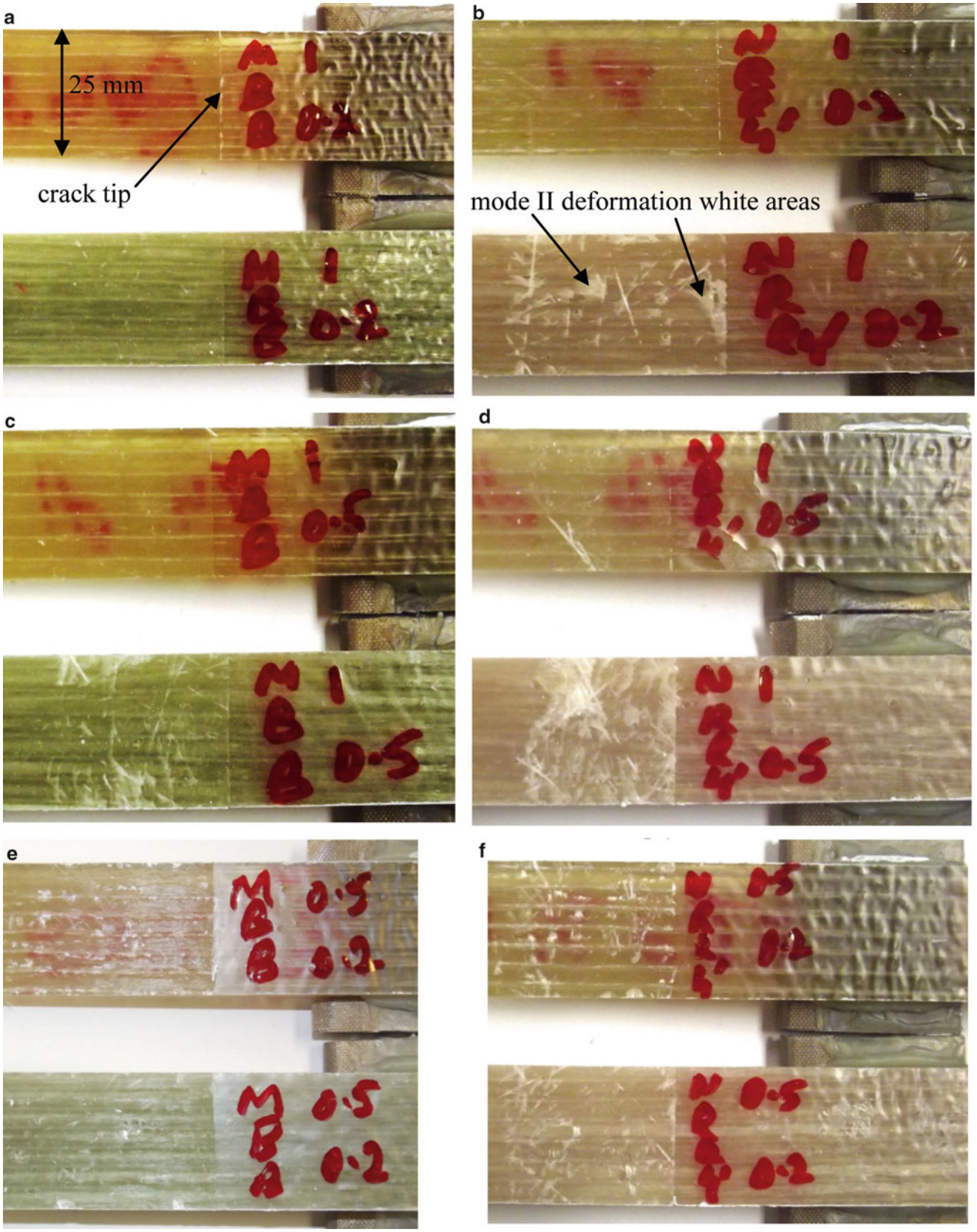

Fig. 6.13 Images of surfaces fractured under different mixed mode I–mode II loads. (**a**) 1 ply R1 $G_{II}/G = 0.2$. (**b**) 1 ply R2 $G_{II}/G = 0.2$. (**c**) 1 ply R1 $G_{II}/G = 0.5$. (**d**) 1 ply R2 $G_{II}/G = 0.5$. (**e**) Partial ply R1 $G_{II}/G = 0.2$. (**f**) Partial ply R2 $G_{II}/G = 0.2$. (**g**) Partial ply R1 $G_{II}/G = 0.5$. (**h**) Partial ply R2 $G_{II}/G = 0.5$. (**i**) 1 ply R1 $G_{II}/G = 0.8$

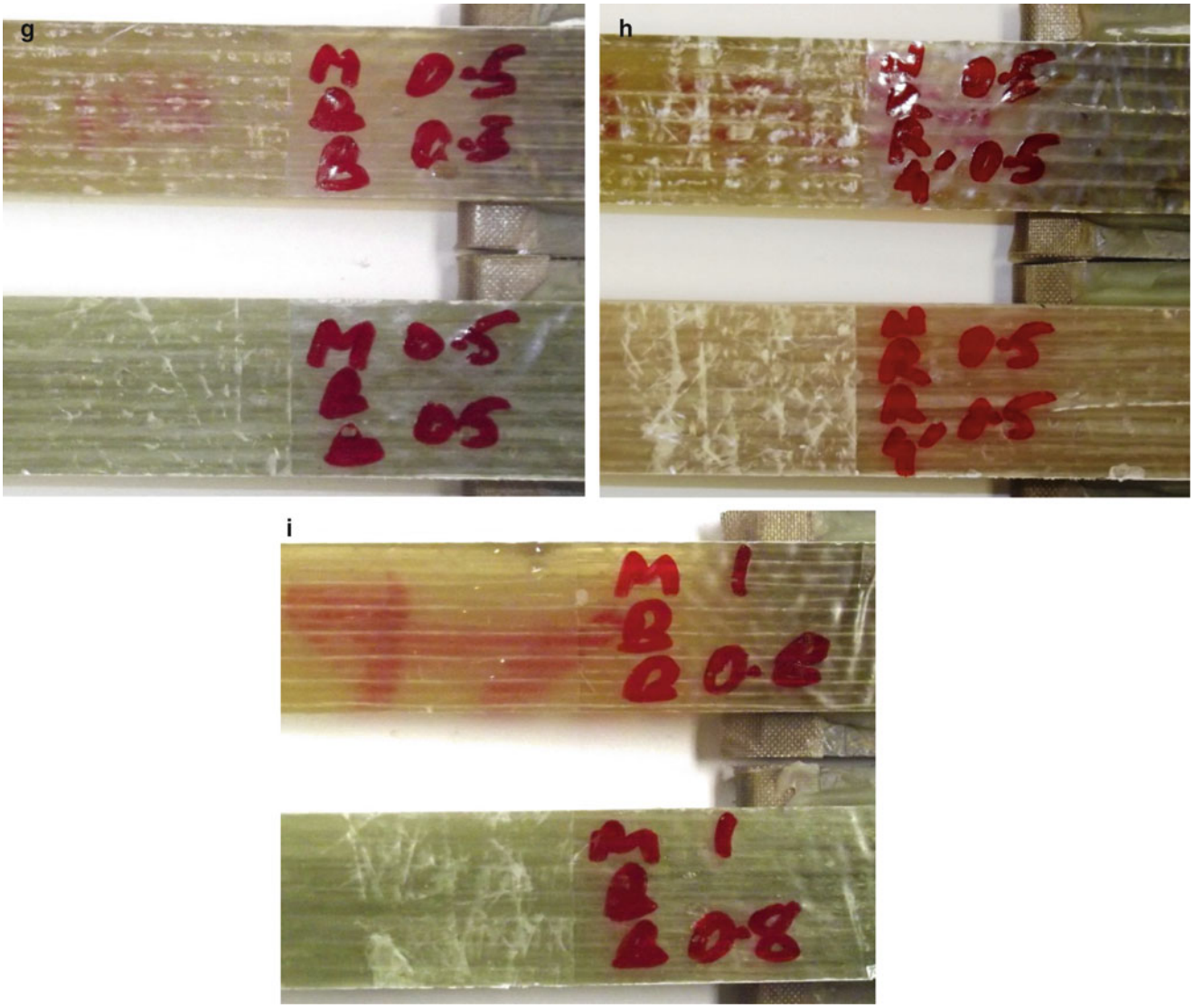

Fig. 6.13 (continued)

Since repairs on wind turbine blades damaged while in service are carried out in the field with the blades still attached to the wind turbine main support, it is difficult to maintain a constant grinding depth. Visual signs, such as reaching the backing of a ply or encountering cross weave while grinding are recorded as markers for gaging the depth ground. Future work is proposed that can involve finding a suitable grinding depth of the top parent ply to achieve optimum fracture toughness and some means to have the top ply ground to that depth consistently every time before repairs are carried out.

Acknowledgements The authors acknowledge financial support of this work by LM Wind Power and the Department of Mechanical Engineering, University of North Dakota.

References

1. ASTM International (2006) Standard test method for mixed Mode I – Mode II interlaminar fracture toughness of unidirectional fiber reinforced polymer matrix composites. ASTM International, West Conshohocken, PA. doi:10.1520/D6671M-06, ASTM D 6671 – 06, www.astm.org
2. Singh S, Partridge IK (1995) Mixed-mode fracture in an interleaved carbon-fibre/epoxy composite. Compos Sci Technol 55(4):319–327, ISSN 0266-3538
3. Naghipour P, Schneider J, Bartsch M, Hausmann J, Voggenreiter H (2009) Fracture simulation of CFRP laminates in mixed mode bending. Eng Fract Mech 76(18):2821–2833, ISSN 0013-7944

4. Feret V, Ghiasi H, Hubert P (2013) Effect of fibre volume fraction on mixed-mode fracture of a fabric carbon/epoxy composite. Appl Compos Mater 20(4):415–429
5. Fan X, Sun Q (2012) Study on mixed-mode interlaminar fracture of laminated composites. Applied Mechanics and Materials 110–116: 1345–1352. doi:10.4028/www.scientific.net/AMM.110-116.1345
6. Benzeggagh ML, Kenane M (1996) Measurement of mixed-mode delamination fracture toughness of unidirectional glass/epoxy composites with mixed-mode bending apparatus. Compos Sci Technol 56(4):439–449, ISSN 0266-3538
7. Ducept F, Davies P, Gamby D (1997) An experimental study to validate tests used to determine mixed mode failure criteria of glass/epoxy composites. Compos A Appl Sci Manuf 28(8):719–729, ISSN 1359-835X
8. Ducept F, Gamby D, Davies P (1999) A mixed-mode failure criterion derived from tests on symmetric and asymmetric specimens. Compos Sci Technol 59(4):609–619, ISSN 0266-3538
9. Ducept F, Davies P, Gamby D (2000) Mixed mode failure criteria for a glass/epoxy composite and an adhesively bonded composite/composite joint. Int J Adhes Adhes 20(3):233–244, ISSN 0143-7496
10. Dharmawan F, Simpson G, Herszberg I, John S (2006) Mixed mode fracture toughness of GFRP composites. Compos Struct 75(1–4):328–338, ISSN 0263–8223
11. Marat-Mendes RM, Freitas MM (2010) Failure criteria for mixed mode delamination in glass fibre epoxy composites. Compos Struct 92(9):2292–2298, ISSN 0263-8223
12. Blake SP, Berube KA, Lopez-Anido RA (2012) Interlaminar fracture toughness of woven E- glass fabric composites. J Compos Mater 46(13):1583–1592
13. Chawla T, Cavalli MN (2011) Fracture testing of simulated FRP repairs. Paper presented at the Conference proceedings of the society for experimental mechanics series, vol. 6, Berlin: Springer, pp. 253–258

Chapter 7
Through Thickness Fracture Behavior of Transversely Graded Ti/TiB Material

Behrad Koohbor, Silas Mallon, and Addis Kidane

Abstract Fracture behavior of a Ti/TiB graded material with a crack perpendicular to the gradient direction was investigated. Three-point bending experiment was conducted and full-field displacement fields were measured on both faces of the specimen, metallic and ceramic-rich surfaces, using 2D digital image correlation technique. Stress intensity factors were calculated using the displacement fields obtained on both faces of the specimen, and were compared to the effective fracture toughness determined from fracture load data. The overall fracture toughness was found to be very close to the stress intensity factor determined using the displacement field on ceramic-rich side. However, the stress intensity factors calculated on both surfaces using the displacement fields, showed different values. In addition, scanning electron microscope observations were performed to examine the fracture surface of the material. It was observed that the crack front is inclined, indicating that the fracture may have initiated in the ceramic side and followed by a very fast propagation to the metallic side.

Keywords Functionally graded materials • Stress intensity factor • Digital image correlation • Transversely graded • Three-point bend

7.1 Introduction

Owing to their unique properties, functionally graded materials (FGMs) have recently been utilized in a wide range of applications. Among all FGMs, special attention has been drawn towards the study of ceramic/metal FGMs due to their potential application in extreme environments. Their quasi-static and dynamic constitutive behavior at different temperature has been studied [1]. One of the limiting factors towards the use of this class of materials is their relatively low fracture resistance [2]. This has triggered extensive research works with the purpose of developing more profound knowledge and understanding about the fracture response of such materials [3–7]. However, the majority of the research performed in this field has been devoted to the study of fracture response of cracked bodies with cracks initiating from one side and propagating trough the gradient direction. Recently, there have been very few studies, investigating the fracture response of transversely graded FGMs, numerically and using model FGM materials [3, 4].

The purpose of the present work is to study the fracture behavior of a Ti/TiB graded material system, more importantly the variation of the stress intensity factor (SIF) across the specimen thickness, i.e. the gradient direction. The DIC technique in conjunction with a crack tip opening displacement (CTOD) analysis were utilized to find the stress intensity factor present at each side of the specimen at the moment of fracture. The results found in this stage were compared to the fracture toughness of the material determined using the far-field load. In addition, fracture surface of the broken specimen was also examined to give a better understanding of the fracture response of the utilized material system.

B. Koohbor (✉) • S. Mallon • A. Kidane
Department of Mechanical Engineering, University of South Carolina, 300 Main Street, Columbia, SC 29208, USA
e-mail: koohbor@email.sc.edu

J. Carroll and S. Daly (eds.), *Fracture, Fatigue, Failure, and Damage Evolution, Volume 5: Proceedings of the 2014 Annual Conference on Experimental and Applied Mechanics*, Conference Proceedings of the Society for Experimental Mechanics Series,
DOI 10.1007/978-3-319-06977-7_7,

Table 7.1 Composition and material properties of the Ti/TiB material system [2]

Layer no.	Ti vol% (TiB vol%)	Layer thickness (mm)	E (GPa)	ν
1	100 (0)	0.2032	106	0.340
2	85 (15)	0.3810	170	0.278
3	70 (30)	0.3810	227	0.238
4	55 (45)	0.3810	262	0.205[a]
5	40 (60)	0.3810	289	0.177[a]
6	25 (75)	0.3810	303	0.152
7	15 (85)	1.0668	316	0.140

[a]Interpolated using chemical composition and the rule of mixture

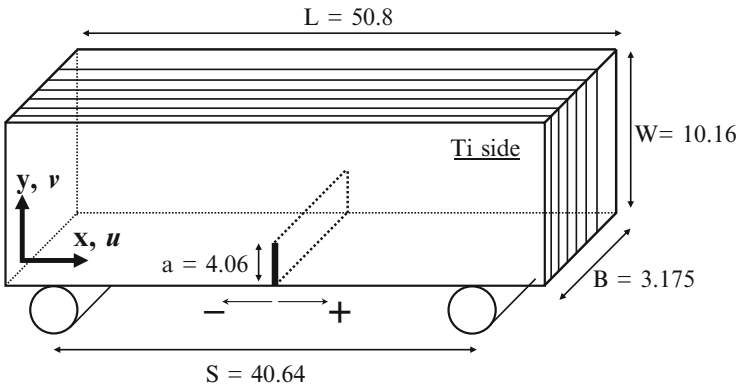

Fig. 7.1 Three-point bend test specimen used in this work. Dimensions are in mm

7.2 Materials and Specimen Geometry

A 3.175 mm thick seven-layered Ti/TiB FGM specimen fabricated by BAE systems was examined in this work. The seven layers ranged from pure titanium on one side to 85 % TiB/15 % Ti on the other, with no distinct interface layers. The properties of the examined material are listed in Table 7.1. Three-point bend test specimens were extracted from the stock using EDM. An initial notch was also cut on the middle section of the specimen using EDM wire of 0.0508 mm diameter making the initial crack front parallel to the gradient direction. An schematic view of the test specimen is shown in Fig. 7.1.

7.3 Experimental Procedure

To study the fracture response of the material, quasi-static three-point bend experiments were performed in room temperature and under displacement control condition at a constant load tip velocity of 0.25 mm/min. The full-field displacement distribution on each side of the specimen was obtained using 2D DIC technique during the loading stage. The cameras located at each side of the specimen (see Fig. 7.2) were synchronized prior to the onset of the experiments, to make it possible to study the deformation history at each side simultaneously. The load cell was also synchronized with the cameras. Images of $1{,}024 \times 1{,}024$ pixel resolution were captured during the loading stage, and were then exported to the software Vic-2D® for further analysis. In this software, a 19×19 pixel correlation window with 3-pixel step size was used to analyze the data.

7.4 Stress Intensity Factor

In the present work, the stress intensity factor (SIF) present at the moment of crack initiation was calculated using two different approaches. The far-field load along with the specimen geometry was first utilized to determine the stress intensity factor based on the linear elastic fracture mechanics formulation proposed for the case of three-point bend test as [1]:

$$SIF = \frac{P}{B\sqrt{W}} f(a/W) \tag{7.1}$$

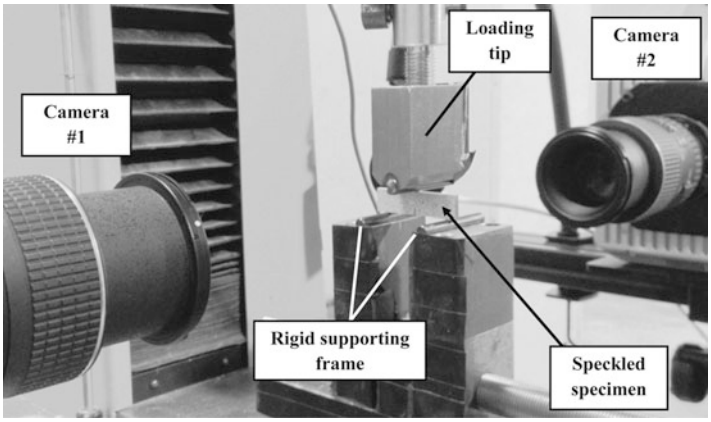

Fig. 7.2 Experimental setup showing the camera configuration

Where, P is the critical load at fracture. B and W are specimen thickness and width, respectively. a denotes the initial crack length and $f(a/W)$ is the geometric factor defined in [1].

The other approach to calculate the SIF utilizes the opening displacement component obtained from DIC, to calculate the stress intensity factor based on a crack tip opening displacement (CTOD) criterion. The CTOD approach is utilized on each side of the specimen to find the corresponding SIF, and to compare these local SIF's with that obtained from the far-field load measurement.

Horizontal and vertical displacement components in a general cracked body under mixed mode fracture (Mode-I and II) conditions can be expressed as [8]:

$$u_x = \frac{K_I}{\mu}\sqrt{\frac{r}{2\pi}}\cos\frac{\theta}{2}\left[\frac{\kappa-1}{2}+\sin^2\frac{\theta}{2}\right]+\frac{K_{II}}{\mu}\sqrt{\frac{r}{2\pi}}\sin\frac{\theta}{2}\left[\frac{\kappa+1}{2}+\cos^2\frac{\theta}{2}\right] \tag{7.2}$$

$$u_y = \frac{K_I}{\mu}\sqrt{\frac{r}{2\pi}}\sin\frac{\theta}{2}\left[\frac{\kappa+1}{2}-\cos^2\frac{\theta}{2}\right]+\frac{K_{II}}{\mu}\sqrt{\frac{r}{2\pi}}\cos\frac{\theta}{2}\left[\frac{1-\kappa}{2}+\sin^2\frac{\theta}{2}\right] \tag{7.3}$$

Where μ is the material's shear modulus, and r and θ and are radial and angular coordinates of an arbitrary point in the vicinity of the crack tip. κ is a parameter dependent on the material's Poisson's ratio written as:

$$\kappa = \begin{cases} (3-\upsilon)/(1+\upsilon) & \text{Plane-stress} \\ 3-4\upsilon & \text{Plane-strain} \end{cases} \tag{7.4}$$

The CTOD of the crack in Mode-I can be expressed as [8]:

$$\Delta u = u\left(r_c, 0^+\right) - u\left(r_c, 0^-\right) = \frac{\kappa+1}{\mu}\sqrt{\frac{r_c}{2\pi}}K_I \tag{7.5}$$

Here, superscripts "+" and "−" denote the displacement component at right and left crack surfaces, respectively (see Fig. 7.1). r_c is also the radial distance behind the crack tip.

7.5 Results and Discussion

Horizontal and vertical components of the displacement on metal and ceramic-rich sides were obtained from DIC. The opening displacement components on ceramic and metal sides as a function of the far-field load are shown in Fig. 7.3. The crack tip opening displacement components at either side increase almost identically up to a load magnitude of about 200 N, and diverge from that point on. A similar observation was made in the far-field load curve, where a gradual change in the slope of then load curve takes place at about 200 N load, as shown in Fig. 7.4. This could be attributed to the formation of microcracks within the more brittle layers during the loading stage.

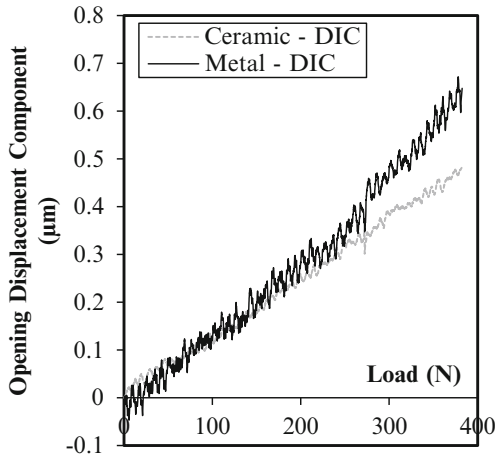

Fig. 7.3 Crack-tip opening displacement on both sides of the specimen as a function of far-field load

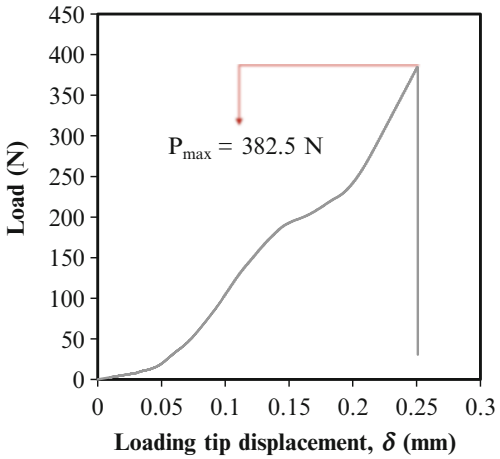

Fig. 7.4 Typical far-field load as a function of loading tip displacement

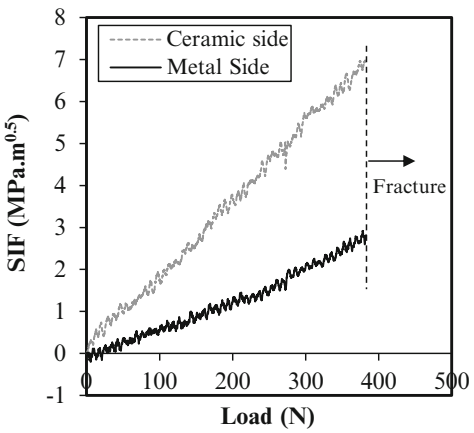

Fig. 7.5 Evolution of the stress intensity factors during the loading stage on the ceramic and metallic surfaces

To determine the value of SIF, the approach explained earlier was utilized. In order to avoid any effects of near crack tip non-linearity, a point 1 mm behind the original crack tip was taken and the SIF values at each side were evaluated accordingly. The evolution of the SIF values at each side as a function of far-field load has been depicted in Fig. 7.5. The stress intensity factors at the moment of fracture calculated from the displacement fields on the ceramic and metal side are 7.04 and 2.92 MPa$\sqrt{\text{m}}$, respectively. It should be emphasized that the values reported here do not represent the fracture toughness of either metal or ceramic, rather these are merely the stress intensity factors present at the moment of crack propagation at each side of the examined FGM.

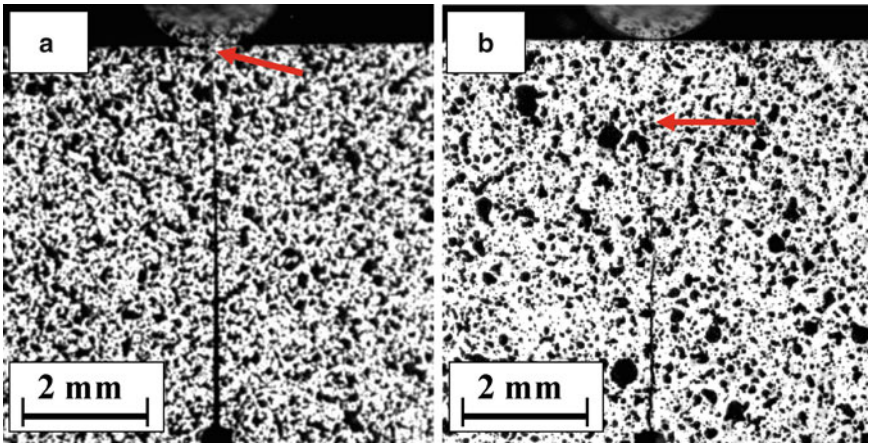

Fig. 7.6 Propagated crack on (**a**) ceramic-rich and (**b**) metallic sides of the examined material, at the time of fracture (maximum load). The crack tip has been marked

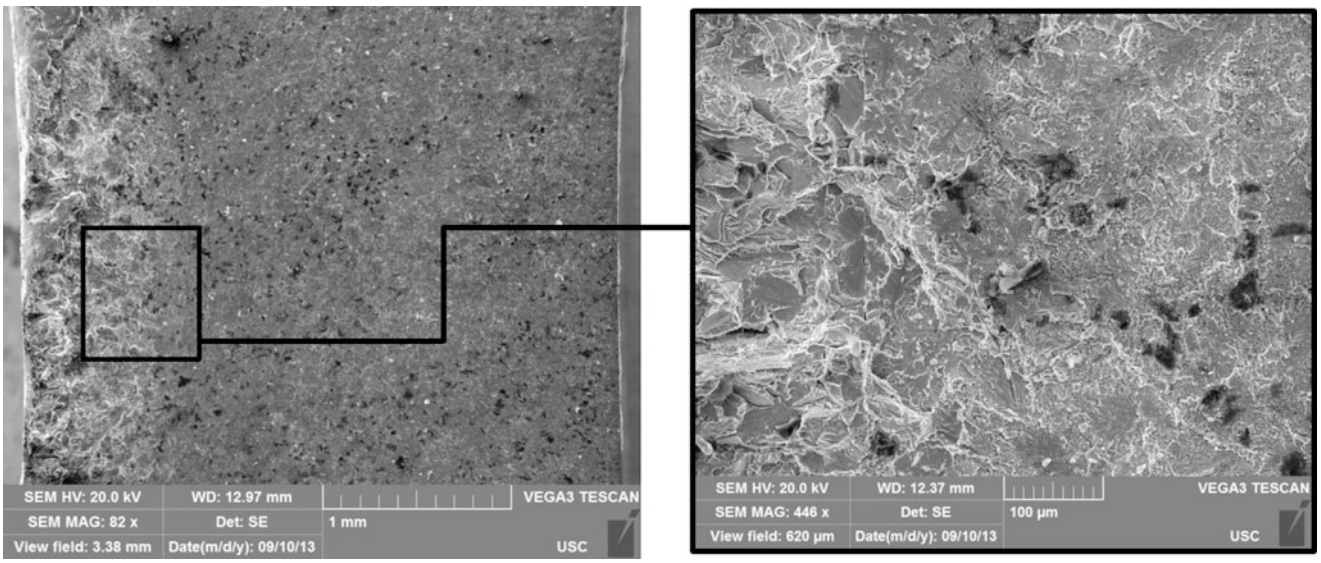

Fig. 7.7 Fracture surface image taken from the graded specimen, showing the quasi-cleavage fracture surface on the Ti side

The effective fracture toughness of the specimen was also determined using the recorded far-field load in conjunction with the mathematical formulation mentioned earlier, and a value of 6.82 MPa$\sqrt{\text{m}}$ was obtained. This value lies between the SIF values determined on the specimen sides.

An interesting point in this regard is that the magnitude of the material's fracture toughness is very close to the stress intensity factor obtained on the ceramic side. It should be noted that in the case of transversely graded materials, although the material is toughened by its metallic component, the overall fracture toughness will still be governed by the brittle nature of the ceramic components. This can be observed by tracking the crack propagation at two sides of the specimen. As shown in Fig. 7.6, the crack first initiates on the ceramics side leaving a very thin ligaments in the metallic side, which eventually leads to a complete fracture.

The fracture surface of the graded specimen exhibits completely different fracture morphology across the thickness of the specimen, as shown in Fig. 7.7. The SEM images illustrate a quasi-cleavage fracture surface on the metal side, indicating that a slight plastic deformation might have taken place on this side [9]. The observed surface behavior remarkably changes to a brittle fracture surface in the ceramic-rich layers.

Acknowledgement The authors would like to thank Dr. Sandeep Abotula for his help during the experiments.

References

1. Kidane A, Shukla A (2008) Dynamic constitutive behavior of Ti/TiB FGM under thermo-mechanical loading. J Mater Sci 43:2771–2777
2. Kidane A, Shukla A (2010) Quasi-static and dynamic fracture initiation toughness of Ti/TiB layered functionally graded material under thermo-mechanical loading. Eng Fract Mech 77:479–491
3. Kommana R, Parameswaran V (2009) Experimental and numerical investigation of a cracked transversely graded plate subjected to in plane bending. Int J Solids Struct 46:2420–2428
4. Wadgaonka SC, Parameswaran V (2009) Structure of near-tip stress field and variation of stress intensity factor for a crack in a transversely graded material. J Appl Mech 76:1–9
5. Hill MR, Carpenter RD, Paulino GH, Munir Z, Gibeling JC (2002) Fracture testing of a layered functionally graded material. In: Salem JA, Quinn GD, Jenkins MG (eds) Fracture resistance testing of monolithic and composite brittle materials. American Society for Testing and Materials, West Conshohocken, PA
6. Kidane A, Chalivendra V, Shukla A, Chona R (2010) Mixed-mode dynamic crack propagation in graded materials under thermo-mechanical loading. Eng Fract Mech 77(14):2864–2880
7. Kidane A, Chalivendra V, Shukla A (2010) Thermo-mechanical stress fields and strain energy associated with a mixed-mode propagating crack. Acta Mech 215:57–69
8. Ma F, Deng X, Sutton M, Newman JC (1999) A CTOD-based mixed mode fracture criterion. In: Miller KJ, McDowell DL (eds) Mixed-mode crack behavior. American Society for Testing and Materials, West Conshohocken, PA, pp 86–110
9. Hull D (1999) Fractography – obsrving, measuring and interpreting fracture surface topography. Cambridge University Press, Cambridge, UK

Chapter 8
Coalescence and Growth of Two Semi-Elliptical Coplanar Cracks in API-5L Grade B Steel

Abdallah Al Tamimi and Mohammad Modarres

Abstract The purpose of this research is to investigate the interaction of two adjacent cracks under cyclic loading. A series of tests at different loads and frequencies were conducted under uniaxial constant amplitude fatigue loads on API-5L grade B steel samples. Crack growth rate of two initial semi-elliptical cracks was investigated. Marker band testing technique was employed to study the crack growth rate before and after interaction. Real time optical microscopy was used to observe crack coalescence on the specimens' surface. Moreover, SEM analysis of the fracture surface was performed for comprehensive understanding of cracks behavior.

Keywords Multi-site damage • Cracks coalescence • Cracks interaction • Marker bands • Carbon steel

8.1 Introduction

Oil and gas transport through piping systems is a vital cog in the oil and gas industry. It is considered as an essential subsystem in the overall oil and gas transport system. Based on the nature of its functions, a combination of straight pipes, pipe-bends, dissimilar welded joints and many other parts are all attached to each other. This system operates under severe conditions: Internal pressure, cyclic load, internal and external harsh environments. The combination of these different parameters can lead to a potential increase in the risk of damage and unexpected fractures. In fact pressure cycling has contributed to fatigue failures in crude oil transmission pipelines. For example, the July 2002 rupture of a 34-in. pipeline near Cohasset, MN was due to fatigue cracking [1].

However, the cost of pipeline replacement, maintenance and inspection has meant that there are now aging systems whose continued operation requires special analysis and improved crack detection techniques. This demands continuous safety and performance improvement toward increasing service life of pipeline networks, maintenance and cost control. Additionally, this necessitates stronger prevention and control measures to avoid the likelihood of structural failures linked to fatigue especially multi-site damage (MSD) which is caused by multiple cracks interacting and forming a bigger crack. Such cracks originate from multiple sources of damage including preexisting flaws and dents, surface deformities caused by mechanical forces, pitting,

The service life of a transport pipeline in the oil and gas industry can potentially introduce MSD which may jeopardize the structural integrity of the transport system. A safety assessment of a structure that contains neighboring cracks in close proximity must take crack interaction into consideration. Inspection intervals are usually directed at the presence of a single crack, but may be inadequate in the presence of MSD. In reality, during routine inspections, different types of defects are found in oil and gas transport pipelines varying between irregularly shaped defects and adjacent defects. But these irregularities in shape make it hard to assess and model these defects.

A. Al Tamimi (✉)
Center of Risk and Reliability, University of Maryland, College Park, MD 20742, USA

Abu Dhabi National Oil Company, ADNOC, Abu Dhabi, UAE
e-mail: altamimi@umd.edu

M. Modarres
Center of Risk and Reliability, University of Maryland, College Park, MD 20742, USA

J. Carroll and S. Daly (eds.), *Fracture, Fatigue, Failure, and Damage Evolution, Volume 5: Proceedings of the 2014 Annual Conference on Experimental and Applied Mechanics*, Conference Proceedings of the Society for Experimental Mechanics Series,
DOI 10.1007/978-3-319-06977-7_8,

In this research, we investigate the coalescence of two co-planar semi-elliptical cracks in specimens subjected to fatigue loading. It is intended to develop a more realistic probabilistic life prediction model that accounts for cracks interaction and more accurately assesses crack growth.

8.2 Background Information

According to Bayley [2], the process of the two independent cracks growing together and joining to form one crack is known as crack interaction and coalescence. The interaction between adjacent cracks is evidence that adjacent cracks can impact the growth rate of each other.

Numerous researchers have studied cracks interaction, including: Harrington [3], Leek and Howard [4–6], Soboyejo [7], Kishimoto [8], Twaddle [9], and O'Donoghue [10]. Most of their research was directed toward understanding the cracks coalescence mechanism of two coplanar surface cracks. When two coplanar and adjacent surface cracks grow by fatigue there are four stages to their interaction as illustrated by Leek and Howard [4] and DeBartolo and Hillberry [11]:

1. The separate phase, when the separating distance (S in Fig. 8.1), between the cracks is large enough for interaction to be completely negligible
2. Interaction, pre-coalescence phase: neighboring cracks are independent and behave as an isolated crack. The interaction between the two cracks increases when the crack tips approach each other.
3. Re-characterization, the coalescence phase: the inner tips of the neighboring cracks come into contact forming a single concave crack. The crack grows more at the concave position, leading to the disappearance of the concave front. This occurs when the two cracks are close enough to be considered a single crack, and they are re-characterized as one. At the end of this stage, there is one crack present.
4. The post-coalescence phase: begins immediately after the two cracks are re-characterized as one and ends when the crack has resumed a uniform shape and continues to propagate as it did before interaction began.

Figure 8.1 shows two neighboring cracks and illustrates their dimensions where, a, is crack depth, c is the crack radius, t_{wall} is the thickness and S and L are the separation distance between two cracks.

8.3 Experimental Procedure and Material

The material used in this study is API-5L Grade B, a material widely used in oil and gas transport pipelines. This grade of carbon steel is used by some oil transport companies because of its high corrosion resistance.

8.3.1 Material Properties

An EDX analysis was done to determine the elemental composition of the test coupons. Results are illustrated in Fig. 8.2. Moreover, a tensile test on an un-notched specimen was performed to determine the mechanical properties of the material. Figure 8.3 presents the stress-strain curve obtained from the tensile test. The yield and the ultimate strength of the material are listed in Table 8.1.

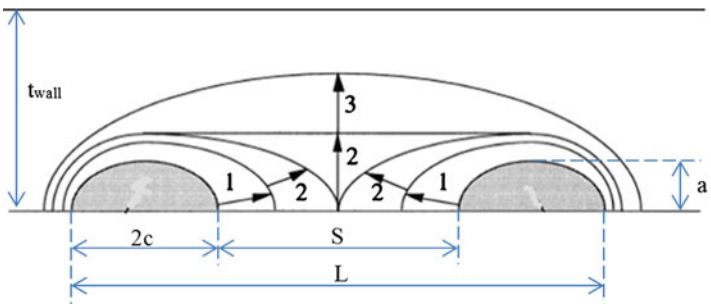

Fig. 8.1 Stages of crack growth: *1*: cracks interaction *2*: cracks re-characterization *3*: cracks coalescence [11]

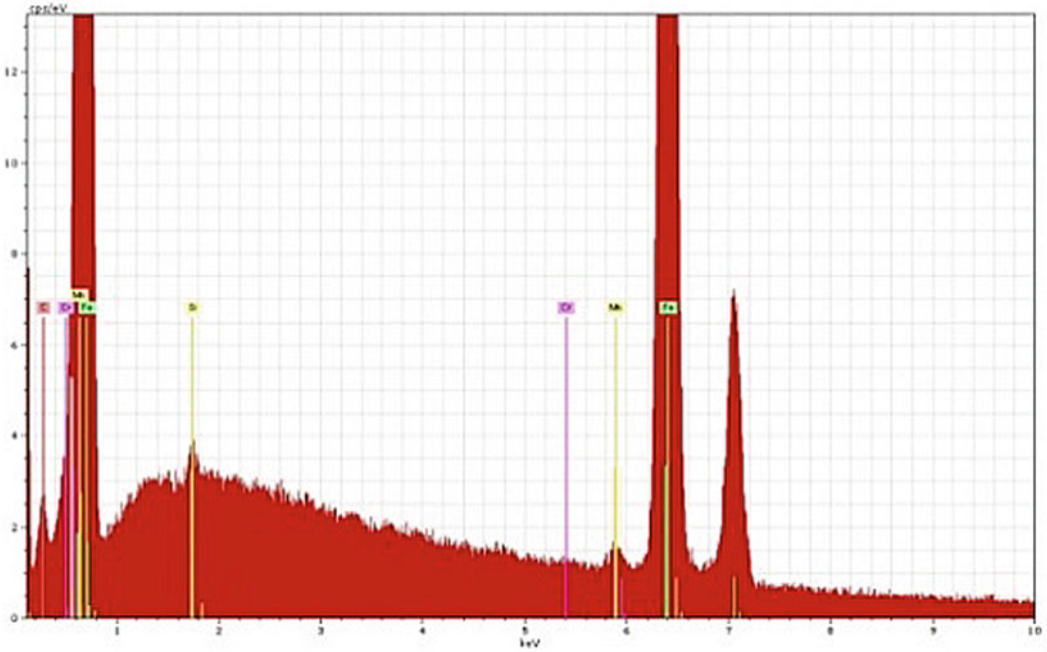

Spectrum: 3055

El	AN	Series	unn. C [wt.%]	norm. C [wt.%]	Atom. C [at.%]	Error [%]
Fe	26	K-series	94.81	97.85	95.54	2.8
Mn	25	K-series	1.04	1.07	1.07	0.1
C	6	K-series	0.57	0.59	2.67	0.1
Cr	24	K-series	0.25	0.25	0.27	0.1
Si	14	K-series	0.23	0.24	0.46	0.0
		Total:	96.90	100.00	100.00	

Fig. 8.2 Elemental composition of the material

Fig. 8.3 Stress-Strain curve for API-5L grade B

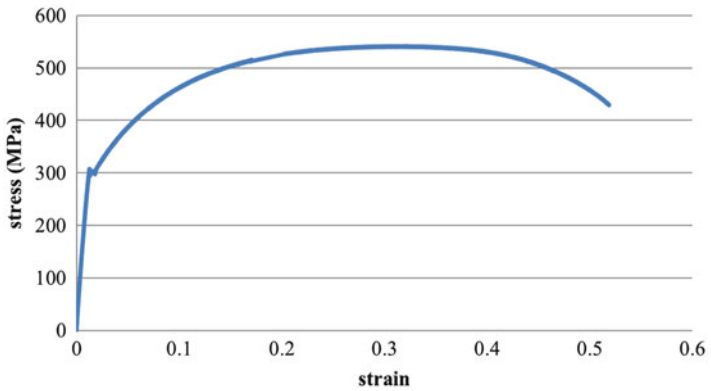

Table 8.1 Mechanical properties of API-5L grade B

Yield strength (MPa)	329
Ultimate strength (MPa)	541

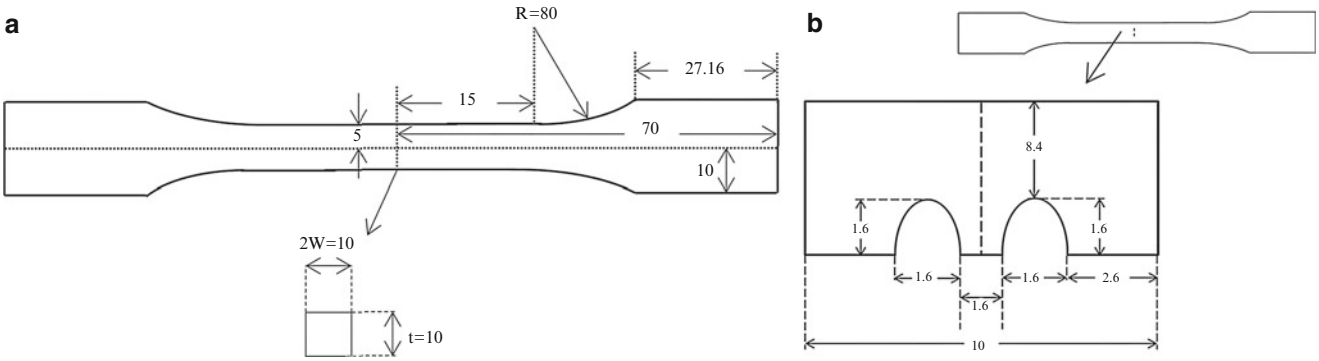

Fig. 8.4 (**a**) Test specimen geometry (**b**) notches geometry, all dimensions are in mm

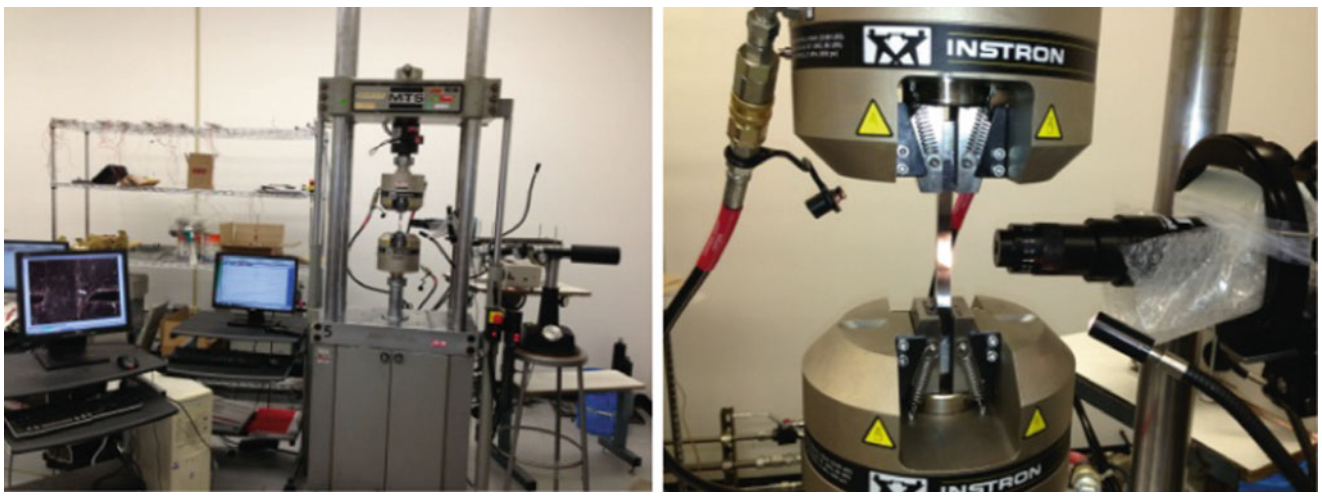

Fig. 8.5 Experimental setup

8.3.2 Specimen Preparation and Geometry

Specimens were manufactured from an actual pipeline that was previously used in the oil and gas industry. Specimens are dog bone shaped following the ASTM E466-07, Standard Practice for Conducting Force Controlled Constant Amplitude Axial Fatigue Tests of Metallic Materials. Figure 8.2a shows the geometry and dimensions of the specimen. Two initial cracks were machined on the sample using the electric discharge machining (EDM) technique. The two cracks are identical, semi-elliptical and co-planar. The notches have a thickness of 0.1 mm, to assure a co-planar growth of the cracks which leads to an idealized interaction between the two cracks. Figure 8.4 illustrates the initial cracks, notches, geometry and dimensions considered for the fatigue experiments.

8.3.3 Test Procedure

Experiments were carried out at room temperature in air. An MTS fatigue-testing machine with capacity of 100 kN in tension and compression and frequency range up to 30 Hz was used. Figure 8.5 shows the testing setup. An optical microscope was also used to monitor the crack coalescence on the surface. The microscope is equipped with a camera to capture and save images of the specimen surface as the crack grows. Experiments are performed at constant amplitude, stress controlled cyclic loading. Frequencies of 0.2 and 2 Hz were chosen for the loadingcyclics. Table 8.2 shows the fatigue testing conditions:

The cycles consist of fatigue loading blocks and marker blocks. The marker blocks are primarily used to investigate the crack growth rate. This will shed light on the mechanism of interaction between the two cracks. The marker block consists of load cycles with the same maximum stress applied as in fatigue block; however, the minimum stress was increased to 80 %

Table 8.2 Testing conditions

Loading cycles				Marker band cycles				
Stress (MPa)				Stress (MPa)				
Max	Min	Loading ratio	# of cycles	Max	Min	Loading ratio	# of cycles	Frequency (Hz)
270	27	0.1	13,000	270	215	0.8	2,000	2
280	28			280	220			0.2
280	28			280	220			2
290	29			290	230			0.2
290	29			290	230			2

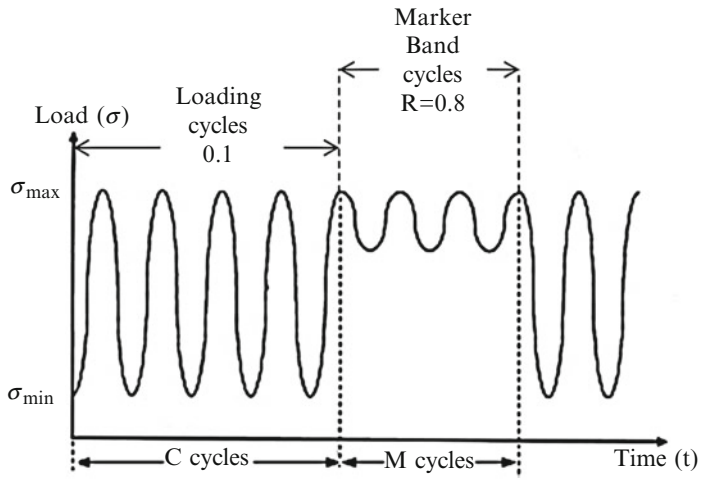

Fig. 8.6 Loading pattern with the marker band loads [12]

of the maximum stress. According to [12], it was observed that marking block with high stress ratio yields a better marking impression which is of better visibility. A typical loading ratio used in marker blocks varies from 0.5 to 0.8 (Fig. 8.6).

According to [13], one of the methods to determine the crack length at different numbers of cycles along with monitoring the fatigue crack front history after testing is to use the marker bands technique. A selective marking of the fatigue surface could do this with a coded marker bands generated by applying a series of fatigue under-loads predetermined intervals.

Also, as stated by [13], the marker bands are groups of microscopic striations that when generated in the proper fashions are readily identifiable by optical and scanning electron microscopy.

8.4 Results and Discussion

There are many factors affecting crack growth including the type of stresses affecting the structure, microstructure and the environment. Figure 8.7 illustrates different factors that affect fatigue crack growth in different fatigue stages.

When neighboring surface cracks are in close proximity, they can interact and grow, achieving what is called cracks coalescence. This phenomenon adds significant complications to the crack growth analysis. Neighboring cracks interaction and coalescence lower the fatigue life of structures and components. Life decrease with increasing cracks density which results in interactions among different cracks (Fig. 8.8).

8.4.1 Surface Crack Monitoring

Measurements of the surface crack growth around the two cracks during the tests were recorded. A real-time microscopy method was employed during the fatigue tests to keep a record of the surface crack growth both between the two cracks and near the sample edge. Figure 8.9 shows the gradual interaction between the two cracks until they achieve coalescence. However, Fig. 8.10 shows the crack on the right growing towards the sample edge.

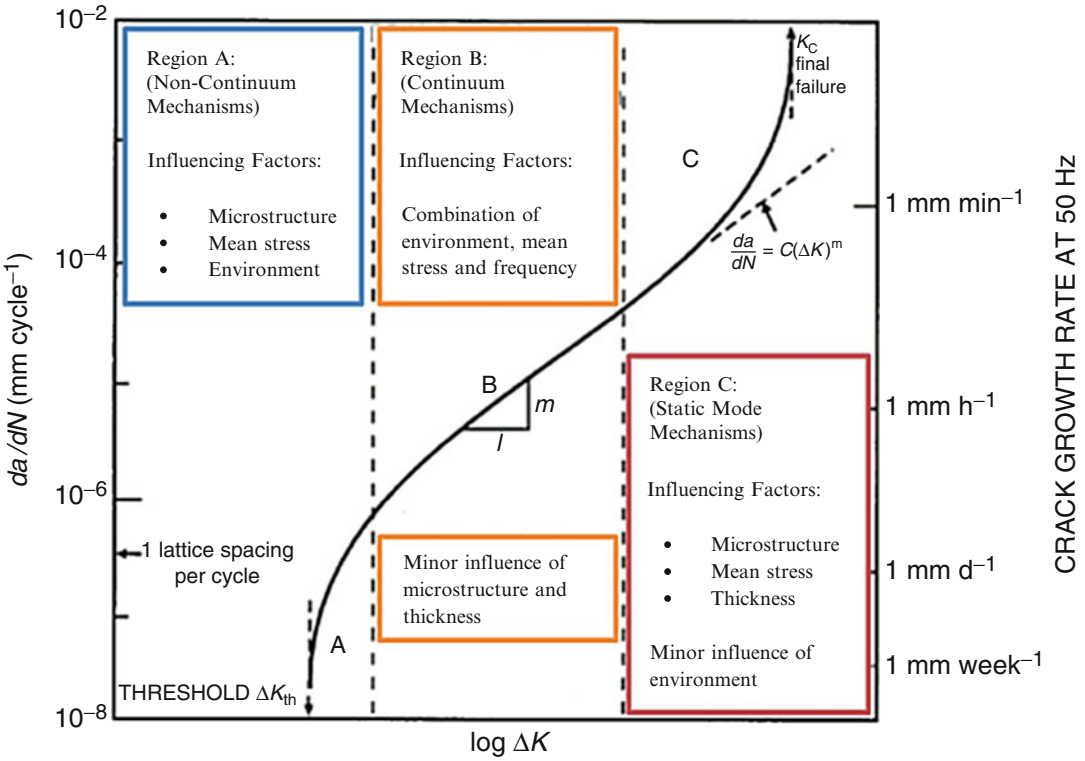

Fig. 8.7 The typical variation in fatigue-crack growth rates da/dn, as a function of the applied stress-intensity range ΔK in metallic materials and the influencing factors in each crack growth regime [14]

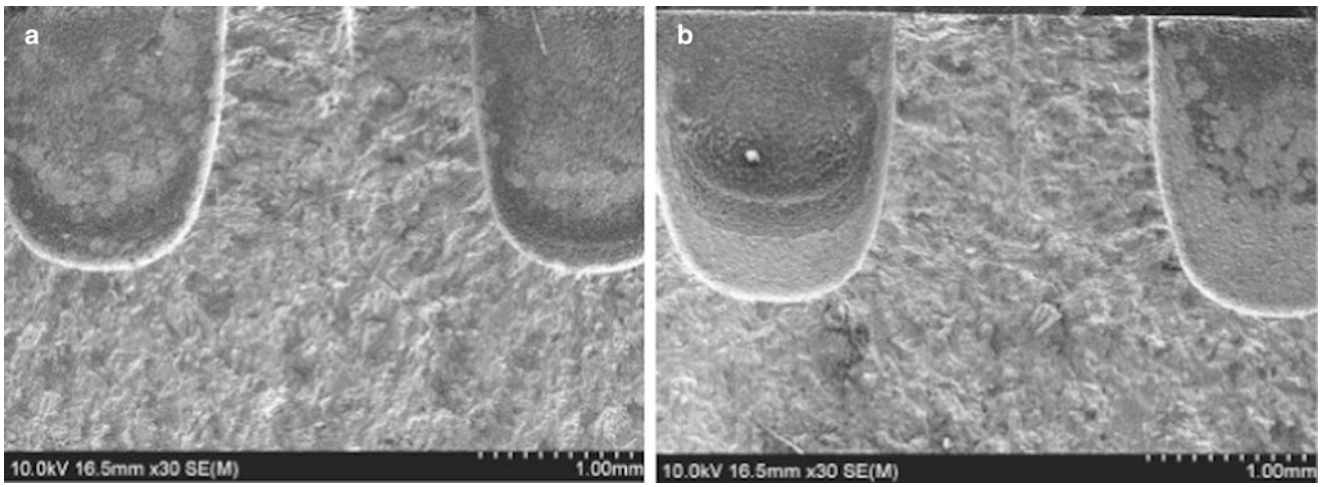

Fig. 8.8 SEM image of the fracture surface under an axial stress of 280 MPa, (**a**) 0.2 Hz (**b**) 2 Hz

One main conclusion drawn was that the surface crack growth rate between the two cracks keeps increasing as result of the cracks interaction effect on the stress intensity factor along the crack tips. As the two surface cracks approaches each other, the stress intensity factor at the inner crack tips increases leading to an increasing crack growth rate. On the other hand, Fig. 8.10 shows the surface crack growth rate after coalescence and until failure. A sudden change in the surface crack behavior was noticed after cracks coalescence. The surface crack growth increases rapidly until it gets closer to the sample edge where the sample corner edge effect on stress intensity factor becomes effective. This effect leads to an increasing crack growth rate as the crack propagates toward the sample edge. The surface crack growth was plotted versus the number of cycles for different stresses and frequencies as illustrated below (Table 8.3):

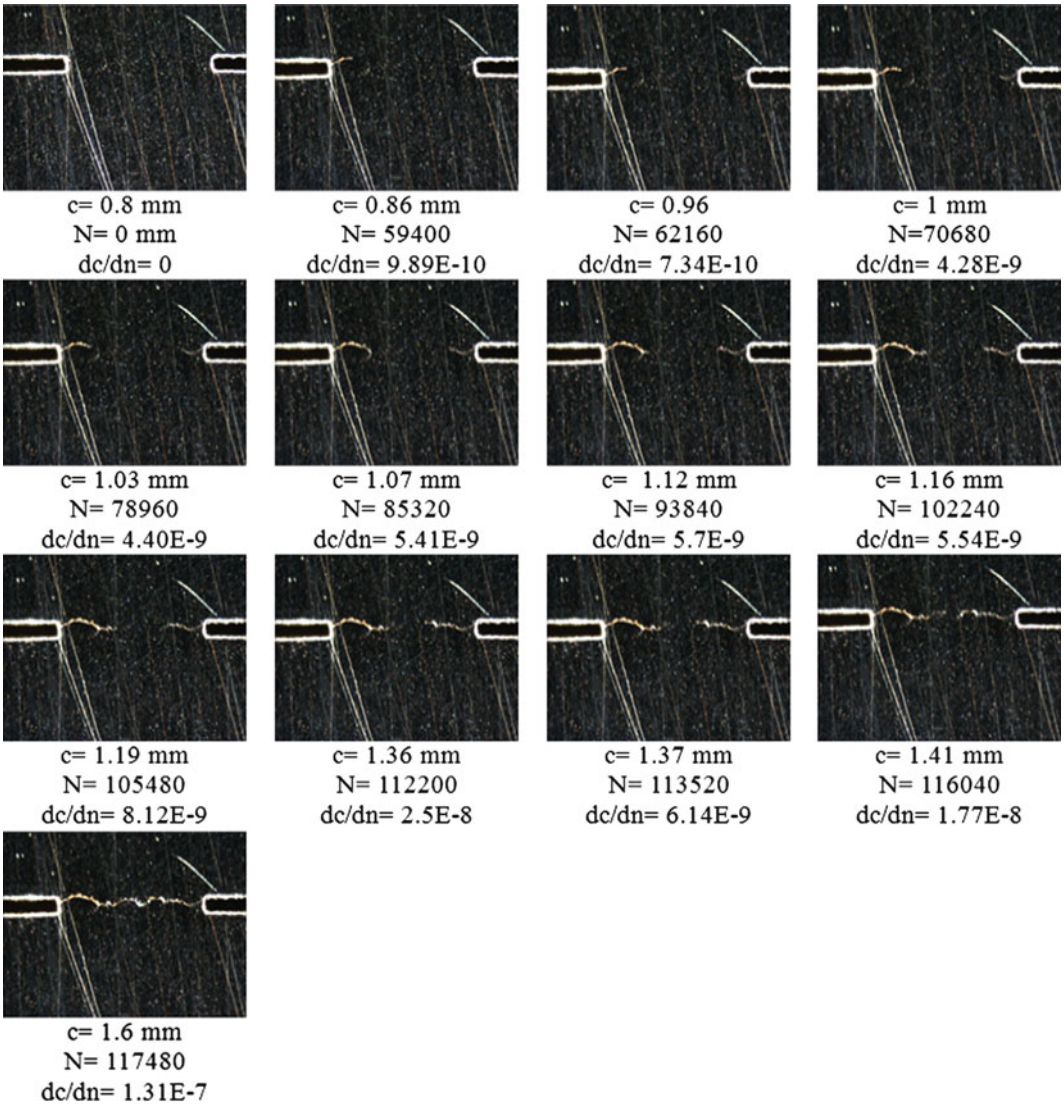

Fig. 8.9 Surface crack growth before coalescence, σ = 270 MPa, f = 2 Hz

The red data points, illustrated in Fig. 8.11, show the surface crack measurements before coalescence. Contrariwise, the green data points show the surface crack growth measurements after coalescence. The graph shows that higher stresses shorten the fatigue life dramatically. Moreover, it shows a slight effect of frequency. Further investigations are required to understand the effect of frequency on the fatigue life of steel materials.

8.4.2 Crack Depth Monitoring

In order to find the depth crack growth rate, the marker bands technique was used. SEM fractography was performed for a closer look at the marker bands as illustrated in Fig. 8.12:

Moreover, Fig. 8.13 shows the fracture surface of two fatigued samples. Different contours could be seen on the surface as a result of the continuously changing loading ratio during the fatigue process. Different materials could behave differently

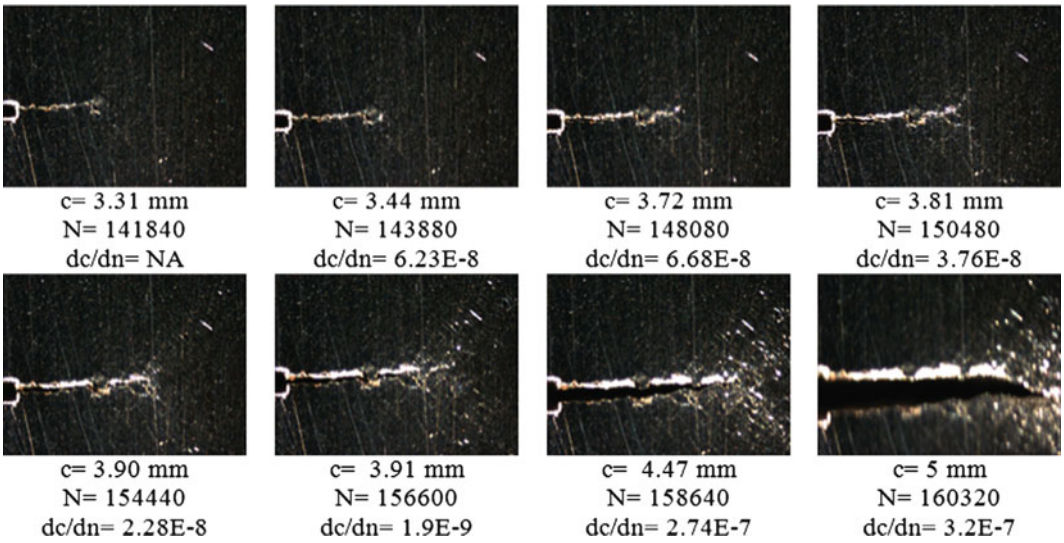

Fig. 8.10 Surface crack growth after coalescence, σ = 270 MPa, f = 2 Hz

Table 8.3 Cycles to failure vs. frequency

Frequency (Hz)	Cycles to failure
0.2	117,140
2	107,980

Fig. 8.11 Surface crack length vs. number of cycles, S = σ(MPa), F(Hz)

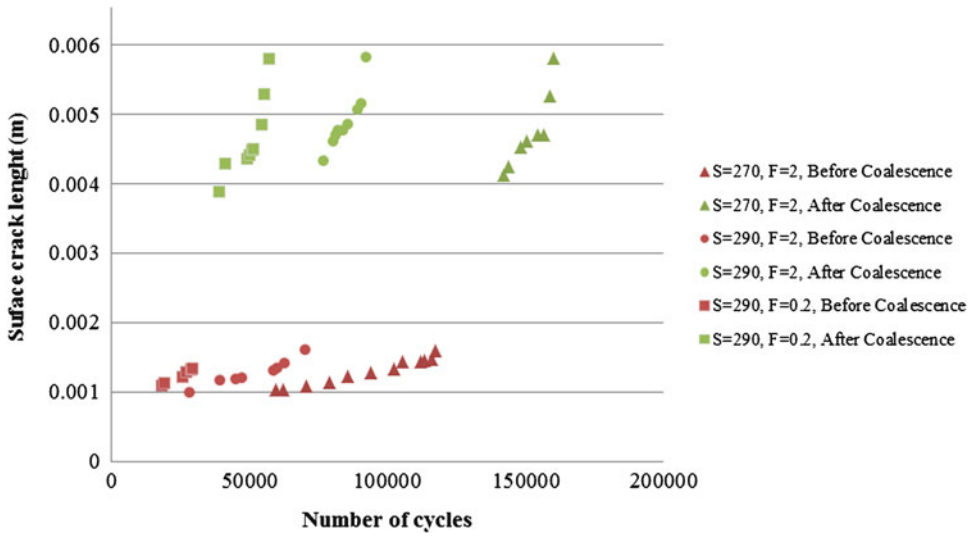

in this kind of tests. API-5L grade B showed high ductility making it harder to see the marker band contours on the fracture surface. For that reason, image processing was required to analyze the fracture surface and observe the marker bands. Image processing software, Image J, was used to analyze the pictures taken for the failed samples cross sections.

This kind of fracture surface analysis allowed finding the crack depth at different numbers of cycles and at different stages of the coalescence process. This led to constructing a da/dN vs. ΔK curve as illustrated in Fig. 8.14.

Figure 8.15 shows the crack depth growth behavior during the fatigue processes. A mild increase in crack depth was observed before the two cracks coalesced. During the cracks interaction processes, a continuously increasing growth rate could be noticed leading to a sudden failure after the complete coalescence of the two cracks.

Performing the same experiment at different stresses, frequencies and crack geometries would allow collecting enough information that could be used to model the phenomena probabilistically. This would be the next step of this research.

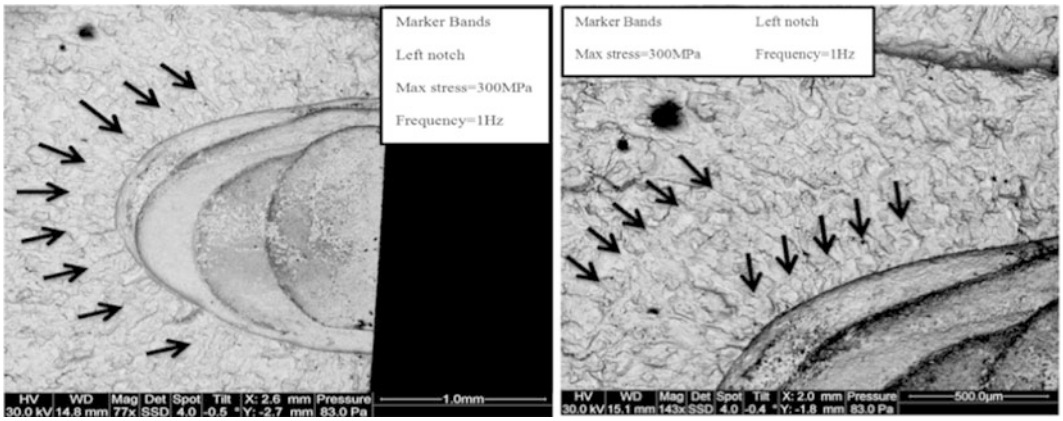

Fig. 8.12 Marker bands SEM illustration

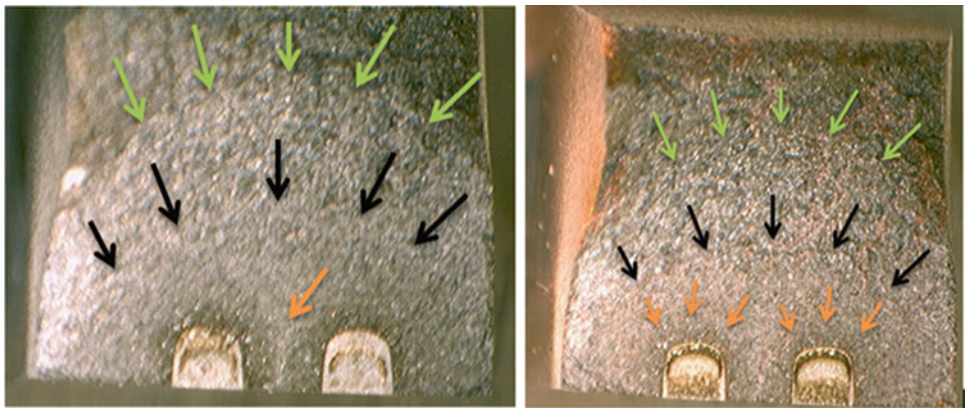

Fig. 8.13 A cross section of a failed testing sample that shows different marker bands

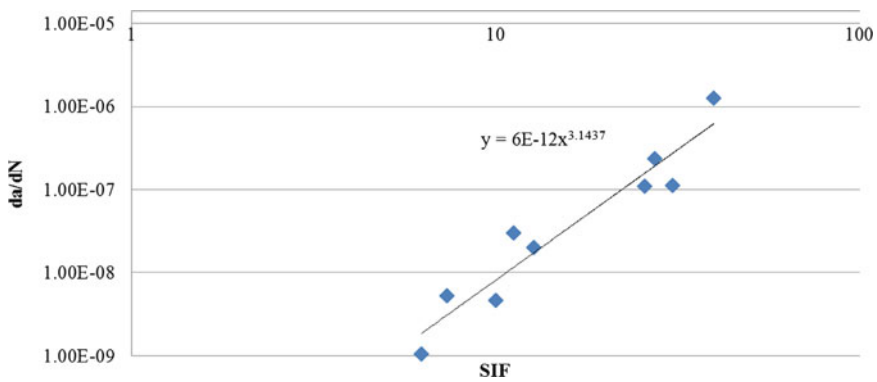

Fig. 8.14 Crack growth rate vs. SIF, S = 290 MPa, F = 2 Hz

8.5 Conclusions

The purpose of this research is to investigate the interaction of two identical adjacent cracks under cyclic loading. A series of tests at different loads and frequencies were conducted under uniaxial constant amplitude fatigue loads on API-5L grade B. The crack growth rate was investigated using the marker band testing technique before and after cracks coalescence. Real time optical microscopy was used to observe crack coalescence on the fracture surface.

The experimental method used combines the use of microscopic fractorgraphy analysis of both surface crack and crack depth to find information about the crack growth rate in the depth directions. This method is a practical method that could be used to understand cracks coalescence and interactions in different types of materials. Moreover, the image processing technique used allows better analysis of the fracture surface in ductile materials. Locating the marker bands on the fracture surface could be challenging, but it could be overcome by using proper image processing techniques.

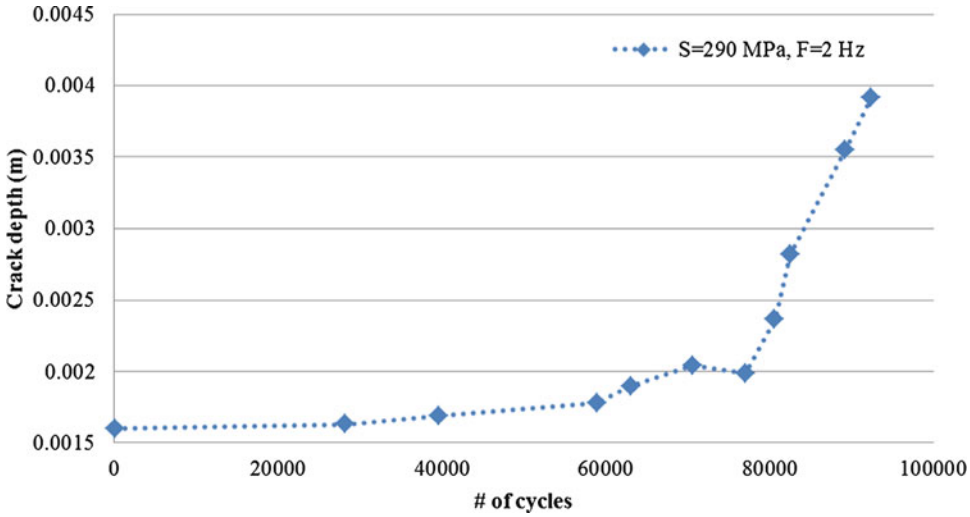

Fig. 8.15 Crack depth at different number of cycles, S = 290 MPa, F = 2 Hz

Future work will address various geometrical combinations of cracks under the effect of fatigue. The end result of this experimental work is to develop a probabilistic life prediction model that describes the process of cracks interaction and coalescence.

Acknowledgments The authors would like to thank Abu Dhabi National Oil Company (ADNOC), Abu Dhabi Company for Onshore Oil Operations (ADCO) and the Petroleum Institute (PI). Also, we would like to thank Dr. Mehdi Amiri for his efforts and support.

References

1. NTSB (2002) Rupture of enbridge pipeline and release of crude oil near Cohasset. NTSB/PAR-04/01, Washington, DC
2. Bayley C (1997) Parametric investigation on the coalescence of coplanar fatigue cracks. Masters' thesis, Carleton University, Ottawa
3. Harrington D (1995) Fatigue crack coalescence and shape development and experimental investigation. Masters Thesis, Carleton University, Department of Mechanical and Aerospace Engineering
4. Leek T, Howard I (1994) Rules for the assessment of interacting surface cracks under mode I load. Int J Press Vessel Pip 60:323–339
5. Leek T, Howard I (1996) An examination of methods of assessing interacting surface cracks by comparison with experimental data. Int J Press Vessel Pip 68:181–201
6. Leek T (1990) The interaction and growth of two surface cracks under fatigue loading. PhD Thesis, University of Sheffield, UK
7. Soboyejo W, Knott J (1990) Fatigue crack propagation of coplanar semi-elliptical cracks in pure bending. Eng Fract Mech 37(2):323–340
8. Kishimoto K, Soboyejo W, Smith R, Knott J (1989) A numerical investigation of the interaction and coalescence of twin coplanar semi elliptical fatigue cracks. Int J Fatigue 11(2):91–96
9. Twaddle J, Hancock B (1988) The development of cracks by defect coalescence. Engineering Materials Advisory Service, Warrington, pp 185–198
10. O'Donoghure T, Nishioka P, Atluris N (1984) Multiple surface cracks in pressure vessels. Eng Fract Mech 20(3):545–560
11. DeBartolo E, Hillberry B (1998) Effects of constituent particle clusters on fatigue behavior of 2024-T3 aluminum alloy. Int J Fatigue 20: 727–735
12. Terrell J (1988) Effect of cyclic frequency on the fatigue life of ASME SA-106-B piping steel in BWR environments. J Mater Eng 10:193–203
13. Willard SA (1997) Use of marker bands for determination of fatigue crack growth rates and crack front shapes in pre-corroded coupons. NASA, Hampton, VA
14. Ritchie R (1999) Mechanisms of fatigue-crack propagation in ductile and brittle solids. Int J Fract 100:55–83

Chapter 9
Measurement of Crack Tip Displacement Field in Desiccating Paste

Tatsuya Arai and Kenichi Sakaue

Abstract Desiccation cracking is a phenomenon in which cracks are caused by shrinkage of drying paste material. In the present study, digital image correlation, DIC, is applied to measure the displacement field at the crack tip in a drying paste. In order to obtain magnified images around the crack tip, the control method for crack nucleation position and crack propagation direction is newly developed. Furthermore, stress intensity factors are evaluated by iterative procedure from the measured displacement field. The results show that the stress intensity factors are varied during crack propagation because of kinked crack path ant the fracture toughness depends on the paste thickness even the paste is composed of the same powder. In addition, it is found that the fracture toughness is independent of the crack propagation speed. The dependence of the fracture toughness on the paste thickness is noticeable results to analyze the fracture of desiccation cracking.

Keywords Fracture mechanics • Digital image correlation • Stress intensity factor • Paste material • Desiccation cracking

9.1 Introduction

Desiccation cracking is a phenomenon in which cracks are caused by shrinkage of drying paste material. The desiccation cracking is observed in natural world as cracks in dried mud and columnar joint. The regular crack pattern of the desiccation cracking is an interesting phenomenon from the viewpoint of statistical physics. On the other hand, from the engineering viewpoint, it is important to prevent the initiation of the desiccation cracking in concrete structures. Thus, the mechanism of the desiccation cracking should be clarified.

The desiccation cracking have been studied by many researchers. In experimental studies, the crack pattern is mainly examined. Groisman and Kaplan [1] presented the relation between the cell size and the paste thickness. They showed that the crack pattern varies by the paste thickness, and the cell size is proportional to the paste thickness. Through these and other experiments [2–7], statistical characteristics such as the cell size, crack patterns etc. have been studied.

Theoretical studies revealed stress distribution in the desiccating paste. Kitsunezaki [8–10] analyzed stress evolution and the cracking process by using a spring-mass system. Otsuki [11] also solved the stress in the paste by the approach of continuum mechanics in order to make clear Nakahara effect [12]. These theoretical analyses assumed that the paste is an elastic material. These studies concluded that the stress in the paste increases as desiccation progress, and the stress becomes larger with increasing the spatial size and with decreasing the paste thickness. Furthermore, assuming the fracture stress and the mechanical properties of the paste, fragmentation of the paste is simulated. The results of these simulations showed the relation between the final cell size and the paste thickness. These studies give the basic understandings of the desiccation cracking.

Further studies need the characteristics of mechanical properties and strength of the paste in order to simulate the desiccation cracking precisely. However, the characteristics of pastes are not well known due to the difficulties on

T. Arai • K. Sakaue (✉)
Department of Mechanical Engineering, Shibaura Institute of Technology, 3-7-5 Toyosu, Koto-ku, Tokyo 135-8548, Japan
e-mail: sakaue@sic.shibaura-it.ac.jp

J. Carroll and S. Daly (eds.), *Fracture, Fatigue, Failure, and Damage Evolution, Volume 5: Proceedings of the 2014 Annual Conference on Experimental and Applied Mechanics*, Conference Proceedings of the Society for Experimental Mechanics Series,
DOI 10.1007/978-3-319-06977-7_9,

experiments. Especially, the measurement of fracture stress or fracture toughness is extremely difficult because pastes are soft at the instant of cracking. Moreover, it is difficult to predict the crack nucleation position because the cracks appear randomly.

In the present study, a new experimental method to control the crack nucleation position and propagation direction in the desiccating paste is developed. This method makes it possible to provide careful observation of crack propagation behavior and to take magnified images around the crack tip. Furthermore, the present method enables digital image correlation [13], DIC, to apply the magnified images before and after cracking in order to measure the crack tip displacement. Through the measurement of displacement field by DIC, stress intensity factors representing crack tip stress field are evaluated by iterative procedure [14, 15]. Moreover, the dependence of the stress intensity factor on the paste thickness is revealed. The present study is the first result evaluating the crack tip stress field of the desiccation cracking.

9.2 Experimental Methods

In the present study, the paste for the experiment of desiccation cracking is composed of magnesium carbonate ($MgCO_3$) and water. The size of particle of $MgCO_3$ is less than 75 μm. The mass of paste m is changed from 80 to 190 g for a powder mass ratio ϕ_p of 30 %. Also the paste of $m = 60$ g and $\phi_p = 25$ % is used. Firstly, the paste is poured into a petri dish with a diameter of 120 mm and the surface of the paste is smoothen by tapping.

Then, in order to control the crack nucleation position, two T-shaped glass plates are inserted at the center of the petri dish as shown in Fig. 9.1. The paste between the glass plate is constrained the shrinkage direction perpendicular to the glass plates. One of the glass plates has a glass chip to provide stress concentration in the paste. The present method using the glass plates can control the crack nucleation position and propagation direction. The petri dish is put on the heater at a temperature T_h of 70 or 90 °C to facilitate desiccation and crack nucleation.

The image of the surface of the paste is continuously taken by a CCD camera from above of the paste to measure the displacement field by digital image correlation, DIC. The DIC is performed between the reference image taken before desiccation and the deformed pattern image taken during crack propagation. DIC requires a random pattern for image matching. In the present study, the surface of the paste is patterned by iron powder.

9.3 Evaluation Method of Stress Intensity Factors

From the measured displacement field around a crack by DIC, stress intensity factors are evaluated by approximating measured displacement field by theoretical one. Kitsunezaki [8–10] and Otsuki [11] supposed that the paste is an elastic material. In the present study, the paste is also supposed to be an elastic material. For the plane problem of mode-I and mode-II cracks, the displacement field around a crack tip is given by infinite series expansion and the displacement field is expressed as

$$\begin{aligned} u &= \sum_{n=1}^{\infty} A_{\mathrm{I}n} \ f_{\mathrm{I}n}(r,\theta) - \sum_{n=1}^{\infty} A_{\mathrm{II}n} \ f_{\mathrm{II}n}(r,\theta) + T_x - R y_k, \\ v &= \sum_{n=1}^{\infty} A_{\mathrm{I}n} \ g_{\mathrm{I}n}(r,\theta) - \sum_{n=1}^{\infty} A_{\mathrm{II}n} \ g_{\mathrm{II}n}(r,\theta) + T_y + R x_k, \end{aligned} \tag{9.1}$$

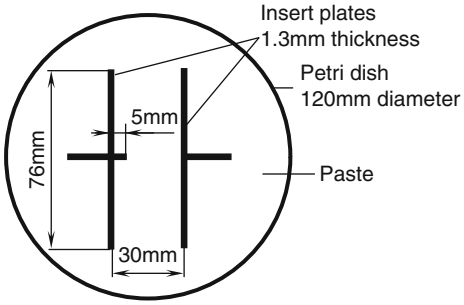

Fig. 9.1 Container in order to control the nucleation position of desiccation crack

where

$$
\begin{aligned}
f_{In}(r,\theta) &= \frac{r^{n/2}}{2G}\left\{\kappa\cos\frac{n}{2}\theta - \frac{n}{2}\cos\left(\frac{n}{2}-2\right)\theta + \left\{\frac{n}{2}+(-1)^n\right\}\cos\frac{n}{2}\theta\right\},\\
f_{IIn}(r,\theta) &= \frac{r^{n/2}}{2G}\left\{\kappa\sin\frac{n}{2}\theta - \frac{n}{2}\sin\left(\frac{n}{2}-2\right)\theta + \left\{\frac{n}{2}-(-1)^n\right\}\sin\frac{n}{2}\theta\right\},\\
g_{In}(r,\theta) &= \frac{r^{n/2}}{2G}\left\{\kappa\sin\frac{n}{2}\theta + \frac{n}{2}\sin\left(\frac{n}{2}-2\right)\theta - \left\{\frac{n}{2}+(-1)^n\right\}\sin\frac{n}{2}\theta\right\},\\
g_{IIn}(r,\theta) &= \frac{r^{n/2}}{2G}\left\{-\kappa\cos\frac{n}{2}\theta - \frac{n}{2}\cos\left(\frac{n}{2}-2\right)\theta + \left\{\frac{n}{2}-(-1)^n\right\}\cos\frac{n}{2}\theta\right\}.
\end{aligned}
\tag{9.2}
$$

In Eqs. 9.1 and 9.2, u and v are the displacement component in x-direction and y-direction, respectively; T_x and T_y represent the rigid body translations along the x-direction and y-direction, respectively; R is rigid body rotation; r and θ are polar coordinate at a crack tip. The unknown coordinate of the crack tip is represented by the polar coordinates as follows:

$$
\begin{aligned}
r &= \sqrt{(x-x_0)^2+(y-y_0)^2},\\
\theta &= \tan^{-1}\left(\frac{y-y_0}{x-x_0}\right),
\end{aligned}
\tag{9.3}
$$

where x_0 and y_0 represent the position of a crack tip with respect to the arbitrary Cartesian coordinate system in the image. κ is substituted with $(3-\nu)/(1+\nu)$ for plane stress and $3-\nu$ for plane strain where ν is Poison's ratio. The coefficients of the first terms, A_{I1} and A_{II1} relate to stress intensity factors, K_I and K_{II}, through the relations of

$$
\begin{aligned}
A_{I1} &= K_I/\sqrt{2\pi},\\
A_{II1} &= -K_{II}/\sqrt{2\pi}.
\end{aligned}
\tag{9.4}
$$

A_{In}, A_{IIn}, T_x, T_y, R, x_0 and y_0 are unknown parameters and are determined by an iterative procedure based on the Newton-Raphson method [14, 15]. Therefore, the stress intensity factors can be evaluated if the measured crack tip displacement field can be approximated by Eqs. 9.1 and 9.2. Furthermore, the crack tip position (x_0, y_0) is also determined exactly. Equation 9.2 is the theoretical solution for a semi-infinite crack in elastic material. The boundary effects of finite-size specimen and the interaction between cracks appear in higher-order terms [14, 15].

9.4 Experimental Result

A whole image example of a completely desiccated paste is shown in Fig. 9.2a. It is found that a crack nucleates from the stress concentration point and propagates straightly between the glass plates because of restricting the shrinkage direction of the paste with the glass plates. This fact means that the present method can control the crack nucleation position.

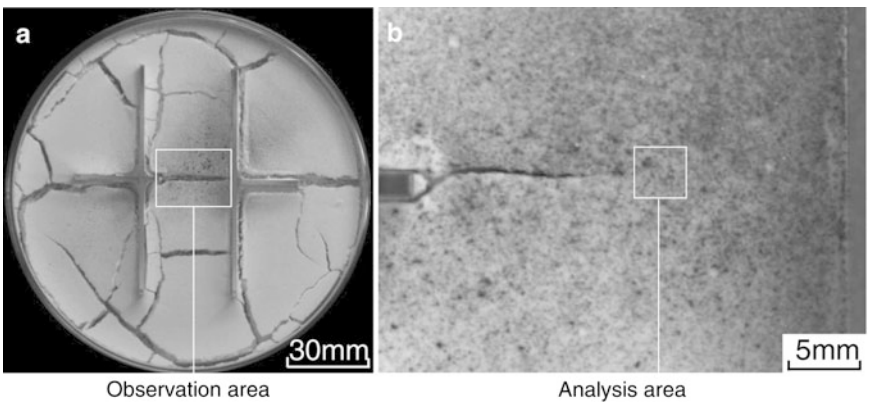

Fig. 9.2 An example of the desiccation crack that is controlled the nucleation position between the glass plates. (**a**) Whole image taken after desiccation and (**b**) magnified image during crack propagation

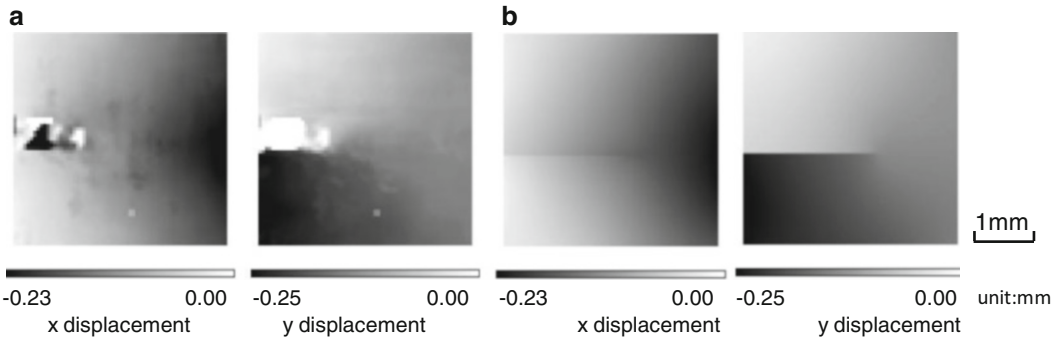

Fig. 9.3 Contour maps of displacement field (**a**) measured displacement field by DIC and (**b**) reconstructed displacement field

Therefore, magnified crack images can be obtained easily. Figure 9.2b shows an example of the magnified image during crack propagation in the observation area of Fig. 9.2a. The crack is clearly observed in the magnified image, thus the displacement field at the crack tip can be measured by DIC with a high spatial resolution.

Figure 9.3a shows the crack tip displacement field measured by DIC that is evaluated between the reference image before desiccation and the deformed pattern image as shown in Fig. 9.2b. The size of analysis area of DIC is 3.5 mm square, and the area is centered on the crack tip. As shown in Fig. 9.3a, the magnitude of the displacement in y-direction of the upper crack surface is quite lager than that of the lower surface. Therefore, the crack is mainly subjected to the load of opening mode, mode-I. Figure 9.3a indicates that the displacements near the crack surfaces cannot be obtained by DIC due to the discontinuity of the displacement across the crack surface. By excluding the invalid data near the crack surfaces, the fracture parameters, A_{I} and A_{II}, related to stress intensity factors are determined. Figure 9.3b shows the displacement field reconstructed by using the determined fracture parameters, A_{In} and A_{IIn}. Ten terms in the series expansion are used for the reconstruction of the displacement field shown in Fig. 9.3b. In addition, the paste is supposed to be an elastic material whose Poison's ratio ν is 0.3. Figure 9.3b indicates that the present method can reconstruct the measured displacement fields.

Figure 9.4a shows the time variation of the stress intensity factors of the crack shown in Fig. 9.2. The stress intensity factors are evaluated during the crack propagation within 10 mm at the center region between the glass plates. The vertical axis indicates the ratio of stress intensity factors and Young's modulus, K_{I}/E and K_{II}/E, because Young's modulus E of the paste is unknown. The mode-I stress intensity factor K_{I} is varied as shown in Fig. 9.4a. This fact is affected by kinked crack path. Therefore, the shear mode stress intensity factor K_{II} appears. The fraction of stress intensity factor $K_{\mathrm{II}}/K_{\mathrm{I}}$ is varied from 1/10 to 1/4. Therefore, the effect of mode-II cannot be neglected.

In the case of the mixed mode crack, fracture toughness K_{IC} is evaluated by maximum tangential stress criterion [16]. Crack propagation direction θ_{I} and fracture toughness K_{IC} in the direction of θ_{I} are expressed by the maximum tangential stress criterion as follows:

$$\theta_{\mathrm{I}} = 2\tan^{-1}\left\{\left(K_{\mathrm{I}} - \sqrt{{K_{\mathrm{I}}}^2 + 8{K_{\mathrm{II}}}^2}\right)/4K_{\mathrm{II}}\right\},$$

$$K_{\mathrm{IC}} = K_{\mathrm{I}}\cos^3(\theta_{\mathrm{I}}/2) - 3K_{\mathrm{II}}\sin(\theta_{\mathrm{I}}/2)\ \cos^2(\theta_{\mathrm{I}}/2). \tag{9.5}$$

Figure 9.4b shows the time variation of the fracture toughness K_{IC}/E evaluated by Eq. 9.5. Figure 9.4b also indicates the average value of the fracture toughness during the crack propagation. By using similar method of Fig. 9.4b, fracture toughness is evaluated for different experimental conditions of m, ϕ_p and T_h. Figure 9.5 shows that the relation between the paste thickness T after desiccation and the fracture toughness K_{IC}/E. The fracture toughness has time variation as shown in Fig. 9.4b. Thus, the average value and the dispersion of K_{IC}/E are shown as a circle and bar, respectively. And, the measurement results of K_{IC}/E at T_h of 70 and 90 °C are indicated as solid circle and open circle, respectively. As shown in Fig. 9.5, with increasing the paste thickness the fracture toughness becomes larger even in considering the dispersion. Figure 9.5 means that the fracture toughness depends on the paste thickness T.

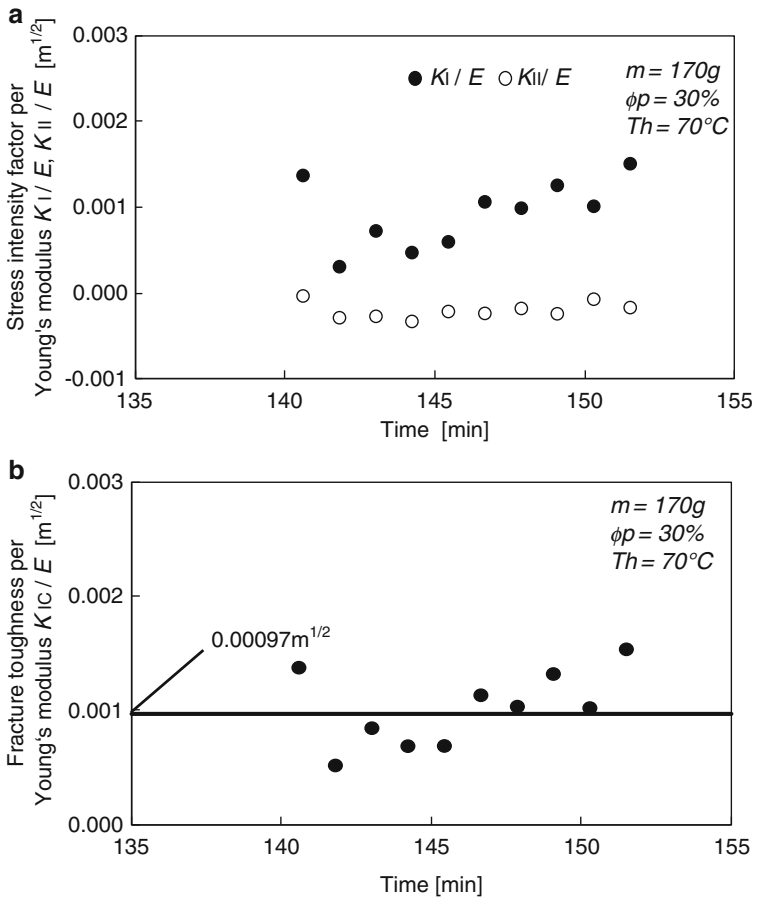

Fig. 9.4 Time variation of (**a**) stress intensity factor and (**b**) fracture toughness

9.5 Discussion

From the viewpoint of material strength, the dependence of K_{IC}/E on the paste thickness is interesting even if the paste is composed of the same powder. In general, smaller on thinner materials have relativity high strength compared to balk materials, it is so called "size effect". However, Fig. 9.5 shows the inverse size effect. Here, the causes of the inverse size effect are discussed.

In Fig. 9.5, fracture toughness is presented by the value of K_{IC}/E because evaluation of Young's modulus is difficult. It is known that the paste desiccates from the surface [2], and it is thought that the distribution of Young's modulus exists in the direction of thickness. If the powder mass ratio ϕ_p of the whole paste is the same in the pastes with different thickness, it is considered that the Young's modulus on the surface of a thick paste is higher than that of a thin paste. If the distribution of E exists in the direction of thickness and K_{IC} is assumed to be a constant for various thickness T, K_{IC}/E is inversely proportional to T. Figure 9.5 shows that K_{IC}/E is proportional to T. Therefore, the dependence of K_{IC}/E on T in Fig. 9.5 is not caused by the distribution of E in the direction of the paste thickness.

Because the paste is a porous material, the mechanical property depends on the apparent density of paste. Therefore, in order to clarify the relation between K_{IC}/E and T, it should be revealed the dependence of the density and the paste thickness. The measurement of the paste thickness after desiccation indicates that the paste thickness is linearly proportional to net powder mass in the paste. This fact means that the density does not depend on the paste thickness. Therefore, the density is not thought to be a cause of the dependency of K_{IC}/E on the thickness. Therefore, it is still an unsolved problem as to why the fracture toughness depends on the paste thickness.

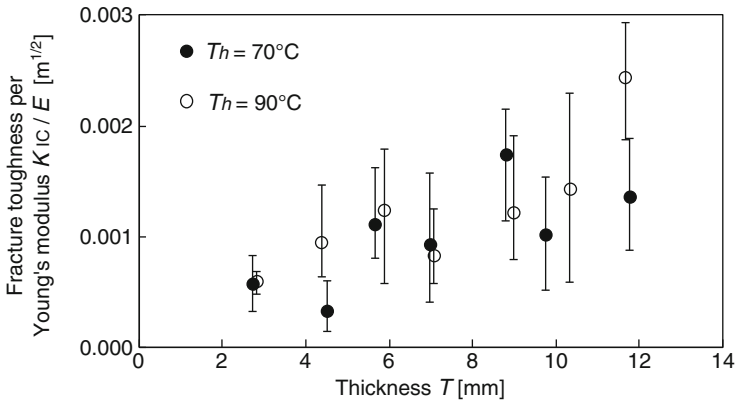

Fig. 9.5 Relation between fracture toughness and paste thickness

9.6 Conclusions

In the present study, the new experimental method is developed to control the crack nucleation position and propagation direction in the desiccation paste. By using this method, digital image correlation is used to measure the crack tip displacement field and the stress intensity factor and the fracture toughness are evaluated. The results show that the dependence of the fracture toughness on the paste thickness is revealed. It is usually thought that mechanical properties are independent of the paste thickness. In fact, this postulate is used in theoretical studies to simulate fragmentation phenomenon of paste. Therefore, the revealed relation between the fracture toughness and the paste thickness is important for precise prediction of desiccation cracking.

Acknowledgements We thank S. Yoneyama for providing the software of digital image correlation.

References

1. Groisman A, Kaplan E (1994) An experimental study of cracking induced by desiccation. Europhys Lett 25:415–420
2. Mizuguchi T, Nakahara A, Kitsunezaki S, Yamazaki Y, Aoki I (2005) Directional crack propagation of granular water systems. Phys Rev E 71:056122
3. Kitsunezaki S (2009) Crack propagation speed in the drying process of paste. J Physical Soc Japan 78(6):064801
4. Bohn S, Platkiewicz J, Andreotti B, Adda-Bedia M, Couder Y (2005) Hierarchical crack pattern as formed by successive domain divisions. II. From disordered to deterministic behavior. Phys Rev E 71:046215
5. Shorlin KA, de Bruyn JR, Graham M, Morris SW (2000) Development and geometry of isotropic and directional shrinkage-crack patterns. Phys Rev E 61(6):6950
6. Dibyendu M, Suparna S, Tapati D, Mitra S, Sujata T (2007) Formation of crack patterns in clay films: desiccation and relaxation. J Physical Soc Japan 76:014801
7. Bohn S, Pauchard L, Couder Y (2005) Hierarchical crack pattern as formed by successive domain divisions. I. Temporal and geometrical hierarchy Memory effect on the formation of drying cracks. Phys Rev E 71:046214
8. Kitsunezaki S (2010) Crack growth and plastic relaxation in a drying paste layer. J Physical Soc Japan 79(12):124802
9. Kitsunezaki S (2011) Crack growth in drying paste. Adv Powder Technol 22:311–318
10. Kitsunezaki S (1999) Fracture patterns induced by desiccation in a thin layer. Phys Rev E 60(6):6449–6464
11. Otsuki M (2005) Memory effect on the formation of drying cracks. Phys Rev E 72:046115
12. Nakahara A, Matsuo Y (2005) Imprinting memory into paste and its visualization as crack patterns in drying process. J Physical Soc Japan 74(5):1362–1365
13. Sutton MA, McNeill SR, Helm JD, Chao Y-J (2000) Advances in two- and three-dimensional computer vision. In: Rastogi PK (ed) Photomechanics. Springer, Berlin, pp 323–372
14. Yoneyama S, Ogawa T, Kobayashi Y (2007) Evaluating mixed-mode stress intensity factors from full-field displacement fields obtained by optical methods. Eng Fract Mech 74:1399–1412
15. Sakaue K, Uchiyama Y, Tanaka H, Yoneyama S, Takashi M (2008) Evaluation of crack tip stress and strain fields under nonproportional loading in a viscoelastic material. Eng Fract Mech 75:4140–4150
16. Erdogan F, Sih GC (1963) On the crack extension in plates under plane loading and transverse shear. Trans ASME J Basic Eng 85(4):519–523

Chapter 10
Characterization of Fracture Behavior of Multi-Walled Carbon Nanotube Reinforced Cement Paste Using Digital Image Correlation

Nima Zohhadi, Behrad Koohbor, Fabio Matta, and Addis Kidane

Abstract This paper reports on the fracture behavior of MWCNT-reinforced cement paste based on evidence from three-point bending tests of single-edge notched beam samples. Digital image correlation (DIC) was used to measure full-field displacements at different stages of fracture in reinforced and unreinforced samples. Strain maps extracted from displacement data were used to characterize the morphology of the fracture process zone (FPZ). The DIC principal tensile strain maps from nanoreinforced samples consistently highlighted the development of a larger FPZ prior to failure. Evidence from scanning electron microscopy analysis of fracture surfaces further supports the hypothesis that highly-dispersed and well-bonded MWCNTs contribute to toughness through crack-bridging.

Keywords Cement paste • Digital image correlation • Fracture properties • Carbon nanotubes

10.1 Introduction

The physical and mechanical properties of carbon nanofilaments and nanotubes, such as multi-walled carbon nanotubes (MWCNTs), make them suitable as a chemically compatible internal reinforcement for the strengthening and toughening of otherwise quasi-brittle cement-based composites [1]. The main challenges in the incorporation of MWCNTs in cement composites are to attain a uniform dispersion within the composite matrix as well as an effective chemical bond with cement hydrates [2]. Due to their high hydrophobicity and attractive Van der Waals forces MWCNTs tend to agglomerate and form entangled aggregates [3]. As a result a stable and homogeneous dispersion of nanotubes cannot be obtained without functionalization [4]. In addition, due to the small dimensions of MWCNTs, mechanical bonding and physical anchorage can hardly be relied upon, and the primary bonding mechanism is reasonably due to the formation of chemical bonds between the functionalized MWCNTs and the cement matrix [5].

Several functionalization techniques have been proposed by different researchers to address these challenges. The most common methods include: ultrasonication [6], acid-functionalization [7], and surfactant-coating [8]. Among these techniques acid-functionalization is preferred since the formation of chemically active carboxyl (COOH) and hydroxyl (OH) groups attached to the surface of MWCNTs facilitate the formation of covalent bonds with the cement hydrates [9]. Once uniform dispersion and effective bonding are achieved, MWCNTs can act as reinforcement for cementitious composites [10]. Previous research focused mainly on the effect of MWCNTs on compressive and flexural strength of cement paste and mortar, as well as physicochemical properties such as early-age shrinkage [11], porosity [12], and electrical conductivity [13]. For example, Li et al. [14] reported up to 19 and 25 % enhancement in compressive and flexural strength of mortar with the addition of 0.5 % in weight of cement (herein denoted as '%') acid-treated MWCNTs. Manzur et al. [15] used ultrasonication to disperse

N. Zohhadi (✉) • F. Matta
Department Civil and Environmental Engineering, University of South Carolina, 300 Main St., Columbia, SC, USA
e-mail: zohhadi@email.sc.edu; fmatta@sc.edu

B. Koohbor • A. Kidane
Department of Mechanical Engineering, University of South Carolina, 300 Main St., Columbia, SC, USA
e-mail: koohbor@email.sc.edu; kidanea@cec.sc.edu

J. Carroll and S. Daly (eds.), *Fracture, Fatigue, Failure, and Damage Evolution, Volume 5: Proceedings of the 2014 Annual Conference on Experimental and Applied Mechanics*, Conference Proceedings of the Society for Experimental Mechanics Series,
DOI 10.1007/978-3-319-06977-7_10,

0.3 % MWCNTs in mortar and obtained up to 29 % increase in compressive strength. In another study, incorporation of 0.048 % surfactant-treated MWCNTs increased the fracture load and Young's modulus of cement paste by 25 % and 40 %, respectively [16].

This paper presents early experimental evidence from an ongoing project aimed at investigating the effect of highly-dispersed acid-functionalized MWCNTs on the fracture behavior of cement paste. First, the homogeneous distribution of MWCNTs in cement mortar was verified based on evidence from compressive strength characterization and scanning electron microscopy (SEM) analysis of plain and nanoreinforced mortar samples. The effect of MWCNTs on fracture characteristics of cement paste was studied by means of three-point bending tests of single-edge notched beams. Digital image correlation (DIC) was enlisted to obtain full-field displacement maps in the notch region. Strain maps extracted from the displacement data were used to study the effect of MWCNTs on the morphology of the fracture process zone (FPZ).

10.2 Experimental Program

10.2.1 Materials

Ordinary Portland cement (OPC) Type I and ASTM C778 silica sand were used to fabricate the specimens. The MWCNTs (Cheap Tubes Inc, cat# sku-030101, Brattleboro, VT) were used as-received. Salient properties of the MWCNTs as provided by the supplier are presented in Table 10.1.

10.2.2 Preparation of MWCNT-Reinforced Cement Paste and Mortar

The MWCNTs were dispersed in water and the resulting suspension was mixed with cement (and sand in case of the mortar cubes used for the characterization of compressive strength) in accordance with ASTM C305. To enhance dispersion in water and bonding with cement hydrates, MWCNTs were first functionalized using an acid-treatment technique.

In a typical procedure, the MWCNTs were soaked in an aqueous solution containing ammonium persulfate, $(NH_4)_2S_2O_8$ (Sigma Aldrich, cat# 215589) and sulfuric acid, H_2SO_4 (Sigma Aldrich, cat# 339741) and the resulting suspension was stirred for 24 h using a magnetic stirrer. The resulting solution was sonicated for 10 min using an ultrasonic processor (S-4000 Ultrasonic Processor, Misonix, Inc., Farmingdale, NY) to mechanically separate nanotube clusters and ensure that the acids reach the innermost nanotubes. The solution was then stirred for another 24 h. At this point, the MWCNTs reached a pH of about 1 and were not suitable for mixing with cement. Therefore, the MWCNTs were washed with deionized water to raise the pH to 7, and then dried and stored as dry powder. The acid-functionalized MWCNTs were added to water and sonicated for 20 min before incorporating them in the cement mixtures for mortar (used to fabricate the compression test samples) and cement paste (used to fabricate the fracture mechanics test samples).

10.2.3 Specimens, Test Setup and Protocol

Compressive strength characterization—The effect of functionalized MWCNTs on the compressive strength of cement mortar was evaluated using compression tests on 2-in. (50-mm) cube specimens in agreement with ASTM C109. The specimens were fabricated with mortar having OPC:sand:water weight proportion of 1:2.75:0.484 in agreement with ASTM C109. Two reinforcement concentrations of 0.05 and 0.5 % were used to prepare three specimens per group. The specimens were moist-cured for 24 h and then demolded and kept under saturated lime water until the age of 28 days. Compression tests were performed using a test frame (MTS 810 Material Testing System, MTS Systems Inc., Eden Prairie, MN) under displacement-control mode with a displacement rate of 0.625 mm/min.

Visual characterization of MWCNT dispersion in mortar—The dispersion of acid-treated MWCNTs in cement mortar was investigated by means of SEM analysis of samples collected from fracture surfaces of failed cube specimens. SEM

Table 10.1 Properties of as-received MWCNTs

Outer diameter [nm]	Inner diameter [nm]	Specific surface area [m^2/g]	Length [μm]	Purity [%]
<8	2–5	500	10–30	>95

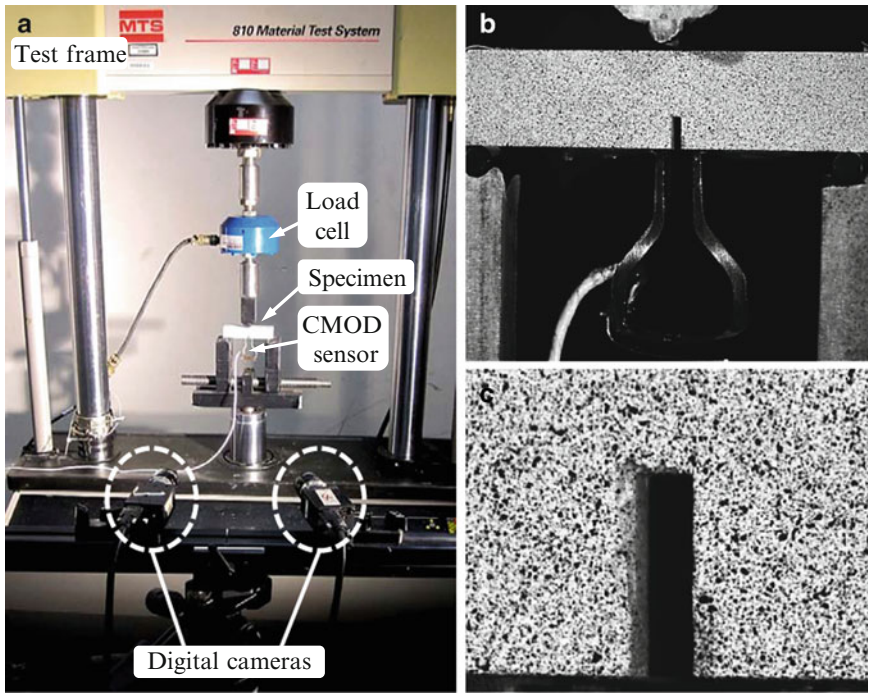

Fig. 10.1 Fracture mechanics testing and DIC measurement: (**a**) test setup; (**b**) close-up photograph of notched beam specimen; and (**c**) close-up view of speckle pattern around 2 × 6 mm notch

micrographs were acquired using a Zeiss Ultra Plus Field Emission Scanning Electron Microscope. All samples were oven-dried for 24 h at 60 °C and gold-sputtered prior to being tested.

Fracture mechanics characterization—The experimental evidence to assess the effect of MWCNTs on the fracture behavior of cement paste was obtained by means of three-point bending test on single-edge notched beam specimens with dimensions of 20 × 20 × 80 mm, as illustrated in Fig. 10.1. Two reinforcement concentrations of 0.05 and 0.5 % were considered and three specimens per group were fabricated. A 0.5 w/c ratio was used for the Type I OPC paste. Specimens were moist-cured for 24 h and then demolded and kept under saturated lime water until the age of 28 days. A water-cooled diamond saw was used to cut 6-mm long and 2-mm wide notches at midspan (Fig. 10.1b, c). A clip gage was used to measure the crack mouth opening displacement (CMOD). The load tests were performed in displacement-control mode at a rate of 0.01 mm/min.

DIC measurements—A thin layer of white wash was applied on the surface of the specimens and a dark speckle pattern was then spray-painted on the white washed background (Fig. 10.1b, c). A pair of five MP cameras (Grasshopper GRAS-50S5M-C, Point Grey, Richmond, Canada) equipped with 35-mm lenses was utilized to acquire images at a 5 fps rate (Fig. 10.1a). The DIC analysis was performed using the software Vic-3D (v7, Correlated Solutions Inc., Columbia, SC) using a subset size of 49 × 49 pixels with a step of 15 pixels.

10.3 Results and Discussion

10.3.1 Compressive Strength

The increase in compression strength is greatly affected by the dispersion of carbon nanoreinforcement [6, 15], and was used as an indirect means to assess the effectiveness of the functionalization technique. Poorly-dispersed MWCNTs tend to produce defect sites at the locations of entangled MWCNTs, thereby contributing to reducing the compressive strength [15]. A summary of the compression test results is presented in Table 10.2.

All nanoreinforced mortar specimens consistently exhibited a higher compressive strength than the counterpart plain mortar specimens, suggesting that a homogeneous dispersion was attained. The strength gain increased for the higher nanoreinforcement concentration (0.5 % in weight of cement). The average strength increased by 24 % and 41 % for MWCNT additions of 0.05 % and 0.5 %, respectively.

Table 10.2 Results of compression tests

Group	Compressive strength [MPa]	Δ [%]
Control	32 ± 3	–
MWCNT 0.05 %	39 ± 1	24
MWCNT 0.5 %	44 ± 4	41

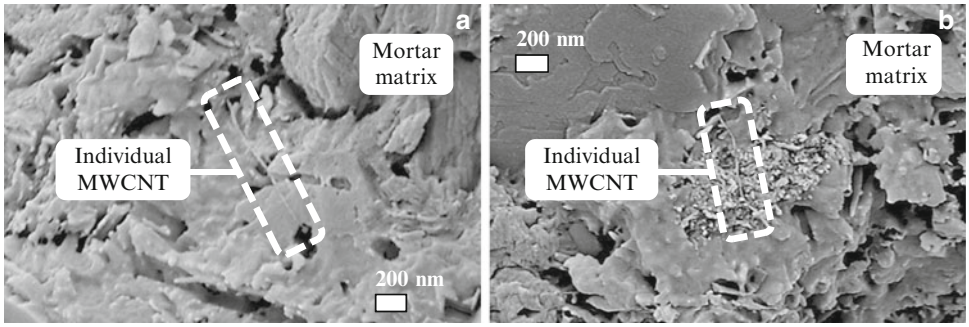

Fig. 10.2 Dispersion of MWCNTs in cement mortar at different concentrations: (**a**) 0.05 %; and (**b**) 0.5 %

Table 10.3 Results of fracture mechanics tests

Specimen group	Maximum load [N]	Stiffness [N/mm]
Control	111 ± 3	4,862 ± 276
MWCNT 0.05 %	139 ± 16	9,400 ± 1,060
MWCNT 0.5 %	135 ± 12	8,981 ± 1,465

10.3.2 SEM Analysis

Portions of fracture surfaces of failed mortar cubes were inspected via SEM to assess the dispersion of MWCNTs in the cement composite. Representative micrographs are presented in Fig. 10.2.

At both 0.05 and 0.5 % concentrations MWCNTs were mostly found as individual nanotubes, indicating that a satisfactory dispersion was attained. In addition, at the majority of the locations inspected, MWCNTs were found partially embedded in cement hydrates, indicating a good chemical compatibility between the acid-functionalized nanoreinforcement and the cement matrix.

10.3.3 Flexural Strength, Stiffness, and Fracture Behavior

The effect of highly-dispersed MWCNTs on the flexural response and fracture characteristics of cement paste was studied by means of three-point bending tests of single-edge notched beams. A summary of the test results is presented in Table 10.3.

The incorporation of MWCNTs in concentrations of 0.05 % and 0.5 % led to an increase in the average maximum load of 25 % and 22 %, respectively, and an increase in the average stiffness of 93 % and 85 %, respectively, consistent with the strength enhancement obtained for mortar cubes. A major stiffness increase was also reported by other researchers [16] and may be attributed primarily to a reduced porosity and refinement of the pore structure [12, 13, 17], which may not further improve at increasing MWCNT concentrations in part due to the difficulty to consistently ensure uniform dispersion.

Representative examples of load-CMOD response of unreinforced and nanoreinforced notched beams are presented in Fig. 10.3. The significant stiffness increase for MWCNT-reinforced samples can be clearly noted. The unreinforced control specimens experienced a sudden drop in the load resisted after attaining the maximum (peak) load, whereas the nanoreinforced specimens exhibited a more progressive damage development and retained a higher residual strength past the peak load.

To better understand the influence of MWCNTs, the load-CMOD curves were divided in three stages: linear elastic, non-linear pre-peak load, and post-peak load. For each group, Table 10.4 compares the energy absorbed in these three stages. A 15 % deviation from linearity in the slope of the load-CMOD curves was used to determine the beginning of the non-linear pre-peak load stage.

The energy absorbed in the stiffer nanoreinforced samples in the linear elastic stage was on average smaller than that in the unreinforced specimens. However, in the second stage (non-linear pre-peak) where nano-cracks form and coalesce into

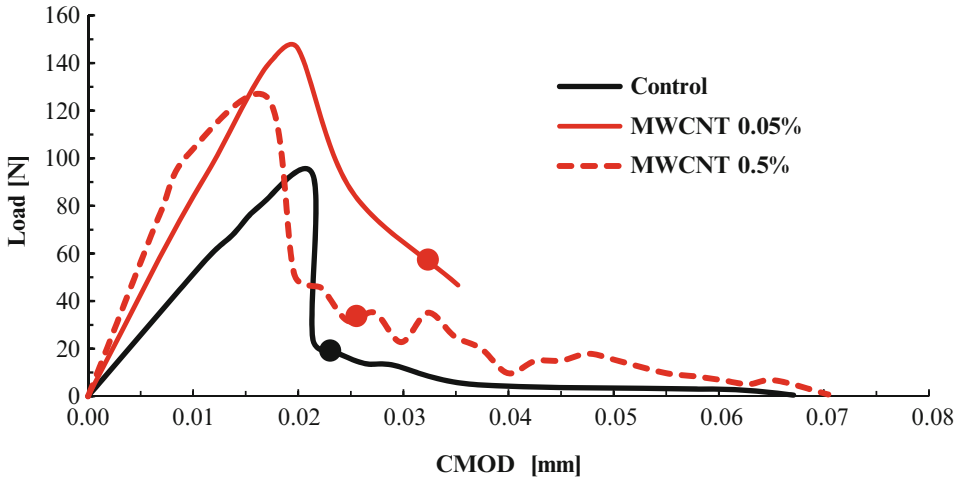

Fig. 10.3 Representative load-CMOD curves. Markers indicate load-CMOD coordinates for DIC strain maps in Fig. 10.5

Table 10.4 Energy at different stages of load-CMOD curve

Specimen group	Total energy [N-mm]	Linear elastic	Non-linear pre-peak load	Post-peak load
Control	1.63 ± 0.05	0.79 ± 0.09	0.38 ± 0.10	0.46 ± 0.08
MWCNT 0.05 %	2.14 ± 0.70	0.60 ± 0.47	0.60 ± 0.24	0.94 ± 0.67
MWCNT 0.5 %	2.09 ± 0.54	0.59 ± 0.10	0.56 ± 0.24	1.08 ± 0.46

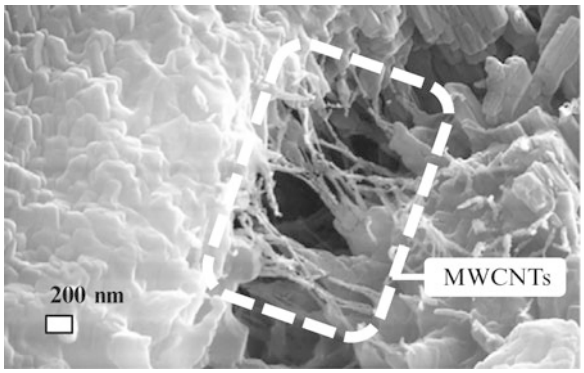

Fig. 10.4 SEM micrograph showing potential crack-bridging contribution of MWCNTs in cement paste

micro-cracks, the energy was significantly higher for the reinforced samples. This behavior is reasonably attributed to the presence of well-dispersed MWCNTs, which may contribute to enhancing the fracture toughness through a crack- or defect-bridging effect, similar to that provided at a larger scale by micro-fiber reinforcement in fiber-reinforced cement composites, as suggested the SEM micrograph in Fig. 10.4.

Defect- and crack-bridging action requires effective bonding between the nanoreinforcement and the surrounding cement paste, and the rupture and progressive pull-out of well-bonded MWCNTs can contribute to fracture toughness [13]. In fact, the influence of MWCNTs is more evident in the third stage of the load-CMOD curve (post-peak load), thus past the maximum load, where unreinforced specimens rapidly collapse. The average energy absorbed in the post-peak load stage by specimens reinforced with 0.05 % and 0.5 % MWCNTs was 104 % and 135 % higher than the unreinforced specimens, respectively, highlighting the toughening contribution of well-dispersed and bonded MWCNTs. As a result, the total energy increased by 31 % and 28 % in the case of nanoreinforced specimens with 0.05 % and 0.5 % MWCNTs, respectively.

10.3.4 Fracture Process Zone

The fracture process zone (FPZ) is the intermediate space between the cracked and uncracked regions ahead and around the crack tip [18]. The effect of MWCNTs on the FPZ of cement paste was investigated by comparing the DIC principal tensile strain maps of unreinforced and nanoreinforced specimens using the images acquired with the stereo-vision system

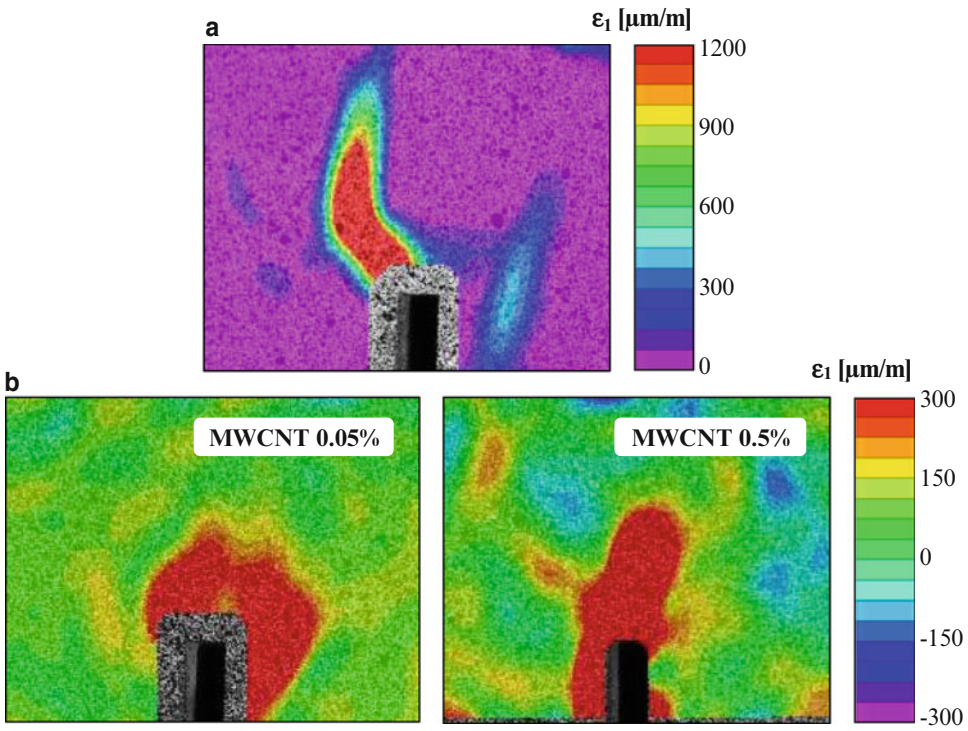

Fig. 10.5 Representative DIC principal tensile strain map in cement paste notched beam specimens in post-peak load stage: (**a**) unreinforced (control) beam; and (**b**) MWCNT-reinforced beams

in Fig. 10.1. Representative DIC principal tensile strain maps at the post-peak load stage (at the load-CMOD coordinates indicated by the circular markers in Fig. 10.3) are presented in Fig. 10.5.

The FPZ for unreinforced cement paste specimens is visualized as a relatively narrow and well-defined damage area at the crack tip. The FPZ for MWCNT-reinforced specimens is significantly larger and has a more progressive strain distribution in the vicinity of the notch, indicating a more damage tolerant zone where damage is more effectively distributed. This evidence is consistent with the load-CMOD curves presented in Fig. 10.3, the associated energy data summarized in Table 10.4, and the possible crack- and defect-bridging effect illustrated in Fig. 10.4.

10.4 Conclusions

Based on the experimental evidence presented in this paper, the following conclusions are drawn.

1) Acid-functionalization of MWCNTs resulted in well-dispersed nanoreinforcement in cement composite matrices for both a 0.05 and 0.5 % MWCNT concentration in weight of cement.
2) The incorporation of 0.05 % and 0.5 % of highly-dispersed acid-functionalized MWCNTs resulted in an average increase in compressive strength of cement mortar of 24 % and 41 %, respectively.
3) The fracture behavior of MWCNT-reinforced cement paste was assessed using three-point bending tests of notched beams. The incorporation of 0.05 % and 0.5 % of highly-dispersed acid-functionalized MWCNTs resulted in an average increase in peak flexural strength of 25 % and 22 %, respectively, and an average increase in flexural stiffness 93 % and 85 %, respectively. The load-CMOD curves show that the nanoreinforced specimens provide enhanced damage tolerance compared to the unreinforced counterparts, resulting in an increase in absorbed energy of 31 % and 28 % when using a 0.05 % and 0.5 % MWCNT concentration, respectively. Visual evidence from SEM analysis suggests the likelihood of a defect- and crack-bridging effect provided by the nanoreinforcement. There seem to be no additional benefit to damage tolerance in increasing the concentration of nanoreinforcement from 0.05 to 0.5 % in weight of cement.
4) The effect of MWCNTs on the FPZ of cement paste was evaluated based on DIC principal tensile strain maps around the beam notch. In the case of the unreinforced cement paste specimens, the FPZ is visualized as a narrow damage area, clearly reflecting a quasi-brittle behavior. In the case of the MWCNT-reinforced specimen, the FPZ is significantly larger and exhibits a more progressive strain distribution in the vicinity of the notch, providing promising experimental evidence of an enhanced damage tolerance as a result of incorporating well-dispersed and chemically compatible nanoreinforcement.

Acknowledgements The support of the University of South Carolina (USC) through a Promising Investigator Research Award (PIRA) to the third author, the State Center for Mechanics, Materials and Non-Destructive Evaluation, and the Magellan Program for undergraduate research is gratefully acknowledged. Special thanks are extended to: Ms. English Player (formerly undergraduate research assistant and USC Magellan mini-grantee), Prof. Navid Saleh and Mr. Nirupam Aich (formerly graduate student) for their assistance in processing of MWCNTs; and Prof. Michael Sutton, Prof. Anthony Reynolds, and Mr. Dan Wilhelm (USC Department of Mechanical Engineering) for their assistance in the use of the load test frame, CMOD sensor and DIC equipment. Correlated Solutions, Inc. (Columbia, SC) generously provided the Vic-3D v7 software used for the DIC analysis.

References

1. Yazdanbakhsh A, Grasley Z, Tyson B, Abu Al-Rub R (2012) Challenges and benefits of utilizing carbon nanofilaments in cementitious materials. J Nanomater 371927
2. Parveen S, Rana S, Fangueiro R (2013) A review on nanomaterial dispersion, microstructure and mechanical properties of carbon nanotube and nanofiber reinforced cementitious composites. J Nanomater 710175
3. Hilding J, Grulke EA, Zhang ZG, Lockwood F (2003) Dispersion of carbon nanotubes in liquids. J Disper Sci Technol 24(1):1–41
4. Vaisman L, Wagner HD, Marom G (2006) The role of surfactants in dispersion of carbon nanotubes. Adv Colloid Interfac 128:37–46
5. Makar JM, Beaudoin JJ (2004) Carbon nanotubes and their application in the construction industry. Sp Publ Roy Soc Chem 292:331–342
6. Musso S, Tulliani JM, Ferro G, Tagliaferro A (2009) Influence of carbon nanotubes structure on the mechanical behavior of cement composites. Compos Sci Technol 69(11):1985–1990
7. Cwirzen A, Habermehl-Cwirzen K, Nasibulin AG, Kaupinen EI, Mudimela PR, Penttala V (2009) SEM/AFM studies of cementitious binder modified by MWCNT and nano-sized Fe needles. Mater Charact 60(7):735–740
8. Metaxa ZS, Konsta-Gdoutos MS, Shah SP (2013) Carbon nanofiber cementitious composites: effect of debulking procedure on dispersion and reinforcing efficiency. Cement Concrete Comp 36:25–32
9. Nasibulina LI, Anoshkin IV, Nasibulin AG, Cwirzen A, Penttala V, Kauppinen EI (2012) Effect of carbon nanotube aqueous dispersion quality on mechanical properties of cement composite. J Nanomater 169262
10. Raki L, Beaudoin J, Alizadeh R, Makar J, Sato T (2010) Cement and concrete nanoscience and nanotechnology. Materials 3(2):918–942
11. Konsta-Gdoutos MS, Metaxa ZS, Shah SP (2010) Multi-scale mechanical and fracture characteristics and early-age strain capacity of high performance carbon nanotube/cement nanocomposites. J Cement Concrete Res 32:110–115
12. Wang B, Han Y, Liu S (2013) Effect of highly dispersed carbon nanotubes on the flexural toughness of cement-based composites. Constr Build Mater 42:8–12
13. Luo J, Duan Z, Li H (2009) The influence of surfactants on the processing of multi-walled carbon nanotubes in reinforced cement matrix composites. Phys Status Solidi A 206(12):2783–2790
14. Li GY, Wang PM, Zhao X (2005) Mechanical behavior and microstructure of cement composites incorporating surface-treated multi-walled carbon nanotubes. Carbon 43(6):1239–1245
15. Manzur T, Yazdani N (2010) Strength enhancement of cement mortar with carbon nanotubes. Transp Res Record 2142(1):102–108
16. Konsta-Gdoutos MS, Metaxa ZS, Shah SP (2010) Highly dispersed carbon nanotube reinforced cement based materials. Cement Concrete Res 40(7):1052–1059
17. Nochaiya T, Chaipanich A (2011) Behavior of multi-walled carbon nanotubes on the porosity and microstructure of cement-based materials. Appl Surf Sc 257(6):1941–1945
18. Orsuka K, Date H (2000) Fracture process zone in concrete tension specimen. Eng Fract Mech 65:111–131

Chapter 11
Characterization of Structural Scale Ductile Fracture of Aluminum Panels Using Digital Image Correlation

K. Nahshon, W.A. Hoffman, and C.B. Ullagaddi

Abstract The use of lightweight aluminum construction has become prevalent in marine structures and it is therefore critical that the performance of such structures in the inelastic regime be characterized. A key aspect of this is the ductile fracture behavior of panels and structural details. Here, the results of ductile fracture tests conducted on large pre-notched aluminum panels seeking to characterize this inelastic response and resulting fracture are reported. Plates fabricated from 5083-H116 and 6061-T6 panels, including a welded panel, were tested with a geometry designed to induce macro-plasticity prior to fracture. Testing was performed using a newly developed heavy steel fixture of sufficient rigidity and included the use of Digital Image Correlation (DIC) strain measurement. Through extensive data collection and analysis, the full extent and severity of plastic deformation prior to fracture were obtained. It is anticipated that this data will be of utility in the calibration and validation of numerical modeling of ductile fracture in large structures.

Keywords Ductile fracture • Plasticity structural testing • Digital image correlation • Welded structures

11.1 Introduction

The use of lightweight aluminum construction has become prevalent in both the commercial and naval ship industries as a result of the increased desire for high vessel speed. Aluminum alloys, specifically 5000 and 6000 series alloys, are attractive primary hull materials for lightweight, high-speed, vessels due their inherent weldability, corrosion resistance, and stiffness to weight ratio [1]. While the operational use of such vessels has been highly successful, there is no data on the behavior of relevant structures in the inelastic regime. Such an inelastic response could arise from severe sea-states, collision, grounding, or weapons loads.

The large-panel fracture tests described herein seek to bridge the gap between large structural tests, which are expensive and complex to perform, and coupon-level testing where it is often difficult to extend results to overall structural performance. For example, the process of localization, necking, and fracture is in a sheet or plate is known to be strongly influenced by the prevailing strain, as evidenced by forming limit diagrams. In addition, Welds and other local details can have a significant impact on mechanical behavior. In their work on large-panel fracture tests, Simonsen and Törnqvist [2] showed that such tests had significant value in bridging the length scales associated with ductile fracture in large structures. A key feature of their test configuration was the relatively large size of the test panels, thus allowing for the development of significant panel plastic deformation prior to rupture. In addition, it was found that large panels facilitated a commonality of element sizes and fracture modeling methodologies between numerical simulations of the test itself and of a separate large scale grounding test. Further utilization of this test data by Neilson and Hutchinson [3] exhibited the utility that these tests have in calibrating cohesive zone models for ductile fracture. It is noted that Zheng et al. [4, 5] performed similar tests on a large extruded corrugated-core Gas Metal Arc (GMA) welded AL 6061-T6 panels in order to evaluate the performance of such panels during a railcar collision.

Motivated by the work in [2], a new test fixture was designed and fabricated to perform large-panel fracture tests. This fixture included a floating arm configuration to allow for testing of extruded panels of significant thickness. Tests were

K. Nahshon (✉) • W.A. Hoffman • C.B. Ullagaddi
Naval Surface Warfare Center Carderock Division, 9500 MacArthur Boulevard, West Bethesda, MD 20817, USA
e-mail: ken.nahshon@navy.mil

J. Carroll and S. Daly (eds.), *Fracture, Fatigue, Failure, and Damage Evolution, Volume 5: Proceedings of the 2014 Annual Conference on Experimental and Applied Mechanics*, Conference Proceedings of the Society for Experimental Mechanics Series,
DOI 10.1007/978-3-319-06977-7_11,

performed with Digital Image Correlation (DIC) measurements during testing. DIC provides full-field surface strain measurements that are able provide a complete picture of the plastic deformation, localization, and crack propagation process. This data facilitates understanding the local and near-crack plastic deformation preceding rupture.

11.2 Experimental Setup

All tearing testing was performed at the Naval Surface Warfare Center Carderock Division (NSWCCD) Structural Testing Laboratory using a 2,440 kN (550 kip) servo-hydraulic MTS tensile load frame with hydraulically actuated grips along with a newly designed test fixture. The test fixture consists of four arms and two compression struts, all nominally 117.5 mm (4.625 in.) thick, connected to two nominally 203 mm (8 in.) thick load heads, all fabricated from A514 steel. A view of the installed fixture is shown in Fig. 11.1a, and a side view showing critical dimensions in Fig. 11.1b.

The fixture is operated by displacing the load heads apart using the load frame actuator. Two compression struts maintain a fixed distance at the edge of the load arms. Thus, the two edges of the test panel are subjected to a linear displacement gradient resulting in deformation, crack propagation, and panel rupture. The positioning of the compression members ensures that the entire coupon is in tension thus avoiding the need for buckling restraints to constrain out of plane motion. All fixture components are linked through spherical bearings so as to minimize the potential for fixture binding. Clamping force is provided by twelve heavily torqued 38.1 mm (1.5 in.) bolts that provide approximately 3,555 kN (800 kips) of clamping force on each arm through an internal gripping system shown in Fig. 11.1b.

All test panels were fabricated from AL5083-H116 and AL6061-T6/651 plates; both are important alloys in marine structures. The overall dimensions of test panels were $1{,}067 \times 798$-mm with a gauge section of 902×798-mm. A 60° V-notch, with an overall length of 50.8-mm (2 in.), was machined on one edge using Electrical Discharge Machining (EDM). All test panels were fabricated so that crack propagation would be aligned with the plate rolling direction.

Test instrumentation included string potentiometers, strain gauges, a crack opening displacement gauge, and DIC to measure displacement and strain. Load was measured using the tensile fixture load-cell. The arrangement of string potentiometers and strain gauges is shown in Fig. 11.2. Load-deflection curves are reported using the deflection measured at the crack edge, SP2, to avoid the effects of machine or fixture compliance on displacement.

All DIC setup and measurements were performed with the assistance of Trillion Systems, Inc. using an ARAMIS 5M system. The ARAMIS 5M system is stereoscopic in nature, this allowing full-field, non-contact strain measurement of 3D deformation. The hardware consists of two CCD cameras, with a resolution of $2{,}448 \times 2{,}050$ pixels (5 Megapixels) along with a digital controller and data acquisition system. Two separate speckle patterns, 'Coarse' and 'Fine,' were utilized during testing and were applied using commercial spray paint. The pattern densities are shown in Fig. 11.3.

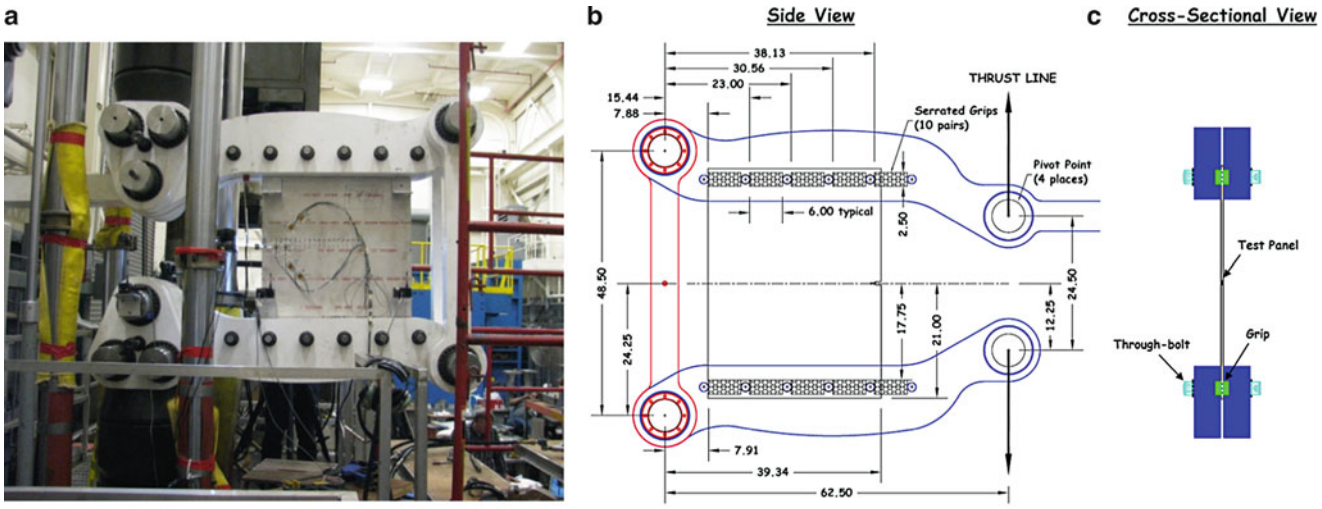

Fig. 11.1 As-installed view (**a**), dimensioned drawing (**b**), and cross-sectional view of gripping system (**c**) of tearing fixture. Dimensions are shown in inches

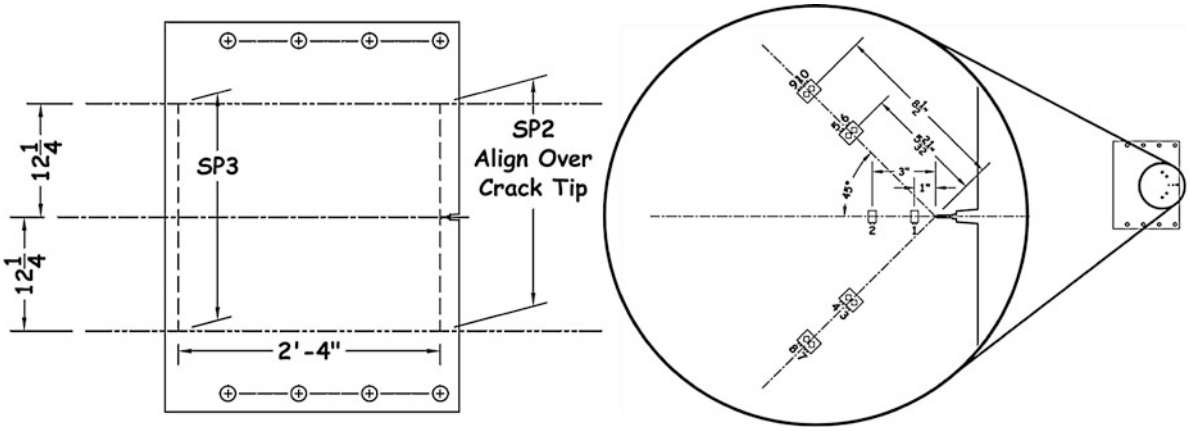

Fig. 11.2 String potentiometer and strain gage layout

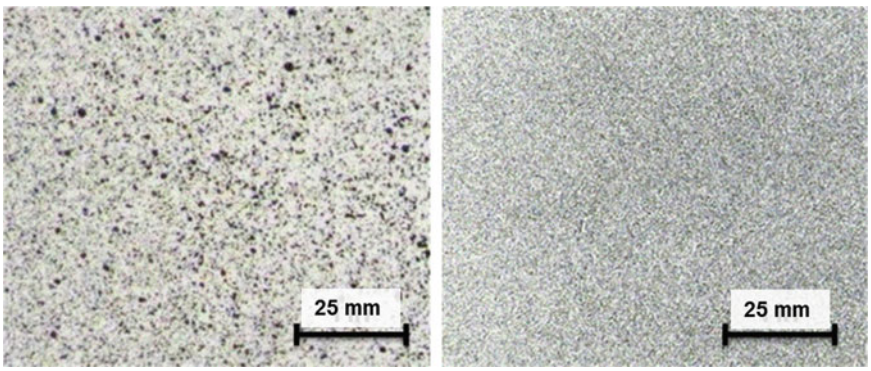

Fig. 11.3 Coarse (L) and fine (R) speckle patterns used in DIC measurements

Table 11.1 Test matrix for panel fracture tests

Test ID	Material ID	Thickness mm (in)	$\sigma_{y,0.2\%}$ MPa	σ_{UTS} MPa	Elongation % (50.8-mm GL)	RA %
Al83-2	5083-H116	6.35 (0.250)	248.9	368.9	14	18
Al83-3	5083-H116	6.35 (0.250)	248.9	370.9	14	21
Al83-6	5083-H116	9.53 (0.375)	246.1	382.7	19	22
Al83-7	5083-H116	9.53 (0.375)	233.0	368.9	23	26
Al83W-1	5083-H116, Weld	6.35 (0.250)	N/A	N/A	N/A	N/A
Al61-1	6061-T6	6.35 (0.250)	281.3	324.7	14	29
Al61-2	6061-T6	6.35 (0.250)	281.3	324.7	14	29
Al61-3	6061-T6	6.35 (0.250)	281.3	324.7	14	29
Al61-4	6061-T651	3.18 (0.125)	276.5	328.9	15	23
Al61-5	6061-T651	3.18 (0.125)	276.5	328.9	15	23

Tensile properties reported transverse to rolling direction

11.3 Test Matrix

Ten tests were conducted with AL5083-H116 and AL6061-T6/651 panels with thicknesses ranging from 3.18 to 9.53 mm (0.125–0.375 in.). A single 5083-H116 panel was fabricated with a Gas Metal Arc (GMA) butt weld aligned with the notch so that the crack would propagate along the weld or Heat Affected Zone (HAZ). All tests were performed under quasi-static conditions with an actuator displacement speed of 0.3 mm/in (0.01 in./min). A summary of the test matrix, along with uniaxial tension test data, can be found in Table 11.1.

11.4 Test Results

A summary of all load deflection curves is shown in Fig. 11.4. All tests, with the exception of AL83W-1 (welded 5083-H116) exhibited several common features. Namely, smooth load-deflection curves were observed until crack propagation occurred, fracture was highly controlled and ductile in nature, significant plasticity was seen to occur away from and ahead of the moving crack, and steady-state crack propagation was observed after the crack extended several plate thicknesses in length. The start of this steady-state mode coincided with the transition from a flat to a slant fracture mode. The single welded 5083-H116 panel failed in a quasi-brittle manner and no plastic deformation was observed outside of the weld region. All tests were terminated after the load decreased below approximately 89 kN (20 kips). It was found that terminating at this load resulted in approximately 2/3 of a meter of crack extension. After removal of each test panel, it was confirmed that no slipping of the panel between the grips was evident.

Load deflection data for 5083-H116 panels, shown in Fig. 11.4a, illustrate that the response up to and beyond peak load is smooth and that unloading occurs in a steady and controlled manner (with the exception of the single welded panel). Both 6.35 mm (0.250 in.) 5083-H116 plates, both from the same manufacturer, exhibit nearly indistinguishable responses. However, the response of two 9.53 mm (0.375 in.) plates, from different manufacturers, is quite different in the plastic regime: substantially different values of both peak load and amounts of plastic work, as inferred from the area under the force-displacement curve, are observed. The reasons for this discrepancy are under investigation. Load deflection data for all 6061-T6 panels shown in Fig. 11.4b, shows similar trends. It is seen that the tests are highly repeatable in nature for both plate thicknesses tested.

Typical DIC measurements for two separate tests of equal thickness plates of both alloys are shown in Fig. 11.5. The quantity plotted is vertical strain (aligned with the loading direction). It is seen that initial yielding occurs in a highly localized manner but that as the crack progresses a plastic pre-cursor field develops. The size and qualitative nature of this yielding pattern does not appear to be significantly different for both alloys despite the differing strain-hardening behavior.

A detailed picture of the yielding and crack propagation process is observed by comparing two separate tests, AL83-2 and AL83-3, of the same alloy and thickness but differing regions of DIC measurement; AL83-2 was configured for far-field measurements and AL83-3 for near field ones. It is seen in Fig. 11.6 that significant crack extension occurs prior to reaching peak load (points 'B' and 'G') and that nearly the full peak load is carried by the panel well after significant crack extension (point 'C' and 'H'). In addition, the transition from flat (point 'F') to slant crack (point 'G') is observed in both the strain output and a photo of the test panel.

Testing of a single butt-welded 6.35 mm (0.250 in.) 5083-H116 panel, AL83W-1, was conducted to evaluate the effect of the presence of a weld on fracture behavior. This was of interest given the under-matched, or weaker, nature of welds in the alloys of interest. Referring to Fig. 11.4, it is seen that the load-deflection curve is smooth until peak load but exhibits little extension (and corresponding plastic dissipation) beyond this point. The unloading behavior is uncontrolled and fracture propagation was found to be rapid; drops in load were accompanied by load cracking noises indicating unstable crack growth. The low fracture toughness of the weldment as compared to the parent material prevents arrest and allows for rapid crack advance driven by elastic unloading of the surrounding plate.

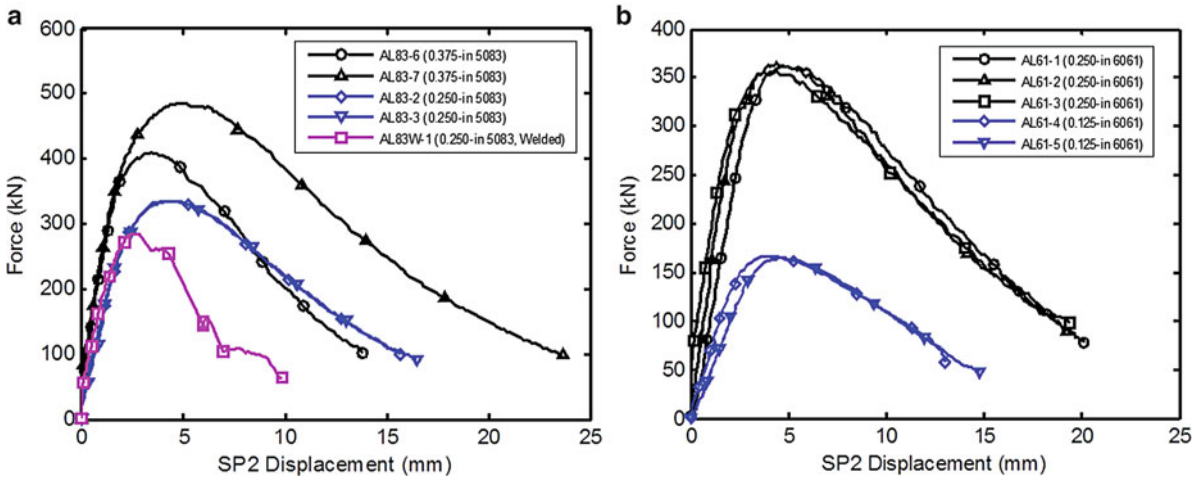

Fig. 11.4 Load versus displacement behavior for 5083-H116 (**a**) and 6061-T6 (**b**) panels

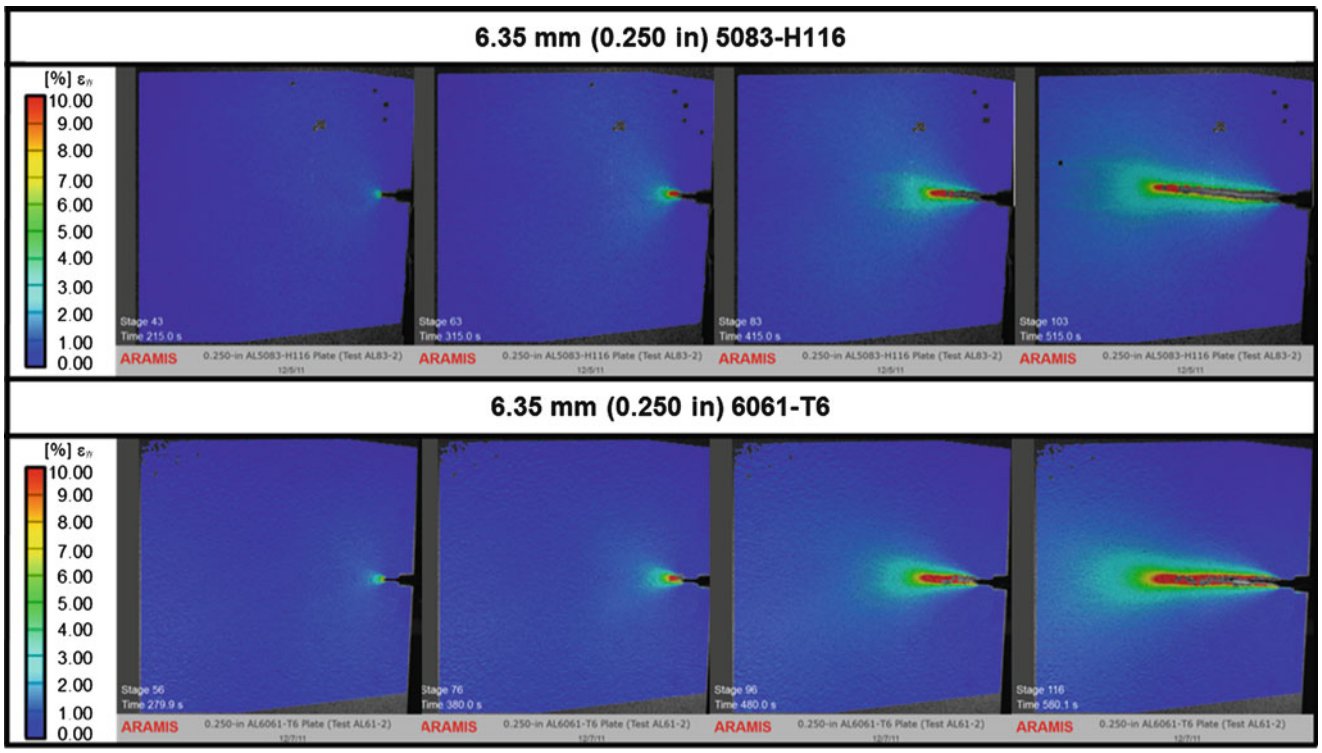

Fig. 11.5 DIC-derived vertical strain fields for 6.35 mm (0.250-in.) 5083-H116 (AL83-2) and 6061-T6 (AL61-2) panels

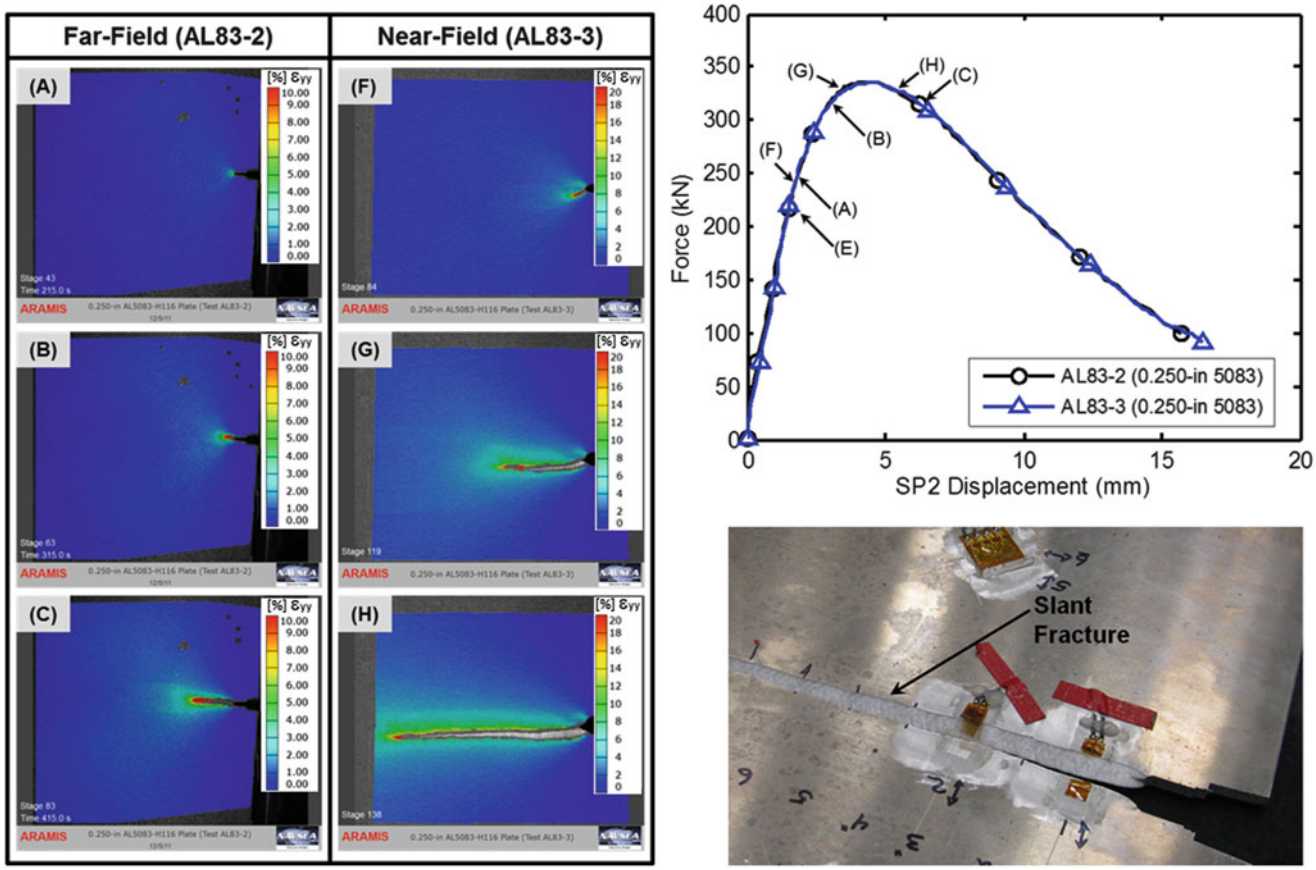

Fig. 11.6 Load versus displacement for 0.250-in 5083-H116 panels

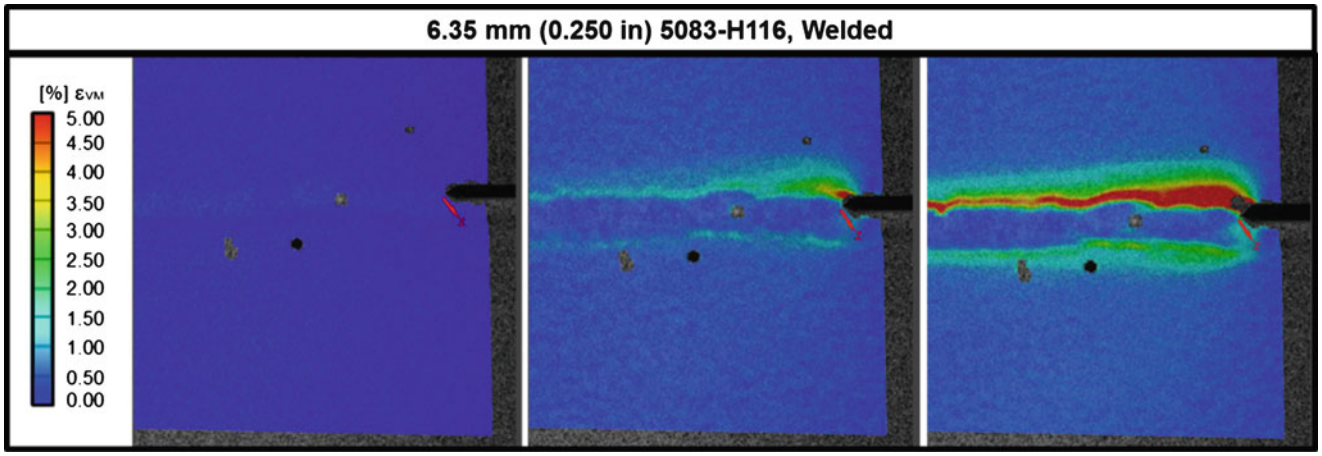

Fig. 11.7 DIC derived contours of in-plane effective strain, welded 6.35 mm (0.250 in.) 5083-H116

Direct comparison of the welded panel with un-welded panels of the same thickness reveals several features. Importantly, the load-deflection curves are nearly identical up to 60 % of the peak load of the un-welded panel and as the welded panel approaches peak load, a drop in modulus is observed. The welded panel displays approximately 85 % of the load carrying capacity of the un-welded panel but the rapid rupture and non-graceful degradation in strength after peak load results in tremendous loss of capacity to deform in the plastic regime as compared to the parent material.

Surface strain measurements from DIC, shown in Fig. 11.7, highlight the role of stress concentration at the toe of the weld in limiting plasticity away from the weld region. The localization of plastic strain and subsequent cracking at the toe of the weld are readily observed. However, due to the surface-measurement nature of the DIC technique, no information is provided on the strain-concentrations in weld metal internal to the joint.

11.5 Conclusions

Fracture tests on large panels using a newly developed tearing test fixture were conducted in order to generate data on the ductile fracture behavior of marine aluminum alloys. The test fixture and panel configuration were proven to provide the required background plasticity as well as ductile crack propagation phenomena under sufficiently rigid boundary conditions. Key findings include:

- The test provides a controllable and repeatable methodology for quantitatively describing the propagations of cracks through a large panel with prior plastic deformation in the zone ahead of the crack.
- Both marine aluminum alloys investigated, 5083-H116 and 6061-T6, exhibited consistently smooth load-deflection curves well beyond initial crack propagation.
- A single welded 5083-H116 panel indicated that locally weak regions of a structure can cause a precipitous drop in plastic capacity while having only a modest effect on peak strength. In addition, the quality of the weldment itself is an important driver of overall panel performance.
- DIC strain-mapping was found to be an important tool in determining the mechanism, overall deformation levels, and extent of crack propagation in the panels that were tested.

The obtained data has increased the understanding of failure of aluminum structures and is likely to prove valuable in developing numerical models of ductile fracture. In particular, the DIC-derived strain fields will readily facilitate comparison with between numerical and experimental results. Due to the ability to model the test configuration in a manner similar to that of a large marine structure, i.e., commonality of element sizes and fracture modeling methodologies, the experimental data can be easily used in the validation and method development of non-linear FE modeling of marine structures subjected to severe loads resulting in rupture.

References

1. Collette MD (2007) The impact of fusion welds on the ultimate strength of aluminum structures. The 10th international symposium on practical design of ships and other floating structures, Houston, TX
2. Simonsen BC, Törnqvist R (2004) Experimental and numerical modeling of ductile crack propagation in large-scale shell structures. Mar Struct 17(1):1–27
3. Neilsen K, Hutchinson J (2011) Cohesive traction-separation laws for tearing of ductile metal plates. Int J Impact Eng 48:15–23
4. Zheng L, Petry D, Rapp H, Wierzbicki T (2009) Mode I fracture of large-scale welded thin-walled AA 6061 extruded panels. Thin-Walled Struct 47(4):375–381
5. Zheng L, Petry D, Rapp H, Wierzbicki T (2008) Mode III fracture of a large-scale welded extruded aluminum panel. Thin-Walled Struct 46(11):1262–1273

Chapter 12
Creep Damage Quantification and Post-fire Residual Strength of 5083 Aluminum Alloy

Y. Chen, S.W. Case, and B.Y. Lattimer

Abstract One of the major concerns regarding the use of lightweight materials in ship construction is the response of those materials to fire scenarios, including the residual structural performance after a fire event. This paper presents a study on creep damage evolution in 5083 marine-grade aluminum alloy and its impact on residual mechanical behavior. Samples were tested at 400 ° C and at different stress levels and times selected to achieve specified creep strain levels. Scanning electron microscopy (SEM) and high resolution optical microscopy were utilized to characterize the creep damage. The damage is primarily manifested as cavitation, grain elongation, and dynamic microstructural evolution. The cavitation morphology, orientation and grain structure evolution were investigated on three perpendicular sample surfaces (rolling, transverse, and normal faces). The competing process between cavitation and grain structure evolution were studied to develop an understanding of the creep damage mechanism. The post-fire residual strength of the Al5083 at 400 °C reveals that the cavitation counteracts the strengthening by grain elongation.

Keywords Creep • Cavity nucleation • Growth • Coalescence • Grain elongation • Residual strength • Fire response

12.1 Introduction

Aluminum alloys are important for lightweight structural applications such as in aerospace and ship engineering. One potential concern with the use of aluminum is the possibility of extreme fire conditions. Under these conditions, the mechanical properties of the material will be degraded and premature failure may occur because of the accumulation of fire damage. This damage to aluminum is complex and may be a combination of grain elongation, precipitate cracking, and cavity formation [1–3]. In situations where the fire is extinguished and yet the structure remains intact, a key concern is the future performance of the structure. In order to predict this post-fire performance, a detailed understanding of the damage that has developed is necessary.

Cavity nucleation, growth, and the subsequent coalescence are the main cause of creep failure. Cavity nucleation requires significant stress concentration that is orders of magnitude greater than the applied stress [4, 5]. The early idea of vacancy agglomeration was from the stable voids (nuclei) [6]. Grain boundary sliding and dislocation pile-up will generate sufficient local stresses and promote the formation of cavities, particularly when they occur against precipitates on the grain boundaries [7, 8]. Existing cavities will also cause stress concentration and lead to new cavity formation as the damage progresses [9]. Once formed, cavity growth is primarily driven by two different mechanisms: vacancy diffusion and creep plasticity [10–12]. The comparison between diffusive cavity growth and plastic cavity growth demonstrated that cavities grow faster when driven by plasticity. Grain boundary sliding has also been considered as another mechanism for cavity growth [13].

A number of creep damage studies have been performed on superplastic aluminum alloys [14–17]. The effects of thermal exposure and stress state on the cavitation evolution were investigated. It was found that diffusive cavity growth and the effect of creep plasticity in the surround material can be coupled. Cavity growth was verified to be controlled by diffusion when

Y. Chen (✉) • S.W. Case
Department of Engineering Science & Mechanics, Virginia Tech, Blacksburg, VA 24061, USA
e-mail: yanyun@vt.edu

B.Y. Lattimer
Department of Mechanical Engineering, Virginia Tech, Blacksburg, VA 24061, USA

J. Carroll and S. Daly (eds.), *Fracture, Fatigue, Failure, and Damage Evolution, Volume 5: Proceedings of the 2014 Annual Conference on Experimental and Applied Mechanics*, Conference Proceedings of the Society for Experimental Mechanics Series,
DOI 10.1007/978-3-319-06977-7_12, © The Society for Experimental Mechanics, Inc. 2015

cavities are small, then controlled by power-law creep when they are large [18]. Cavities may grow initially by diffusion, then by coupling of diffusion and creep plasticity, and finally by creep plasticity alone. A plastic cavity growth model was proposed, implying that with an initial cavity volume fraction value, cavities grow exponentially with the increase of creep strain [14].

In addition to cavitation, grain size, shape and texture have been found to evolve during the continuous creep deformation. Dynamic recrystallization also takes place during the high temperature creep deformation. Material strength change with the grain size has also been investigated. The Hall-Petch relation established an effective method to estimate material strength caused by average grain size change [19]. The effect of grain shape change on the material strength has also been studied [20]. Grain aspect ratio evolution has been proposed to cause the material yield strength change. Yield strength will increase as structure evolves from equiax grain structure to high aspect ratio grains. Model coupling grain orientation and grain size/shape effect has been developed [21].

Despite these efforts, there is still lack of understanding on the effect of creep cavity growth and dynamic microstructure evolution on the residual material strength for the 5083 aluminum alloy. In this paper, a uniaxial stress state was adopted to perform the tensile creep tests to simulate the fire exposure condition. Damage associated with the creep behavior was examined by both scanning electron microscopy and high resolution optical microscopy. The cavitation and dynamic grain structure evolution in 5083-H116 aluminum alloy during the creep process were examined to study the damage mechanism. Residual mechanical properties were also determined to evaluate the post fire performance of the material. The competing process between cavitation and grain structure evolution was investigated and correlated to the residual material strength.

12.2 Materials and Sample Geometry

For this work, the marine-grade aluminum alloy 5083-H116 is investigated. Aluminum 5083-H116 is a work-hardened alloy that contains 4–4.9 % of magnesium as its major alloying element. The nominal chemical composition is shown in Table 12.1. This alloy is known for exceptional performance in extreme environments and its excellent resistance to seawater and corrosive chemicals. Thus, it is frequently used in ship construction. The material was supplied by Alcoa in the form of 6.35 mm inch thick sheets.

The test sample geometry, illustrated in Fig. 12.1, was selected based on the ASTM standard E21-09. Samples were 304.8 mm long dog-bone samples cut from the aluminum sheet with 6.35 mm uniform thickness. The sample gage length is 190.5 mm. All test samples were machined by using a Tormach PCNC 1100 Mill.

12.3 Experimental Methods

12.3.1 Creep Tests

To induce creep damage to the material, a specified temperature and stress level were selected to simulate the thermo-mechanical loading condition to an aluminum structure. Previous work on the Al5083 alloy revealed that 400 °C was a critical temperature at which grain recrystallization process had been completed and the lowest post-fire yield and ultimate strengths occurred after 400 °C exposure [22], thus 400 °C was chosen to study the creep damage in this paper. All creep

Table 12.1 Chemical composition of Al 5083 material (wt.%)

Chemical element	Al	Mg	Mn	Si	Fe	Zn	Ti	Cr	Cu
Al5083	Balance	4.0–4.9	0.4–1.0	0.4	0.4	0.25	0.1	0.05–0.25	0.1

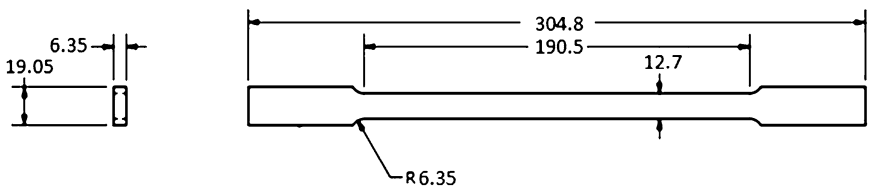

Fig. 12.1 Tensile test specimen geometry (cm)

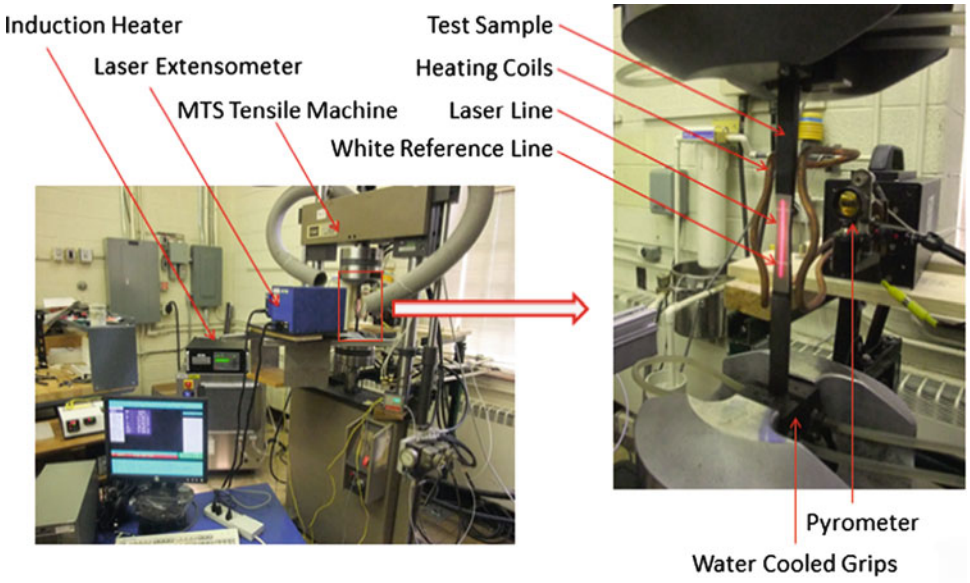

Fig. 12.2 Simulated fire-load conditioning test set up

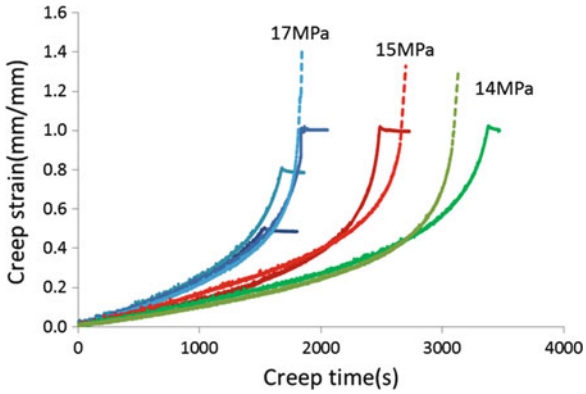

Fig. 12.3 Creep curves of the fire-load conditioning tests for Al5083 samples

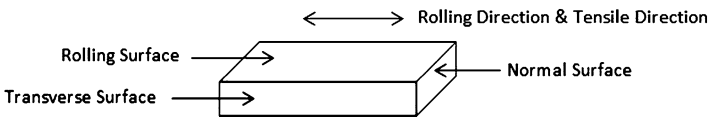

Fig. 12.4 Sectioning terminology

tests were performed using an MTS 880 Test Frame and Ameritherm 5060LI Induction heater. Samples were heated from room temperature to 400 °C at a controlled heating rate of 50 °C/min. After the sample temperature reached 400 °C, a pre-selected engineering tensile stress of 17, 15, or 14 MPa was applied. Samples were then soaked in constant loading and temperature to achieve specified creep strain. During the test, a Micro-Epsilon Infrared Pyrometer was used to control the sample temperature. A lens was mounted in front of the infrared sensor to help focus and precisely measure the center temperature of the sample. Strains were measured over a 22 mm gage length using a Fiedler Optoelektronik GmbH Laser Extensometer, as shown in Fig. 12.2. During the test, water was circulated continuously through the grips to cool the sample ends.

As shown in Fig. 12.3, the creep tests were interrupted at engineering strains of 50, 80, 100, 143 % for 17 MPa applied stress samples; 100, 133 % for 15 MPa tests; and 100, 144 % for 14 MPa. As expected, these samples demonstrated necking in the center of the gauge region, indicating the presence of creep-induced damage. Sections were cut from the sample necking region (6 mm in length) to examine the creep damage. Characterization was performed using two-dimensional techniques on all three surfaces (rolling, transverse and normal surfaces as shown in Fig. 12.4) to observe the cavity morphology and grain structure. To link the microstructural details above to mechanical properties, duplicated creep samples were prepared and used to perform room temperature tensile tests for measurement of residual mechanical properties.

12.3.2 Microstructure Quantification

Two-dimensional damage quantification was performed with FEI Quanta 600 FEG Scanning Electric Microscopy and Hirox Optical Microscopy. Samples were first polished with 240, 320, 400, 600, 800 and 1200 grit sandpaper, followed with 3 and 1 μm diamond suspension and MgO powder, then examined by SEM using the second electron detector.

To study the creep damage, 30 SEM images for each sample, 10 images for each surface (rolling, transverse and normal), were collected. Images taken at 500× magnifications were selected to study the cavity evolution. This magnification shows a sample surface area of 512 × 443 μm, which is the optimal size to analyze cavities of sizes greater than 1 μm and represent the overall damage state of the creep samples. To estimate the cavity volume fraction, grey-scale SEM images were converted to binary images using a thresholding process in Matlab. The threshold value was adjusted for each SEM images based on their different brightness. The average cavity size was calculated based on the total cavity area and the number of cavities in each image (assuming spherical cavities and circular cross-sections).

To study dynamic microstructural evolution, samples were etched using an etchant consisting of 12 mL HCl (conc.), 26 mL HNO_3 (conc.), 1 mL HF (48 %), 17 mL H_2O and 4.8 g chromic acid. Etchant was held at room temperature for 4 h before sample etching. High resolution optical microscopy and SEM investigation were then applied to observe the cavitation and grain structure evolution.

12.4 Results and Discussion

12.4.1 Creep Samples

Figure 12.5 shows the tested samples stopped at multiple creep strain for 400 °C exposure and different applied stresses. Both unfractured and fractured creep samples tested at 17, 15 and 14 MPa are shown in Fig. 12.5a–c with the fractured samples on the right side of the images. Large plastic deformation and severe necking were observed in those fractured samples. The fracture surfaces are almost necked to a thin line, with 90 % of reduced area, indicating highly ductile failure of those fracture samples. Figure 12.5d shows a zoomed in view of the necking portion for the 14 MPa, 144 % strain sample with several cracks observed on the rolling surface indicating impending failure. Similar cracks are shown for the 17 MPa, 143 % strain creep sample. Moreover, the 143 and 144 % creep samples have similar extension with the fracture ones on their right; indicating they has reached the just-before-fracture state. For the 15 MPa, 133 % strain sample, necking is not so severe as the 143 and 144 % ones, and no crack was observed on the sample surface, implying that this sample was approaching failure but had not reached the just-before-fracture state yet.

12.4.2 Damage Quantification

12.4.2.1 Cavitation Evolution

Figure 12.6 shows the SEM observations of the microstructures of the rolling surface for Al5083 as-received and 17 MPa 50–144 % strain samples. The cavities are randomly distributed and appear darker on the light aluminum background. Creep damage is manifested in the increase in the number of visible cavities as well as the growth of those cavities. No cavities were observed in the as received microstructure; however, some precipitates are randomly distributed, as shown in Fig. 12.6a. Under thermo-mechanical loading condition, significant stress concentration will be generated around the precipitates and on the junction of grain boundaries. New cavities will nucleate at these locations due to sufficient local stress concentrations during plastic deformation.

As the creep strain increases, severe necking indicates more damage occurs in the sample. For creep microstructures at strains lower than 100 %, the cavities appear mostly spherical shape, randomly distributed on the sample inner surface. These cavity sizes are relatively small and similar. As the sample creep strain exceeds 100 % strain, the cavities begin to agglomerate and more irregular cavity shapes are observed in the microstructure. This phenomenon indicates that cavity coalescence begins between 80 and 100 % creep strain level. After the sample creeps beyond 100 % strain and approaches failure, more spherical cavities were stretched and coalesced into crack-like cylindrical cavities, which are parallel to the direction of rolling and loading have lengths ranging from 50 to 150 μm and aspect ratios larger than 5.

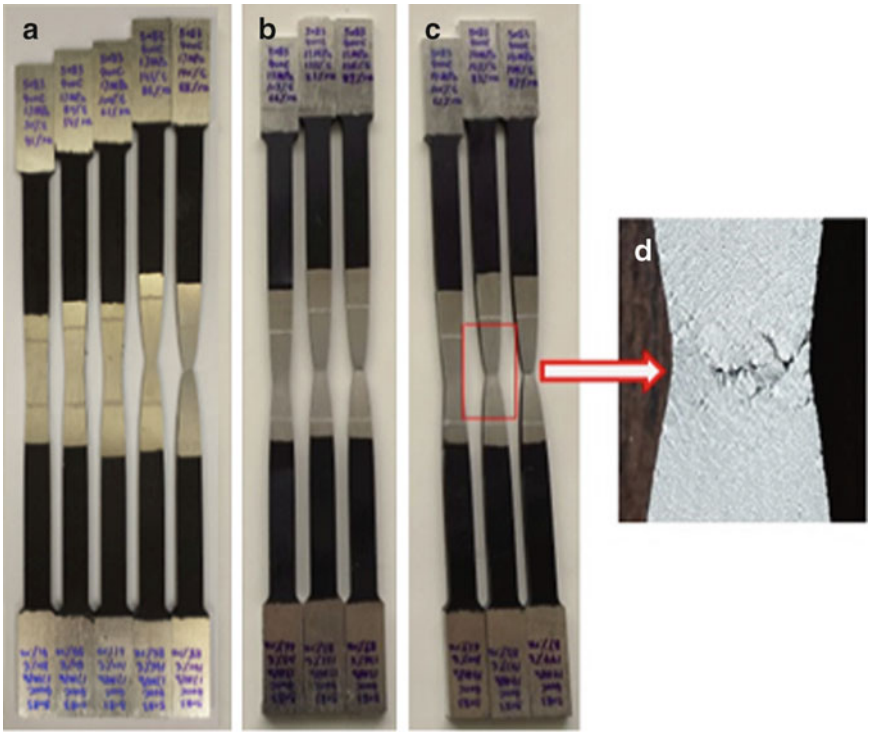

Fig. 12.5 (**a**) 17 MPa, 50, 80, 100, 143 % creep and fracture samples (**b**) 15 MPa, 100, 133 % creep and fracture samples (**c**) 14 MPa, 100, 144 % creep and fracture samples (**d**) Necking region of just-before-fracture sample

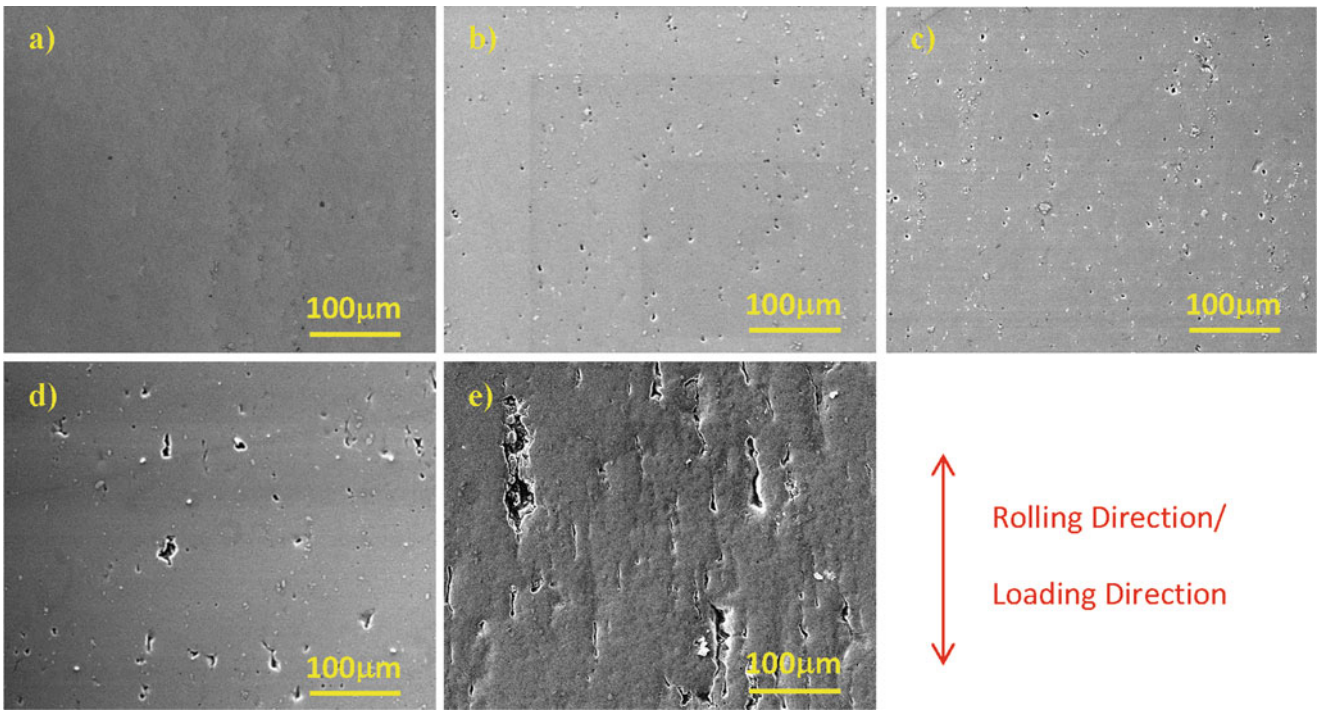

Fig. 12.6 ESEM images (500×, rolling surface) (**a**) As received sample $\varepsilon = 0$ %, and 400 °C 17 MPa applied stress samples (**b**) $\varepsilon = 50$ % (**c**) $\varepsilon = 80$ % (**d**) $\varepsilon = 100$ % (**e**) $\varepsilon = 143$ %

Closer inspection of the three-surface microstructures gives more evidence of the creep cavity orientation. Both rolling and transverse surfaces display vertical crack-like cylindrical cavities along the direction of rolling and loading, while round-like cavities are randomly distributed on the normal surface, as shown in Fig. 12.7. These cavity morphologies on the three surfaces indicate that during high plastic deformation, creep cavities grew from the original spherical shape into the longer, cylindrical shapes along the direction of rolling and loading. Similar cavity morphologies are displayed in all three surfaces

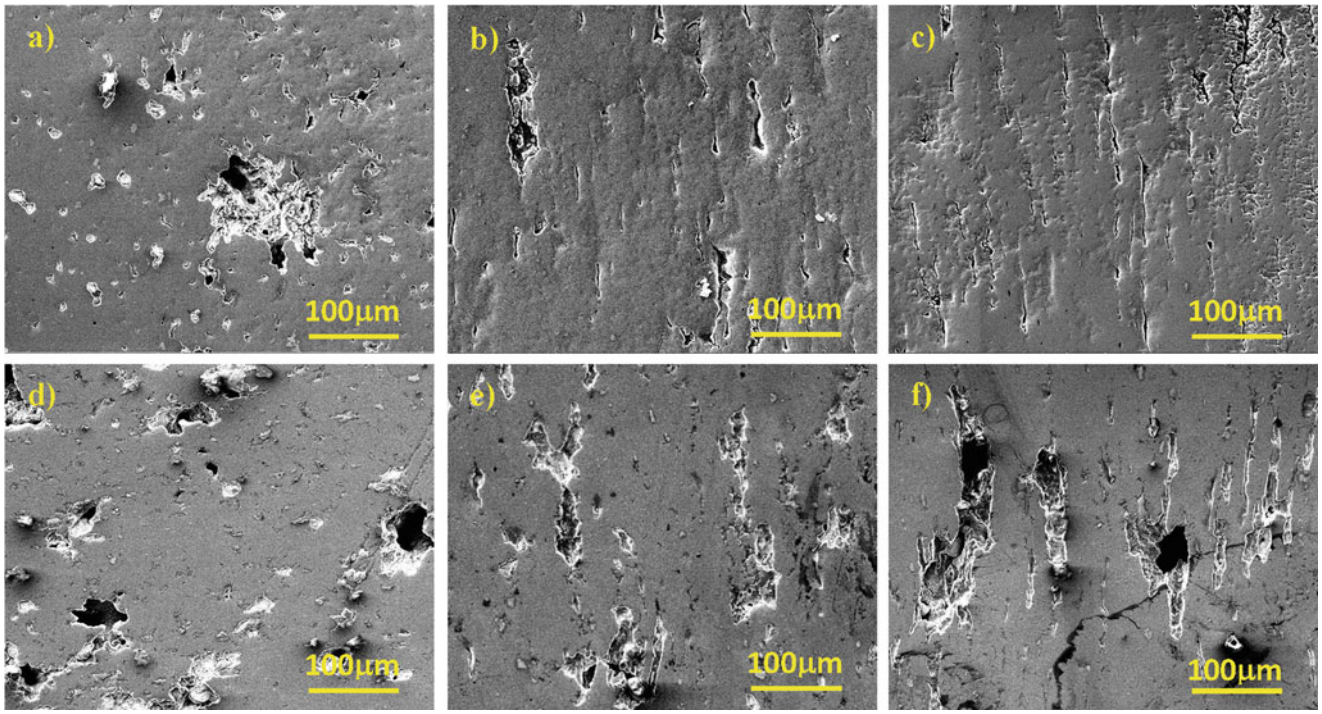

Fig. 12.7 Three surfaces ESEM images (500×) of just-before-rupture samples (**a**) 17 MPa, Normal (**b**) 17 MPa, Rolling (**c**) 17 MPa, Transverse (**d**) 14 MPa, Normal (**e**) 14 MPa, Rolling (**f**) 14 MPa, Transverse

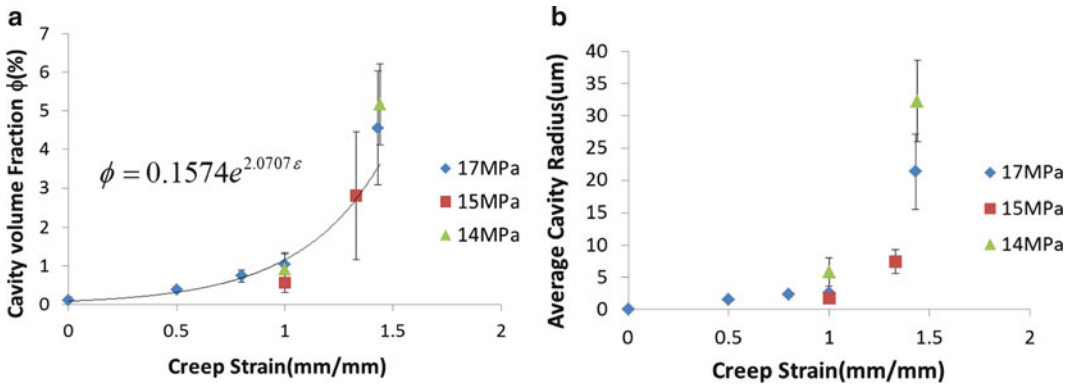

Fig. 12.8 (**a**) Cavity volume fraction versus creep strain (**b**) Average cavity size evolution versus creep strain

of the 17 and 14 MPa samples, indicating similar damage has been developed during the creep tests within 14–17 MPa range. Several small cracks are also observed in some locations of 14 MPa microstructure, as shown in Fig. 12.7f. These cracks grow transversely to the direction of rolling and loading and connect the closely spaced cavities, implying that microcracks will be developed after the coalescence of the cavities and the following crack propagation will cause sample failure.

Creep damage can be represented as cavity volume fraction and cavity size in the deformed material. The cavitation evolution for the above microstructures are characterized and summarized in Fig. 12.8. As shown in Fig. 12.8a, the cavity volume fraction is quantified for different creep strain and stress levels. For samples tested at 17 MPa stress, the cavity volume fraction shows a gradually increasing trend with the increase of creep strain below 100 %, but the damage value is limited to 1 % cavity volume fraction at 100 % strain level. As the sample continues to deform above a creep strain of 100 %, the sample approaches the failure and the rate of cavity growth dramatically increases. However, the critical value of the cavity volume fraction before sample failure is still relatively small (approximately 4.7 % for the 17 MPa sample).

Similar quantification was performed for 14 and 15 MPa samples. Creep strain levels of 100 % and just-before-fracture (approximately 140 %) were selected to compare the creep damage induced by different applied stress. As shown in Fig. 12.8a, the quantified cavity volume fraction values at 100 % strain level are around 1 % for all 14–17 MPa creep

samples. The just-before-fracture data of 14 and 17 MPa samples also gives similar cavity volume fraction (about 5 %), which corresponds to similar damage states in the three surface microstructures in Fig. 12.7. The 15 MPa, 133 % strain sample captures about 3 % cavity volume fraction, which lies between the 1 % damage at 100 % strain and the 5 % damage at the just-before-rupture state. The 5 % cavity volume fraction can be defined as the critical damage value at the just-before-fracture state. The standard deviations of the cavity volume fraction are 5.8 and 6.4 at the just-before-fracture state, which is quite large compared to the small value below 100 % strain, which is coincident with the observation that cavity coalescence into large crack-like cylindrical cavities after 100 % strain. These large crack-like cylindrical cavities are non-uniformly distributed inside the necking region of the creep sample.

The cavity size evolution with creep strain is similar with the cavity volume fraction evolution. As shown in Fig. 12.8b, the average cavity size gradually increases below 100 % strain and sharply increases when the creep strain exceeds 100 %. Cavity sizes are similar at the same creep strain levels for all 14–17 MPa samples. A larger standard deviation also occurs at the just-before-fracture states.

Previous work has indicated that the cavity growth will switch from diffusion-controlled to plasticity-controlled with the enlargement of cavity size. In the small cavity state, cavity grow is dominated by the diffusion controlled mechanism. In contrast, plasticity controlled growth is the dominant mechanism in large cavity state under high creep strain [23]. The superplastic cavity growth model [24] suggested a critical cavity size of 0.5 μm. When average cavity size is smaller than 0.5 μm, the cavity growth is diffusion controlled; the cavitation is plasticity controlled when the cavity size is greater 0.5 μm. Figure 12.8b shows that the average cavity sizes are greater than 0.5 μm, thus the cavity growth in Al5083 creep tests is primarily controlled by plasticity based on the above condition.

When cavity growth is plasticity-controlled, the cavity volume fraction can be given by a simple model in Eq. 12.1:

$$\varphi = \varphi_0 \exp(\eta\varepsilon) \tag{12.1}$$

where ϕ is the cavity volume fraction at strain ε, ϕ_0 is the initial cavity volume fraction of the as-received material, and η is a growth parameter usually ranging from 2 to 4, which is dependent on material, strain rate, temperature, and grain size. An exponential fit based on the data collected at all stress levels in Fig. 12.8a yields an η of 2.0707, which lies between the upper bound calculated value 2.5 by Cocks and Ashby's model and the conservative predicted value 1 by Budiansky [14].

12.4.2.2 Dynamic Microstructure Evolution

The dynamic microstructure evolution with the increase of creep strain was also investigated. As shown in Fig. 12.9a, large gains parallel with the direction of rolling are observed on the rolling surface of the as-received sample. The average grain size is approximately 80 μm. Several cavities are observed inside the grains due precipitates removed by the etchant. After 400 ºC exposure, the grain recrystallization process is completed and the average grain size decreases to 46 μm with an equiax grain structure as shown in Fig. 12.9b. Through Fig. 12.9a–e, the grains are observed to be stretched along the horizontal direction (direction of rolling and loading) from the equiax structure to thin, long pancake grain structure. Data in Fig. 12.10 shows that gain aspect ratio increases from 0.91 at 1 % strain to 11.1 at 143 % creep strain, which indicates the grains are highly elongated along the tensile direction to accommodate the large plastic deformation during creep.

Small spherical cavities are observed to nucleate at the grain boundary when the sample creeps at moderate strain levels (50 and 80 % strain). The formation of these cavities is promoted by the stress concentrations on the grain boundaries, particularly at the triple junction of grains and where precipitates are located on grain boundaries. As the sample creeps continuously to the high strain levels (100 % strain and before fracture), the cavity growth is controlled by creep plasticity. Large creep strains are produced around the surface of the cavities and small cavities are driven to coalesce into larger ones [14]. Grain boundary sliding also occurs during this plastic creep process to cause significant stress concentration in the plane of the sliding boundary which also promotes the cavity growth [13]. During this stage, small spherical cavities develop into larger crack-like cylindrical cavities along the grain boundaries, as shown in Fig. 12.9e.

Figure 12.11 shows the clear view of cavity growth and coalescence at high creep strain levels. Clear grain boundaries can be identified from the sample surface. Crack-like cylindrical cavities are developed between grains and grow along the grain boundaries. Some closely spaced cavities are observed to coalesce. Cavity coalescence is the final stage of the cavity growth, and the creep plasticity controlled mechanism is an important factor in this stage [25]. In some cases, fracture occurs when these intergranular cavities disintegrate the grains between them and coalesce across grains to develop into the transgranular cavities. However, the coalescence of the intergranular cavities is distributed quite non-homogeneously on the grain boundaries and some boundaries have reached the state of coalescence while others have not yet begun. As a consequence, some grain boundary facets are separated before fracture occurs due to the stress being redistributed

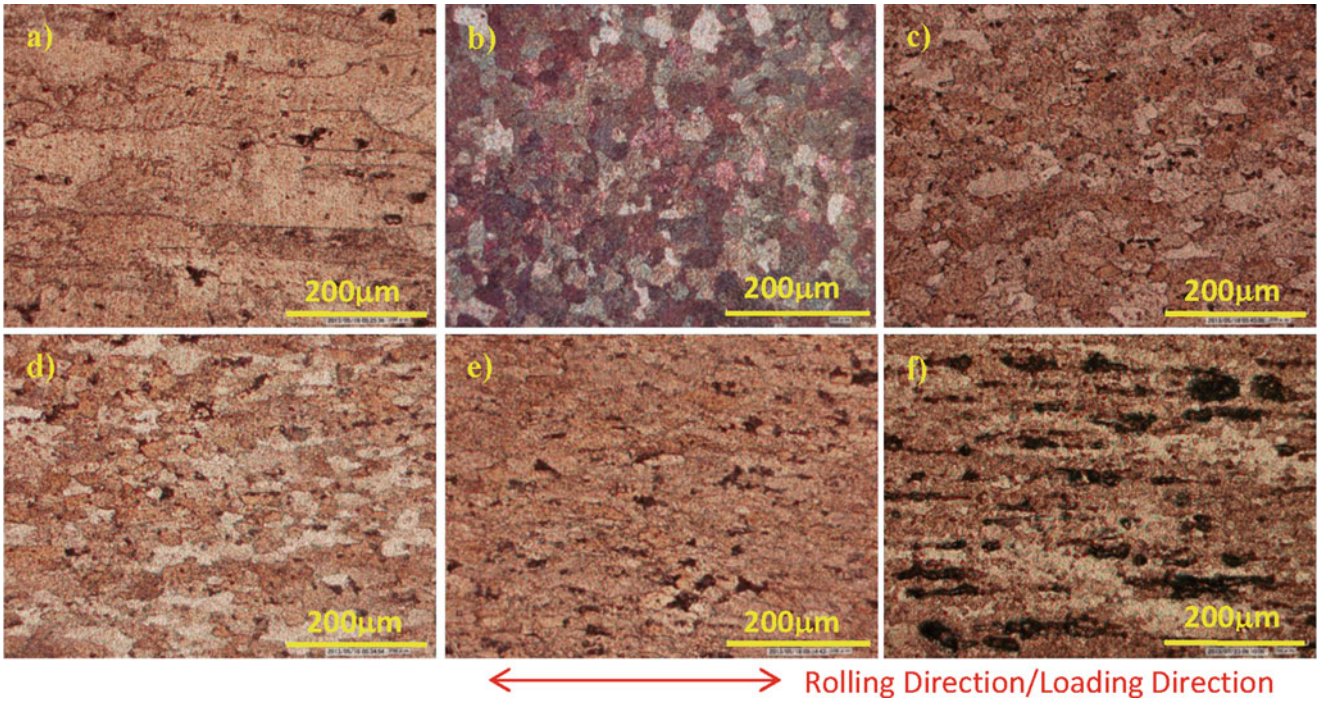

Fig. 12.9 Grain structures evolution (560×, rolling surface) (**a**) As received (**b**) 400 °C, 0 MPa, $\varepsilon = 1$ %, and (**c**)–(**f**) 400 °C, 17 MPa, $\varepsilon = 50$, 80, 100 and 143 %

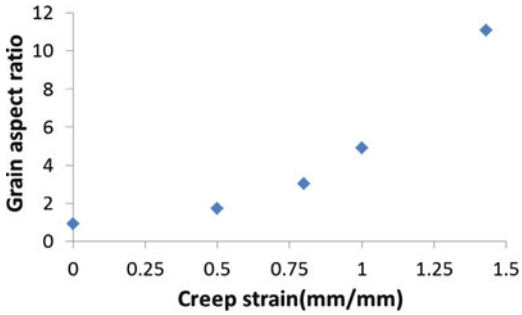

Fig. 12.10 Grain aspect ratio (calculated based on rolling surface grains) versus creep strain for 400 °C, 17 MPa creep samples

during non-homogeneous cavitation. With continuous plastic deformation, the separated grain boundaries will be connected and microcracks will be developed from the coalescence of closely spaced cavities at the just-before-fracture state. The interlinkage and propagation of these microcracks will lead to fracture of the material.

12.4.2.3 Post-fire Residual Material Strength

The post-fire residual mechanical properties of the 400 °C, 17 MPa creep samples were measured through room temperature tensile tests. The 0.2 % offset yield strength and ultimate strength are provided in Fig. 12.12 along for the as-received samples as well as samples heated to 400 °C and crept to various levels of strain. To isolate the residual strength degradation due to the thermal exposure, the post-fire strength of samples exposed to 400 °C without applied stress is also contained in Fig. 12.12. For a sample with only thermal exposure, material strength decreases primarily due to the static grain recrystallization. This results in a decrease of 160MPa and 50MPa in the residual yield and ultimate strengths, respectively. As the soak time increases, residual strength of the thermal exposure samples remains constant, which is due to the fact the material has fully recrystallized by the time the sample reaches 400 °C at the heating rate used in this work.

To better represent the post-fire mechanical properties, residual material strength is calculated based on the deformed cross section area. Compared to a sample subjected to a 400 °C exposure with no applied stress, residual material strengths of the 400 °C, 17 MPa creep samples show similar yield strength at low strain levels (25 and 50 % strain), but gradually increase at the mid to high strain levels. The yield strength increases by 30 MPa at the high strain levels (143 % strain). This

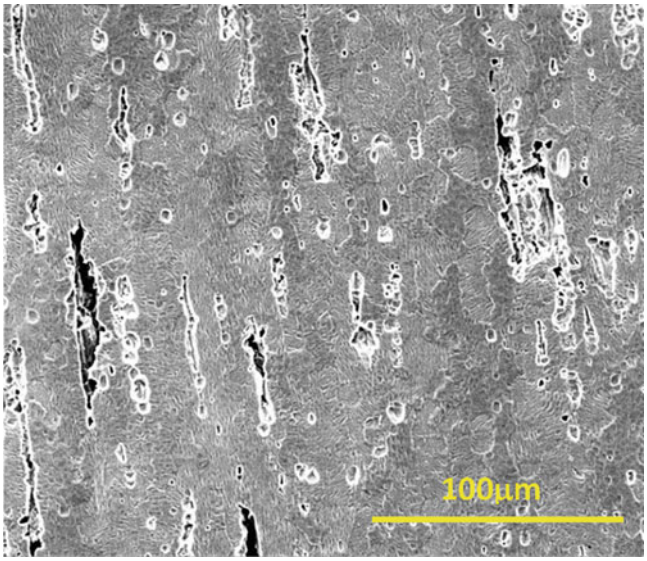

Fig. 12.11 Etched microstructures (1,000×, 400°C, 17 MPa, 143 % creep strain)

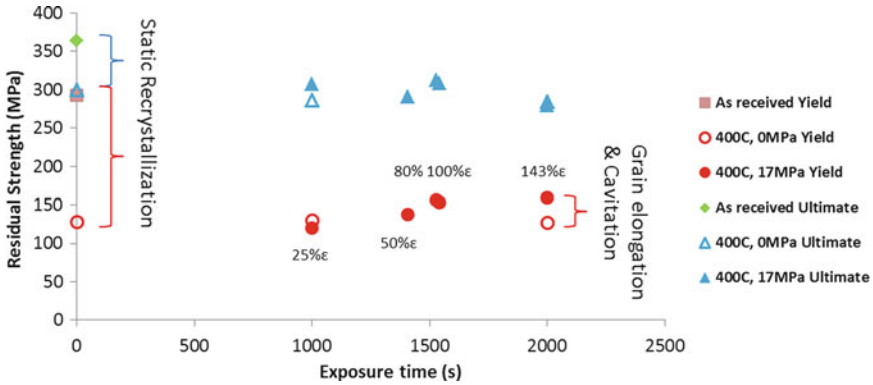

Fig. 12.12 Post-fire Residual material strength versus exposure time for thermal exposure and creep samples

increase in strength is related to the grain structure evolution. Yield strength is suggested to be at a minimum value at the equiax state, then increases with the increase of grain aspect ratio [21]. Since grain aspect ratio was observed to increase from 0.91 to 11.1 with increase in creep strain in Fig. 12.10, the increase of yield strength with strain was attributed to the strengthening by grain elongation during plastic deformation at high stain levels.

Previous discussion reveals two completing mechanisms during creep deformation: cavitation which degrades the residual strength by introducing defects inside the material and grain elongation which strengthens the material by strain hardening of the grains. From Figs. 12.8a and 12.10, effects of these two mechanisms are enhanced with an increase in creep strain. From Fig. 12.12, almost no change in strength was measured up to strains of 25 % due to the small amount of cavitation and grain elongation as seen in Figs. 12.8 and 12.10. At high strain levels (143 %) where cavitation is significant and grains become highly elongated, the two effects counteract each other resulting in only a small difference in the yield strength of thermal exposure and creep samples.

12.5 Conclusion

This work examined the creep damage evolution of Al5083 due to a thermal exposure of 400 °C with selected applied stress. Cavitation and grain structure evolution at multiple creep strain levels were quantified and analyzed to study the creep damage mechanism. Stress concentration promotes cavity formation on the grain boundaries while creep plasticity dominates the subsequent cavity growth. Cavity morphology changes from a small spherical shape at low strain level to a large crack-like cylindrical shaped cavity at higher strain with the length of the cylinder orientated along the direction of rolling and loading. Cavity volume fraction increases as a function of creep strain. Simultaneously, dynamic microstructural evolution causes grains to evolve from an equiax grain structure to a textured thin pancake grain structure at high strains.

Grain aspect ratio increases significantly with the increase of creep strain. At high strains, the reduction in strength due to cavitation is counteracted by the strengthening of grain elongation. As a result, high strain levels caused an small increase in strength over unstressed samples despite significant cavitation.

Acknowledgements The authors would like to thank the Office of Naval Research for funding this work under Grant N00014-11-1-0875, scientific monitor Dr. William Mullins.

References

1. Leckie FA, Hayhurst DR (1974) Creep rupture of structures. Proc R Soc Lond A 340:323–347
2. Lin J, LIU Y, DEAN TA (2005) A review on damage mechanisms, models and calibration methods under various deformation conditions. Int J Damage Mech 14:299–319
3. Hénaff G, Odemer G, Journet B (2011) Creep and creep fatigue crack growth in aluminium alloys. Aluminium alloys, theory and applications. InTech, Rijeka, Croatia, pp 259–282
4. Evans HE (1984) Mechanisms of creep fracture. Elsevier Applied Science, London
5. Kassner ME, Hayes TA (2003) Creep cavitation in metals. Int J Plast 19:1715–1748
6. Greenwood JN, Miller DR, Suiter JW (1954) Intergranular cavitation in stressed metals. Acta Metall 2:250–258
7. Yoo MH, Trinkaus H (1986) Interaction of slip with grain-boundary and its role in cavity nucleation. Acta Metall 34:2381–2390
8. Trinkaus H, Yoo MH (1987) Nucleation under time-dependent supersaturation. Phil Mag A Phys Condens Matt Struct Def Mech Prop 55:269–289
9. Anderson PM, Shewmon PG (2000) Stress redistribution and cavity nucleation near a diffusively growing grain boundary cavity. Mech Mater 32:175–191
10. Hulla D, Rimmera DE (1959) The growth of grain-boundary voids under stress. Phil Mag 4:673–687
11. Hancock JW (1976) Creep cavitation without a vacancy flux. Metal Sci 10:319–325
12. Raj R, Ashby MF (1975) Intergranular fracture at elevated-temperature. Acta Metall 23:653–666
13. Chen IW (1983) Mechanisms of cavity growth in creep. Scr Metall 17:17–22
14. Kannan K, Hamilton CH (1998) Inhomogeneities in initial cavity distribution in a superplastic Al 5083 alloy. Scr Mater 38:299–305
15. Chandra N, Chen Z (2000) Cavity nucleation in Al5083 alloys. Mater Res Soc 601:235–246
16. Hsiao IC, Huang JC (2002) Deformation mechanisms during low- and hightemperature superplasticity in 5083 Al-Mg alloy. Metall Mater Trans A 33A:1373–1384
17. Kaibyshev FMR, Lesuer DR, Nieh TG (2003) Superplastic behavior of an Al–Mg alloy at elevated temperatures. Mater Sci Eng A342:169–177
18. Cocks ACF, Ashby MF (1982) Creep fracture by coupled power-law creep and diffusion under multiaxial stress. Metal Sci 16:465–474
19. Hall EO (1951) The deformation and ageing of mild steel: III discussion of results. Proc Phys Soc Sec B 64:747
20. Bunge HJ, Wagner F, Welch PI, Vanhoutte P (1985) A new way to include the grain shape in texture simulations with the Taylor model. J Phys Lett 46:1109–1113
21. Sun S, Sundararaghavan V (2012) A probabilistic crystal plasticity model for modeling grain shape effects based on slip geometry. Acta Mater 60:5233–5244
22. Matulich RD (2011) Post-fire mechanical properties of aluminum alloys and aluminum welds. M.S. thesis, Virginia Tech
23. Tsutomu Tanaka KH (2004) Cavitation behavior in superplastically deformed Zn-22 mass%Al alloy at room temperature. Mater Trans 45:2547–2551
24. Rao MK, Kashyap BP, Mukherjee AK (1984) Cavity growth during superplastic deformation in 7475 aluminum alloys. Pergamon Press, Oxford, pp 2311–2317
25. Goods SH, Nix WD (1978) Coalescence of large grain-boundary cavities in silver during tension creep. Acta Metall 26:753–758

Chapter 13
Nanoindentation Measurements on Rocks

Priyavrat Shukla, Shantanu Taneja, Carl Sondergeld, and Chandra Rai

Abstract Young's modulus and hardness of shale are important parameters for the design of hydraulic fractures and the selection of proppant. Nanoindentation has shown applicability in fine grained rocks and provides a method to measure these parameters using core fragments and drill cuttings. Nanoindentation measurements on horizontal and vertical samples can be used to quantify anisotropy. Indentation Young's modulus correlates well with dynamic modulus obtained from acoustic velocity data on core plugs. Nanoindentation is thus a viable method to measure mechanical properties of fine grained shale. Young's moduli obtained by nanoindentation are related to composition and porosity, e.g., total organic carbon (TOC), porosity and mineralogy. Young's modulus showed a trends with both TOC and porosity and warrants further study to establish more robust relationships. The primary aim of this paper is to study the applicability of nanoindentation to shale and this is established by comparing nanoindentation results with standard dynamic pulse-transmission velocity measurements. Nanoindentation on Wolfcamp shale, Lyons sandstone, Sioux quartzite, Indiana limestone and pyrophyllite was performed to test whether the nanoindentation test gives representative results of the whole sample with variation in grain size. The experimental results indicate that nanoindentation measures the grain Young's modulus due to all indentations on a single grain for coarse grained rocks and thus, resulting in incorrect Young's modulus of rock. However, for rock with smaller grain (<indenter area), nanoindentation results are representative of multiple grains and hence correlating well with the dynamically determined Young's modulus.

Keywords Nanoindentation • Young's modulus • Shale • Sandstone • Limestone

13.1 Introduction

US oil and gas industry has witnessed resurgence with the development of shale resources. With the advent of horizontal drilling and development of hydraulic fracturing, shales have not only surpassed our understating of its capacity to produce economically but has contributed to US natural gas production of 23 trillion cubic feet (Tcf) in 2011 and is expected to dominate production by 2040 [1]. Shale is the most abundant sedimentary rock in earth's crust. Shale, which is primarily composed of fine grained clastics and carbonates, are characterized by complex microstructure with low matrix porosity and permeability which differentiates it from conventional reservoir rocks. Shale production requires hydraulic fracturing. Mechanical properties of shale are important inputs in hydraulic fracture designs and the industry has either depended on dynamic or static measurements on core plugs or sonic logs to obtain these mechanical properties, primarily Young's modulus. The pulse-transmission technique is a standard dynamic method to measure elastic properties of rocks. The ends of a core plugs are attached to transducers to measure first-break traveltimes of compressional and shear waves. The measured compression or shear wave velocities and density are used to calculate Young's modulus and Poisson's ratio. Nanoindentation provides an alternative reliable method to obtain Young's modulus which agrees well with this dynamic measurement technique, and it provides a means to obtain reliable measurement of Young's modulus on small, millimeter sized, rock samples, It is a viable technique to obtain Young's modulus from core fragments and drill cuttings in absence of core plugs. In addition to measuring Young's modulus, nanoindentation provides a measure of the mechanical anisotropy in shales when

P. Shukla (✉) • S. Taneja • C. Sondergeld • C. Rai
University of Oklahoma, 100 E. Boyd Street, Norman, OK 73069, USA
e-mail: priyavrat.shukla@gmail.com

J. Carroll and S. Daly (eds.), *Fracture, Fatigue, Failure, and Damage Evolution, Volume 5: Proceedings of the 2014 Annual Conference on Experimental and Applied Mechanics*, Conference Proceedings of the Society for Experimental Mechanics Series,
DOI 10.1007/978-3-319-06977-7_13,

bedding directions are known. Shales are found to contain a variable amount of organic matter which not only contributes to anisotropy [2] but also contains significant pore volume.

Hydraulic fracturing is necessary to create a conductive pathway for hydrocarbons to flow in most shales. Fracturing fluid is pumped at high pressures to initiate fracture and is followed by proppants to keep fracture open and maintain conductivity. It is observed that the fracture conductivity can degrade due embedment of proppants in shale under the influence of closure stress. Guo and Liu [3] and Akrad et al., [4] have concluded that the probability of proppant embedment increases with increase in soaking time which makes the rock weaker. Guo and Liu [3] indicated that embedment depends on Young's modulus. They explained the embedment characteristics of various shales using their proppant embedment model and concluded that shales, characterized by higher Young's moduli and low closure stress showed gradual embedment. Akrad et al., [4] conducted tests on Bakken, Barnett, Eagle Ford and Haynesville shales after exposing them to fracturing fluids at 300 °F for 48 h and observed significant drop in Young's modulus using a nanoindentation technique.

13.2 Objective

The primary objective of this study is to understand the applicability of nanoindentation on rocks. However, the most critical aspect of nanoindentation is sample preparation and instrument calibration. Instrument calibration is out of scope of this paper and more details about same can be found in Shukla [5]. This paper describes the procedures followed for making measurements on rock fragments. We then discuss results on the following coarse grained rocks: Lyons sandstone, Sioux quartzite, Indiana limestone and pyrophyllite. Measurements on shale are also presented.

13.3 Sample Preparation

Nanoindentation testing requires samples in the form of discs with thickness no more than 8 mm, and, diameter no more than one inch. However, rock fragments can also be used as long as they are embedded in a host medium [5]. Measurement requires a flat and smooth target surface; contact area is calculated on the basis of contact depth and indented area ([5], [6]). It is challenging to achieve a perfectly smooth surface, but combination of polishing and ion milling reduce errors in nanoindentation results. Samples are progressively polished on abrasive papers from 60 to 3,000 grit size to make the top and bottom surfaces parallel to ± 0.01 mm thickness variation [5]. An alternative method to dry mechanical polishing is use of precision polisher that involves sample polishing using a rotating disc at the bottom and a shaft that rotates the sample. Presence of water or oil between the disc and rock surface provides lubrication and cooling. Mechanical polishing is followed by broad beam argon ion milling to further reduce surface asperities. Ion milling is carried out by accelerating ionized argon gas and impinging it on sample surface at angles almost parallel to sample surface under vacuum. Power of ion beam and duration of milling may be varied based on sample composition. Figure 13.1 shows survey scans of an ion-milled sample and un-ion-milled sample [5]. The variation in roughness scale in ion-milled sample is from 0 to 1,546 nm while that in the un-ion milled sample is from 0 to 3,243 nm. Variations in results due to inefficient polishing are shown in Fig. 13.2 where histograms of Young's modulus on ion-milled and un-ion-milled shale sample are presented [5]. Un-ion milled samples show larger scatter. Similar results were also observed by Kumar ([7], [8]).

13.4 Results

This study investigates whether the small area of investigation during a nanoindentation test gives a representative result for the whole sample. Scanning Electron Microscope (SEM) studies show that indenter senses multiple grains in shales, but this is not true in coarse grained rocks. Also nanoindentation results, due to smaller depth of investigation are fairly independent of cracks present inside the rock sample. These data should be close to crack free Young's moduli of core plugs obtained at higher confining pressures from dynamic pulse-transmission experiments. Figure 13.3 shows the image of the four core plugs of different lithologies used for testing [5]. This section provides indentation results and compares them to results from dynamic velocity measurements. Table 13.1 provides summary of results of tests performed on Wolfcamp shale, Lyons sandstone, Sioux quartzite, Indiana limestone and pyrophyllite [5].

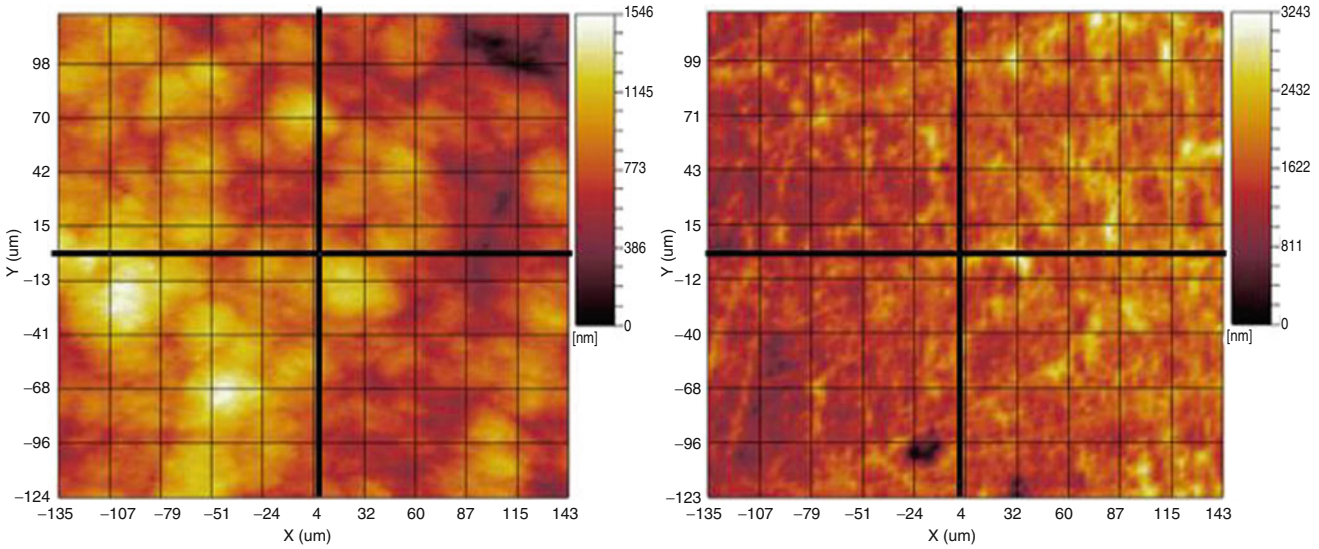

Fig. 13.1 Survey scanning topography of two shale samples, ion-milled (*left*), un-ion-milled (*right*) [5]. Variation in topography for ion milled sample is from 0 to 1,546 nm while for un-ion milled variation is 0–3,243 nm. Variation in topography controls surface roughness which affects the orthogonality of the indent

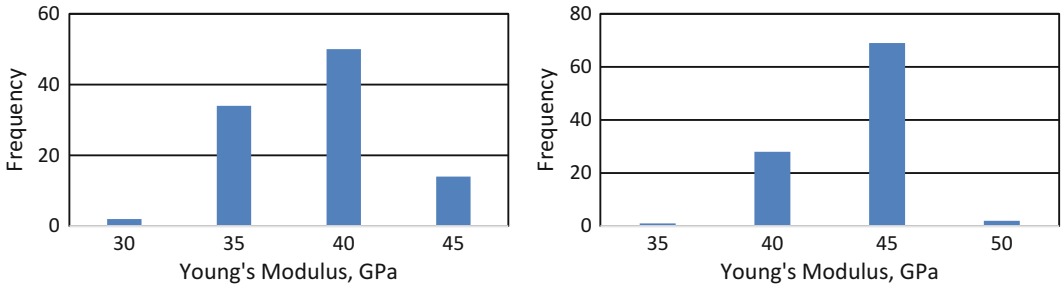

Fig. 13.2 Histogram of Young's modulus measured on Wolfcamp shale sample without ion milling (*left*) and with ion milling (*right*) [5]. Greater standard deviation is observed for un-ion milled sample as compared to ion milled sample

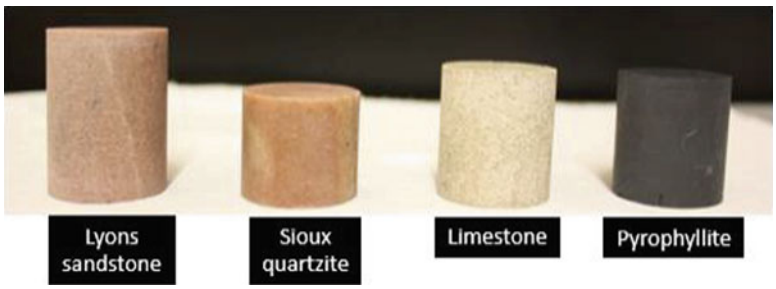

Fig. 13.3 Core plug images for (*left* to *right*) Lyons sandstone, Sioux quartzite, Indiana limestone and pyrophyllite [5]

13.5 Wolfcamp Shale

Mechanical properties of shales have been studied extensively by Kumar, ([7], [8]) and Shukla, [9]. They studied samples from Wolfcamp, Woodford, Barnett, Hayensville, Eagle Ford, Collingwood, and Kimmeridge shales. A more detailed analysis of mechanical properties of shale and its dependence on mineralogy, porosity and TOC can be found in Kumar, ([7], [8]) and Shukla, [9]. In this study, we present results of Fourier Transform Infrared Spectroscopy (FTIR), low pressure pycnometer porosity (LPP) and dynamic pulse transmission measurements along with nanoindentation measurements on a specific sample of Wolfcamp shale. The sample was prepared following the procedure explained above. FTIR mineralogy results showed that sample is primarily composed of 47 % clays, 22 % quartz and 13 % carbonates. LPP was used to measure porosity and showed porosity of 7.3 %. Total organic content (TOC) of the sample was also analyzed using LECO C844

Table 13.1 Summary of porosity, grain density, grain size and Young's moduli [5]

	Wolfcamp Shale	Lyons Sandstone	Sioux Quartzite	Indiana Limestone	Pyrophyllite
Porosity (%)	7.3	5.7–8.9	2.5	15.6	4.3–5.9
Mineralogy (Wt %)	47 % Clays, 22 % quartz, 13 % carbonates	80–85 % Quartz, 7–11 % mixed clays	99 % Quartz	89 % Carbonates, 6 % clays	Pyrophyllite minerals
Grain density (g/cm^3)	– (Bulk density—2.58 g/cm^3)	2.64–2.66	2.65	2.7	2.83–2.84
Grain size	Very fine	190 μm	Fused grains	500 μm	Very fine
Dynamic Young's Modulus (GPa)	46	57–60	71–82	36–41	30–34
Indentation Young's Modulus (GPa)	33–50	84–96	90–100	42–55	34–40

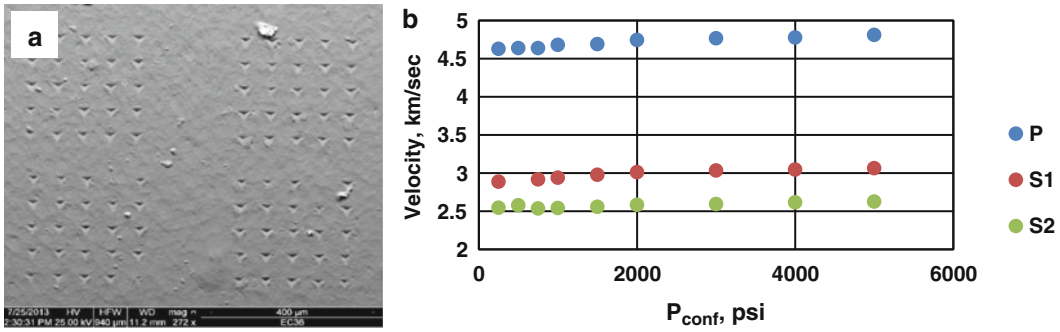

Fig. 13.4 (**a**) SEM image of Wolfcamp shale showing 100 indentations. (**b**) Pressure dependence of compressional (P) and shear (S) wave velocities in the native state Wolfcamp shale sample [5]

instrument. Bathija et al. [10] and Mba and Prasad [11] have indicated that organic matter contributes to a lower Young's modulus. Nanoindentation was performed on the selected sample and an SEM image of the sample with indentations is shown in Fig. 13.4a [5]. Figure 13.4b shows the variation of compressional wave velocity (P) and shear wave velocities (S1 and S2) with confining pressure. The Young's modulus obtained from nanoindentation ranged from 33 to 50 GPa while the Young's modulus obtained from dynamic method was 46 GPa [5]. We observe a good correlation between the Young's moduli measured by these two methods. It is observed in Fig. 13.4b that P does not show dependence on confining pressure indicating that there were not many cracks present in the sample [5]. Nanoindentation is not sensitive to cracks inside the sample due to its small depth of investigation.

13.6 Lyons Sandstone

Lyons sandstone is aeolian in origin. The average grain size of Lyons sandstone was determined to be 190 μm. Kumar [7] reported that size of a nanoindentation to be greater than 30 μm for a force of 30–50 mN. The size of nanoindentation is smaller than the grain size of Lyons sandstone. It is expected that the indentation modulus would correspond to modulus of single grain. Mineralogy data (from FTIR) indicates that Lyons sandstone is primarily composed of quartz. The average grain density was measured using LPP and yielded an average value of 2.65 g/cm^3 which is the density of quartz. Nanoindentation was performed and the indentation Young's modulus ranged from 84 to 96 GPa as expected. However, the velocity measurement yielded much smaller Young's modulus, i.e., from 57 to 60 GPa. This can be explained by observing the dynamic method results (Fig. 13.5b) which show that velocities increase even at high pressure due to the presence of cracks. Thus, we conclude that presence of these cracks can be sensed by macro-measurements on core plugs but such effects are completely absent in nanoindentation results. Due to larger grain size, all indentations during a nanoindentation experiment are on a single grain.

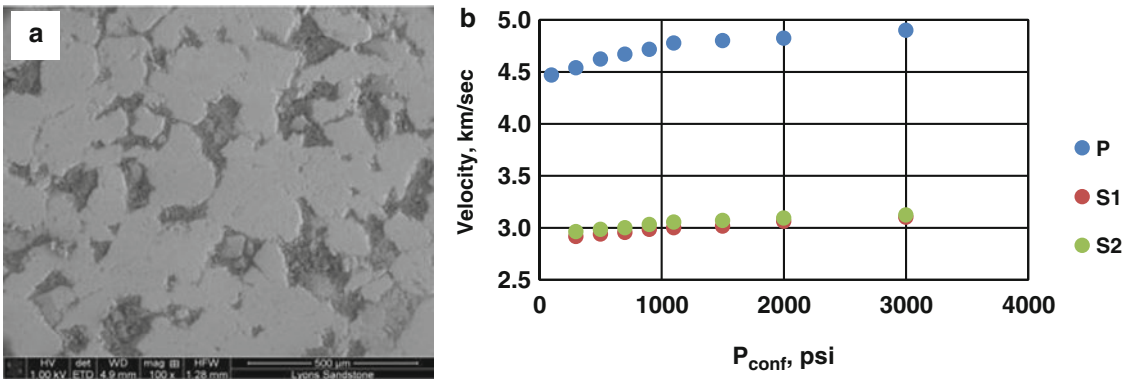

Fig. 13.5 (**a**) SEM image of Lyons sandstone with a field of view ∼1,200 μm across. *Light grey* portions indicate grains while *dark grey* portions are surface depressions. (**b**) Pressure dependence of P and S wave velocities in the dry sample. Velocities show strong dependence on confining pressure [5]

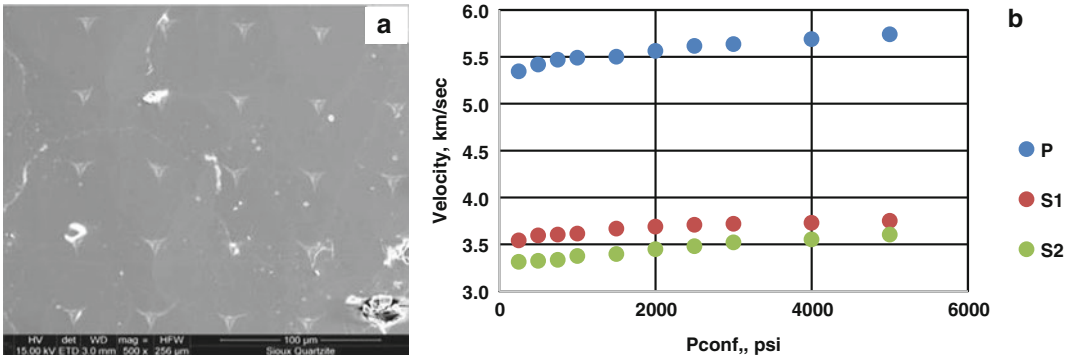

Fig. 13.6 (**a**) SEM image of Sioux quartzite with a field of view ∼220 μm across. All grains appear to be fused. (**b**) Pressure dependence of P and S wave velocities in a dry sample [5]

13.7 Sioux Quartzite

Sioux quartzite is primarily composed of quartz. Grain size of Sioux quartzite is composed of round and fused grains ranging in size from 125 to 500 μm. Measured grain density is same as quartz, 2.65 g/cm^3. The indentation Young's moduli ranged from 90 to 100 GPa which is close to that of quartz. The Young's moduli measured using acoustic velocities correlated well with the nanoindentation moduli and ranged from 71 to 82 GPa. Figure 13.6b [5] show the variation of P, S1 and S2 velocities with confining pressure; velocities are relatively constant after confining pressure of 3,000 psi indicating that most of the cracks are close at low pressure. The dynamic Young's moduli approaches to the value for pure quartz at high pressure. Figure 13.6a shows a SEM image of Sioux quartzite and a 5×5 indentation array [5].

13.8 Indiana Limestone

A limestone core plug was selected with FTIR mineralogy results showing 89 % carbonates and 6 % clays. Nanoindentation and acoustic measurements were performed on cores from same sample. The grain size of limestone was found to be 500 μm. Nanoindentation Young's moduli ranged from 42 to 55 GPa and the Young's moduli from dynamic measurement ranged from 36 to 41 GPa. Nanoindentation Young's moduli and dynamic Young's moduli show good agreement. Figure 13.7b is a plot of P, S1 and S2 with confining pressure [5]. It is evident that velocities become constant after 2,000 psi which indicates that cracks are closed at this pressure. Hence, the Young's moduli from both measurements become very similar at higher pressures.

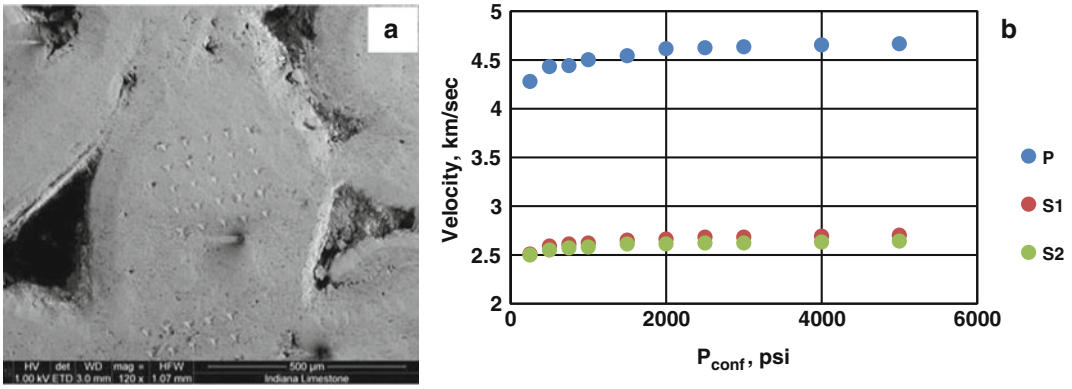

Fig. 13.7 (**a**) SEM image of limestone with a field of view ~1,200 μm across. *Light grey* portions indicate grains while *black* portions are surface depressions between grains. (**b**) Pressure dependence of P and S-wave velocities in a dry sample [5]

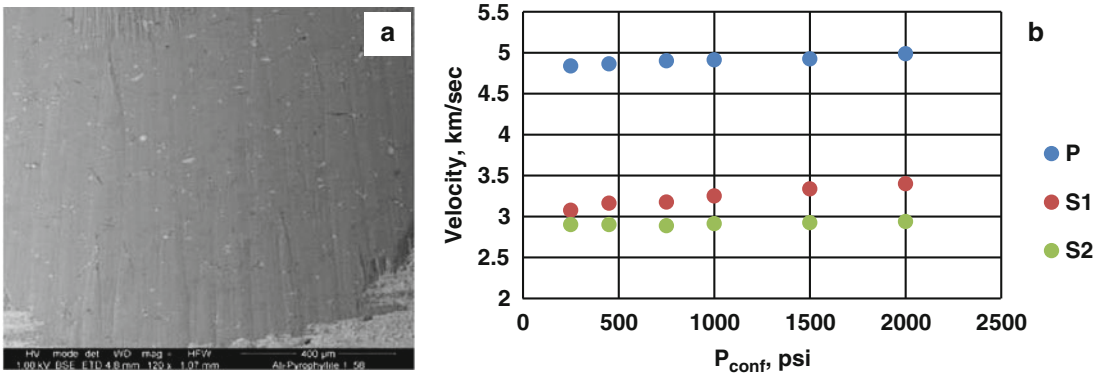

Fig. 13.8 (**a**) SEM image of pyrophyllite with a field of view ~1,000 μm across. Image shows no grain boundaries due to extremely fine grains present. (**b**) Pressure dependence of P and S-wave velocities in a dry sample [5]

13.9 Pyrophyllite

Pyrophyllite is a fine grained, strongly foliated, anisotropic rock which is composed almost exclusively of the clay mineral pyrophyllite. Nanoindentation and dynamic experiments were performed on samples with same fabric direction. Grain size was determined to be about 2–4 μm and the measured grain density was 2.83–2.84 g/cm^3. Figure 13.8a shows an SEM image of pyrophyllite sample which shows very fine grains with no clear grain boundaries [5]. Dynamic Young's modulus varied from 30 to 34 GPa, while nanoindentation Young's modulus ranged from 34 to 40 GPa. These values are in good agreement. Figure 13.8b [5] shows the pressure behavior of the P, S1 and S2 velocities; note the difference between S1 and S2 velocity results from the anisotropy in pyrophyllite. It is evident that there is very little change in velocities upto 2,000 psi indicating that the sample is crack free.

13.10 Conclusion

Nanoindentation results on shales and other rocks were tested to study the applicability of nanoindentation. The experimental results indicate that for coarse grained rocks, nanoindentation may not measure the correct Young's modulus of the rock, rather it measures the grain Young's moduli due the relative indentation area to grain size ratio. Coarse grained rocks with low crack density yield nanoindentation Young's moduli that agree with moduli measured from dynamic measurements on core plugs as observed in the limestone sample. Finer grained rocks, shales and pyrophyllite, where the indention area is larger than the average grain size yield moduli values which are representative of the rock. Evidence for this comes from the agreement between nanoindentation moduli and core plug measurements. We believe that grain size is an important parameter that distinguishes application of nanoindentation on rocks.

Acknowledgement We are thankful to Gary Stowe and Jeremy Jernigen for their support during the project. The support to purchase the nanoindentor came from Apache Corp. We also thank the Experimental Rock Physics and Unconventional Shale Gas Consortia members for their continued support. This research has been conducted by Priyavrat Shukla for his MS degree at University of Oklahoma.

References

1. U.S. Energy Information Administration (2013) Annual energy outlook 2013, http://www.eia.gov/forecasts/aeo/pdf/0383(2013).pdf, August 25, 2013
2. Vernik L, Nur A (1992) Ultrasonic velocity and anisotropy of hydrocarbon source rocks. Geophysics 57(5):727–735. doi:10.1190/1.1443286
3. Guo J, Liu Y (2012) Modeling of proppant embedment: elastic deformation and creep deformation. Paper SPE 157449 presented at the SPE international production and operations conference and exhibition, Doha, Qatar, 14–16 May 2012
4. Akrad O, Miskimins J, Prasad M (2011) The effects of fracturing fluids on shale rock mechanical properties proppant embedment. Paper SPE 146658 presented at the SPE annual technical conference and exhibition, Denver, CO, USA, 30 October–2 November 2011
5. Shukla P (2013) Nanoindentation studies on shales. MS Thesis, University of Oklahoma, Norman, OK, USA
6. Hay JL, Pharr GM (2000) Instrumented indentation testing. ASM handbook. ASM, Materials Park, OH, pp 232–243
7. Kumar V (2012) Geomechanical characterization of shales using nanoindentation. MS Thesis, University of Oklahoma, Norman, OK, USA
8. Kumar V, Sondergeld CH, Rai CS (2012) Nano- to macro- mechanical characterization of shale. SPE 159804 Presented in SPE annual technical conference and exhibition, San Antonio, TX, 8–10 October 2012
9. Shukla P, Kumar V, Curtis M, Sondergerld CH, Rai CS (2013) Nanoindentation studies on shales. Paper ARMA 13-578 presented at 47th US rock mechanics/geomechanics symposium, San Francisco, CA, 23–26 June 2013
10. Bathija PL, Prasad M, Liang H, Upmanyu M, Lu N, Batzle M (2009) Elastic properties of clay minerals. Extended abstract, SEG annual meeting, Las Vegas, NV, USA, 9–14 November, 2009
11. Mba KC, Prasad M (2010) Mineralogy and its contribution to anisotropy and kerogen stiffness variations with maturity in the bakken shales. SEG extended abstract presented at Annual meeting, Denver, CO, USA. 17–22 October 2010

Chapter 14
Anelasticity in Al-Alloy Thin Films: A Micro-mechanical Analysis

J.P.M. Hoefnagels, L.I.J.C. Bergers, and M.G.D. Geers

Abstract Micro-electromechanical systems enable many novel high-tech applications. Aluminum alloy thin films would be electrically favorable, but mechanical reliability forms fundamental challenges. Notably, miniaturization reveals detrimental time-dependent anelasticity in free-standing Al-alloy thin films. Yet, systematic experimental studies are lacking, perhaps due to challenges in microscale testing.

To this end, a microbeam bending methodology (with <4 $\mu\varepsilon$ strain resolution) and nano-tensile tester (with $\sim$70 nN and <6 $\mu\varepsilon$ resolution) have been developed for reproducible long-duration characterization of anelasticity of on-wafer 5 μm-thick Al-(1 wt%)Cu test structures under real-time in situ microscopy. Time-dependent anelasticity was indeed observed, both in bending and in tension, and a multi-mode visco-elastic model was found to described and predict the non-linear anelastic behavior between $\sim$1 and $\sim$105 s.

To gain insight in the underlying micro-mechanisms, time-dependent anelasticity was characterized under systematic variation of the grain boundary density and copper precipitate state/distribution (carefully analyzed using HRTEM/EBSD/WAXD/EDX/SEM), yielding a wealth of information. Surprisingly, both microstructural features were excluded as the (primary) cause of the time-dependent anelasticity. Based on dynamic strain aging effects observed in nano-indentation, an underlying micromechanism responsible for time-dependent anelasticity was hypothesized.

Keywords MEMS • Anelasticity • Micro-mechanics • Microscopic analysis • In situ mechanical testing

14.1 Introduction

Micro-electromechanical systems (MEMS) enable novel high-tech applications in, e.g., aerospace, biomedicine and wireless communications by integrating electrical and mechanical functionalities to address increasing demands: higher performance, more functionality, smaller dimensions. Although aluminum alloy thin films are electrically favorable, the compromised mechanical reliability still forms a fundamental challenge. Miniaturization has revealed detrimental size-dependent behavior in time-dependent elasticity, i.e., anelasticity, for free standing Al-alloy thin films, see Fig. 14.1. However, systematic experimental analyses of these mechanics have yet to be performed, partly due to the challenges of microscale testing. This work therefore aimed to develop on-wafer mechanical characterization methods and to acquire insights into the underlying physical micro-mechanisms responsible for anelastic size-effects.

14.2 On-Wafer Mechanical Tests for Characterization of Long-Term Anelasticity

Two methodologies were developed for reproducible characterization of anelasticity of on-wafer test structures in combination with microscopy. The specimens were 5 μm-thick aluminum and Al-(1 wt%)Cu films fabricated in a MEMS fabrication process. A microbeam bending methodology [1, 2], see Fig. 14.2, and a nano-tensile test methodology [3],

J.P.M. Hoefnagels (✉) • L.I.J.C. Bergers • M.G.D. Geers
Department of Mechanical Engineering, Eindhoven University of Technology, Den Dolech 2, Eindhoven, 5612AZ The Netherlands
e-mail: j.p.m.hoefnagels@tue.nl

J. Carroll and S. Daly (eds.), *Fracture, Fatigue, Failure, and Damage Evolution, Volume 5: Proceedings of the 2014 Annual Conference on Experimental and Applied Mechanics*, Conference Proceedings of the Society for Experimental Mechanics Series,
DOI 10.1007/978-3-319-06977-7_14,

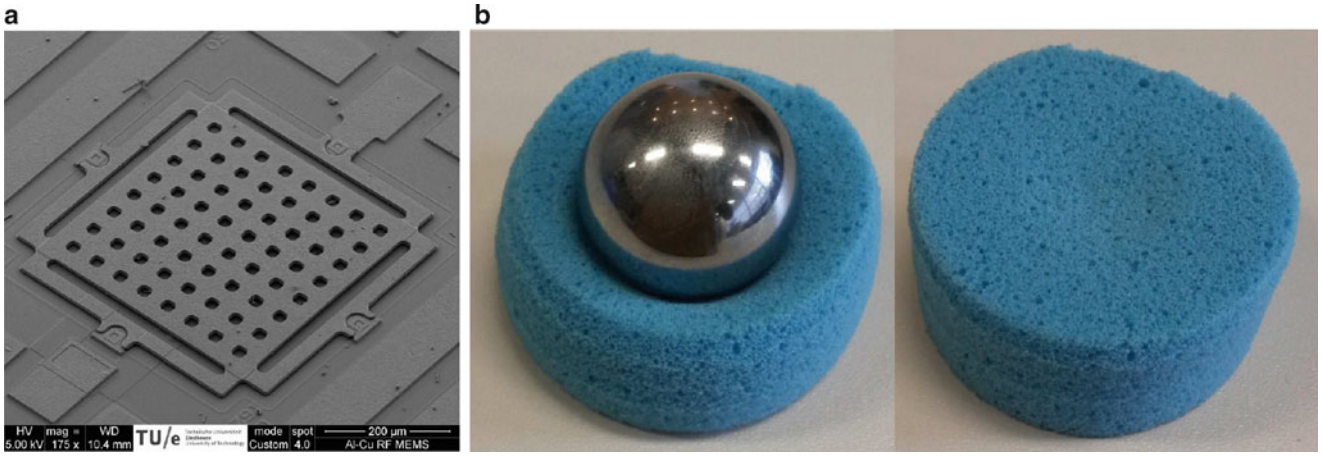

Fig. 14.1 (**a**) A scanning electron microscope image of a radio-frequency microelectromechanical system: a capacitive switch consisting of a perforated square plate suspended at its corners by hinging beams that are fixed to four points on the chip substrate. The plate and beams are made of an aluminum-alloy. It suffers from time-dependent anelasticity, which is commonly known in polymers as visco-elasticity as demonstrated by polymer foams, known as memory foam, (**b**) that recover their shape slowly after being deformed

see Fig. 14.3, were developed. To measure minute strains involved in anelasticity, both methodologies relied on novel improvements and developments to optical imaging and processing techniques: digital holographic microscopy, confocal optical profilometry, bright field optical microscopy, global digital image correlation. This ensured reproducible deformation measurements of $<6 \times 10^{-6}$ strain during time spans of days. The microbeam bending method relied on a multi-mode anelasticity model to yield key characteristics of the mechanical behavior without an explicit force measurement. For the nano-tensile testing drift-compensated force measurements achieved resolution down to 70 nN and maximum forces up to 200 mN. Hence, the two micromechanical techniques enabled characterization of anelasticity of these thin metal films.

14.3 Characterization of Al-(1 wt%)Cu Specimens [4]

Subsequently, the microstructure of pure aluminum and Al-(1 wt%)Cu thin films were characterized to investigate the influences of grain boundaries and alloy microstructure, i.e., solute concentration, precipitate type, size and distribution [4]. The grain boundaries of various microstructures were characterized with electron backscatter diffraction. The influence of precipitates was investigated by altering their state through heat treatments for homogenization and aging. Backscatter electron contrast imaging, energy dispersive spectroscopy, wide angle X-ray diffraction and high resolution transmission electron microscopy [4] revealed the variations of precipitate type and distribution in the Al–Cu alloy microstructure. Interestingly, the precipitation in the thin films was different compared to precipitation in bulk. The precipitation appeared to occur sooner and did not yield θ' precipitates. This difference was hypothesized to be due to preferential nucleation of θ at the grain boundary grooves and surface, see Fig. 14.4, which could result in a lower free energy of the system with respect to bulk precipitation.

14.4 Results on Time-Dependent Anelastic Mechanics [5]

Finally, the two mechanical characterization techniques were applied to measure the time-dependent anelastic response as function of the microstructural variations [5]. The influence of grain boundaries and precipitation state was probed with the microbeam bending methodology on the Al–Cu specimens. However, results suggest a negligible influence of either grain boundaries or precipitate size or state, see Fig. 14.5. Nano-tensile tests on Al–Cu and pure Al revealed nearly identical anelastic behavior as compared to the Al–Cu microbeams. These observations suggest that the grain boundaries, precipitates and even Cu-solutes did not influence the time-dependent anelasticity [5]. This led to the hypothesis that the underlying micromechanism responsible for time-dependent anelasticity could be related to dislocation junctions and entanglements and their diffusion-limited formation and relaxation.

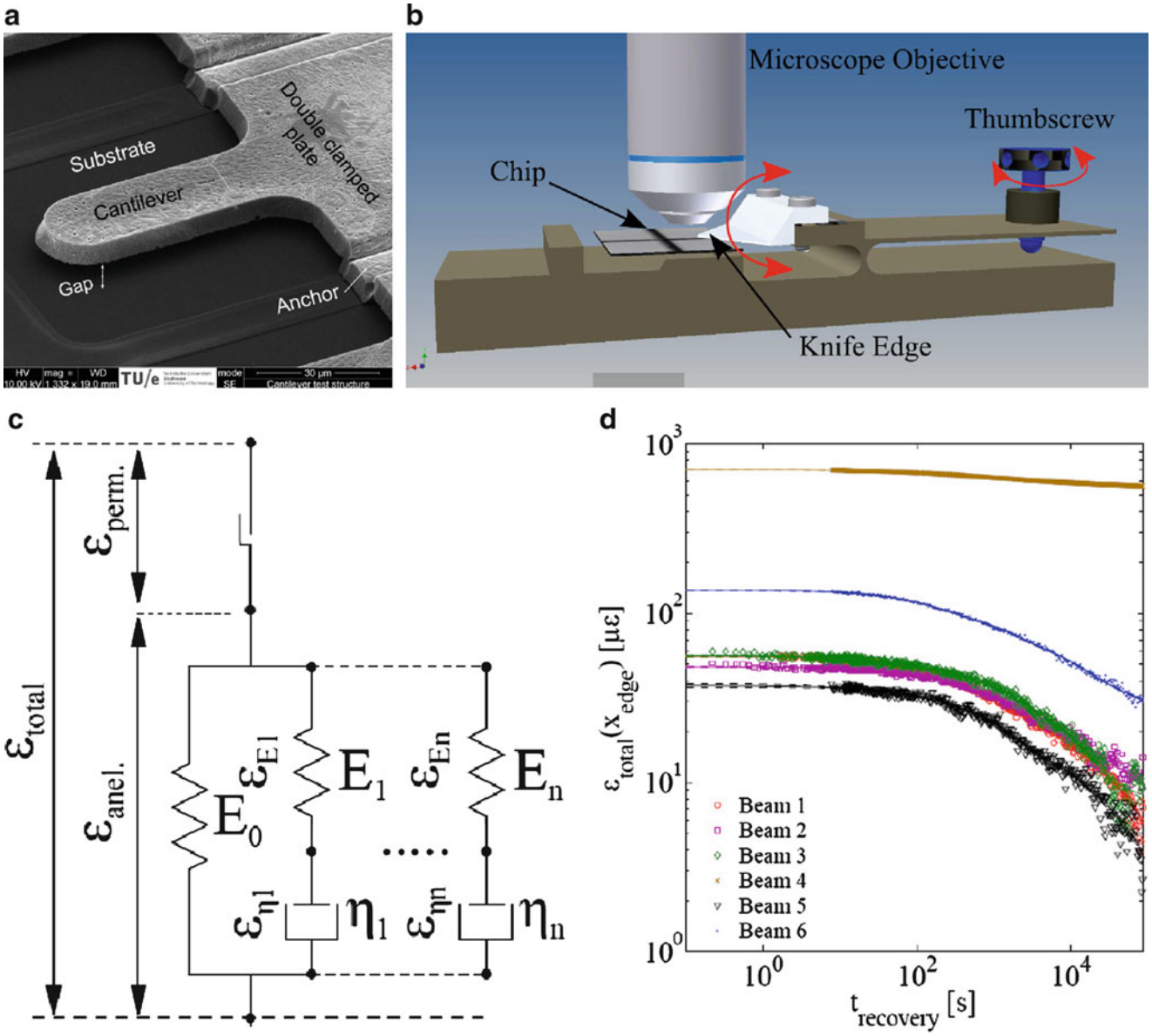

Fig. 14.2 The microbeam bending methodology [1, 2]: (**a**) A SEM-image of a test cantilever beam that is attached to a free-standing plate clamped on three sides by an anchor. (**b**) Schematic side view of the micro-clamp used to deflect on-chip cantilevers with high resolution under a profilometer. Thermal and mechanical drift effects in the load are minimized through a dedicated thermomechanical design. (**c**) Time-dependent behavior described by a standard solid multi-mode viscoelastic model with plastic dissipation resulting in permanent deformation. (**d**) Strain recovery evolution with individual model responses

14.5 Conclusions

A microbeam bending methodology (with <4 $\mu\varepsilon$ strain resolution) and nano-tensile tester (with ~70 nN and <6 $\mu\varepsilon$ resolution) have been developed for reproducible long-duration characterization of anelasticity of on-wafer 5 μm-thick Al-(1 wt%)Cu test structures under real-time in situ microscopy. Time-dependent anelasticity was indeed observed, both in bending and in tension, and a multi-mode visco-elastic model was found to described and predict the non-linear anelastic behavior between ~1 and 10^5 s. Time-dependent anelasticity was carefully analyzed characterized under systematic variation of the grain boundary density and copper precipitate state/distribution. Surprisingly, both microstructural features were excluded as the (primary) cause of the time-dependent anelasticity. An underlying micromechanism responsible for time-dependent anelasticity was hypothesized.

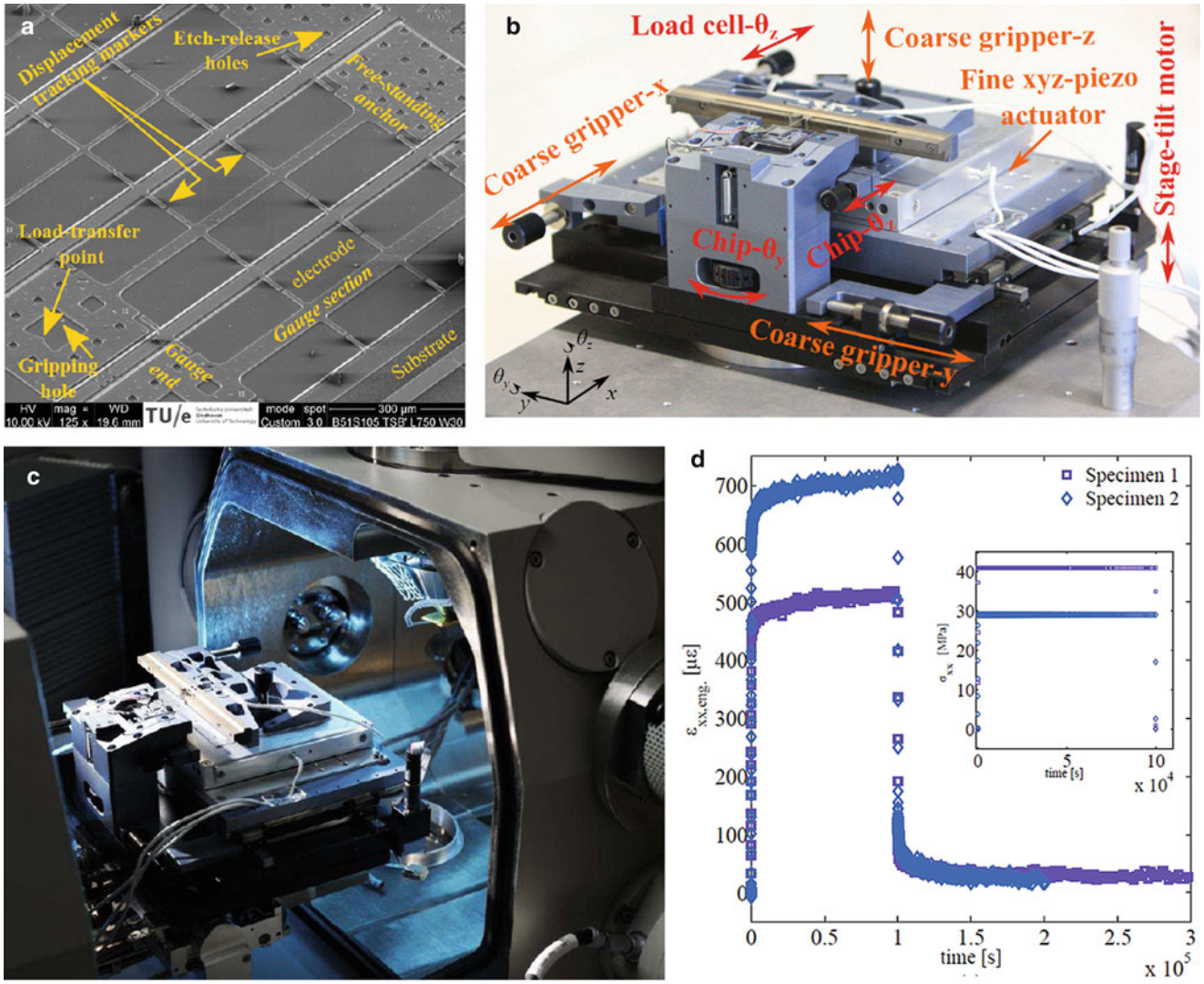

Fig. 14.3 The nano-tensile test methodology [3]: (**a**) Scanning electron micrograph of a free-standing tensile specimen that is fixed at one end along the perimeter of the anchor. At the free-standing gauge-end a gripping hole is made with load-centering feature. Along the substrate and the length of the beam several displacement tracking markers are fabricated to measure the substrate displacement and the gauge deformation. (**b**) Overview of the nano-tensile tester highlighting manual precision manipulators for angular alignment, coarse xyz-positioning and a xyz-piezo actuator for nm-positioning. (**c**) Nano-tensile stage placed in a FEI Quanta 600 ESEM. (Photo courtesy of Bart van Overbeeke Fotografie.) (**d**) Tensile creep experiment at constant stress (see inset) followed by time dependent anelasticity recorded for a tensile specimen

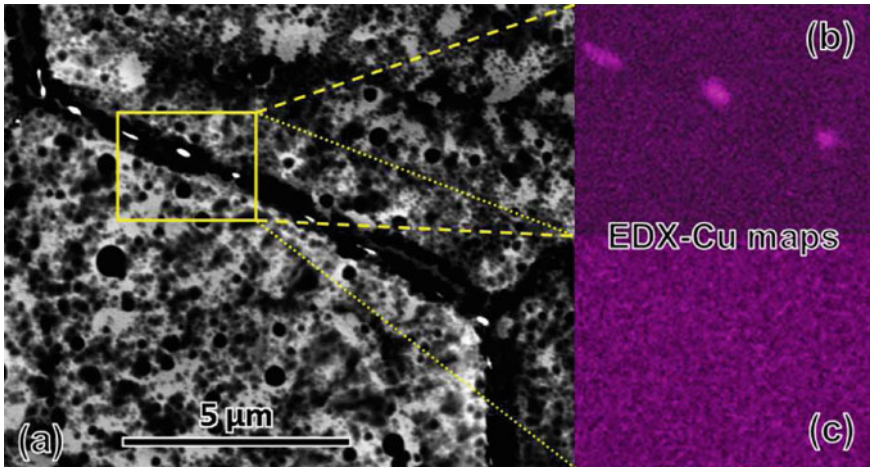

Fig. 14.4 The effect of the homogenization step at 550 °C on the precipitate state in the as-received Al-(1 wt%)Cu material. (**a**) back-scatter electron (BSE) image of large θ precipitates (with sizes up to half a micrometer) aligned on a grain boundary. (**b**, **c**) EDS maps of the copper concentration (**b**) before and (**c**) after the solution heat treatment, showing that all copper has been dissolved. BSE and EDS performed in a FEI Sirion FEG-SEM with EDAX EDS system and Apollo SDD detector. BSE obtained with Ebeam = 15 kV, EDS measured with Ebeam = 20 kV

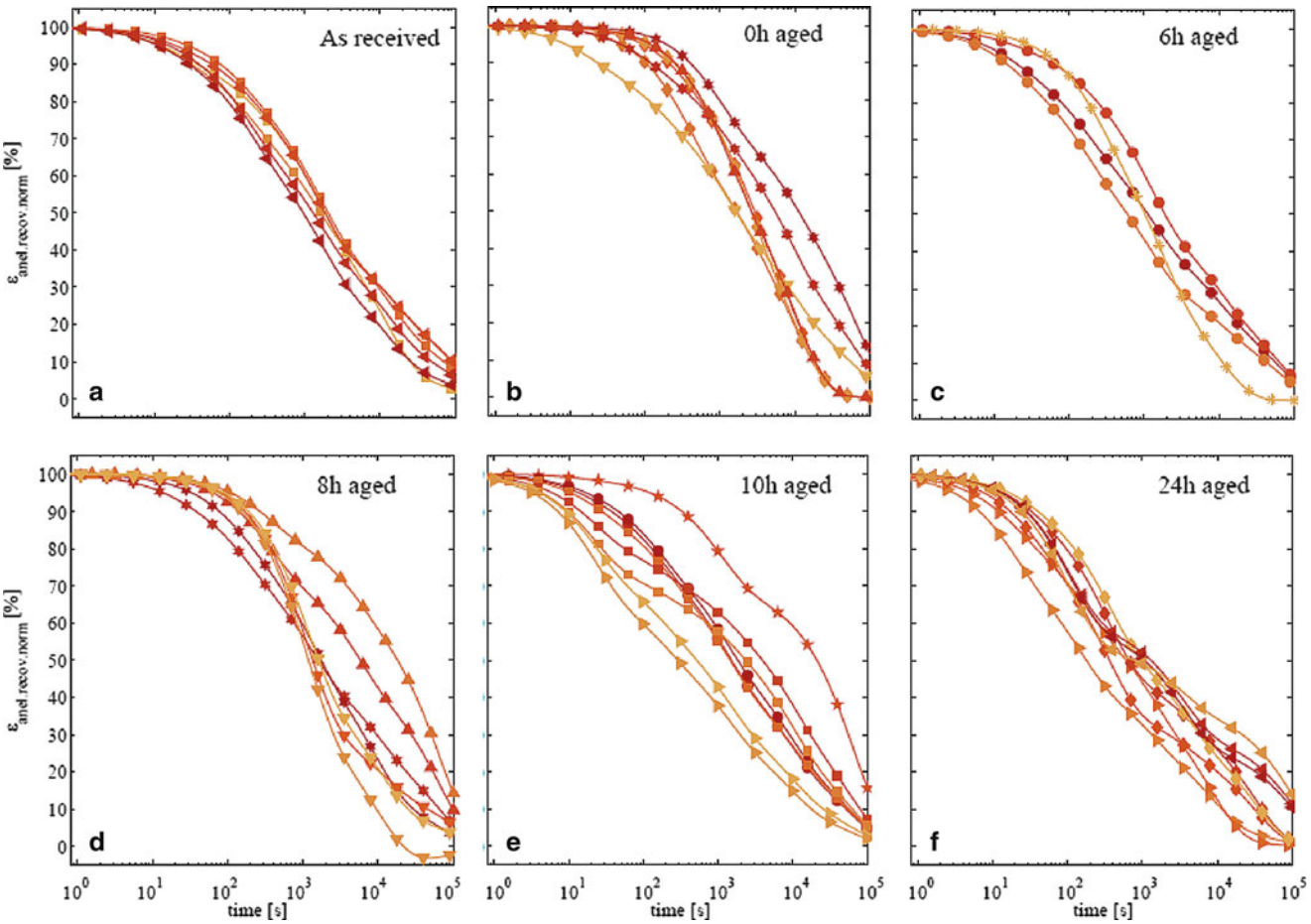

Fig. 14.5 Influence of the grain boundary density on the normalized anelastic recovery evolution for specimens (**a**) as-received and (**b**) 0 h, (**c**) 6 h, (**d**) 8 h, (**e**) 10 h and (**f**) 24 h aged condition. The color intensity (ranging from *light orange* to *dark red*) corresponds to the increase in grain boundary density, ρ'_{GB}. These results suggest a negligible influence of either grain boundaries or precipitate size or state (Color figure online)

Acknowledgements The authors acknowledge dr. Y. Bellouard for discussions about DHM. Dr.ir. M.A.J. van Gils and ir. J.A. Bielen at EPCOS Netherlands B.V. are greatly acknowledged for their cooperation, support and fruitful discussions in this work. Furthermore, the authors acknowledge the aid of dr.ir. M.A.J. van Gils, and ir. A. den Dekker of EPCOS Netherlands BV and dr.ir. E. van den Heuvel and E. Alexander-Moonen of Philips Innovations Services during the design and fabrication of the specimen wafers. The authors acknowledge ir. E.C.A. Dekkers, ir. R.J.L.J de Regt and P. Minten of the Engineering and Prototyping Center and S. Garenfeld and P.W.C. van Hoof of the Dept. of Mech. Eng. of the Eindhoven University of Technology for collaborating on the design and realization of the nano-tensile stage. Prof. dr. J.Th.M. de Hosson and dr. J. Rao of the Materials Science group, Department of Physics at the University of Groningen are gratefully acknowledged for the TEM analyses. For preliminary X-ray diffraction and subsequent discussions the authors acknowledge M.M.R.M. Hendrix at the Department of Chemical Engineering and Chemistry, Eindhoven University of Technology. ir. M. van Drongelen is thanked for providing beam-time and performing WAXD measurements at the DUBBLE beamline at the ESRF. B.Sc., B.A., Göttgens is acknowledged for his work on the material characterization, microbeam bending and nano-indentation measurements. Finally, Marc van Maris is gratefully acknowledged for his general support on (in situ) mechanical experiments in the Multi-Scale lab.

References

1. Bergers LIJC, Hoefnagels JPM, Delhay N, Geers MGD (2011) Measuring time-dependent deformations in metallic MEMS. Microelectron Reliab 51:1054–1059
2. Bergers LIJC, Hoefnagels JPM, Geers MGD (2014) Characterizing time-dependent anelastic microbeam bending mechanics. J Phys D (2014)
3. Bergers LIJC, Hoefnagels JPM, Geers MGD (2014) On-wafer time dependent nano-tensile testing, submitted for publication
4. Bergers LIJC, Hoefnagels JPM, de Hosson JThM, Geers MGD (2014) Observations on θ precipitation in Al-(1wt%)Cu thin films, submitted for publication
5. Bergers LIJC, Hoefnagels JPM, Geers MGD (2014) On the underlying micromechanisms in time-dependent anelasticity in Al–Cu alloy thin films, submitted for publication

Chapter 15
Oxide Driven Strength Degradation on (111) Silicon

Scott J. Grutzik and Alan T. Zehnder

Abstract Previous results have suggested that oxidation of nanoscale Si structures is correlated with a reduction in strength. The mechanism by which this occurs is unknown however. It is possible that the process of oxidation causes some irreversible change in the surface of the crystalline Si. It may also be possible that the change in strength is due to the presence of the oxide itself, perhaps changing the atomic or electronic distribution in some way. In this work, we allow a set of nominally identical nanoscale Si beams to oxidize over approximately five weeks while taking periodic fracture strength measurements. The oxide is then removed and strength is measured a final time. We see that after removing the oxide, strength does not recover at all, suggesting that the change is strength is indeed due to a change in the Si surface.

Keywords Silicon • Nanoscale strength • Nanoscale testing • Oxide • Atomic force microscope

15.1 Introduction

Micro- and nanoelectromechanical systems (MEMS and NEMS) play an increasing role in many fields such as telecommunications, defense, microelectronics, and biomedical devices. These systems can be subjected to sustained loads, oscillating loads, dynamic shock loading, or a combination of all three. The small size of these devices make accurate predictions and measurements of strength and durability difficult. As a result they may be designed with overly large factors of safety with respect to mechanical failure. More efficient design will require accurate knowledge of the stochastic nature of fracture at these length scales.

For a variety of reasons, it is difficult to extrapolate macroscale material failure behavior down to the length scales required for MEMS and NEMS design. Components of these systems are often small enough that they contain few or no defects other than those introduced during processing. Also, because of their high surface to volume ratio, surface properties tend to play a larger role than volumetric properties. Nonetheless, it is possible to make some general predictions. From a continuum mechanics perspective, a smoother surface should give rise to a stronger structure. Any pit or ledge on the surface will act as a stress concentrator under loading and act as a potential nucleation point for fracture. It is also expected that if the surface can be maintained in a compressive state, strength should increase. The compressive stress would act to hold the faces of any existing cracks together, making it more difficult for cracks to propagate.

Alan et al. [1] have reported results that agree with the first of these expectations. Their results suggest that the surface roughness of nanoscale Si beams strongly affects their strength and that if the surface is smooth enough the strength can be close to the ideal strength derived from atomistic simulations. Alan et al. [2] have also reported results that are somewhat at odds with the second expectation that a compressive surface stress should increase fracture strength. Their data show a decrease in strength with increasing surface oxidation and, that if oxidation is prevented, the initially high strength is maintained. What makes this an unexpected result is that silicon dioxide grown on a Si surface grows in a compressive state. From our continuum mechanics reasoning oxidation should lead to an increase in fracture strength, not a decrease as the data suggests. The work presented here is part of an effort to understand the mechanisms behind how oxidation affects nanoscale strength.

S.J. Grutzik • A.T. Zehnder (✉)
Field of Theoretical and Applied Mechanics, Cornell University, Ithaca, NY 14853, USA
e-mail: atz2@cornell.edu

J. Carroll and S. Daly (eds.), *Fracture, Fatigue, Failure, and Damage Evolution, Volume 5: Proceedings of the 2014 Annual Conference on Experimental and Applied Mechanics*, Conference Proceedings of the Society for Experimental Mechanics Series,
DOI 10.1007/978-3-319-06977-7_15,

15.2 Sample Fabrication

Accurate measurement of mechanical properties such as stiffness or fracture strength on micro- and nanoscale samples is difficult. The small sizes and forces involved introduce challenges at every step of the process, from sample fabrication to gripping the specimen to measuring small forces and displacements. Several methods have been proposed, including adapting macroscale techniques like three point bending to the nanoscale [3], high precision piezo-controlled loading devices [4], high throughput tests consisting of a chain of nanoscale rings [5], and a test specimen shaped like the Greek letter Θ which allows the crossbar to be easily put in a state of pure tension [6]. Each of these approaches has advantages and disadvantages. The chain of rings method, for example, can produce a lot of data with relatively little effort but requires a complex fabrication process and special testing apparatus.

Here we use a method developed by Alan et al. [1, 2] similar to that of Namazu et al. [3] in which a force is applied at the midpoint of a suspended single crystal beam via an atomic force microscope (AFM). A scanning electron micrograph of such a beam after testing is shown in Fig. 15.1. The test specimens are fabricated from Si (111) wafers using standard micromachining techniques in the process outlined in Fig. 15.2 [7]. The long axis of the beam is parallel to the $[1\bar{1}0]$ direction.

The "dog bone" shape of the sample ensures that the fracture stress occurs reproducibly in the center of the beam, where the small width leads to highest stress. If the beam were uniform width, there would be stress concentrations at the attachment points which would complicate analysis.

The fabrication process involves using two consecutive steps of photolithography and reactive ion etching. The first lithography and etch step, denoted by (a) in Fig. 15.2, defines the shape of the beam. The depth of this first etch roughly controls the thickness of the beam. After the first etch step, a 100 nm layer of thermal oxide is grown, as shown in Fig. 15.2b. A second round of lithography and etching defines a deep trench on both sides of the beam. After this step, the beam is still connected to the substrate by a pillar of Si.

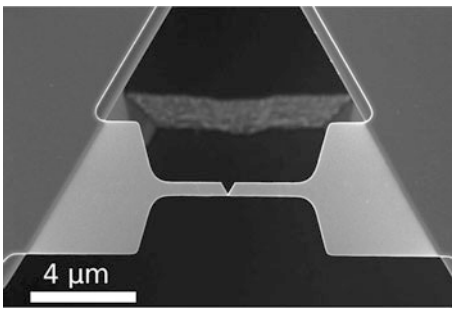

Fig. 15.1 Scanning electron micrograph of a fractured nanobeam. The V shaped notch is not part of the fabricated design but a characteristic of the failure mode

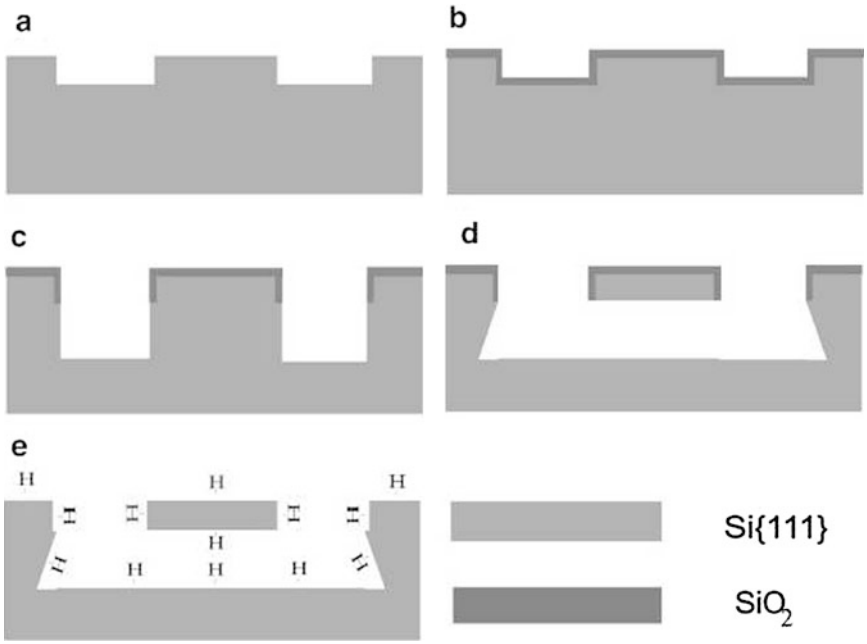

Fig. 15.2 Diagram of Si nanobeam fabrication process

The beams are released with an anisotropic etchant that rapidly removes all non-{111} exposed Si surfaces, leaving behind an atomically clean, H-terminated surface. To prevent uncontrolled oxidation of the H-terminated surface, the beams are only released just prior to fracture testing. The unreleased beams are first cleaned with a modified RCA clean [8]. The RCA cleaning procedure involves immersing the beams in 5:1:1 solution of H_2O (water), H_2O_2 (hyrdogen peroxide), and NH_4OH (ammonium hydroxide) at 80 °F for 10 min followed by immersion in a 5:1:1 solution of H_2O, H_2O_2, and HCl (hydrochloric acid) at 80 °F for 10 min. The first solution removes any organic contaminants and the second any metallic contaminants. The beams are then anisotropically etched with potassium hydroxide (KOH) and tetramethyl ammonium hydroxide (TMAH). These etchants produce the Si {111} terminated structure in Fig. 15.2e. This procedure slowly etches the backside of the beam; however, top and sides of the beam are protected by the oxide layer. The oxide layer is then removed with a buffered HF solution (a 5:1 mixture of NH_4F:HF) and rinsed in ultrapure water. This leaves all surfaces hydrogen terminated. For this experiment, the Si beams were allowed to naturally oxidize in a normal laboratory atmosphere for 5 weeks while taking periodic fracture strength measurements. The oxide was then removed, using the same buffered HF solution as before, and the strength was measured a final time.

15.3 Fracture Testing Procedure

After fabrication and chemical modification, an AFM is used to apply a force at the center of the beam, as shown in Fig. 15.3. This method has been previously used by Alan et al. The test has two parts. First, the beam is imaged by scanning the AFM cantilever over its surface to obtain its shape. Once the center of the beam is located, the cantilever is brought to this point and pushed straight down until the beam breaks. During the deformation, the displacement applied to the base of the cantilever by the peizo in the AFM head, δ_{piezo}, and the output signal of the photodetector are recorded simultaneously until the beam fractures, as indicated by a sharp discontinuity in photodetector signal. Importantly, both the cantilever and the beam bend during this process. By repeating this deflection test on an effectively rigid area of the wafer surface, the photodetector signal can be calibrated to the cantilever deflection, $\delta_{\text{cantilever}}$. The beam deflection, δ_{beam} is then calculated from $\delta_{\text{beam}} = \delta_{\text{piezo}} - \delta_{\text{cantilever}}$. If the stiffness of the AFM cantilever is known, $\delta_{\text{cantilever}}$ can be converted to the force F applied to the beam. This procedure quantifies the applied force F and beam deflection δ_{beam} at the time of failure. A variety of well characterized methods exist for measuring cantilever stiffness, most using mechanical or thermodynamic relations to determine stiffness [9, 10]. Due to the high stiffness required to generate enough force to fracture the Si beams used in the tests described here, the standard methods are not effective and a reference cantilever method was utilized instead [11].

Before the beam deflection and applied force at failure can be converted to maximum stress at failure, the thickness of the beam must be determined. To do this, we measure the resonant frequency of the beam by driving it inertially with a swept sine signal. Deflection during this measurement is transduced by optical interferometry [7]. The in-plane dimensions of the beam can be measured using SEM or the initial AFM scan which was used to locate the beam center. The thickness can then be calculated using the finite element method (FEM). The thickness in the FEM model is adjusted until the calculated resonant frequency agrees with the measured one. The validity of the FEM model can be verified by including higher order resonant frequencies in the thickness determination and by comparing the shape of the FEM generated load-deflection curve prior to failure to the experimental one. In both the physical and finite element beams, the long axis is aligned with the $[1\bar{1}0]$ direction. The material is assumed to be orthotropic with linear elastic modulii C_{1111} = 166 GPa, C_{1212} = 64 GPa, and C_{4444} = 79.6 GPa [12]. All strength testing was done on an Asylum MFP3D AFM (Asylum Research, Santa Barbara, CA). Finite element simulations were performed using ABAQUS (Dassault Systèmes, Waltham, MD) By applying the force at fracture to this FEM model, the fracture stress can be calculated.

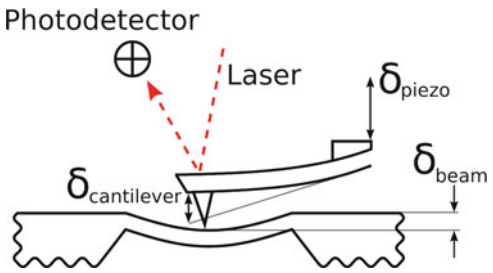

Fig. 15.3 Side view schematic of the AFM based fracture testing process

15.4 Fracture Strength Data

Figure 15.4 shows a typical force-deflection curve of one of the silicon beams from onset of loading to failure, indicated by termination of the blue line. The structural response of the beam is governed by geometric nonlinearity. As the center of the beam is pushed by the AFM cantilever the ends remain fixed and the entire beam is put in a state of tension. The resulting membrane stress vastly overwhelms the linear bending behavior. Even though linear bending is negligible in the total structural response of the beam, bending is sharply localized near where the load is applied. As a result, a significant portion of the fracture stress does result from bending.

Because the Si is brittle, it fails in a stochastic manner and a number of beams must be tested to obtain an accurate strength measurement. For the results presented in Fig. 15.5, each strength point consists of 10–15 individual fracture strength tests. The data is then fit to a three parameter Weibull distribution,

$$P_{\text{fracture}}(\sigma) = 1 - e^{l(\sigma/\sigma_0)^{\rho}}. \tag{15.1}$$

Each stress point shown in Fig. 15.5 is the Weibull strength, σ_0, for that data set. As the Si oxidizes, it reduces in strength, in agreement with Alan et al. [2]. Between the last two data points, the oxide is removed, restoring the Si to an H-terminated surface. The strength does not recover, and in fact reduces slightly, demonstrating that oxidation driven weakening must be the result of changes to the Si surface and not due to the presence of the oxide itself.

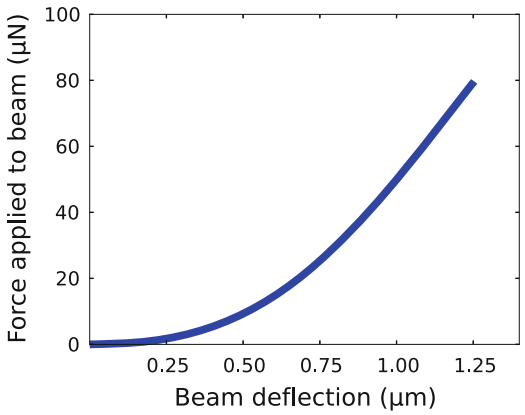

Fig. 15.4 A typical force-deflection curve for a silicon beam from onset of loading to failure

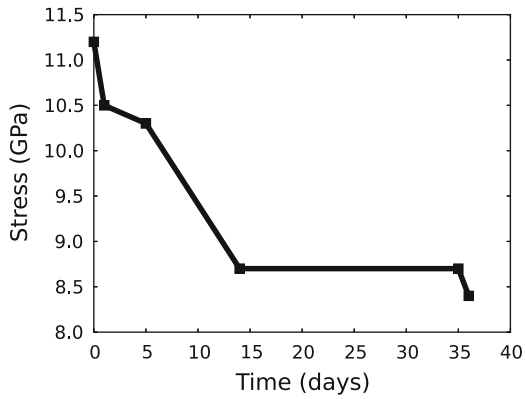

Fig. 15.5 Weibull strength decreases as the Si surface is allowed to oxidize. Between the final two points, the oxide is removed

15.5 Summary

The fracture strength nominally identical nanoscale Si beam specimens was measured over a period of approximately five weeks. The oxide was then removed and strength was measured a final time. Fracture strength decreases as the Si oxidizes as expected but does not recover at all after the oxide is removed. This suggests the reduction in strength is due to an irreversible change in surface of the crystalline Si.

Acknowledgements This work was funded by the National Science Foundation (NSF) grant CMMI-0856488. SJG acknowledges support from the NSF IGERT program (DGE-0654193). It was performed in part at the Cornell NanoScale Facility, a member of the National Nanotechnology Infrastructure Network, which is supported by NSF Grant ECS-0335765 and made use of the Cornell Center for Materials Research Shared Facilities which are supported through the NSF MRSEC program (DMR-1120296). We would also like to express our gratitude to the Nanomechanical Properties Group at the National Institute of Standards and Technology for their aid in reference cantilever calibration.

References

1. Alan T, Hines MA, Zehnder AT (2006) Effect of surface morphology on the fracture strength of silicon nanobeams. Appl Phys Lett 89:091901
2. Alan T, Zehnder AT, Sengupta D, Hines MA (2006) Methyl monolayers improve the fracture strength and durability of silicon nanobeams. Appl Phys Lett 89:231905
3. Namazu T, Isono Y, Tanaka T (2000) Nano-scale bending test of Si beam for MEMS. In: The thirteenth annual international conference on micro electro mechanical systems, pp 205–210
4. Tsuchiya T, Tabata O, Sakata J, Taga Y (1998) Specimen size effect on tensile strength of surface micromachined polycrystalline silicon thin films. J Microelectromech Syst 7:106–113
5. Reedy ED Jr, Boyce BL, Foulk JW III, Field RV Jr, Ohlhausen JA, de Boer MP, Hazra SS (2010) Predicting fracture in micron-scale polycrystalline silicon MEMS structures. Technical report SAND2010–6701, Sandia National Laboratory
6. Gaither MS, DelRio FW, Gates RS, Fuller ER Jr, Cook RF (2010) Strength distribution of single-crystal silicon theta-like specimens. Scripta Materialia 63(4):422–425
7. Wang Y, Henry JA, Zehnder AT, Hines MA (2003) Surface chemical control of mechanical energy dissipation in micromachined silicon devices. J Phys Chem B 107:14270
8. Kern W, Puotinen DA (1970) Cleaning solutions based on hydrogen peroxide for use in silicon semiconductor technology. RCA Rev 31: 187–206
9. Ohler B (2007) Practical advice on the determination of cantilever spring constants. Technical report, Veeco Instruments Inc
10. Veeco Instruments, Inc. NanoScope V controller manual
11. Grutzik SJ, Gates RS, Gerbig YV, Smith DT, Cook RF, Zehnder AT (2013) Accurate spring constant calibration for very stiff atomic force microscopy cantilevers. Rev Sci Instruments 84(11):113706
12. McSkimin HJ, Andreatch P (1964) Elastic moduli of silicon vs hydrostatic pressure at 25.0 °C and -195.8 °C. J Appl Phys 35(7):2161–2165

Chapter 16
Impact of Speckle Pattern Parameters on DIC Strain Resolution Calculated from In-situ SEM Experiments

Jennifer L.W. Carter, Michael D. Uchic, and Michael J. Mills

Abstract The advent of small-scale testing procedures coupled with scanning electron microscopy (SEM) imaging allow for high-resolution digital image correlation (DIC) studies to examine strain localization at the grain size length scale. A systematic study was performed to determine how speckle patterning parameters (speckle density and shape) affect strain resolution of DIC using SEM imaging. Strain resolution increased with increased speckle density from 23 to 58 % area fraction. Patterns with less than 23 % area fraction exhibited significant signal noise, and a loss in strain resolution due to inadequate correlation. It was also observed that when the edges of square speckles were aligned with SEM rastering directions, the noise in the e_{yy} data was double the noise in the e_{xx} data. Rotating the speckle to eliminate edge alignment with the rastering direction significantly decreased the e_{yy} strain noise. Competing optimization requirements for the correlation parameters were needed to minimize strain intensity noise or maximize spatial resolution. Application of the optimization techniques to high temperature in-situ studies of Ni-based superalloys will also be presented.

Keywords Digital image correlation • Speckle patterning • In-situ deformation

16.1 Introduction

Characterization of localized strain accommodation processes within microstructural features is a budding field of research. Digital image correlation (DIC) techniques provide full-field deformation information, and have been used to examine localized deformation mechanism in various materials and loading conditions. Some examples include; monotonic loading of bulk and thin film materials [1, 2], fatigue damage accumulation and fatigue crack growth [3, 4], and stress induced transformations in shape memory alloys [5]. These few examples demonstrate the flexibility of the DIC for studying localized deformation behavior in heterogeneous material systems.

Recently, DIC utilizing scanning electron microscopy (SEM) imaging has allowed for higher resolution studies of strain localization on the grain scale of engineering materials with conventional grain sizes, 50–500 μm [3, 6–10]. In order to use SEM imaging systems for DIC, it is necessary to establish a vacuum compatible, electronically conductive, rigidly adhered pattern on the sample surface. Several techniques are available for applying such patterns including chemical vapor deposition, sputter deposition through transmission electron sample grids, and electron beam lithography [11, 12]. Electron beam (e-beam) lithography provides the most control over the patterns created, and allows for optimization of the pattern parameters to enhance strain resolution. Pattern parameters that can be optimized include: random speckle shape (e.g. square, diamond, and round) and random speckle density. E-beam lithography also permits the experimentalist to apply both a random pattern of speckles and an organized set of linear grid markers for grain boundary sliding measurements [13]. For elevated temperature experiments it is advantageous to know if strain accumulation measured from DIC is a product of intragranular and/or intergranular mechanisms such as grain boundary sliding. Strain associated with grain boundary sliding

J.L.W. Carter (✉) • M.J. Mills
The Ohio State University 477 Watts Hall, 2041 College Rd. Columbus, OH 43210, USA

Case Western Reserve University, 10900 Euclid Ave, Cleveland, OH 44106, USA
e-mail: jennifer.w.carter@case.edu

M.D. Uchic
Air Force Research Laboratory, Materials & Manufacturing Directorate, AFRL/RXCM, Wright Patterson AFB, Dayton, OH 45433, USA

J. Carroll and S. Daly (eds.), *Fracture, Fatigue, Failure, and Damage Evolution, Volume 5: Proceedings of the 2014 Annual Conference on Experimental and Applied Mechanics*, Conference Proceedings of the Society for Experimental Mechanics Series,
DOI 10.1007/978-3-319-06977-7_16,

has been conventionally calculated by measuring discrete steps in linear markers [14]. In addition to strain from DIC analysis, we desire to measure discrete steps in linear markers for grain boundary sliding analysis; this requires that there be limited overlap between the linear markers and the random speckle pattern. This provides an example of an experimental design in which limiting the density of the random speckle pattern for DIC would be preferred. Therefore, it is advantageous to understand how speckle shape and pattern density can affect the strain resolution of DIC calculations.

This paper will focus on how speckle pattern, and analysis parameters affect localized strain measurements from SEM DIC experiments. For these experiments, Correlated Solutions VIC-2D software was used. The VIC-2D DIC algorithm partitions the image into subsets and correlates the motion of rigidly adhered speckles in images taken during deformation with their original position in an image taken prior to deformation. Local strain is measured by iteratively applying a deformation tensor to subsets in the deformed image relative to a subset in the reference image, and minimizing the error associated with the unique gray-scale. By stepping the subsets across the imaged region by a particular overlap, the deformation field on the surface of the specimen can be assessed [15]. As a result of this algorithm, for particular imaging conditions, the strain resolution of DIC analysis is a function of the speckle pattern, subset size and step size used during the DIC analysis. The effect of each of these parameters on strain measurement resolution are addressed in this paper. Noise in the full field strain measurements has both intensity and spatial components, and decreasing the noise will increase the strain resolution of the measurement. As such, these two terms "signal noise" and "strain resolution" are used interchangeably through this paper. Each component of the signal noise will be addressed; the intensity component dictates how much strain above/below its neighbors a data point must experience to be considered a localization site, and the spatial component dictates how localized a strain measurement can be (important for characterizing very localized deformation at slip traces and grain boundaries).

16.2 Experimental

Random speckle patterns were applied to samples of a wrought nickel-based superalloy, Rene-104, using e-beam lithography techniques. Samples were polished for metallographic examination prior to patterning using standard polishing procedures on an Allied Multi-prep system, finishing with a 0.2 μm colloidal silica vibratory polish. Microstructural analysis was conducted prior to speckle patterning using electron backscatter diffraction. Samples were spin coated with PMMA, followed by e-beam lithography in a Vistec EBPG 5000 e-beam lighography equipment at 50 keV with an 800 $\mu C/cm^2$ dose. The resist was developed and hafnium oxide was deposited on the sample surface using e-beam evaporation. Specifics about patterning procedures, and EBSD analysis and alignment are presented in J.L. Walley (Carter) et al. [13].

Correlated Solutions VIC-2D digital image correlation software was used to analyze local deformation fields. Digital image correlation for deformation measurements using random speckles is best when the speckles are at least three pixels in diameter [15]. Lagrangian strains were calculated from the displacement measurements using a 15 pixel Gaussian smoothing decay filter [16]. For small strains, principle engineering strain can be calculated from Lagrangian strains by the following equation: $\epsilon_{engr} = \sqrt{1 + 2e_{11}} + 1$ [15]. Strain resolution is a function of initial calculation length scales, which are defined by the DIC parameters: subset and the step size.

Two sets of experiments were conducted to assess the how patterning and DIC parameters affected noise in the strain measurements. First, DIC analysis parameters were optimized for the image acquisition settings, where the DIC parameters were systematically varied from 20 pixels to 100 pixels for subset size, and 1–10 pixels for step size. This analysis was conducted on a sample under zero load condition, and sets of five or more images taken over the same region of interest, without varying the speckle pattern parameters. Since the strain accumulated from one image to the next should be zero, this technique allows us to assess the noise in the strain measurements due to image acquisition and how DIC parameters can be optimized to minimize this noise through averaging. Second, when there is no strain applied it is also possible to determine if the DIC measurements are dependent on speckle pattern density and speckle shape. Finally, non-optimized and optimized DIC parameter sets were applied to strain data collected on a sample deformed at 700 °C at constant load and comparisons were made to show how parameter optimization affects data interpretation [17].

The material examined for this study has an average grain size of 32±4 μm, and it was desired to make the subset sizes vary from one third to half the average linear grain size. This subset size was selected such that the majority of subsets would not overlap multiple grain boundaries and experience an affine deformation environment. Image resolution was set at 2048 × 1768 $pixels^2$ and contrast and brightness of the secondary electron images were adjusted to utilize the entire gray-scale. For an image to incorporate 15 grains across the longest dimension of the image frame, a 6.8 pixel/μm magnification is required. Based on these resolution requirements, and the minimum speckle size criteria of three pixels per speckle, the minimum speckle size is 0.2 μm. Random speckle patterns of variable densities were generated using square speckles with edge lengths between 0.2 to 0.7 μm. Table 16.1 enumerates the different pattern densities developed for this study.

Table 16.1 Area fraction of the speckle coverage for each pattern examined

Pattern	Area fraction (%)
0	12
1	23
2	30
3	35
4	37
5	58

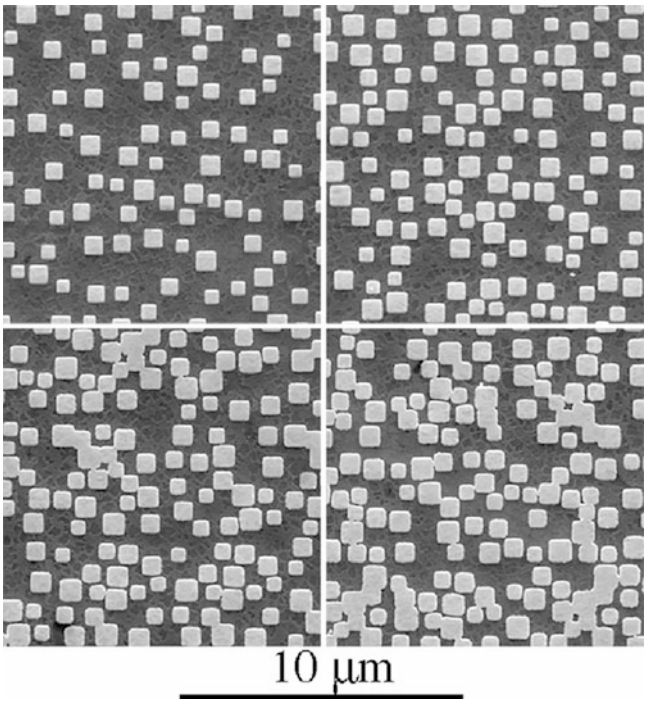

Fig. 16.1 SE image of the speckle pattern densities (*top-left corner* to *bottom-right corner* are 12 %, 23 %, 35 %, and 37 % area fraction)

Strain resolution as a function of speckle orientation was also assessed by comparing patterns of the same speckle density with both square and diamond shaped speckles. In the experiments to assess the effect of speckle density on signal noise, the specimen was aligned so that edges of square speckles were aligned parallel to the rastering directions of the SEM images.

Biery et al. concluded that when the square grids used for DIC analysis are aligned with the discrete electron beam rastering direction, there is a reduction in strain resolution along the imaging direction that corresponded to the discrete raster direction [9]. To determine if this conclusion would apply to DIC analysis with random speckeles, a second experiment was conducted to assess the effect of speckle shape on signal noise, with the specimen was aligned so that square edges were oriented 30° with respect to the rastering direction.

Sutton et al. concluded that DIC analysis from SEM images created by integrating the image intensity over eight images creates lower intensity strain noise as compared to images acquired with longer dwell, single scan rasters [6]. This observation was confirmed prior to conducting these experiments. All the images for this paper were acquired using 1 μs dwell time with eight images integration using the FEI integration option for a total image acquisition time of 28.8 s. The SEM used for this experiment was an FEI Quanta SEM with a field emission source, at 15 kV and a spot size of 3. A secondary electron (SE) image of the speckle patterns, densities 1 through 4, is shown in Fig. 16.1.

16.3 Results and Discussion

16.3.1 Speckle Pattern

Independent of the chosen DIC parameters, there was consistent and substantial reduction of signal noise intensity between the pattern density with 12 % area fraction coverage and 23 % area fraction coverage. Above this threshold, increasing the area fraction (i.e. speckle density) resulted in statistically insignificant reduction of signal noise with increased pattern

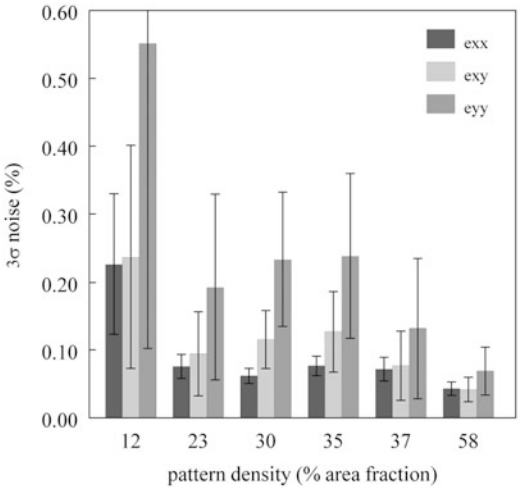

Fig. 16.2 Strain intensity noise as a function of speckle density of a 40 pixel subset size and a 3 pixel step size. The error bars for each show the standard deviation in the noise calculated from multiple images

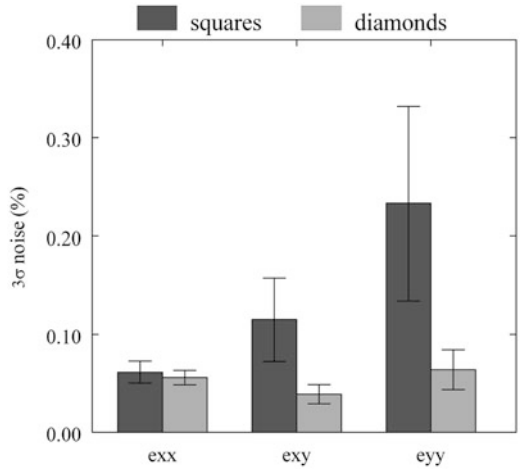

Fig. 16.3 Strain intensity noise as a function of speckle orientation for 30 % pattern, with 40 pixel subset and 3 pixel step sizes

density, until the pattern density was greater than 42 %. When the speckle pattern has a density greater than 50 % area fraction, the underlying material becomes the speckle, therefore the pattern density of 58 % is equivalent to 42 %. Figure 16.2 shows these trends in noise intensity variability for a 40 pixel subset size and a 3 pixel step size. For all speckle densities, with speckles edges parallel to the rastering direction, the e_{yy} signal noise was approximately double the e_{xx} noise. Images acquired at zero load (zero average strain) over the course of 30 min showed no systematic variation in the signal noise intensity.

Previous work, by Biery et al. [9], had indicated that the increased noise intensity in the y-direction is caused by the interaction between the rastering characteristic of SEM and the top and bottom edges of square speckles in a regular array. SEM images are acquired in a simple raster pattern, where pixels in the x-direction are sampled continuously along a row before stepping the beam down in the y-direction to sample the next row of pixels. The comparatively long time between sampling pixels in the y-direction leads to higher probability of image drift that can affect strain calculations. This leads to noise increased noise when the speckle edge is aligned along the horizontal image direction. Since a similar relationship was observed for random square pattern densities, a series of images were acquired by rotating the patterns relative to the rastering direction by 30°. A comparison of the strain noise for the same pattern density with speckles aligned (square) or not aligned (diamond) with the rastering directions (pattern 2, 30 % area fraction) is presented in Fig. 16.3. It was observed that rotating square speckles so that the cube edge was not aligned with the SEM beam rastering decreased the signal noise in the $e_{xy}$and e_{yy} data so that they were similar in magnitude to the noise in the e_{xx}. This is in agreement with the conclusions of Biery et al. [9]. It is expected that round or randomly shaped speckles would eliminate this direction bias in the intensity noise.

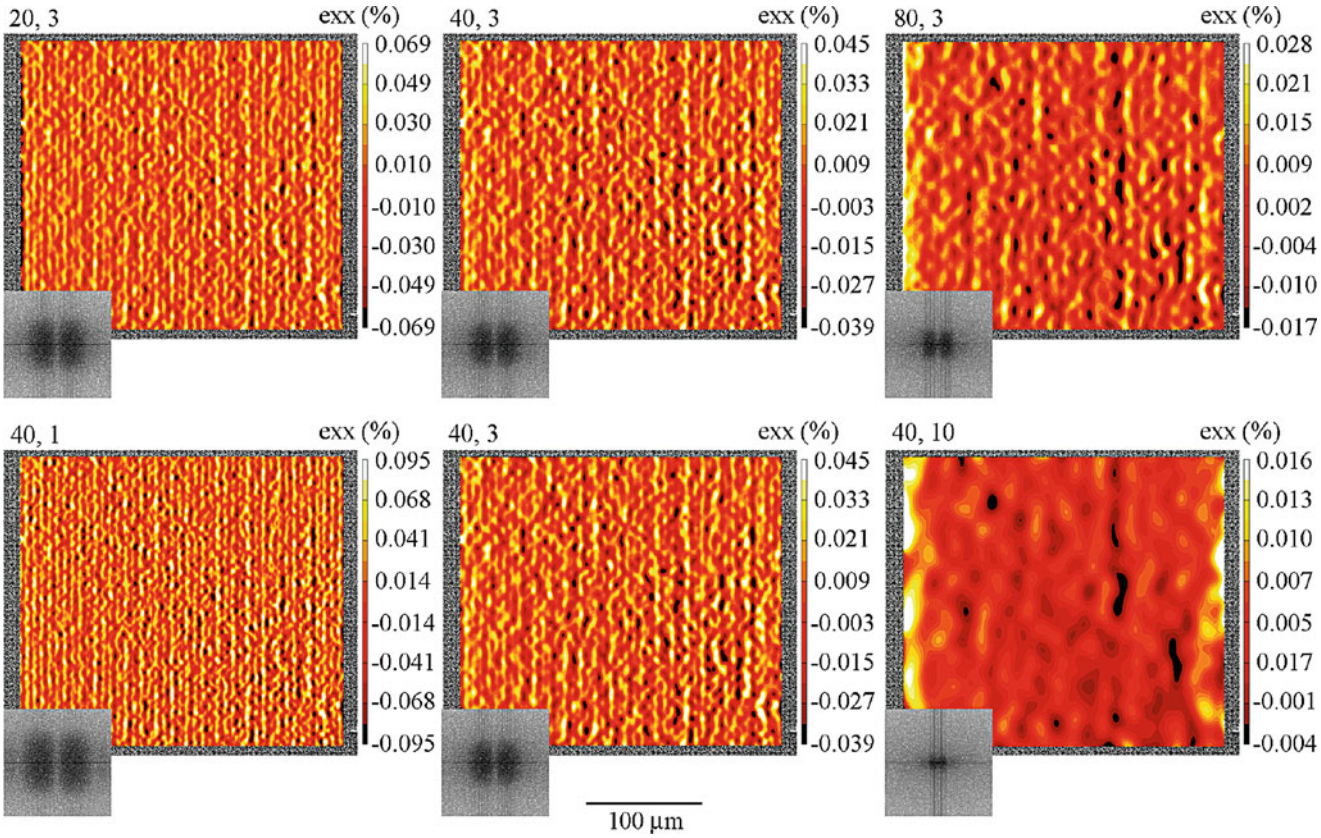

Fig. 16.4 Intensity noise and spatial resolution of strain maps decrease with increasing subset and step sizes. The subset and step size (pixels) is indicated at the top left of each strain map, and the Fourier transforms in the lower left of each strain map show the vertical alignment of the elliptical noise spots

16.3.2 VIC-2D Parameters

The density of the speckle pattern had a very small effect on the spatial resolution of the DIC measurements, expect that the spacing between speckles can set the minimum applicable subset size. When the subset size was similar to the speckle spacing, there was be an increase in the number of regions that could not analyzed since they did not exhibit a unique random gray-scale distribution. The data indicates that a minimum speckle density of about 25 % area fraction is needed so that the speckle pattern does not limit the spatial resolution of the DIC measurements. If additional spatial resolution was required, than higher resolution images should be collected, and smaller speckle size and spacing should be incorporated into the speckle pattern.

The VIC-2D DIC parameters had dramatic effect on the intensity and spatial distribution of the noise in the strain data. Increasing the subset or step sizes effectively decreased the intensity of the strain noise, independent of speckle pattern density. This is a trade-off, as increasing the subset and step size also decreased spatial resolution. It has previously been shown that VIC-2D calculation of strain introduces a non-random spatial distribution of elliptical spots with the long axis perpendicular to the strain measurement [13]. Increasing the subset or step size parameters increases the size and decreases the periodicity of these elliptical spots, while also decreasing their relative intensity, and effectively smoothing out the data. The spatial noise as a function of subset and step size for the 35 % area fraction pattern is presented in Fig. 16.4, with a table of noise intensities presented in Table 16.2. Figure 16.4 indicates that larger subsets and step sizes increase intensity noise near the outer edges of the correlated region. Data presented in Table 16.2 was calculated by averaging the strain measurement at each pixel location and multiplying by three.

Comparison of the spatial distributions and the intensity variations in the signal noise indicates that increasing the subset size to reduce signal noise intensity produces less spatial resolution loss than increasing the step size. Therefore, the optimum method for minimizing signal noise while maintaining the best spatial resolution would be to minimize step size while using a moderate subset size. This optimization method is subjective depending on the measurement requirements, (measuring elastic strains requires low intensity noise, while plastic strain localization at grain boundaries requires high spatial resolution).

Table 16.2 Noise in the strain data as a function of select VIC-2D parameters

Subset size (pixels)	Step size (pixels)	3σ noise (%)
20	3	0.0874
40	3	0.0540
60	3	0.0360
80	3	0.0264
40	1	0.1257
40	3	0.0540
40	10	0.0114

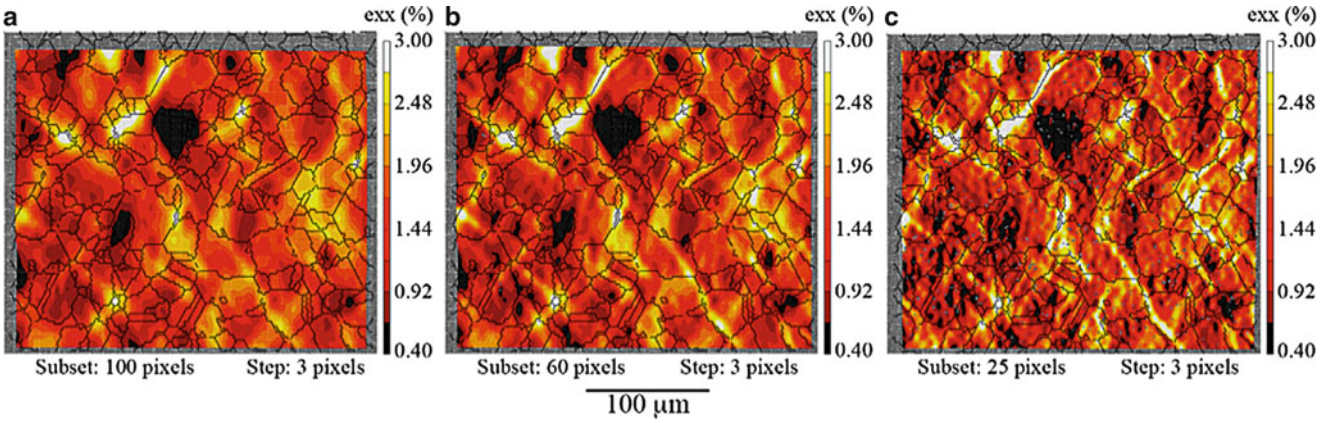

Fig. 16.5 The effect of VIC-2D parameters on the spatial and intensity resolution of the DIC data from a sample tested at constant stress (1,100 MPa) at 700 °C to approximately 1.6 % total macroscopic strain. (**a**) Optimal intensity settings to minimize noise, (**b**) optimal settings for best trade off between strain noise and spatial resolution, and (**c**) optimal settings for maximum spatial resolution. Variations in strain noise are clearly visible in the grains showing little strain accumulation

For the patterns and image resolution used for these experiments, the optimum parameters for characterizing plastic strain accumulation at grain boundaries were subjectively determined, to minimize the signal noise while maintaining good spatial resolution: 60 pixel subset size and 3 pixel step size. These parameters set the strain resolution limit for this data at approximately 360 μ-strain (as shown in Table 16.2).

Speckle pattern density can limit the smallest possible subset size that could be applied to the data sets. When the subset size was on the same order of magnitude as the spacing between speckles, the DIC software was unable to make correlation measurements between the reference image and subsequent images. This issue was observed with the 12 % area fraction pattern, using subset sizes less than 30 pixels.

Spatial resolution was maximized with small subset and step size DIC parameters. The smaller the subset size, the better the spatial resolution and the worse the intensity noise distribution. The minimum subset size is a function of the speckle density. For the lowest density speckle pattern the minimum subset size was 30 pixels, while for the denser patterns the minimum subset size was limited by the DIC software not the speckle pattern. The best spatial resolution is obtained by minimizing subset and step sizes, while increasing the intensity noise. Therefore, optimum parameters are set to minimize intensity noise while maximizing spatial resolution. For the experiments conducted, these parameters were 60 pixel subset and 2 pixel step size.

16.3.3 Deformed Samples

A comparison of actual data can be seen in Fig. 16.5. This in-situ experiment was conducted at constant stress (1,100 MPa) at 700 °C to approximately 1.6 % total macroscopic strain. The strain data has been integrated with electron backscatter diffraction information on grain boundary information to visualize how the spatial distribution of strain correlates with microstructural features. Figure 16.5 provides visualization of how changing DIC analysis parameters changes the relative hot spot intensities and shapes. Since increasing the subset size reduces the intensity noise and the spatial resolution, increasing the subset size to 100 pixels broadens the strain data around the grain boundaries. Increasing the subset size also reduces the peak intensities of the hot-spots since the strain is being averaged over a larger area. When parameters are used to optimize spatial resolution (25 pixel subset and 3 pixel step), the strain becomes highly localized at the grain boundaries, though this

increases the noise intensity in grains exhibiting average strain accumulation. Optimal parameters for minimizing intensity noise are also shown, it can be seen that these optimized parameters maximize the spatial resolution but minimize the effects of intensity noise.

16.4 Conclusions

This work examined the optimization of e-beam lithography produced speckle patterns for DIC measurements on nickel-based superalloys tested in elevated temperature, constant stress conditions. The speckle pattern distribution (size, spacing, shape) used for DIC analysis should be optimized for the desired spatial and intensity resolution. The Vistec EBPG 5000 e-beam lithography system used for this study can repeatability produce patterns with resolution of 25 nm. This makes it easy to produce a variety of repeatable patterns for DIC. Though, if much smaller or larger speckles are required, the lithography exposure voltage and current densities used in this study should be varied to provide accurate edge retention. A speckle pattern with 50 % area fraction would provide optimum intensity resolution, but patterns with at least 25 % area fraction and optimum speckle size exhibit little loss in intensity resolution. There was a slight decrease in the spatial resolution with low density patterns when the spacing between speckles was on the same order of magnitude as the analysis subset size. This work indicates that decreasing the speckle density to add secondary information, grid markers for grain boundary sliding measurements and alphanumeric markers for subsequent alignment for example, will not greatly reduce the effectiveness of the DIC measurements.

We also confirmed that square speckles were not the optimal speckle geometry for DIC analysis of random speckle patterns in SEM images. Alignment with the rastering direction of the SEM imaging system led to a pixilated edge. This was particularly apparent with this pattern because speckles were only 9–49 pixel^2 in size. A diamond pattern dramatically decreased the intensity noise in the e_{yy} measurements, and by extension a round speckle would be the optimum speckle geometry.

Optimizing intensity and spatial resolution of the DIC measurement proved to be contradictory requirements. Decreasing intensity noise and thus increasing intensity resolution by increasing subset and step sizes simultaneously lowers spatial resolution. Therefore, parameters should be tailored depending on data required. Since optimal spatial resolution is often more important than the absolute intensity value in assessing plastic deformation distribution, the smallest subset and steps possible should be used when analyzing data sets.

Acknowledgements Funding was provided by the Air Force Research Laboratory (AFRL) STW-21 program FA9550-09-1-0014. The authors would like to thank Aimee Price, Research Associate of the Institute for Materials Research at The Ohio State University for the assistance in producing the patterns used for this study.

References

1. Tong W (1997) Detection of plastic deformation patterns in a binary aluminum alloy. Exp Mech 37(4):452–459
2. Read D, Cheng Y, Keller R, McColskey DJ (2001) Tensile properties of free-standing aluminum thin films. Scripta Materialia 45(5):583–589
3. Carroll J, Abuzaid W, Lambros J, Sehitoglu H (2010) An experimental methodology to relate local strain to microstructural texture. Rev Sci Instruments 81(8):083703–083703–9
4. Efstathiou C, Sehitoglu H, Lambros J (2010) Multiscale strain measurements of plastically deforming polycrystalline titanium: role of deformation heterogeneities. Int J Plast 26:93–106
5. Kim K, Daly S (2010) Martensite strain memory in the shape memory alloy nickel-titanium under mechanical cycling. Exp Mech 51:641–652
6. Sutton MA, Li N, Joy DC, Reynolds AP, Li X (2007) Scanning electron microscopy for quantitative small and large deformation measurements part i: SEM imaging at magnifications from 200 to 10,000. Exp Mech 47:775–787
7. Sutton MA, Li N, Garcia D, Cornille N, Orteu JJ, McNeill SR, Schreier HW, Li X, Reynolds AP (2007) Scanning electron microscopy for quantitative small and large deformation measurements part II: experimental validation for magnifications from 200 to 10,000. Exp Mech 47:789–804
8. Tschopp M, Bartha B, Porter W, Murray P, Fairchild S (2009) Microstructure-dependent local strain behavior in polycrystals through in-situ scanning electron microscope tensile experiments. Metallurgical Mater Trans A 40:2363–2368
9. Biery N, de Graef M, Pollock TM (2003) A method for measuring microstructural-scale strains using a scanning electron microscope: applications to gamma-titanium aluminides. Metallurgical Mater Trans A 34(10):2301–2313
10. Jin H, Haldar S, Bruck HA, Lu W-Y (2011) Grid method for microscale discontinuous deformation measurement. Exp Mech 51:565–574
11. Scrivens WA, Luo Y, Sutton MA, Collette SA, Myrick ML, Miney P, Colavita PE, Reynolds AP, Li X (2006) Development of patterns for digital image correlation measurements at reduced length scales. Exp Mech 47:63–77

12. Kammers AD, Daly S (2013) Digital image correlation under scanning electron microscopy: methodology and validation. Exp Mech 53(9):1743–1761
13. Walley JL, Wheeler R, Uchic MD, Mills MJ (2012) In-situ mechanical testing for characterizing strain localization during deformation at elevated temperatures. Exp Mech 52(4):405–416
14. Langdon T (2006) Grain boundary sliding revisited: developments in sliding over four decades. J Mater Sci 41:597–609
15. Sutton M, Orteu J, Schreier H (2009) Image correlation for shape, motion and deformation measurements basic concepts, theory and applications. Springer, New York
16. C. Solutions, VIC-2D testing guide (2009)
17. Carter J, Zhou N, Sosa J, Shade P, Pilchak A, Kuper M, Wang Y, Fraser H, Uchic M, Mills M (2012) Characterization of strain accumulation at grain boundaries of nickel-based superalloys. In: Superalloys 2012 (Warendale). TMS, pp 43–52

Chapter 17
Very High-Cycle Fatigue Resistance of Shot Peened High-Strength Aluminium Alloys: Role of Surface Morphology

M. Benedetti, V. Fontanari, and M. Bandini

Abstract The present paper is aimed at investigating the effect of shot peening on the very-high cycle fatigue resistance of the Al-7075-T651 alloy. Pulsating bending fatigue tests ($R = 0.05$) were carried out on smooth samples exploring fatigue lives comprised between 10^5 and 10^8 cycles. Three peening treatments with different intensity were considered to explore different initial residual stress profiles and surface microstructural conditions. An extensive analysis of the residual stress field was carried out by measuring with the X-ray diffraction (XRD) technique the residual stress profile before and at the end of the fatigue tests, so as to investigate the onset of a stabilized residual stress field. Fatigue crack initiation sites have been investigated through scanning electron microscopy (SEM) fractography. The surface morphology modifications induced by shot peening were evaluated using an optical profilometer. The influence of surface finishing on the fatigue resistance was quantified by eliminating the surface roughness in some peened specimens through a tribofinishing treatment.

Keywords Shot peening • Very high-cycle fatigue • Al-7075-T651 • Residual stresses • Tribofinishing

17.1 Introduction

Aluminium alloys are an attractive class of materials for aircraft and automotive industry because of their high specific static strength. In aerospace, aluminium alloys face ever stiffer competition from composites. In the automotive context, more and more engine parts are being made from them. Usually, high static mechanical properties are induced in aluminium alloys by dispersion hardening through solution and ageing heat treatments. However, aluminium alloys exhibit poor plain fatigue resistance and high notch fatigue sensitivity. Accordingly, stress raisers, like holes, fillets and grooves, always present in machine parts, are particularly detrimental to the fatigue response of these alloys, thus limiting their use in highly stressed mechanical components characterized by complex shapes. For this reason, aluminium alloys are frequently subjected to shot peening, particularly effective in incrementing the plain and notch fatigue strength of steels and light alloys. The shot peening mainly results in three fatigue related modifications of the surface layers: roughness, residual stresses and work hardening. Clearly, the surface roughening after shot peening is detrimental to the fatigue resistance due to the stress concentration exerted by the surface dimples. In the literature, it is commonly accepted that the improvement of fatigue strength is mainly induced by the introduction of compressive residual stresses in the surface region, responsible for both retarded fatigue crack initiation and lower small crack growth rates [1, 2]. The role of work hardening on the fatigue response is essentially indirect, since it strongly affects the stability of residual stresses by preventing them from relaxing due to accumulation of plastic deformation [3].

The authors recently studied the effect of three types of shot peening treatments on the plain and notch high-cycle fatigue response of the Al-7075-T651 alloy ($R = -1$) [4–8]. In particular, it was shown that (i) residual stress relaxation occurs when the superposition between the compressive residual stress and the compressive peak stress produced by reverse bending

M. Benedetti (✉) • V. Fontanari
Department of Industrial Engineering, University of Trento, via Mesiano 77, Trento 38100, Italy
e-mail: matteo.benedetti@ing.unitn.it

M. Bandini
Peen Service s.r.l., via Pollastri 7, Bologna 40138, Italy
e-mail: m.bandini@peenservice.it

J. Carroll and S. Daly (eds.), *Fracture, Fatigue, Failure, and Damage Evolution, Volume 5: Proceedings of the 2014 Annual Conference on Experimental and Applied Mechanics*, Conference Proceedings of the Society for Experimental Mechanics Series,
DOI 10.1007/978-3-319-06977-7_17,

exceeds the material's cyclic yield stress; (ii) the plain fatigue response is directly correlated with the surface residual stress as successfully predicted using a multiaxial fatigue criterion incorporating the stabilized residual stress field as mean stresses; (iii) gentle peening treatments conducted using small ceramic beads are more effective than more intense treatments employing larger peening media (iv) shot peening reduces the fatigue notch sensitivity; (v) the notch fatigue resistance can be satisfactorily predicted by the a multiaxial fatigue criterion incorporating stabilized residual stresses and combined with a line method based on the critical distance theory to account for the notch sensitivity. However, the current state-of-the-art-knowledge lacks for investigations proving whether the beneficial effect of shot peening is still present in the very-high cycle fatigue regime.

The present paper is aimed at investigating the effect of shot peening on the very-high cycle fatigue resistance of the Al-7075-T651 alloy. Pulsating bending fatigue tests ($R = 0.05$) were carried out on smooth samples exploring fatigue lives comprised between 10^5 and 10^8 cycles. Three peening treatments with different intensity were considered to explore different initial residual stress profiles and surface microstructural conditions. An extensive analysis of the residual stress field was carried out by measuring with the X-Ray Diffraction (XRD) technique the residual stress profile before and at the end of the fatigue tests, so as to investigate the onset of a stabilized residual stress field. Fatigue crack initiation sites have been investigated through Scanning Electron Microscopy (SEM) fractography. The surface morphology modifications induced by shot peening were evaluated using an optical profilometer. The influence of surface roughness on the fatigue resistance was quantified by eliminating the surface roughness in some peened specimens through a tribofinishing process.

17.2 Materials and Experimental Procedures

The experimentation was performed on the aluminium alloy Al-7075-T651, widely used for aeronautical applications, supplied in the form of 4 mm thick rolled plate. The bulk material properties were determined on five standard monotonic tensile tests (initial strain rate of 1×10^{-3} s^{-1}) performed in the longitudinal orientation. The results, summarized in Table 17.1, show a yield strength higher than 500 MPa, combined with a good ductility (total elongation of 16 %).

The fatigue characterisation was carried out on hourglass specimens whose geometry, according to the standard ISO 3928, is illustrated in Fig. 17.1. The microstructure has been tested with the stress axis parallel to the L-direction. The samples present a fillet radius large enough to make any notch fatigue effects negligible.

Part of the specimens was subjected to controlled shot peening: the parameters of the three peening treatments considered are summarized in Table 17.2. Each treatment was performed using non-metallic beads, which lend light alloys higher fatigue performance as compared with steel shots without introducing undesired galvanic effects [6]. The basic idea was (i) to apply a widely used commercial peening treatment, termed Z425, employing beads of medium-small size (diameter 150 μm), which introduces some surface roughness and a deep cold worked layer (depth 100 μm), (ii) to explore an innovative peening treatment, called B120, with small ceramic beads leading to a gentle and superficial effect, (iii) and finally to investigate a fine particle shot peening treatment, termed V40, with very fine glass beads, which is known to greatly enhance the fatigue resistance of aluminium alloys [9].

In order to investigate the effect of the surface roughness induced by shot peening on the fatigue strength, three specimens previously subjected to the treatment B120 and V40 were then subjected to tribofinishing using a controlled vibrating tank with an aqueous medium containing high quality granulates and additives (mainly surfactants). During the process, the

Table 17.1 Monotonic tensile properties of the Al-7075-T651 alloy

E (GPa)	$\sigma_{Y0.2}$ (MPa)	UTS (MPa)	σ_F (MPa)	T.E. (%)	R.A. (%)
73 (±1)	510 (±5)	580 (±5)	780 (±10)	16 (±2)	22 (±2)

E elastic modulus, $\sigma_{Y0.2}$ 0.2 % yield stress, *UTS* ultimate tensile strength, σ_F true fracture stress, *T.E.* total elongation, *R.A.* reduction in area

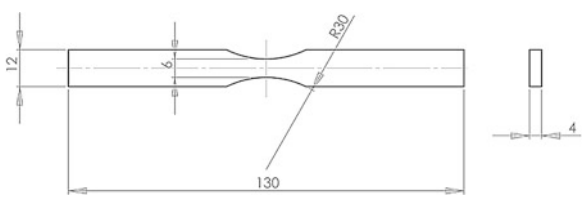

Fig. 17.1 Geometry of the smooth hourglass specimen used in this study for bending fatigue tests. All dimensions are given in mm

Table 17.2 Shot peening parameters

Treatment	Material	Bead size [μm]	Bead hardness [HV_1]	Bead composition	Almen intensity	Angle of impingement	Coverage [%]
Z150	Ceramic	150 ÷ 210	700	ZrO_2 67 %	12 N	90°	100
B120	Ceramic	63 ÷ 125		SiO_2 31 %	4.5 N		
V40	Glass	40 ÷ 70	550	SiO_2 31 %	4.2 N		
				Na_2O 14 %			

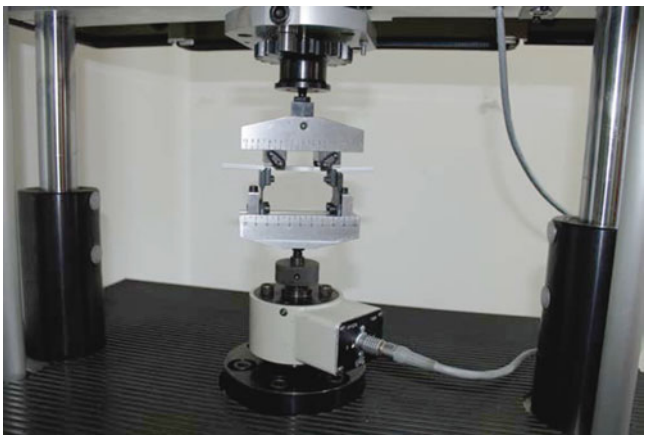

Fig. 17.2 4-point bending fatigue test apparatus used in the present study

specimen surface was periodically observed with an optical microscope to make sure that polishing is stopped just after removing all the dimples created by the shot peening treatments. A material surface layer of approximately 5 ÷ 10 μm thickness was removed in this way.

Pulsating (R = 0.05) load-controlled 4-point bending fatigue tests were carried out in air, at room temperature, and at a nominal frequency of 110 Hz using a resonant testing machine Rumul Mikrotron 20 kN equipped with a 1 kN load cell (Fig. 17.2). Different stress levels corresponding to fatigue lives in the range between nearly 10^5 and 10^8 cycles were considered. Tests were terminated at 10^8 cycles when no fracture occurred. The fatigue curves corresponding to 50 % of failure probability, represented by the S-N curve:

$$\sigma_{P50} = \sigma_{0P50} \times N_f^{-\frac{1}{k}} \tag{17.1}$$

were determined by fitting the $\log(N_f)$ vs. $\log(\sigma)$ results. The uncertainty range was assumed to be constant and approximated by its centroid value. As a representative value of the scatter, the following expression was used:

$$T\sigma = 1 : \sigma_{P90}/\sigma_{P10} \tag{17.2}$$

P_{90}, P_{10} denote the 90 % and 10 % levels of failure probability, respectively.

The modifications of the surface layers produced by the shot peening treatments were investigated through microhardness, surface roughness and residual stress profile measurements. To this regard, microhardness profiles were measured to characterize the material's work hardening. Cross-sections were prepared by low-speed cutting with a diamond saw. To preserve the material work-hardening state, samples were cold-mounted in epoxy resin and then mechanically polished. A diamond Vickers indenter was used applying a maximum force of 1 N. The load was applied gradually at a constant 0.1 N/s rate with a dwell time of 10 s. Five measurements were performed at each depth and averaged in order to account for material's heterogeneity and measurement errors.

A confocal optical profilometer WLI Sensofar Plu Neox (plane surface spatial resolution of 0.31 μm, z-axial measurement resolution of 0.02 μm), was used to observe the samples surface. Three dimensional surface topography and roughness were evaluated.

Residual stress analysis was performed by X-Ray Diffraction (XRD) technique using an AST X-Stress 3000 X-ray diffractometer. Measurements were made with Cr Kα radiation in the longitudinal direction in the gage region. The analysis zone was limited by a collimator of 1 mm^2 in area. The classical $\sin^2\psi$ method was applied for stress evaluation with the use of nine diffraction angles (2θ) scanned between −45° and +45° for each stress value. The ⟨311⟩ diffracting planes were chosen (i) in order to obtain high angle measurements (2θ angle 139.0°) with higher strain sensitivity, and (ii) because they

do not accumulate significant intergranular stresses and hence exhibit similar behavior as that of the bulk. Calibration of the system was checked by collecting a diffraction pattern from a standard polycrystalline Al powder prior to conducting the experiment. The in-depth measurements were conducted step-by-step using an electro-polishing device by removing a very thin layer of material in a region (2 mm × 2 mm) localized at the gauge section of the specimens.

Both initial and stabilized residual stress fields were measured. For this purpose, measurements were performed on tested smooth specimens after failure in a region far enough from the fracture surface (about 2 mm) so that the material rupture was supposed not to have altered the residual stress field [4]. Measurements were carried out on both specimen sides, subjected to tensile and compressive bending stresses, respectively.

17.3 Results and Discussion

17.3.1 Surface Characteristics

The effect on the surface roughness exerted by the shot peening treatments is quantified in Table 17.3, where the results of the optical profilometer measurements made on an assessment area 636×477 μm^2 are summarized. It can be noted that the shot peening treatments increase the surface roughness with the respect to the as-received condition and that the most intense treatment Z150 results in a larger roughness increment with respect to the gentler processes B120 and V40. The tribofinishing is able to reduce the surface roughness of the peened samples below that of the virgin material. The as-received and the peened variants have a skewness close to zero, index of a symmetric height distribution (i.e. with as many peaks as valleys), while the tribofinished conditions have a negative skewness due to the fact that the surface asperities were removed by the polishing process. The maximum peak to valley height (S_z) and the mean spacing between profile peaks (D_p) can be used to estimate the stress concentration effect exerted by the surface dimples caused by shot peening according to the following expression proposed by [10]:

$$K_t = 1 + 4\left(\frac{S_z}{D_p}\right)^{1.3} \tag{17.3}$$

The surface morphology of the virgin, Z150, B120, tribofinished B120, V40 and tribofinished V40 conditions is depicted in Fig. 17.3, respectively. Notably, the surface morphology of the as-received condition is characterized by striations caused by the rolling process. The large beads used in the most intense peening treatment, i.e. Z150, created large and deep impact craters. Dimples of smaller size, typical of gentle superficial peening treatments, are visible on the surfaces of the B120 and V40 conditions. The superficial structure of impact craters is not visible on the tribofinished variants.

The surface morphology of the virgin, Z150, B120, tribofinished B120, V40 and tribofinished V40 conditions is depicted in Fig. 17.3, respectively. Notably, the surface morphology of the as-received condition is characterized by striations caused by the rolling process. The large beads used in the most intense peening treatment, i.e. Z150, created large and deep impact craters. Dimples of smaller size, typical of gentle superficial peening treatments, are visible on the surfaces of the B120 and V40 conditions. The superficial structure of impact craters is not visible on the tribofinished variants.

A comparison among the microhardness profiles measured for both the peening treatments and the as-received condition is illustrated in Fig. 17.4. Noticeable differences, which are directly correlated to the surface work hardening experienced by the material as well as to the depth of the surface layer interested by the plastic deformation, can be observed: B120 and V40

Table 17.3 3D surface roughness properties

Condition	S_a [μm]	S_q [μm]	S_z [μm]	S_{sk}	S_{ku}	S_{dr} [%]	S_{pk} [μm]	S_k [μm]	S_{vk} [μm]	D_p [μm]	K_t
As-received	0.29	0.38	1.44	0.19	5.98	1.10	0.59	0.81	0.41	–	–
Z150	3.79	4.83	21.29	0.29	8.60	40.61	8.09	11.56	3.56	200	1.22
B120	1.24	1.54	7.12	0.14	3.03	6.07	1.75	3.96	1.42	110	1.11
B120 trib.	0.19	0.26	0.99	−1.21	12.17	0.60	0.29	0.55	0.38	–	
V40	1.33	1.66	7.66	−0.01	2.96	3.79	2.12	4.23	1.24	100	1.14
V40 trib.	0.17	0.23	0.87	−1.30	12.52	0.61	0.28	0.49	0.33	–	

S_a average roughness, S_q root mean square roughness, S_z maximum peak to valley height, S_{sk} skewness, S_{ku} kurtosis, S_{dr} developed interfacial area ratio, S_{pk} reduced peak height, S_k core roughness depth, S_{vk} reduced valley depth, D_p mean spacing between profile peaks, K_t stress concentration factor due to surface roughness

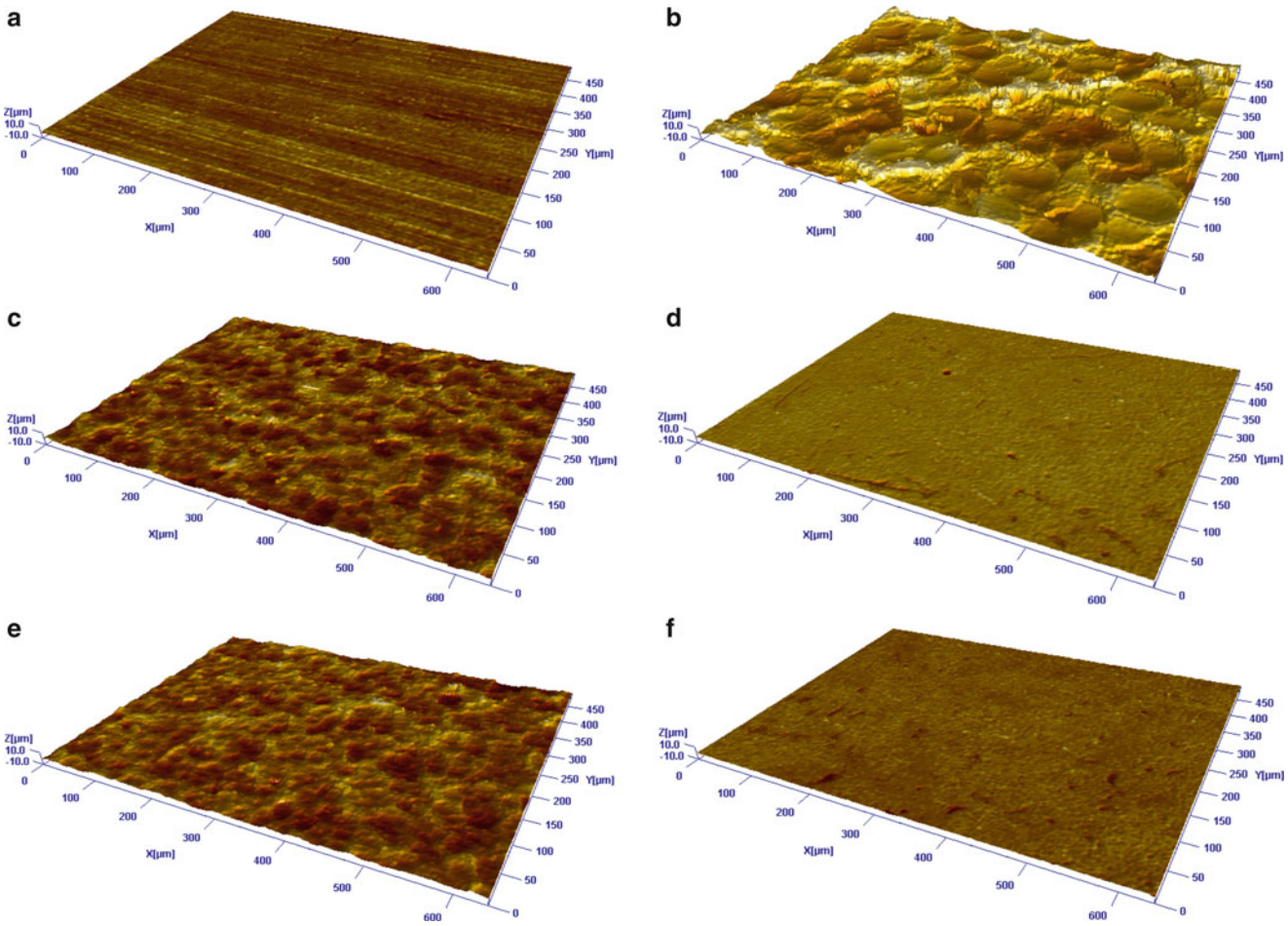

Fig. 17.3 Surface morphologies measured through optical profilometer. (**a**) As-received, (**b**) Z150 peened, (**c**) B120 peened, (**d**) B120 peened and tribofinished, (**e**) V40 peened, (**f**) V40 peened and tribofinished. The assessment area is $636 \times 477\ \mu m^2$

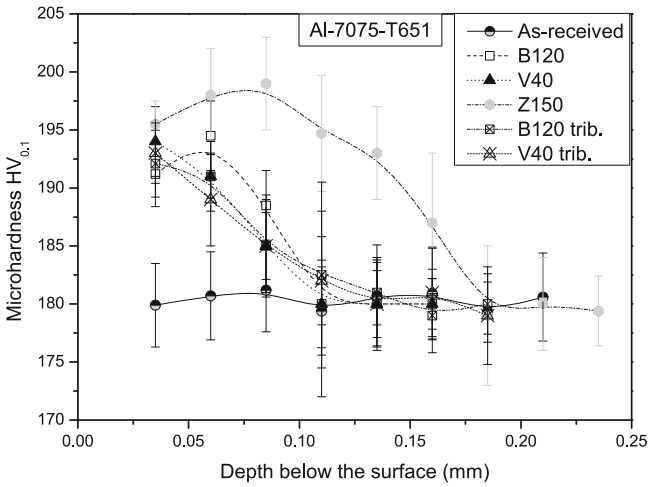

Fig. 17.4 Microhardness profiles of the as-received and peened variants, obtained by averaging the results of five tests

peening treatments are very superficial, the maximum hardness is within 60 μm from the surface, the depth of the surface layer interested by the plastic deformation is about 100 μm. The B120 treatment causes a more intense work hardening of the sub-superficial layers, and hence higher microhardness values, while the V40 treatment introduces higher microhardness values down to 40 μm below the surface. The Z150 treatment induces a sub-superficial microhardness peak, where the Hertzian pressure is nearly maximal; the effect of shot peening vanishes at approximately 0.17 mm below the surface. The tribofinishing treatment slightly modifies the microhardness profiles, mainly due to the removal of the outer material layer without significantly altering the work-hardening state.

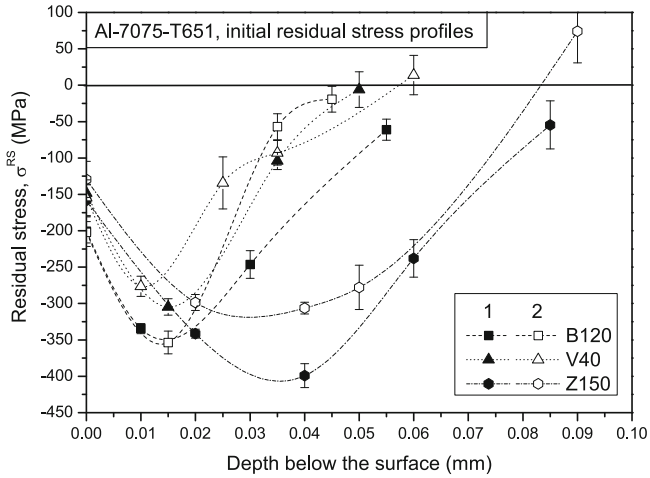

Fig. 17.5 Initial residual stress profiles of the peened variants measured by XRD technique. Two measurements per peened variant were carried out in order to account for the variability in the residual stress field

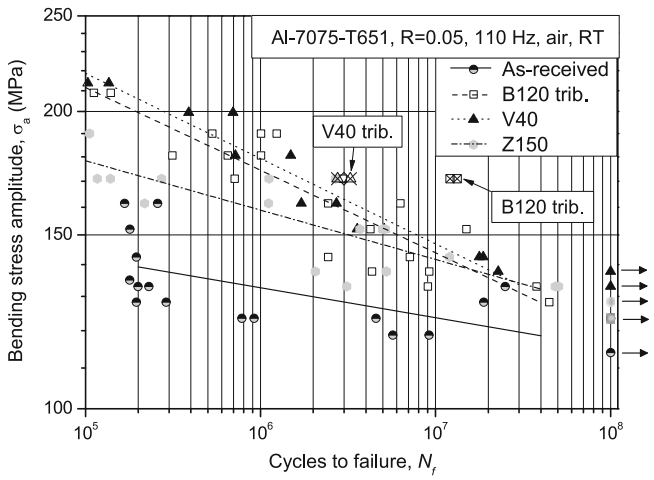

Fig. 17.6 Pulsating bending fatigue curves of the as-received and peened conditions. Run-out tests are marked by *arrows*

XRD measurements were carried out on the fatigue samples in order to characterize the residual stress field prior to fatigue testing. The obtained stress profiles are illustrated in Fig. 17.5. Two measurements per peening variant were performed in order to account for the variability in the residual stress field. The peening treatments B120 and V40 display a sub-superficial compressive residual stress peak located nearly 15 μm below the surface and a depth of the surface layer interested by compressive residual stresses equal to about 50 μm. The B120 treatment induces higher residual stresses as compared with the V40 treatment. The most intense peening treatment Z150 is characterized by lower compressive surface residual stress, by higher sub-superficial compressive peak, and by deeper compressive residual stress profiles (about 90 μm) with respect to the gentler treatments. The repeatability of the residual stress measurements is very good within a depth of about 20 μm, where the fatigue response is mostly dictated [4], while it increases noticeably at higher depths, presumably due to the very elongated grain structure of the internal material layers that have not undergone recrystallization and hence grain refinement during shot peening.

17.3.2 Fatigue Curves

The results of the pulsating bending fatigue tests as well as the P50 fatigue lines are shown in Fig. 17.6 in the different material conditions considered and compared with those of the tests carried out on the two tribofinished variants. The parameters representing the fatigue curves corresponding to 50 % of failure probability, according to Eq. 17.1 and the results scatter, expressed by Eq. 17.2 are listed in Table 17.4.

All the peening treatments were effective in prolonging the fatigue life of the material as well as in reducing the large scatter in fatigue results displayed by the virgin material. This improvement depends on the applied load, being more remarkable for load levels corresponding to shorter fatigue lives, leading however to higher values of the slope in the P50

Table 17.4 Principal results of fatigue tests

Condition	k	σ_{0P50} [MPa]	Tσ
As-received	33	200	1:1.22
Z150	20	315	1:1.17
B120	12	555	1:1.19
V40	12	590	1:1.10

k, σ_{0P50} slope and y-intercept of the Wöhler curve according to Eq. 17.1, $T\sigma$ results scatter according to Eq. 17.2

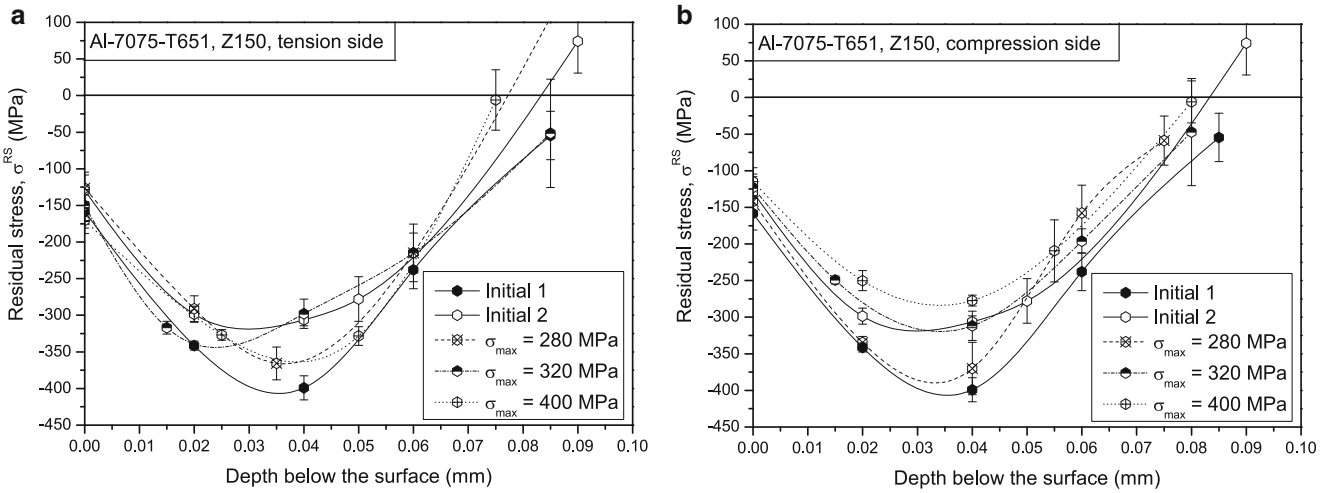

Fig. 17.7 Evolution of the residual stress profile during fatigue life in samples subjected to Z150 treatment. (**a**) Tensioned, (**b**) compressed side. Specimen tested at 280 (320, 400) maximum stress MPa failed after 50.6×10^6 (5.1×10^6, 106,000) cycles

fatigue line. Therefore, the increment in fatigue resistance due to shot peening steadily declines during fatigue life. The lightest V40 peening treatment, despite lower surface residual stresses and slightly higher roughness, is more effective in improving the plain fatigue resistance with respect to the B120 treatment, which, in turn, performs better than the most intense treatment Z150. Finally, it can be noted that the tribofinished samples displayed a fatigue performance significantly higher with respect to the corresponding peened condition: the increment in fatigue strength due tribofinishing is about 5 % for the V40 and even 20 % for the B120 condition. The fact that the tribofinishing increments the fatigue performes of V40 in less extent than B120 condition suggests the hypothesis that the particular surface morphology of the V40 condition, characterized by lower values of developed interfacial area ratio and reduced valley depth, exerts a less detrimental effect on the fatigue response as compared with that exhibited by B120.

17.3.3 Residual Stress Evolution During Fatigue Life

Figures 17.7, 17.8 and 17.9 illustrate the evolution of the residual stress field at two loading levels for the Z150, B120 and V40 treatment, respectively. Figures 17.7 (17.8, 17.9) and 17.7 (17.8, 17.9) refer to the specimen surface subjected to compressive and tensile bending stresses, respectively. It can be noted that some relaxation of the residual stress field occurred on the outer layer of the specimen side subjected to compressive bending stresses, the more pronounced the higher the load levels, especially in the B120 and Z150 conditions. Conversely, significantly lower relaxation occurred on the specimen side subjected to tensile bending stresses. This confirm the observations made in [4, 5] that relaxation is more like a "quasi-static" effect, due to the achievement of the material's plasticization when the compressive bending stresses are superimposed to the compressive surface residuals stress field. Cyclic relaxation seems to be negligible, since the application of tens of millions fatigue cycles do not significantly alter the surface residual stress field on the tensioned side of the samples.

Figure 17.10 illustrate the comparison between the initial (prior to tribofinishing) and the stabilized residual stress profiles for the tribofinished B120 and V40 variants, respectively. It can be noted that the material removal exposes on the surface the residual stress that was present at the corresponding depth prior to polishing. Moreover, tribofinishing caused some stress redistribution in the subsuperficial peak, while the depth of the surface layer interested by compressive residual

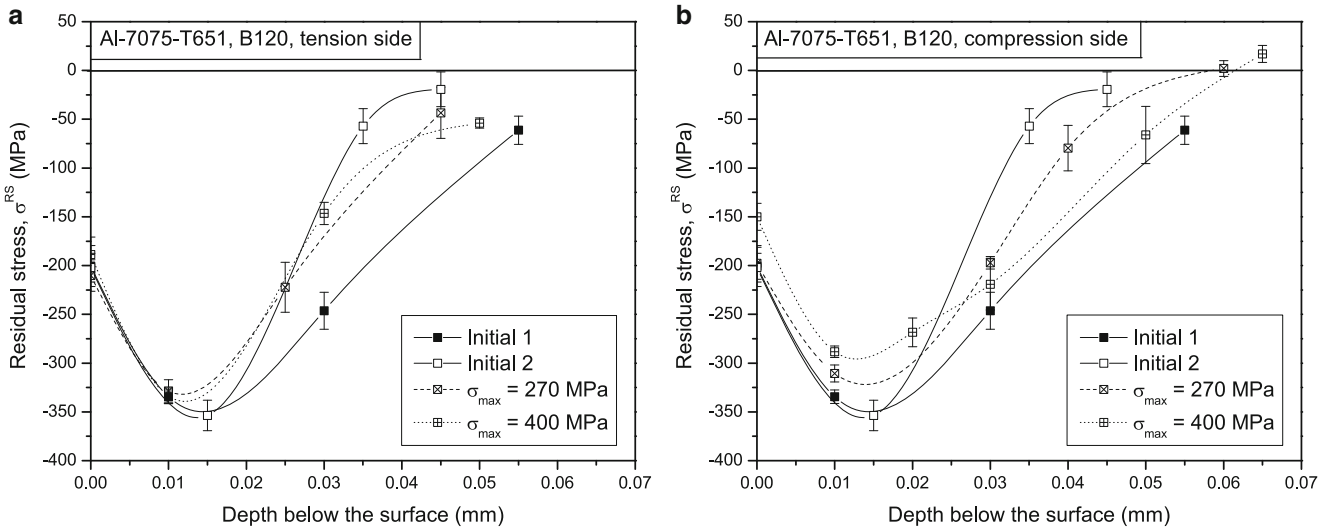

Fig. 17.8 Evolution of the residual stress profile during fatigue life in samples subjected to B120 treatment. (**a**) Tensioned, (**b**) compressed side. Specimen tested at 270 (400) maximum stress MPa failed after 44.6×10^6 (530,000) cycles

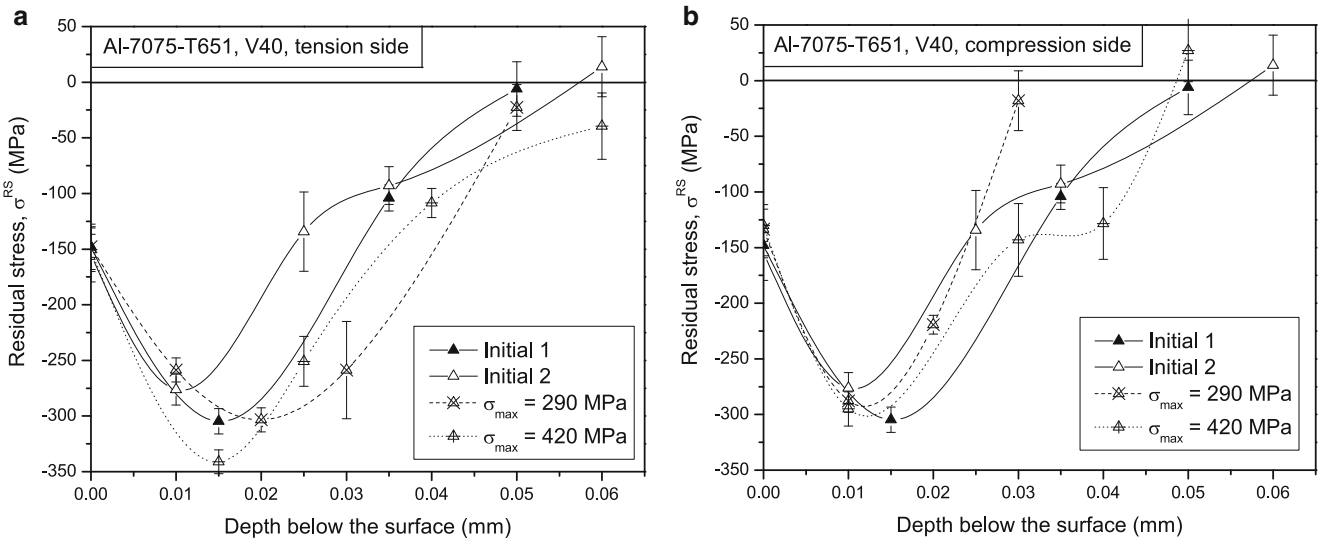

Fig. 17.9 Evolution of the residual stress profile during fatigue life in samples subjected to V40 treatment. (**a**) Tensioned, (**b**) compressed side. Specimen tested at 290 (420) MPa maximum stress failed after 22.8×10^6 (390,000) cycles

stresses remained nearly unaffected. Residual stress profiles are very similar on the tensioned and the compressed side of the specimen, thus suggesting that no residual relaxation occurred at the investigated stress level.

17.3.4 SEM Analysis of Fracture Surfaces

The fracture surfaces of all the fatigue samples were analyzed with the SEM. The analysis of the unpeened specimens revealed surface crack initiation throughout the entire fatigue life interval explored, even in the very high-cycle fatigue regime, as shown in Fig. 17.11. In the peened variants, surface crack initiation was found in the medium-cycle fatigue regime ($N_f < 1 \times 10^6$), as depicted in Fig. 17.11 for the B120 condition. At longer fatigue lives ($N_f > 2 \times 10^6$), almost all crack initiation sites were found below the surface. Moreover, the fracture surfaces near the crack initiation sites show several crystallographic planes. This is frequently observed in Al alloys when fatigue tests are conducted under vacuum and can be explained by the fact that the first propagation stages of sub-superficial cracks occur at very low partial pressures of

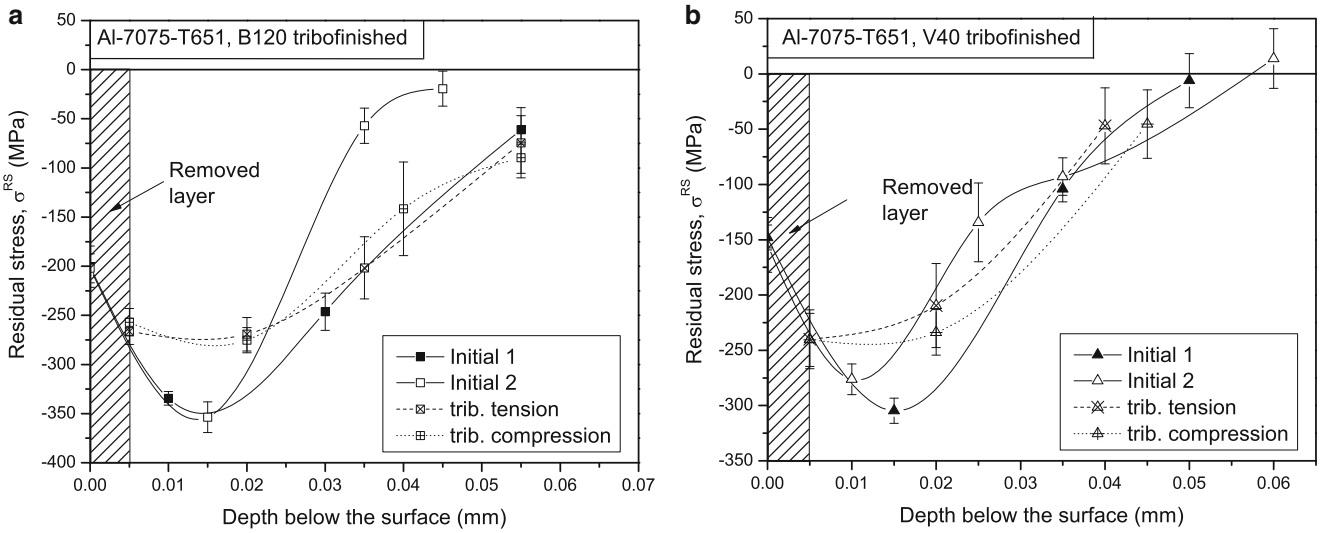

Fig. 17.10 Evolution of the residual stress profile during fatigue life in peened and tribofinished samples. (**a**) B120, (**b**) V40 peening. Specimens were tested at 360 MPa maximum stress and failed after (**a**) 13.3106 and 3.3106 cycles

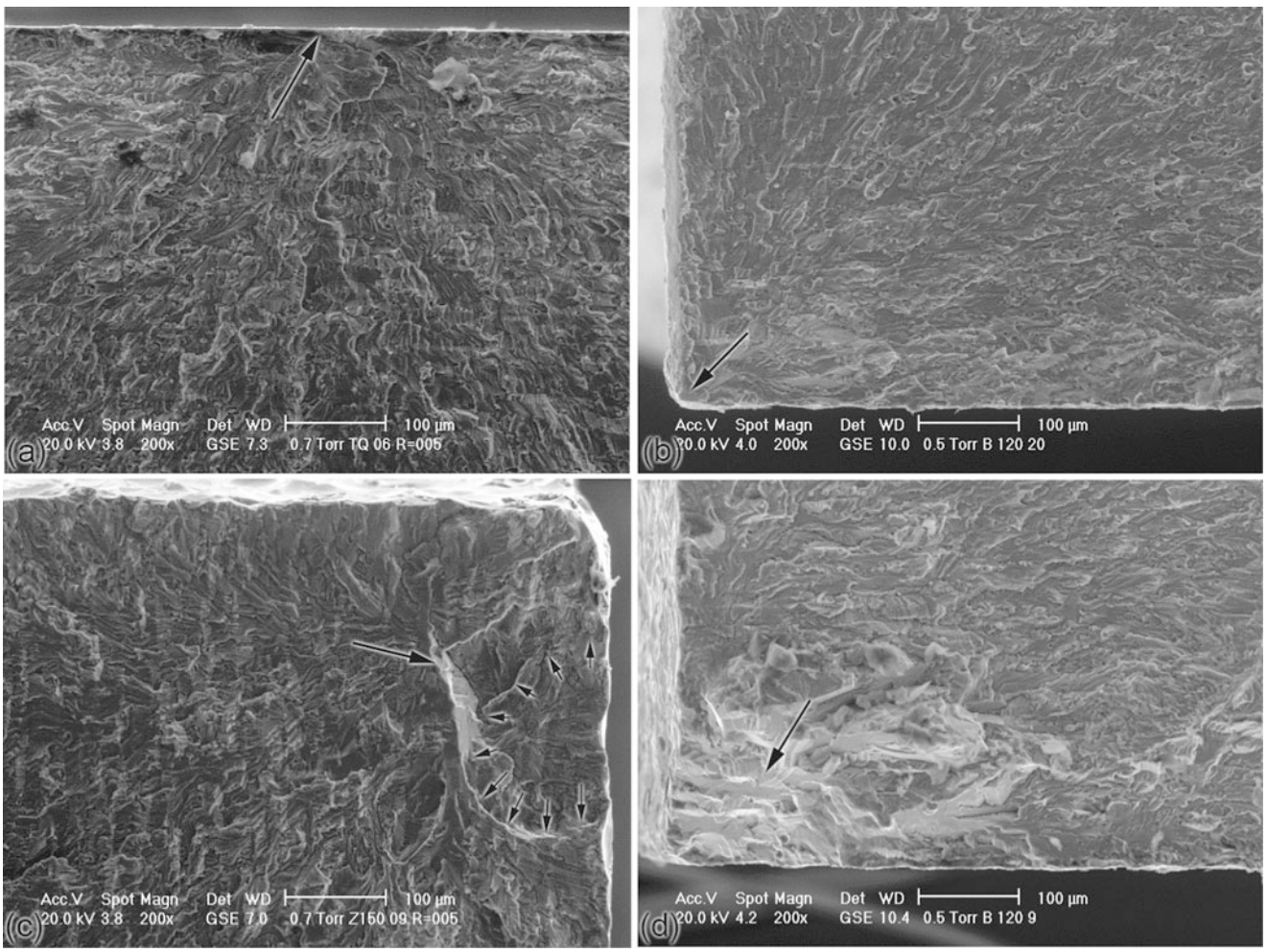

Fig. 17.11 SEM micrographs of the fracture surfaces around the fatigue crack initiation sites. (**a**) As-received ($\sigma_a = 133$ MPa, $N_f = 25.0 \times 10^6$), (**b**) B120 ($\sigma_a = 209$ MPa, $N_f = 139{,}000$), (**c**) Z150 ($\sigma_a = 133$ MPa, $N_f = 48.2 \times 10^6$), (**d**) B120 ($\sigma_a = 162$ MPa, $N_f = 6.3 \times 10^6$)

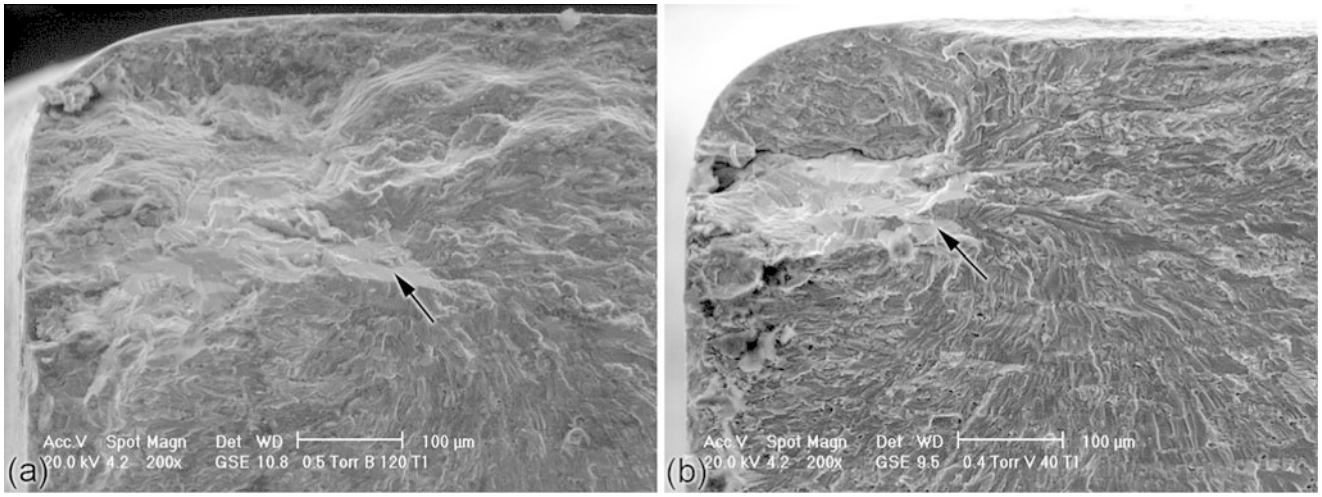

Fig. 17.12 SEM micrographs of the fracture surfaces around the fatigue crack initiation sites in the tribofinished specimens. Prior to tribofinishing the specimens were subjected (**a**) B120, (**b**) V40 peening treatment. Specimens were tested at $\sigma_a = 171$ MPa and failed after 13.3×10^6 and 3.3×10^6 cycles, respectively

oxygen. In general, specimens that failed at a number of cycles less than that corresponding to P50 probability show a non-propagating crack at the surface, near the subsuperficial initiation site of the main crack, as shown exemplarily in Fig. 17.11, while specimens that failed at a number of cycle significantly higher than that corresponding to P50 probability do not exhibit surface crack initiation, as depicted in Fig. 17.11. Apparently, non propagating cracks, initiated on the surface because of the stress concentration effect exerted by surface roughness, and arrested by the closing effect exerted by compressive residual stresses, promote crack initiation in the underlying layer, thus leading to a shorter fatigue life.

Figure 17.12 show the fracture surface of the tribonished B120 and V40 conditions, respectively. It can be noted that in both cases subsuperficial crack initiation occurred, but the extension of crystallographic crack growth is larger in the B120 than in the V40 condition. Apparently, the deeper compressive residual stress profile of the B120 condition was more effective in retarding crack propagation up to the surface than that of the V40 variant.

17.3.5 Simulation of the Fatigue Response

Recently, Benedetti et al. [8] conducted multiaxial fatigue tests on both unpeened and peened Al samples in order to identify the most suitable fatigue criterion. They found that the Crossland criterion was able to predict the fatigue strength with a relative error lower than 15 %, provided that the Stabilized Residual Stress (SRS) on the surface and the stress concentration factor due to surface roughness are considered. This approach clearly implies that the surface crack is the fatigue controlling parameter. In the present paper, the fatigue response of the peened samples has been predicted using the same material parameters of the Crossland fatigue criterion found in [8]. The SRS was assumed to depend on the applied external stress. For a given external stress level, the corresponding SRS was calculated by linearly interpolating the experimental values obtained at two stress levels on the tensioned side of the fatigue samples. Then, an iterative procedure was used to search for the SRS to be used in the fatigue criterion, in a similar way to that presented in [6, 7].

The comparison between the experimental data and the calculated mean fatigue curve is illustrated in Fig. 17.13 for the Z150, B120 and V40 conditions, respectively. The indication of the crack initiation site (superficial, subsuperficial or superficial assisted by a superficial non-propagating crack) of each fatigue tests is also provided. It can be noted that when the initiation of the dominant crack occurs on the surface, the agreement between experiments and predictions is very good, since the calculation model is based on the assumption of superficial crack initiation. On the contrary, if the shot peening treatment is able to suppress surface crack initiation and to push it beneath the layer affected by compressive residual stresses, as in the case of the tribofinished specimens and some specimens subjected to B120 and Z150 treatments, the predictions greatly underestimate the fatigue life. When the subsuperficial crack initiation is promoted by a non-propagating surface crack, the experiments are still in fairly good agreement with the prediction in the high-cycle fatigue regime ($N_f < 5 \times 10^6$), while the predictions underestimate the fatigue strength in the very high-cycle fatigue regime ($N_f > 10 \times 10^6$). Presumably,

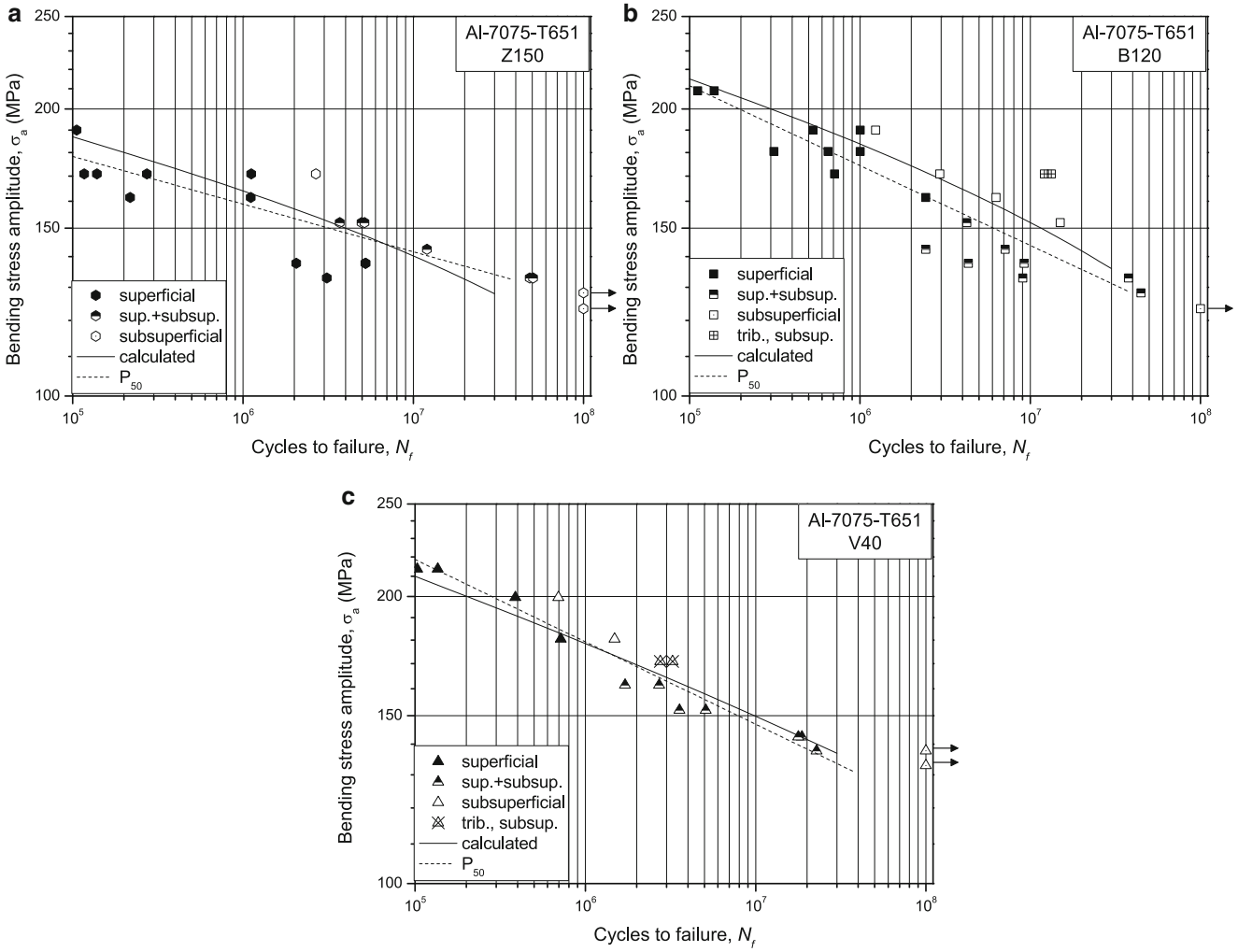

Fig. 17.13 Comparison between experimental and calculated P_{50} fatigue curves of the peened conditions. (**a**) Z150, (**b**) B120, and (**c**) V40 peening treatment. The experimental fatigue data are marked according to the crack initiation mechanism: (**a**) superficial crack initiation (*closed symbols*), (**b**) subsuperficial crack initiation (*open symbols*), (**c**) subsuperficial crack initiation promoted by a non-propagating surface crack (*half-closed symbols*)

in the former case, as soon as a crack initiates on the surface and is arrested, a crack quickly initiates below the surface leading to the sample fracture. In the latter case, a longer fatigue life is spent after surface crack arrest to initiate a superficial dominant crack.

17.4 Conclusions

The plain fatigue strength of shot peened aluminium alloy Al-7075-T651 was experimentally investigated exploring fatigue lives comprised between 10^5 and 10^8 cycles. Experiments were conducted on specimens subjected to three different shot peening treatments. The surface morphology was characterized using an optical profilometer. To quantify the influence of the change in surface morphology induced by shot peening upon the fatigue response, some peened samples were tribofinished with the aim of eliminating surface roughness and preserving the surface residual stress field. XRD measurements were carried out to determine the initial and the stabilized residual stress field. The following conclusions can be drawn:

1. Residual stress relaxation occurs mainly when compressive bending stresses are superimposed to the surface compressive residual stress field.

2. The effect exerted by shot peening is a complicated interaction between residual stresses and surface roughness, greatly impacting the mechanism of fatigue crack initiation and early propagation.
3. Shot peening conducted at low intensities with small beads is more effective in incrementing the fatigue resistance as compared to more intense treatments with larger shots, since it causes a lower roughnening of the surface and induces the maximum compressive residual stress as close as possible to the surface where crack initiation is likely to occur.
4. In the very high cycle regime, the initiation of the crack leading to final failure occurs in the subsuperficial layers and may be promoted by the presence of non-propagating surface cracks. By eliminating surface roughness through a tribofinishing treatment, the occurrence of surface crack initiation is suppressed, thus further incrementing the beneficial effect of shot peening. The extent of this additional improvement depends on the type of shot peening treatment, being more significant if the layer interested by compressive residual stresses is deeper.

References

1. Guagliano M, Vergani L (2004) An approach for prediction of fatigue strength of shot peened components. Eng Fract Mech 71:501–512
2. Wagner L (1999) Mechanical surface treatments on titanium, aluminum and magnesium alloy. Mater Sci Eng A263:210–216
3. McClung RC (2007) A literature survey on the stability and significance of residual stresses during fatigue. Fatigue Fract Eng Mater Struct 30:173–205
4. Benedetti M, Fontanari V, Scardi P, Ricardo CLA, Bandini M (2009) Reverse bending fatigue of shot peened 7075-T651 aluminium alloy: the role of residual stress relaxation. Int J Fatigue 31:1225–1236
5. Benedetti M, Fontanari V, Monelli BD (2010) Numerical simulation of residual stress relaxation in shot peened high-strength aluminium alloys under reverse bending fatigue. ASME J Eng Mater Technol 132:011012-1-9
6. Benedetti M, Fontanari V, Santus C, Bandini M (2010) Notch fatigue behaviour of shot peened high-strength aluminium alloys: experiments and predictions using a critical distance method. Int J Fatigue 32:1600–1611
7. Benedetti M, Fontanari V, Bandini M (2014) A simplified and fast method to predict plain and notch fatigue of shot peened high-strength aluminium alloys under reverse bending. Surf Coat Technol 243:2–9. doi:10.1016/j.surfcoat.2011.12.008
8. Benedetti M, Fontanari V, Bandini M, Taylor D (2014) Multiaxial fatigue resistance of shot peened high-strength aluminum alloys. Int J Fatigue 61:271–282
9. Oguri K (2011) Fatigue life enhancement of aluminum alloy for aircraft by Fine Particle Shot Peening (FPSP). J Mater Proc Technol 211:1395–1399
10. Li JK, Yao M, Wang D, Wang R (1992) An analysis of stress concentration caused by shot peening and its application in predicting fatigue strength. Fatigue Fract Eng Mater Struct 15(12):1271–1279

Chapter 18
Experimental Characterization of Semi-Rigidity of Standardized Lattice Beam Using the Grid Method

Eric Fournely, Rostand Moutou Pitti, Evelyne Toussaint, and Michel Grediac

Abstract Timber structures often exhibit shear and tension perpendicular to grain. This phenomenon induces brittle failure if it is not controlled. This is particularly the case in joining zones, and even more when the beam elements are thin. These thin elements can be found for example in lattice beams. Standardized lattice timber beams appear as an efficient solution for economical, ecological and mechanical aspects. This study focuses on the mechanical behavior of notched beams. Experiments are carried out with a classic loading device and LVDT measurements as well as with the grid method which provides full-field displacement and strain measurements. Tests are conducted for various orientations of annual rings of the wood. The evolutions of strains in the zone affected by shear and tension stresses are analyzed.

Keywords Notched beam • Grid method • Experimental analysis

18.1 Introduction

In wood material, shear and tension perpendicular to grain generally induce brittle fracture if they are not controlled. This is particularly the case in joining zones and even more when the beam elements are thin. These thin elements can be found for example in lattice beams [1, 2]. Standardized lattice timber beams appear as an efficient solution for economical, ecological and mechanical reasons. Many uses of this type of structure can be found in the field of industrial buildings as well as in small and collective housings. This study focuses on the stress distribution in notched beams specimens cut in chord elements of a timber truss beam previously studied with various connector or adhesives [3]. The orientation of the annual rings, the direction of the grain and the knot area ratio are important parameters which drive the global mechanical behavior of theses beams.

In the literature, few authors have shown the influence of the connections [1, 4] on the global behavior of structures and especially of timber structures. In fact, digital image correlation is generally employed in order to evaluate mechanical displacements during the test [5]. The present work is aimed at studying the mechanical behavior of notched beams using another measurement technique, namely the grid method [6]. This method has been recently successfully employed in various cases such as the characterization of notched aluminum specimens [7] or the failure of wooden specimens for instance [8, 9]. In particular, the grid method enables one to obtain here the evolution of the strain field in the zone affected by shear and tension stresses.

E. Fournely • E. Toussaint
LaMI - CNRS - Blaise Pascal University, BP 265 - Campus de Cezeaux, Aubiere Cedex 63175, France

M. Grediac
LaMI, Campus de Clermont-Ferrand, Les Cezeaux, BP 265, Aubiere Cedex 63175, France

R. Moutou Pitti (✉)
Universite Blaise Pascal, Polytech Clermont-Ferrand, 24 Avenue des Landais, PB 206, Aubiére, Auvergne 63174, France
e-mail: rostand.moutou_pitti@puniv-bpclermont.fr

J. Carroll and S. Daly (eds.), *Fracture, Fatigue, Failure, and Damage Evolution, Volume 5: Proceedings of the 2014 Annual Conference on Experimental and Applied Mechanics*, Conference Proceedings of the Society for Experimental Mechanics Series,
DOI 10.1007/978-3-319-06977-7_18,

The wood specimens and the different orientations of the annual rings are presented in the first part of the paper. Various configurations tests, the experimental procedure, the experimental device and the grid technique are then recalled. Then, the deformations and the displacements maps located at the support point, where cracks can be appear and growth, are shown and discussed.

18.2 Experimental Setup

18.2.1 Specimen and Loading Conditions

Numerous tests on notched beams were carried out on Zwick testing machine. A schematics of the test is shown in Fig. 18.1. The forces were measured by two 5 kN sensors. One of these sensors is placed at the center, at point B where force F1 is applied; the second is placed at point A where F2 is applied. Force F3 located at point C is calculated as the difference of the previous two forces. For the boundary conditions, two spherical contacts placed at points A and B enable us to avoid any potential parallelism defects between the notched face and the faces where F1 and F2 are applied. The support plate is fixed close to the notch; its width is 20 mm. The quick trimmer (UPE80) provides the support of the force sensor and position of the central displacement sensor, which records the global deflection. A second sensor records the evolution of beam's height near the notch. The dimensions shown in Fig. 18.1 are in agreement with the configuration described before. Figure 18.2 shows a picture of the specimen in real configuration test with the testing machine.

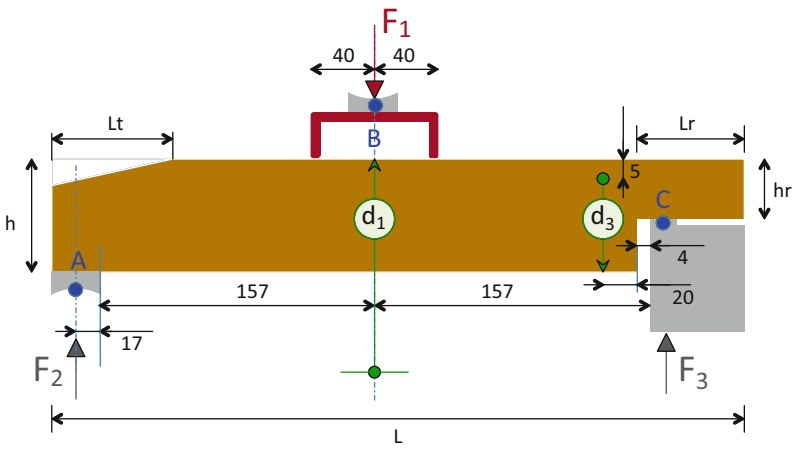

Fig. 18.1 Configuration and geometry of experimental tests

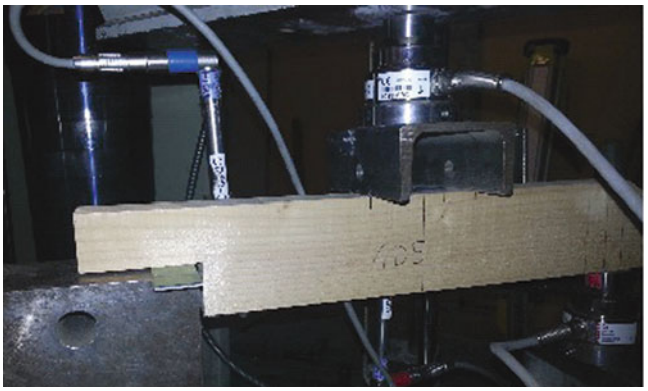

Fig. 18.2 Real experimental device

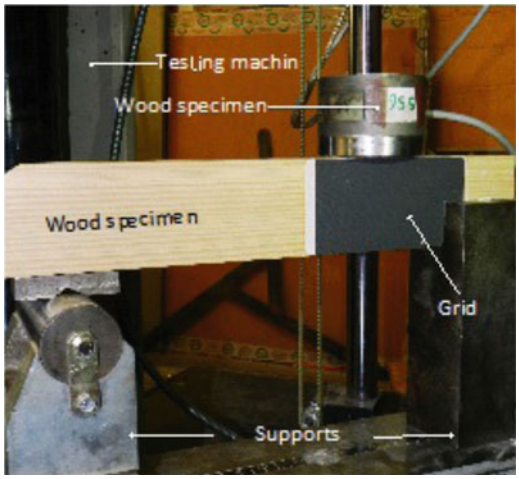

Fig. 18.3 Experimental device with grid

18.2.2 The Grid Method

The grid method consists first in depositing a crossed grid on the surface under investigation in order to track the slight change in the grid as loading increases. The 2D displacement and strain fields are deduced from the images of the grid taken during the test. The grid is deposited using the procedure described in [10]. The pitch of the grid is equal here to 0.2 mm along both directions. Processing images of the grid classically provides phase and phase derivative change maps of this quasi-periodical marking. These quantities are directly proportional to the in-plane displacement and strain components, respectively. It has been shown that the metrological performance of this technique could be significantly improved (especially for strain measurements) by getting rid of most of the grid marking defects, which unavoidably occur when grids are printed on their polymeric support before transfer on the specimen [6]. This leads to a good compromise between resolution and spatial resolution of the measurements. In the current case, a 12-bit/1,040 × 1,376 pixel SENSICAM camera connected to its companion software CamWare is employed. The strain maps are obtained directly from the images of the grids taken by the camera. Full details on small strain calculation can be found in Ref. [6].

Figure 18.3 presents the experimental device employed during the tests. The wood specimen in bending can be seen as well as the load sensor and the supports of a classic 200 kN testing machine.

18.3 Results and Discussions

Typical horizontal and vertical displacement fields measured before crack appearance are shown in Figs. 18.4 and 18.5, respectively. Dimensions are given in pixels (1 pixel = 40 μm). These fields are rather smooth despite the small spatial resolution employed in the grid image processing. This spatial resolution can be estimated to be equal to 30 pixels only. The magnitude of the displacement is small too: some tenths of mm only but the maps are not noisy. The impact of the annual rings is not visible on these displacement maps.

The ε_{xy} and ε_{yy} strain maps are shown in Figs. 18.6 and 18.7 (the ε_{xx} maps is not considered here because of the too low amplitude of this quantity). These maps are obtained at the same loading level as the displacement maps discussed above. The effect of the material heterogeneity due to the annual rings is clearly visible, especially in the ε_{yy} map : the transverse tensile strain strongly changes from one ring to each other. This transverse tensile straining causes a crack to appear at the corner of the notch for a higher loading level, and then to propagate horizontally.

18.4 Conclusion

This paper presents an experimental study on notched thin beam with thin different configurations. Strength values obtained in this experimentation study are in a good agreement with EN1995.1.1 predictions. Grid method analysis exhibits interesting results in order to give more information on lattice beams with equivalent cross-section chord beams. This extension will be completed soon by a FEM analysis.

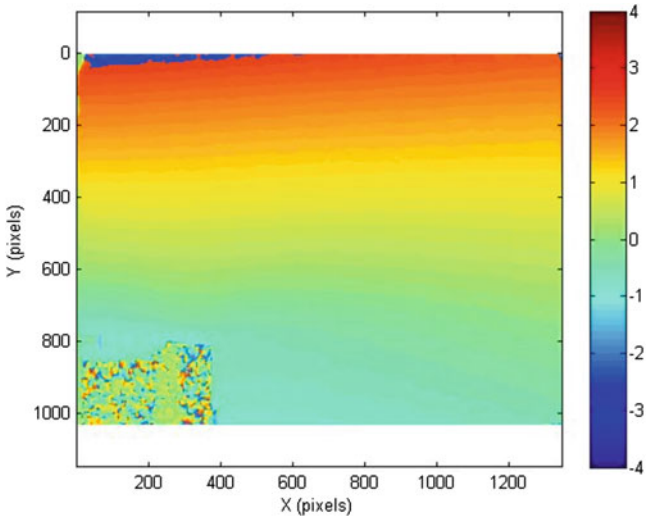

Fig. 18.4 Typical horizontal displacement field (all dimensions in pixel, 1 pixel = 40 μm)

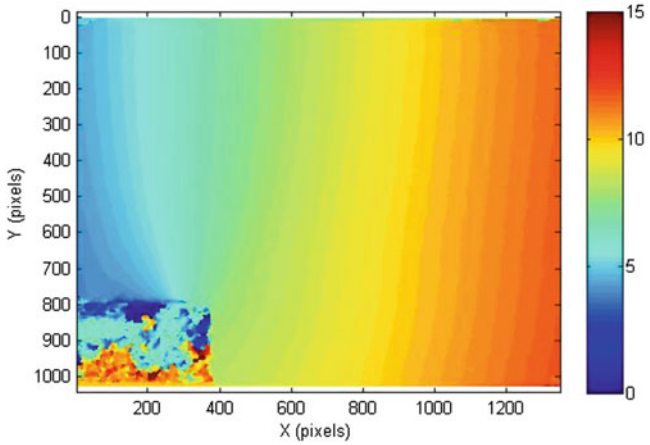

Fig. 18.5 Typical vertical displacement field (all dimensions in pixel, 1 pixel = 40 μm)

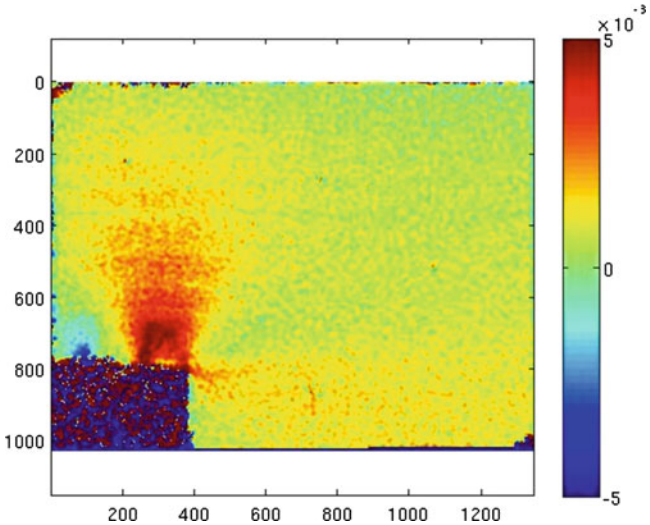

Fig. 18.6 ε_{xy} map

Fig. 18.7 ε_{yy} map

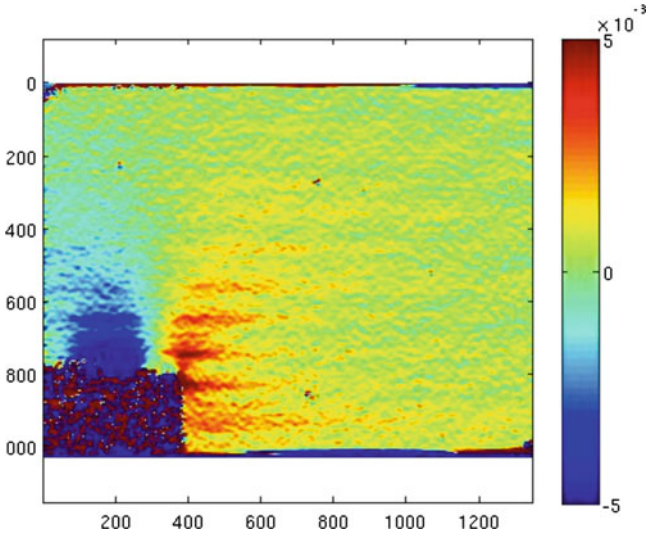

References

1. Fournely E, Moutou Pitti R, Bouchair A (2012) Behaviour of timber lattice beam with semi-rigid joints: analytical and experimental study. Pro Ligno 8:19–41
2. Fournely E, Moutou Pitti R, Bouchair H, Dubois F (2012) Experimental analysis of the semi-rigidity joint in the standardized timber beam. Springer 34:357–366. doi:10.1007/978-1-4614-4226-4_42
3. AFNOR, NF EN 408 (2004) Structures en bois, Bois de structure et bois lamellé collé, détermination de certaines propriétés physiques et mécaniques. Mars, p 32
4. Leichti RJ, Hyde RA, French ML, Camillos SG (2000) The continuum of connection rigidity in timber structures. Wood Fiber Sci 32:1–19
5. Méité M, Dubois F, Pop O, Absi J (2013) Mixed mode fracture properties characterization for wood by digital images correlation and finite element method coupling. Eng Fract Mech 105:86–100
6. Badulescu C, Grédiac M, Mathias J-D (2009) Investigation of the grid method for accurate in-plane strain measurement. Meas Sci Technol 20(9):095102. doi:10.1088/0957-0233/20/9/095102
7. Moutou Pitti R, Badulescu C, Grédiac M (2014) Characterization of a cracked specimen with full-field measurements: direct determination of the crack tip and energy release rate calculation. Int J Fract. doi:10.1007/s10704-013-9921-5
8. Lachhab A, Moutou Pitti R, Toussaint E, Grédiac M (2014) Evaluation of energy release rate in dried wood material using the grid method. In: ECWM7, seventh European conference on wood modification, Lisbone, Spain, 10–12 March 2014
9. AFNOR, Eurocode 5 (2005) Conception et calcul des structures en bois—généralités, règles communes et règles pour les bâtiments, NF EN 1995-1.1
10. Piro JL, Grédiac M (2004) Producing and transferring low-spatial-frequency grids for measuring displacement fields with moiré and grid methods. Exp Tech 28(4):23–26

Chapter 19
Characterization of Martensitic Transformation Morphology in Wide Hysteresis Shape Memory Alloys

Reginald F. Hamilton, Asheesh Lanba, and Osman Ozbulut

Abstract NiTi (aka Nitinol) shape memory alloys can be alloyed with Nb in order facilitate a wider thermal hysteresis. The ternary alloy thermal hysteresis is nearly 100 °C, which is considerably higher than binary Nitinol. The wider hysteresis for NiTiNb makes the alloy suitable for the civil engineering operating temperature ranges. Thus the alloys are promising for integration into structures and can lead to the development of SMA hybrid composite smart structures. The wider hysteresis is attributed to the presence of second phases within the microstructure. The microstructure consists of a matrix, which undergoes the martensitic transformation and thus gives rise to shape memory behavior. A eutectic-like microstructure constituent is evident, with a substantial volume fraction of nano-precipitates dispersed throughout, and neither takes part in the transformation. Consequences of tailoring the microstructure via thermo-mechanical treatments are explored. In this work, the interaction of the non-transforming microstructural constituents with the martensitic transformation morphology is characterized using a fundamental thermo-mechanical framework. The bulk scale deformation measurement are reported as well as the meso-/micro-structure scale full-field and local deformation analyses. The technique used in this work is in-situ Digital Image Correlation (DIC). With this, the current work assesses the surface strain morphology in order to elucidate the influence of microstructure on the bulk scale shape memory responses.

Keywords Shape memory alloy • NiTiNb • Digital image correlation • Solid-solid phase transformation • Full-field strain measurement

19.1 Introduction

SMAs undergo a thermoelastic martensitic transformation (MT), which is a solid-solid phase transformation between a high temperature austenitic phase and a low temperature martensitic phase. During cooling, the high temperature austenitic phase (A) transforms to a low temperature martensitic phase (M). This forward $A \rightarrow M$ transformation begins at a temperature designated as M_s and ends at lower temperature M_f. Upon heating, the reverse $A \leftarrow M$ transformation from austenite to martensite begins at A_s and ends at A_f. A thermal hysteresis exists and there is a temperature differential between the forward and reverse transformation temperatures. When an SMA is cooled to a martensitic state, the martensite can be deformed and the original shape is recovered heated above A_f, which is referred to as the shape memory effect. At a constant temperature above A_f, the transformation can be stress-induced and the forward transformation takes place over a seemingly constant stress or plateau in the stress-strain response. Once the material is unloaded, the material will return to its original shape, albeit a stress hysteresis exists. In the stress-induced case, the SMA behavior is referred to as the pseudoelastic effect.

The transformation temperatures of NiTiNb alloys are well-suited for operating temperature ranges that are required for civil engineering applications, e.g., pre-stressing concrete beams [1, 2]. NiTi has been the most commercially successful SMA to date. Alloying NiTi with Nb has been shown to nearly double the thermal hysteresis [3]. A comparison of NiTiNb and NiTi thermal hysteresis ($=\Delta T_H$) is illustrated in Fig. 19.1. The NiTiNb alloys are typically thermo-mechanically processed

R.F. Hamilton (✉) • A. Lanba
Department of Engineering Science and Mechanics, The Pennsylvania State University, University Park, PA, USA
e-mail: rfhamilton@psu.edu

O. Ozbulut
Department of Civil and Environmental Engineering, University of Virginia, Charlottesville, VA, USA

J. Carroll and S. Daly (eds.), *Fracture, Fatigue, Failure, and Damage Evolution, Volume 5: Proceedings of the 2014 Annual Conference on Experimental and Applied Mechanics*, Conference Proceedings of the Society for Experimental Mechanics Series,
DOI 10.1007/978-3-319-06977-7_19, © The Society for Experimental Mechanics, Inc. 2015

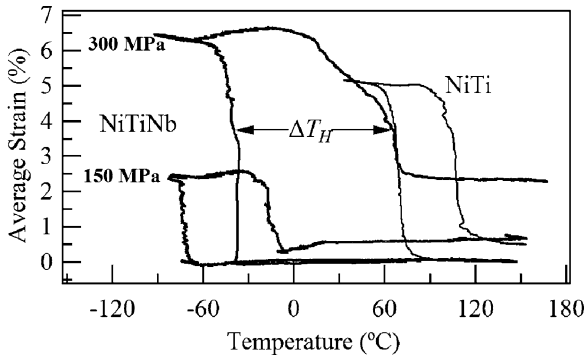

Fig. 19.1 Strain-temperature response of as-processed $Ni_{47.7}Ti_{43.5}Nb_{8.8}$ (at%) material at constant stresses of 150 and 300 MPa. A $Ni_{49.4}Ti_{50.2}$ (at%) result loaded to 120 MPa is included for comparison

(e.g. rolling) after casting. Authors have rationalized the wider hysteresis in the as-processed materials by assessing the impact of the deforming microstructure on the reverse transformation temperatures. Zhang et al. [4] proposed that plastic deformation of Nb-rich particles during the stress-induced martensitic transformation relaxes strain energy of martensite interfaces. This is accompanied by plastic deformation of the parent phase. Kusagawa et al. [5] found that after heating specimens that had been deformed in the austenitic state between M_s and A_s, residual strain was always present. Recently, Schryvers et al. [6] found evidence of plastic deformation in Nb-rich nano-precipitates after it had interacted with a growing martensite plate. A few works report on the fundamental thermo-mechanical deformation in order to understand microstructure-property relationships [4–9]. The current work utilizes in-situ digital image correlation analysis in order to ascertain the surface morphology during the stress-induced MT and expound on the impacts of microstructure changes.

Fundamental thermo-mechanical characterization of SMAs reports on the shape memory effect, i.e. deformation of thermal induced martensite and subsequent recovery during heating, which is illustrated in Fig. 19.1. The characterization may also report on the superelastic/pseudoelastic effect as a result of the stress-induced reversible A $\Longleftrightarrow$ M transformation at a constant temperature. The digital image correlation (DIC) analysis has primarily been used to characterize the superelastic effect in-situ, i.e. throughout deformation [10–12]. The authors have observed general trends as DIC strain contours evolve during the pseudoelastic shape memory response. A summary of the trends with respect to the macro-scale measurements for the stress-strain response follows. The elastic response facilitates homogeneous strain fields and localization is not observed in the full-field DIC strain maps. Upon further loading, a critical value of stress is reached, the stress-strain response deviates from linearity, and a stress plateau develops. That critical stress brings about the stress-induced A $\rightarrow$ M transformation and transformation strain is accrued over a constant stress plateau. DIC measurements illustrate the transformation morphology by delineating a boundary between high strains that appear in local regions corresponding to martensite from strikingly lower strain levels corresponding to not yet transformed austenite. Multiple and differently oriented boundaries may exist. Single bands of transforming material may be evident between boundaries or multiple bands can interact and overlap. After the plateau, the stress-strain response may transition to a second linear-elastic type response, which corresponds to elastic deformation of a fully martensitic microstructure. The high, local strain regions are no longer present and the appearance of the contours is similar to the initial linear-elastic response of austenite, albeit the strain levels are much higher. An ideal pseudoelastic stress-strain unloading curve will follow the elastic loading curve. However, the reverse transformation A $\leftarrow$ M, takes place over a lower constant stress plateau and thus a hysteresis exists. Finally, the initial deformed austenite recovers elastically. It is well understood that the reverse A $\leftarrow$ M MT morphology is the reverse of that for the forward A $\rightarrow$ M. Hence, the DIC strain fields during unloading disappear in the reverse sequence that they appear during loading.

Based on the aforementioned fundamental understandings, the reversible pseudoelastic shape memory alloy response can be related to the martensitic transformation morphology using DIC surface strain measurements. Utilizing in-situ DIC, the current work elucidates the martensitic transformation morphology of a $Ni_{47.7}Ti_{43.5}Nb_{8.8}$ (at%) SMA. The bulk material was supplied after thermo-mechanical deformation into a rolled strip. Compared to the as-cast material, the microstructure becomes highly oriented after rolling. The evolution of full-field strains is assessed throughout the stress-strain response with the temperature held constant. Furthermore, after unloading the strains are assessed during heating under null load. It is well known that the transformation stress is temperature dependent. The dependence is modeled using a Clausius-Clapeyron relationship and the stress increases with increasing constant temperature. Thus we contrast DIC measurements for different test temperatures. The influence of microstructure is studied by characterizing the thermo-mechanical response for material in the as-processed (or rolled strip) state and after solution annealing.

19.2 Experimental Methodology

A NiTiNb rolled strip with composition $Ni_{47.7}Ti_{43.5}Nb_{8.8}$ (at%) was obtained from Medical Metals LLC. The strip was 6 mm wide and 0.25 mm thick. Dog-bone specimens with a gage length of 10 mm and gage width of 3 mm were micro-machined from this strip. Some specimens were solution annealed at 900 °C for 1 h in an Ar atmosphere within a Lindberg/blue-box furnace (BF51732 series) and then quenched in room temperature water. Scanning electron microscopy (SEM) was performed at room temperature in a Philips XL30 ESEM in back-scattered mode. Alloying NiTi with Nb leads to the formation of Nb-rich precipitates embedded in the NiTi matrix. The lower magnification image of an as-cast $Ni_{47.3}Ti_{44.1}Nb_{8.6}$ (at%) material is shown in Fig. 19.2a. The constituents are a eutectic-like microstructure (light inclusions) and matrix (darker background). Zooming into an area reveals that the eutectic structure consists of lighter Nb-rich particles, which are shown in Fig. 19.2b. Processing leads to deformation of these particles. For the $Ni_{47.7}Ti_{43.5}Nb_{8.8}$ (at%) rolled strip investigated in this work, the microstructure is shown in Fig. 19.2c. The lighter striations along the rolling direction (direction the white arrow) result from the particles elongated in the rolling direction. The micrograph in Fig. 19.2e shows a cross-section view and these particles speckle the matrix. Only the matrix material participates in the MT. SEM micrographs of the as-processed material in Fig. 19.2d, e can be compared to the annealed material in Fig. 19.3. Figure 19.3a shows the rolling direction and the cross-section is in Fig. 19.3b. After annealing, the long striations of Nb-rich particles break up into particles that are aligned in the rolling direction. The cross-sectional images reveal that the Nb-rich particles are larger after solution annealing.

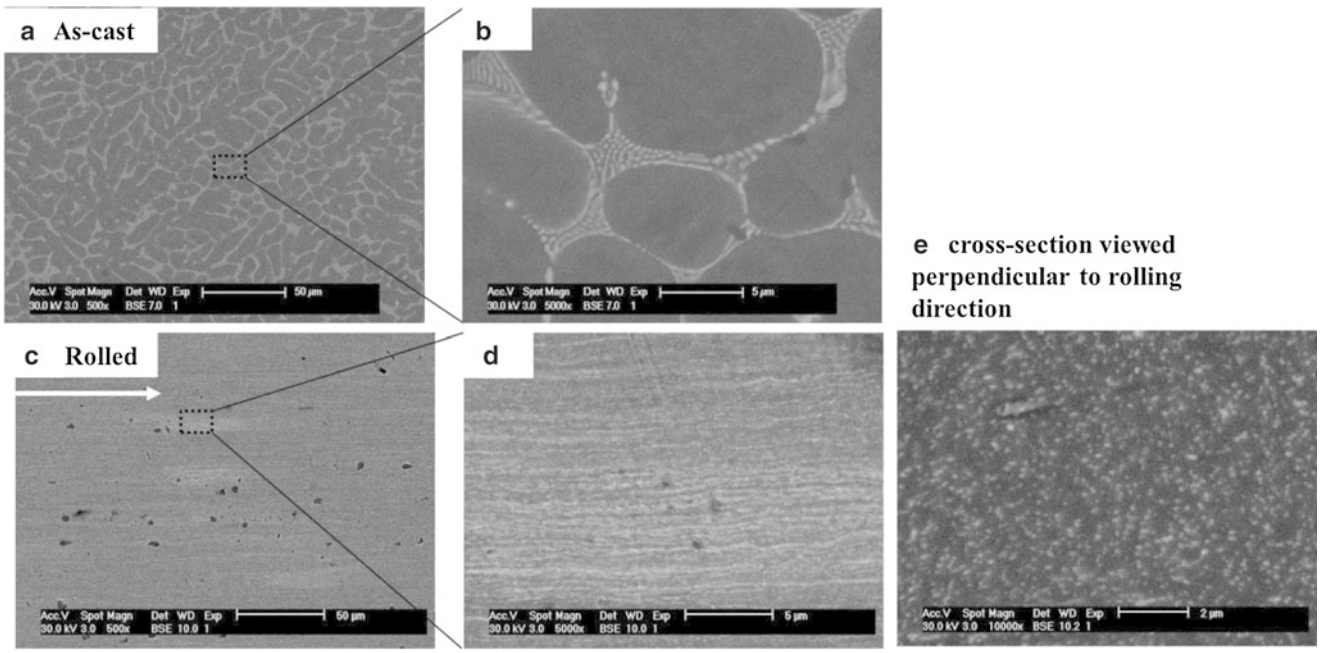

Fig. 19.2 Scanning electron micrographs showing white Nb-rich particles in an as-cast microstructure of $Ni_{47.3}Ti_{44.1}Nb_{8.6}$ (at%) material in (**a**) at 500× magnification and (**b**) at 5,000× magnification. (**c**) The microstructure of the as-processed material $Ni_{47.7}Ti_{43.5}Nb_{8.8}$ (at%), investigated in this work, shown in the rolling direction at 500× magnification and (**d**) at 5,000× magnification. (**e**) The cross-section view of the rolled strip material at 10,000× magnification. In the text, (**d**) and (**e**) are contrasted with the solution annealed microstructure in Fig. 19.3

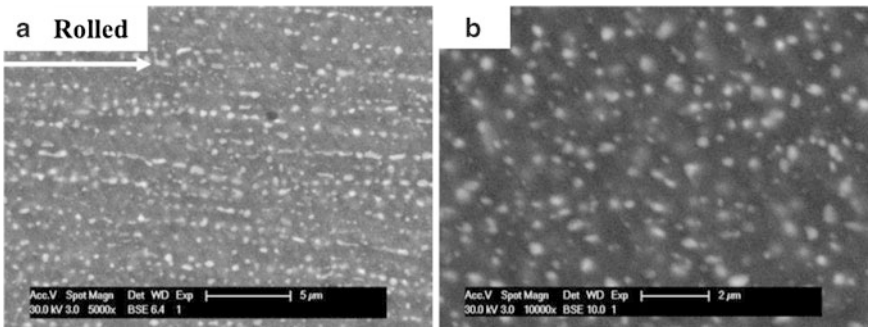

Fig. 19.3 SEM micrographs showing the white Nb-rich particles of the annealed material (900 °C for 1 h) in the (**a**) rolling direction at 5,000× and (**b**) cross-section at 10,000×. These images are compared to the as-processed microstructure in Fig. 19.2

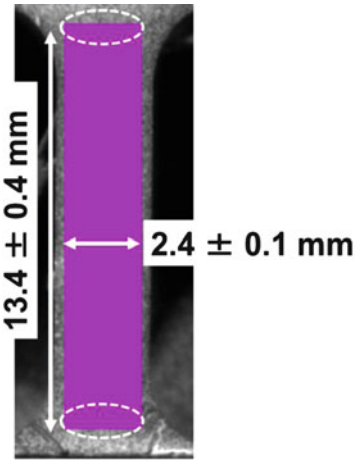

Fig. 19.4 Region of interest covering the speckle pattern on the specimen surface. The ROI dimensions used in the DIC analysis are included. The *dashed ovals* at the *top* and *bottom* mark that the ROI extends into the specimen grip section. Consequently, those regions remain unchanged during deformation in Figs. 19.5–19.7

The thermo-mechanical experiments were conducted on an MTS 810 servo hydraulic load frame. The heating was accomplished via induction heating of the grips and the specimen. The average strain is based on actuator displacement. The temperature was measured via a thermocouple attached to the specimen. For the mechanical loading/unloading at a constant temperature, the specimen was first heated under zero load to the test temperature. It was then loaded in displacement control 0.0028 mm/s, which corresponds to an average strain rate of 1.7×10^{-4}/s. After loading, the specimen was unloaded in force control at an equivalent stress rate of 1.2 MPa/s. After unloading, the specimen was heated in force control at a rate of 10–15 °C/min with the load set to zero in order to try and recover residual deformation.

In-situ full-field deformation fields were obtained along the gage length using digital image correlation (DIC). DIC is an optical technique that measures displacement fields by tracking a high intensity pattern on the specimen surface. This pattern is applied by painting a thin, uniform white coating of Golden Airbrush Titanium White (#8380) on the surface, followed by a speckle pattern of Golden Airbrush Carbon Black (#8040). The pattern was applied using an IWATA Micron-CMB airbrush in order to paint micron size speckles. In-situ images of the specimen surface were captured using a Grasshopper GRAS-20S4M/C CCD camera (1,600 × 1,200 pixels). The image capture was synched with the data capture and was collected using Vic-Snap software from Correlated Solutions. The images and data were captured at a frequency of 1 Hz. The images that were captured have a spatial resolution of 18 μm/pixel. The correlation is performed in an region of interest (ROI) that is selected in a reference image. The definition of the ROI is shown in Fig. 19.4. This region is divided into subsets and the pixel intensity of each subset is calculated and tracked in deformed images by optimizing the displacements and displacements gradients (strains). Each subset is a square region that is approximately 450 μm^2 in size. The DIC was performed via the software Vic-2D from Correlated Solutions, Inc. The general theory of DIC is explained in the works of Sutton et al. [13–15].

19.3 Results and Discussion

Figure 19.5a shows the stress-strain response for the as-processed $Ni_{47.7}Ti_{43.5}Nb_{8.8}$ (at%) specimen. The specimen is deformed to 8 % average strain at room temperature (RT = 21 °C). Inset images show strain contours (calculated based on full-field DIC measurements) at selected points. The contours are the normal component of strain, which coincides with the loading direction. Initially, the specimen exhibits a linear elastic response. At an average strain of 1.4 %, the stress drops and the response transitions onto a stress plateau. At an average strain of 5.8 %, the response becomes linear, with the stress increasing until the average strain reaches the 8 % target value.

The inset DIC strain contours show that during the stress drop, a localized band of high strain appears at the top of the image. As the specimen is further deformed, the lower boundary of the band travels towards the bottom of the image and the localized region of strain grows across the gage length. The maximum localized (or micro-scale) strains within the band remain unchanged at around 9.5 % as it grows across the gage length. Note that serrations appear in the plateau, which are delineated within a dashed box. At the onset of the serrations, the distinct local small bands appear which are circled: one with the same orientation as the original band and another with a different orientation. The original band and two auxiliary bands grow together until the average strain reaches 5.8 %. Within the bands the DIC strain measurements approach 10 %. The band stops growing throughout the image at the end of the plateau and the onset of the increase in load. Throughout the

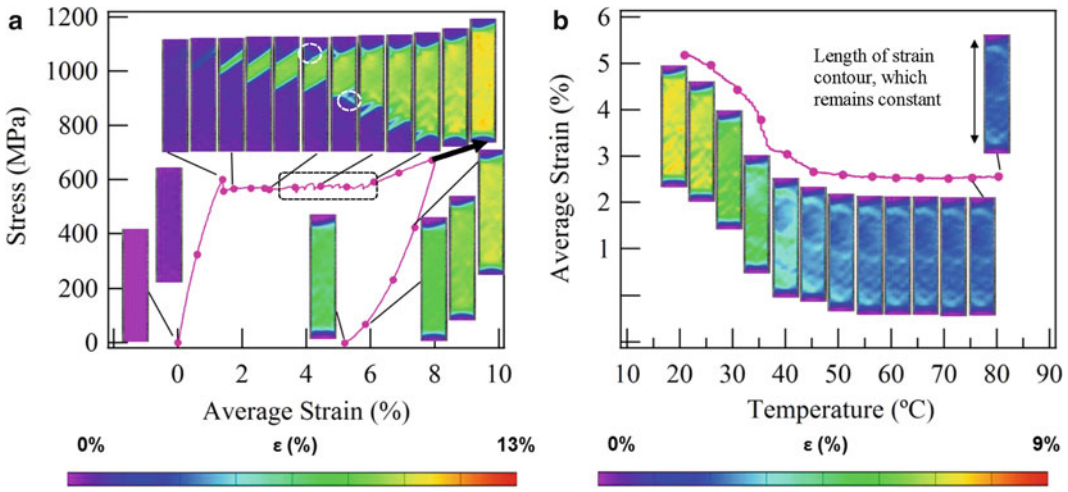

Fig. 19.5 (**a**) The stress-strain response of as-processed material deformed at RT up to 8 % average target strain and unloaded. (**b**) The strain-temperature response after unloading and during heating at null load. DIC strain contours are *inset* at selected points. The strain in the deformation fields is measured in the loading direction. In part (**b**), the scale has been adjusted to highlight the changes in strain contours during heating

linear hardening-like response, the length of the corresponding DIC strain contour remains uniform. The results stress-strain curve exhibits a strain hardening like increase while the load increases; however, the slope is nearly linear as opposed to the non-linear strain hardening response observed in conventional ductile metals. Though the length of the DIC strain contour remains uniform, the strain reaches around 11 % despite the average strain only reaching the 8 % target value. The DIC strain fields during unloading indicate that the length of the high strain contours does not shrink. Instead, localized strain values within the region decrease to around 7 %.

Once the specimen is completely unloaded, it is heated under null load. Figure 19.5b shows the strain-temperature response of the specimen during heating. Upon heating, average strain recovery ensues immediately at 21 °C and recovers 2.6 % until the temperature reaches 51 °C and average recovery strain saturates. Inset DIC images illustrate that strain recovery is highly localized. During this recovery, the length of the region of high strain does not decrease in size. Locally, however strains decrease from 7 % to nearly 2.5 %. The recovery of strains reflects that stress-induced martensite is stabilized during loading. Heat input was necessary to facilitate the reversion of that martensite via the shape memory effect. As permanent residual strain remains after heating, we presume that it is due to irreversible plastic deformation.

The stress-strain response for a specimen deformed to 8 % average strain at a constant temperature of 60 °C is shown in Fig. 19.6. Initially, the stress-strain response exhibits a linear elastic type of response. Upon reaching an average strain of 1.7 %, there is a transition from linearity to a non-linear response, similar to a strain-hardening type response. At 2.7 % average strain, there is a stress-drop. Relative the room temperature response in Fig. 19.5a, the slope of the stress-strain curve rises linearly. The accompanying DIC strain contour measurement that corresponds to the transition from the initial linear elastic response (i.e., at the average strain of 1.7 %) exhibits a uniform blue color that implies a uniform increase in strain. When the stress drops, a local region (outlined with a dashed white circle) of high strain appears at the center of the full-field contour. In the following image, the local strain within the dashed boundary increases further. As the specimen is further loaded, the upper and lower boundaries of the central region, respectively, grow in the upward and downward vertical directions. The bold black arrow mark when the length of the deformed region becomes constant. In subsequent images the local strains increase in a diffuse manner. As the specimen is further loaded to 8 % average strain, the length of the high strain region does not grow in size, however, the strains increase uniformly to around 12.5 %. The DIC strain fields during unloading indicate that the length of the high strain contours does not shrink. Instead, localized strain values within the region decrease from about 13 % to around a minimum of 8 %.

After complete unloading, the specimen was heated under null load. The strain-temperature response is shown in Fig. 19.6b. Instead of local strains decreasing immediately upon heating, the specimen must be heated by about 10 °C in order to initiate strain recovery. The specimen only recovers 0.2 % average strain between the temperatures of 70 and 100 °C. This recovered strain is over an order of magnitude less than the average strain of 2.6 % that was recovered for the specimen deformed at RT. Furthermore, the evolution of the full field strains during heating is much more diffuse and miniscule compared to the recovery during heating of the specimen initially deformed at RT. The accompanying DIC deformation fields indicate that the strains within the deformed region decrease uniformly by a small amount from 8 to 7 %. The stark contrasts in deformation and recovery suggest that plastic deformation is dominant throughout loading rather than the reversible martensitic deformation.

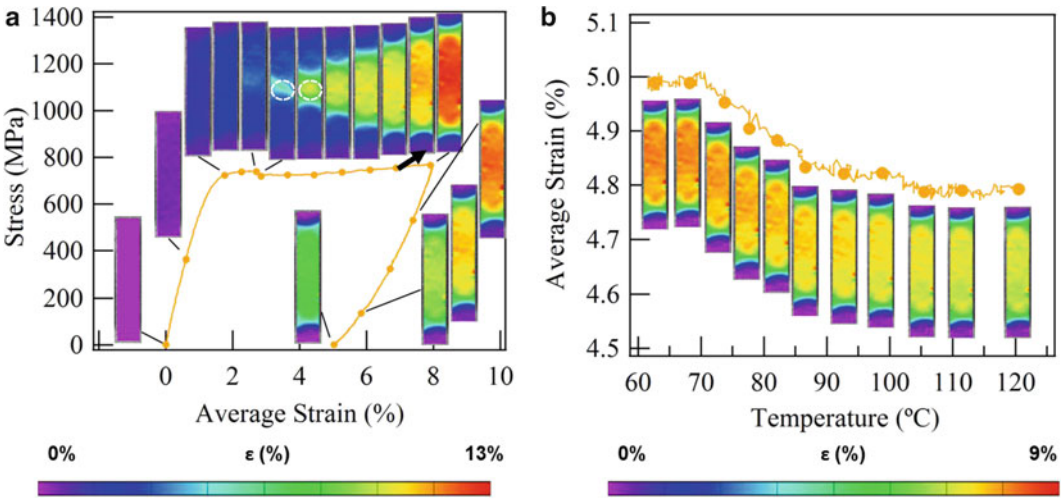

Fig. 19.6 (**a**) The stress-strain response at 60 °C, the material is deformed to 8 % average strain and unloaded. (**b**) After unloading, the strain-temperature response during heating at null load. *Inset* images of strain contours are shown along selected points on both curves. The strain is in the loading direction. In part (**b**), the scale has been adjusted to highlight the changes in strain contours during heating

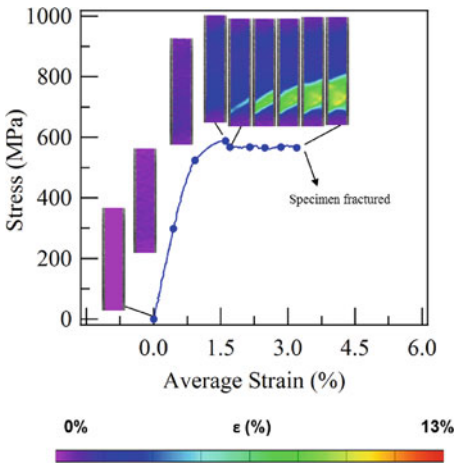

Fig. 19.7 The stress-strain response when annealed material is deformed at RT along with accompanying DIC strain fields at selected points. The strain in the deformation fields is calculated in the loading direction

The RT response of a solution annealed specimen is shown in Fig. 19.7. The accompanying DIC deformation fields along selected points during the deformation are also shown. During the initial elastic response, the strains in the DIC deformation fields increase homogeneously. The curve deviates from linearity around an average strain of 1 % and strains continue to increase uniformly across a large region in the gage section till an average strain of around 1.6 %. At an average strain of 1.6 %, there is a stress drop and a localized band appears towards the bottom of the specimen. As the specimen is loaded, the uppermost boundary of the band grows towards the top of the specimen. The strains outside the bands remain unchanged, while the strains within the band increase slightly to around 10 %. This band grows as the deformation proceeds throughout a stress plateau. At an average strain of 3.2 %, the specimen fractures. The fracture initiates at the uppermost boundary of the high strain region.

19.4 Conclusions

In this paper, the effects of test temperature on the full-field deformations of $Ni_{47.7}Ti_{43.5}Nb_{8.8}$ (at%) rolled strip material have been characterized. Both the RT and 60 °C stress-strain loading responses are accompanied by a stress-drop and a transition onto a stress plateau via the formation of a high strain band that grows. The behavior can be attributed to the initiation of the stress-induced forward MT. Throughout the stress plateau, at both temperatures, the local transformations measured using DIC analysis reach about 13 %. On the other hand, the average strain determined from the crosshead displacement is set to

reach a target value of 8 %. Contrasts in the evolution of the full-field strain contours throughout the plateau suggest that the large local strain levels arise from different deformation mechanisms. At room temperature, multiple bands appear that do not exist during deformation at the elevated temperature. Upon heating, both specimens recover local strains uniformly across the deformed region. However, the specimen deformed at RT recovers a larger amount of strain via the shape memory effect. The much lower level of local recoverable strains at 60 °C as well as the slight diffuse change of stress contours suggest that shape memory effect recovery is miniscule. Thus plastic deformation dominates the martensitic transformation at the elevated temperature.

In the case of the solution annealed response, there is a region between the deviation from linearity and the stress-drop where the strains increase homogeneously across a large area of the gage section. The stress-strain response for the as-processed and solution annealed specimen at RT show that the stresses at which the response deviates from linearity are similar. The solution annealed specimen fractures during the stress plateau region at 3.2 % strain. Also, the solution annealed specimen fractures at the top of the high strain region that grows during the stress plateau. Recalling the microstructures of the as-processed and annealed specimens in Figs. 19.2 and 19.3, the deformation results suggest that the breaking up of the elongated particles and the increase in size of the particles after annealing weakens the material.

Acknowledgements This study has been supported by the Mid-Atlantic Universities Transportation Center (MAUTC) Pooled Research Program issued by the Research and Innovative Technology Administration of the US DOT (Grant No. DTRT12-G-UTC03).

References

1. Choi E, Chung Y-S, Choi J-H, Kim H-T, Lee H (2010) The confining effectiveness of NiTiNb and NiTi SMA wire jackets for concrete. Smart Mater Struct 19(3):035024
2. Li L, Li Q, Zhang F (2007) Behavior of smart concrete beams with embedded shape memory alloy bundles. J Intell Mater Syst Struct 18(10):1003–1014
3. Siegert W, Neuking K, Mertmann M, Eggeler GF (2002) Influence of Nb content and processing conditions on microstructure and functional properties of NiTiNb shape-memory alloys. Mater Sci Forum 394–395:361–364
4. Zhang CS, Zhao LC, Duerig TW, Wayman CM (1990) Effects of deformation on the transformation hysteresis and shape memory effect in a Ni47Ti44Nb9 alloy. Scr Metall Mater 24:1807–1812
5. Kusagawa M, Nakamura T, Asada Y (2001) Fundamental deformation and recovery behaviors of NiTiNb shape memory alloy. JSME Int J 44(1):57–63
6. Schryvers D, Shi H, Martinez GT, Van Aert S, Frenzel J, Van Humbeeck J (2013) Nano- and microcrystal investigations of precipitates, interfaces and strain fields in Ni-Ti-Nb by various TEM techniques. Mater Sci Forum 738–739:65–71
7. Piao M, Miyazaki S, Otsuka K (1992) Characteristics of deformation and transformation in Ti44Ni47Nb9 shape memory alloy. Mater Trans JIM 33(4):346–353
8. Wang M, Jiang M, Liao G, Guo S, Zhao X (2012) Martensitic transformation involved mechanical behaviors and wide hysteresis of NiTiNb shape memory alloys. Prog Nat Sci Mater Int 22(2):130–138
9. Zheng Y, Cai W, Luo Y, Zhao L (1997) Effects of heat treatment on tensile properties and shape memory effects of Ni-Ti-Nb alloy. Trans Nonferrous Met Soc China 7(4):92–96
10. Hamilton RF, Sehitoglu H, Aslantas K, Efstathiou C, Maier HJ (2008) Inter-martensite strain evolution in NiMnGa single crystals. Acta Mater 56(10):2231–2236
11. Hamilton RF, Dilibal S, Sehitoglu H, Maier HJ (2011) Underlying mechanism of dual hysteresis in NiMnGa single crystals. Mater Sci Eng A 528(3):1877–1881
12. Daly S, Ravichandran G, Bhattacharya K (2007) Stress-induced martensitic phase transformation in thin sheets of Nitinol. Acta Mater 55(10):3593–3600
13. Chu TC, Ranson WF, Sutton MA, Peters WH (1985) Applications of digital-image-correlation techniques to experimental mechanics. Exp Mech 25(3):232–244
14. Sutton MA, Walters WJ, Peters WH, Ranson WF, Mcneil SR (1983) Determination of displacements using an improved digital correlation method. Image Vis Comput 1(3):133–139
15. Sutton M, Mingqi C, Peters W, Chao Y, McNeill S (1986) Application of an optimized digital correlation method to planar deformation analysis. Image Vis Comput 4(3):143–150

Chapter 20
Study of Phase Transformation Intermittency in S.M.A. Using the Grid Method

Noemi Barrera, Xavier Balandraud, Michel Grédiac, Paolo Biscari, and Giovanni Zanzotto

Abstract The objective of this study is to show experimentally the intermittency of the phase transformation in a shape memory alloy using a kinematical full-field measurement method. The specimen is a Cu-Al-Be single crystal with $Ms = -2\,°C$. A uniaxial loading was applied by using a device based on gravity. In practice, a drop-by-drop device controlled by water pumps enabled us to apply a perfectly monotonic loading with very small force increments. The grid method was used to measure the strain fields on the specimen surface during the test. It is observed that the plateau which is classically obtained when the specimen transforms from austenite to martensite is actually characterized by an intermittency of the phase change. It means that the events, in terms of appearance of martensite needles and propagation, occur with an irregular alternation. The paper presents the experimental setup, the image processing and some typical results.

Keywords Shape memory alloy • Full-field measurement • Grid method • Phase transformation • Intermittency

20.1 Introduction

Shape-memory alloys (SMAs) feature specific mechanical properties such as superelasticity, memory effect and good damping properties. These properties result from a reversible austenite/martensite phase change that occurs within the material when it is subjected to a mechanical load or a temperature change. Martensite generally appears in austenite through typical microstructures such as martensite twins, habit planes, wedges, needles, crossing bands or X-shaped microstructures [1]. These microstructures were largely studied through theoretical approaches based on crystallographic considerations for a better understanding of the reversibility of the phase transformation [1–3]. Alternatively, classic experimental means such as microscopes are generally used to analyze the microstructures, but the recent development of full-field measurement techniques has made possible the analysis of martensitic microstructures in terms of strains fields. For instance, moiré interferometry was used in Ref. [4] to analyze the displacement field due to martensitic transformation in a monocrystalline Cu-Al-Ni SMA. The technique used in more recent studies to measure displacement fields is digital image correlation (DIC). The idea is to track speckles which are randomly deposited on the surface under investigation, and to deduce the displacement field by image processing [5]. DIC was for instance used to study intermartensitic transformations in a Ni-Fe-Ga single crystal [6], to compare experimental strain fields with their numerical counterparts in a Cu-Al-Be SMA multicrystal [7],

N. Barrera
Dipartimento di Matematica, Politecnico di Milano, Piazza Leonardo da Vinci 32, Milan 20133, Italy

Clermont Université, Université Blaise Pascal, Institut Français de Mécanique Avancée, Institut Pascal UMR 6602, BP 10448, Clermont-Ferrand 63000, France

X. Balandraud (✉) • M. Grédiac
Clermont Université, Université Blaise Pascal, Institut Français de Mécanique Avancée,
Institut Pascal UMR 6602, BP 10448, Clermont-Ferrand 63000, France
e-mail: xavier.balandraud@ifma.fr

P. Biscari
Dipartimento di Matematica, Politecnico di Milano, Piazza Leonardo da Vinci 32, Milan 20133, Italy

G. Zanzotto
DMMMSA-DPG, Università di Padova, Via Venezia 8, Padova 35131, Italy

J. Carroll and S. Daly (eds.), *Fracture, Fatigue, Failure, and Damage Evolution, Volume 5: Proceedings of the 2014 Annual Conference on Experimental and Applied Mechanics*, Conference Proceedings of the Society for Experimental Mechanics Series,
DOI 10.1007/978-3-319-06977-7_20,

to study the development of martensite in Nitinol [8, 9] or to investigate local transformations in precipitated Ni-Ti single crystals [6]. A comparison between DIC and digital speckle pattern correlation to measure displacement fields in a Cu-Al-Be SMA was presented in Reference [10]. The grid method [11] was used on a monocrystalline Cu-Al-Be [12], including a specific procedure to limit some negative effects of unavoidable grid defects [13, 14]. This procedure limited the use of spatial filtering to reduce noise in strain maps, leading to a good compromise between strain resolution and spatial resolution in strain, and thus making possible the detection of very localized phenomena such as appearance and development of thin martensite needles. The same technique was employed in the present study to analyze the microstructure changes in the same specimen, but using a specific loading device based on gravity. The application here is the analysis of phase transformation intermittency, a topic which is addressed in some recent studies in which acoustic emission is used as an experimental mean [15, 16].

20.2 Material and Experimental Setup

The specimen was a Cu-Al-Be single-crystal with a martensite-start temperature *Ms* equal to −2 °C. The test consisted of a uniaxial loading at ambient temperature. A specific device with a can and a drop-by-drop device controlled by water pumps was used to load the specimen: see Fig. 20.1. This device enables us to ensure a perfectly monotonic loading with very small force increments which are not possible to obtain with classic testing machines. A similar experimental approach can be found in Reference [17]. The complete transformation from austenite to martensite was obtained in more than 24 h. Special attention was paid to maintain a constant ambient temperature at 14 ± 0.5 °C over the whole test duration. The dimensions of the portion of the specimen studied here is $0.94 \times 17.78 \times 72$ mm^3. A crossed-grid was first transferred on one side using the procedure described in Reference [18]. The pitch of the grid was equal to 0.2 mm along both directions. A 1040×1376 pixel Sensicam QE CCD camera was used to capture images of the grid during the test. These images were then processed with a specific procedure described in Reference [13] which enabled us to deduce the 2D strain fields on the surface of the specimen.

20.3 Results

Figure 20.2 shows three fields of longitudinal Green-Lagrange strain measured at three different loading levels. Figure 20.2a corresponds to a loading level of 25 % of the transformation stress plateau. Microstructures consist of parallel martensite needles crossing the whole width of the specimen. Different local strain levels are observed in this map. However, it can be expected that all the martensitic zones in the specimen are characterized by a fixed transformation strain whose order of magnitude is 0.10 [12]. The different levels of local strain in the martensitic zones actually result from the image processing, which is based on the windowed Fourier transform (WFT): this value is underestimated if the martensite needle width is

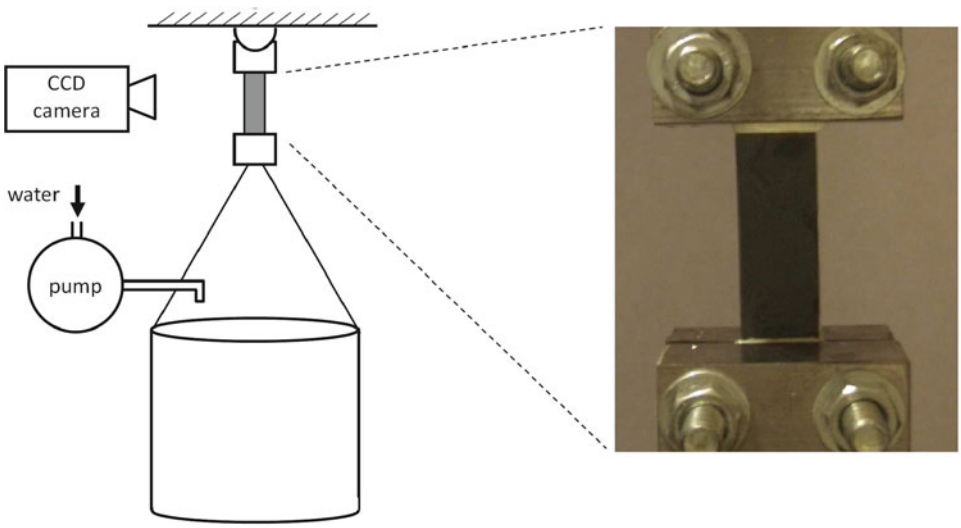

Fig. 20.1 Scheme of the experimental setup

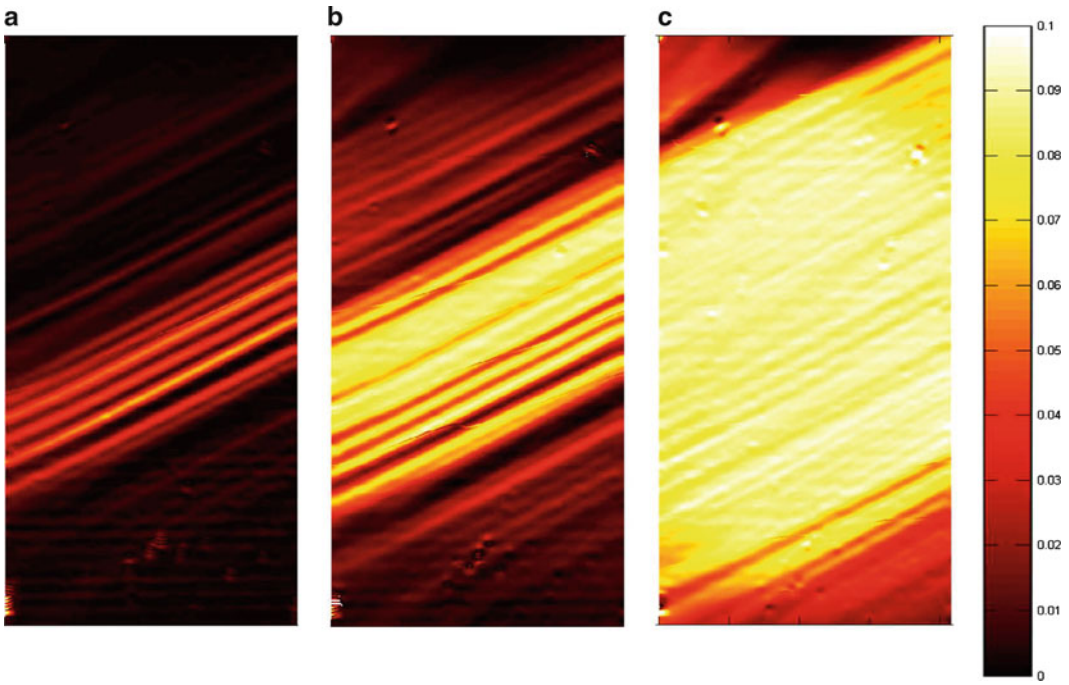

Fig. 20.2 Longitudinal strain field at three different loading levels

too small. This is due to the fact that the strain value provided by the image processing is equal to the actual strain value convolved by the envelope of the kernel employed in the WFT [19]. Figure 20.2b corresponds to a loading level of 50 % of the transformation stress plateau. The maximum strain is equal to 0.10 in the central part of the specimen, as a consequence of the merge of martensite needles which now form a large band. Figure 20.2c corresponds to the strain map for the maximum applied load (end of the transformation stress plateau). The central zone of the specimen is entirely transformed in martensite, whereas two triangular zones at both ends of the specimen are not completely transformed into martensite. The whole series of strain maps which are captured can be used to study the intermittency of the phase transformation in the specimen. By plotting the strain variation along a longitudinal profile, it can be observed that the strain rate does not evolve continuously but changes following an irregular mode. The microstructure change occurs according to an irregular alternation. The statistic quantification of the events in terms of appearance and propagation of martensite needles can be used to extract the main features of the phase transformation intermittency.

20.4 Conclusion

The grid method was applied in this study on a SMA single crystal subjected to a mechanical loading based on gravity. The good spatial resolution of the strain measurement and the small force increments resulting from the specific mechanical device enabled us to follow the phase transformation in terms of appearance and propagation of martensite needles. It is observed that the austenite-to-martensite transformation is actually characterized by an intermittency of the microstructural events, whose analysis is in progress.

References

1. Bhattacharya K (2003) Microstructure of martensite: why it forms and how it gives rise to the shape-memory effect. Oxford University Press, Oxford
2. James RD, Hane KF (2000) Martensitic transformations and shape memory materials. Acta Mater 48:197–222
3. Balandraud X, Delpueyo D, Grédiac M, Zanzotto G (2010) Almost compatible microstructures in shape memory alloys. Acta Mater 58:4559–4577

4. Zhang X, Xou T, Sun QP, Tong P (1997) On the full-field deformation of single crystal Cu-Al-Ni shape memory alloys-stress-induced β_1-γ_1' martensitic transformation. J Phys IV 11:555–560
5. Sutton M, Orteu JJ, Schreier H (2009) Image correlation for shape, motion, and deformation measurements: basic concepts, theory and applications. Springer, New York
6. Efstathiou C, Sehitoglu H (2008) Local transformation strain measurements in precipitated NiTi single crystals. Scr Mater 59:1263–1266
7. Merzouki T, Collard C, Bourgeois N, Zineb TB, Meraghni F (2010) Coupling between measured kinematic fields and multicrystal SMA finite element calculations. Mech Mater 42:72–95
8. Daly S, Ravichandran G, Bhattacharya K (2007) Stress-induced martensitic phase transformation in thin sheets of nitinol. Acta Mater 55:3593–3600
9. Daly S, Rittel D, Bhattacharya K, Ravichandran G (2009) Large deformation of nitinol under shear dominant loading. Exp Mech 49:225–233
10. Sanchez-Arevalo F, Garcia-Fernandez T, Pulos G, Villagran-Muniz M (2009) Use of digital speckle pattern correlation for strain measurements in a Cu-Al-Be shape memory alloy. Mater Charact 60(8):775–782
11. Surrel Y (2000) Fringe analysis. In: Rastogi PK (ed) Photomechanics, vol 77, Topic applied physics. Springer, New York, pp 55–102
12. Delpueyo D, Grédiac M, Balandraud X, Badulescu C (2012) Investigation of martensitic microstructures in a monocrystalline Cu-Al-Be shape memory alloy with the grid method and infrared thermography. Mech Mater 45:34–51
13. Badulescu C, Grédiac M, Mathias J-D (2009) Investigation of the grid method for accurate in-plane strain measurement. Meas Sci Technol 20(9):095102
14. Badulescu C, Grédiac M, Mathias J-D, Roux D (2009) A procedure for accurate one-dimensional strain measurement using the grid method. Exp Mech 49(6):841–854
15. Niemann R, Baro J, Heczko O, Schultz L, Fahler S, Vives E, Manosa L, Planes A (2012) Tuning avalanche criticality: acoustic emission during the martensitic transformation of a compressed Ni-Mn-Ga single crystal. Phys Rev B 86(21):214101
16. Planes A, Manosa L, Vives E (2013) Acoustic emission in martensitic transformations. J Alloys Compd 577(1):S699–S704
17. Carrillo L, Ortin J (1997) Avalanches in the growth of stress-induced martensites. Phys Rev B 56(18):11508
18. Piro JL, Grédiac M (2004) Producing and transferring low-spatial-frequency grids for measuring displacement fields with moiré and grid methods. Exp Tech 28(4):23–26
19. Sur F, Grédiac M (2014) Towards deconvolution to enhance the grid method for in-plane strain measurement. Inverse Probl Imaging 8:259–291

Chapter 21
In-Situ X-Rays Diffraction and Multiscale Modeling of Shape Memory Alloys

M.D. Fall, O. Hubert, K. Lavernhe-Taillard, and A. Maynadier

Abstract Increasing use of Shape Memory Alloys (SMA) for complex applications requires a robust modeling of phenomena governing their behavior. The development of micro-macro multiaxial model is relevant. Such approach relies the definition of transition scale rules, depending on the microstructure, and a description of the behavior of constituents. On the other hand, it requires experiments for identification of parameters such as enthalpies or kinetic constants and validation of the model. In this paper, in situ X-Ray Diffraction (XRD) measurements are performed during tensile tests and heating-cooling cycles. XRD permits monitoring of the average volume fraction of phases in presence. Results will be used for the validation of a multiscale and multiphased model.

Keywords Shape memory alloys (SMA) • Phase transformation • Pseudoelasticity • X Ray diffraction (XRD)

21.1 Introduction

Shape Memory Alloys (SMA) are widely used in many industrial fields such as aerospace, automotive, biomedical, and even the clothing industry. Their interest lies in their ability to recover their original shape (as suggest their name!) by simply heating them. Indeed, they combine two interesting properties: the so-called shape memory effect and a pseudo elastic behavior (shape recovery after large deformation above 8 %). Such interesting properties are to be associated to the occurrence of a solid-solid phase transformation involving a high temperature stable phase called *austenite* (A) and a lower symmetry low temperature stable phase called *martensite* (M) exhibiting many variants. Indeed SMA behavior exhibits a high thermomechanical coupling since phase transition can be driven thermally and/or mechanically. Democratization of the use of such materials requires nevertheless the overcome of some major difficulties regarding their behavior and so their modeling. One first difficulty is that the phase transformation is associated with thermal phenomena: heat loss for A to M transformation and heat absorption for the inverse transition. These thermal phenomena are at the origin of strain localizations during a strengthening. Phenomena like martensite reorientation by variant selection under complex multiaxial mechanical loadings is another major difficulty. A final difficulty is the appearance of some intermediate R (rhombohedral)-phase depending on the temperature-stress path. A multiaxial multiscale modelling for SMA thermomechanical behaviour has been developed at LMT-Cachan [1]. This model allows to reproduce appearance/disappearance/re-orientation of A, R-Phase or M variants at the microscale depending on their free energy associated to various loading conditions. Localization and homogenization rules are used for scale transitions. Among other results, this model permits an estimation of phase fractions and orientation so that in situ X-Ray Diffraction (XRD) may represent an interesting tool in order to validate the modeling. This paper is focused on the presentation of the experimental set-up that allowed us to get the measurements of phase volume fractions' evolution under simple loadings i.e. cooling and heating at zero stress and tensile tests at room temperature, by X Ray measurements. Diffractograms reported in the text have been obtained with a texturized nickel-titanium SMA exhibiting both martensitic and intermediate R-phase transformation. They consist in intensities as function of

M.D. Fall (✉) • O. Hubert • K. Lavernhe-Taillard
LMT Cachan (ENS Cachan/CNRS UMR 8535/PRES UniverSud Paris), 61 Avenue du Président Wilson, 94235 Cachan Cedex, France
e-mail: fall@lmt.ens-cachan.fr

A. Maynadier
LaMCoS (INSA Lyon/UMR 5229), 18-20, rue des Sciences, 6962 Villeurbanne, Cedex, France

J. Carroll and S. Daly (eds.), *Fracture, Fatigue, Failure, and Damage Evolution, Volume 5: Proceedings of the 2014 Annual Conference on Experimental and Applied Mechanics*, Conference Proceedings of the Society for Experimental Mechanics Series,
DOI 10.1007/978-3-319-06977-7_21,

Bragg angular positions. Powder diffraction databases are almost used for identification of diffracting planes and associated phases. Quantitative analysis (estimation of volume fraction ratio) consists in measuring integrated intensities (or heights) and comparing the intensities ratio taking account of the crystallographic texture of the material [2].

21.2 Motivation

Increasing use of Shape Memory Alloys (SMA) for complex applications requires a robust modeling of phenomena governing their behavior. The development of micro-macro multiaxial model is relevant. Such approach relies the definition of transition scale rules, depending on the microstructure, and an appropriate description of the behavior of constituents. A multiscale model has been proposed at LMT Cachan [1]. This model is able to predict the phase constituents and orientation at a given multiaxial stress level and temperature. It has been developed in a pseudo reversible framework. Indeed the model is based on the comparison of the free energies of each variant and calculation of associated volume fractions thanks to a probabilistic approach at the single crystal scale. Averaging operations allow calculating the macroscopic quantities at the polycrystalline scale. Obviously some experiments are required for identification of parameters and/or validation of the model. This second point is addressed in the paper. In situ X-Ray Diffraction (XRD) measurements are performed during tensile tests and heating-cooling cycles. XRD permits monitoring of the average volume fraction of phases in presence [3, 4]. Its operation requires the coupling of three different models: the multiscale modeling, diffraction pattern and geometric diffraction apparatus modeling on the other hand. Comparisons between experimental and modeled diffratograms lead to conclude about the model quality.

21.3 Material and Experimental Set Up

21.3.1 $Ni_{49.95at\%}Ti$ Sample

The specimen consists in a thin plate of polycrystalline nickel-titanium (Ni-$_{49.95at\%}$Ti) SMA. Samples have a rectangular section of 20×2 mm^2. The forming process consists in a cold-rolling followed by a heat treatment of 2 min at 480 °C in salt bath. For Nickel-titanium SMA, the phase transformation consists usually in the appearance of a low temperature monoclinic martensite phase inside a high temperature mother body-cubic-centered austenite phase. Depending on exact composition and manufacture process, martensitic transition is sometimes preceded by the appearance of an intermediate phase called R-phase which unit cell is rhombohedral [5]. A Differential Scanning Calorimetry (DSC) measurement has first been performed to get the main characteristics of our sample. Results reported in Fig. 21.1 show that the sample undergoes a double phase transition. Two successive thermal peaks occur during cooling associated to austenite to R-phase for the high temperature peak, and R-phase to martensite for the low temperature peak. DSC measurements also give an estimation of the associated

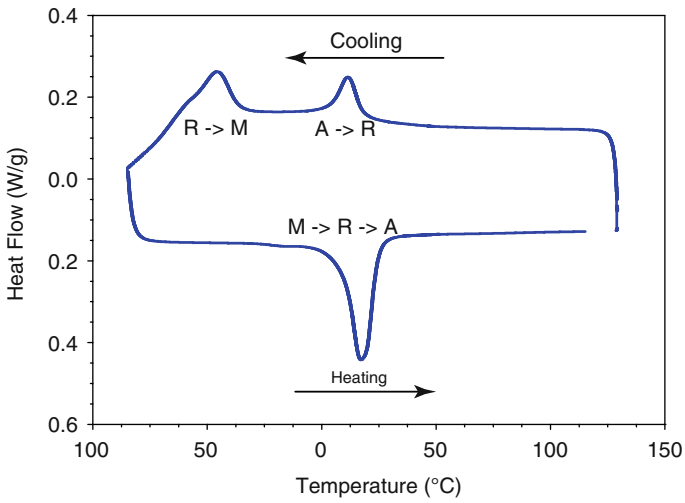

Fig. 21.1 DSC analysis of Ni-$_{49.95at\%}$Ti sample (courtesy of V.Delobelle—SIMAP-GPM2)

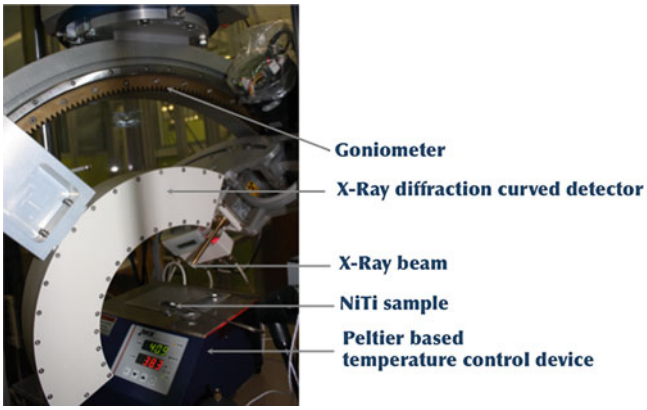

Fig. 21.2 Temperature controlled experimental device

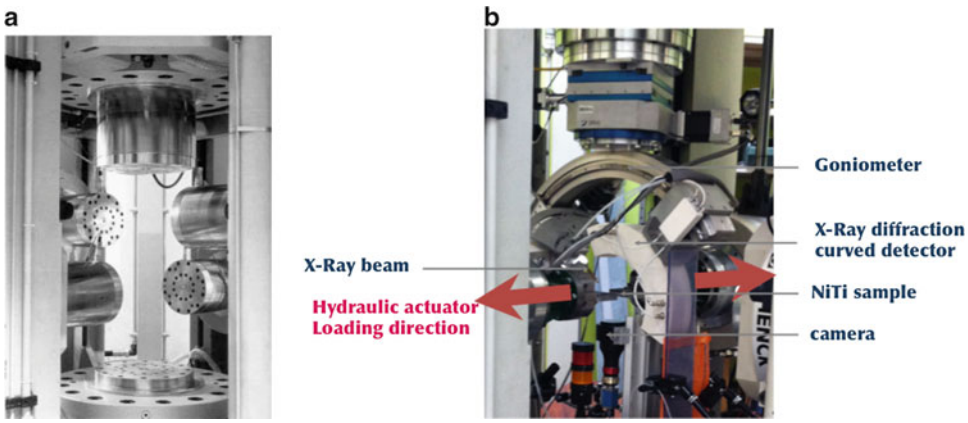

Fig. 21.3 (**a**) ASTREE: a complex multiaxial loading machine composed of six hydraulic actuators (**b**) Uniaxial tensile loading experimental device

transition temperatures ($T_{A\to R} = 11.20$ °C et $T_{R\to M} = -45.75$ °C) and associated mass enthalpies ($\Delta H_{A\to R} = 6.946$ J.g^{-1} et $\Delta H_{R\to M} = 18.22$ J.g^{-1}). Transition temperatures are not the same while heating. Peaks are shifted to the right with respect to cooling. This leads to the unique peak observed in the figure corresponding to a martensite-austenite transition ($T_{M\to A} = 16.86$ °C et $\Delta H_{M\to A} = 24.13$ J.g^{-1}). This heat absorption may involve a transient R-phase transformation.

21.3.2 Tests and Experimental Devices

We use an in situ X ray diffractometer (Figs. 21.2 and 21.3). It consists on a goniometer for positioning the incident beam and X ray tube. Source chosen for diffraction is Cobalt (Kα ray—0.1789 nm). Diffracted rays are measured thanks to a curved detector (INEL CPS 180) covering a large range of angular detection (2θ range = 120°). A 1 mm diameter beam with fixed 50° incident angle is used. For an improved ratio between main peaks and background, acquisitions duration is fixed to 10 min under 20 mA current and 30 kV acceleration voltage. Sample's upper surface underwent an electrochemical polishing to improve the X ray diffraction quality. The first test performed is a cooling/heating cycle. Temperature is controlled using a Peltier effect apparatus made of a heating or cooling plate and a thermocouple for feedback control (Fig. 21.2). The plate can heat up to 50 °C but can't reach low temperature needed for full martensitic transition. A liquid nitrogen flow is added to reach the martensitic transition temperature. This flow avoids the appearance of ice crystals. The second experience is a uniaxial tensile test at room temperature. Sample gauge length is 80 mm. Measurements were done on a hydraulic device available at LMT-Cachan (ASTREE) allowing us to keep fixed the central point of sample (Fig. 21.3). We use two coaxial horizontal hydraulic actuators for the uniaxial loading. Loading force and global displacement are measured. Loading is displacement controlled, with rate set to 0.01 mm/s. The test is performed at room temperature (26 °C), the material being consequently initially in the austenitic state.

21.4 Results

21.4.1 Reference Measurement: Austenite Diffractogram at 50 °C

Theoretical powder diffraction data reported in Fig. 21.4 are used for identifying corresponding diffracting planes for the three possible phases. We performed a first measurement at 50 °C temperature without any external solicitation. Measured Difractogram is given in Fig. 21.5. According to the DSC curve in Fig. 21.1, the sample should be fully austenitic at 50 °C. We observe a global good agreement between the theoretical diffractogram of the austenitic phase (Fig. 21.4a), but some differences occur. For both, main austenite peak is the {110} planes diffraction. But intensity ratios between main peak and the others are slightly different from powder diffraction theory. In addition one of the main peaks of austenite corresponding to {200} planes does not appear on experimental pattern. We also observe small low angle peak ($2\theta = 44.3°$) that doesn't match any possible austenite reflection. According to the sample composition and the Ni-Ti phase diagram, $NiTi_2$ precipitates can form during cooling in quasi equi atomic Ti-rich nickel-titanium alloys. $NiTi_2$ have a cubic centered unit cell and the first experimental peak match the peak {422} of $NiTi_2$. On the other hand, the relevance of a comparison between experiment carried out on a thin plate sample and a powder diffraction can be questioned due to possible texture effect. EBSD analysis has been performed at ambient temperature. Sample is mainly austenitic according to DSC measurements. EBSD pole

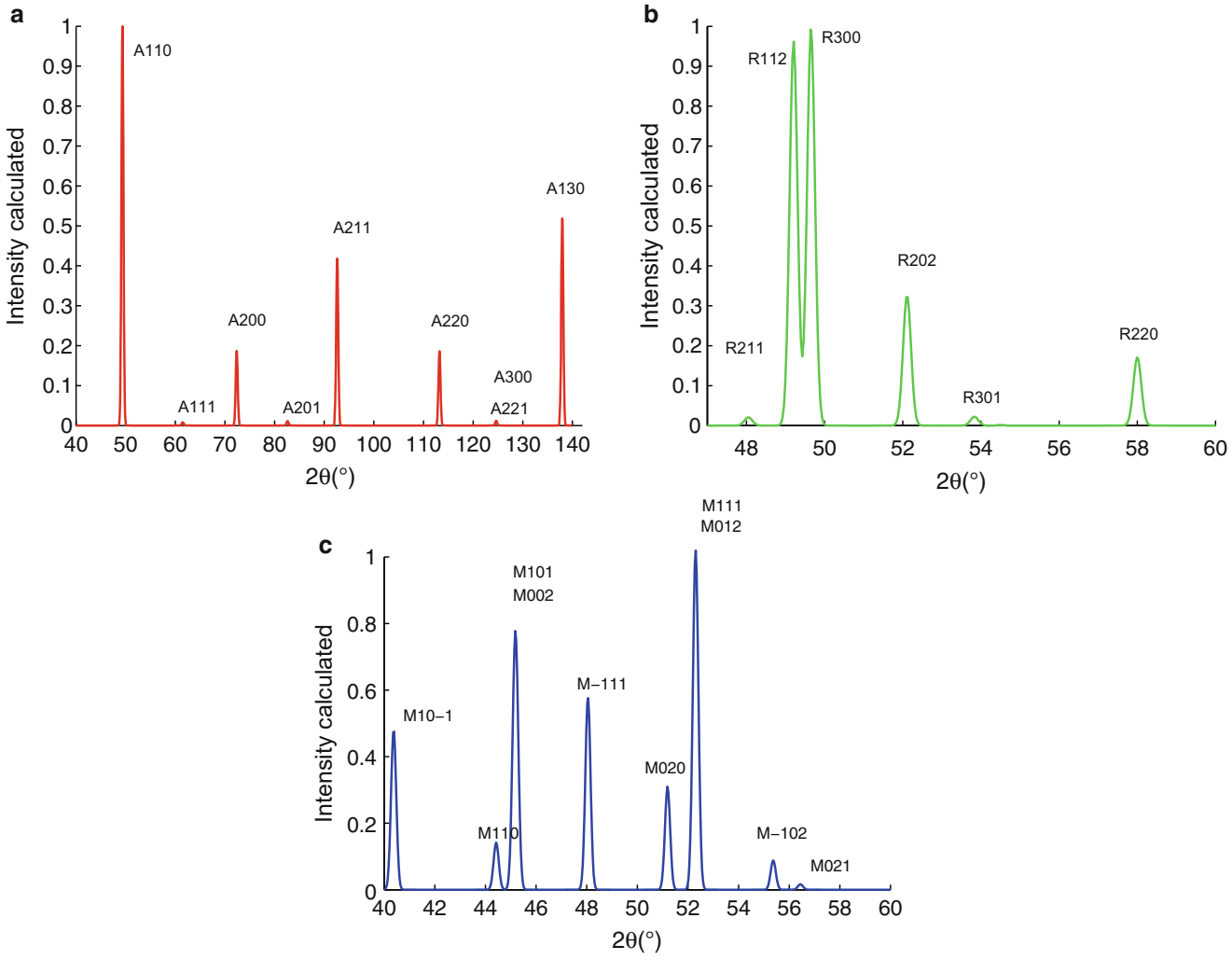

Fig. 21.4 Calculated powder diffraction for austenite (**a**), R-phase (**b**) and martensite (**c**) phases

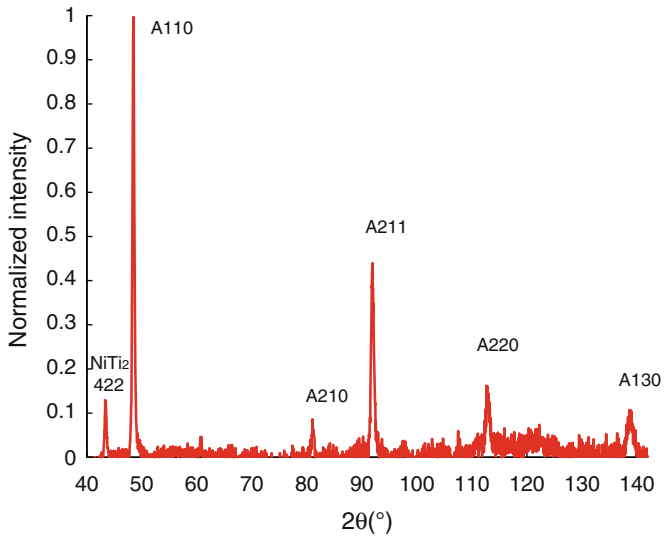

Fig. 21.5 Experimental diffraction pattern at 50 °C

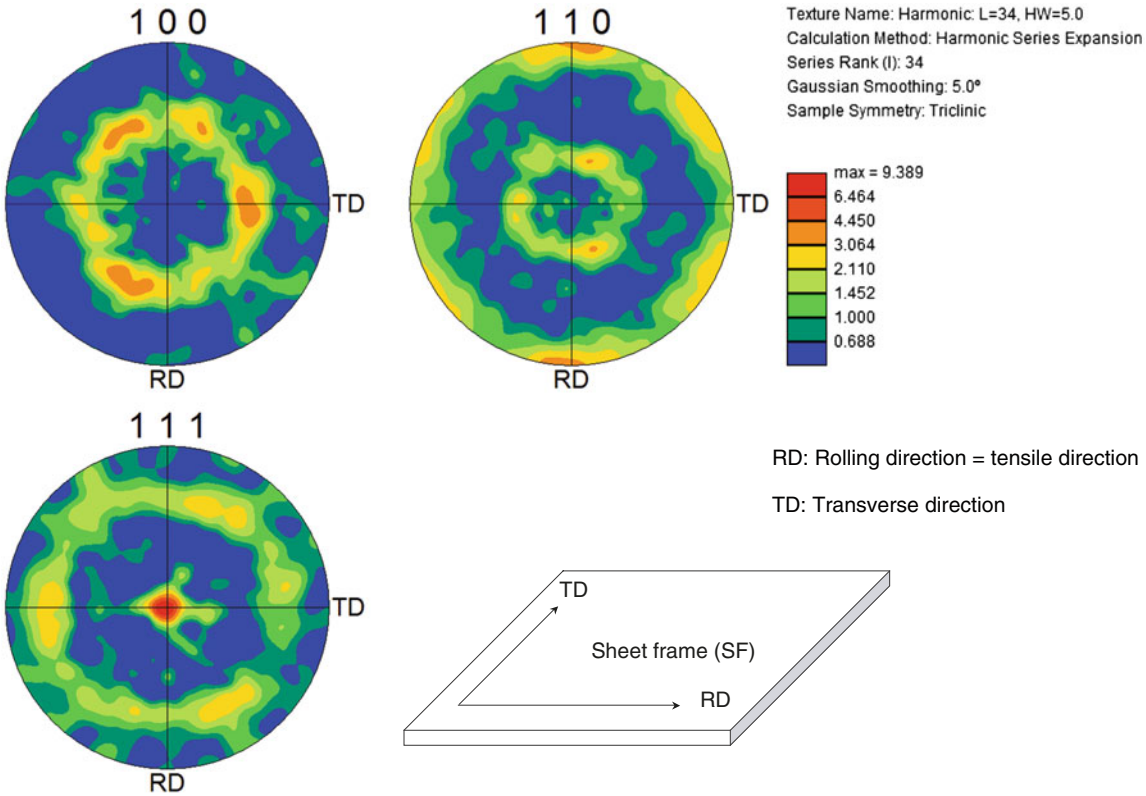

Fig. 21.6 {100}, {110} and {111} poles figures of austenitic phase and associated densities from EBSD analysis

figures in Fig. 21.6 highlights a transverse isotropic texture inherited from the forming process. Hence, according to grain orientation, some planes are more or less in favorable diffraction conditions. Presence of texture may consequently alter some diffracting intensities associated with peculiar planes and have an influence on intensities of peaks associate to generated phases (martensite or R-phase). A modeling of the diffracting conditions confirm that the decrease of {200} A intensity is associated to the transverse isotropic texture. For further discussions, we will consider a smaller range of 2θ between 40° and 60°.

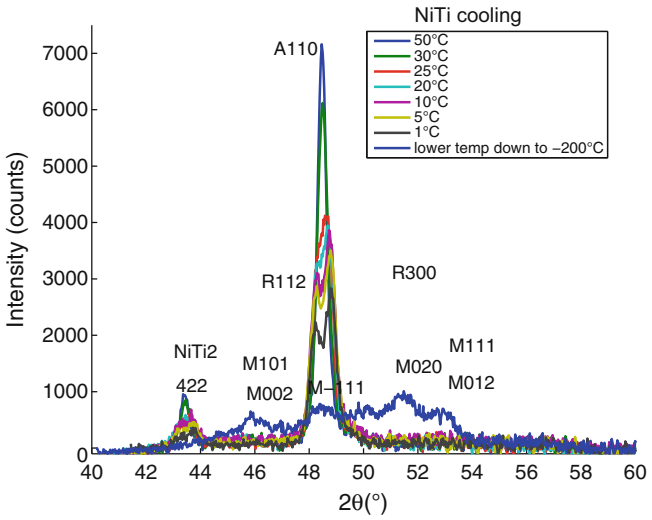

Fig. 21.7 NiTi diffraction pattern during cooling test

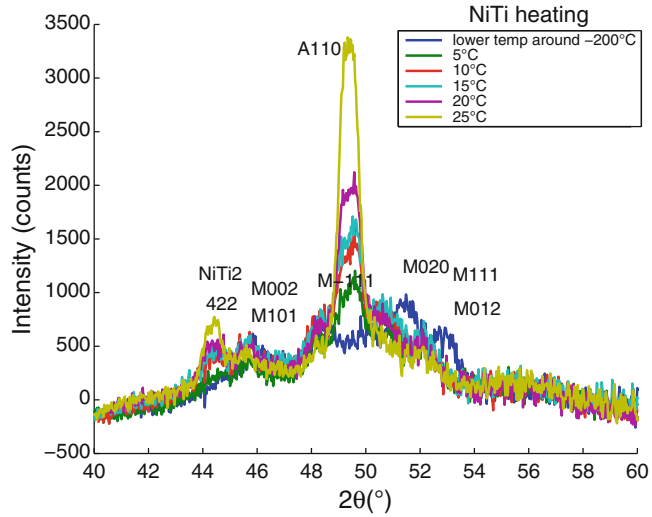

Fig. 21.8 NiTi diffraction pattern during heating test

21.4.2 Results Obtained Under Thermal Solicitations

Sample is first heated to 50 °C. We will first consider a cooling from 50 °C to −200 °C (Fig. 21.7), then a heating from −200 °C to 50 °C (Fig. 21.8). As previously said, sample is mainly austenitic at 50 °C with a small amount of $NiTi_2$ precipitates. We see the austenite main pic A{110} ($2\theta = 49.4°$) and $NiTi_2${422} peak ($2\theta = 44.3°$). Cooling to 30 °C, we notice a slight decrease of two peaks. The sample stands mainly austenitic at that temperature. Cooling down to 25 °C then to 20 °C, A{110} peak progressively transforms while $NiTi_2${422} peak is still decreasing. At 10 °C, A{110} peak splits clearly into to new peaks that can be identified as R{112} ($2\theta = 49.2°$) and R{300} ($2\theta = 49.6°$) peaks (see Fig. 21.4b). Precipitate peak is still decreasing. Diffraction pattern is quite the same from 10 °C to 5 °C. We just notice a slight decrease in R-phase's peaks. R-phase peaks consequently decrease from 5 °C to −5 °C. At −5 °C (diffraction pattern not reported in Fig. 21.7), new peaks appear that may correspond to ice. In fact, down to 0 °C, ice starts forming on the cooling plate and indeed on the sample surface. This can cause false interpretation and estimation for quantitative analysis. We used then a liquid nitrogen flow to reach a very low temperature down to −200 °C. Temperature hardly stabilizes under this flow. So we did just one measurement at lower temperature then heated the sample back. This unique measurement permits identification of the main martensite peaks (see Fig. 21.4c).

Figure 21.8 gives the diffraction results for the sample heated from −200 °C to 25 °C in order to observe the inverse transformation. The main observation is that inverse and the direct transition patterns are different. This result is in accordance with the DSC predictions since reverse and direct transformations do not occur at the same temperature. On the other hand it seems clear now that the martensite transforms directly in austenite without any transient transformation into R-phase. The sample is quite mainly austenitic at 25 °C. A precise quantitative analysis would require to quantify first the texture effect on

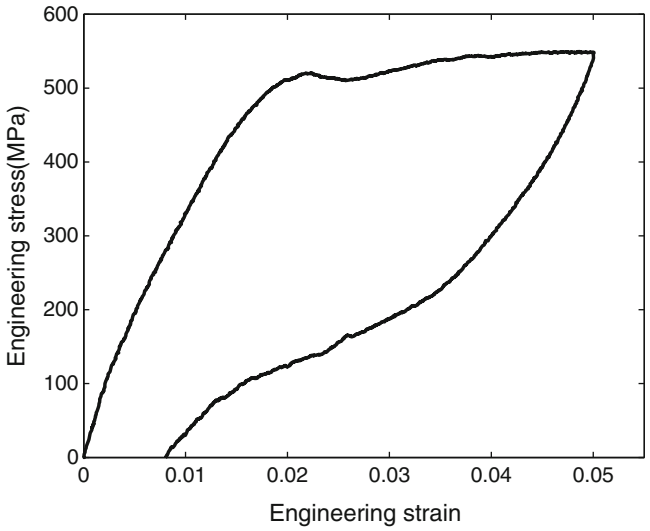

Fig. 21.9 Engineering stress-strain curve for NiTi SMA at the room temperature (rate: 0.01 mm/s)

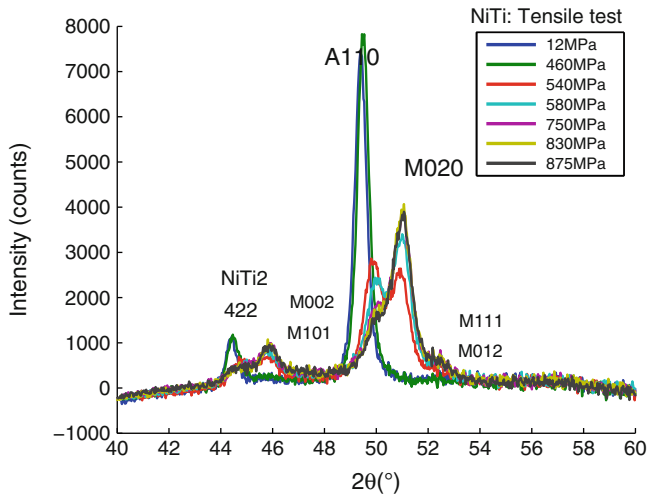

Fig. 21.10 NiTi diffraction pattern during uniaxial tensile loading at the room temperature

the austenite diffraction pattern, and secondly its effect on R phase and martensite patterns. Besides many errors can occur since martensite peaks are quite weak comparing to the background. Some other limits for identification can be addressed: diffuse transformation, convoluted peaks, doubled peaks . . . Quantitative estimation of phase fraction requires a very careful analysis of the dispersion sources. This work is in progress.

21.4.3 Results Obtained During Uniaxial Tensile Test at the Room Temperature

The measured engineering stress ($\sigma = F/S_0$) versus engineering strain ($\varepsilon = \Delta l/l_0$) curve is given in Fig. 21.9. The observed plateau is specific to pseudoelastic behavior, i.e. stress induces a transformation from austenite to martensite. Diffraction measurements have been carried out for various stress/strain points of this curve. The diffraction is realized perpendicularly to the applied stress. Results are reported in Fig. 21.10. At the room temperature ($T = 26\ °C$) and without applied stress (12 MPa—sample positioned in the machine), the austenitic state is clearly dominant. Applying 460 MPa stress level, we observe a little change in the peaks position. This shift is associated with a small change of lattice parameters due to stress. Increasing applied stress to 540 MPa, we notice a clear decrease of A{110} and $NiTi_2$ {422} peaks and a concomitant appearance of martensite M{020} peak. Increasing applied stress from 540 MPa to 750 MPa, $NiTi_2$ {422} peak progressively disappears. A{110} peak is still decreasing while M{020} peak intensity is increasing. Meanwhile smaller martensite peaks like M{101} and M{002} just appear. Peaks position continue a progressive shifting to higher angles due to increasing stress. Up to 750 MPa diffraction pattern does no longer evolve. In stress driven transformation, we see that M{020} is the

main diffracting plane. Unlike uniform temperature driven transformation, martensite variants oriented along the loading direction are preferably selected with the mechanical loading. Another important feature is the complete absence of R-phase planes. This result is in accordance with the small transformation strain of this phase and small associated thermomechanical coupling [5]. Quantitative estimation of phase volume fraction would require the same precaution than for results carried out under thermal loading.

21.5 Conclusion

In Situ X ray measurements offer an efficient way for characterizing martensitic transition at the microscale. Some valuable information have been carried out concerning the studied NiTi sample: presence of $NiTi_2$ precipitates; transient R-phase appearance with temperature; path differences between heating and cooling due to germination effects; martensite variants selection during the mechanical loading and non activation of R-phase transformation during stress driven tests. This work offers a lot of interesting perspectives. In situ X ray diffraction is especially a very promising tool to validate multiscale and multiphased model estimations [6]. Of course, quantitative analysis over diffraction pattern is needed to extract fractions from experiments. For a good quality quantitative analysis, we need to accurately control the test conditions (e.g. appearance of ice during cooling), the acquisition precision (peak height versus background) and sample's history (presence of precipitates, texture effect, residual stress level). These parameters should be taken into account for identification as well as volume fraction evaluation. The sample texture influences austenite diffractogram pattern. Its role on the X-ray signature of derived phases (R-phase and martensite) must be carefully taken into account. Some others limits like the small signal/background ratio for martensite peaks for example do exist. A Rietveld quantitative analysis taking into account texture correction for each phase will be implemented to get a more precise estimation of phase volume fractions. The multiscale model developed at LMT-Cachan is able to predict thermomechanical SMA behavior under thermal and multiaxial loadings. Hence, it would be very interesting in a second approach to perform quantitative in situ X ray diffraction under complex conditions mixing multiaxial stress and thermal loading.

References

1. Maynadier A, Depriester D, Lavernhe-Taillard K, Hubert O (2011) Thermo-mechanical description of phase transformation in Ni-Ti Shape Memory Alloy. Procedia Eng 10:2208–2213
2. Cullity BD (1978) Elements of X-ray diffraction, 2nd edn. Addison-Wesley, Reading, MA
3. Pattabi M, Ramakrishna K, Mahesh KK (2007) Corrigendum to "Effect of thermal cycling on the shape memory transformation behavior of NiTi alloy: powder X-ray diffraction study". Mater Sci Eng A 448:33–38
4. Uchila J, Braz Fernandesb FM, Mahesha KK (2007) X-ray diffraction study of the phase transformations in NiTi shape memory alloy. Mater Character 58:243–248
5. Battacharya K (2003) Microstructure of martensite: why it forms and how it gives rise to the shape memory effect? Oxford series on materials modelling
6. Fall MD, Lavernhe-Taillard K, Maynadier A, Hubert O (2014) Validation of shape memory alloys multiscale modeling thanks to in-situ X-rays diffraction. In: 16th International Conference on Experimental Mechanics (ICEM 2014)

Chapter 22
Failure Mode Transition in Fiber Composite Fatigue

Mohammad Rasheduzzaman and M.N. Cavalli

Abstract Previous work has shown that, under some circumstances, failure of polymer-matrix fiber composites under bending fatigue loading can transition from compressive/local buckling failure to tensile/fiber fracture failure. For low cycle fatigue, failure tends to be compressive in nature and can be modeled based on kink band theory. For high cycle fatigue, failure tends to be tensile and can be modeled based on a fatigue damage/wear-out model. In this work, we investigate the effect of load ratio on the transition from low cycle/compressive failure to high cycle/tensile failure for a unidirectional polyester/glass fiber composite. The stiffness degradation of the beams under changing loading conditions is also investigated.

Keywords Glass fiber-reinforced polymers • Bending fatigue • Fatigue testing • Buckling • Failure transition

22.1 Introduction

Cyclic (fatigue) loading of materials leads to the accumulation of damage and eventual failure. The rate of damage accumulation and the resulting change in material properties depend on the original material properties (on both the macro- and micro-scales), as well as the loading history. Fatigue of composite materials can be particularly complicated because of the number potential variables that can affect material behavior. Examples of previous work related to fatigue of composites include research focused on fatigue life assessment [1, 2], damage modeling and propagation of failure [3–11], the effect of stress in off-axis fiber [12], failure criteria [13, 14], and developing model for fatigue life prediction [2, 8, 15–21].

Under compressive loading, an isotropic material can typically fail by shear or fracture (depending on its toughness) or macroscopic buckling. In the case of unidirectional fiber-reinforced composite materials, an additional failure mode of delamination/local buckling is possible. For axial fatigue with a positive stress ratio (defined as $R = \sigma_{min}/\sigma_{max}$ during a fatigue cycle), the material is never in compression and this failure mode is not active. However, in bending deformation, both tensile and compressive stresses can be present in the material. Failure can occur in the region of tensile stresses due to fracture of the matrix and fiber or in the region of compressive stresses due to delamination and local buckling. The purpose of this work is to investigate the conditions under which a transition from compression-dominated failure to tension-dominated failure occurs for unidirectional glass-reinforced polyester composites tested under four-point bending. Experimental results are compared with available theory.

22.2 Experimental Methods

Composite plates were fabricated using Vacuum Assisted Resin Transfer Molding (VARTM). The unidirectional E-glass fibers used had a thin layer of randomly-oriented chopped fibers attached to one side. Analysis indicated approximately 95 % of the glass was contained in the unidirectional fibers. The resin was GT 125 Polylite 413 (Reichhold). An initiator

M. Rasheduzzaman • M.N. Cavalli (✉)
Department of Mechanical Engineering, University of North Dakota, 243 Centennial Drive, Stop 8359, Grand Forks, ND 58202-8359, USA
e-mail: mohammad.rasheduzzam@my.und.edu; matthew.cavalli@engr.und.edu

J. Carroll and S. Daly (eds.), *Fracture, Fatigue, Failure, and Damage Evolution, Volume 5: Proceedings of the 2014 Annual Conference on Experimental and Applied Mechanics*, Conference Proceedings of the Society for Experimental Mechanics Series,
DOI 10.1007/978-3-319-06977-7_22,

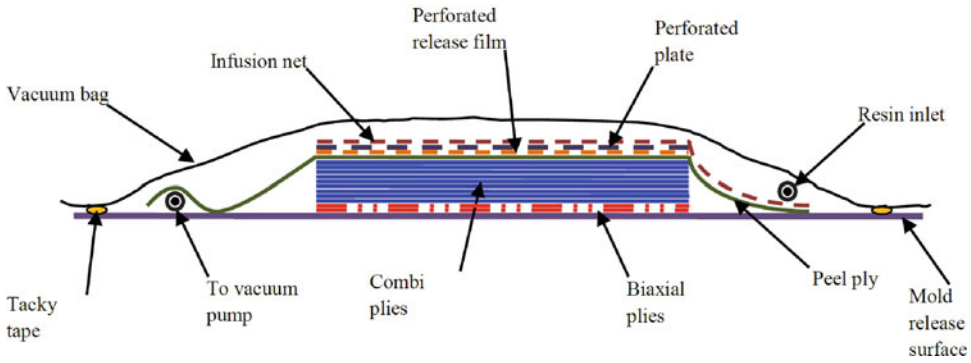

Fig. 22.1 Schematic of VARTM process [22]

concentration of 1.5 % was mixed with the resin prior to starting the infusion process. Figure 22.1 shows a schematic of the VARTM process [22].

Ten layers of glass were used. Fabricated plates measured approximately $610 \times 305 \times 8.5$ mm. After curing for 24 h at room temperature, plates were post-cured for 14 h at 65 °C. Fiber burnoff tests indicated a fiber volume fraction of about 54 %.

After post-curing, 305×25.4 mm samples were cut from the larger plate for testing. Both static and cyclic testing of these samples were performed. Sample geometry followed the requirements of ASTM 6272 [23]. For both types of testing, the support span was 203 mm and the load span was 68 mm. Static testing was conducted on a Shimadzu AG-IS system at a displacement rate of approximately 9 mm/min. Cyclic loading was conducted using a Bose Electroforce 3510 machine at a frequency of 5 Hz. Four different load ratios were investigated during the cyclic loading, $R = 0.1$, 0.3, 0.5 and 0.7. The load form was a sine wave. Infinite fatigue life was defined as 2 million cycles.

Following cyclic testing, images of the compressive and tensile sides of the beams were captured. Image analysis was performed to compare the fracture of visible damage present on both sides of the beam.

22.3 Modeling

The "wear out" model of Sendeckyj [24] has been shown to capture the high-cycle fatigue behavior of fiber-reinforced composites. It takes the form of a power law as shown in (22.1).

$$S = AN_f^n \tag{22.1}$$

S is the failure stress, N_f is the number of fatigue cycles, and A and n are material constants determined by fitting experimental data. The fitting parameters only apply to the portions of the S-N curve for which the failure mechanism remains the same.

In the case of a failure transition in the low-cycle fatigue regime, an alternative model is required. Slaughter and Fleck proposed a model for compressive fatigue failure of composites [20]. They termed this type of failure 'plastic collapse'. The fatigue model is an extension of earlier work by Budiansky and Fleck [19] related to monotonic loading. Both models are based on the concept of kink bands. Figure 22.2 illustrates the geometry of a kink band. Under an applied compressive stress, σ^∞, a kink forms at an angle, β, to the axis of the rest of the fiber with width, ω.

Equilibrium for the kink band can be represented by (22.2):

$$S^\infty = \frac{t}{\overline{\omega} + \eta} \tag{22.2}$$

where

$$S^\infty = \frac{\sigma^\infty}{G^*} \tag{22.3}$$

$$t = \frac{\tau_e}{\tau_y} \tag{22.4}$$

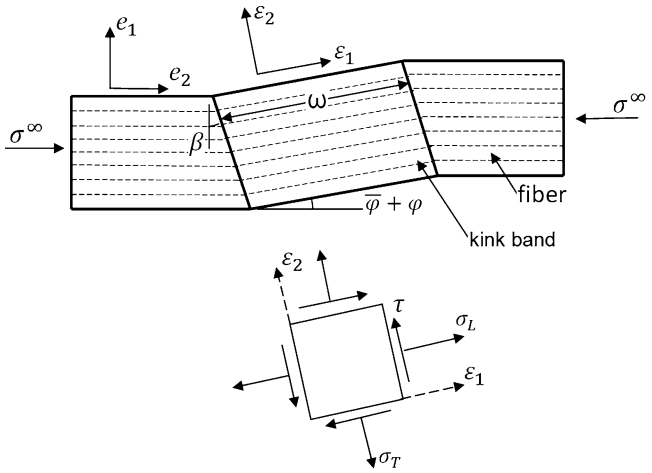

Fig. 22.2 Kink band geometry

$$\eta = \frac{\gamma_e}{\gamma_y} \tag{22.5}$$

$$\overline{\omega} = \frac{\varphi}{\gamma_y^*} \tag{22.6}$$

and

$$G^* = \alpha^2 G \tag{22.7}$$

$$\gamma_y^* = \frac{\gamma_y}{\alpha} \tag{22.8}$$

The 'e' subscript indicates effective stress or strain and the 'y' subscript indicates yield stress or strain. The parameter α is defined by:

$$\gamma_e = \alpha\varphi \tag{22.9}$$

and

$$\alpha = \sqrt{1 + R^2 tan^2\beta} \tag{22.10}$$

$$R = \frac{\sigma_{Ty}}{\tau_y} \tag{22.11}$$

where the 'Ty' subscript indicates transverse yield strength. A Considere Diagram, as shown in Fig. 22.3, can be used to determine the solution for the onset of microbuckling, assuming the composite follows a Ramsberg-Osgood constitutive law.

Using Fig. 22.3, the critical stress and strain for the onset of microbuckling, tc and S_c^∞, respectively, can be determined as:

$$t_c = \left[\frac{7\overline{\omega}}{3\,(n-1)}\right]^{1/n} \tag{22.12}$$

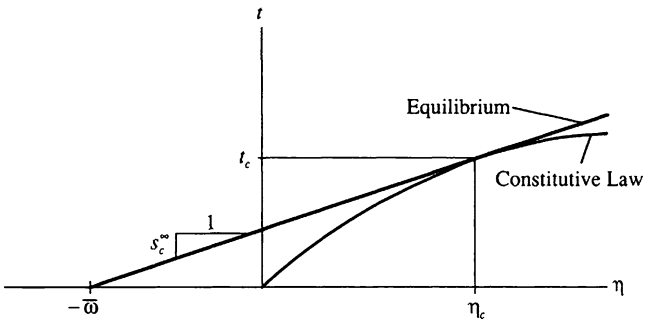

Fig. 22.3 Considere diagram for use in determining parameters for the onset of microbuckling [19]

$$S_c^\infty = \frac{1}{1 + n\left(\frac{3}{7}\right)^{1/n}\left(\frac{\bar{\omega}}{n-1}\right)^{(n-1)/n}} \tag{22.13}$$

where n is a material parameter. From these results, Eqs. (22.14 and 22.15) can be solved for t_2 and Δt, respectively, and then plugged into (22.16), which has the form of a Coffin-Manson fatigue law.

$$t_2 - S_{max}^\infty \left(t_2 + \frac{3}{7}t_2^n + \bar{\omega}\right) = 0 \tag{22.14}$$

$$\Delta t - \left(1 - \frac{S_{min}^\infty}{S_{max}^\infty}\right) t_2 + S_{min}^\infty \left(\Delta t + \frac{6}{7}(\Delta t)^n + \bar{\omega}\right) = 0 \tag{22.15}$$

$$\frac{\Delta\eta}{2} = \frac{\gamma_f'}{y_y}(2N_f)^c \tag{22.16}$$

In (22.16), γ_f' and c are material properties determined through fitting the model curve to experimental data. $\Delta\eta$ is the increment in effective plastic strain during the fatigue cycle. Slaughter and Fleck [25] found that the results of this analysis are expected to have a strong dependence on c and a weaker dependence on γ_f'. Expected values of c are in the range of -0.5 to -0.7. The model predicts an abrupt change in slope as the applied stress reaches S_c^∞ and the onset of microbuckling begins.

22.4 Results

Static testing of the composite beams showed a failure stress of 791 ± 19 MPa. All static samples failed via delamination and local buckling on the compressive face of the beam.

Figure 22.4 shows the S-N curve for the fatigue testing for each of the load ratios. The highest value of maximum stress applied during fatigue testing was 90 % of the static failure load (710 MPa). At this stress level, all samples failed by compressive buckling. For lower stress levels, a combination of compressive and tensile failure was observed. Any samples reaching 2 million cycles were stopped prior to failure (runout).

Figure 22.5 shows images of the tensile and compressive surfaces as a function of the applied maximum stress for a sample with load ratio $R = 0.3$. The lighter areas represent regions of fracture and delamination. Note that this data does not show damage progression, since all results are taken after failure. The amount of damage on the tensile side of the beam increases as the maximum applied stress decreases. Similarly, the amount of damage on the compressive side of the beam increases as the maximum load applied during the fatigue cycle goes up.

To quantify the damage region in the failed samples, image analysis was conducted. ImageJ [26] was used to convert the images Fig. 22.5 (and for other load ratios) to black and white images where white corresponded to failed material and black regions in the image had not failed. A range of thresholding values were used for the conversion to determine the uncertainty

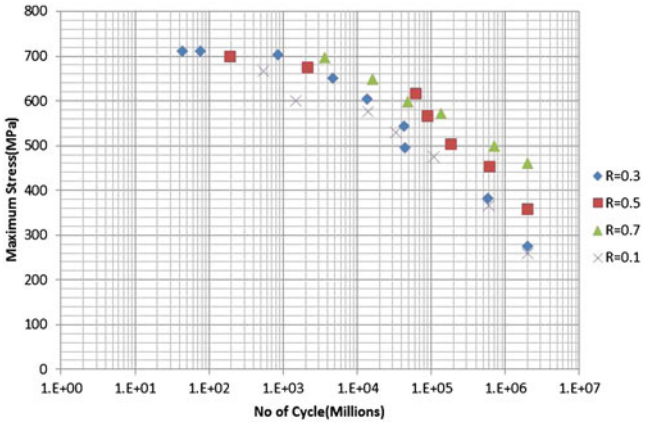

Fig. 22.4 S-N curve for four-point composite beams under fatigue loading

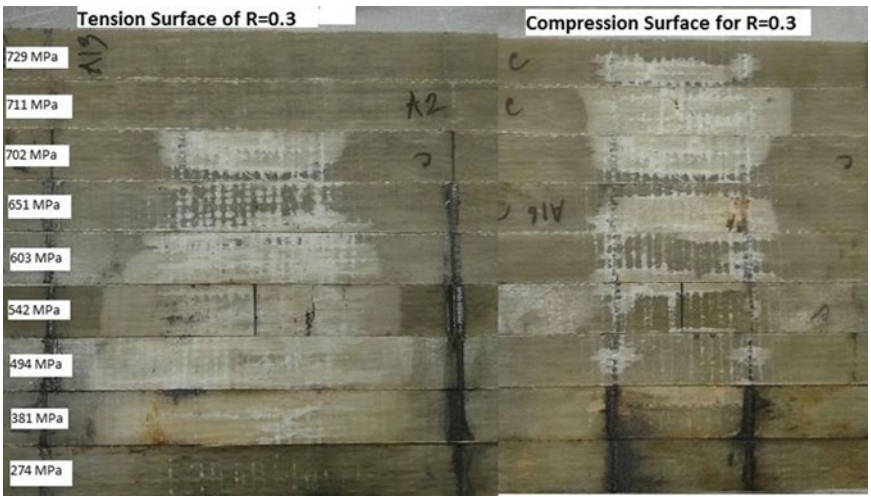

Fig. 22.5 Comparison of tension (*left*) and compression (*right*) faces of fatigue specimens after failure

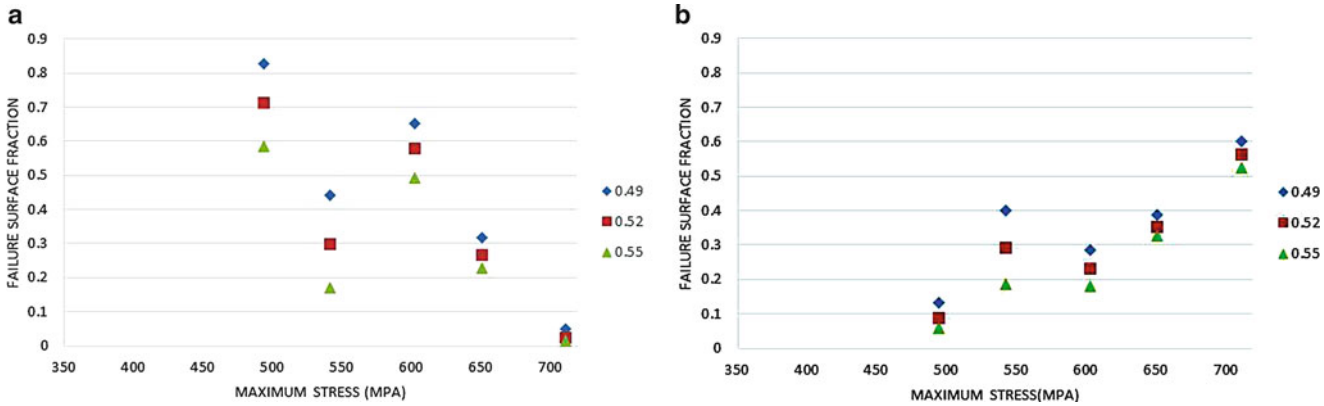

Fig. 22.6 Damage estimate on (**a**) tension surface and (**b**) compression surface of failed specimens for R = 0.3

in the process. The results for two load ratios, R = 0.3 and R = 0.5, are shown in Figs. 22.6 and 22.7, respectively. In general, observed damage on both sides of the material appears to follow a predictable trend.

As damage accumulates in the material, it is expected that the effective stiffness of the beams will go down. To understand the progression of damage leading to the results shown in Fig. 22.5, the effective stiffness of the beams was plotted as a function of the number of loading cycles. The results can be seen in Fig. 22.8. The y-axis is the normalized stiffness, or the measured stiffness at a given load cycle divided by the stiffness of the pristine material. The x-axis is the normalized loading cycle, or the fatigue cycle divided by the fatigue life for that applied stress level. For most samples, the normalized results collapse into a relatively tight window, with a slow degradation of material stiffness throughout the fatigue life followed by an abrupt stiffness reduction after about 90 % of the fatigue life has been completed.

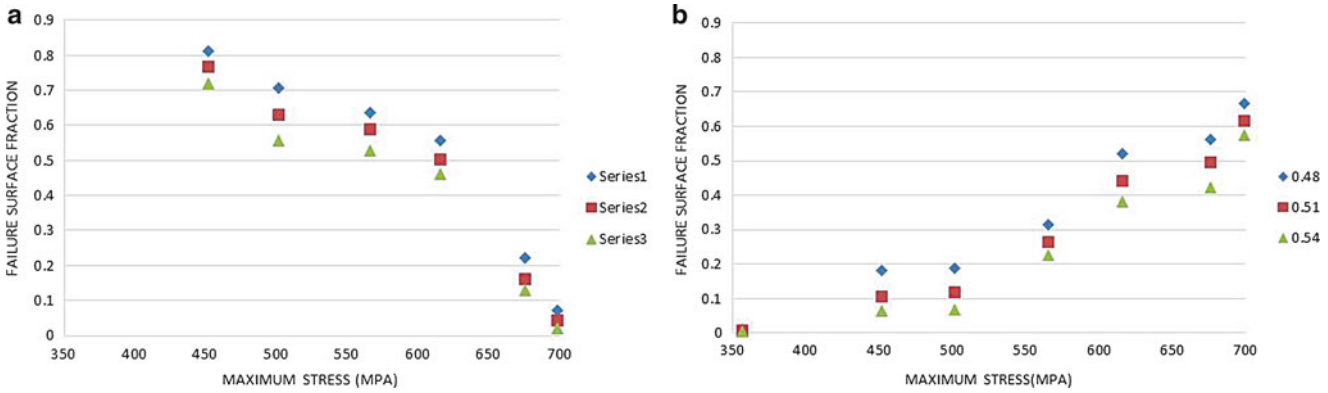

Fig. 22.7 Damage estimate on (**a**) tension surface and (**b**) compression surface of failed specimens for R = 0.5

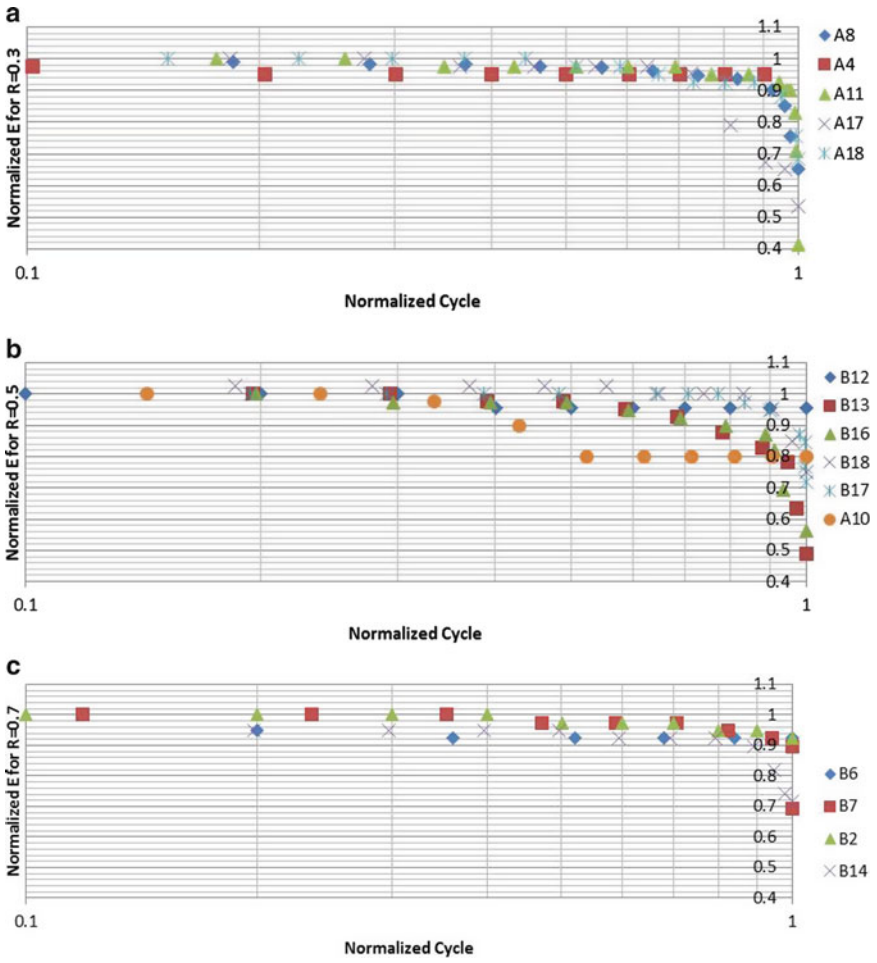

Fig. 22.8 Stiffness degradation of composite beams under fatigue loading

For modeling, the transverse yield strength and shear modulus were taken to be the same as those of Reimbayev [27]. Static loading data was determine from the testing described earlier in this section. Additional details about the intermediate calculations can be found in [27]. Figure 22.9 shows and example of the fitting process for R = 0.5. Three different model predictions with three different sets of parameters are shown in comparison with the experimental data (diamonds). Table 22.1 lists the final fitting parameters for R = 0.1, 0.3, and 0.5.

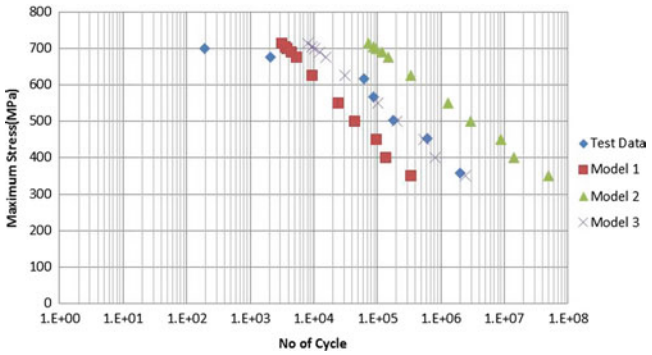

Fig. 22.9 Example of the fitting process to determine the Slaughter-Fleck model parameters

Table 22.1 Best-fit parameters for R = 0.1, 0.3, and 0.5

Load ratio, R	c	$\frac{\gamma'_f}{y_y}$
0.1	−0.6	35
0.3	−0.7	35
0.5	−0.98	45

22.5 Conclusions

Fiber-reinforced polyester samples tested in four-point bending demonstrate a transition in failure morphology from local microbuckling at high maximum stress to fiber fracture at low maximum stress. The transition from microbuckling-dominated to fiber fracture-dominated failure is a function of the applied load ratio. The onset of the transition tends to occur at higher cycles as the stress ratio increases. As cyclic loading continues, damage accumulates in the material. This manifests itself as a steady decrease in effective stiffness of the samples during testing. Results show that the decrease in stiffness is relatively slow for the first 90 % of the total fatigue life with the stiffness of the beam at about 90 % of the initial stiffness after 90 % of the life. At this point, the decrease in fatigue life accelerates significantly until the final onset of failure.

The microbuckling failure model of Budiansky, Fleck and Slaughter has been successfully applied to capture the transition in failure mode observed in this work. The fitting parameters are a function of load ratio.

References

1. Makeev A, Nikishkov Y (2011) Fatigue life assessment for composite structure. In: Proceedings of the 26th ICAF symposium (June 1–3), Montreal
2. Momenkhani K, Sarkani S (2006) A new method for predicting the fatigue life of fiber-reinforced plastic laminates. J Compos Mater 40(21):1971–1982
3. Labeas GN et al (2012) Adaptive progressive damage modeling for large-scale composite structures. Int J Damage Mech 21:441–462
4. Varvani-Farahani A et al (2006) A fatigue damage parameter for life assessment of off-axis unidirectional GRP composites. J Compos Mater 40(18):1659–1670
5. Van der Meer FP, Sluys LJ (2009) Continuum models for the analysis of progressive failure in composite laminates. J Compos Mater 43(20):2131–2156
6. Riccio A (2005) Effects of geometrical and material features on damage onset and propagation in single-lap bolted composite joints under tensile load: part II – numerical studies. J Compos Mater 39(23):2091–2112
7. Subramanian S et al (1995) A cumulative damage model to predict the fatigue life of composite laminates including the effect of a fibre-matrix interphase. Int J Fatigue 17(5):434–351
8. Wu F, Yao W (2010) A fatigue damage model of composite materials. Int J Fatigue 32:134–138
9. Mao H, Mahadevan S (2002) Fatigue damage modeling of composite materials. Compos Struct 58:405–410
10. Shi W et al (2011) A damage mechanics model for fatigue life prediction of fiber reinforced polymer composite lamina. Acta Mechanica Solida Sinica 24(5):399–410
11. Owen MJ, Howe RJ (1972) The accumulation of damage in a glass-reinforced plastic under tensile and fatigue loading. J Phys D Appl Phys 5:1637–1653
12. Kawai M, Suda H (2004) Effects of non-negative mean stress on the off-axis fatigue behavior of unidirectional carbon/epoxy composites at room temperature. J Compos Mater 38(10):833–854
13. Davila CG et al (2005) Failure criteria for FRP laminates. J Compos Mater 39(4):323–345
14. Yeh H-Y et al (2008) An investigation of failure criterion for new orthotropic ceramic matrix composite materials. J Reinforc Plast Compos 28(4):441–459

15. Hanus E, Ericsson T (1995) Influence of four-point bending fatigue on the residual stress state of a pressure-rolled, particulate-reinforced metal matrix composite. Mater Sci Eng A 194:147–156
16. Epaarachchi JA, Clausen PD (2003) An empirical model for fatigue behavior prediction of glass fibre-reinforced plastic composites for various stress ratios and test frequencies. Composites A 34:313–326
17. Momenkhani K, Sarkani S (2005) Development and application of a model using center of gravity hysteresis loops to predict fatigue damage accumulation in fiber-reinforced plastic laminates. J Compos Mater 39(6):557–575
18. Dowling NE (2004) Mean stress effects in stress-life and strain-life fatigue. SAE Technical Paper 2004-01-2227
19. Budianski B, Fleck NA (1993) Compressive failure of fibre composites. J Mech Phys Solid 41(1):183–211
20. Slaughter WS, Fleck NA (1993) Compressive fatigue of fibre composites. J Mech Phys Solid 41(8):1265–1284
21. Diao X et al (1995) A statistical model of residual strength and fatigue life of composite laminates. Compos Sci Technol 54:329–336
22. Chawla T (2013) Mechanical characterization of composite repairs for fiber-glass wind turbine blades. Ph.D. Thesis, University of North Dakota
23. ASTM D6272–10 (2010) Standard test method for flexural properties of unreinforced and reinforced plastics and electrical insulating materials by four-point bending. ASTM, West Conshohocken, PA
24. Sendeckyj GP (1981) Fitting models to composite material fatigue data. In: Test methods and design allowables for fibrous composites
25. Slaughter WS, Fleck NA (1993) Compressive fatigue failure of fiber composites. Cambridge University, Engineering Department, Cambridge, UK
26. ImageJ: Image processing and analysis in Java. National Institutes of Health. Accessed from http://imagej.nih.gov/ij/ on 3/8/14
27. Reimbayev M (2012) Fatigue behavior of continuous fiber-reinforced composite beams. M.S. Thesis. University of North Dakota

Chapter 23
Fracture Toughness and Impact Damage Resistance of Nanoreinforced Carbon/Epoxy Composites

Joel S. Fenner and Isaac M. Daniel

Abstract In this study, the objective was to develop, manufacture, and test hybrid nano/microcomposites with a nanoparticle reinforced matrix and demonstrate improvements to damage tolerance properties in the form of Mode-II fracture toughness and related impact damage absorption. The material employed was a woven carbon fiber/epoxy composite, with multi-wall carbon nanotubes (CNT) as a nano-scale reinforcement to the epoxy matrix. A direct-mixing process, aided by a block copolymer dispersant and sonication, was employed to produce the nanoparticle-filled epoxy matrix used in composite fabrication. Composite samples were tested as End Notched Flexure (ENF) specimens in three point bending to determine the static Mode-II fracture toughness, showing improvement of approx. 30 % for nano-reinforced composite over reference material. Certain testing and material difficulties were noted with useful implications for both the testing technique as applied to woven composite materials and the material properties of the nano-reinforced composite. Impact tests were then performed in a falling-weight drop tower to generate delamination damage in samples of hybrid and reference composite. Impact damaged specimens were imaged by ultrasonic c-scans to assess the size and internal geometry of the damage zone, showing a consistently smaller mean damage zone diameter (approx 15 %) for hybrid composite over reference material. This translated to a nominally higher Mode-II fracture toughness in the hybrid composite (approx 30 %) regardless of specific impact energy, agreeing with static Mode-II fracture toughness tests.

Keywords Nanocomposites • Hybrid nano/microcomposites • Test Methods • Fracture toughness • Impact damage

23.1 Introduction

The effect of nanoparticles on the mechanical properties of composite materials is a topic of continuing importance in contemporary research [1–15]. The motivation for these studies is the significant enhancement to various properties that can be obtained from the inclusion of relatively small quantities of nanoparticles in a composite material. The ability to substantially modify material properties of a composite, especially though small manufacturing or composition changes, allows for materials more tailored to specific applications and serves as an attraction to more widespread use.

Damage tolerance enhancements are to be expected from the addition of nanoparticles to a composite material owing to additional energy-absorbing mechanisms that arise. In the case of carbon nanotubes, mechanisms such as nanotube pullout from matrix, nanotube fracture, and nanotube stretching cause additional energy absorption at the nanoscale (Fig. 23.1) [2]. These mechanisms contribute to bulk macroscopic energy absorption, which in turn improves overall fracture toughness and fatigue life, as well as related properties such as compressive and shear strength and impact damage tolerance.

This objective of this study was to examine the effect of nanoparticles, namely carbon nanotubes (CNT), on the damage tolerance and energy-absorption properties of composites, especially impact damage and associated Mode-II fracture toughness, which often dominates interlaminar damage in impact [10, 13–15].

J.S. Fenner • I.M. Daniel (✉)
Center for Intelligent Processing of Composites, Northwestern University, Evanston, IL 60208, USA
e-mail: JoelFenner2012@u.northwestern.edu; imdaniel@northwestern.edu

J. Carroll and S. Daly (eds.), *Fracture, Fatigue, Failure, and Damage Evolution, Volume 5: Proceedings of the 2014 Annual Conference on Experimental and Applied Mechanics*, Conference Proceedings of the Society for Experimental Mechanics Series,
DOI 10.1007/978-3-319-06977-7_23,

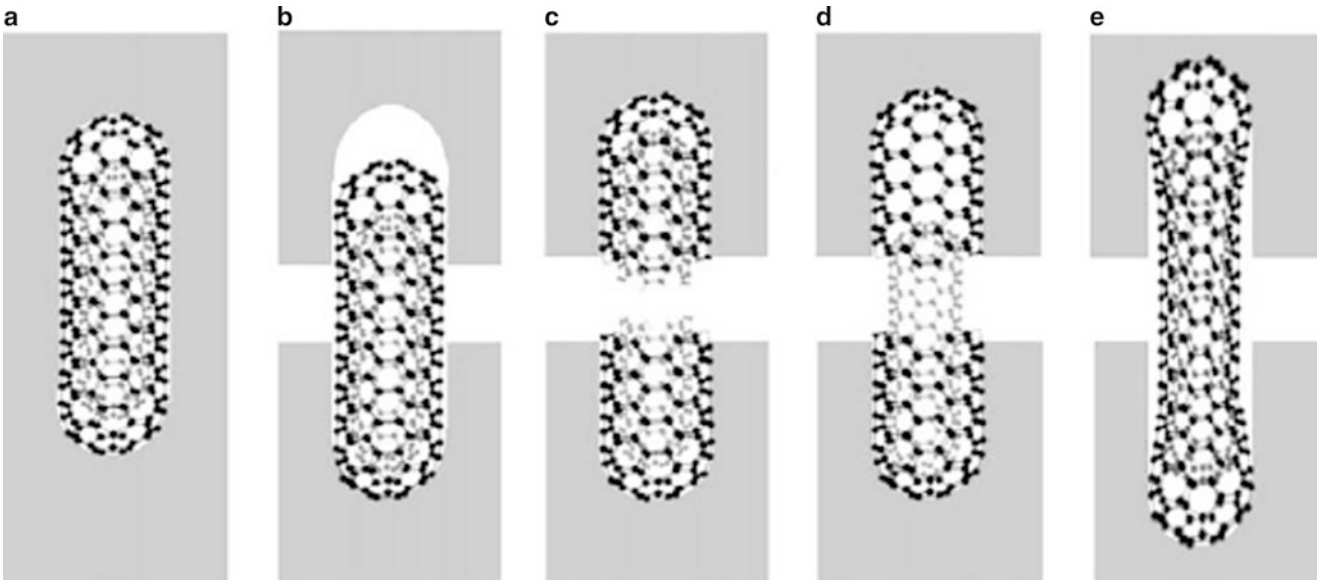

Fig. 23.1 Illustration of possible energy-absorbing mechanisms of CNTs embedded in matrix: (**a**) initial state, (**b**) pullout following CNT/matrix debonding, (**c**) fracture of CNT, (**d**) telescopic pullout-fracture of outer layer and pullout of inner layer, (**e**) partial debonding and stretching [2]

Fig. 23.2 Schematic diagram of composite fabrication mold

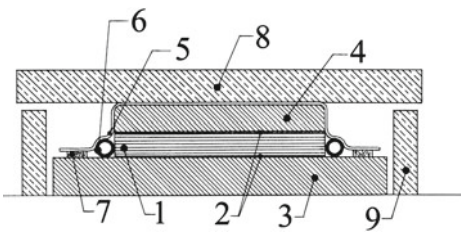

1 – Composite laminate
2 – PTFE-coated release layers
3 – Lower tool plate
4 – Pressure plate
5 – Vacuum bag
6 – Resin outlet gallery
7 – Tacky-tape seal
8 – External pressure plate
9 – Gauge block (for thickness control)

23.2 Material Processing

The material employed in this investigation was a woven carbon fiber/epoxy composite with matrix reinforcement provided by short multi-wall carbon nanotubes. The major mechanical reinforcement was provided by a 5-harness satin weave carbon fabric dry preform (Hexcel, AGP370-5H, AS4 fibers, 6 k tows). The matrix was a typical Bisphenol-A epoxy resin (DGEBA, Huntsman GY 6010) cured with an anhydride hardener (Methyltetraphthalic anhydride, Huntsman HY 917) and an additional amine accelerator (1-Methylimidazole, Huntsman DY 070). The nominal mixture ratio was 100:90:1 (resin:hardener:accelerator) by weight. The resin was reinforced with short multi-wall carbon nanotubes (Helix Material Solutions) of 1–2 μm in length and 10–30 nm in outer diameter. A polyester block copolymer supplied in solution with a weakly volatile organic solvent (Disperbyk-2150, BYK Chemie) was used to facilitate dispersion of the CNTs.

Preparation of the nanoparticle enhanced matrix was carried out primarily by simple mixing and sonication. A weighed amount of DGEBA was mixed with 0.5 %wt of nanotubes and an appropriate amount of copolymer solution. The materials were mixed together thoroughly and then vacuum degassed at an elevated temperature (80 °C) to remove the organic solvent. Anhydride hardener was then added and mixed thoroughly, followed by a repeat vacuum degassing. The resulting mixture was subjected to sonication (90 W at 20 kHz for 30 min.) to disperse the nanotubes. Just prior to composite infusion, the accelerator amine was then added, and the resin mixture infused into the carbon fiber preform, layer by layer, in a wet layup process. The wetted perform stack was subjected to final degassing and then brought to elevated temperature (150 °C) in a mold to achieve full cure. The construction of the mold (Fig. 23.2) allowed for careful control of finished laminate thickness and controlled removal of excess resin during curing. This process was developed and adapted to problems related to a marked increase in resin viscosity due to the presence of nanotubes and a filtration effect on nanotubes encountered in

VARTM processing. The same procedure was used for the reference and nano-reinforced (hybrid) composites. After curing, composite plates were rough cut into specimens by means of diamond-abrasive cutting wheels, and wet-polished with SiC abrasive papers to final dimensions and smoothness.

23.3 Mode-II Interlaminar Fracture Toughness

Initial tests were performed to quantify Mode-II fracture toughness of the composite. The standard three-point End Notched Flexure (ENF) test was chosen for its overall simplicity in testing and analysis (Fig. 23.3) [16, 17]. Specimens were prepared with nominal dimensions $L = 25$ mm, $a_0 = 7.6$ mm, $b = 12$ mm, $2h = 4$ mm (8 plies).

Tests were carried out on numerous specimens of each material type (reference and hybrid composite), giving numerous curves of the form shown in Fig. 23.4. From these curves, calculation of the Mode-II strain energy release rate was made by various methods. From the peak load at crack advance alone, the strain energy release rate G_{II} is given by the relation

$$G_{II} = \frac{9a^2P^2}{16E_1b^2h^3}\left(1 + 0.2\frac{E_1}{G_{13}}\left(\frac{h}{a}\right)^2\right) \tag{23.1}$$

where a is the crack length
b is the specimen width
$2h$ is the specimen thickness
P is the applied load at the central roller
E_1 is the elastic modulus along the beam span
G_{13} is the shear modulus in the plane of bending

For reasonably slender specimens of a material with a higher bending modulus than shear modulus ($a >> h$ and $E_1 >> G_{13}$) may be approximated as

$$G_{II} = \frac{9a^2P^2}{16E_1b^2h^3} \tag{23.2}$$

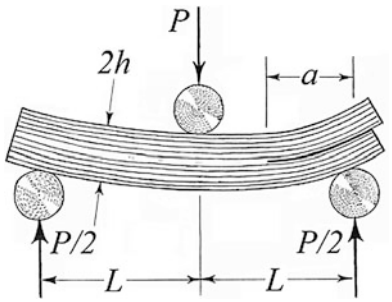

Fig. 23.3 Diagram of end notched flexure (ENF) specimen

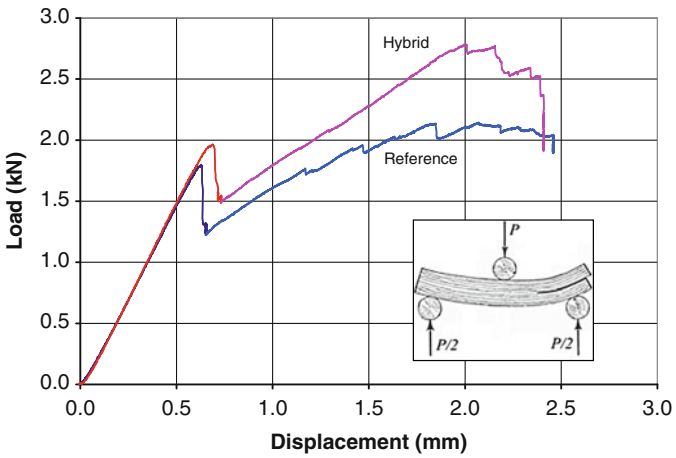

Fig. 23.4 Representative curves of load-deflection behavior for Mode-II ENF fracture specimens

Table 23.1 Mode-II fracture toughness from ENF tests, as calculated by different methods

	By peak load (J/m^2)	By peak load and initial compliance (J/m^2)	By total work of fracture—compliances (J/m^2)	By total work of fracture—Measured crack lengths (J/m^2)
Reference	553	590	1,614	3,868
Hybrid	729	789	1,852	3,734

Alternatively, the fracture toughness was computed making use of the loading (until first peak) and unloading (immediately after first peak) compliances of the specimen to determine the crack length. Neglecting shear effects as in (23.2), the specimen compliance is given by

$$C = \frac{2L^3 + 3a^2}{8E_1 bh^3} \tag{23.3}$$

This permitted simple calculation of the crack length a pre- and post- peak from the measured specimen compliances. Fracture toughness was then calculated by the area method as

$$G_{II} = \frac{P_1\delta_2 - P_2\delta_1}{2b\,(a_2 - a_1)} \tag{23.4}$$

Calculation of the Mode-II fracture toughness purely by peak load or by peak load with initial compliance correction showed an increase of 30 % in GII in hybrid composite over reference composite (Table 23.1). Depending on the method of calculation, however, some disparate "apparent" values of G_{II} were obtained from the data, such as those obtained using post-peak compliance or manually-measured crack lengths. In prior work on Mode-I fracture toughness with identical material [12], differing methods of calculation typically resulted in very good agreement. The lesser degree of self-agreement in these experiments indicates that the crack growth process is not as well behaved as the Mode-I crack growth studied previously.

23.4 Mode-II Fracture Toughness

Because the composite used in this study was manufactured from woven carbon fibers, this introduced additional complications to both testing and analysis. In a woven composite, the crimps in the weave have a strong tendency to self-interfere from ply-to-ply in a Mode-II failure, as in Fig. 23.5. The effect is that sliding motion between plies is generally impeded by mechanical interference of one ply upon an adjacent ply, becoming worse for longer crack lengths as more overall ply sliding is necessary. This situation is quite different from that of a unidirectional composite, as there are no fiber crimps in the latter to impede the deformation of a specimen. One effect is that specimens with longer cracks experience more self-interference at the crack interface, violating assumptions for specimen behavior and making compliance based calculations (like (23.3)) less accurate. This partially explains the unusual fracture toughness values in Table 23.1 when using post-peak specimen compliance. Alternatively, this situation may be viewed as one where the crimp mechanical interference behaves in a manner effectively equivalent to exceptionally high "interfacial friction" between plies, effectively preventing the requisite ply-on-ply sliding that is needed for crack growth to occur This provides an explanation for the unusually large numerical values of G_{II} obtained from measured post-peak crack length, as mechanical self-interference of the fabric plies effectively prevented crack growth beyond the initial peak.

Another feature of note is the unusually "stable" character of the post-peak failure process in these specimens. The nature of an ENF specimen is that crack growth under displacement-controlled conditions is theoretically unstable for crack lengths less than approx. $0.7L$ [17], which is significantly longer than the pre-crack length employed in this study. While these specimens do exhibit an initial load peak during testing, the peak transitions into a gradual re-loading process, and hence the initial peak does not represent an overall peak load for a given test as would be expected. A theoretical test would exhibit a strong instability at peak load, achieving sudden crack growth followed by rapidly diminishing specimen stiffness (Fig. 23.6). Instead, all ENF specimens tested presented an increasing load with increase in deflection, regardless of material composition. This is further justification of the supposition that the fabric crimps interfere with the crack growth process, imparting error to post-peak behavior and calculations that depend on it.

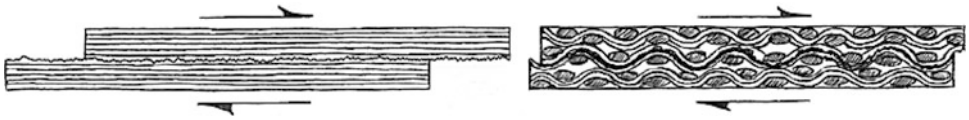

Fig. 23.5 Illustration showing Mode-II sliding failure difference between unidirectional composite (*left*) and woven composite (*right*) with respect to ply-on-ply interference

Fig. 23.6 Plot of load-displacement characteristic of theoretical/ideal ENF test, showing expected instability, peak, and post-peak behavior for the given specimen geometry

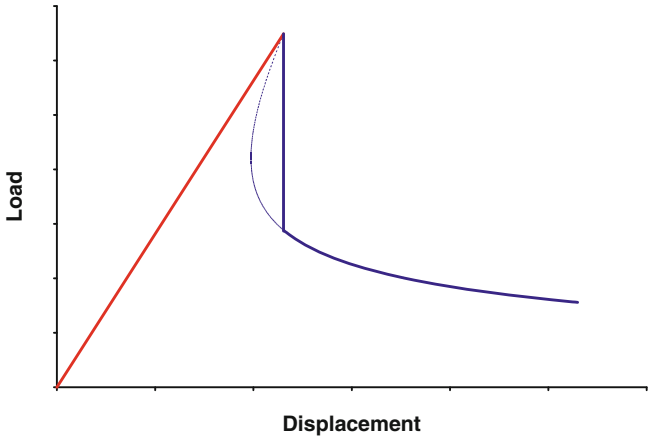

Fig. 23.7 Drop tower employed in impact tests

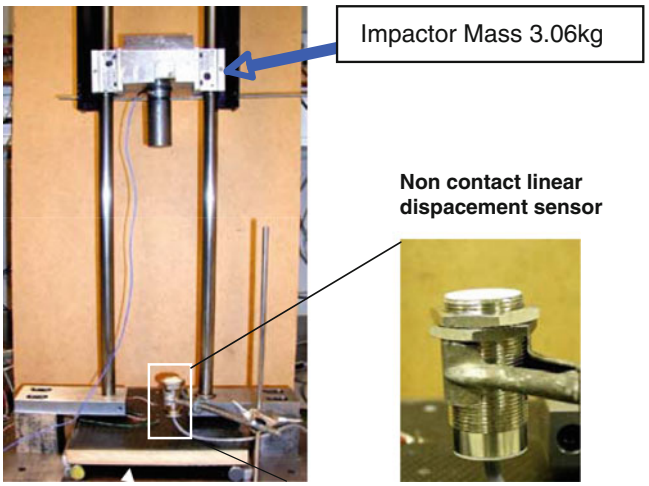

23.5 Impact Testing

Following the numerous difficulties associated with conventional Mode-II fracture toughness tests, and a desire to examine a more macroscopic failure process, impact tests were performed on sample plates of the two composite materials. Testing was carried out in a falling-weight drop tower (Fig. 23.7) with a hemispherical indenter of 25.4 mm diameter. Tests were conducted in pairs (one reference sample followed by one hybrid sample) at the same impact energy. Impact energy was verified by simultaneous measurement of impactor velocity (by means of a non-contact capacitive position sensor) and by measurement of the impact force by means of a piezoelectric (quartz) load cell. Nominal specimen dimensions were 4 in. × 6 in. × 0.2 in. (16 plies). Impactor kinetic energy ranged from 13.5 to 46 J among the various tests.

Following impact, each sample was imaged ultrasonically in a water-immersion scanning tank utilizing a 5 MHz focused probe. Ultrasonic C-scan timing gates were specified to collect reflected wave signals separately for each of the 16 plies in the composite, permitting through-thickness imaging of the damage zone. These various C-scan images (Fig. 23.8) were then examined to quantitatively assess the size of the damage zone at each of the 16 plies.

The sets of C-scan images, sequentially, allow for modest quantitative assessment of the damage zone through the thickness of the sample. Measuring the diameter of the damage zone, in each image, along the sample axes and taking

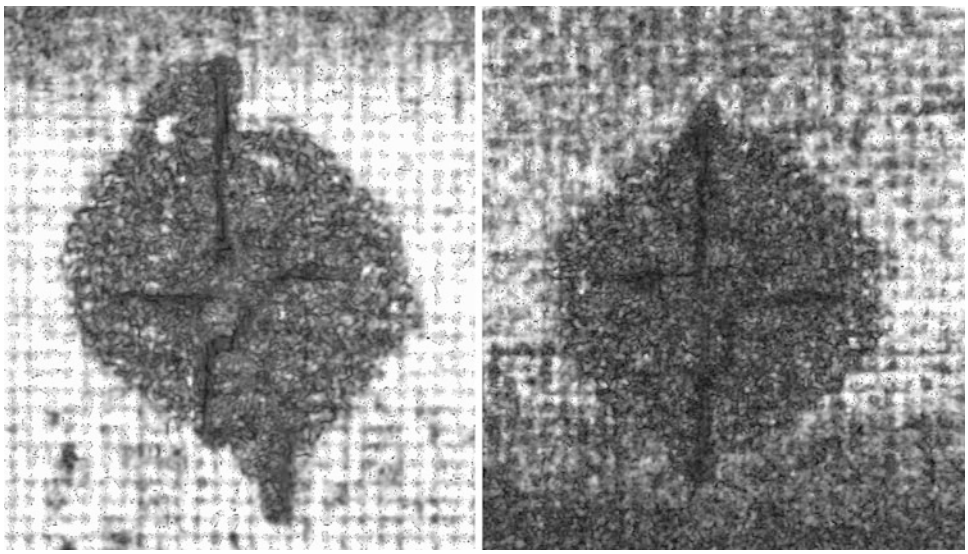

Fig. 23.8 Ultrasonic C-scans of impact damage specimens, backwall echo (ply 16), impactor energy 46 J. *Left*: Reference composite, *Right*: Hybrid composite

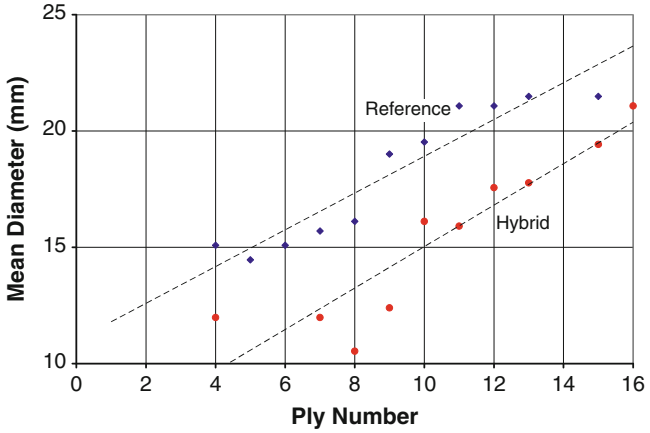

Fig. 23.9 Plot of mean damage zone diameter from ultrasonic C-scan vs ply number (13.5 J impactor energy for both samples)

an average produced values for mean damage zone diameter ($½d_{major} + ½d_{minor} = d_{mean}$) at each ply. Plots of mean damage zone diameter (Fig. 23.9) consistently showed a smaller damage zone size at a given ply and impactor energy for the hybrid composite over the reference material. This behavior was observed regardless of the specific impactor energy applied to the pair of specimens.

For comparison purposes, the ratio of mean damage zone diameters (d_{hybrid}/d_{ref}) was computed for each comparable pair (same impact energy) of specimens at each ply. This allowed simultaneous comparison of test pairs at different impact energies (Fig. 23.10). In spite of the scatter at lower ply numbers, which occur nearer the site of impact, there is a clear overall tendency of the mean diameter ratio to remain less than unity at any given ply. This reaffirms the notion that the hybrid composite requires more energy to form a given amount of damage than the reference composite. From Fig. 23.10, the average diameter ratio across all plies and all energies is about 0.85, showing an overall 15 % decrease in mean damage zone diameter in hybrid composite over reference composite.

As an approximate means of characterizing the Mode-II fracture toughness from the impact test data, the total absorbed fracture energy of a test may be assumed as

$$E_{impact} \approx G_{II} A_{damage} \tag{23.5}$$

where A_{damage} is the mean damage zone area as observed ultrasonically

This may be rewritten as

$$G_{II} \approx 4\frac{E_{impact}}{\pi d^2} \tag{23.6}$$

where d is the mean damage zone diameter

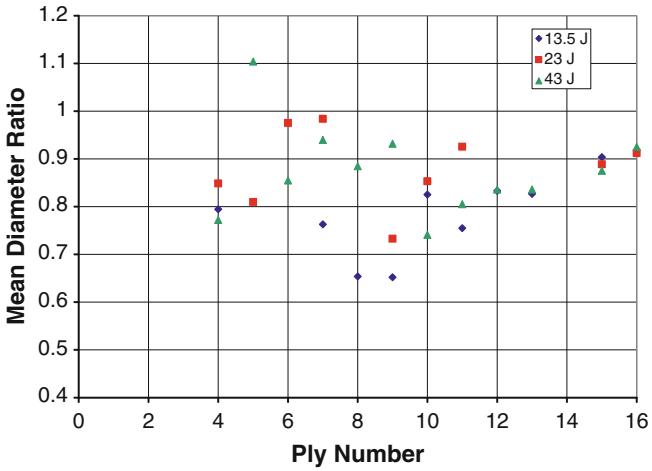

Fig. 23.10 Plot of ratio of mean damage zone diameters (d_{hybrid}/d_{ref}) between reference and hybrid composites, ply by ply

Using this approach, the mean Mode-II fracture toughness of the reference composite was found to be 768 J/m^2 and the mean Mode-II fracture toughness of the hybrid composite was found to be 1,010 J/m^2, showing an increase of approximately 30 %. Since the relation in (23.5) is approximate, however, these are not exact values of fracture toughness. The fact that there is a 30 % increase, however, agrees with static ENF Mode-II fracture toughness tests in Table 23.1 obtained from data up until peak load. Alternatively, from the mean damage zone ratios in Fig. 23.10, it is possible to calculate a ratio of mean damage zone areas of 0.71, or a 30 % decrease in mean damage zone area in hybrid composite over reference. By (23.6), this also implies a 30 % higher Mode-II fracture toughness in the hybrid composite over the reference composite, which is also in agreement with the change in ENF Mode-II fracture toughness tests.

23.6 Conclusions

This study demonstrated that damage tolerance of fiber-reinforced composite materials can be significantly improved by nanoparticle reinforcement of the matrix at low concentrations. The presence of nanoparticles in a hybrid nano/microcomposite can offer a significant increase in interlaminar Mode-II fracture toughness, improving resistance to internal sliding delamination. Furthermore, nanoparticles also can reduce the size of internal delamination developed from impact damage to composites, reducing the overall size of an internal delamination in both diameter and through-thickness volume. Furthermore, the increase in Mode-II fracture toughness correlates well on a relative basis with the overall reduction in impact damage observed through the addition of carbon nanotubes to a composite.

The result of this study is significant in that it shows how overall damage tolerance of a composite, and hence its resistance to impact damage as is seen in realistic service, may be enhanced by introduction of a fairly modest quantity of nanoparticles and simple additional material processing. This not only translates to the possibility of developing more durable or robust composite materials for a broader range of applications, but also for materials that will survive significantly longer in a given application, as in high-cost systems (aircraft, wind turbines, etc.) or mass-production applications (e.g. automotive).

Acknowledgment This work was supported by the Office of Naval Research (ONR). We are grateful to Dr. Y. D. S. Rajapakse of ONR for his encouragement and cooperation.

References

1. Iwahori Y, Ishiwata S, Sumizawa T, Ishikawa T (2005) Mechanical properties improvements in two-phase and three-phase composites using carbon nano-fiber dispersed resin. Compos Appl Sci Manuf 36:1430
2. Gojny FH, Malte MHG, Fiedler B, Schulte K (2005) Influence of different carbon nanotubes on the mechanical properties of epoxy matrix composites-a comparative study. Compos Sci Technol 65:2300–13
3. Dean D, Obore AM, Richmond S, Nyairo E (2006) Multiscale fiber-reinforced nanocomposites: synthesis, processing and properties. Compos Sci Technol 66:2135

4. Siddiqui NA, Woo RSC, Kim JK, Leung CCK, Munir A (2007) Mode I interlaminar fracture behavior and mechanical properties of CFRPs with nanoclay-filled epoxy matrix. Compos Appl Sci Manuf 38:449
5. Bekyarova E, Thostenson ET, Yu A, Kim H, Gao J, Tang J, Hahn HT, Chou TW, Itkis ME, Haddon RC (2007) Multiscale carbon nanotube-carbon fiber reinforcement for advanced epoxy composites. Langmuir 23:3970
6. Cho J, Chen JY, Daniel IM (2007) Mechanical enhancement of carbon fiber/epoxy composites by graphite nanoplatelet reinforcement. Scr Mater 56:685
7. Qiu JJ, Zhang C, Wang B, Liang R (2007) Carbon nanotube integrated multifunctional multiscale composites. Nanotechnology 18:275708
8. Cho J-M, Daniel IM (2008) Reinforcement of carbon/epoxy composites with MWCNTs and dispersion enhancing block copolymer. Scr Mater 58:533–536
9. Daniel IM, Cho J-M (2010) Multiscale hybrid nano/microcomposites-processing, characterization, and analysis, Chapter 12. In: Gilat R, Banks-Sills L (eds) Advances in mathematical modeling and experimental methods for materials and structures. Springer, The Netherlands, pp 161–172
10. Davis DC, Whelan BD (2011) An experimental study of interlaminar shear fracture toughness of a nanotube reinforced composite. Composites B 42:105–116
11. Joshen SC, Dikshit V (2011) Enhancing interlaminar fracture characteristics of woven CFRP Prepreg composites through CNT dispersion. J Compos Mater 46:665–675
12. Fenner JS, Daniel IM (2013) Fracture toughness and fatigue behavior of nanoreinforced carbon/epoxy composites. In: Proc. of SEM XIII international congress and exposition on experimental and applied mechanics
13. Lin JC, Chang LC, Nien MH, Ho HL (2006) Mechanical behavior of various nanoparticle filled composites at low-velocity impact. Compos Struct 74:30
14. Iqbal K, Khan SU, Munir A, Kim JK (2009) Impact damage resistance of CFRP with nanoclay-filled epoxy matrix. Compos Sci Technol 69:1949
15. Hosur MV, Chowdhury FH, Jeelani S (2006) Processing and low-velocity impact performance of nanophased woven carbon/epoxy composite laminates. In: Proceedings of the twelfth US-Japan conference on composite materials 114
16. Pankow M, Waas AM, Yen CF, Ghiorse S (2011) Resistance to delamination of 3D woven textile composites evaluated using End Notch Flexure (ENF) tests: cohesive zone based computational results. Compos Appl Sci Manuf 42:1863
17. Carlsson LA, Gillespie JW, Pipes JR, Pipes RB (1986) On the analysis and design of the end notched flexure (ENF) specimen for mode II testing. J Compos Mater 20:594

Chapter 24
Fatigue Behavior of Glass-Bubbles Modified Adhesively Bonded Composite Joints

Ermias G. Koricho, Anton Khomenko, and Mahmoodul Haq

Abstract Adhesive joining is gaining acceptance in aerospace, automotive, and marine industries as it allows joining of similar and dissimilar materials, eliminates secondary machining processes, minimizes stress due to mechanical joining and most importantly reduces structural weight. One way of improving the performance of adhesively bonded joints is the use of nano-/micro- particle reinforcement of the adhesive or composite matrix. While considerable literature exists on nano-modified composite substrates to improve their mechanical and thermal properties, the work on nano-/micro- modified adhesively bonded joints and their fatigue behaviour is relatively limited.

Therefore, in this paper, the fatigue behaviour of single lap-joints (SLJs) made of S-glass/epoxy substrates were studied. Adhesives with and without glass-bubbles (microspheres) modification were evaluated. The specimens were subjected to different fatigue (tension–tension) loadings with the maximum loading level of 90 % of the bond shear strength. As expected, the fatigue life of adhesive joints in both cases, pristine and glass bubble modified adhesives, depend on the applied cyclic loadings. Inclusion of glass bubbles improves the tensile strength and the fatigue life of single-lap joints. The observations from the experimental fatigue data and its correlation with failure could be considered as valuable information for better design of composite joints and related components.

Keywords Adhesive • Fatigue • Single lap joint (SLJ) • Glass bubbles • Tensile-shear • Composite joints

24.1 Introduction

Adhesive joints are increasingly used in automotive, aeronautic, naval, and ground vehicle sectors. One of the main advantage of using adhesive joints is their high fatigue loading resistance and durability relative to conventional joining techniques. Other advantages of adhesive joints include uniform stress distribution, prevention of stress risers such as holes, high strength to weight ratio, low cost, ability to join similar and dissimilar materials, introduce sealing effect, and ability to damp the noise and vibration [1–3].

Similarly, composite materials are also gaining acceptance in transportation sectors because of their enhanced crash-worthiness and mainly lightweight. For instance, critical sub-systems of vehicles such as bumper assembly, hood, and monocoque are being substituted by composite materials. Hence, understanding the emerging materials, joining techniques and their response under different loading conditions in the complex structure is crucial. The assembled/joined parts of bumper subsystem must be able to absorb enough energy in an impact event to protect the occupants while maintaining the desired structural integrity.

Considerable work have been performed over the past four decades on adhesively bonded joints to understand their responses for fatigue loading [1–6]. Most results indicate that the failure in adhesive joints generally initiated at moderate stress level [4–6]. It is acknowledged that the critical section for crack initiation and propagation is at the edge point that generally affects the fatigue life of the joint. Furthermore, it is commonly agreed that there are two types of approaches to

E.G. Koricho • A. Khomenko • M. Haq (✉)
Composite Vehicle Research Center, Michigan State University, 2727 Alliance Drive, Lansing, MI 48910, USA
e-mail: haqmahmo@egr.msu.edu

J. Carroll and S. Daly (eds.), *Fracture, Fatigue, Failure, and Damage Evolution, Volume 5: Proceedings of the 2014 Annual Conference on Experimental and Applied Mechanics*, Conference Proceedings of the Society for Experimental Mechanics Series,
DOI 10.1007/978-3-319-06977-7_24,

predict the fatigue life of adhesively bonded joints namely, the stress-life approach and fatigue crack initiation/propagation approaches [4]. In stress-life approach, the joints are tested at selected load levels under cyclic loading in order to obtain the S-N curves. Whereas, in fatigue crack initiation/propagation approach, although there are two phases of fatigue lifetime namely, crack initiation and crack propagation, several researchers have analyzed mainly the crack propagation phase. One of the main reasons for neglecting the crack initiation is the difficulties to correlate the crack nucleation in modeling and to detect and monitor the crack initiation. The fatigue life prediction based on fatigue crack propagation involves fracture parameters, such as strain energy release rate and the crack growth rate. The well know fatigue crack propagation for adhesively bonded joint is a log plot of crack growth rate against maximum strain energy release rate over time.

Different additives have been used in adhesive joint to improve the mechanical, thermal, and electrical conductivity of the adhesive materials. Srivastava [7] has investigated the effect of the addition of inorganic nano-particles and demonstrated that multi-walled carbon nanotube (MWCNT) filled epoxy resin adhesive gives higher bonding strength for C/C and C/C-Si substrates than the unmodified epoxy resin bonded substrate. Vega et al. [8] have studied single-walled carbon nanotubes (SWCNTs) as a sensor and proved that SWCNTs could be used to monitor the internal stress developed during the curing process of thermoset materials.

In this paper, the fatigue behaviour of single lap joints (SLJ) made of S-glass/epoxy substrates was studied. Adhesives with and without glass-bubbles (microspheres) modification were used. Load controlled tensile fatigue tests with stress ratio R of 0.1 were conducted. The specimens were subjected to varying fatigue loadings with the maximum loading level of up to 90 % of the bond shear strength. As expected, the level of reduction on shear strength and stiffness were found to depend on the level of fatigue loading. The observations from the experimental fatigue data and its correlation with failure provide valuable information for better design of composite joints and related components.

24.2 Materials

In this paper, the vacuum assisted resin transfer molding (VARTM) technique was used to manufacture the composite substrates for the lap joints. The reinforcement used for the adherent was S2-glass plain weave fabric (Owens Corning ShieldStrand S) with a real weight of 818 g/m^2. The resin used was a two part toughened epoxy, namely SC-15 (Applied Poleramics Inc., CA). Betamate® 1440 (Dow Automotive, MI) was used as the structural adhesive for bonding. Tensile properties of the adhesive were obtained per ASTM D638 and the samples were manufactured by placing the adhesive in the silicon mold. High strength, low density glass microsphere bubbles (iM16K®, 3 M Inc, MN) were used as reinforcement for the adhesive. The choice of iM16K® was because of its low density and ability to withstand high compressive. The SC-15/glass-fiber adherends were cured in a convection oven at 60 °C for 2 h followed by a post cure of 4 h at 94 °C. The pristine adhesive, glass-bubble modified adhesive and resulting joints were cured in a convection oven at a temperature of 180 °C for 30 min.

24.2.1 Processing of Glass-Bubble Modified Adhesives and Manufacturing of Samples

Two approaches were attempted to homogeneously mix the glass bubbles in the highly viscous Betamate adhesive. The shear mixing method was used with and without the solvent. The solvent 2-Propanol was mixed with the glass bubbles modified adhesive with a weight ratio of 1:2 to reduce the viscosity of the adhesive. After thorough mixing process, the solvent removal was carried by maintaining the temperature of the solution at 80 °C for 1 h followed by 24 h at room temperature. The resulting adhesive was then used for adhesive joint production. Regarding the samples for the adhesive joints, the geometry was according to ASTM D5898 standards. The substrates size was 25 mm × 100 mm and thickness of 4.8 mm. The overlap area was 25 mm by 25 mm. The adhesive thickness was 0.2 mm.

Preliminary experimental test results revealed weak bonding strength which is attributed to the residual solvent, as shown in Fig. 24.1. During the curing cycle of the adhesive joints (180 °C at 30 min.), the residual solvent evaporated creating voids in the adhesive bond-line thereby reducing the joint strength. Based on the aforementioned observations, the experimental testing program in this work used only the shear-mixing of glass-bubbles without the use of a solvent.

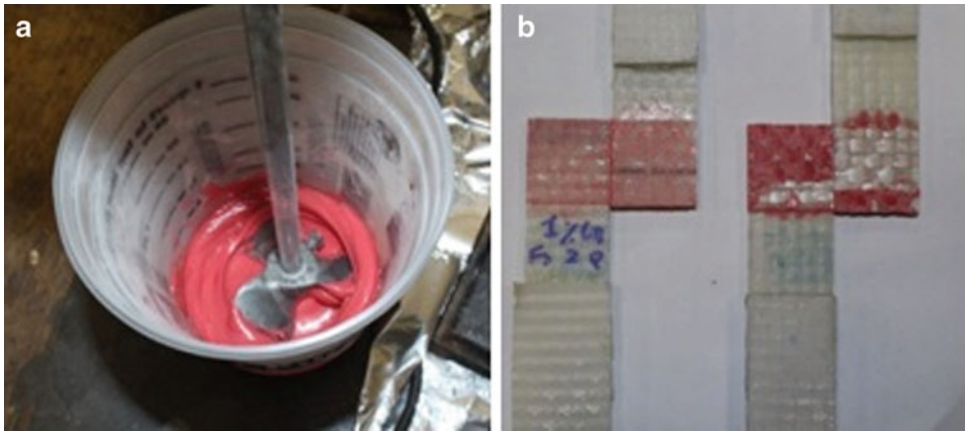

Fig. 24.1 Mixing process of glass bubbles: (**a**) Shear mixing, (**b**) Failure mode glass bubbles modified adhesive joint (*left*: with solvent, *right*: without solvent)

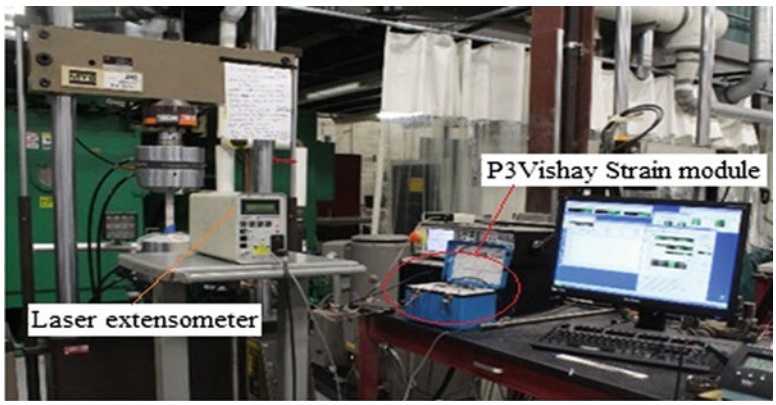

Fig. 24.2 Experimental setup for material characterization and single lap-joint tests

24.3 Experimental Setup

Prior to testing of bonded joints, the tensile properties of GFRP (glass-fiber reinforced plates) adherends and bulk adhesives were experimentally obtained according to ASTM D3039 and D638, respectively. All tests were performed using servo-hydraulic testing machine (MTS 810) and a typical test setup is shown in Fig. 24.2. The machine is equipped with a standard 50 kN load cell and an in-built cross-head displacement measuring device. Additionally, an external laser extensometer was used to accurately measure relative displacements within the sample. Both GFRP and Betamate bulk adhesive specimens were also instrumented by strain gages to measure Young's modulus (Ex) and Poisson's ratio (ν_{xy}). A Vishay Model P3 Strain Indicator and Recorder was used for strain gage data acquisition.

In this work, five tests were carried out for each static test configurations, and three tests were carried out for each fatigue static test configurations. The average shear strength of the joint was calculated by dividing the maximum load of each test divided by the overlap area. The specimen was clamped using hydraulic wedge grips. In the case of GFRP, to eliminate the influence of tab and gripping pressure, the experimental setup was modified based on earlier studies by the authors [9]. As per ASTM D3039, GFRP specimens were subjected to monotonic tensile loading with a stroke rate of 2 mm/min. The static behavior of the joints was investigated by tensile-(lap-shear) tests as per ASTM D5898 standards. The fatigue tests were carried out under load control, with sinusoidal wave, frequency of 10 Hz, load ratio $R = 0.1$, and data recording rate of 100/s.

To plot the S-N curve of the adhesive joint, the experimental fatigue testing was carried out at various load levels, namely, 90 %, 75 %, 60 %, and 45 % of the static shear strength of adhesively bonded joint. Fatigue tests were run continuously up to 10^6 cycles for 45 % load level, whereas for 60 %, 75 % and 90 % load levels, the tests were performed until failure. For 45 % load level, after the fatigue tests were stopped, tensile tests were run on the pre-cycled specimens to measure the joint residual shear strength and stiffness. Test procedure for measurement of the residual properties was the same as that for measurement of the ultimate properties on virgin specimens.

24.4 Result and Discussion

24.4.1 Tensile Test

The tensile properties of adhesive (pristine and glass-bubble modified) and glass-fiber reinforced plastics (GFRP, S-glass/epoxy) are shown in Tables 24.1 and 24.2, respectively. As it can be been seen in Table 24.1, inclusion of 1 wt.% of GB has slightly detrimental effects on the tensile strength and modulus of elasticity of the adhesive. Similarly, the Poisson's ratio of glass bubble (GB) modified adhesive exhibited higher value relative to pristine adhesive. This is attributed to the morphology, spherical shape of the GB. While fillers with higher aspect ratios such as nanoclay have been found to introduce a reinforcement effect, thereby increasing the tensile strengths and modulus at lower concentrations, similar effect was not observed with GB.

Representative tensile behavior of pristine and GB modified adhesives are illustrated in Fig. 24.3. For pristine adhesive, the non-linear portion of the curve covers approximately 91.4 % of the total strain, while in the case of the GB modified adhesive it covers about 83.7 % of the total strain. It is clearly evident from the figure that the total strain of GB modified adhesive is less than that of pristine adhesive's total strain, approximately by 26.9 %, at expense of mainly the tensile strength. Hence, for a joint that requires dimensional stability at relatively high load level, GB fillers can significantly reduce the plastic strain, which is the major part of total strain in viscoelastic materials.

24.4.2 Single-Lap Joint Static Tests

Prior to fatigue tests, quasi-static, tensile-shear tests were performed on pristine (unmodified) and GB modified SLJs. Figure 24.4 shows a comparison of the tensile tests for pristine and GB modified SLJs. Unlike quasi-static tensile tests of bulk adhesives, the static tensile-shear strength of GB modified SLJs seems to be significantly better than that of the pristine SLJs. Specifically, the lap-shear strengths of GB modified SLJs was found to be 9.30 ± 0.38 kN relative to 8.80 ± 0.17 kN for pristine SLJ.

Table 24.1 Materials properties of adhesives

Adhesive	Max. tensile stress (MPa)	E (GPa)	ν
Pristine adhesive (Betamate)	41.51	2.45	0.407
1 % GB Adhesive	39.42	2.38	0.438

Table 24.2 Material properties of substrate

Composite	Weave type	Fiber fraction (wt%)	Tensile strength (MPa)	E_x(Gpa)	G_{xy}(Gpa)	ν_{xy}
0/90S-Glass/Epoxy	Plain	0.61	476.264	23.18	4.0	0.08

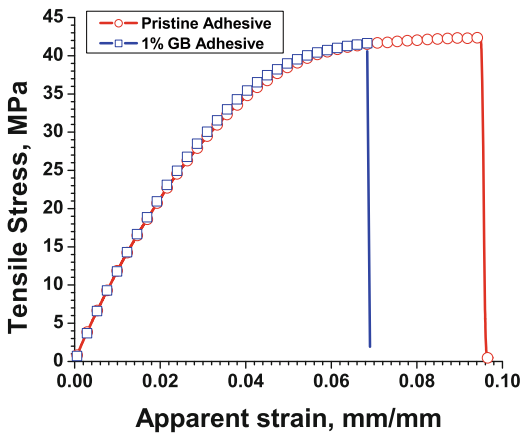

Fig. 24.3 Tensile stress-strain curves of adhesive materials

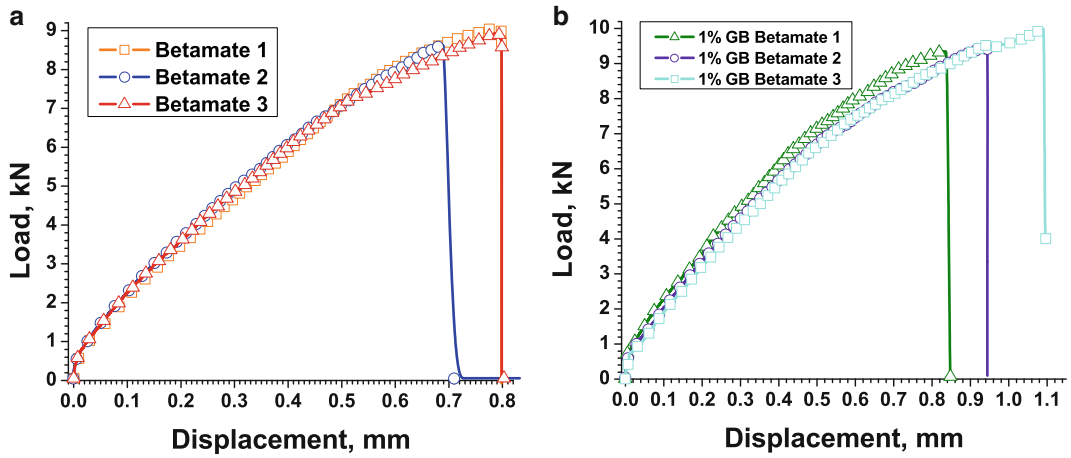

Fig. 24.4 Tensile strength of SLJ: (**a**) Pristine SLJs; (**b**) 1 % GB SLJs

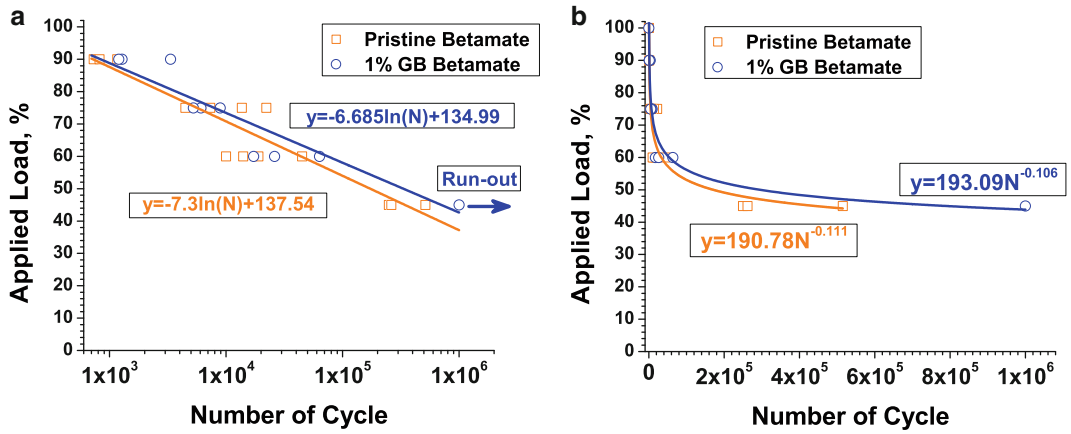

Fig. 24.5 S-N curves: (**a**) Linear scale, and (**b**) logarithmic scale

24.4.3 Fatigue Tests

The results of fatigue tests for both pristine and GB modified SLJs are presented in the form of S-N (stress versus number of cycles) diagrams in Fig. 24.5a, b. Figure 24.5a presents the median curves for both SLJs configurations. As it can be observed, the median curve of GB modified SLJs translated to the right, which implies better performance of fatigue life for the same load percentage of ultimate failure load (UFL) relative to pristine SLJs. This result indicates that as the applied load level decreases, i.e., 45 % of UFL, the fatigue life of adhesive joint is categorized as under the endurance limit of the joint, which exhibits continuous longer life. In this paper, the lowest applied load level was restricted at 45 % of UFL. Hence, found results showed that only GB modified SLJs exhibited run-out data.

Figure 24.5b shows standard S-N curves for both pristine and GB modified SLJs. In the figure, each load level in the S-N graph is represented by at least three experimentally tested specimens. The Fig. 24.5b can be used to predict the endurance limit of pristine and GB modified SLJs. When the fatigue loading is 30–35 % for pristine SLJs, and 45 % for GB modified SLJs, the number of cycles becomes greater or equal to 10^6.

In Fig. 24.6, standard S-N curves of pristine and 1 % GB modified SLJs are presented. As it can be observed that for a given number of cycles, GB modified SLJs have better performance with a greater maximum amplitude stress than that of the pristine SLJs. For a given stress ratio of R = 0.1, the life of pristine and GB modified SLJs can be predicted using Eq. (24.1).

$$\sigma = a * logN + b \tag{24.1}$$

$$N = 10^{(\sigma - b)a} \tag{24.2}$$

where a and b are constants obtained experimentally as shown in Fig. 24.6 and N is number of cycles.

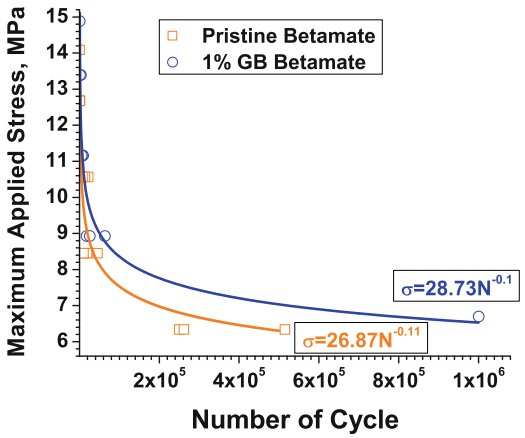

Fig. 24.6 Stress-versus number of cycles diagrams of pristine and 1 % GB modified SLJs

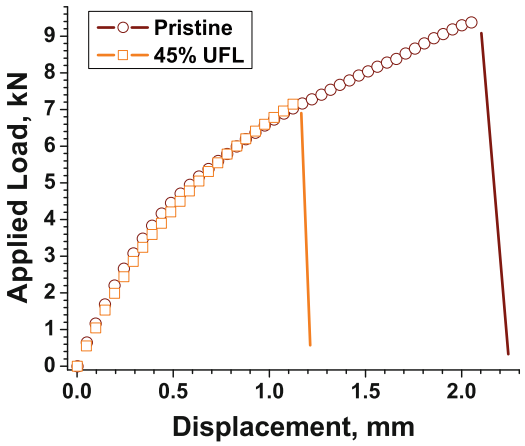

Fig. 24.7 Load-displacement diagram of as-fabricated and pre-cycled 1 % GB SLJ at one million cycles

For GB modified SLJs, which were subjected to 45 % of UFL, the fatigue tests were interrupted at one million cycles and quasi-static tensile-shear tests were performed to obtain the residual strength. Figure 24.7 provides the tensile-shear test comparison of as-fabricated (pristine) and fatigued (one-million cycle at 45 % UFL) specimens. As expected, the pre-cycled specimens showed considerable strength reduction, in this particular case by 21.49 %. Overall, the use of glass-bubble modified adhesive joints showed enhanced fatigue performance relative to their pristine counterparts. Nevertheless, a detailed study taking into account all the parameters including the variation in concentrations of glass-bubbles, chemical functionalization and statistically significant experimental testing is essential to fully exploit the benefits offered by these materials.

24.5 Conclusion

In this work, the static and fatigue behavior of pristine and micro glass-bubbles (GB) modified adhesives on single lap-joints (SLJ) were investigated. The results are briefly summarized as follows:

- GBs (1 wt.%) had a slight detrimental effect on the tensile modulus (3 %) and strength (5 %) of the bulk adhesive used.
- Conversely, SLJs with GB modified adhesive had higher tensile-shear strengths of 5.7 % relative to pristine adhesive joints.
- Generally, GB modified SLJs exhibited better fatigue performance relative to pristine SLJs.
- At 45 % of ultimate failure load (UFL), only GB modified SLJs sustained the load up to one million cycles.
- Quasi-static tensile-shear test results of pre-cycled (1 million cycles) GB modified SLJs revealed that the residual strength was approximately 78.5 % of the as-fabricated (pristine) joints.

Generally, the observations from the experimental static and fatigue data and their correlations with failure could provide valuable information for better design of innovative composite joints and their related components in automotive applications. Besides, filler materials, such as GBs, could play a significant role in improving the fatigue life of joints and allows introducing a concept of light-weighting of adhesive joints in vehicle design. Overall, the work shows great promise in use of novel fillers, but considerable care and detailed experimental characterization are essential to fully exploit the benefits these materials have to offer.

Acknowledgements This work was supported by US Army under TACOM/MSU Cooperative Agreement No. W56HZV-07-2-0007. The authors also acknowledge the in-kind material contribution (iM16K®) by 3 M Center, MN.

References

1. Mactabi R, Rosca ID, Hoa SV (2013) Monitoring the integrity of Adhesive during fatigue loading using carbon nanotube. Compos Sci Technol 78:1–9
2. Kahraman R, Sunar M, Yilbas B (2008) Influence of adhesive thickness and filler content on the mechanical performance of aluminum single-lap joint bonded with aluminum powder filer epoxy adhesive. J Mater Process Technol 205(1–3):183–9
3. Pereira AM, Ferreira JM, Antunes FV, Bartolo PJ (2009) Study on the fatigue strength of AA 6082-T6 adhesive lap joints. Int J Adhesion Adhesives 29(6):633–8
4. Wahab MMA (2012) Fatigue in adhesive bonded joints: a reviews. ISRN material Science 2012; Article ID 746308
5. Renton WJ, Vinson JR (1975) Fatigue behavior of bonded joints in composite structures. J Aircraft 12(5):442–7
6. Kreiger RB (1979) Fatigue testing of structural adhesives. SAMPE Proc 24(1):1102–25
7. Srivastava VK (2011) Effect of carbon nanotubes on the strength of adhesive lap joints of C/C and C/C-SiC ceramic fiber composites. Int J Adhesion Adhesives 31:486–9
8. Vega A, Kinloch IA, Young RJ, Bauhofer W, Schulte K (2011) Simultaneous global and local strain sensing in SWCNT-epoxy composites by Raman and impedance spectroscopy. Compos Sci Technol 71:160–6
9. Belingardi G, Paolino DS, Koricho EG (2011) Investigation of influence of tab types on tensile strength of E-glass/epoxy fiber reinforced composite materials. Proceedia Engineering (ICM11) 10; 3279–3284

Chapter 25
Experimental Observations of Dynamic Delamination in Curved [0] and [0/90] Composite Laminates

I. Uyar, M.A. Arca, B. Gozluklu, and D. Coker

Abstract Curved composite parts are increasingly replacing metal ribs and box structures in recent civil aerospace structures and wind turbine blades. Delamination of L-shaped composite laminates occurs by interlaminar opening stresses in addition to the interlaminar shear stresses at the curved region. An experimental setup is designed to investigate dynamic delamination in L-shaped composite brackets under quasi static shear loading. The materials are unidirectional $[0]_{17}$and cross-ply $[0/90]_{17}$ epoxy/graphite composite laminates. The load displacement curves are recorded and subsequent dynamic delamination is captured with a million fps high speed camera. The failed specimens are analyzed under a microscope. It is seen that layup differences change the failure mechanism in composites. Multiple delaminations in one load drop are observed in failure of unidirectional laminate whereas sequential delamination at each discrete load drop is seen in cross ply laminates. In the [0] laminate single delamination in the center ply followed by symmetric delamination nucleations around the two crack tips are observed. In the 0/90 cross-ply laminate, multiple load drops are recorded and delaminations start near the inner radius by peeling of 0/90 plies sequentially at each load drop. In both layups, first time observation of intersonic delamination speeds up to 2,200 m/s are made.

Keywords Delamination • Curved composite laminates • Dynamic crack growth • High-speed camera

25.1 Introduction

Composite materials are preferred for both aerospace and wind turbine industries due to their high stiffness and low weight. Replacing the metallic structures with composites is an increasing demand in both industries especially for load carrying members of the structure like L-shaped beams. Although external loads are the same, the material response and fracture modes are highly different due to the anisotropic behavior of composites. When external loads on a wing structure is investigated, the loading in a typical L-shaped beams can be reduced to three simple loading cases namely, axial load which is parallel to the arm (P), shear load which is perpendicular to the arm (V), and the moment (M) (shown in (Fig. 25.1a). These external loads cause delamination in the composite laminates in the curved region because of the low through-the-thickness strengths of composites. This paper contains the results of our experimental investigation on delamination of L-shaped composite laminates subjected to shear loading.

The delamination failure in L-shaped composite laminates under perpendicular loading to the arm was investigated in the past. In the 1990s, Martin et al. [1, 2] determined numerically the location of highest radial stress in curved region where

I. Uyar • M.A. Arca
Department of Aerospace Engineering, Middle East Technical University, 06800 Ankara, Turkey

B. Gozluklu
Department of Aerospace Engineering, Middle East Technical University, 06800 Ankara, Turkey

Helicopter Group, Turkish Aerospace Industries (TAI), 06980 Ankara, Turkey

D. Coker (✉)
Department of Aerospace Engineering, Middle East Technical University, 06800 Ankara, Turkey

METU Center for Wind Energy, Middle East Technical University, 06800 Ankara, Turkey
e-mail: coker@metu.edu.tr

J. Carroll and S. Daly (eds.), *Fracture, Fatigue, Failure, and Damage Evolution, Volume 5: Proceedings of the 2014 Annual Conference on Experimental and Applied Mechanics*, Conference Proceedings of the Society for Experimental Mechanics Series,
DOI 10.1007/978-3-319-06977-7_25,

delamination is assumed to initiate. They showed that delamination propagates in to the arms of the laminate predominantly in opening mode using energy release rate analysis. In their experimental work, delamination growth was found to be unstable but the growth of delamination was not captured. In 2000s, Wimmer et al. [3] studied the same problem. Their computational models using VCCT showed unstable crack growth for the case without any initial crack and a stable crack growth for a 3-mm pre-crack. In their experimental work they showed that instantaneous load drop in load displacement curve occurred during crack propagation. Feih and Shercliff (2005) [4] also investigated the failure of L-shaped composite laminates positioned between a composite base and vertical rib for shear loading perpendicular to arm. The finite element model was carried out on ABAQUS with UMAT subroutines combined with Hashin's failure criteria for matrix and fiber cracking and with Tong-Norris delamination onset criterion. They outlined the failure sequence and compared the surface strains with results obtained from strain gages. Gozluklu and Coker (2012) [5] carried out explicit finite element analysis with cohesive elements to model delamination in composite L-beams subjected to parallel loading instead of perpendicular loading. In their simulations they showed that during the unstable crack growth that occurs during a single load drop, the crack tip speed reaches the shear wave speed of the composite laminate.

The objective of this study is to investigate the effect of lay-up on delamination process for unidirectional and cross-ply lay-ups. Experiments were carried out on L-beams subjected to quasi-static loading shear loading (V) in conjunction with high speed camera system. Load displacement plots, delamination process and speeds were compared.

25.2 Experimental Method

L-shaped composite specimens used in experiments were manufactured by hand lay-up technique. For $[0]_{17}$ and $[90/0]_{17}$ specimens HexPly® AS4/8552 UD carbon pre-pregs having 0.18 mm cured thicknesses are laid up using right angled male tool. The dimensions of the composite specimens used in experiments are tabulated in Fig. 25.1b. In Table 25.1, the lamina properties for pre-pregs and in Table 25.2, engineering constants for the laminate which are calculated using with classical lamination theory are tabulated.

Shimadzu Autograph AGS-J series 10 kN screw-driven displacement controlled tensile-compression testing machine was used in experiments. In these tests the effect of machine compliance may be neglected. All tests are conducted at a cross-head speed of 3 mm/min at the room temperature. The fixture was designed to create a displacement load perpendicular to the

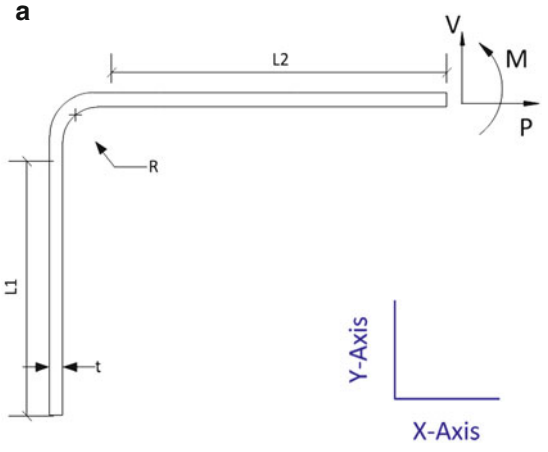

b

	$[0]_{17}$	$[0/90]_{17}$
L_1 (mm)	90	90
L_1 (mm)	150	150
R (mm)	10	10
t (mm)	3.13	3.13
w (mm)	30	30

Fig. 25.1 (**a**) Loads applied on L-beam structure and the symbols of dimensions (**b**) Dimensions of composite specimen

Table 25.1 Lamina properties [6]

	E_1 (GPa)	$E_2 = E_3$ (GPa)	$G_{12} = G_{13}$ (GPa)	ν	Ply thickness (mm)	Density (g/cm^3)	Nominal fiber volume (%)
AS4/8552 UD	135.0	8.5	4.2	0.29	0.184	1.59	57.42

Table 25.2 Laminate properties

	E_x (GPa)	E_y (GPa)	G_{xy} (GPa)	ν_{xy}	ν_{yx}
$[0]_{17}$	135.0	8.5	2.8	0.35	0.02
$[0/90]_{17}$	68.5	75.9	2.8	0.04	0.04

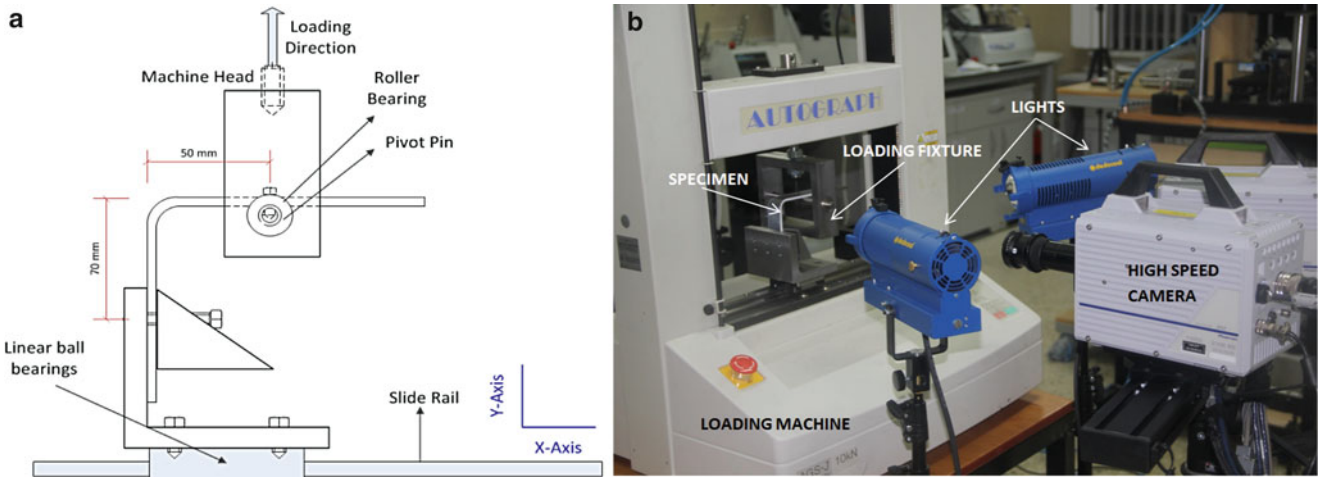

Fig. 25.2 (**a**) Loading Fixture for perpendicular loading of the arm; (**b**) Experimental setup showing Photron SA5 high speed camera and specimen after failure

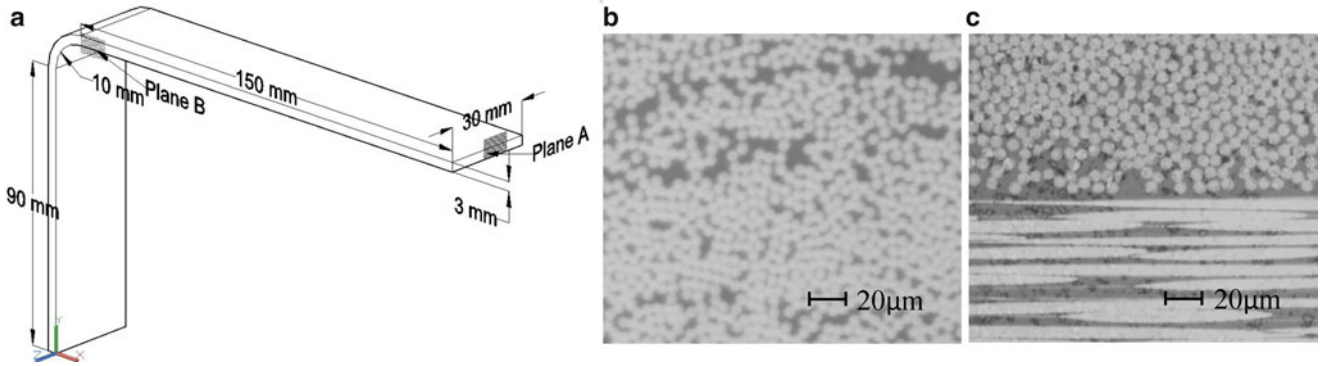

Fig. 25.3 (**a**) Cross section planes A and B for microscopic analysis (**b**) Optical micrographs of composite specimens showing cross sectional distribution of fibers and epoxy matrix for (**b**) $[0]_{17}$with ×100 magnification, (**c**) $[90/0]_{17}$ with ×100 magnification

upper arm. By using a pivot pin bearing system which is free to rotate, the applied load remains parallel to the lower arm during the experiment. The specimen is bolted to the pivot pin to fix the loading arm with respect to the corner of the L-beam. The lower arm of the specimen is clamped and bolted to the fixture. Lower fixture is mounted on a linear motion bearing system to give smooth precision motion along the x-axis that removes the reaction force along the x-axis at the upper arm. In Fig. 25.2a, the drawing of the fixture and Fig. 25.2b, the experimental setup is shown.

In this study, $[0]_{17}$ and $[(90/0)_4, \overline{90}]_s$ specimens were tested under perpendicular loading as discussed above and the delamination initiation and propagation was captured with high speed camera system. By using the high speed camera pictures the crack length and crack speeds were calculated. The shear wave speed calculation was conducted by following the steps described in [7]. After calculating the laminate properties for both lay-ups, the stiffness matrices are obtained. $[0]_{17}$ laminate is assumed to be transversely isotropic and [90/0] cross-ply laminate is assumed to be orthotropic. The relations between wave speeds and stiffness components as follow [7],

$$c_l^{\parallel} = \left(\frac{c_{11}}{\rho}\right)^{1/2}, \quad c_l = \left(\frac{c_{22}}{\rho}\right)^{1/2}, \quad c_s = \left(\frac{c_{66}}{\rho}\right)^{1/2}$$

where $\mathbf{c_l^{\parallel}}$ denotes the dilatational wave speed parallel to fibers while $\mathbf{c_l}^{\perp}$ denotes the dilatational wave speed perpendicular to the fibers, $\mathbf{c_s}$ is the shear wave speed and $\boldsymbol{\rho}$ is density. For the Rayleigh wave speed calculation, the same steps in [7] were followed.

The specimen was cut through the width direction (Plane A) with a diamond saw cutter and prepared for microscopic analysis. In Fig. 25.3b, c, optical micrographs are showing cross sectional distribution of carbon fibers in the epoxy matrix for the [0] and [90] laminate, respectively.

25.3 Results

25.3.1 Unidirectional $[0]_{17}$ Lay-up

In this study, the general behavior of delamination and the effect of lay-up on failure mechanisms are discussed. The load-displacement curves of three different $[0]_{17}$ experiments under quasi-static shear loading are shown in Fig. 25.4. After a linear elastic loading behavior, a load drop occurs at failure with the load dropping to less than 15 % of the maximum value. An instant high level breaking sound was heard during load drop. After the crack propagation ends, the multiple delaminations were observed post-mortem. After the load drop, the specimen lost all its load carrying capacity. In Fig. 25.4, the loading stiffness shows a large variation.

In Fig. 25.5, the high speed camera images of Specimen 1 captured during delamination initiation and propagation are shown. The time interval between two pictures is 1.613 μs, and the total time for process is approximately 20 μs. There are several observations as a result of high speed monitoring. An initial crack occurs in the mid-part of the curved region (Fig. 25.5a). After the initial crack grows to 8.6 mm, four symmetric delaminations (Fig. 25.5c) start simultaneously and place symmetric with respect to the crack tips. These symmetric cracks merge and propagate together through the arms and also small crack branches occur near the big cracks (Fig. 25.5e). In the final picture of failure, there are multiple delaminations observed from inner radius to outer radius which explains the loss in load carrying capacity.

The right crack tip location as a function of time was determined from high speed pictures starting from the nucleation point (Fig. 25.6a). The average crack tip speeds are calculated using backward difference method. In Fig. 25.6b, the right crack tip speed is shown together with material wave speeds (the shear wave speed (C_s), Rayleigh wave speed (C_R) and dilatational wave speeds parallel and perpendicular to the fiber directions ($C_I^{||}$, $C_I^{\perp}$)). The first calculated speed (1,033 m/s) is already near the Rayleigh wave speed of the material (1,224 m/s) and then reaches intersonic speed (2,401 m/s) as the crack tip as under mixed-mode loading as discussed in [7].

25.3.2 Cross-ply $[(90/0)_4, \overline{90}]_s$ Lay-up

The same experimental procedure was conducted for [90/0] cross-ply oriented laminates. In Fig. 25.7, the load-displacement curves of three different specimens are seen; there are three or four sudden load drops with each load drop corresponding to delamination initiation and propagation. When the failed composite specimens were reloaded, they continued carrying applied load at a slightly lower stiffness. In Fig. 25.4, [0] laminates can carry up to 1,300 N, while the maximum load of [90/0] cross ply laminate is 745 N (Fig. 25.7). The difference between maximum loads can be explained with the difference between longitudinal modulus of composite laminate as is tabulated in Table 25.2 which makes the laminate stronger in longitudinal direction. Therefore, $[0]_{17}$ laminate is stronger than the $[90/0]_{17}$ along the loading direction until initiation of delamination. After reloading of the [90/0] cross ply specimen, the load increases to 75 % or more of the initial maximum load before the next load drop occurs. The load carrying capacity is preserved albeit with a lower stiffness value for 3 or more load-drops until the experiment is ended.

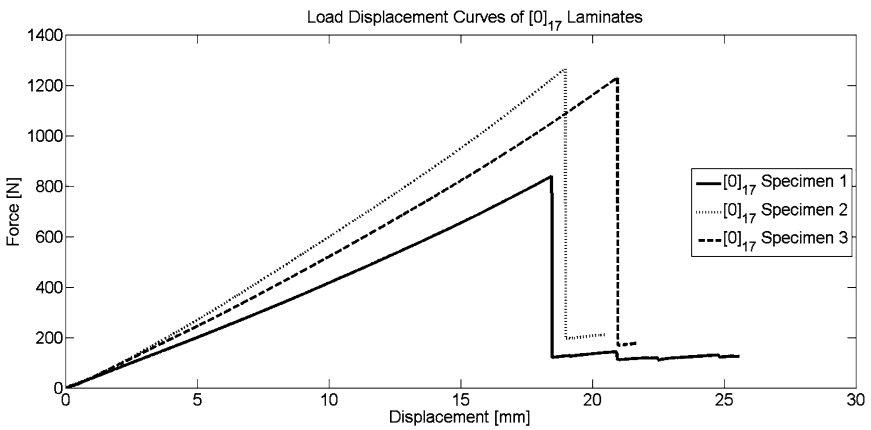

Fig. 25.4 $[0]_{17}$ specimen load displacement curve under perpendicular loading

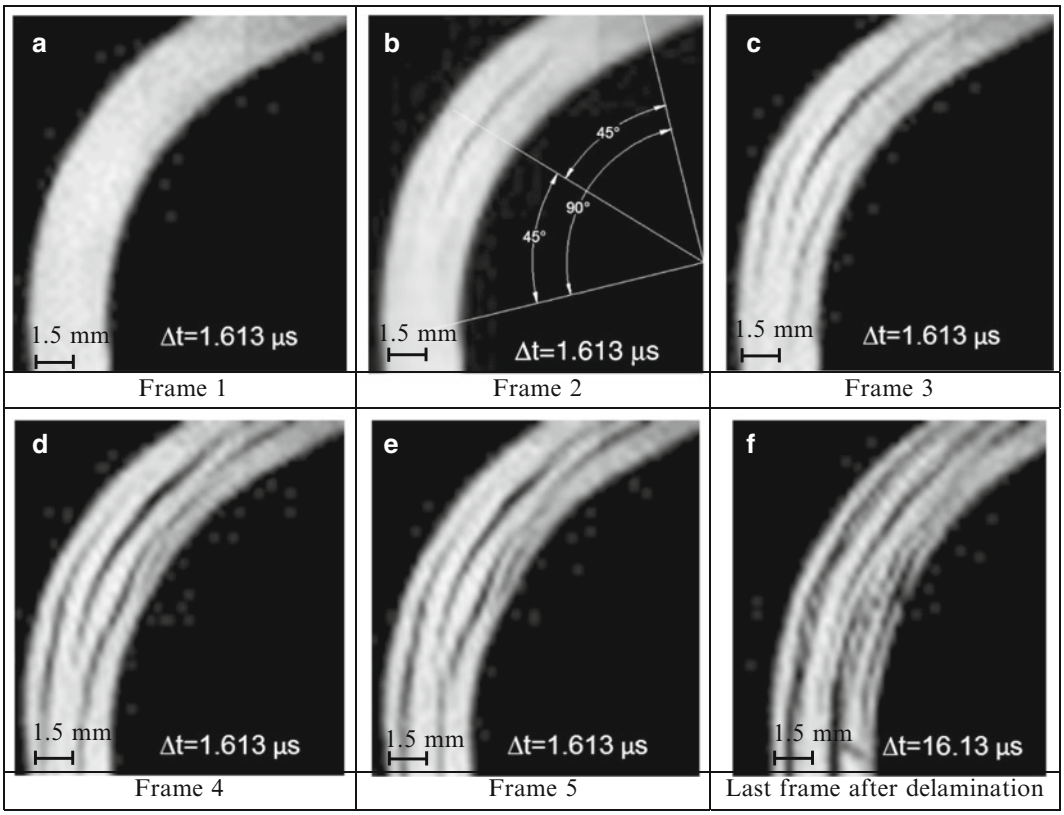

Fig. 25.5 High speed images of Specimen 1 taken at 620,000 fps with 1.613 μs time increment

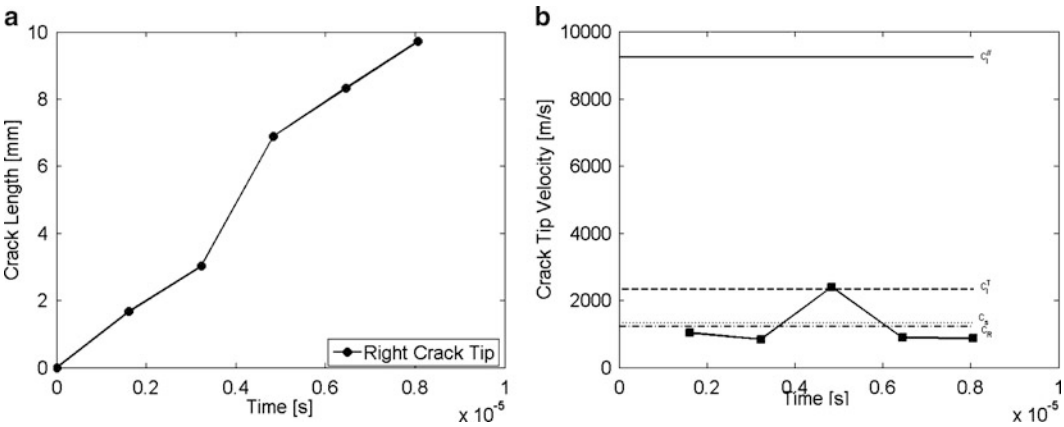

Fig. 25.6 (**a**) The right crack tip progress during delamination propagation. (**b**) Crack tip speed history for initial crack of $[0]_{17}$ specimen subjected to shear loading

The high-speed camera results for Specimen 3 taken at 465,000 fps show the details of the delamination failure during the sudden load drops. In this case, each single delamination corresponds to a single load drop. In Fig. 25.8a, a single delamination occurs in the inner part of the curved region between third and fourth layers of the laminate and propagates all the way through until the end of first load drop. After the first load drop, as the specimen is loaded a second delamination occurs when the load reaches 435 N Fig. 25.8b albeit with a lower stiffness. Upon further loading the stiffness of the specimen slightly decreases and the specimen can still carry load up to 430 N before the third and fourth delamination occurs Fig. 25.8c. Delaminations start near the inner radius by peeling of 0/90 plies sequentially at each load drop. The crack nucleation angle was calculated to be 13° from the middle of the curved region (Fig. 25.8a Frame2). Unlike the $[0]_{17}$ laminate, the crack initiation point is not symmetric with respect to both arms.

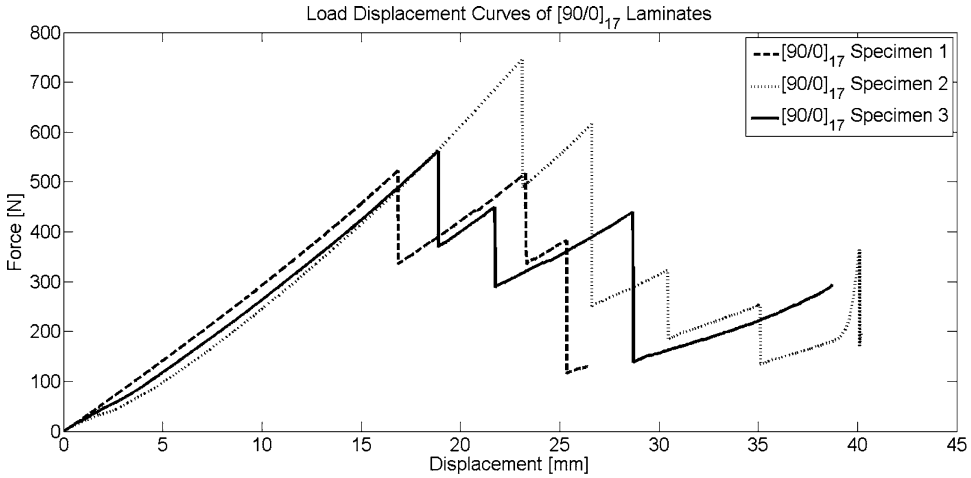

Fig. 25.7 Load displacement of $[90/0]_{17}$ specimens curve under perpendicular loading

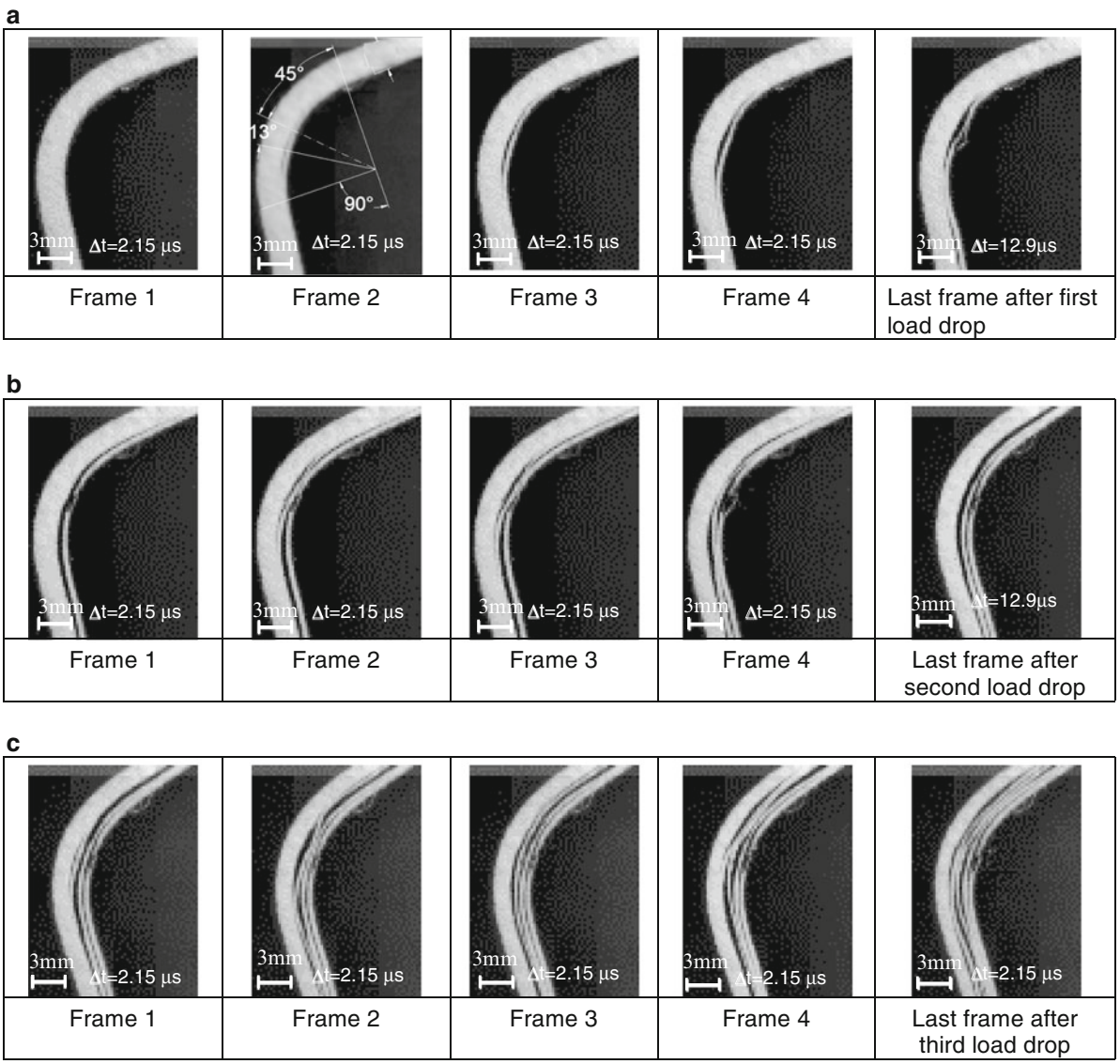

Fig. 25.8 [90/0] cross-ply progressive damage pictures taken at 465,000 fps (**a**) first load drop (**b**) second load drop (**c**) third load drop

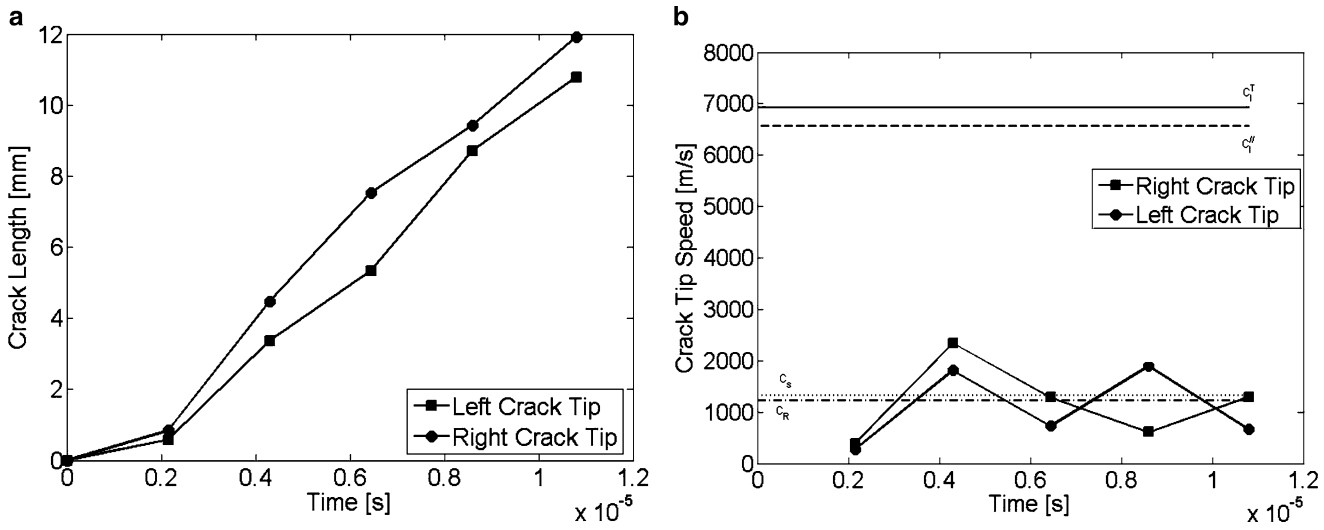

Fig. 25.9 (**a**) The right and left crack tip progress during delamination propagation (**b**) Crack tip speed history for initial crack of $[90/0]_{17}$ specimen under perpendicular loading

From the first five pictures of delamination process the crack tip positions and crack tip speeds are calculated with respect to the crack initiation point shown in Fig. 25.9a, b. The right and left crack tip locations as a function of time was determined (Fig. 25.9a). The crack propagation rate is approximately the same for both crack tips. With the crack initiation point taken as the crack origin, the crack tip speeds are separated as right and left crack tip speeds with respect to this origin. The crack tip speeds were calculated using backward difference method and is plotted in Fig. 25.9b.

In Fig. 25.9b, the crack tip speeds are shown together with the material wave speeds (the shear wave speed (C_s), Rayleigh wave speed (C_R) and dilatational wave speeds parallel and perpendicular to the fiber directions ($C_I^{||}$, $C_I^{\perp}$)). The first calculated speeds (391 m/s and 270 m/s) are smaller than the Rayleigh wave speed of the material (1,224 m/s). However, the following points exceed the Rayleigh wave speed with the crack tip speeds reaching intersonic speeds of 2,340 and 1,810 m/s. The fracture mode near the crack tip is mixed-mode as discussed in [7].

25.4 Conclusions

Dynamic delamination of L-shaped composite brackets with [0] and [90/0] layups were investigated. Experiments were conducted in which L-shaped brackets were subjected to quasi-static shear loading and subsequent dynamic delamination was captured with a million fps high speed camera. In addition the load displacement curves were also recorded. The major conclusions were as follows;

1. Delamination initiation mechanism was different between two plies. In the [0] laminate, crack initiates near the center ply followed by two cracks nucleated symmetrically near each tip of the original crack. In the [90] laminate, sequential delaminations occur from the inner part to the outer part of the laminate.
2. In the [0] laminate, there is single load drop were the structure loses most of its load carrying capacity. In the [90/0] ply three smaller load drops until losing all their load carrying capacity.
3. In the [0] all delaminations occur in a single load drop. In the [90/0] laminate one or two delaminations occurred at each load drop.
4. After the load drop in the [0], the load carrying capacity reduces to one tenth of its initial value whereas in a [90/0] plies small decreases are observed after each load drop.
5. In both cases the crack tip speeds vary from sub-Rayleigh speeds of 900 m/s to intersonic speeds of 2,200 m/s.
6. Finally the micrographs showed that [0] laminate has interlaminar cracks whereas in the [90/0] the delamination occurs between the interface of 90° and 0° plies.

References

1. Martin RH, Jackson WC (1991) Damage prediction in cross-plied curved composite laminates, NASA Technical Memorandum 104089, USAAVSCOM Technical Report 91-B-009
2. Martin RH (1992) Delamination failure in a unidirectional curved composite laminate. Compos Mater Test 10:365–83
3. Wimmer G, Kitzmüller W, Pinter G, Wettermann T, Pettermann HE (2009) Computational and experimental investigation of delamination in L-shaped laminated composite components. Eng Fract Mech 76:2810–2820
4. Feih S, Shercliff HR (2005) Composite failure prediction of single-L joint structures under bending. Composites A 36:381–395
5. Gozluklu B, Coker D (2012) Modeling of the dynamic delamination of L-shaped unidirectional laminated composites. Compos Struct 94: 1430–1442
6. AS4/8552 Product Data Retrieved from: http://www.hexcel.com/Resources/DataSheets/Prepreg-Data-Sheets/8552_eu.pdf
7. Coker D, Rosakis AJ (2001) Experimental observations of intersonic crack growth in asymmetrically loaded unidirectional composite plates. Philos Mag A 81(3):571–595

Chapter 26
Fatigue Failure of Polyethylene Electrofusion Joints Subject to Contamination

Pedrom Tayefi, Stephen. B.M. Beck, and Rachel A. Tomlinson

Abstract In the UK, water companies renew their aging water network using novel techniques and robust materials. The most common type of material used for network rehabilitation is Polyethylene (PE) pipe. A common method of jointing PE pipe is electrofusion welding. Here, electricity is used to heat a coil that melts the fitting and the host pipe of the same material. When the joint cools it forms a bond. However, premature failure of these can occur if best practice installation principles are not followed on site.

A novel experimental rig, designed to be retrofitted to an existing servo-hydraulic fatigue testing machine, has been used to cyclically pressurise PE fittings that have been created with a controlled element of 'poor workmanship'. Extensive fatigue tests have shown the relationship between joint failure and the dynamic pressures experienced in water distribution systems. Furthermore, the effects of poor workmanship have shown to have a detrimental effect on asset integrity.

A post-failure analysis of the fittings using non-destructive ultra-sonic methods has shown the failure paths of the fittings. Additionally, a bespoke ultra-sonic rig was designed and built to monitor the crack propagation of the fittings during live dynamic tests to confirm the mode of failure.

Keywords Polyethylene pipe • Electrofusion • Fatigue • Ultrasonic analysis

26.1 Introduction

Polyethylene (PE) has been used in the water industry since the early 1950s [1]. With the improvement of industry standards, the products developed from low density PE (LDPE) to today's high density PE (HDPE). This meant a more reliable and robust material was used in the industry which had a better resistance to crack growth than its predecessor, PVCu [2]. Today, the preferred material of choice for rehabilitating aging pipework is polyethylene (PE) pipe [3].

Two ways in which PE pipes are joined together are known as butt fusion and electrofusion (EF) welding. Buttfusion welding usually takes place above ground as the equipment used to join the pipes is quite large; whereas EF welding can be performed in smaller spaces such as trenches. Regardless of the welding method, in the UK a particular procedure highlighted in Water Industry Standard (WIS) 4-32-08 [4] should be followed to reduce the risks of premature failure due to poor installation. With regards to PE failures within the water industry, Trew & Mills [5] found a UK national failure rate of 8 failures per 100 km per year between 2005 and 2009.

A coupler can be used to EF weld two pipes together. However, to connect the host main to the end user, a service connection is usually used: these are known as tapping tees (See Fig. 26.1). To create an EF weld, the pipe surface needs to be scraped to remove the oxidised layer as well as being free from contaminants. Electricity can then be passed through the filament wire to heat the polymer of the host pipe and the fitting. Once a target heating time is reached, the fitting is required to cool and here the bond is formed. Pipes are typically pressure tested post-installation using water to check for leakage.

P. Tayefi • S.B.M. Beck • R.A. Tomlinson (✉)
Department of Mechanical Engineering, University of Sheffield, Mappin St., Sheffield S1 3JD, UK
e-mail: r.a.tomlinson@sheffield.ac.uk

J. Carroll and S. Daly (eds.), *Fracture, Fatigue, Failure, and Damage Evolution, Volume 5: Proceedings of the 2014 Annual Conference on Experimental and Applied Mechanics*, Conference Proceedings of the Society for Experimental Mechanics Series,
DOI 10.1007/978-3-319-06977-7_26,

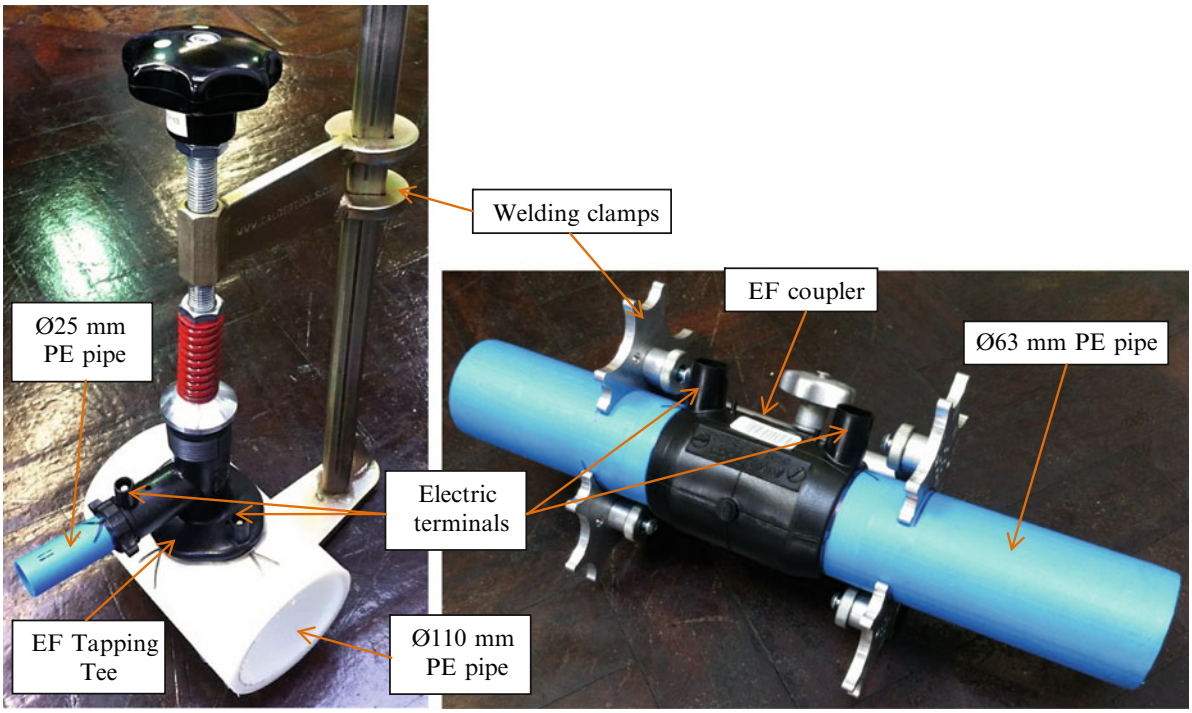

Fig. 26.1 Typical EF tapping tee (*left*) and coupler (*right*)

Research has shown that premature failures of EF joints in service can occur if the correct procedures are not followed, with the main causes of failure being poor scraping, misalignments and contamination [3, 6, 7]. Scraping of the pipe and correctly aligning the joint assembly can arguably be overcome by the implementation of appropriate tooling and training. However, contamination is an environmental issue that may be harder to overcome.

A surge can be defined as the fluctuation in pressure that occurs in a relatively short space of time [8]. With regards to water distribution networks, surges can occur with the opening and closing of valves as well as the starting and stopping of pumping stations [9]. Fatigue can be described as the loss of strength as a result of repeated loading over a period of time [10]. Bowman [11] explains that pipe systems may be subject to two types of 'fatigue': firstly, a diurnal fatigue by which the demand on the network causes fluctuations in pressure; secondly, the operation of pumps and valves changing pressures.

An experiment was designed to observe the fatigue performance of incorrectly installed EF joints. More specifically, EF tapping tees were subject to a talc particulate contaminant and tested under dynamic load.

26.2 Fatigue Experiment

An experimental hydraulic rig was designed and built at the University of Sheffield to be retrofitted onto an existing servo-hydraulic machine. The rig was designed to house two tests; (1) a short term burst test specified in WIS 4-32-08 [4] and (2) a dynamic (fatigue) test. The aim of the latter experiment was to observe the fatigue-life performance of EF tapping tees that have been subject to a talc contamination prior to welding. Talc is used as it replicates 'dirt' which could contaminate the weld. The fittings were identical products purchased off-the-shelf and the pipe was provided by a single manufacturer.

The fatigue test followed a trapezoidal loading pattern with a fixed mean pressure. The mean was calculated as half of the average failure pressure of five specimens tested to the aforementioned short term burst test. The pressure ranges for the trapezoidal loading regime was deduced as a percentage factor of the average failure pressure from the short term burst test. For details refer to [12].

The results from the experiment are shown in Fig. 26.2.

Figure 26.2 suggests that as the pressure range is decreased, the spread of results becomes greater. Therefore the predictability of the number of cycles to failure becomes more difficult. Furthermore, at the lowest testing pressure range, 40 % $P_{mat,\,max}$, shows results that exceed 1,000 cycles which may suggest that there is a fatigue limit to this testing programme.

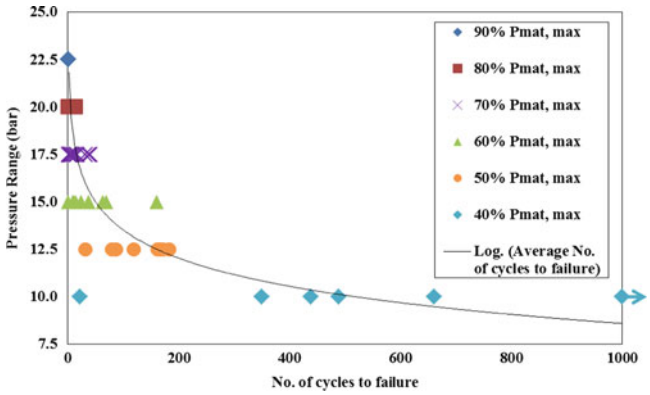

Fig. 26.2 Pressure range vs. number of cycles to failure for the fatigue test [12]

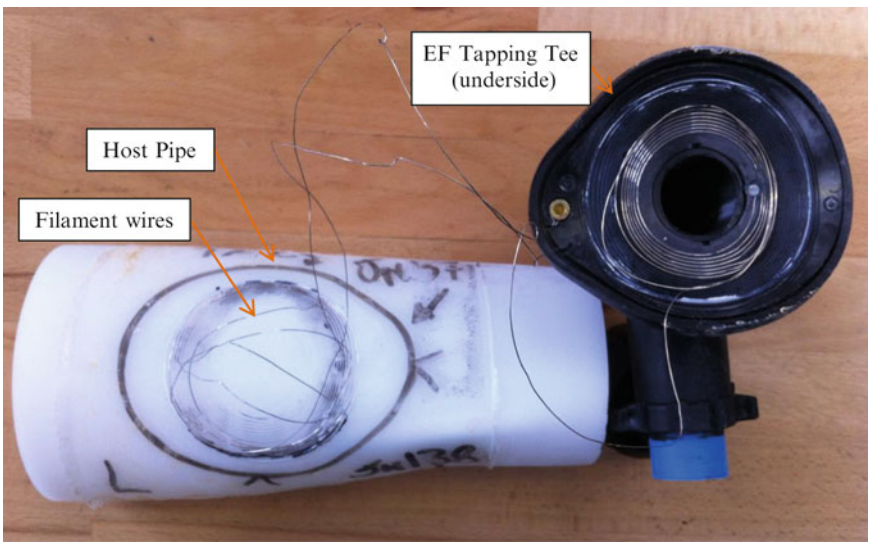

Fig. 26.3 Talc contaminated specimen subject to crush test

A secondary set of experiments are currently being conducted to observe the fatigue-life under a fixed range but variable mean; following the same trapezoidal loading pattern as mentioned previously.

With regards to Fig. 26.2, the most logical failure mechanism would be crack propagation [10] of the jointing surface. This hypothesis was explored further through the use of destructive and non-destructive methods of analysis.

26.3 Destructive Tests

Destructive tests were performed to observe the failure modes by comparing contaminated joints visually to those that had been manufactured to best practice principles. A crushing decohesion test was performed in accordance with ISO 13955 [13] on EF tapping tees. The results showed the failure mode was brittle about the joint when the welding interface was subject to contamination prior to welding (Fig. 26.3). Notice that there are remnants of black polymer on the surface of the pipe and white polymer on the tapping tee where it appears a bond was beginning to form. Filament wires also appear to be still embedded into the host pipe.

Contrarily, joints welded to best practice principles showed fully ductile behaviour about the jointing interface. Figure 26.4 shows the tapping tee after it was subject to the maximum crushing distance. There appears to be preliminary signs of crazing about the jointing interface after the pipe had been crushed. It is interesting to note that removing the tapping tee from the host pipe proved extremely difficult. This was mainly because there was minimal room to operate a lever to prise the fitting away from the pipe. Secondly, the joint had a distinct difference in mechanical strength compared to the brittle failure of the contaminated joint; which fell apart during the crush test.

The decohesion test proved useful in showing the comparable difference in strength and failure mode between joints that are subject to contamination and joints done to best practice principles.

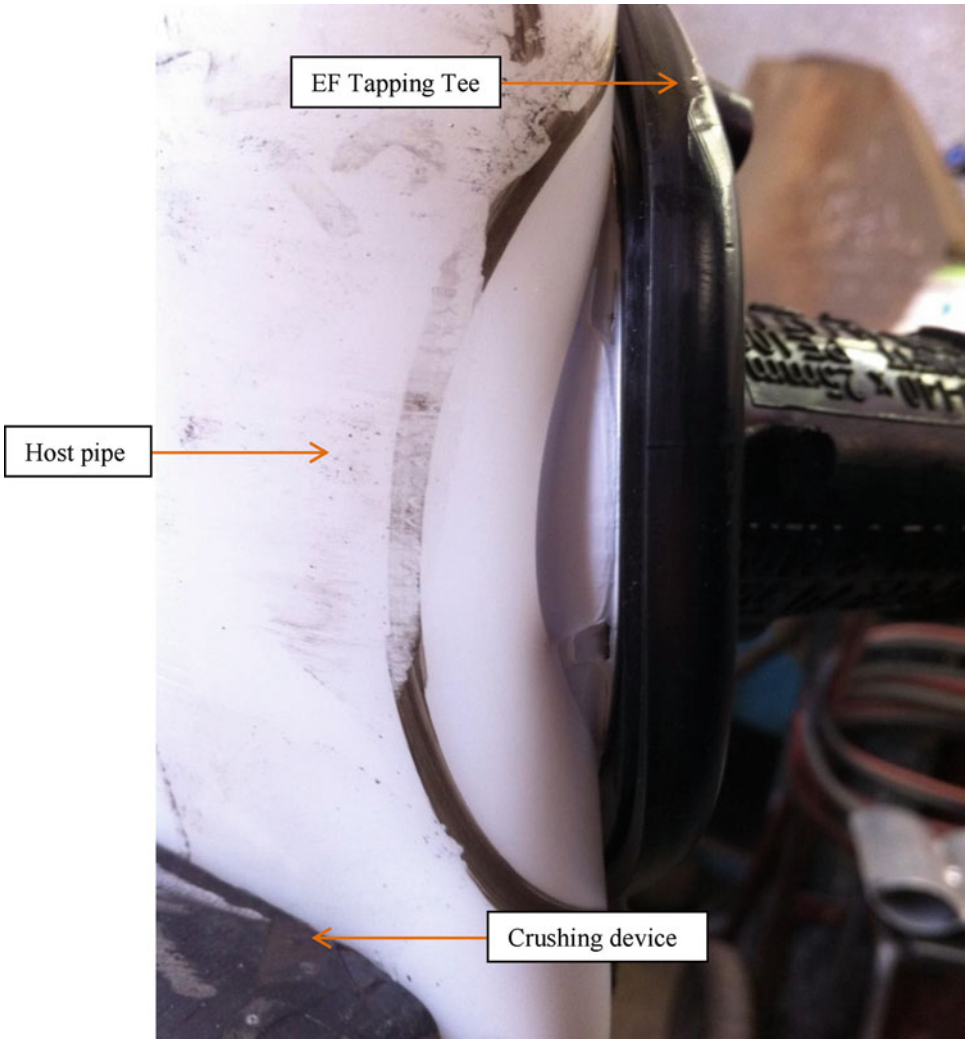

Fig. 26.4 Post-crush of 'perfect' specimen

As Fig. 26.3 shows evidence of bonding beginning to take place it was assumed that the crack growth would be visible if non-destructive methods of analysis were used to observe the crack growth (i.e. leak paths) of joints failed to the fatigue testing regime highlighted in Fig. 26.2.

26.4 Ultrasound Experiment

A rig was designed and built to observe the leak paths of failed joints. The rig consisted of an ultrasonic focussing lens attached to a stepper motor stage (Fig. 26.5). The stepper motor stage allowed for line scans to be performed. Joints that have been tested to failure in the fatigue programme (Fig. 26.2) were cut in half using a bandsaw, along the centre line of the pipe. This left the internal bore and the underside of the tapping tee exposed so that the ultrasonic transducer could focus on the internal bore of the pipe. Furthermore, the focussing lens transmitted pulses perpendicular to the internal bore of the PE pipe and fitting assembly.

Preliminary line scans were conducted on the internal bore of the pipe in order to observe the delaminated surface of the fusion interface. The line scans were then knitted together to create a map of the fusion zone thus observing the leak path (Fig. 26.6).

Once the map was created, the predicted leak path was confirmed by applying a flow of water through the EF tapping tee fitting. This was achieved using a basic hand pump.

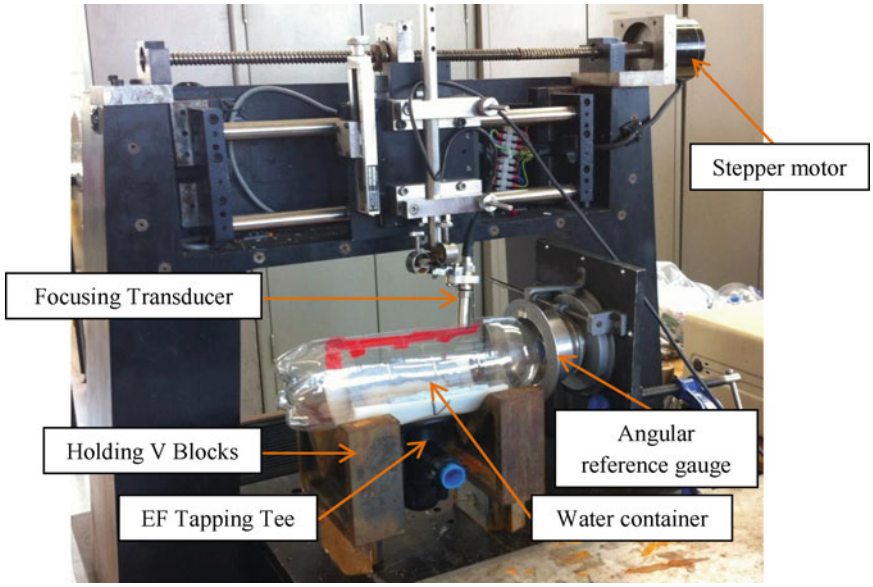

Fig. 26.5 Ultrasound focussing transducer arrangement

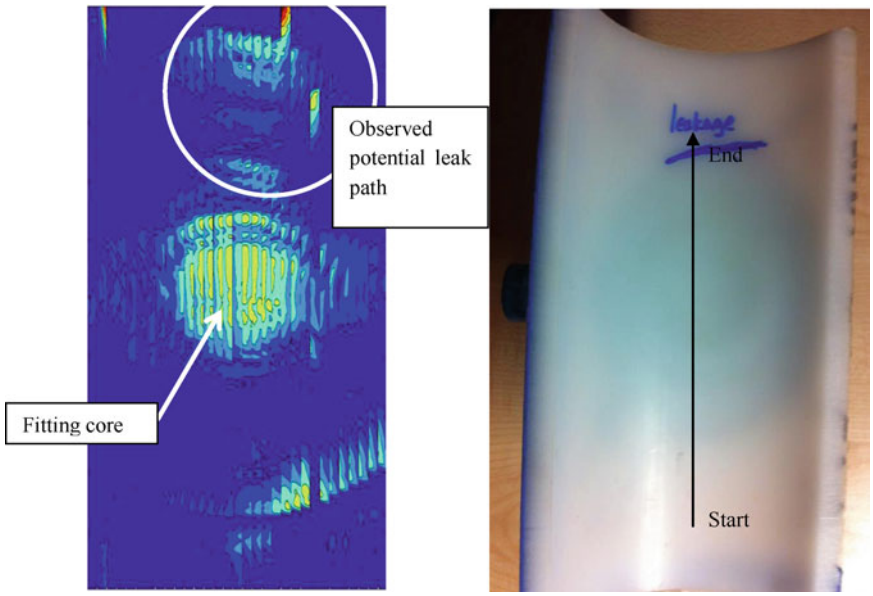

Fig. 26.6 Preliminary line scan results showing leak path (*Left*) and scan direction (*right*)

Following on from the degree of success with single transducer ultrasonic analysis, a bespoke ultrasonic sensor array was designed and built to monitor the crack propagation during a live fatigue test. The aim of the experiment was to observe crack growth of EF tapping tees whilst they are subject to a pressure fatigue test. The outcomes of this experiment will be shown at the conference.

26.5 Discussion and Conclusions

There is a dramatic decrease in joint performance when EF tapping tees are subject to contamination prior to the welding process. It is clear from Fig. 26.2 that if the jointing interface were to be contaminated, failures associated with fatigue can occur in a relatively short space of time. It should be noted that the pressure amplitudes used in the fatigue test were aimed to replicate the pressures that may be expected in surge events. However, the frequency of the pressure ranges are slower than a surge, as the frequencies used were between 0.007 and 0.016 Hz (90 to 40 % $P_{mat,\ max}$ respectively). The predictability of failure also becomes more difficult as the pressure range decreases—this was evident due to the increase in scatter as the pressure range was reduced.

It is interesting to note that the destructive tests showed a visually distinct difference in mechanical failure if the joint were to be subject to a talc contaminant prior to welding. With regards to the specimen subject to contamination (Fig. 26.3), there was evidence to suggest that a bond was beginning to form. Some filament wires were still present once the fitting was removed from the host pipe. This suggests that the filament wire may have been providing some degree of structural strength to the joint assembly which may let the fitting pass the initial pressure test before it is put in service. However, the joint would still fail in a brittle manner if it were subject to the fatigue testing regime.

The leak path investigation using non-destructive ultrasonic methods showed promising preliminary results. Being able to observe the directions of which the leak paths (cracks) have formed gives an insight into the failure mechanics of the fitting. Furthermore, in principle this can be confirmed using the same methods but during the live fatigue test.

Acknowledgements The authors would like to thank the Engineering and Physical Sciences Research Council (EPSRC), Severn Trent Water and WRc PLC for their sponsorship and support of this project. The authors would also like to thank Kai Yan Siaw and Naomi Shipway of the University of Sheffield for their efforts to date with the ultrasound analysis.

References

1. O'Connor C (2012) The nature of polyethylene pipe failure, Pipeline & Gas Journal 239 (12)
2. UKWIR (1997) Plasitc pipeline systems—analysis of system failures. UK Water Industry Research Limited, London
3. UKWIR (2011) Leakage in PE pipe systems. UK Water Industry research Limited, London
4. WIS 4-32-08 (2002) Specification for the fusion jointing of polyethylene pressure pipeline systems using PE80 and PE100 materials. WRc PLC, Swindon
5. Trew J, Mills D (2011) National sewers and water mains failure database. Cast study no. 1: Polyethylene pipe failures on water mains. WRc PLC for UK Water Industry Research Limited, Swindon
6. UKWIR (1996) Pipeline innovation final report. UK Water Industry Research Ltd, London
7. UKWIR (1997) Plastic pipeline systems—pipeline innovation. UK Water Industry Research Ltd, London
8. Wylie EB, Streeter VL, Suo L (1993) Fluid transients in systems. Prentice Hall, Englewood Cliffs
9. Beech SH, Headford A, Hunt S, Sandilands G (1995) The resistance of polyethylene water pipeline systems to surge pressure. In: Plastic pipes IX, Edinburgh
10. Hertzberg RW, Manson JA (1980) Fatigue of engineering plastics. Academic, London
11. Bowman J (1990) The fatigue response for polyvinyl chloride and polyethylene pipe systems. In: ASTM special technical publication issue, no. 1093, pp 101–121
12. Tayefi P, Beck S, Tomlinson R (2014) The fatigue performance of electrofusion tapping tees subject to contamination, Int. J. Pressure Vessels and Piping (under review)
13. ISO 13955 (1997) Plastic pipes and fittings—crushing decohesion test for polyethylene (PE) electrofusion assemblies. International Organisation for Standardization, London

Chapter 27
Creep Crack Growth in High-Temperature Impure Helium Environments

D. Grierson, G. Cao, A. Glaudell, D. Kuettel, G. Fisher, P. Pezzi, P. Brooks, T. Allen, K. Sridharan, and W.C. Crone

Abstract Next Generation Nuclear Plant (NGNP) designs for very-high-temperature reactors (VHTR) employ intermediate heat exchanger (IHX) for which the material demands are extreme. Currently, Alloy 617 and Alloy 800H are considered to be among the candidate materials for the high-temperature, helium-cooled environments that are planned for these systems. The primary helium coolant is expected to operate at temperatures at or above 750 °C, and creep crack growth (CCG) of these candidate alloys is of particular concern for their reliability in VHTRs for long-term service. Using an apparatus that was designed and constructed in-house, CCG testing was conducted on compact tension specimens at temperatures up to 850 °C in controlled environments, including air and impure helium, following ASTM standard E 1457-07. Overall, our CCG testing revealed that Alloy 617 exhibits superior resistance to creep crack growth compared to Alloy 800H. Trends observed in the mechanical behavior and microstructure of the candidate alloys as a function of environment will be discussed.

Keywords Creep crack growth (CCG) • High-temperature testing • Inconel 617 • Alloy 800H • ASTM E 1457-07

27.1 Introduction

Next Generation Nuclear Plants (NGNPs) are being designed with a very-high-temperature helium-cooled reactor (VHTR) for generating electricity and co-generating hydrogen using the process heat from the reactor. The chosen coolant for these high-temperature reactor systems is helium, which is expected to be at 850–1,000 °C. Candidate alloys for intermediate heat exchangers (IHXs) are Inconel 617, Haynes 230, Alloy 800H and Hastelloy X. The helium coolant inevitably contains low levels of impurities during steady-state operation that are problematic because these alloys can experience significant long-term corrosion by the gaseous impurities present at elevated temperatures. These corrosion reactions, which may involve oxidation, carburization or decarburization, can substantially affect long-term mechanical properties. Little is known about the effects of impurities on the creep crack initiation and growth rate of these alloys at elevated temperatures. Scoping studies and eventually code studies are needed to provide specific guidelines for engineering design of IHXs in the presence of impure helium at high temperatures, and creep crack growth testing of candidate alloys in prototypical environments is an important component of those studies [1].

An apparatus for conducting creep crack growth (CCG) studies for candidate alloys at elevated temperatures and in controlled environments, including impure helium, was developed and described by the authors previously [2, 3]. Our work testing creep crack initiation and creep crack growth focused on two candidate materials, namely Inconel 617 and

D. Grierson • G. Cao • A. Glaudell • D. Kuettel • P. Pezzi • P. Brooks • T. Allen • K. Sridharan • W.C. Crone (✉)
Department of Engineering Physics, University of Wisconsin-Madison, 543 Engineering Research Building, 1500 Engineering Dr., Madison, WI 53706, USA
e-mail: crone@engr.wisc.edu

G. Fisher
Department of Mechanical Engineering, University of Wisconsin-Madison, Madison, WI, USA

J. Carroll and S. Daly (eds.), *Fracture, Fatigue, Failure, and Damage Evolution, Volume 5: Proceedings of the 2014 Annual Conference on Experimental and Applied Mechanics*, Conference Proceedings of the Society for Experimental Mechanics Series,
DOI 10.1007/978-3-319-06977-7_27,

Alloy 800H, and CCG tests were performed within the temperature range 700–850 °C, which falls within the range stipulated by the "Nuclear Energy University Program Research Needs" released in December 2008 [4]. Here we will briefly discuss our observations of creep crack growth resistance in these materials. A full paper on the topic is in preparation.

27.2 Experimental Methods

The CCG testing apparatus developed by the authors relied on ASTM standard E 1457-07 [5] for performing creep crack growth measurements on metals and alloys. The apparatus simultaneously tests three compact tension (CT) specimens within an environmental chamber and under dead-weight loading. Samples are loaded within a retort tube that allows for high-temperature testing within a controlled environment. Tension rods, fabricated out of Inconel 617 alloy, deliver a constant load to the specimens throughout the testing duration.

Two candidate alloys were studied in detail: Alloy 617 and Alloy 800H. Alloy 617 is the leading candidate alloy for intermediate heat exchangers. It has been reported that Alloy 617 can be used at temperatures as high as 982 °C. Alloy 800H is currently approved under ASME code for nuclear service for up to 760 °C and could be used immediately in a lower-temperature reactor.

Table 27.1 presents the chemical compositions of the as-received alloys. All 617 and 800H samples used in these studies were provided by Dr. Richard Wright at Idaho National Laboratory (INL), Idaho Falls, ID, USA. The materials from INL were cut from much larger samples and were solution annealed. Before creep crack growth testing, both Alloy 617 and Alloy 800H were solution treated (ST) at 1,200 °C for 1 h, then quenched in water, then aged for 2,000 h in air at 850 °C. Aging of the alloys prior to CCG testing was done because the Alloy 617 and Alloy 800H materials will ultimately be used for extended periods of time and at high temperatures during heat exchanger service. The composition of the impure helium gas was 12 ppm CO, 1.5 ppm CO_2, 0.5 ppm O_2, 05 ppm N_2, 05 ppm Ar, 0.2 ppm H_2O moisture, with balance helium. The impure helium gas was premixed and certified by Airgas.

Numerous tests were conducted under various temperature and environmental conditions for Inconel 617 and Alloy 800H. Table 27.2 provides a summary of the tests that were successfully taken to completion. The direct current potential drop technique (DCPD) was used to conduct real-time monitoring of crack growth within each CT specimen (results to be presented in a future publication). The results presented herein focus on scanning electron microscopy (SEM) images taken of the cracks after the specimens were removed from the CCG testing apparatus. For all CCG tests, the direction of crack propagation was parallel to the rolling direction, and the cracks were prevented from propagating through the samples entirely in order to calibrate the DCPD measurements by quantifying the final crack length. To get reliable CCG data, the stress intensity for CCG testing of Alloy 800 has to be significantly lower as compared to the case of Inconel 617 at the same test temperature (700 °C).

Table 27.1 Chemical compositions of the tested alloys [6]

Element Alloy	Ni	Cr	Fe	Co	Mo	Ti	Al	C	Si	Mn	Cu	P	B	S
Alloy617	54.1	22.2	1.6	11.6	8.6	0.4	1.1	0.05	0.1	0.1	0.04	–	<0.001	<0.002
Alloy800H	30.65	19.7	46.24	0.1	–	0.54	0.56	0.061	0.42	1.27	0.2	0.024	–	0.001

Table 27.2 CCG tests completed on 617 and 800H samples. ST indicated solution treated

Test #	Alloy	Stock #	Pretreatment	Temperature (°C)	Environment	Stress intensity (MPa $\sqrt{m}$)
2	617	1	ST + aged	700	Air	16
4	617	1	ST + aged	850	Air	4
7	800H	1	ST + aged	700	Air	5
8	617	3	None (as-received)	700	He	16
9	800H	1	ST + aged	700	He	5
10	617	2	ST + aged	700	He	16
11	617	2	ST + aged	850	He	4

27.3 Results and Discussion

The cracks that formed during CCG testing were investigated by SEM imaging. The major cracks visible on the outer surfaces (images not shown here) extended through the thickness of the samples, and crack branching was readily observed in all specimens. After cutting the CT specimens in half, it was found in all cases that major cracks within the interior of the specimens were longer than those found on the surface. The length of the longest crack within the interior of each specimen was used to quantify crack growth during CCG testing.

Figures 27.1 and 27.2 present SEM images of the crack morphologies of Alloy 617 specimens tested at 700 °C in air and in helium, respectively. One major crack is observed in the sample tested in air. There are many small crack branches in samples tested in helium. In both cases, some small crack initiations and/or cavitations are observed in front of the crack tip. In Fig. 27.1, crack propagation along the grain boundaries can be seen. It appears that the cracks initiated primarily from the triple point grain boundary junctions and near the carbide regions.

Figures 27.3 and 27.4 present SEM images of cracks in Alloy 617 specimens tested at 850 °C in air and helium, respectively. The crack morphologies appear to be similar to one another; namely, there is one major crack and many small cracks. It can be seen from the saw-shaped cracks in Fig. 27.3 that there is significant strain in Alloy 617 tested in air. In both cases, the cracks are intergrannular, and cracks appear to have initiated from the triple point grain boundary junctions and carbide regions.

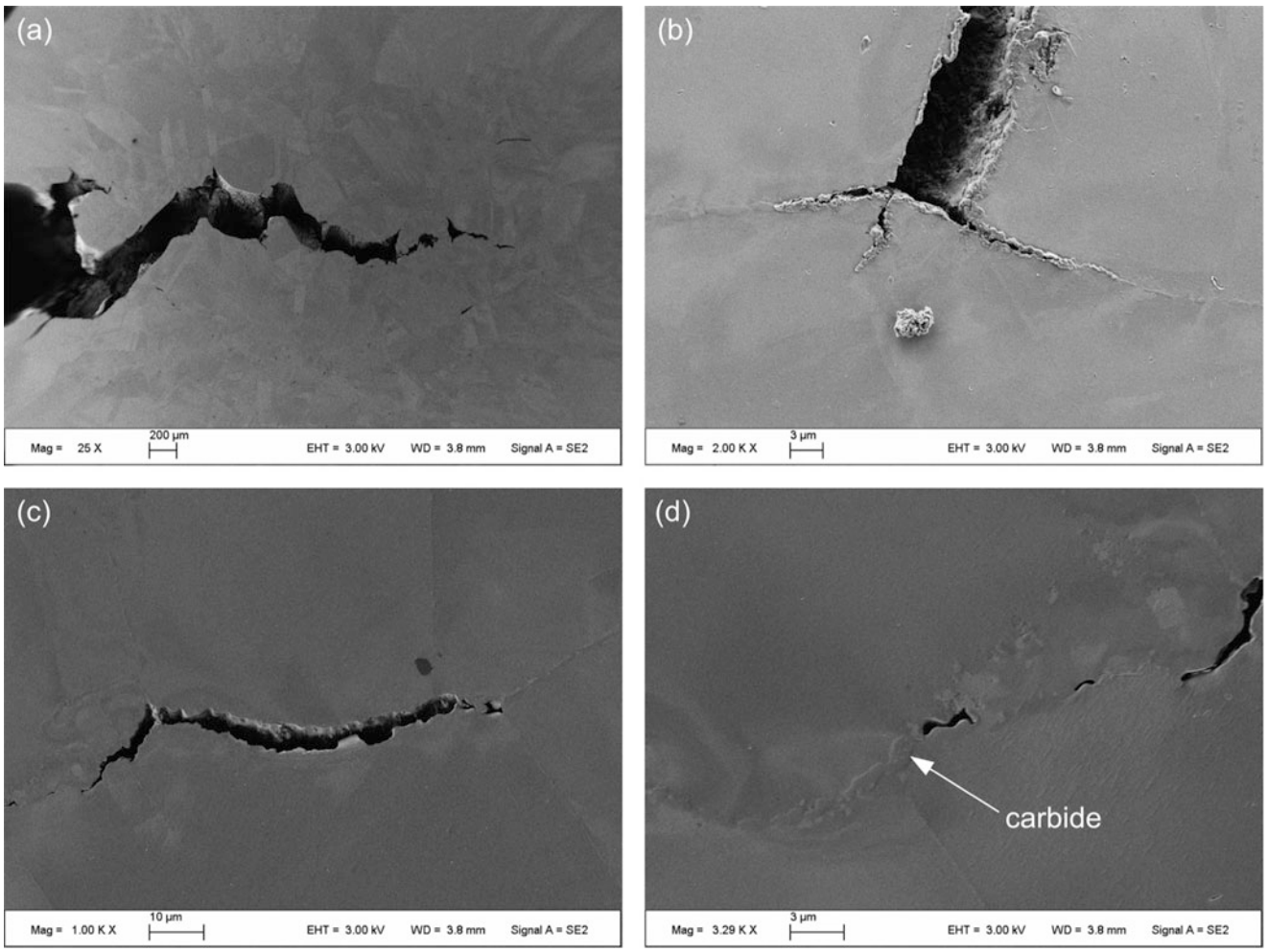

Fig. 27.1 Crack, crack tip, crack cavitation, and crack initiations in Alloy 617 tested in air at 700 °C (Test 2). (**a**) Overall crack, (**b**) magnified crack tip in (**a**), (**c**) micro crack ahead of the crack tip, (**d**) crack initiation. The cracks initiated and propagated along grain boundaries. The cracks appeared to have initiated at the grain triple points and near the carbide areas

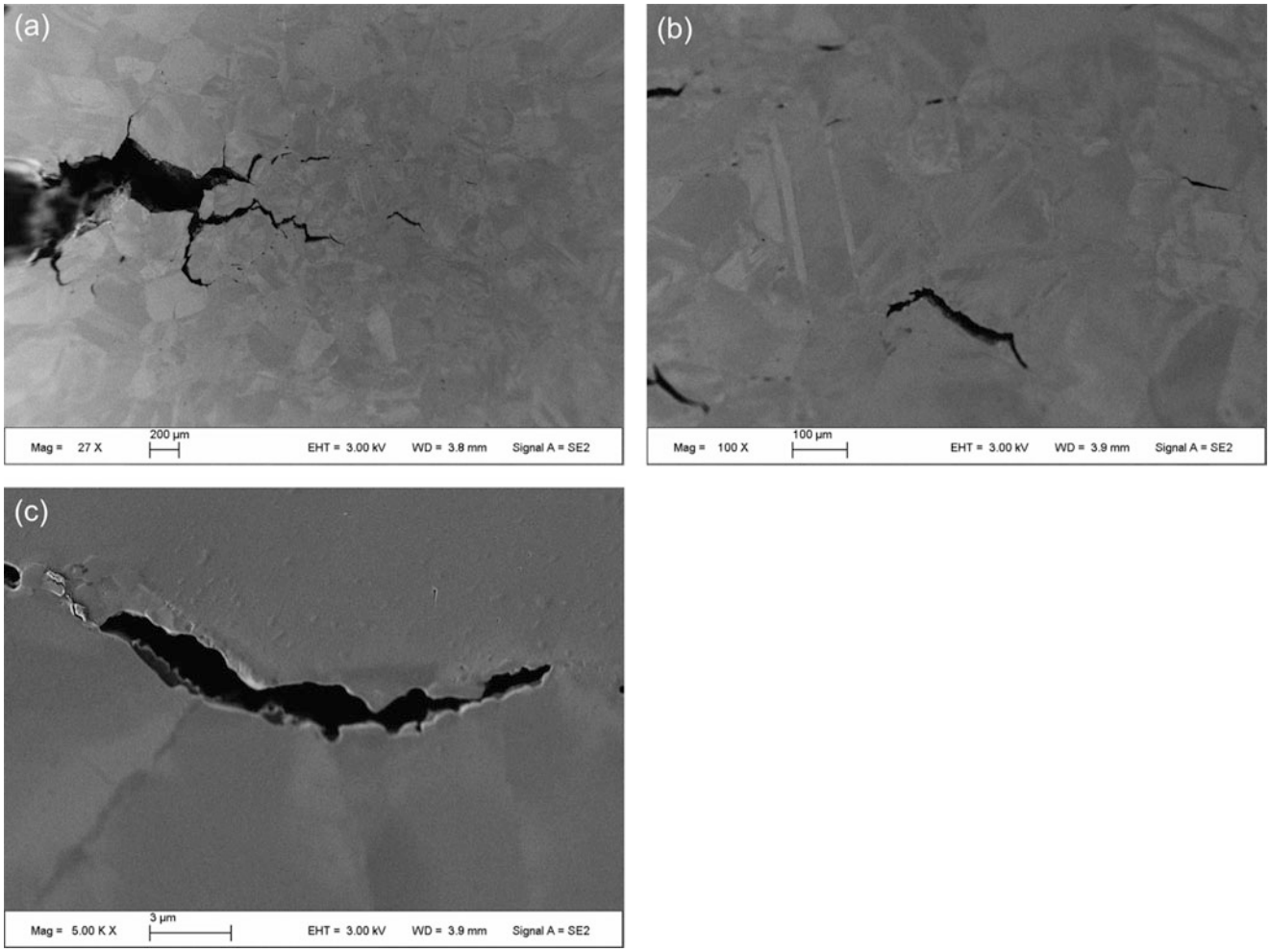

Fig. 27.2 Cracks in Alloy 617 tested at 700 °C in helium (Test 10). (**a**) Overall crack, (**b**) crack tip in (**a**), (**c**) a crack initiation ahead of crack tip. Cracks are intergrannular and appear to have initiated at triple points

Figures 27.5 and 27.6 presents SEM images of the cracks in Alloy 800H specimens tested at 700 °C in air and in helium, respectively. One major crack is observed in each sample, and the crack tips are significantly oxidized. The cracks appear to have propagated along the grain boundaries and around the carbide phases.

27.4 Conclusion

An experimental testing apparatus was used to conduct creep crack growth studies for candidate alloys Alloy 617 and Alloy 800H at elevated temperatures and in controlled environments. The results obtained provide scoping information pertaining to long-term service in VHTR-type environments. CCG testing of candidate alloys revealed the effects of temperature and environment on crack-growth resistance within the parameter space explored. The creep cracks formed in both materials (Alloy 617 and Alloy 800H) tested at 700 and 850 °C in air and in helium were determined to be intergrannular. Alloy 617 was found to have superior CCG resistance to that of Alloy 800H under the conditions tested.

Acknowledgements The authors would like to thank Dr. Richard Wright of INL and Dr. Sam Sham of ORNL for helpful discussions regarding sample processing and testing. This research was performed using funding received from the U.S. Department of Energy Office of Nuclear Energy's Nuclear Energy University Programs under Battelle Energy Alliance, LLC Standard Research Contract No. 00088925, entitled "Assessment of Embrittlement of Very High Temperature Reactor Structural Alloys in Impure Helium Environments," to the University of Wisconsin, under Prime Contract No. DE-AC07-05ID14517.

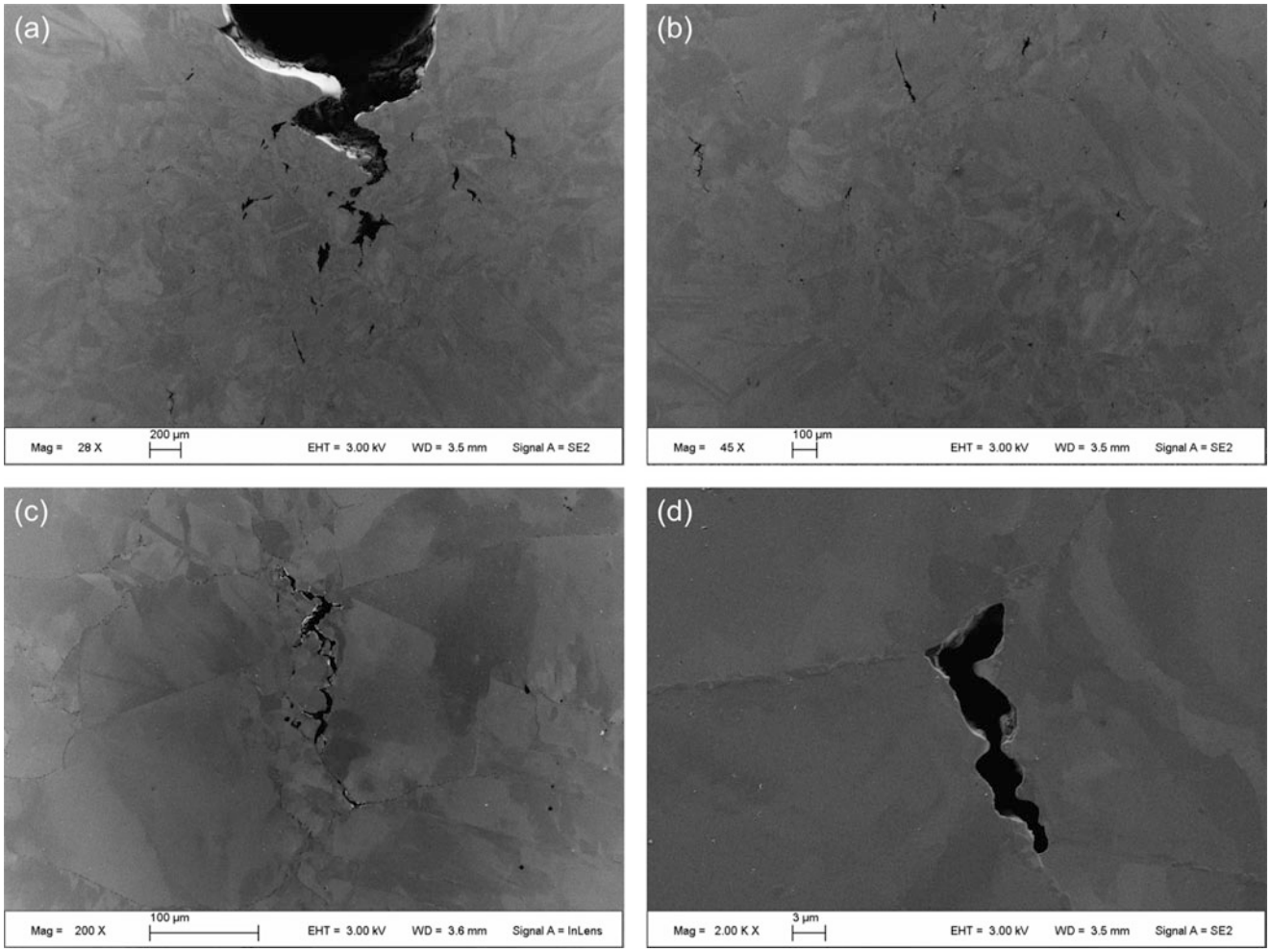

Fig. 27.3 Cracks in Alloy 617 tested at 850 °C in air (Test 4). (**a**) Overall crack, (**b**) crack tip area, (**c**) crack ahead of crack tip, (**d**) a crack initiation ahead of crack tip. Many small cracks are observed. Cracks are intergrannular, and cracks appear to have initiated from the triple points and near carbide regions

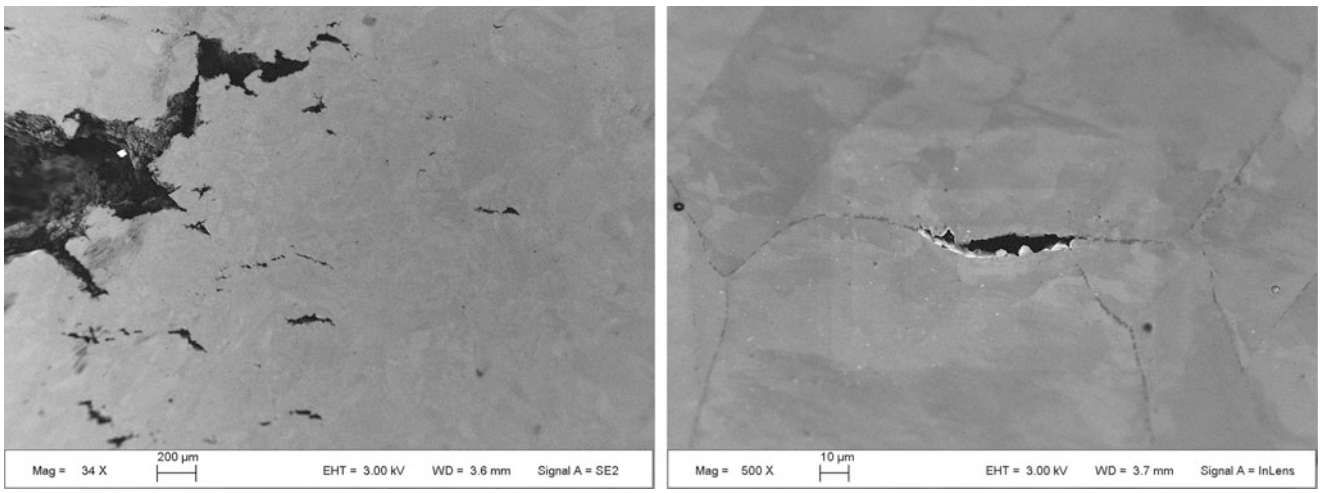

Fig. 27.4 Cracks in Alloy 617 tested at 850 °C in helium (Test 11)

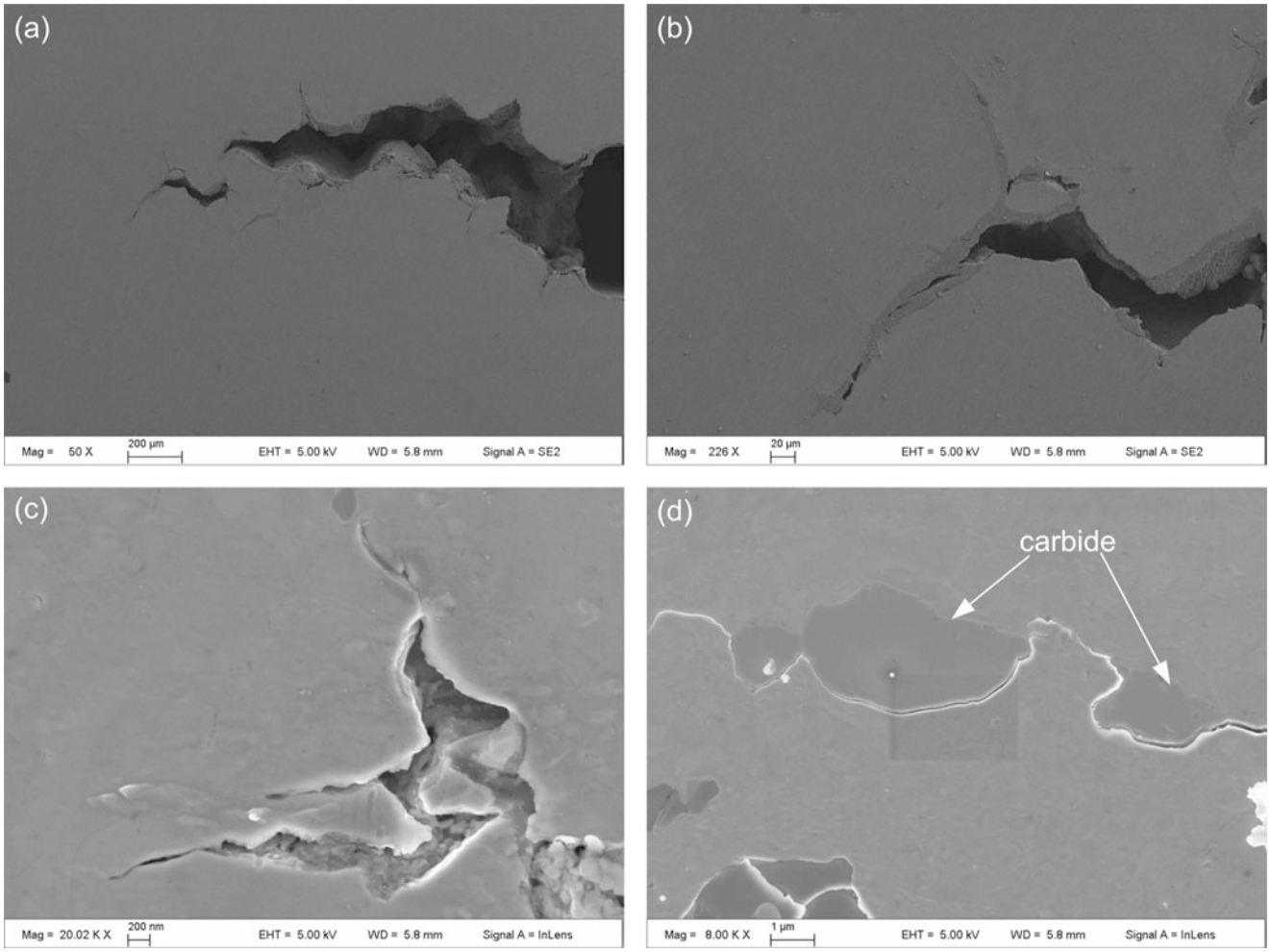

Fig. 27.5 SEM images of cracks in Alloy 800H tested at 700 °C in air (Test 7). (**a**) Overall crack, (**b**) crack tip, (**c**) magnified crack tip area, (**d**) a crack initiation ahead of major crack. One major crack is seen, and significant oxidation in the crack tip region is observed

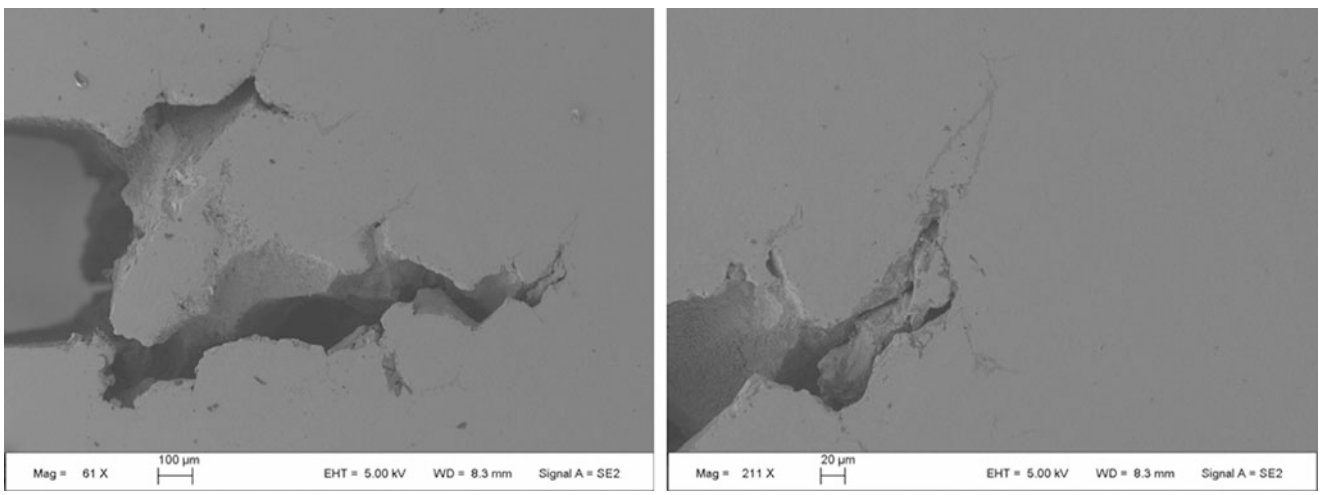

Fig. 27.6 SEM images of cracks in Alloy 800H tested at 700 °C in helium (Test 9), One major crack is seen, and signs of oxidation in the crack tip and along grain boundary immediately in front of the crack tip are apparent

References

1. Shah VN, Majumdar S, Natesan K (2003) Review and assessment of codes and procedures for HTGR components NUREG/CR-6816, ANL-02/36
2. Grierson D, Cao G, Brooks P, Pezzi P, Glaudell A, Kuettel D, Fisher G, Allen T, Sridharan K, Crone WC. Experimental method for creep crack growth testing in controlled environments at high temperatures. Submitted to Experimental Mechanics
3. Grierson D, Cao G, Brooks P, Pezzi P, Glaudell A, Kuettel D, Fisher G, Allen T, Sridharan K, Crone WC (2013) An apparatus for creep crack growth testing in controlled environments at high temperatures. In: Proceedings of the 2013 SEM annual conference and exposition on experimental and applied mechanics, Albuquerque
4. Center for Advanced Energy Studies, Idaho National Laboratory (2008) Nuclear Energy University programs research needs, p 35
5. ASTM International. (2013) Standard test method for measurement of creep crack growth times in metals, ASTM E 1457-13
6. Haynes International, Inc. (2014) Corrosion-resistant & high-temperature alloys. http://www.haynesintl.com/. Accessed 5 March 2014

Chapter 28
High-Frequency Resonance Phenomena in Materials Subjected to Mechanical Stress

G. Lacidogna, B. Montrucchio, O. Borla, and A. Carpinteri

Abstract The elastic energy released by micro-cracking yields to macroscopic fracture whose mechanical vibrations are converted into electromagnetic (EM) oscillations over a wide range of frequencies, from few Hz to MHz, and even up to microwaves. As regards Acoustic Emission (AE), the classical monitoring techniques allow an observation over a range of frequencies up to hundreds of kHz. In this paper the authors investigate if, during compression tests on brittle materials, which involve catastrophic fractures, it is possible to identify in the stressed materials mechanical oscillations in a frequency range higher than that characteristic of the AE and comprised between MHz and THz. This excited state of matter could be a precursor of subsequent resonance phenomena of nuclei able to produce neutron bursts, especially in the presence of sudden catastrophic fractures. This phenomenon has been also very recently argued from a theoretical physical point of view by Widom et al. In this investigation experimental evidences emerge by means of a confocal sensor able to measure the resonance frequency of the specimen. The basic idea is to use a laser light focused onto a spot of the specimens surface subjected to mechanical compression. A photo-detector measures the intensity of the reflected light and then gives the frequency variation that is proportional to the vibration frequency of the spot particles.

Keywords Brittle Failure • Acoustic Emission • Electromagnetic Emission • Neutron Emission • Laser measurements

28.1 Introduction

This paper discusses the phenomenon of energy emissions from brittle material specimens under mechanical loading. The authors have recently found experimental evidence that energy emission of different forms occurs from solid-state fractures. By subjecting quasi-brittle materials such as granitic rocks to compression tests, for the first time, bursts of neutron emission (NE) during the failure process were observed for the first time [1–5], necessarily involving nuclear reactions, besides the well-known acoustic emission (AE) [6–15], and the phenomenon of electromagnetic radiation (EM) [16–21], which is highly suggestive of charge redistribution during material failure. As regards neutrons, these emissions are due to piezonuclear reactions, which depend on the different modalities of energy release during the tests. For specimens with sufficiently large size and/or slenderness, a relatively high energy release is expected, and hence a higher probability of neutron emission at the time of failure [1–5].

The phenomenon of EM emissions is regarded as an important precursor of critical phenomena in Geophysics, such as rock fractures, volcanic eruptions, and earthquakes [22, 23]. For example, anomalous radiation of geo-electromagnetic waves are observed before major earthquakes. At the laboratory scale, rocks and concrete under compression generate AE and EM emission nearly simultaneously. This evidence suggests that also NE emissions are generated during crack growth, reinforcing the idea that the NE phenomenon could be associated with seismic activity [24].

The experimental analysis carried out by the authors may open a new possible scenario, in which the stress state of the elements firstly involves the generation of microcracks, accompanied by mechanical energy release in the field of ultrasonic

G. Lacidogna (✉) • O. Borla • A. Carpinteri
Department of Structural, Geotechnical and Building Engineering, Politecnico di Torino, Corso Duca degli Abruzzi 24, 10129 Torino, Italy
e-mail: giuseppe.lacidogna@polito.it

B. Montrucchio
Department of Control and Computer Engineering, Politecnico di Torino, Corso Duca degli Abruzzi 24, 10129 Torino, Italy

J. Carroll and S. Daly (eds.), *Fracture, Fatigue, Failure, and Damage Evolution, Volume 5: Proceedings of the 2014 Annual Conference on Experimental and Applied Mechanics*, Conference Proceedings of the Society for Experimental Mechanics Series,
DOI 10.1007/978-3-319-06977-7_28,

vibrations that can be measured using suitable AE equipments. Hence, the formation of coherent EM fields occurs over a wide range of frequencies, from few Hz to MHz, and even up to microwave frequencies. This excited state of the matter could be the cause of subsequent resonance phenomena of nuclei able to produce neutron bursts. This hypothesis is also confirmed by Widom et al. [25, 26]. As a matter of fact, the microcracking elastic energy release ultimately yields the acoustic vibrations, which are converted into electromagnetic oscillations. The electromagnetic waves accelerate the condensed matter particles producing neutrons and neutrinos.

In this paper the authors—after presenting previous experimental results about the different forms of energy emitted during compression tests on brittle materials such as magnetite and basalt rocks—describe a first attempt to identify mechanical oscillations in a frequency range higher than the usual one for AE and comprised between MHz and THz.

The materials presently considered are mortar enriched with iron dioxide, magnetite, gypsum and Luserna stone, a metamorphic rock deriving from a granitoid protolith. In particular the experimental results of the cementitious sample ($4 \times 4 \times 8$ cm^3) are reported. The data obtained from the remaining specimens are still under processing. The experimental approach is based on a confocal sensor able to measure the specimen resonance frequency. The basic idea is to use besides the AE detection also a laser light focused onto a spot on the specimen surface during mechanical compression. A photo-detector measures the intensity of the reflected light and then gives the frequency variation that is proportional to the vibration frequency of the spot particles. The phenomenon under investigation is unique, because we are analyzing the specimen vibration under stress, but the two used devices capture two different frequencies ranges.

28.2 Material and Methods

28.2.1 Acoustic Piezoelectric Transducer

The AE activity emerging from the compressed specimens was detected by attaching to the specimen surface a wideband piezoelectric (PZT) transducer, capable to detect frequencies comprised between 50 and 800 kHz, which converts the high-frequency surface movements due to the acoustic wave into an electric signal (the AE signal). Wideband sensors are typically used in applications where frequency analysis of the AE signal is required, and in helping to determine the predominant frequency band of AE sources. In these applications, various AE wave-modes can be detected, providing more information about the AE source and distance of the AE event. Whereas broadband sensors are commonly used in research applications, a choice of resonant sensors covering the frequency range of interest would demonstrate superior sensing. As a matter of fact, resonant sensors are more sensitive than broadband sensors, which are characterized by a flat frequency response in their working range, and then they can be successfully used in monitoring of large-sized structures [14, 15].

28.2.2 EM Detecting Device

The EME detecting device is constituted by three pickup coils with a different number of turns, made of a 0.2 mm copper wire, that are positioned around the monitored specimen. This instrumentation, which acquires data in the frequency range from few Hz up to 4 MHz, exploits the induction Faraday's law: the induced voltage in a closed circuit (loop) is proportional to the change in the magnetic flux throughout the circuit. The first coil, constituted by five turns, works in a frequency range from 300 kHz to 4 MHz. The other two coils constituted by 125 turns and 500 turns, work in the frequency range from few kHz to 20 kHz, and from few Hz to 1 kHz, respectively.

28.2.3 He^3 Neutron Proportional Counter

The He^3 detector used in the compression tests under monotonic displacement control, and by ultrasonic vibration, is a He^3 type (Xeram, France) with electronics of preamplification, amplification, and discrimination directly connected to the detector tube. The detector is powered with 1.3 kV, supplied via a high voltage NIM (Nuclear Instrument Module). The logic output producing the TTL (transistor-transistor logic) pulses is connected to a NIM counter. The device was calibrated for the measurement of thermal neutrons; its sensitivity is 65 cps/$n_{thermal}$ ($\pm$10 % declared by the factory) i.e., a thermal neutron flux of 1 thermal neutron/s cm^2 corresponds to a count rate of 65 cps.

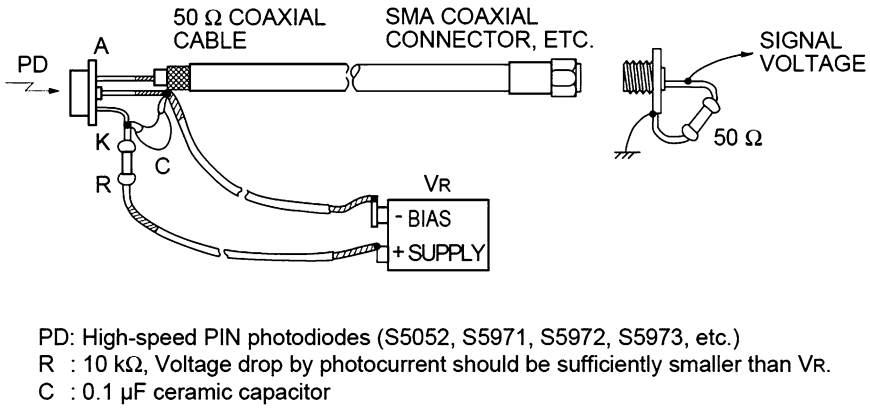

Fig. 28.1 High-speed light detector

28.2.4 High-Speed Light Detector

The employed circuit to analyze the laser pulses utilizes no active components, and since no signal amplification is performed, it is mainly used for detection at relatively high light intensity levels. The impedance matching load resistance of 50 Ω can be directly connected to the 50 Ω terminal of an oscilloscope or other measurement equipment. High speed photodiodes designed for the GHz range can be used with this circuit. The photodiode generate signals and the conductors of the coaxial cable, where high-speed frequency flows, should be made as short as possible. A scheme of the high-speed light detector used during the experimental analysis is shown in Fig. 28.1. For this experimental tests a Hamamatsu S5973 photodiode, and a Lasiris 635nmclass IIIb 10 mW laser are employed.

28.2.5 Agilent 3000 Series Oscilloscope

The Agilent 3000 Series oscilloscope used is a portable digital storage oscilloscopes (DSOs) that deliver powerful features as maximum sample rate equal to 1 GSa/s, automatic voltage and time measurements, advanced triggering (edge, pulse width, and video) and math function waveforms (add, subtract, multiply, FFT), vertical resolution of 8 bits, peak detection of 5 ns.

28.3 Experimental Results

28.3.1 Compression Tests on Brittle Rock Specimens

In this section, the tests previously carried out on magnetite and basalt rocks specimens are synthesized to describe the first attempts to identify mechanical oscillations in a frequency range up to MHz. The utilized devices were AE transducers, EM antenna, and Neutron proportional counter [27]. A total of 29 cylindrical specimens (27 of magnetite and 2 of basalt) with different size and slenderness were tested.

The specimens were tested in compression up to failure under displacement control by setting constant piston velocities of the MTS machine. In the following, the experimental results on two magnetite specimens will be examined (Fig. 28.2). They showed a brittle response with a rapid decrease in load-carrying capacity when deformed beyond the peak load. Experimental evidence indicates the presence of AE, EME, and NE activity (see Fig. 28.3). In the specimen P1 (diameter 40 mm, slenderness 1), whose behaviour is described by the load vs. time curve in Fig. 28.3 (left), the observed bursts of AE and EME activity can be clearly correlated to the stress drops occurring before the collapse, Fig. 28.3 (upper and middle left). The specimen P2 failure (diameter 90 mm, slenderness 1) was preceded by two closely correlated bursts of AE and EME activity at nearly 80 % of the peak load, Fig. 28.3 (upper and middle right). This activity, particularly as regards electromagnetic emission, can be due to the behavior under loading of magnetite that—being rich in iron, about 65 % in weight—determines the formation of magnetic charges generated by friction during the loading process, and their spontaneous release independently of the formation of macro-cracks at the time of final collapse.

Fig. 28.2 The experimental setup for the magnetite specimen P1 (diameter 40 mm, slenderness 1) under compression by using a MTS servo-controlled hydraulic testing machine. The AE sensor is attached on the specimen surface, while the EM antenna is around it positioned. The He^3 detector is placed at a distance of 10 cm from the test specimen and enclosed in a polystyrene case to avoid that the results are altered by mechanical stresses. In the *photo* a set of passive neutron detectors (*BDT* Bubble Dosimeter Thermal, *BD-PND* Bubble Dosimeter-Personal Neutron Dosimeter models) also used to detect the neutron emissions are visible. The results of this last analysis are reported in [27]

As regards the NE measurements, the He^3 neutron detector was switched on at least 1 h before the beginning of each compression test, in order to reach the thermal equilibrium of electronics, and to make sure that the behaviour of the device was stable with respect to intrinsic thermal effects. For the considered specimens P1, P2 the average measured background level ranges from $(4.00 \pm 1.00) \times 10^{-2}$ to $(6.40 \pm 1.60) \times 10^{-2}$ cps. In particular, for the neutron measurements of specimen P2, the neutron emissions achieved values up to three orders of magnitude higher than the ordinary background.

In Table 28.1, the experimental data concerning all the tested specimens are summarized. The results obtained from this analysis show how the crack generation is accompanied by mechanical energy release in the field of ultrasonic vibrations detected by AE sensors. It was also observed that, for constant specimen diameter, the AE signals reached high frequency peaks for low slenderness values, whereas the EME frequencies increase with the sample size. The highest neutron emissions occurred from specimens with EME detected in the field of MHz. This shows that the formation of coherent EM fields occurs over a wide range of frequencies, from few Hz to MHz and even up to microwaves, during the fracture propagation. This excited state of the matter could be a cause of subsequent resonance phenomena of nuclei able to produce neutron bursts in the presence of stress-drops or sudden catastrophic fractures.

28.3.2 Preliminary Test on High Frequency Vibration Detection

As anticipated in the Introduction, different materials were taken into account: a prismatic cement mortar specimen enriched with iron dioxide, measuring $4 \times 4 \times 8$ cm^3, a Luserna stone and a gypsum specimen (diameter 50 mm, slenderness 2), and a rock sample of magnetite (diameter 50 mm, slenderness 1.5), see Fig. 28.4. They were tested under compression by an electronically controlled servo-hydraulic press with a maximum capacity of 600 kN. This machine makes it possible to carry out tests in either load control or displacement control.

In particular, in this section the experimental results on the mortar specimen are reported. The data obtained from the other specimens are still under elaboration and we will discuss about them in a further report. The test on the mortar sample was performed by piston load control, setting loading steps of 20 kN, up to load of 120 kN. Every load increment had a lasting time of 1 min, and before being incremented by additional 20 kN, it was kept constant for 4 min. The periods in which the force was maintained constant were used to analyze with accuracy also in real time the vibration frequencies obtained from the photodiode. Once the planned value of 120 kN was reached, the load continued to grow until the final collapse of the specimen. The experimental set up is reported in Fig. 28.5.

The load vs. time diagram, the AE cumulated curve, and the associated counting rate are shown in Fig. 28.6. A widespread AE activity during all the loading steps was observed, with a maximum counting rate up to 11 hits per second which diminished when the force was kept constant. The mortar sample failure was preceded by an intense increment of AE burst activity at nearly 90 % of the peak load. As an example, a typical AE signal when the peak load is approaching, and its

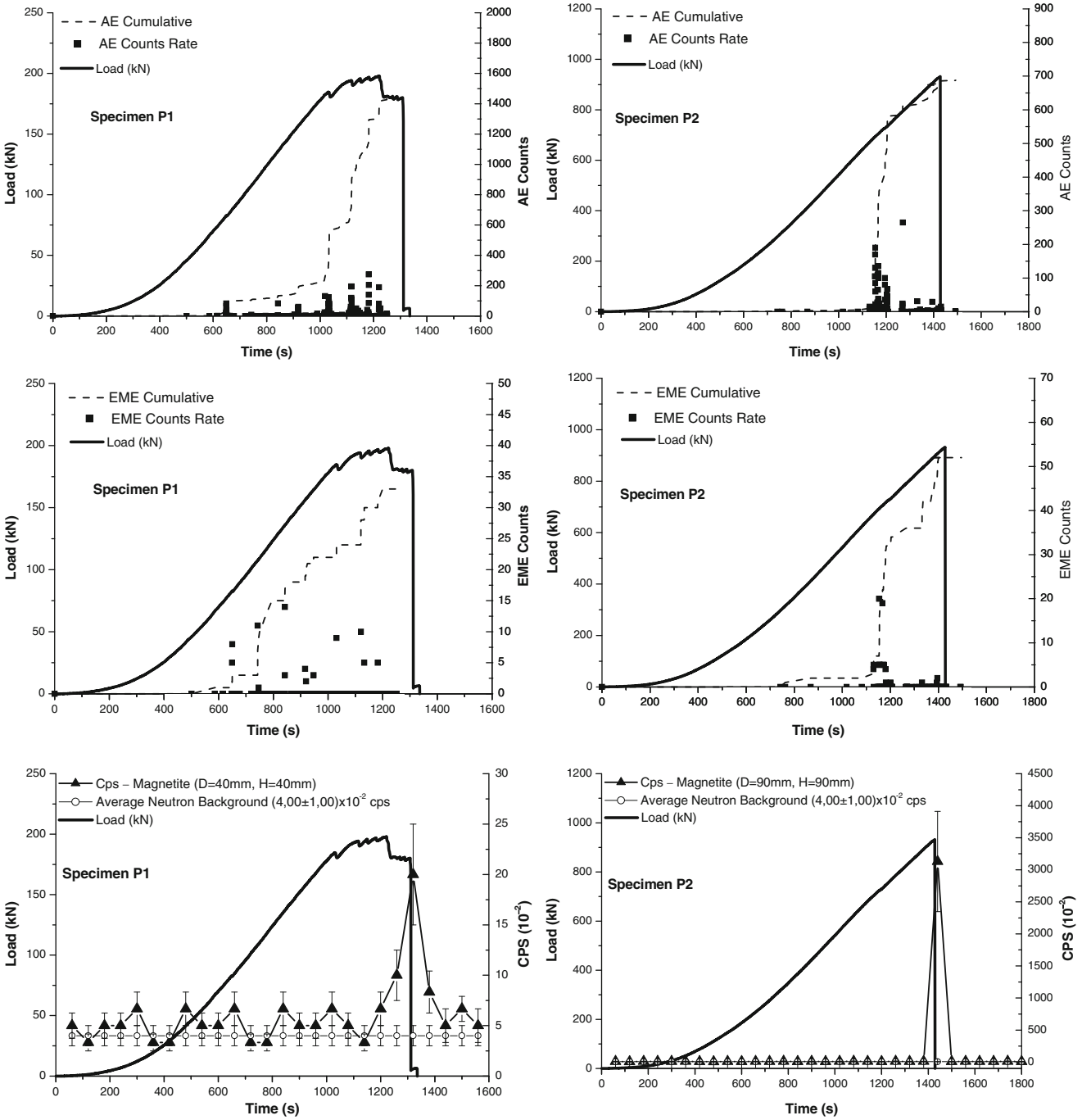

Fig. 28.3 Load vs. time diagram of the magnetite specimen P1 (M-40-1 type) (*left*); accumulated number and rate of AEs (*upper left*); accumulated number and rate of EMEs (*middle left*); NE count rate (*lower left*). Load vs. time diagram of the magnetite specimen P2 (M-90-1 type) (*right*); accumulated number and rate of AEs (*upper right*); accumulated number and rate of EMEs (*middle right*); NE count rate (*lower right*)

FFT (Fast Fourier Transform) analysis are shown in Fig. 28.7. The frequency spectrum, calculated by FFT analysis, is characterized by a wide range of frequencies, up to 250 kHz. In particular a mean frequency of 75 kHz was detected.

During the compression test, the sample vibration frequencies were measured by detecting the reflected laser light focused on a spot on the specimen surface trough a photo-detector (see Fig. 28.5). Before the beginning of the test, in order to increase the intensity of the reflected light, a reflecting paint was previously deposited on the specimen surface. The photo-detector evaluated the intensity of the received light, providing a frequency variation that is proportional to the vibration frequencies of the spot particles.

Table 28.1 Tested specimens and their mechanical characteristics

Specimens	Specimens number	Dimension		Piston velocity [m/s]	Volume [mm^3]	Average peak load [kN]
		Diameter [mm]	Slenderness [λ]			
Magnetite						
M-20-0.5	5	20	0.5	5×10^{-7}	3,140	67.46
M-20-1	2	20	1	5×10^{-7}	6,280	48.20
M-20-2	4	20	2	5×10^{-7}	12,560	45.88
M-40-0.5	2	40	0.5	1×10^{-6}	25,120	159.25
M-40-1	6	40	1	1×10^{-6}	50,240	146.87
M-40-2	4	40	2	1×10^{-6}	100,480	109.40
M-90-1	4	90	1	2×10^{-6}	572,265	849.89
Basalt						
B-50-2	2	50	2	1×10^{-6}	196,250	177.64

Specimens	AE		EME		NE	
	Average frequency [Hz]	Average highest frequency [Hz]	Average frequency [Hz]	Average highest frequency [Hz]	Average neutron background [10^{-2} cps]	Average count rate at the neutron emission [10^{-2} cps]
Magnetite						
M-20-0.5	20,975	56,990	19,622	>46,000	4.84 ± 1.21	Background
M-20-1	25,889	49,488	—	—	5.90 ± 1.48	Background
M-20-2	23,569	42,984	32,312	>55,000	5.70 ± 1.42	Background
M-40-0.5	53,354	133,133	28,278	>49,000	5.50 ± 1.38	Background
M-40-1	60,055	90,997	37,787	>77,000	5.06 ± 1.26	18.75 ± 4.69
M-40-2	33,520	73,385	35,274	>98,000	5.60 ± 1.40	25.96 ± 6.49
M-90-1	52,350	132,062	110,089	>1 MHz	4.95 ± 1.24	901.20 ± 225.30
Basalt						
B-50-2	76,668	165,363	204,417	>335,000	5.60 ± 1.40	14.22 ± 3.55

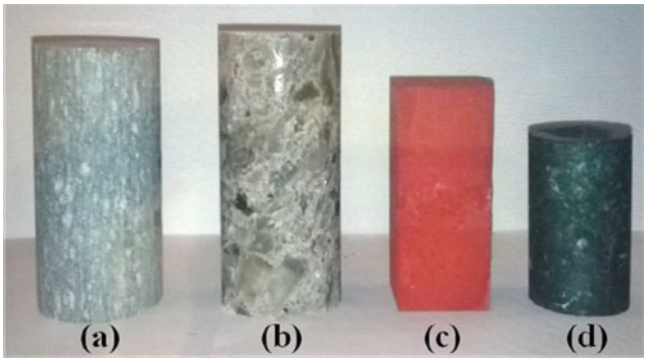

Fig. 28.4 The tested rocks and cement mortar specimens. (**a**) Lusena stone specimen (diameter 50 mm, slenderness 2); (**b**) gypsum specimen (diameter 50 mm, slenderness 2); (**c**) mortar specimen enriched with iron dioxide ($4 \times 4 \times 8$ cm^3); (**d**) magnetite specimen (diameter 50 mm, slenderness 1.5)

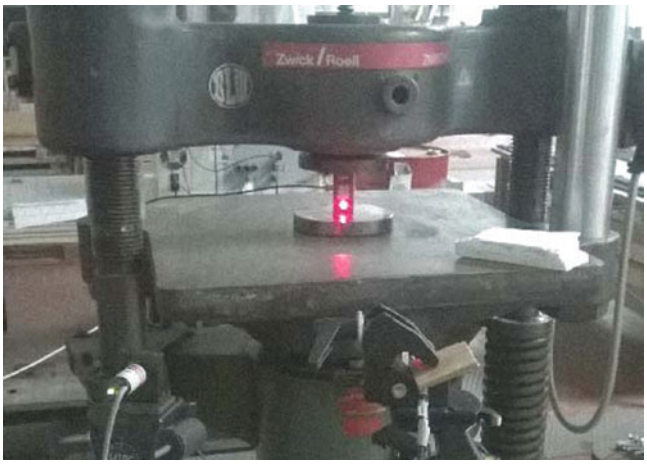

Fig. 28.5 The mortar specimen under compression equipped with the AE sensor and the laser apparatus

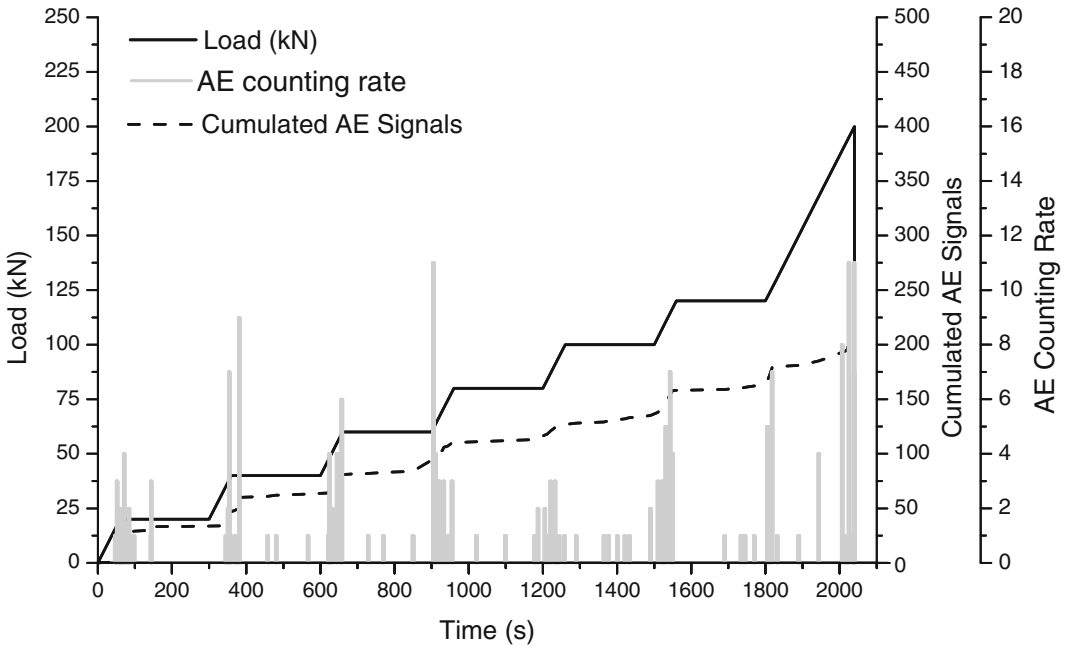

Fig. 28.6 Load vs. time diagram with the AE cumulated curve and the associated AE counting rate

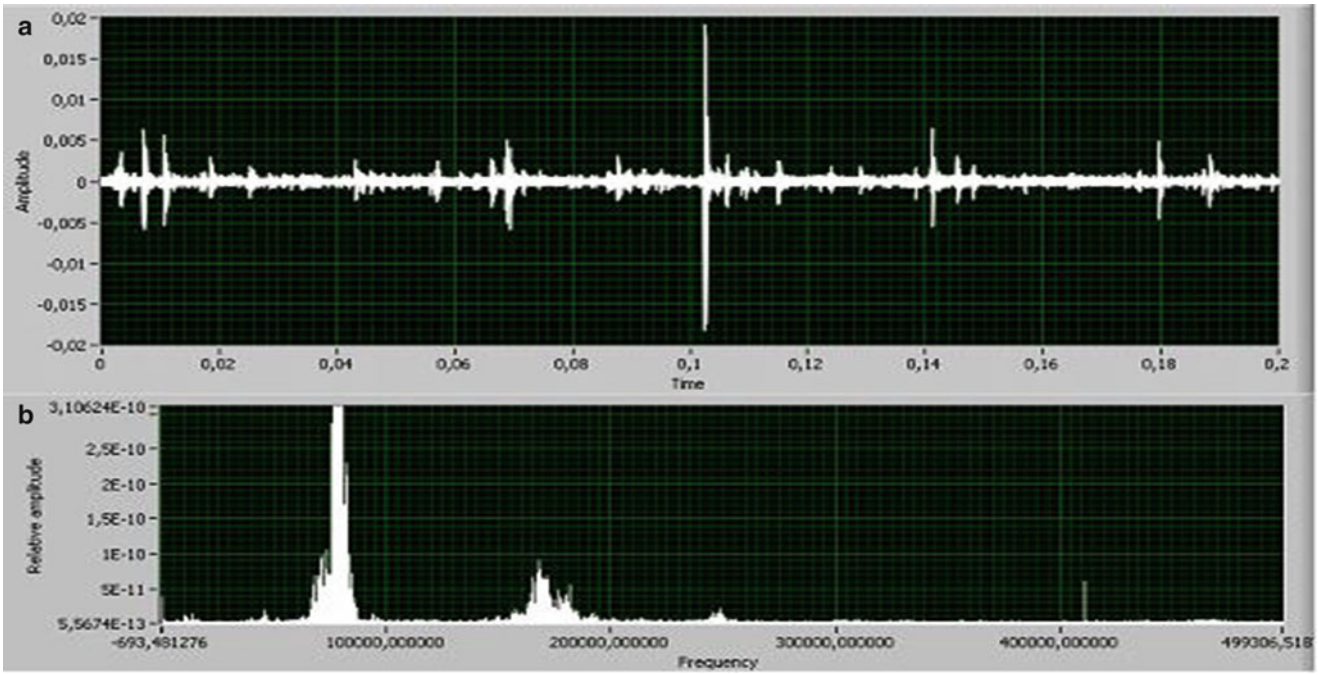

Fig. 28.7 Typical AE emissions at peak load (**a**), with the associated FFT analysis (**b**)

The performed analysis showed two different behaviors of the material under stress. By the AE sensor the signals due to elastic waves produced by crack advancements were detected; at the same time, by the laser apparatus the vibrations coming from the crystal lattice were analyzed in the neighborhood of the monitored spot.

Furthermore, the data obtained from the piezoelectric transducers were acquired at a sampling rate of 1 M-sample per second, while the information coming from the photodiode were obtained by the Agilent oscilloscope at a sampling rate up to 1 G-sample per second. This last solution allowed the signals detection with frequencies up to 100 MHz.

The load vs. time diagram, the main frequencies detected by the piezoelectric transducers, and the optical device are shown in Fig. 28.8. It is interesting to emphasize that the AE signals are characterized by frequencies up to 250 kHz, whereas the mechanical vibrations of the specimen spot reach a wider range of frequencies, from kHz to MHz, with the most intense values of 667 kHz and 3.8 MHz, respectively.

This phenomenon may be attributed to the increase in the applied force acting on the specimen, and to the resulting stress state involving a certain amount of accumulated energy. Increasing the stress the specimen vibrates locally at higher frequencies. During the final specimen collapse, this energy is suddenly released with the creation of macrocracks characterized by typical AE frequencies. Moreover, as it can be seen from the graph of Fig. 28.8, the frequencies detected by the photodiode remain almost unchanged for all the duration of the test, whereas the AE frequencies tend to decrease approaching to the final collapse as has been observed by the authors in previous works [10].

These encouraging preliminary results lead to the conclusion that spot particles could still locally vibrate at frequencies higher than MHz and even up to GHz or microwaves. But the feasibility of this observation depends both on the sensitivity and sampling acquirement rate of the employed apparatus. Moreover, better results will be obtained by processing the data reached from the Lusena stone and gypsum specimens, that are characterized by crystal intrusions and more reflective surfaces. For this reason, the authors are developing a more efficient experimental set-up to detect wider and more intense frequency spectra.

28.4 Conclusions

The experimental evidence presented in this paper confirms that AE, EME and NE signals are failure precursors in brittle rock materials. The highest neutron emissions occurred from specimens with EME detected in the field of MHz. This shows that the formation of coherent EM fields occurs over a wide range of frequencies, from few Hz to MHz and even up to microwaves, during the fracture propagation.

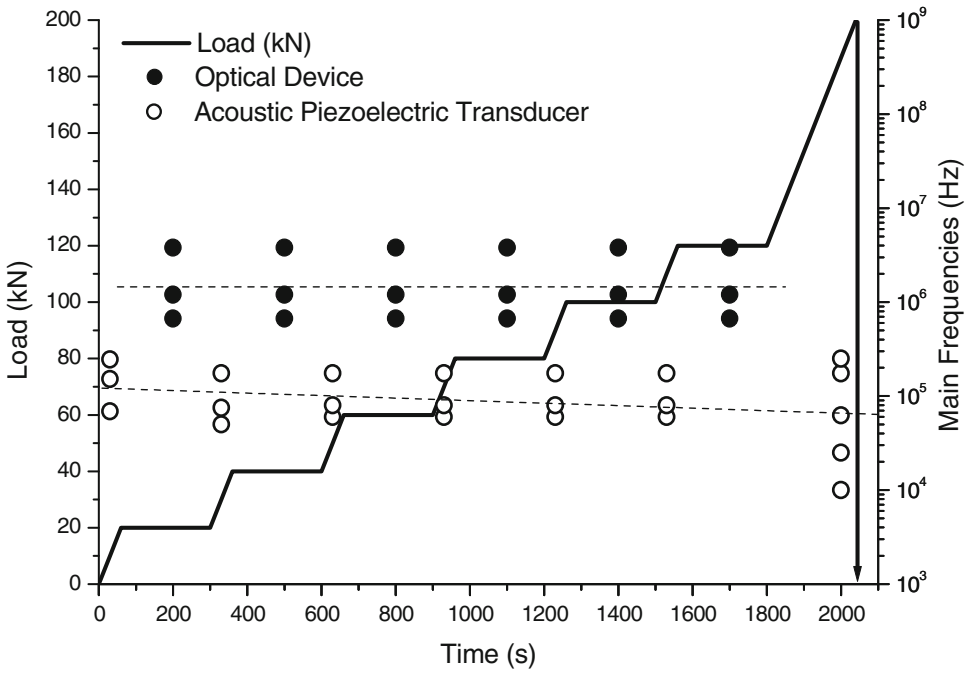

Fig. 28.8 The load vs. time diagram of the mortar specimen with the main frequencies detected by the piezoelectric transducer and the optical device

In addition, a first attempt to analyze mechanical vibrations in a spot of a mortar specimen under compression was carried out. The experimental apparatus was based on a laser pointer and a high-speed light detector. Simultaneously with the laser signals also the AE events were monitored. The AE signals, acquired by a PZT sensor, were characterized by frequencies of few hundreds of kHz, whereas the specimen vibrations, detected by the laser, reached higher values up to 3.8 MHz. This phenomenon may be attributed to the stress increase and to the consequent energy released that induces the solid to vibrate locally over a wide range of frequencies, from kHz to MHz, with the more intense values on 3.8 MHz.

It is important to emphasize that the phenomenon under investigation is unique, because we are analyzing the specimen vibration under stress, but the two used devices capture two different frequencies ranges. As a matter of fact, the obtained experimental results reported in this paper depend on two main factors. The first one connected to the physical characteristics of the sensors, the second one related to the limitations of the used sampling equipment. The AE sensors are sensitive to frequencies comprised between 50 and 800 kHz, for which a sampling rate of 1 M-sample per second was adequate. The signals obtained by the laser instead—characterized by a wide range of frequencies—were analyzed by an oscilloscope operating at a sampling rate of up to 1 G-samples per second, that cannot account for vibrations higher than 100 MHz.

Nevertheless, the hypothesis is that locally the matter could still vibrate at higher frequencies, up to GHz or microwaves. For this reason the authors, to give account of high frequency localized vibrations, linked to an excited state of matter, that could be the cause of subsequent resonance phenomena, are developing a more efficient experimental set-up that can detect wider and more intense frequency spectra.

Acknowledgements The authors wish to thank L. Spagnolo of Politecnico di Torino, Department of Control and Computer Engineering, for his valuable technical assistance with the LabView data processing.

References

1. Carpinteri A, Cardone F, Lacidogna G (2009) Piezonuclear neutrons from brittle fracture: early results of mechanical compression tests. Strain 45:332–339
2. Cardone F, Carpinteri A, Lacidogna G (2009) Piezonuclear neutrons from fracturing of inert solids. Phys Lett A 373:4158–4163
3. Carpinteri A, Borla O, Lacidogna G, Manuello A (2010) Neutron emissions in brittle rocks during compression tests: monotonic vs cyclic loading. Phys Mesomechanics 13:268–274
4. Carpinteri A, Lacidogna G, Manuello A, Borla O (2011) Energy emissions from brittle fracture: neutron measurements and geological evidences of piezonuclear reactions. Strenght Fract Comp 7:13–31
5. Carpinteri A, Lacidogna G, Manuello A, Borla O (2013) Piezonuclear fission reactions from earthquakes and brittle rocks failure: evidence of neutron emission and non-radioactive product elements. Exp Mech 53:345–365

6. Mogi K (1962) Study of elastic shocks caused by the fracture of heterogeneous materials and its relation to earthquake phenomena. Bull Earthquake Res Inst 40:125–173
7. Lockner DA, Byerlee JD, Kuksenko V, Ponomarev A, Sidorin A (1991) Quasi static fault growth and shear fracture energy in granite. Nature 350:39–42
8. Ohtsu M (1996) The history and development of acoustic emission in concrete engineering. Mag Concr Res 48:321–330
9. Rundle JB, Turcotte DL, Shcherbakov R, Klein W, Sammis C (2003) Statistical physics approach to understanding the multiscale dynamics of earthquake fault systems. Rev Geophys 41:1019–1049
10. Niccolini G, Schiavi A, Tarizzo P, Carpinteri A, Lacidogna G, Manuello A (2010) Scaling in temporal occurrence of quasi-rigid-body vibration pulses due to macrofractures. Phys Rev E 82:46115 (1-5)
11. Carpinteri A, Lacidogna G (2006) Damage monitoring of an historical masonry building by the acoustic emission technique. Mater Struct 39:161–167
12. Carpinteri A, Lacidogna G (2006) Structural monitoring and integrity assessment of medieval towers. J Struct Eng (ASCE) 132:1681–1690
13. Carpinteri A, Lacidogna G (2007) Damage evaluation of three masonry towers by acoustic emission. Eng Struct 29:1569–1579
14. Carpinteri A, Lacidogna G, Niccolini G (2006) Critical behaviour in concrete structures and damage localization by acoustic emission. Key Eng Mater 312:305–310
15. Carpinteri A, Lacidogna G, Pugno N (2007) Structural damage diagnosis and life-time assessment by acoustic emission monitoring. Eng Fract Mech 74:273–289
16. Lacidogna G, Carpinteri A, Manuello A, Durin G, Schiavi A, Niccolini G, Agosto A (2010) Acoustic and electromagnetic emissions as precursor phenomena in failure processes. Strain 47(2):144–152
17. Carpinteri A, Lacidogna G, Manuello A, Niccolini A, Schiavi A, Agosto A (2010) Mechanical and electromagnetic emissions related to stress-induced cracks. Exp Tech 36:53–64
18. Misra A (1977) Theoretical study of the fracture-induced magnetic effect in ferromagnetic materials. Phys Lett A 62:234–236
19. Frid V, Rabinovitch A, Bahat D (2003) Fracture induced electromagnetic radiation. J Phys D 36:1620–1628
20. Rabinovitch A, Frid V, Bahat D (2007) Surface oscillations. A possible source of fracture induced electromagnetic oscillations. Tectonophysics 431:15–21
21. Hadjicontis V, Mavromatou C, Nonos D (2004) Stress induced polarization currents and electromagnetic emission from rocks and ionic crystals, accompanying their deformation. Nat Hazards Earth Syst Sci 4:633–639
22. Warwick JW, Stoker C, Meyer TR (1982) Radio emission associated with rock fracture: possible application to the great Chilean earthquake of May 22, 1960. J Geophys Res 87:2851–2859
23. Nagao T, Enomoto Y, Fujinawa Y et al (2002) Electromagnetic anomalies associated with 1995 Kobe earthquake. J Geodyn 33:401–411
24. Borla O, Lacidogna G, Di Battista E, Niccolini G, Carpinteri A (2013) Multiparameter approach for seismic risk evaluation through environmental monitoring. Atti del 21° Congresso Nazionale di Meccanica Teorica ed Applicata (AIMETA), Torino, Italy, CD-ROM
25. Widom A, Swain J, Srivastava YN (2013) Neutron production from the fracture of piezoelectric rocks. J Phys G: Nucl Part Phys 40:15006 (1–8)
26. Widom A, Swain J, Srivastava YN (2013) Photo-disintegration of the iron nucleus in fractured magnetite rocks with magnetostriction. arXiv:1306.6286
27. Lacidogna G, Borla O, Niccolini G, Carpinteri A (2012) Time correlation between different forms of energy emitted from rocks under compression. In: Fracture mechanics for durability, reliability and safety (Proceedings of the 19th European Conference on Fracture, Kazan, Russia, 2012), CD-ROM, Paper N. 609

Chapter 29
Electromagnetic Emission as Failure Precursor Phenomenon for Seismic Activity Monitoring

O. Borla, G. Lacidogna, E. Di Battista, G. Niccolini, and A. Carpinteri

Abstract The electromagnetic (EM) signals detected during failure of brittle materials are analogous to the anomalous radiation of geoelectromagnetic waves observed before major earthquakes, reinforcing the idea that the EM effect can be applied as a forecasting tool for seismic events.

Moreover, it has been argued (Widom-Swain-Srivastava) that the elastic energy released by micro-crack production eventually yields to forming macroscopic fractures, whose mechanical vibrations are converted into electromagnetic oscillations over a wide range of frequencies, from few Hz to MHz, and even up to microwaves.

This excited state of the matter could be a precursor of subsequent resonance phenomena of nuclei able to produce neutron bursts in the presence of stress-drops or sudden catastrophic fractures. As a matter of fact, neutron emissions (NE) measured at seismic areas exceed the usual neutron background up to three orders of magnitude in correspondence to rather appreciable earthquakes.

In this work the Authors measure the EM pulses generated during micro-cracking of rock specimens by a dedicated loop antenna sensitive up to MHz.

Taking into account the relationship between EM, NE and seismic activity, it will be possible to set up a sort of alarm system that could be at the base of a warning network.

Keywords Electromagnetic emission • Loop antenna • Stress-drops • Neutron emission • Seismic activity

29.1 Introduction

Monitoring and detection of the different forms of energy emitted during the failure of natural and artificial brittle materials allow an accurate interpretation of damage in the field of Fracture Mechanics. These phenomena have been mainly measured based on the signals captured by the acoustic emission (AE) measurement systems [1–10], or on the detection of the electromagnetic (EM) charge [11–18]. Nowadays, the AE technique is well-known in the scientific community and applied for monitoring purpose. In addition, based on the analogy between AE and seismic activity, AE associated with microcracks are monitored and power-law frequency vs. magnitude statistics are observed.

The EM signals are usually related to brittle materials in which the fracture propagation occurs suddenly and it is accompanied by stress drops in the stress–strain curve. This behavior is explained according to the model of Frid et al. [15] and Rabinovitch et al. [16]. For this model the EM signals source is due to the rupture of material's bonds during the cracks growth. This involves the breaking of mechanical and electrical equilibrium on the fracture surfaces with creation of ions moving collectively. The resulting oscillating dipoles act as a source of EM emissions.

A number of laboratory studies revealed the existence of EM signals during fracture experiments carried out on a wide range of materials [11]. Studies on electrical properties of rocks have been demonstrated that exists a correlation between electrical resistivity and cumulative damage [19–21]. Moreover, it was observed that the EM signals and electric signals

O. Borla (✉) • G. Lacidogna • E. Di Battista • G. Niccolini • A. Carpinteri
Department of Structural, Geotechnical and Building Engineering, Politecnico di Torino, Corso Duca degli Abruzzi 24, Torino 10129, Italy
e-mail: oscar.borla@polito.it

J. Carroll and S. Daly (eds.), *Fracture, Fatigue, Failure, and Damage Evolution, Volume 5: Proceedings of the 2014 Annual Conference on Experimental and Applied Mechanics*, Conference Proceedings of the Society for Experimental Mechanics Series,
DOI 10.1007/978-3-319-06977-7_29, © The Society for Experimental Mechanics, Inc. 2015

detected during failure of materials are analogous to the anomalous radiation of geoelectromagnetic waves observed before major earthquakes [12, 22], these events reinforce the idea that the EM effect can be applied as a forecasting tool for seismic events.

Very recently it has been also argued by Widom et al. [23, 24] that the elastic energy due to micro-crack production eventually yields to forming macroscopic fractures, whose mechanical vibrations are converted into electromagnetic oscillations over a wide range of frequencies, from few Hz to MHz, and even up to "microwave." This excited state of the matter could be a cause of subsequent resonance phenomena of nuclei able to produce neutron bursts in the presence of stress-drops or sudden catastrophic fractures.

As regards the neutron emissions (NE), original experimental tests were performed by Carpinteri et al. on brittle rock specimens [25–32]. Different kinds of compression tests under monotonic, cyclic and ultrasonic mechanical loading have been carried out fully confirming the hypothesis of piezonuclear reactions, giving rise to neutron emissions up to three orders of magnitude higher than the background level at the time of catastrophic failure.

These phenomena have important implications also at the Earth's crust scale. Recent neutron emission detections by the Authors [33] and other Russian researchers [34–37] have led to consider the Earth's crust as a relevant source of neutron flux variations.

In this work the Authors measure the EM pulses generated during micro-cracking on gypsum specimens by a dedicated loop antenna sensitive up to MHz. The device was calibrated according to metrological requirements and it was also assembled in order to drastically reduce false signals detection due to a wrong antenna-cable coupling at the junction.

Finally, preliminary results, acquired at a gypsum mine situated in the Northern Italy (Murisengo, AL) and related to the evaluation of acoustic and nuclear phenomena are reported. The monitoring system, based on the simultaneous acquisition of the various physical quantities, control the structural stability of the mine carrying out, at the same time, the environment monitoring for the seismic risk evaluation.

Taking into account the relationship between AE, EM, NE and seismic activity it will be possible to set up a sort of alarm systems that could be at the base of a warning network. This warning system could combine the signals from other alarm stations to prevent the effects of seismic events and to identify the earthquakes' epicentres. Similar networks, only based on seismic accelerations, are being utilized all over the World in countries like Mexico, Taiwan, Turkey, Romania and Japan [38].

29.2 Material and Methods

29.2.1 Dedicated Loop Antenna

EM signals was monitored using a device, calibrated according to metrological requirements, constituted by three winding loops with different number of turns that can be positioned around the monitored specimen. The working principle is based on the induction Faraday's law. It states that the electromagnetic force (voltage) in a closed circuit (loop) is proportional to the change of the magnetic flux in the windings section. In fact, the three coaxial coils with an increasing number of turns are capable to perform the measurement from very low (Hertz) to high (MHz) frequencies in the magnetic field. The first coil, constituted by 5 turns, works in a frequency range from 300 kHz to 4 MHz. The other two coils constituted by 125 turns and 500 turns, work in the frequency range from 0 to 20 kHz, and from 0 to 1 kHz, respectively. Each turn is realized by a 0.2 mm copper wire, mounted on two coaxial PVC tubes embedded in a two components resin, in order to allow a large range of measurements.

In Fig. 29.1 the employed antenna and its CAD representation are shown. The antenna was modelled by triangular patches necessary for treating problems of scattering phenomena by numerical procedure based on electric field integral equation calculation [39]. By defining suitable triangulation, defined in terms of an appropriate set of faces, edges, vertices, and boundary edges, as illustrated in Fig. 29.1, it is possible to define all the antenna surface S and so drastically reduce false signals detection during experimental observations.

29.2.2 Acoustic Piezoelectric Transducer

The AE activity emerging from the compressed specimens was detected by a piezoelectric (PZT) transducer glued on the external surface, resonant at 78 kHz, which is able to convert the high-frequency surface motions due to the acoustic wave into electric signals (the AE signal). The transducer sensitivity in the low-frequency range were measured by placing it on

Fig. 29.1 Dedicated loop antenna (*left*) with its CAD representation (*right*)

shaker excited by frequencies in the range 0–10 kHz (white noise). The result of this calibration at low frequencies was 1.2 μV/(mms^{-2}). Resonant sensors are more sensitive than broadband sensors, which are characterized by a flat frequency response in their working range, and then they can be successfully used in monitoring of large-sized structures [6, 7].

29.2.3 ^{3}He Proportional Counter

Since neutrons are electrically neutral particles, they cannot directly produce ionization in a detector, and therefore cannot be directly detected. This means that neutron detectors must rely upon a conversion process where an incident neutron interacts with a nucleus to produce a secondary charged particle. These charged particles are then detected, and from them the neutrons presence is deduced. For an accurate neutron evaluation, a ^{3}He radiation monitor were used.

During the experimental trial the neutron field monitoring was carried out in "continuous mode." The AT1117M (ATOMTEX, Minsk, Republic of Belarus) neutron device is a multifunctional portable instrument with a digital readout consisting of a processing unit (PU) with an internal Geiger-Müller tube and external smart probes (BDKN-03 type). This type of device provides a high sensitivity and wide measuring ranges (neutron energy range 0.025 eV–14 MeV), with a fast response to radiation field change ideal for environmental monitoring purpose.

29.3 Experimental Results

29.3.1 Laboratory Tests on Cylindrical Gypsum Specimens

Preliminary laboratory compression tests on four gypsum specimens were conducted to assess the validity and efficiency of the dedicated loop antenna in view to a permanent installation for in situ monitoring.

Gypsum samples of the same size and shape (diameter D = 52 mm, slenderness $\lambda = 2$) taken from Murisengo mine, were used. For these tests a standard servo-hydraulic press with a maximum capacity of 1,000 kN, equipped with control electronics, was employed. This machine makes it possible to carry out tests in either load or displacement control. The tests were performed in piston travel displacement control by setting, for all the tested specimens, a velocity of 0.001 mm/s during compression.

It is known that flexing, twisting, or transient impacts on cables could cause electromagnetic signal noise (with a spectrum from few Hz to tens THz) due to rapid changes of capacitance between conductors. For these reasons the loop antenna was carefully placed around the sample, as shown in Fig. 29.2, to drastically reduce any sort of triboelectric effect.

Specific tests were previously conducted to assess the EM environmental noise. In particular, the EM probe was used to detect the EM background for about 12 h before to start the compression tests. The typical environmental noise is represented

Fig. 29.2 The electromagnetic coaxial coils device and AE piezoelectric transducer positioned around the monitored gypsum specimen

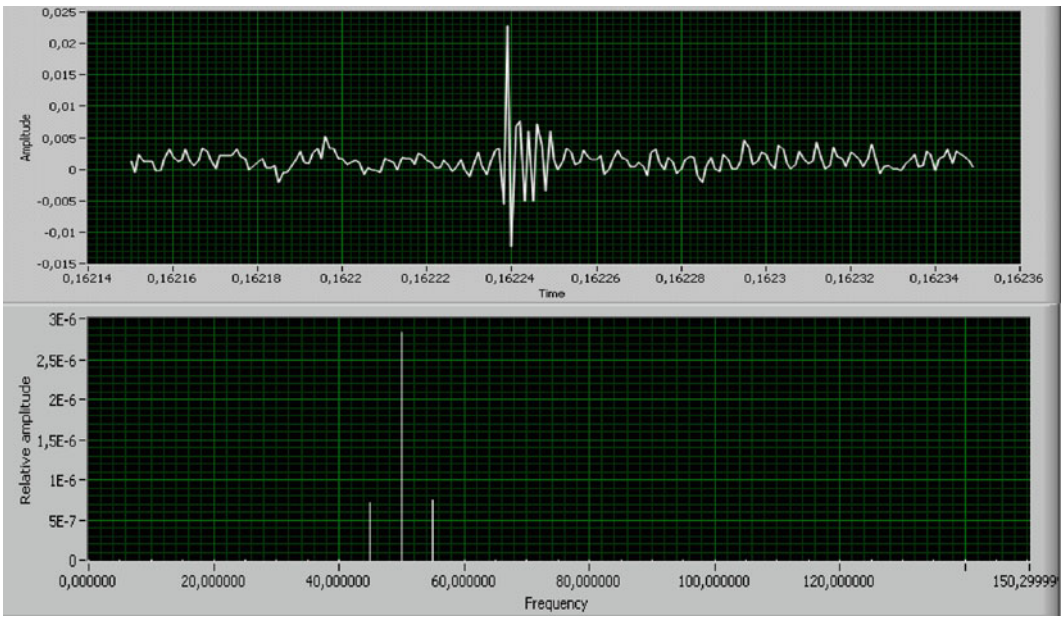

Fig. 29.3 Typical EM environmental noise spectrum (*up*) with the associated FFT (Fast Fourier Transform) analysis (*down*)

in Fig. 29.3 with the associated FFT (Fast Fourier Transform) analysis. It is evident that the main contribution is due to signals with frequency peaked at 50 Hz, the typical domestic power supply, with a maximum "Relative Amplitude" of 2.8×10^{-6} (Fig. 29.3).

In addition, to better monitoring the fracture precursors the AE signals were detected by applying to the sample surface the piezoelectric transducer described above (Fig. 29.2).

In Fig. 29.4a, the load vs. time and the cumulated AE and EM signals for one of the tested gypsum specimen are represented. Similar results were obtained for the other specimens. This sample, that is characterized by an evident ductile behaviour, reached a maximum load of about 40 kN. In particular, starting from the first peak load, a significant increase in AE rate is observed. The AE signals achieved the maximum rate in proximity of the peak loads, while in the post peak phase,

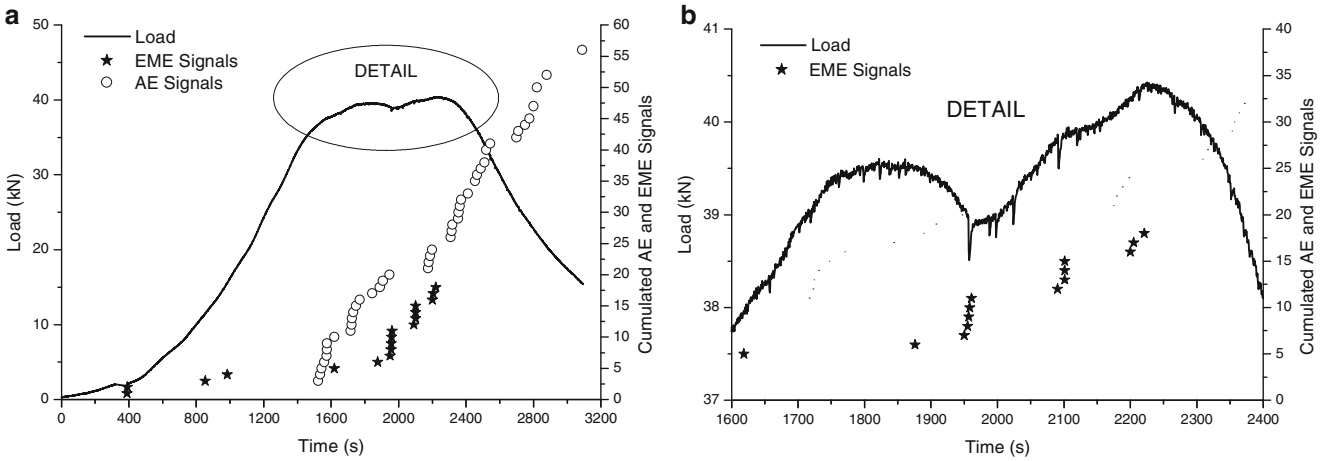

Fig. 29.4 (**a**) Load vs. time curve, AE (*circles*) and EM (*stars*) signals cumulated number. (**b**) Detail of load vs. time curve and EM cumulated number in the vicinity of the peaks load

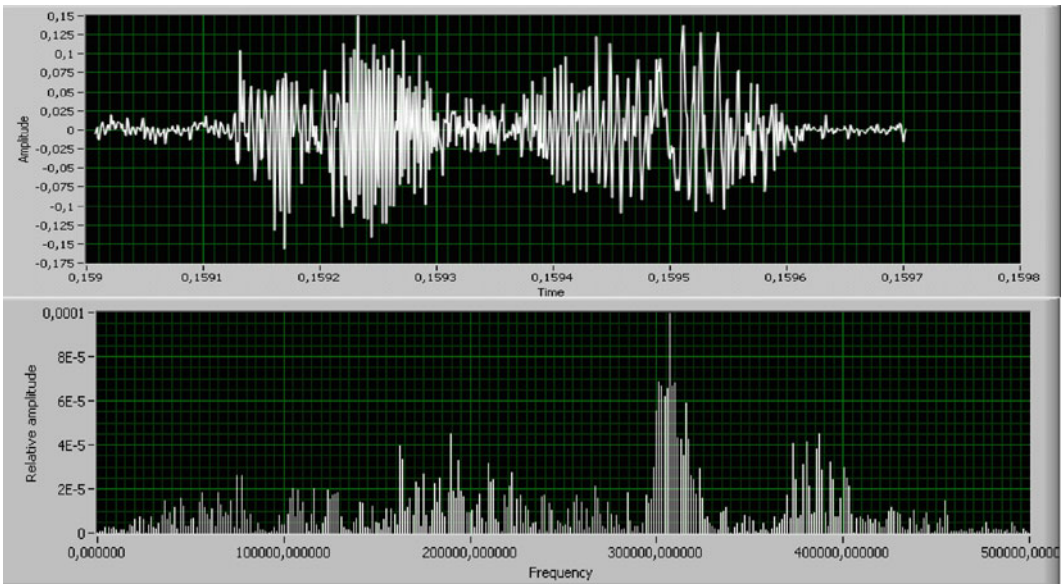

Fig. 29.5 Typical EM emissions at peak load (*up*) with the associated FFT (Fast Fourier Transform) analysis (*down*)

at the end of specimen softening behaviour, the AE rate diminished. On the other hand, EM emissions were detected for all the duration of the experiment, with a sensible growth rate just after the second peak load. This behaviour, both for AE and EM signals clearly represents a precursor of specimen failure.

Moreover, as shown in detail in Fig. 29.4b, it is observed that gypsum is characterized by weak and frequent stress drops, around which EM signals have accumulated. This EM distribution reinforces the idea that in this particular phases the accumulated energy is suddenly released, due to micro-cracks formation, and the mechanical vibrations are converted into electromagnetic oscillations [23, 24].

As an example, in Fig. 29.5 a typical EME signal at the peak load, and its FFT analysis are shown. Confirming the hypotheses of Widom et al. [23, 24], it is evident the wide range of EM spectrum with respect to the one related to environmental noise (see Fig. 29.3). The frequency spectrum, calculated by FFT analysis, is characterized by a wide range of frequencies (up to 500 kHz) with a maximum "Relative Amplitude" of 1.0×10^{-4}. In particular, a main frequency of about 300 kHz is identified, ca. 6,000 times higher than the background level.

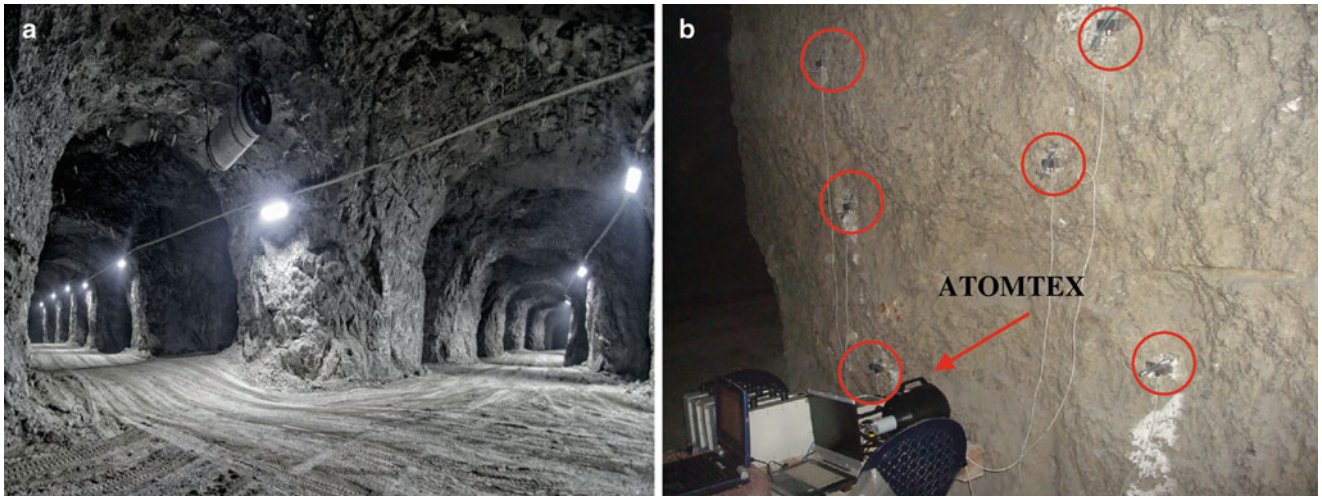

Fig. 29.6 (**a**) San Pietro—PratoNuovo gypsum quarry. (**b**) The six AE devices and the ATOMTEX ^{3}He neutron radiation monitor applied to the selected pillar

29.3.2 In Situ Environmental Monitoring

From June 24, 2013 a dedicated in situ monitoring at the San Pietro—PratoNuovo gypsum quarry located in Murisengo (AL), Italy is started and it is still in progress. The mine is structured in five levels of underground development and from which high quality gypsum is extracted every day (Fig. 29.6a).

The structural stability in each level is assured by an archway-pillar system which unloads over the underlying floor of average thickness of 4 m. Through accurate topographic surveys, it was possible to ensure a good coaxiality of the pillars between the different levels. In this way dangerous loads eccentricity were avoided.

Currently the quarry is subjected to a multiparameter monitoring, by the AE technique and the detection of the environmental neutron field fluctuations, in order to assess the structural stability and, at the same time, to evaluate the seismic risk of the surrounding area. The dedicated "USAM" AE acquisition system consists of 6 PZT transducers, calibrated over a wide range of frequency comprised between 50 and 800 kHz, 6 units of data storage provided of triggers and a central unit for the data synchronization.

The AE signals received by all the transducers are analysed by means of a threshold detection device that counts the signal bursts exceeding a certain electric tension (measured in volts (V)). Throughout the monitoring period, the threshold level for the detection of the input signals coming from the PZT transducers was kept at 100 mV. Based on the authors' experience, in fact, this level is the most significant for the detection of AE signals from damage processes in non-metallic materials.

Figure 29.7 shows a plot of the cumulative AE count obtained on the basis of the number of events detected per monitoring day. The curve was plotted starting from the date of application of the sensors to July 9, 2013. Moreover the AE count rate distribution in terms of events/min compared to the usual seismic activity of the area (green circles)—recorded within a 100-km radius from the quarry site—and to the rock blasting (red triangles) made during the monitoring period is also shown. The experimental observation reveals a correlation between the AE events and the most intense and closed seismic events [40], but not with the rock blasting. As can be seen the highest AE count peak (ca. 150) was detected on June 25, 2013 when the surrounding area was hit by three small quakes [40]. Finally from Fig. 29.7 it is possible to observe that the plot of the cumulative AE count is characterized by jumps reflecting sudden increases in acoustic events, together with frequency and amplitude increment. The discontinuities in the cumulative AE count curve denote the critical moments during which the release of energy from the microcrack formation process is greatest. Moreover the *b*-value estimation indicates also that the monitored pillar is actually undergoing to a damage process [8–10]. As a matter of fact high *b*-values is linked to diffused microcracking, while, to the other hand, low *b*-values correspond to macrocrak growth.

In addition, also a neutron field evaluation was carried out in "continuous mode" by means of the ATOMTEX ^{3}He neutron radiation monitor.

A relative natural background measurement was performed before the beginning of the monitoring campaign. The average natural level was find about one order of magnitude lower with respect to the usual environmental background. This value is in agreement with the location of the mine, which is about 100 m below the ground level.

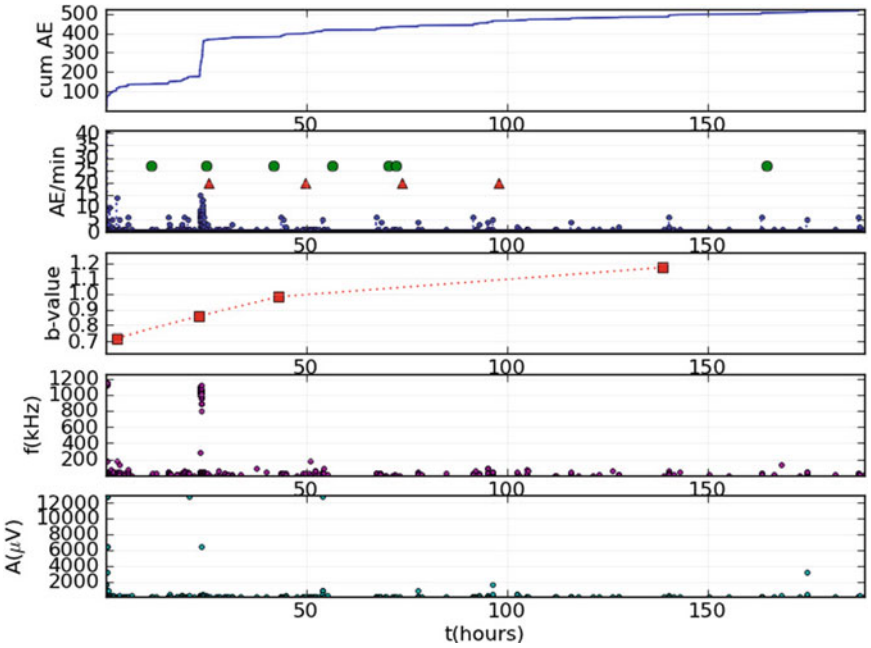

Fig. 29.7 Cumulated AE activity, AE count rate, *b*-value, AE frequency and amplitude relating to the pillar monitored during the experimental campaign

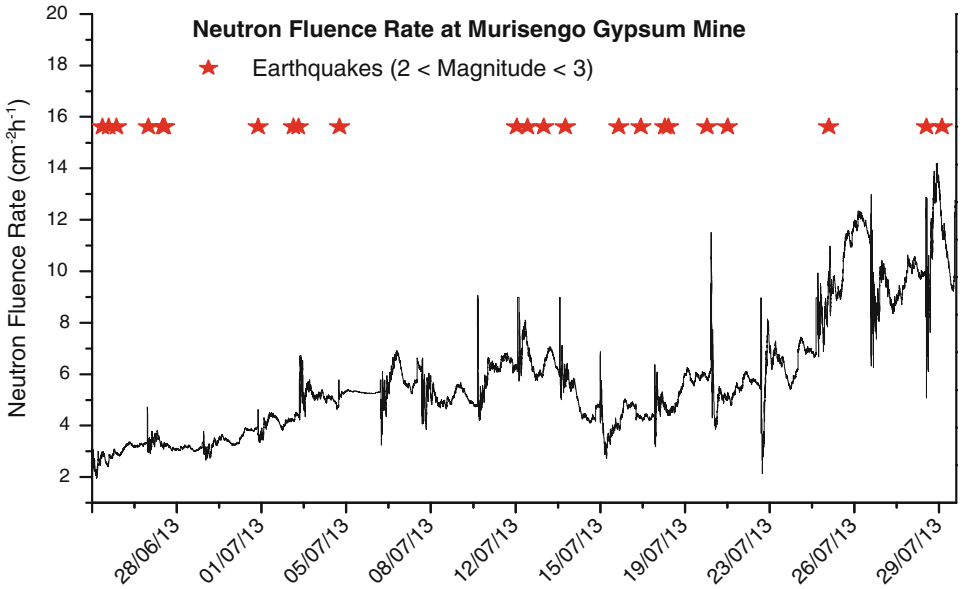

Fig. 29.8 Neutron Ambient fluence rate compared to local seismic activity

Evident peaks in neutron radiation field were detected in the monitored period. Moreover, starting from July 1st, it is possible to observe a continuous and constant increase in the neutron fluence rate with respect to the average natural background. Bursts of neutron radiation of at least 30 min long were also detected.

The comparison between the earthquakes [40] occurred in the immediate vicinity of the monitored area during the experimental campaign was carried out. From Fig. 29.8 it is possible to observe that the most significant neutron emission increments happened before or after quakes occurrence. This further experimental evidence strengthens the idea that integrating neutron fluctuations with acoustic and electromagnetic emissions—and also considering gas radon emission that appears to be one of the most reliable seismic precursors—it will be possible to set up a sort of monitoring systems that could perform a warning environmental monitoring.

29.4 Conclusions

Dedicated loop antenna was used to detect EM emissions generated during micro-cracking. The experimental data strengthen the hypothesis that the released energy due to micro-crack production can yield to forming macroscopic fractures, whose mechanical vibrations are converted into electromagnetic oscillations over a wide range of frequencies, from few Hz to MHz, and even up to microwave.

It is also known that the EM signals detected during failure of materials are analogous to the anomalous radiation of geoelectromagnetic waves observed before major earthquakes, reinforcing the idea that the EM effect can be applied as a forecasting tool for seismic events.

On the other hand, recent neutron emission detections have led to consider also the Earth's crust as a relevant source of neutron flux variations.

Preliminary results, acquired at a gypsum mine related to the evaluation of acoustic, and nuclear phenomena are reported. The experimental data acquired emphasize the close correlation between acoustic, electromagnetic and nuclear emissions and seismic activity. The monitoring campaign is till in progress and additional data will be provided in the next publications.

Thanks to these encouraging result, the Authors will improve their research by using wide frequency range antennas able to detect higher frequencies up to GHz or THz.

By integrating all these signals, it will be possible to set up a sort of alarm systems that combine AE, EM and neutron sensors for the prediction and diagnosis of earthquakes. These sensors could be applied at certain depths in the soil, along the most important faults, or very close to the most seismic areas to prevent well in advance the effects of seismic events and to identify the epicentre of an earthquake.

Acknowledgements The Authors are grateful to Dr. Sandro Gennaro from San Pietro PratoNuovo gypsum mine for his assistance during the in situ environmental monitoring.

References

1. Mogi K (1962) Study of elastic shocks caused by the fracture of heterogeneous materials and its relation to earthquake phenomena. Bull Earthquake Res Inst 40:125–173
2. Lockner DA, Byerlee JD, Kuksenko V, Ponomarev A, Sidorin A (1991) Quasi static fault growth and shear fracture energy in granite. Nature 350:39–42
3. Shcherbakov R, Turcotte DL (2003) Damage and self-similarity in fracture. Theor Appl Fract Mech 39:245–258
4. Ohtsu M (1996) The history and development of acoustic emission in concrete engineering. Mag Concr Res 48:321–330
5. Carpinteri A, Lacidogna G, Pugno N (2006) Richter's laws at the laboratory scale interpreted by acoustic emission. Mag Concr Res 58:619–625
6. Carpinteri A, Lacidogna G, Niccolini G (2006) Critical behaviour in concrete structures and damage localization by acoustic emission. Key Eng Mater 312:305–310
7. Carpinteri A, Lacidogna G, Pugno N (2007) Structural damage diagnosis and life-time assessment by acoustic emission monitoring. Eng Fract Mech 74:273–289
8. Carpinteri A, Lacidogna G, Niccolini G (2009) Fractal analysis of damage detected in concrete structural elements under loading. Chaos Soliton Fract 42:2047–2056
9. Carpinteri A, Lacidogna G, Puzzi S (2009) From criticality to final collapse: evolution of the b-value from 1.5 to 1.0. Chaos Soliton Fract 41:843–853
10. Carpinteri A, Lacidogna G, Niccolini G, Puzzi S (2009) Morphological fractal dimension versus power-law exponent in the scaling of damaged media. Int J Damage Mech 18:259–282
11. Miroshnichenko M, Kuksenko V (1980) Study of electromagnetic pulses in initiation of cracks in solid dielectrics. Sov Phys Solid State 22:895–896
12. Warwick JW, Stoker C, Meyer TR (1982) Radio emission associated with rock fracture: possible application to the great Chilean earthquake of May 22, 1960. J Geophys Res 87:2851–2859
13. O'Keefe SG, Thiel DV (1995) A mechanism for the production of electromagnetic radiation during fracture of brittle materials. Phys Earth Planet Inter 89:127–135
14. Scott DF, Williams TJ, Knoll SJ (2004) Investigation of electromagnetic emissions in a deep underground mine. Proceedings of the 23rd international conference on ground control in mining, Morgantown, 3–5 Aug 2004, pp 125–132
15. Frid V, Rabinovitch A, Bahat D (2003) Fracture induced electromagnetic radiation. J Phys D 36:1620–1628
16. Rabinovitch A, Frid V, Bahat D (2007) Surface oscillations. A possible source of fracture induced electromagnetic oscillations. Tectonophysics 431:15–21
17. Lacidogna G, Carpinteri A, Manuello A, Durin G, Schiavi A, Niccolini G, Agosto A (2011) Acoustic and electromagnetic emissions as precursor phenomena in failure processes. Strain 47(2):144–152
18. Carpinteri A, Lacidogna G, Manuello A, Niccolini A, Schiavi A, Agosto A (2012) Mechanical and electromagnetic emissions related to stress-induced cracks. Exp Tech 36:53–64

19. Russell JE, Hoskins ER (1969) Correlation of electrical resistivity of dry rock with cumulative damage, the 11th U.S. symposium on rock mechanics (USRMS), Berkeley, CA, 16–19 June 1969
20. Brace WF, Orange AS (1968) Electrical resistivity changes in saturated rocks during fracture and frictional sliding. J Geophys Res 73(4): 1433–1445
21. Lacidogna G, Carpinteri A, Manuello A, Piccolini G, Agosto A, Borla O (2011) Acoustic emission and electrical properties of quasi-brittle materials under compression. Proceedings of SEM annual conference and exposition on experimental and applied mechanics, Uncasville, 13–16 June 2011, Paper N. 112
22. Fidani C (2012) The Central Italy Electromagnetic Network and the 2009 L'Aquila earthquake: observed increases in anomalies. Geosciences 1:3–25
23. Widom A, Swain J, Srivastava YN (2013) Neutron production from the fracture of piezoelectric rocks. J Phys G Nucl Part Phys 40:015006 (8pp)
24. Widom A, Swain J, Srivastava YN (2013) Photo-disintegration of the iron nucleus in fractured magnetite rocks with magnetostriction. arXiv:1306.6286
25. Carpinteri A, Cardone F, Lacidogna G (2009) Piezonuclear neutrons from brittle fracture: early results of mechanical compression tests. Strain 45:332–339
26. Cardone F, Carpinteri A, Lacidogna G (2009) Piezonuclear neutrons from fracturing of inert solids. Phys Lett A 373:4158–4163
27. Carpinteri A, Cardone F, Lacidogna G (2010) Energy emissions from failure phenomena: mechanical, electromagnetic, nuclear. Exp Mech 50:1235–1243
28. Carpinteri A, Borla O, Lacidogna G, Manuello A (2010) Neutron emissions in brittle rocks during compression tests: monotonic vs cyclic loading. Phys Mesomech 13:268–274
29. Carpinteri A, Lacidogna G, Manuello A, Borla O (2010) Evidence of piezonuclear reactions: from geological and tectonic transformations to neutron detection and measurements. Proceedings of SEM annual conference and exposition on experimental and applied mechanics, Indianapolis, 7–10 June 2010, Paper N. 458
30. Carpinteri A, Lacidogna G, Manuello A, Borla O (2011) Energy emissions from brittle fracture: neutron measurements and geological evidences of piezonuclear reactions. Strenght Fract Complex 7: 13–31
31. Carpinteri A, Chiodoni A, Manuello A, Sandrone R (2010) Compositional and microchemical evidence of piezonuclear fission reactions in 248 rock specimens subjected to compression tests. Strain 47(2): 282–292
32. Carpinteri A, Manuello A (2010) Geomechanical and geochemical evidence of piezonuclear fission reactions in the Earth's crust. Strain 47(2): 267–281
33. Borla O, Lacidogna G, Di Battista E, Niccolini G, Carpinteri A (2013) Multiparameter approach for seismic risk evaluation through environmental monitoring. Atti del 21° Congresso Nazionale di Meccanica Teorica ed Applicata (AIMETA), Torino, Italy, CD-ROM
34. Volodichev NN, Kuzhevskij BM, Nechaev OY, Panasyuk M, Podorolsky MI (1999) Lunar periodicity of the neutron radiation burst and seismic activity on the Earth. Proceedings of the 26th international cosmic ray conference, Salt Lake City, 17–25 Aug 1999
35. Kuzhevskij M, Nechaev OY, Sigaeva EA (2003) Distribution of neutrons near the Earth's surface. Nat Hazards Earth Syst Sci 3:255–262
36. Kuzhevskij M, Nechaev OY, Sigaeva EA, Zakharov VA (2003) Neutron flux variations near the Earth's crust. A possible tectonic activity detection. Nat Hazards Earth Syst Sci 3:637–645
37. Antonova VP, Volodichev NN, Kryukov SV, Chubenko AP, Shchepetov AL (2009) Results of detecting thermal neutrons at Tien Shan high altitude station. Geomagn Aeronomy 49:761–767
38. Allen R (2011) Seconds before the big one. Seismology. ScientificAmerican.com, 54–59
39. Rao SM, Wilton DR, Glisson AW (1982) Electromagnetic scattering by surface of arbitrary shape. IEEE Trans Antenn Propag 30(3):409–418
40. ISIDe Working Group (INGV, 2010) Italian Seismological Instrumental and parametric database. http://iside.rm.ingv.it. Accessed July 2013

Chapter 30
Wireless Acoustic Emission Monitoring of Structural Behavior

A. Manuello, G. Lacidogna, G. Niccolini, and A. Carpinteri

Abstract The few non-visual methodologies make use of wired devices. Systems based on wireless transmission should be cost efficient and adaptive to different structures. The Acoustic Emission (AE) technique is an innovative monitoring method useful to detect damage, as well as to evaluate the evolution and the location of cracks. This paper shows the capability of a new data processing system based on a wireless AE equipment, very useful to long term monitoring of steel, concrete, and masonry structures. To this purpose, computer-based procedures, including an improved AE source location based on the Akaike algorithm, are implemented. These procedures are performed by automatic AE data processing and are used to evaluate the AE results in steel structures monitored during fatigue loading condition. In the most critical cases, or in some cases requiring long in situ observation periods, the AE monitoring method is fine tuned for a telematic procedure of processing AE data clouds to increase the safety of structures and infrastructural networks.

Keywords AE monitoring • Telematic procedure • Damage evolution • Akaike algorithm • Seismic risk

30.1 Introduction

Continuous structural health monitoring should provide data in order to better understand structural performances and to predict durability and remaining life-time.

In the last few years, the Acoustic Emission (AE) technique has been used in several applications due to its capability to detect crack growth, damage accumulation and AE source localizations in historical monuments, concrete structures, and infrastructures [1–7]. In Europe, the sudden collapse of a training hall in Bad Reichenhall (Germany) in early January 2006 and the collapse of a new trade building in Katowice (Poland) some weeks later, confirm dramatically the necessity of structural control of civil structures [8]. In U.S.A., the tragedy (August, 2007) of the highway bridge collapse in Minneapolis, Minnesota, raises the question of whether U.S.A., bridges are unsafe. In particular, recent events such as the reconstruction of the Noto Cathedral in 2007, after the collapse and the effects of the L'Aquila earthquake in April 2009, brought the problem of structural safety as a priority in the maintenance of Italian civil structures and monuments. These recent events lead to the conclusion that a large number of structures need monitoring and inspection procedures, reliable, inexpensive, and easy to implement.

During the last years the AE technique has been used during long-term monitoring in order to analyze the time evolution of microcracking phenomena [9–19]. According to this technique, it is possible to detect the onset and the evolution of stress-induced cracks. Crack opening, in fact, is accompanied by the emission of elastic waves which propagate within the bulk of the material. These waves can be detected and recorded by transducers applied to the surface of the structural elements. AE monitoring is performed by means of piezoelectric (PZT) sensors, using crystals that give out signals when subjected to a mechanical stress [1–3]. In this way, the AE technique makes it possible to estimate the amount of energy released during the

A. Manuello (✉) • G. Lacidogna • A. Carpinteri
Department of Structural, Geotechnical and Building Engineering, Politecnico di Torino, Corso Duca degli Abruzzi 24, Torino 10129, Italy
e-mail: amedeo.manuellobertetto@polito.it

G. Niccolini
National Research Institute of Metrology – INRIM, Strada delle Cacce 91, Torino 10135, Italy

J. Carroll and S. Daly (eds.), *Fracture, Fatigue, Failure, and Damage Evolution, Volume 5: Proceedings of the 2014 Annual Conference on Experimental and Applied Mechanics*, Conference Proceedings of the Society for Experimental Mechanics Series,
DOI 10.1007/978-3-319-06977-7_30,

fracture process, to obtain information on the criticality of the process underway and to localize the damage source locations [7–16]. The different analysis were used to evaluate the damage of a steel double girder bridge crane subjected to service loads.

In the present paper a new AE equipment based on a wireless data acquisition system is presented. Due to the attenuation of acoustic waves and geometrical spreading, numerous sensors have to be applied to cover all critical parts. These circumstances make the traditional way to apply AE techniques too expensive [8, 9]. Monitoring systems for large structures should be based on a new kind of AE equipment using wireless transmission systems. In the new monitoring system, AE signals are detected by the sensor array, recorded in situ by a synchronisation and storage unit, and, subsequently, they are sent via the GPRS/UMTS system to the central server for the elaboration phases. In this way, it is possible to use a centralised station to control continuously and simultaneously, in real time, individual structures situated in different sites.

30.2 AE Equipment and Wireless Transmission System

In the last few years a computer-based procedure including AE source location, AE event counting, and statistical analysis applied to AE time series has been developed by the authors [7, 17–20]. The final output of the AE data processing code returns a complete description of damage characterization and evolution [7, 17–20]. Today, the most critical cases, or those demanding long in-situ observation periods (infrastructural or monumental buildings), require AE monitoring based on telematic working procedure. Huge structures, such as large concrete structure and infrastructures, should be monitored by means of new type sensors, using efficient algorithms for processing large quantities of data.

To this purpose, the authors are working on a new type of AE equipment able to execute the AE data acquisition in real time by wireless technology. By means of this new equipment, AE signals detected by the sensor array are recorded in situ by a synchronization storage device, and successively sent via GPRS/UMTS system to the central server for the elaboration phase. In this way, it will be possible to use a centralised station to control continuously and simultaneously individual structural elements or entire structures, possibly situated in different places. Moreover, because a correlation exists between the regional seismic activity and the AE signals collected during structural monitoring [7], AE wireless equipment can be also used for the preservation of concrete structural and infrastructural networks from the seismic risk [8]. The new AE instrumentations and the prototype are the result of a technical collaboration between the AE research unit of the Politecnico di Torino and LEANE net. srl, an Italian company leader in the design and implementation of structural monitoring systems. The new AE sensors, calibrated at the National Research Institute of Metrology (INRIM), are designed to optimize weight, size, and applicability to different structural supports (Fig. 30.1a, b). The connection between the sensors and the acquisition module is realized by coaxial cables optimized to reduce the effects of electromagnetic noise. The modules for the signal storage are integrated within the central acquisition unit. The AE data coming from each channel are synchronized and analyzed by a mini-processor. During this phase, the main characteristics of AE signals are recognized (AE amplitude, signal arrival time, duration, signal frequency).

In Fig. 30.2a, b the central unit interface and the modem for the AE wireless transmission system are reported. The scheme of acquisition, pre-processing, and data transmission adopted in the prototype is reported in Fig. 30.3. Each channel consists of an Analog to Digital Converter module (ADC) with the capacity to acquire 10 (mega-sample/s) Ms/s in order to cover the wide band of AE signals frequency range (50−800 kHz). The data exchange is run using a Field Programmable Gate Array (FPGA) connected with a parallel bus and integrated into the central unit (Fig. 30.3). Each channel, connected with the central processor, has a devoted memory of 64 Mb and is able to perform the data synchronization.

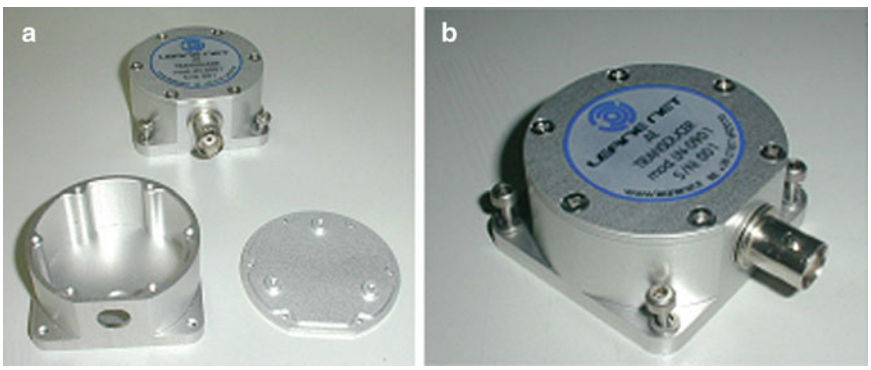

Fig. 30.1 (**a**) New PZT AE sensors. (**b**) The new AE sensors, working in a frequency range between 50 and 800 kHz, are designed to optimize weight, size, and applicability to different structural supports

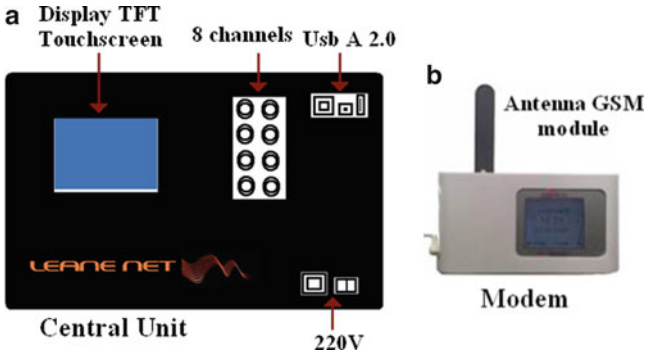

Fig. 30.2 Central Unit interface (**a**) Modem for AE wireless data transmission (**b**)

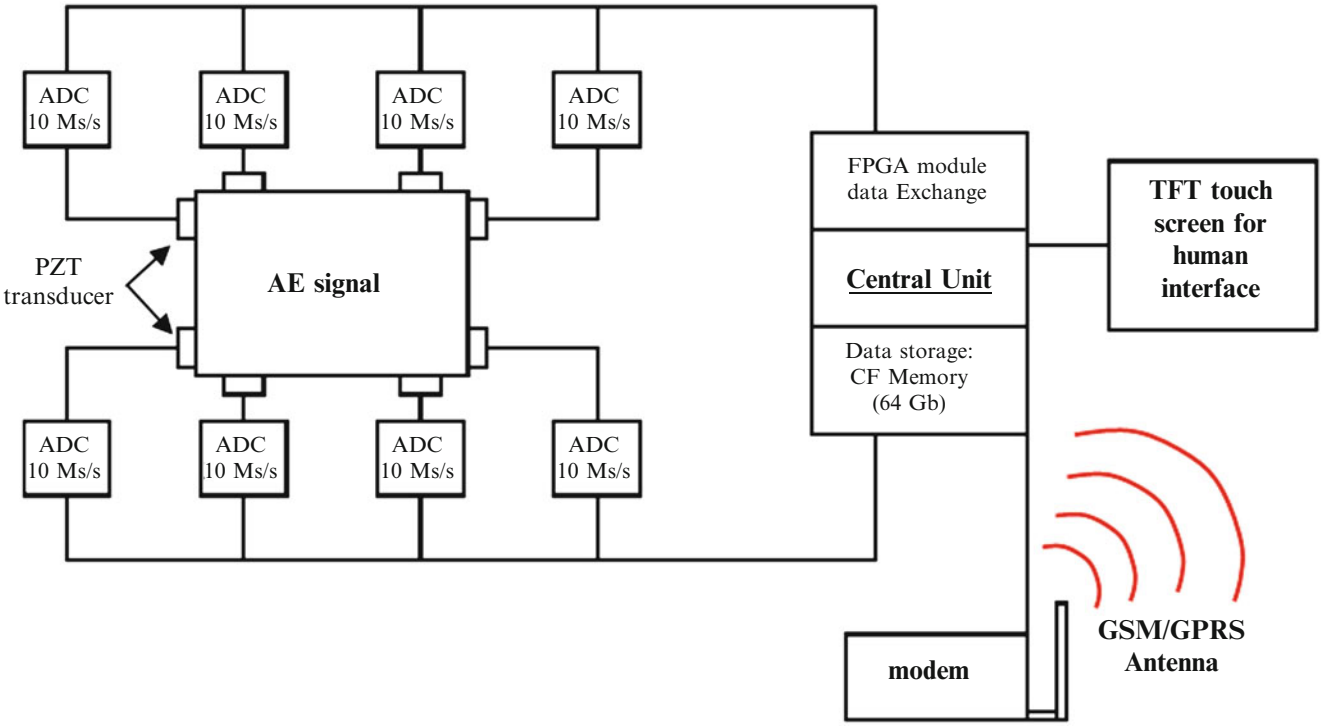

Fig. 30.3 Acquisition, pre-processing, and data transmission of AE signals for the new AE equipment

The central unit is also equipped by a thin film transistor (TFT) touch screen for human interface and first signal processing executable in situ (Fig. 30.2a). The stored data are collected into a Compact Flash memory card (CF 64 Gb) and then sent in real time to the AE laboratory, by GSM/GPRS antenna (Fig. 30.3), for AE signal analysis. The AE sensors adopted for the new monitoring system are of two types: resonant and broadband piezoeletric transducers. These two kind of sensors were used according to different conditions and considering the different structures to be monitored. The sensitivity of the broadband sensor is lower but these sensors are able to acquire data clouds in a wide frequency band and can be used in structures and component of reduced dimensions. In other condition, and specially when the localization of the damage must be particularly accurate the resonant sensors will be used according to their greater sensitivity. These kind of sensors will be used for very large structures or in the case in which the monitored elements are characterized by heterogeneous materials.

30.3 Real Time AE Analysis: Damage Evolution

The new AE equipment perform automatically different kind of analysis. The first analysis are devoted to evaluate the damage evolution of the monitored structure. According to this objective different parameters are computed using the acquired data. The first indicator is represented by the cumulative number of AE signals *N,* detected during the monitoring time. In addition,

the time dependence of the structural damage observed during the monitoring period, identified by parameter η, can also be correlated to the rate of propagation of the micro-cracks. If we express the ratio between the cumulative number of AE counts recorded during the monitoring process, N, and the number obtained at the end of the observation period, N_d, as a function of time, t, we get the damage time dependence on AE [1, 2]:

$$\eta = \frac{E}{E_d} = \frac{N}{N_d} = \left(\frac{t}{t_d}\right)^{\beta_t} \tag{30.1}$$

In Equation (30.1), the values of E_d and N_d do not necessarily correspond to critical conditions ($E_d \leq E_{max}$; $N_d \leq N_{max}$) and the t_d parameter must be considered as the time during which the structure has been monitored. By working out the β_t exponent from the data obtained during the observation period, we can make a prediction as to the structure's stability conditions. If $\beta_t < 1$, the damaging process slows down and the structure evolves towards stability conditions, in as much as energy dissipation tends to decrease; if $\beta_t > 1$ the process diverges and becomes unstable; if $\beta_t = 1$ the process is metastable, that is, though it evolves linearly over time, it can reach indifferently either stability or instability conditions [6, 7].

Damage assessment in the structure may be also investigated by the statistical distribution of the AE signal magnitudes fitted by the Gutenberg–Richter (GR) law [6, 7]:

$$LogN\ (\geq M) = a - bM, \tag{30.2}$$

where N is the number of AE events with magnitude greater than M, and a and b (or b-value) are fitting parameters. The b-value is an important parameter for damage assessment of structures as it decreases during damage evolution, reaching final values close to 1 when the failure is imminent [6]. The cumulative number of AE, the β_t exponent and the b-value are computed using the new AE equipment for a concrete notched beam subjected to three point bending.

30.3.1 Basic Principle of AIC Criterion

Initially developed to predict the optimal order of the auto-regressive process fitting the time series in seismology [21–25], the *AIC* criterion can be used to demark the point of two adjacent time series (noise and signal) with different underlying statistics [26–31].

Suppose that a voltage time series $\{x_1, x_2, \ldots, x_n\}$, containing the AE signal, is divided in two segments $i = 1,2$, $\{x_1, x_2, \ldots, x_k\}$ and $\{x_{k+1}, x_2, \ldots, x_n\}$, where k identifies the unknown signal onset time. Both segments are assumed to be two different pseudo-stationary time series, either modeled as an auto-regressive (AR) process of order M with coefficients $\{a^i{}_m\}$:

$$x_j = \sum_{m=1}^{M} a_m^i x_{j-m} + e_j^i \qquad i = 1, 2, \tag{30.3}$$

where $j = M + 1, \ldots, k$ for interval $i = 1$ and $j = k + 1, \ldots, n - M$ for $i = 2$.

The model divides either time series into a deterministic and a non-deterministic part $e^i{}_j$, the latter assumed to be a white noise. Thus, the time series $\{e^i{}_j\}$ is a sample of independent and identically distributed random variables, with mean zero, variance $\sigma_i{}^2$ and density function $f(e^i{}_j) = (\sigma_i 2\pi)^{-1/2}\exp[-(e^i{}_j/\sigma_i)^2/2]$, to which the maximum-likelihood estimation (MLE) can be applied. Then, we look at the joint density function of all variables $\{e^i{}_j\}$—expressed in terms of the observations $\{x_j\}$ by means of Eq. 30.3—considered as fixed parameters, whereas the model parameters $\Theta_i = \Theta_i\ (a^i{}_1, \ldots\ a^i{}_m, \sigma_i{}^2)$ for the i-th interval are allowed to vary freely. In this perspective, the joint density function is the likelihood function L [26–31]:

$$\begin{aligned} L\ (\Theta_1, \Theta_2, k, M\ |x\ ) = \prod_{i=1}^{2} \left(\frac{1}{\sigma_i^2 2\pi}\right)^{n_i/2} \\ \exp\left[-\tfrac{1}{2\sigma_i^2} \sum_{j=p_i}^{q_i} \left(x_j - \sum_{m=1}^{M} a_m^i x_{j-m}\right)^2\right] \end{aligned} \tag{30.4}$$

where $p_1 = M + 1$, $p_2 = k + 1$, $q_1 = k$, $q_2 = n - M$, $n_1 = k - M$ and $n_2 = N - k - M$.

As it is known, the MLE finds the particular values of the model parameters which make the observed results the most probable or, in other words, which maximize the likelihood function L. Working equivalently with the logarithm of Eq. 30.4 and searching for the MLE of the model parameters we get:

$$\frac{\partial \ln L\left(\Theta_1, \Theta_2, k, M \mid x\right)}{\partial \sigma_i} = 0 \qquad i = 1, 2, \tag{30.5}$$

which has the solution:

$$\sigma_{i,max}^2 = \frac{1}{n_i} \sum_{j=p_i}^{q_i} \left(x_j - \sum_{m=1}^{M} a_m^i x_{j-m} \right)^2 \quad i = 1, 2. \tag{30.6}$$

Inserting Eq. 30.6 into Eq. 30.4 we get the maximized logarithmic likelihood function [29–31]:

$$\begin{aligned} &\ln L\left(\Theta_1, \Theta_2, k, M \mid x\right) \\ &\quad = -\frac{k-M}{2} \ln \sigma_{1,max}^2 - \frac{n-k-M}{2} \ln \sigma_{2,max}^2 + C_1 \end{aligned} \tag{30.7}$$

where C_1 is a constant.

The expression in Eq. 30.7 is the basis for the Akaike Information Criterion (*AIC*), in which the *AIC* function is defined as $AIC = 2P - 2\ln(\text{maximized likelihood function})$, where P is the number of parameters in the statistical model. Generally, a model with minimum *AIC* value is thought to be most suitable one among the competing models.

Originally this function was designed to determine the optimal order for an AR process fitting a time series. In the current application, the order M of the AR process is fixed, and therefore the *AIC* function is a measure for the model fit. The point k where *AIC* is minimized, or L is maximized, determines the optimal separation of the two time series—the first representing noise and the second containing the signal—in the least square sense, and is interpreted as the onset time of the signal. In this sense, the *AIC* as a function of k is known as *AIC* picker [29]:

$$\begin{aligned} AIC(k) = &(k-M) \ln \sigma_{1,max}^2 \\ &+ [n-k-M] \ln \sigma_{2,max}^2 + C_2, \end{aligned} \tag{30.8}$$

where C_2 is a constant.

Alternatively, the *AIC* value can be directly calculated from the signal without dealing with the AR coefficients. As $M << n$, Eq. 30.8 can be simplified [29]:

$$\begin{aligned} AIC(k) = &k \ln\left(\text{var}(x[1,k])\right) \\ &+ (n-k-1) \ln\left(\text{var}(x[1+k,n])\right), \end{aligned} \tag{30.9}$$

where k goes through all the signal trace and var is the sample variance.

As *AIC* picker finds the onset point as the global minimum, it is necessary to choose a time window that includes only the segment of interest of the signal. If the time window is chosen properly, *AIC* picker can find the first arrival of the signal (P-wave arrival for AE) accurately. In case of low S/N ratios (as for noisy EM signals) or more seismic phases (as P-wave and S-wave for AE signals) in a time window, global minimum cannot guarantee to indicate the first arrival of the signal. For this reason a pre-selection of this window is necessary to apply the procedure. Here, the onset time is firstly pre-determined using a threshold amplitude level:

$$\left(\sum_{k=i+1}^{10} |x_k| \right) / 10 \geq 4 \left(\sum_{k=1}^{i} |x_k| \right) / i, \tag{30.10}$$

The first value for the index k that makes relation (30.10) fulfilled is named k_0 and it is the first estimation for the onset time. This first estimation is always localized after the actual onset time. Thus, we apply *AIC* picker to the interval $[1,k_0]$ for a rough determination of the onset time, k_1. Then, the application of *AIC* picker to the time window with center in k_1 and width $2(k_1 - k_0)$ gives the value k_{min}, which is regarded as the actual onset time of the analyzed signal.

30.4 AE Monitoring of the Double Girder Bridge Crane

The monitoring results reported in the present study are devoted to the analysis of a steel structure consisted in a double girder bridge crane with a service load of 20×10^3 daN. The structure has over 30 years of service. The AE sensors were installed on one of the two beams of the bridge crane, a pair of sensors for each of the two ends, in correspondence of the supports, and the other four were positioned in correspondence of the middle part of the monitored element (see Fig. 30.4). The monitoring was carried out continuously for 120 h, from November 25 2013 to November 30 2013.

The absence of AE signals during the moving of the structure was verified considering the absence of the service loads. From the analysis of the AE time series it is possible to correlate the AE activity with the most intense activity of the crane. The β_t exponent indicated a substantial structural stability. At the same time the variability of the parameter b-value (between 3.8 and 2.8) is far from critical ($b = 1.5$) or collapse ($b = 1$) condition (see Fig. 30.5).

By means of the localization procedure reported in the previous section triangulation of the AE signals was carried out to identify the AE sources. The localization results are shown in Fig. 30.6, showing an asymmetric distribution of the AE sources, localized prevalently towards a semi-beam of the crane.

30.5 Conclusions

The paper shows the capability of a new AE data processing system based on wireless AE data transmission. The new AE equipment can be employed to realize contemporary long time monitoring of different civil structures and to perform AE signal analysis in real time. This system, cost efficient, easy to install, and adaptive to different types of concrete structural

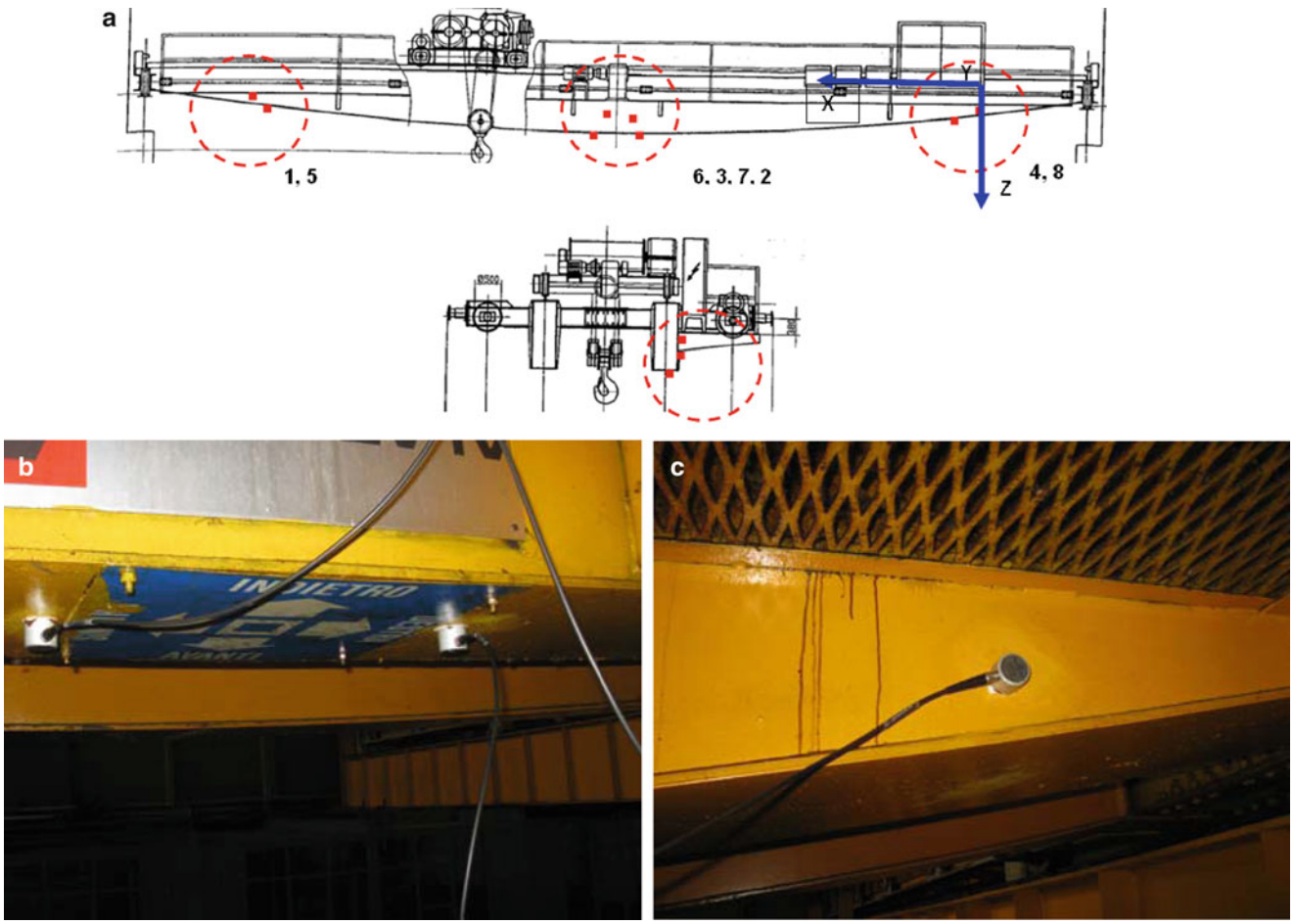

Fig. 30.4 Sensor positions on the double girder bridge crane (**a**). Application of the sensors in the middle of the beam (**b**) and in correspondence of the supports (**c**)

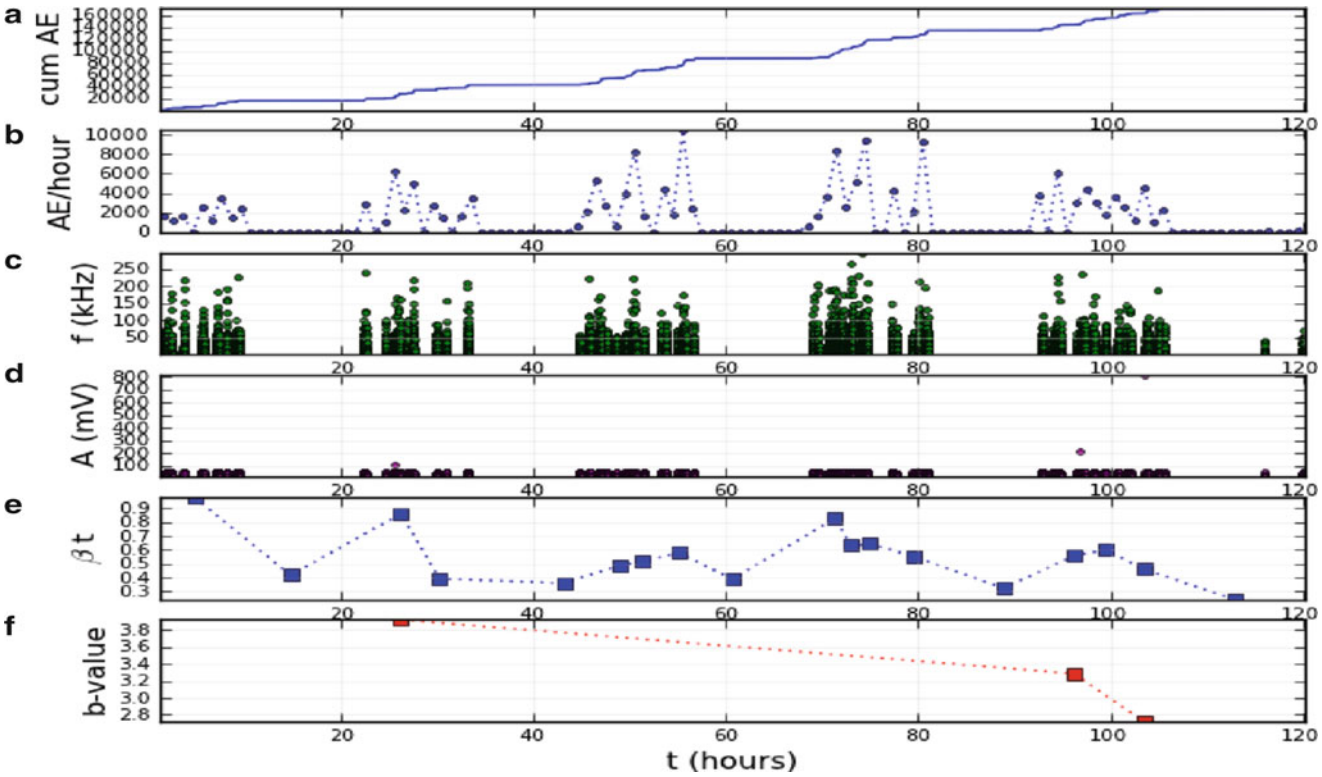

Fig. 30.5 AE cumulated number (**a**), AE number per hour (**b**), Frequency range of AE signals (**c**), Time series of AE amplitudes (**d**), β_t and *b*-value (**e, f**)

Fig. 30.6 Scheme of the sensor positions and Localization of the AE sources

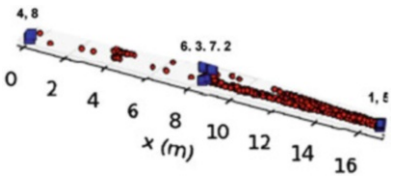

and infrastructural networks, seems to be also very promising for seismic risk monitoring of civil structures and historical monuments. The AE cumulative number, the β_t exponent and the *b*-value have been computed in order to evaluate the damage evolution in a double girder bridge crane subjected to service loads. These analysis are the first parameter extrapolated from the AE data and represent damage indicators obtained in real time by the new AE equipment.

After the AE data acquisition it is possible to perform the localization of the AE sources (micro-cracks). This analysis represents the second kind of data available by the AE monitoring. The position of damage, infact, is particularly useful in damage evaluation of concrete and masonry structures. In particular, the onset of AE signals from rock fracture is determined through the joint auto-regressive modelling of the noise and the signal, and the application of the Akaike Information Criterion (*AIC*) using the onset time as parameter. This so-called *AIC* picker is able to find accurately the onset of genuine signals against the background noise. The presented study suggests the use of AE measurements to enhance monitoring, especially applied to micro-seismicity with potential applications in earthquake forecasting.

The monitoring system fine tuned could be used extending the acquisition to different kind of data in addition to AE signals. The data acquired from the sensor network will be sent electronically to a central server for real time monitoring of the condition of the buildings, by means of correlation algorithms applied to data from the different measured variables. This remote monitoring system will be maintained after the conclusion of the restoration work, allowing for detection and real time monitoring of possible structural deterioration processes of the buildings, thus constituting a useful tool for prevention of structural collapses. This monitoring system, if properly extended, may use the buildings as points of a monitoring network on the territory, useful for reducing the seismic hazard and securing entire metropolitan areas by monitoring the seismic activity.

Acknowledgements The Authors gratefully acknowledge the support of the ALCIATI Ltd (Vigliano d'Asti-Italy) for supplying the materials research. Special thanks for their kind collaboration are due to Dr. M. Spampani and Dr. Michele Pedroni, and Alessandro Mitillo (Leane net. srl) for their valuable cooperation throughout the development of the new AE monitoring system.

References

1. Carpinteri A, Lacidogna G, Pugno N (2004) A fractal approach for damage detection in concrete and masonry structures by the acoustic emission technique. Acoust Tech 38:31–37
2. Carpinteri A, Lacidogna G (2006) Structural monitoring and integrity assessment of medieval towers. J Struct Eng (ASCE) 132:1681–1690
3. Carpinteri A, Lacidogna G (2006) Damage monitoring of an historical masonry building by the acoustic emission technique. Mater Struct 39:161–167
4. Carpinteri A, Lacidogna G, Paggi M (2007) Acoustic emission monitoring and numerical modeling of FRP delamination in RC beams with non-rectangular cross-section. Mater Struct (RILEM) 40:553–566
5. Carpinteri A, Lacidogna G (2007) Damage evaluation of three masonry towers by acoustic emission. Eng Struct 29:1569–1579
6. Carpinteri A, Lacidogna G, Manuello A (2011) Stability of the ancient Athena temple in Syracuse investigated by the *b*-value analysis. Strain 47:243–253
7. Carpinteri A, Lacidogna G, Niccolini G (2006) Critical behaviour in concrete structures and damage localization by acoustic emission. Key Eng Mater 312:305–310
8. Grosse CU, Finck F, Kurz H, Reinhardt W (2004) Monitoring techniques based in wireless AE sensor for large structures in civil engineering, DGZIP-Proceedings, BB-90 CD, pp 691–698
9. Yoon D-J, Lee S, Kim CY, Seo DC (2007) Acoustic emission diagnosis system and wireless monitoring for damage assessment of concrete structures. Proceedings of NDT for safety, 7–9 Nov 2007, Prague, Czech Republic
10. Ohtsu M (1996) The history and development of acoustic emission in concrete engineering. Mag Concr Res 48:321–330
11. Pollock AA (1973) Acoustic emission-2: acoustic emission amplitudes. Non-Destruct Test 6:264–269
12. Brindley BJ, Holt J, Palmer IG (1973) Acoustic emission- 3: the use of ring-down counting. Non-Destruct Test 6:299–306
13. Grosse CU, Reinhardt HW, Finck F (2003) Signal based acoustic emission techniques in civil engineering. ASCE J Mater Civil Eng 15: 274–279
14. Kaiser J (1950) An investigation into the occurrence of noises in tensile tests, or a study of acoustic phenomena in tensile tests. PhD Dissertation, Technische Hochschule München, Munich FRG
15. Carpinteri A, Lacidogna G, Pugno N (2005) Creep monitoring in concrete structures by the acoustic emission technique. In: Pijaudier-Cabot G, Gérard B, Acker P (eds) Creep, shrinkage and durability of concrete and concrete structures (Proceedings of the 7th CONCREEP Conference, Nantes, France, 2005). Hermes Science, London, pp 51–56
16. Shah SP, Li Z (1994) Localization of microcracking in concrete under uniaxial tension. ACI Mater J 91:372–381
17. Carpinteri A, Lacidogna G, Manuello A (2007) An experimental study on retrofitted fiber-reinforced concrete beams using acoustic emission. In: Carpinteri A, Gambarova P, Ferro G, Plizzari G (eds) Proceedings of the 6th international FraMCoS conference, vol 2. Taylor & Francis, London, pp 1061–1068.
18. Carpinteri A, Lacidogna G, Niccolini G (2007) Acoustic emission monitoring of medieval towers considered as sensitive earthquake receptors. Nat Hazards Earth Syst Sci 7:251–261
19. Niccolini G, Xu J, Manuello A, Lacidogna G, Carpinteri A (2012) Onset time determination of acoustic and electromagnetic emission during rock fracture. Progr Electr Res Lett 35:51–62
20. Lacidogna G, Manuello A, Niccolini G, Carpinteri A (2012) Acoustic emission monitoring of Italian historical buildings and the case study of the Athena temple in Syracuse. Arch Sci Rev 1–10. doi:10.1080/00038628.2012.720246
21. Sleeman R, Eck T (1999) Robust automatic P-phase picking: an on-line implementation in the analysis of broadband seismogram recordings. Phys Earth Planet In 113:265–275
22. Earle P, Shearer PM (1994) Characterization of global seismograms using an automatic-picking algorithm. Bull Seismol Soc Am 84:366–376
23. Tong C, Kennett BLN (1996) Automatic seismic event recognition and later phase identification for broadband seismograms. Bull Seismol Soc Am 86:1896–1909
24. Withers M et al (1998) A comparison of select trigger algorithms for automated global seismic phase and event location. Bull Seismol Soc Am 88:95–106
25. Anant KS, Dowla FU (1997) Wavelet transform methods for phase identification in three-component seismograms. Bull Seismol Soc Am 87:1598–1612
26. Kurz J, Grosse C, Reinhardt H (2005) Strategies for reliable automatic onset time picking of acoustic emissions and of ultrasound signals in concrete. Ultrasonics 43:538–546
27. Zhang H, Thurber C, Rowe C (2003) Automatic p-wave arrival detection and picking with multiscale wavelet analysis for single-component recordings. Bull Seismol Soc Am 93:1904–1912
28. Hafez AG, Khan TA, Kohda T (2010) Clear P-wave arrival of weak events and automatic onset determination using wavelet filter banks. Digital Signal Proc 20:715–732
29. Akaike H (1974) A new look at the statistical model identification. Trans Automat Contr 19:716–723
30. Yokota T, Zhou S, Mizoue M, Nakamura I (1981) An automatic measurement of arrival time of seismic waves and its application to an on-line processing system. Bull Earthq Res Inst 55:449–484
31. Maeda N (1985) A method for reading and checking phase times in auto-processing system of seismic wave data. Zisin 38:365–379

Chapter 31
Acoustic Emission Monitoring of Rock Specimens During Fatigue Tests

L. Zhou, A. Manuello, G. Lacidogna, R. Sesana, and A. Carpinteri

Abstract Some of the most significant civil and historical structures, such as bridges, viaducts, dams and ancient monumental buildings, may collapse below the critical loading conditions due to fatigue effects. In the present paper, damage level evolution during fatigue tests of rock specimens will be evaluated by Acoustic Emission technique (AE). The fundamental parameters of AE will be analyzed in order to interpret the damage level evolution. The relationships between the cumulative AE counts and the damage accumulation during fatigue experiments will be considered for different kinds of iron-rich rocks (granite, basalt, magnetite). The achievement of critical conditions will be recognized through synthetic parameters based on AE, such as the *b*-value of the Gutenberg-Richter law and considering the increase in low-frequency components during the damage accumulation.

Keywords Rock fatigue tests • Acoustic emission • Damage evolution • Fatigue • *b*-Value

31.1 Introduction

The monitoring of damage due to static and fatigue loads on rock structures plays an important role in the design and assessment of historical and civil constructions such as monuments, railway, highway tunnels, bridges, hydro-and nuclear power stations. At the same time the geological hazards prediction and the prevention of natural disaster are related to monitoring systems even more innovative and based on wire-less data transmission.

Recent applications of Acoustic Emission technique were used to estimate the damage level and the failure of historical and civil buildings also during in situ constructions and in service structures and components [1–8]. In particular, several concrete, rock and masonry constructions are usually subjected to cyclic loads, such as the traffic, cyclic hydraulic and wind pressure loads. Among the innovative non-destructive monitoring methods, the non-destructive technique based on acoustic emission (AE) proves to be very effective also during fatigue experiments.

A number of techniques have been developed to detect and study crack growth in brittle rock fracture. The most common of these involves the use of strain gauges to measure slight changes in sample deformation that can be related to the closing and opening of cracks [9, 10]. To a lesser extent, AE monitoring has been used to correlate the number of acoustic events with various strain gauge responses [11–13]. Other techniques have involved the use of photoelastics, optical diffraction patterns, scanning electron microscopes, laser speckle interferometry, ultrasonic probing and electrical resistivity [14]. Many of these NDT work by introducing some type of energy into the system to be analysed. In AE tests, the energy input is the mechanical stresses produced by the structure itself through the application of loads [14]. By monitoring a structure by means of the AE technique, it becomes possible to detect the occurrence and evolution of stress-induced cracks. Cracking, in fact, is accompanied by the emission of elastic waves which propagate within the bulk of the material. These waves can

L. Zhou (✉) • A. Manuello • G. Lacidogna • A. Carpinteri
Department of Structural, Geotechnical and Building Engineering, Politecnico di Torino, Corso Duca degli Abruzzi 24, Torino 10129, Italy
e-mail: lili.zhou@polito.it

R. Sesana
Department of Mechanical and Aerospace Engineering, Politecnico di Torino, Corso Duca degli Abruzzi 24, Torino 10129, Italy

J. Carroll and S. Daly (eds.), *Fracture, Fatigue, Failure, and Damage Evolution, Volume 5: Proceedings of the 2014 Annual Conference on Experimental and Applied Mechanics*, Conference Proceedings of the Society for Experimental Mechanics Series,
DOI 10.1007/978-3-319-06977-7_31,

be received and recorded by piezoelectric (PZT) transducers applied to the external surface of the structural elements. The signal is therefore analysed by a measuring system counting the emissions that exceed a certain voltage threshold measured in volts.

By AE monitoring the damage assessment is often obtained analysing synthetic parameters. These parameters are based on the statistical analysis of the AE amplitude distribution emerging from the growing micro-cracks. In particular, the amplitudes of AE signals are distributed according to the Gutenberg-Richter (GR) law and could be described through the *b*-value. This value, mutuated from the seismological analysis, decreases systematically with the damage evolution [15, 16]. Since the cracking is a multiscale phenomenon, recently AE data have been interpreted by statistical and fractal theories considering the relation between the *b*-value and the fractal dimension D in which the damage take place [15, 16]. In the last two decades, the properties of fractality and multifractality of fracture surfaces have been widely recognized in the case of quasi-brittle [17–22]. Carpinteri firstly proposed two geometrical multifractal scaling laws for strength and toughness of disordered materials [18]. In the present paper the achievement of critical conditions will be recognized through these AE parameters, and the *b*-value will be computed in order to discriminate the different failure mechanisms and to interpret the fractal domain of the damage evolution during the cyclic tests.

31.2 Experimental Set Up Materials and AE Equipment

The specimens used during the experiments were obtained from different iron-rich rocks. The tests were conducted on granite, basalt and magnetite specimens. During the experimental campaign, as stated in the introduction, the specimens were subjected to fatigue cycles with a working frequency of about 200 Hz.

From a petrographic point of view, the Luserna stone used for the experimental campaign is a leucogranitic orthogneiss, probably from the Lower Permian Age, that outcrops in the Luserna-Infernotto basin (Cottian Alps, Piedmont), at the border between the Turin and Cuneo provinces (north-western Italy) [23–26]. The stone is characterised by a micro 'Augen' texture, it is grey-greenish or locally pale blue in colour. Geologically, Luserna stone pertains to the Dora-Maira Massif [23, 25], that represents a part of the ancient European margin annexed to the Cottian Alps during Alpine orogenesis [23, 25]. Magnetite blocks come from the San Leone mine [27]. This deposit is located about 30 km southwest of Cagliari, Sardinia (Italy), near the Basso-Sulcis batholit, a granodioritic intrusive of Hercynian age [28]. The mineralization of the deposit is mainly represented by magnetite. The ore bodies within skarn generated by the thermometamorphism of previous paleozoic limestones in contact with granitic intrusions (300×10^6 years ago). The mean iron concentration of the San Leone magnetite is between 72.5 % and 75.0 % [26]. The last material employed during the experimental study is basalt originating from the Mount Etna bacine. Basalt is a very common extrusive igneous rock, the dominant material making up the Earth's oceanic crust, and represents the principal product from volcanic eruptions. The basalt, also called Lava stone, used in the tests reported in this paper, is characterized by a mafic chemistry (with a high content of iron and magnesium), is dark grey and shows porphyritic texture with few mm-sized phenochrists of plagioclase, clinopyroxene and olivine [28]. All the prepared specimens were cylindrical, with a diameter of 50 mm and a height of 100 mm.

As far as the working frequency (200 Hz) is concerned, the cylindrical specimens have been subjected to compression-compression fatigue tests by means of an electromechanical Amsler Vibrofore 10 HPF 422 (see Fig. 31.1a and b). This equipment allows to apply fatigue loading with a frequency range between 100 and 260 Hz, a mean load up to 50 kN, and an alternate load up to 50 kN. The machine working conditions are related to resonance conditions of the system which is composed by two masses (a seismic huge mass and the specimen mass) and two springs (a huge machine spring element and the specimen stiffness) disposed in series (see Fig. 31.1a). Working condition difficulties are often related to specimen damping. In the case of rocks, a tuning activity was needed to reach resonance conditions. The specimens were set between two compression platens, a preload (mean) was set and then alternate loading was applied.

For the fatigue tests a computer-based procedure including AE event counting, and statistical analysis applied to AE time series has been used by the authors [7, 29–31]. The final output of the AE data processing code returns a complete description of damage characterization and evolution [7, 8, 29–31]. The new AE instrumentations and the prototype used for the tests are the result of collaboration between the AE research unit of Politecnico di Torino and LEANE net. srl, an Italian company leader in the design and implementation of structural monitoring systems. The new AE sensors, calibrated at the National Research Institute of Metrology (INRIM), are designed to optimize weight, size, and applicability to different structural supports (Fig. 31.2). The connection between the sensors and the acquisition module is realized by coaxial cables optimized to reduce the effects of electromagnetic noise. The modules for the signal storage are integrated within the central acquisition unit. The AE data coming from each channel are synchronized and analyzed by a mini-processor. During this phase, the main characteristics of AE signals are recognized (AE amplitude, signal arrival time, duration, signal frequency).

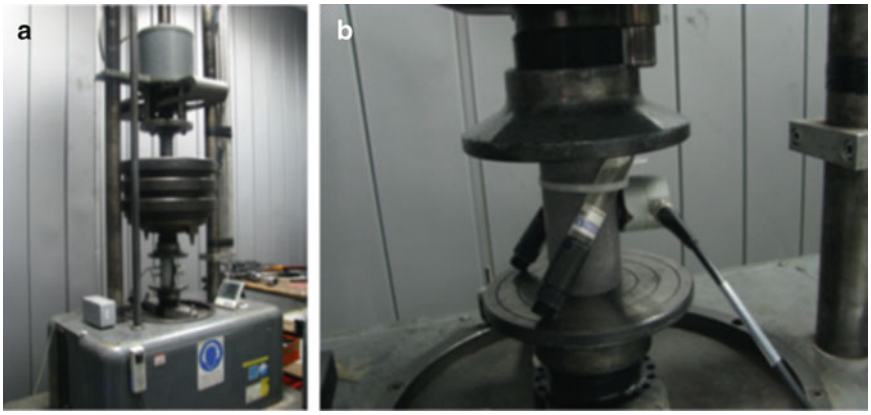

Fig. 31.1 Amsler Vibrofore 10 HPF 422. This equipment allows to apply fatigue loading with a frequency range between 100 and 260 Hz, a mean load up to 50 kN, and an alternate load up to 50 kN (**a**). Basalt specimen during the test (**b**)

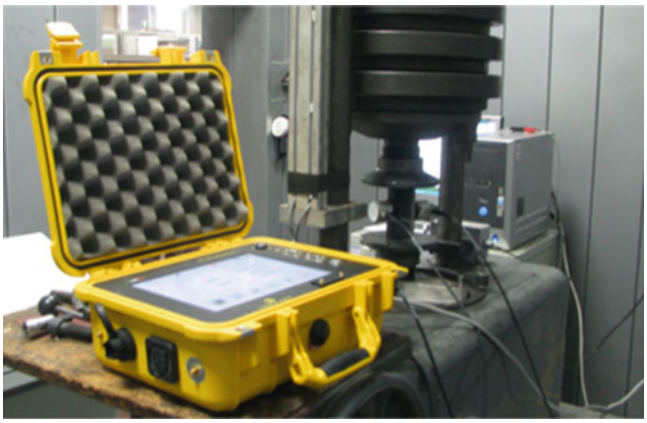

Fig. 31.2 Acquisition, pre-processing, and data transmission of AE signals for the new AE equipment during fatigue tests

Each channel consists of an Analogy to Digital Converter module (ADC) with the capacity to acquire 10 (mega-sample/second) Ms/s in order to cover the wide band of AE signals frequency range (50−800 kHz). The data exchange is run using a Field Programmable Gate Array (FPGA) connected with a parallel bus and integrated into the central unit. Each channel, connected with the central processor, has a devoted memory of 64 Mb and is able to perform the data synchronization.

31.3 AE Analysis: Damage Evolution

31.3.1 Damage Level and Damage Acceleration: Cumulated AE and β_t Exponent

The new AE equipment performs automatically different kind of analysis. According to this objective different parameters are computed using the acquired data. The first indicator is represented by the cumulative number of AE signals N, detected during the monitoring time. In addition, the time dependence of the structural damage observed during the monitoring period, identified by parameter η, can also be correlated to the rate of propagation of the micro-cracks. If we express the ratio between the cumulative number of AE counts recorded during the monitoring process, N, and the number obtained at the end of the observation period, N_d, as a function of time, t, we get the damage time dependence on AE [5, 32]:

$$\eta = \frac{E}{E_d} = \frac{N}{N_d} = \left(\frac{t}{t_d}\right)^{\beta_t} \tag{31.1}$$

In Eq. 31.1, the values of E_d and N_d do not necessarily correspond to critical conditions ($E_d \leq E_{max}$; $N_d \leq N_{max}$) and the t_d parameter must be considered as the time during which the structure has been monitored. By working out the β_t exponent from the data obtained during the observation period, we can make a prediction as to the structure's stability conditions.

If $\beta_t < 1$, the damaging process slows down and the structure evolves towards stability conditions, in as much as energy dissipation tends to decrease; if $\beta_t > 1$ the process diverges and becomes unstable; if $\beta_t = 1$ the process is metastable, that is, though it evolves linearly over time, it can reach indifferently either stability or instability conditions [7, 8].

31.3.2 The b-Value and the Damage Fractal Domain

By analogy with seismic phenomena, in the AE technique the magnitude may be defined as follows [15, 16]:

$$m = log_{10} A_{max} + f(r) \tag{31.2}$$

where A_{max} is the amplitude of the signal expressed in μV and *f(r)* is a correction coefficient whereby the signal amplitude is taken to be a decreasing function of the distance r between the source and the AE sensor. In seismology, the Gutenberg-Richter empirical law [18]:

$$log_{10} N\ (\geq m) = a - bm \quad \text{or} \quad N\ (\geq m) = 10^{a-bm} \tag{31.3}$$

expresses the relationship between magnitude and total number of earthquakes in any given region and time period, and is one of the most widely used statistical relations to describe the scaling properties of seismicity. In Eq. 31.3, N is the cumulative number of earthquakes with magnitude $\geq m$ in a given area and within a specific time range, while a and b are positive constants varying from a region to another and from a time interval to another. Equation 31.3 has been used successfully in the AE field to study the scaling laws of AE wave amplitude distribution. This approach evidences the similarity between structural damage phenomena and seismic activities in a given region of the earth, extending the applicability of the Gutenberg-Richter law to structural engineering. According to Eq. 31.3, the b-value changes systematically at different times in the course of the damage process and therefore can be used to estimate damage evolution modalities [33–35].

Scale effects on the size of the cracks identified by the AE technique entail, by analogy with earthquakes [16], the validity of the following relationship:

$$N\ (\geq L) = cL^{-2b} \tag{31.4}$$

where N is the cumulative number of AE events generated by cracks having a characteristic size ≥L, c is the total number of AE events and $D = 2b$ is the noninteger (or fractal) exponent of the distribution. This interpretation rests on the assumption of a dislocation model for the seismic source and requires that $2 \leq D \leq 3$, i.e., the cracks are distributed in a fractal domain comprised between a surface and the volume of the analysed region [36]. The cumulative distribution 31.4 is substantially identical to the one proposed by Carpinteri [18, 37–39], according to which the number of cracks with size $\geq L$ present in a body is given by:

$$N^*\ (\geq L) = N_{tot} L^{-\gamma} \tag{31.5}$$

In Eq. 31.5, γ is an exponent reflecting the disorder, i.e., crack size scatter and N_{tot} is the total number of cracks present in a body. By equating distributions 31.4 and 31.5, we find that $2b = \gamma$. When the final propagation occurs, defects concentrate along preferential paths, in a narrow band around the final fracture surface. In this case, as shown by Carpinteri et al. [15, 16], the self-similarity condition entails $\gamma = 2.0$. This exponent corresponds to value $b = 1.0$, which is experimentally approached in structural members during the final crack propagation [38]. In this connection, subdividing the loading process into consecutive stages, it is possible to explain the evolution of damage in terms of increasing microcrack density on preferential surfaces.

31.4 Experimental Results

In Fig. 31.3 the total cumulated number of AE for basalt specimen is reported at the end of the cyclic test. It is interesting to note that three different phases may be recognised. The first is characterized by an appreciable increase of AE cumulated number. After this first phase a second phase is characterized by a very low AE activity. Finally in the last phase it is possible to observe a sudden increase in AE cumulated number up to the final failure of the specimen.

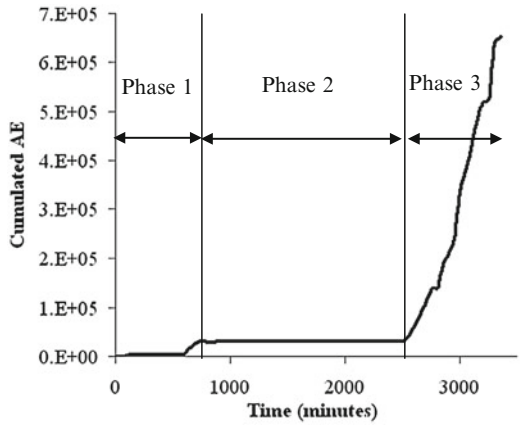

Fig. 31.3 Total Cumulated AE for the specimen made of Etna basalt

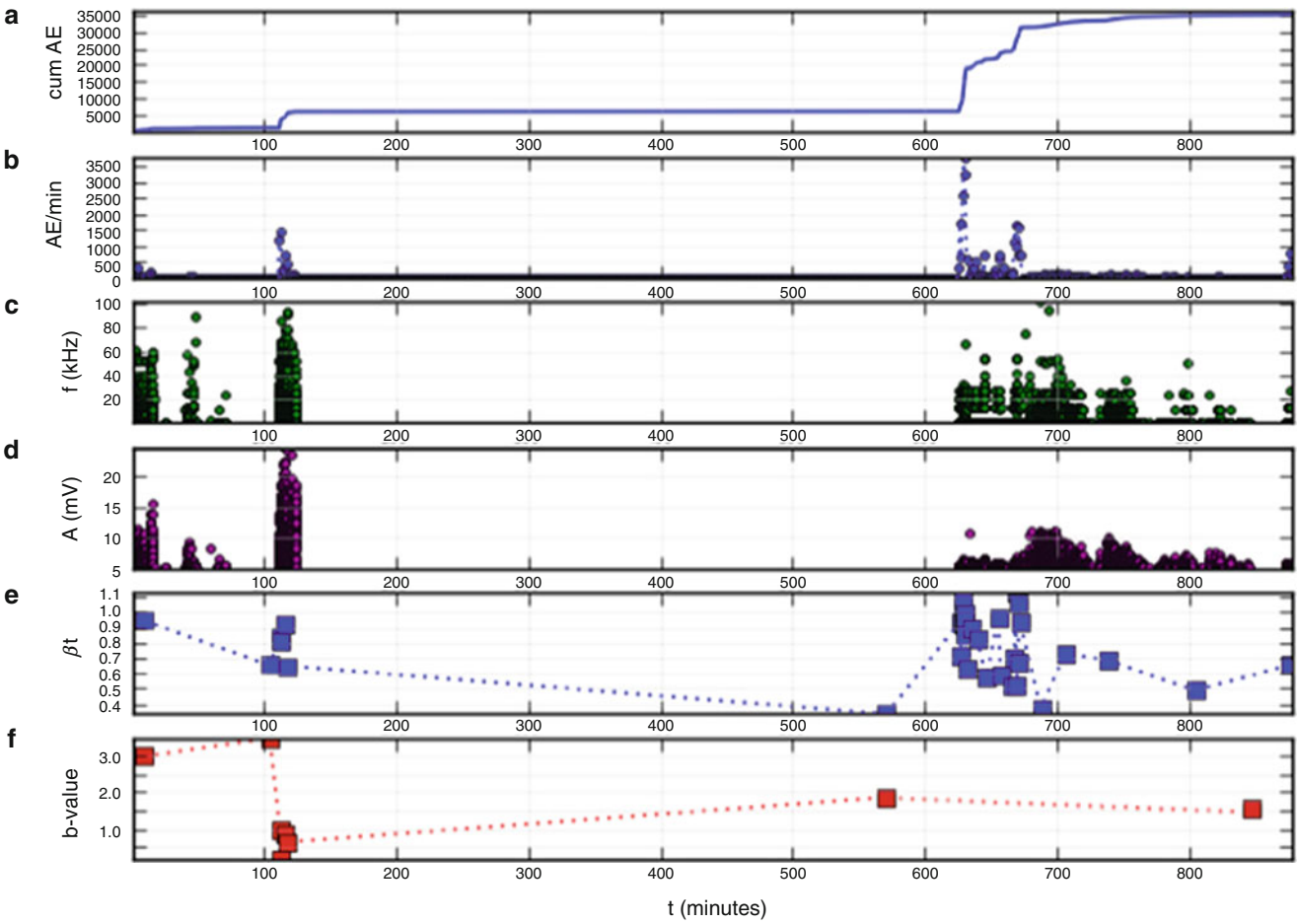

Fig. 31.4 Basalt specimen: First phase. Cumulated AE (**a**), AE/minutes (**b**), AE signal Frequency (**c**), AE Amplitudes (**d**), βt exponent (**e**), b-value (**f**)

In Fig. 31.4 the AE analysis are reported in details for the first phase. It is possible to observe an increasing of the AE cumulate number after 10 min from the beginning of the test. In correspondence of this increment in AE activity significant values in the AE/minutes were observed. This value, in particular, reached a peak value of 1,500 hits/min. During this time interval, between 110 and 120 from the beginning of the test the AE are characterized by a frequency range between 20 and 100 kHz. At the same time also the AE amplitudes increased up to 30 mV.

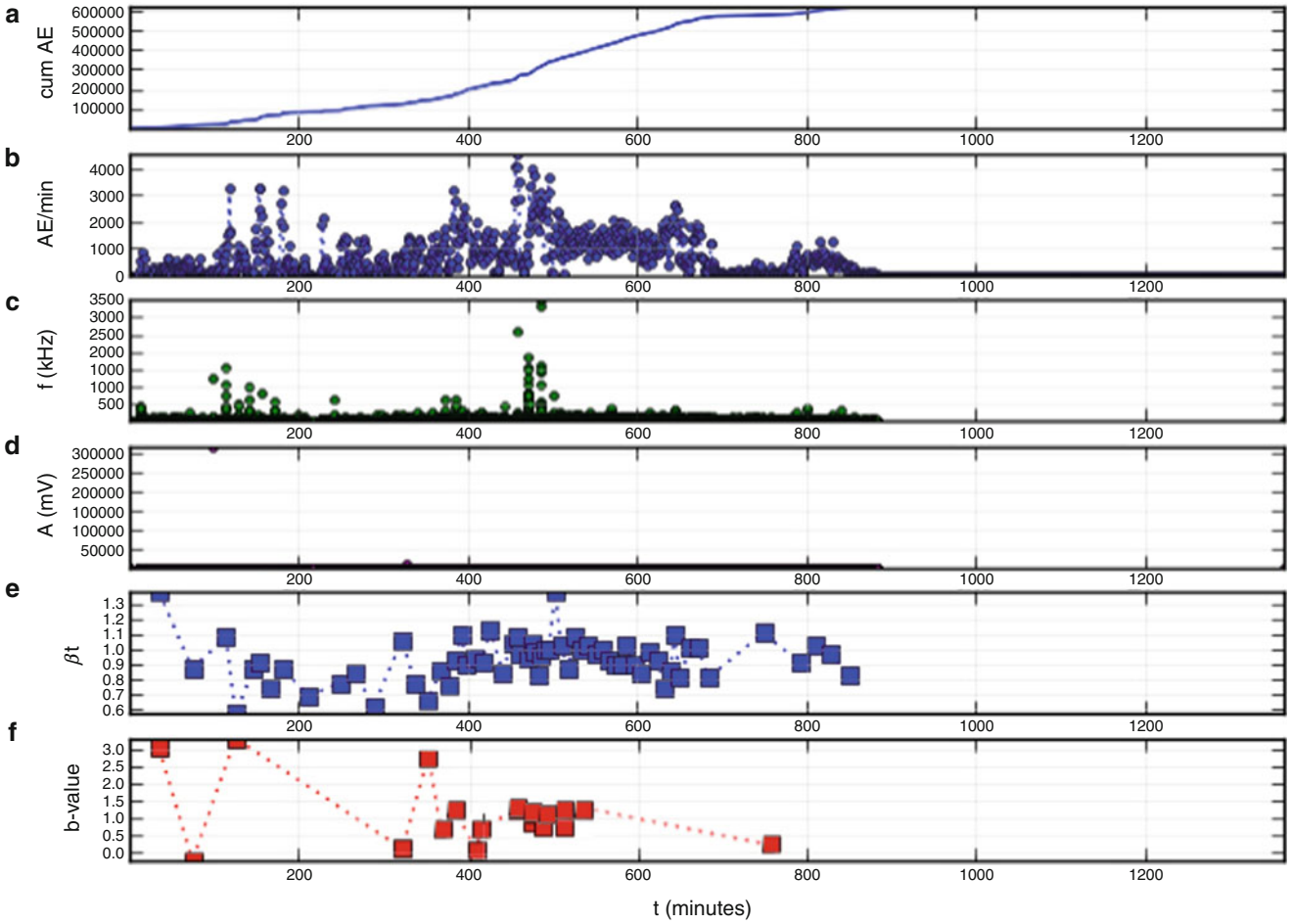

Fig. 31.5 Basalt specimen: Last phase. Cumulated AE (**a**), AE/minutes (**b**), Ae signal Frequency (**c**), AE Amplitudes (**d**), βt exponent (**e**), b-value (**f**)

On the other hand, the increase of AE rate were accompanied by a β_t close to 1 denouncing a metastable condition. This evidence, together with the *b*-value showing a drastic decreasing down to 1, denoted that after 1.32×10^6 cycles a evident damage took place into the monitored specimen. It is interesting to observe that after this first increment of AE activity no signals were observed for about 500 min. A second appreciable increase in AE events was observed only after about 8 h from the beginning of the test and precisely after 610 min. In this case a considerable AE increasing was observed in AE events with greater magnitude respect to their smaller counterparts (Fig. 31.4). The increment in the number of AE with greater magnitude was accompanied by *b*-values changing between 1.8 and 1.5 indicating little variability in signal amplitudes and a damage still distributed in a volume. In Fig. 31.5 the last phase for the basalt specimen is reported and a stronger increase of AE with values between 3,000 and 4,000 for the AE number per unit time were detected. In this phase maximum cumulated AE counts about 20 times greater than cumulated AE counts observed during the first phase (see Fig. 31.4). The trend of β_t shows a progressive increase up to values between 1 and 1.3. As far as the *b*-value is concerned it decreased drastically to values smaller than 1 just in correspondence of the final failure occurred after about 31×10^6 cycles.

Similar results in AE activity were observed in the case of granite and magnetite specimens, in particular the *b*-value trends for the final stages are reported in Fig. 31.6. Also in this case it is possible to observe that the *b*-value changes from higher value down to 1 in correspondence to the final failure of the specimen when the final collapse took place.

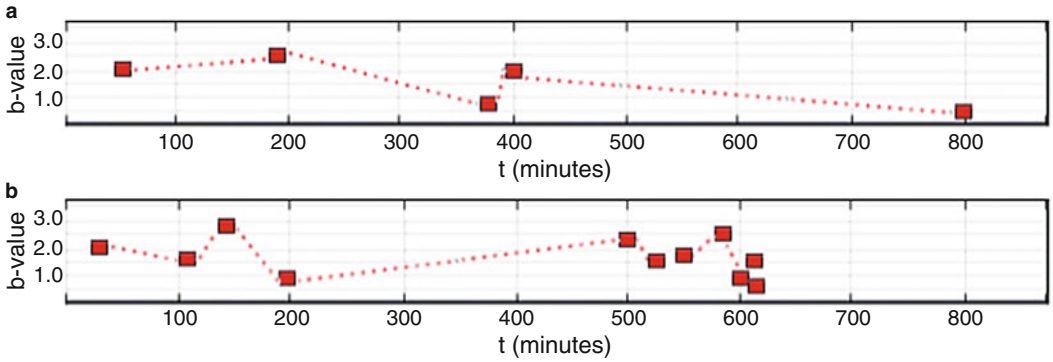

Fig. 31.6 *b*-Values for Granite (**a**) and Magnetite (**b**) specimens: Third phase. The *b*-value changes from higher to lower values close to 1 in correspondence of the final failure of the specimens

31.5 Conclusions

In this paper, laboratory tests were performed on different kind of rocks with the aid a new AE equipment. The cumulated AE number is used to detect the damage evolution during cyclic tests. The fatigue damage evolution obtained by AE data lead to recognize three different phases during the tests. In particular the first and the last phase are characterized by a sudden increment into the AE number. By adopting statistical analysis on AE data was possible to describe the damage accumulation due to fatigue by a fractal description of the damage domain through the *b*-value. The trend observed for this parameter may be useful to recognize in advance the final failure condition in order to prevent the collapse due to fatigue in rock materials.

Aknowledgements The Authors gratefully acknowledge Dr. M. Spampani and Dr. Michele Pedroni, and Alessandro Mitillo (Leane net. srl) for their valuable cooperation throughout the development of the new AE monitoring system.

References

1. Lacidogna G, Manuello A, Niccolini G, Carpinteri A (2012) Acoustic emission monitoring of Italian historical buildings and the case study of the Athena temple in Syracuse. Architect Sci Rev 11(3):359–366
2. Carpinteri A, Lacidogna G, Pugno N (2004) A fractal approach for damage detection in concrete and masonry structures by the acoustic emission technique. Acoustique et Techniques 38:31–37
3. Carpinteri A, Lacidogna G (2006) Structural monitoring and integrity assessment of medieval towers. J Struct Eng (ASCE) 132:1681–1690
4. Carpinteri A, Lacidogna G (2006) Damage monitoring of an historical masonry building by the acoustic emission technique. Mater Struct 39:161–167
5. Carpinteri A, Lacidogna G, Paggi M (2007) Acoustic emission monitoring and numerical modeling of FRP delamination in RC beams with non-rectangular cross-section. Mater Struct (RILEM) 40:553–566
6. Carpinteri A, Lacidogna G (2007) Damage evaluation of three masonry towers by acoustic emission. Eng Struct 29:1569–1579
7. Carpinteri A, Lacidogna G, Manuello A (2011) Stability of the ancient Athena temple in Syracuse investigated by the b-value analysis. Strain 47:243–253
8. Carpinteri A, Lacidogna G, Niccolini G (2006) 2006 Critical behaviour in concrete structures and damage localization by acoustic emission. Key Eng Mater 312:305–310
9. Bieniawski ZT (1967) Mechanism of brittle rock fracture. Part II. Experimental studies. Int J Rock Mech Mining Sci Geomech Abstr 4:407–423
10. Brace WF, Paulding BW Jr, Scholz C (1966) Dilatancy in the fracture of crystalline rocks. J Geophys Res 71:3939–3953
11. Scholz CH (1968) Microfracturing and the inelastic deformation of rock in compression. J Geophys Res 73:1417–1432
12. Ohnaka M, Mogi K (1982) Frequency characteristics of acoustic emissions in rocks under uniaxial compression and its relation to the fracturing process to failure. J Geophys Res 87:3873–3884
13. Khair AW (1984) Acoustic emission pattern: an indicator of mode of failure in geologic materials as affected by their natural imperfections. In: Hardy HR Jr, Leighton FW (eds) Proceedings of the 3rd conference on acoustic emission/microseismic activity in geologic structures and materials, 1981, University Park, PA. Trans Tech Publications, Clausthal, pp 45–66
14. Eberhardt E, Stead D, Stimpson B, Read RS (1998) Identifying crack initiation and propagation thresholds in brittle rock. J Can Geotech 35:222–233
15. Carpinteri A, Lacidogna G, Niccolini G, Puzzi S (2008) Critical defect size distributions in concrete structures detected by the acoustic emission technique. Meccanica 43:349–363
16. Carpinteri A, Lacidogna G, Niccolini G, Puzzi S (2009) Morphological fractal dimension versus power-law exponent in the scaling of damaged media. Int J Damage Mech 18(3):259–282

17. Carpinteri A (1994) Fractal nature of material microstructure and size effects on apparent mechanical properties. Mech Mater 18:89–101, Internal Report, Laboratory of Fracture Mechanics, Politecnico di Torino, N. 1/92; 1992
18. Carpinteri A (1994) Scaling laws and renormalization groups for strength and toughness of disordered materials. Int J Solids Struct 31:291–302
19. Carpinteri A (1994) Strength and toughness in disordered materials: complete and incomplete similarity. In: Size-scale effects in the failure mechanisms of materials and structures. Proceedings of the international union of theoretical and applied mechanics (IUTAM), Turin, Italy. E&FN Spon, London, pp 3–26
20. Carpinteri A, Ferro G (1994) Size effects on tensile fracture properties: a unified explanation based on disorder and fractalilty of concrete microstructure. RILEM Mater Struct 27:563–571
21. Carpinteri A, Chiaia B (1994) Fractals, renormalization group theory and scaling laws for strength and toughness of disordered materials. In: Proceedings of the workshop probabilities and materials: tests, models and applications (PROBAMAT), Cachan, France, Nov 1993. Kluwer, Dordrecht, pp 141–150
22. Carpinteri A, Chiaia B (1995) Multifractal nature of concrete fracture surfaces and size effects on nominal fracture energy. RILEM Mater Struct 28:435–443
23. Vola G, Marchi M (2009) Mineralogical and petrographic quantitative analysis of a recycled aggregate from quarry wastes. The Luserna stone case-study. Proceedings of the 12th euroseminar on microscopy applied to building materials, 15–19 Sept 2009, Dortmund, Germany
24. Sandrone R, Cadoppi P, Sacchi R, Vialon P (1993) The Dora-Maira Massif. In: Von Raumer JF, Neubauer F (eds) Pre-Mesozoic geology in the Alps. Springer, Berlin, pp 317–325
25. Sandrone R, Borghi A (1992) Zoned garnets in the northern Dora-Maria Massif and their contribution to a reconstruction of the regional metamorphic evolution. Eur J Minerals 4:465–474
26. Compagnoni R, Crisci GM, Sandrone R (1983) Caratterizzazione chimica e petrografica degli “gneiss di Luserna” (Massiccio cristallino Dora-Maira, Alpi Occidentali). Rend Soc It Min Petr 38:498
27. Verkaeren J, Bartholomè P (1979) Petrology of the San Leone magnetite skarn deposit (S. W. Sardinia). Econ Geol 74:53
28. Tanguy JC (1978) Tholeiitic basalt magmatism of Mount Etna and its relations with the alkaline series. Contrib Mineral Petrol 66:51
29. Carpinteri A, Lacidogna G, Manuello A (2007) An experimental study on retrofitted fiber-reinforced concrete beams using acoustic emission. In: Proceedings of the 6th international FraMCoS conference, Catania, Italy
30. Carpinteri A, Ferro G, Gambarova P, editors (2007) High-Performance Concrete, Brick-Masonry and Environmental Aspects. In: Proceedings of the 6th International Conference on Fracture Mechanics of Concrete and Concrete, Catania, Italy 2(3):1061–1068
31. Carpinteri A, Lacidogna G, Niccolini G (2007) Acoustic emission monitoring of medieval towers considered as sensitive earthquake receptors. Nat Hazards Earth Syst Sci 7:251–261
32. Niccolini G, Xu J, Manuello A, Lacidogna G, Carpinteri A (2012) Onset time determination of acoustic and electromagnetic emission during rock fracture. Progr Electr Res Lett 35:51–62
33. Carpinteri A, Lacidogna G, Pugno N (2007) Structural damage diagnosis and life-time assessment by acoustic emission monitoring. Eng Fract Mech 74(1–2):273–289
34. Colombo S, Main IG, Forde MC (2003) Assessing damage of reinforced concrete beam using “b-value” analysis of acoustic emission signals. J Mat Civil Eng (ASCE) 15:280–286
35. Rao MVMS, Lakschmi PKJ (2005) Analysis of b-value and improved b-value of acoustic emissions accompanying rock fracture. Curr Sci 89:1577–1582
36. Richter CF (1958) Elementary seismology. W.H. Freeman, San Francisco, CA, London
37. Rundle JB, Turcotte DL, Shcherbakov R, Klein W, Sammis C (2003) Statistical physics approach to understanding the multiscale dynamics of earthquake fault systems. Rev Geophys 41:1–30
38. Carpinteri A (1986) Mechanical damage and crack growth in concrete: plastic collapse to brittle fracture. Martinus Nijhoff, Dordrecht

Chapter 32
Hybrid thermography and acoustic emission testing of fatigue crack propagation in Aluminum Samples

C. Barile, C. Casavola, G. Pappalettera, and C. Pappalettere

Abstract In this paper the crack propagation process was monitored by two different experimental techniques. Acoustic emissions sensors were placed on the sample in order to monitor the evolution of the acoustical events during the test; at the same time the change in temperature was monitored by thermography. Test were run on aluminum samples (Al 5068). Specimens were previously cracked, by cutting notches having known sizes and geometry. Successively, X-Ray diffractometry analysis were performed in order to establish the given initial stress state of each sample. Specimen were then subjected to mechanical tests. During these tests the crack propagation was continuously monitored and recorded by both techniques. Data obtained, in terms of number of hits, amplitude signals and maps' temperature, were critically compared in order to assess the capability of each technique in following the evolution of the damage process.

Keywords Aluminum • Acoustic emission • Crack propagation • Fatigue • Thermography

32.1 Introduction

A release of plastic energy happens every time structural modifications occur inside solid materials, this phenomenon not only produces temperature variations but also generates acoustic emissions (AE). These acoustic signals can be related to several sources i.e. motion of dislocations, crack nucleation, crack propagation etc. The acoustic emissions technique detects stress waves produced during the transient release of energy in materials subjected to heat treatments such as local annealing for relieving residual stress [1–4] or mechanical stresses [5–7], it is a non-invasive technique that can act both in active and in passive way. AE are detected in the ultrasonic range of frequencies by using high sensitivity piezoelectric sensors having the resonance frequency close to the frequency of the ultrasound signal to be monitored.

The AE technique and infrared relieving of temperature by thermography technique are characterized by the possibility to detect the energy release of stressed component even when it depends on a strictly localized phenomenon. In this work, in fact, a live monitoring of crack propagation was performed. In order to better describe fatigue crack evolution, two nondestructive techniques, AE and thermography, were combined.

32.2 Materials and Methods

Experimental tests were carried out on three aluminum samples (Al 5068) with rectangular cross section 20×10 mm^2 and 200 mm length. A notch was cut on each specimen in order to identify a precise location for monitoring both crack nucleation and propagation. Notches were obtained by means of a machine in correspondence of the centerline of the specimen. Notches were observed and measured by an optical microscope in order to calculate the stress intensity factor as function of the notch geometry.

C. Barile, Ph.D. • C. Casavola (✉) • G. Pappalettera, Ph.D. • C. Pappalettere
Dipartimento di Meccanica, Matematica e Management, Politecnico di Bari, Viale Japigia 182, Bari 70126, Italy
e-mail: casavola@poliba.it

J. Carroll and S. Daly (eds.), *Fracture, Fatigue, Failure, and Damage Evolution, Volume 5: Proceedings of the 2014 Annual Conference on Experimental and Applied Mechanics*, Conference Proceedings of the Society for Experimental Mechanics Series,
DOI 10.1007/978-3-319-06977-7_32,

Table 32.1 Main characteristics of the Pico sensor

Peak sensitivity	54 dB
Operating frequency range	200–750 kHz
Resonant frequency	250 kHz
Temperature range	−65 to 177 °C
Dimension	5 × 4 mm

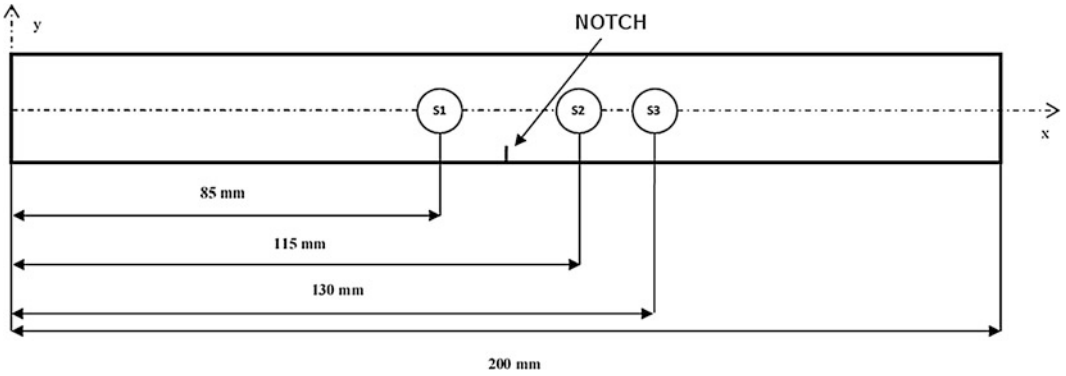

Fig. 32.1 Schematic of acoustic sensor locations on the specimen

Preliminary X-ray measurements were executed on specimens along three different directions on different locations in correspondence of the longitudinal axis and close to the notch in order to evaluate the initial stress field on the specimens.

Fatigue tests were carried out using an amplitude load of ±31 kN and a mean load of 0 kN, acquiring data at 1 Hz frequency. During the cyclic load both acoustic emissions and thermographic images were acquired.

Acoustic emission events are identified by a set of shots (*hits*) [8]. If a voltage threshold value is fixed, the hits represent the number of times the voltage generated from the PZT sensor overcomes that threshold. Every shot is characterized by an intensity value proportional to the energy of the detected event [9].

Three Pico-sensors (Table 32.1 [10]) were placed on the surface of the specimen, two sensors were 30 mm far apart one from each other (Fig. 32.1) and at the same distance from the notch, the third one was placed farther from the notch in order to take account for other possible events.

Thermal images were acquired by using a thermo camera having the following characteristics:

- Resolution: 640 × 480 pixel
- Working distance: >30 cm
- Temperature range: −20 °C ÷ 60 °C
- Acquisition rate: 1 Hz

Acoustic emissions and thermo images were monitored and recorded continuously during the cyclic test.

32.3 Results and Discussion

Monitoring crack propagation has shown some differences in the analysis capability of the two techniques. In particular, analyzing the next figures, it should be noted that AE followed very well the nucleation and the initial behavior of crack propagation; on the other hand thermography technique best appreciates the final phase of propagation and the fracture.

Figure 32.2 shows signal records of the three AE sensors placed on one specimen; they represent the number of hits recorded and cumulate during the test time. The curves distinguish a first trend between 0 and 50 s having a high slope and a second one having a lower slope. This difference can be justified since the first part of curve refers to crack nucleation that generally is characterized by a great number of acoustic events, on the contrary in the second part due to the Kaiser effects, the AE activity become more stationary until the final fracture event occurs. Scientific literature confirms this attitude [11, 12] associating to the sample fracture a low number of events with a high intensity.

In Fig. 32.3 some images recorded by thermo-camera are reported. It is possible to observe a region of higher temperature in correspondence of the notch. In Fig. 32.4 the increment of temperature recorded in an area close to the notch is reported for three specimens. As mentioned above in thermography the final phase of crack propagation and fracture was more evident than in AE graph.

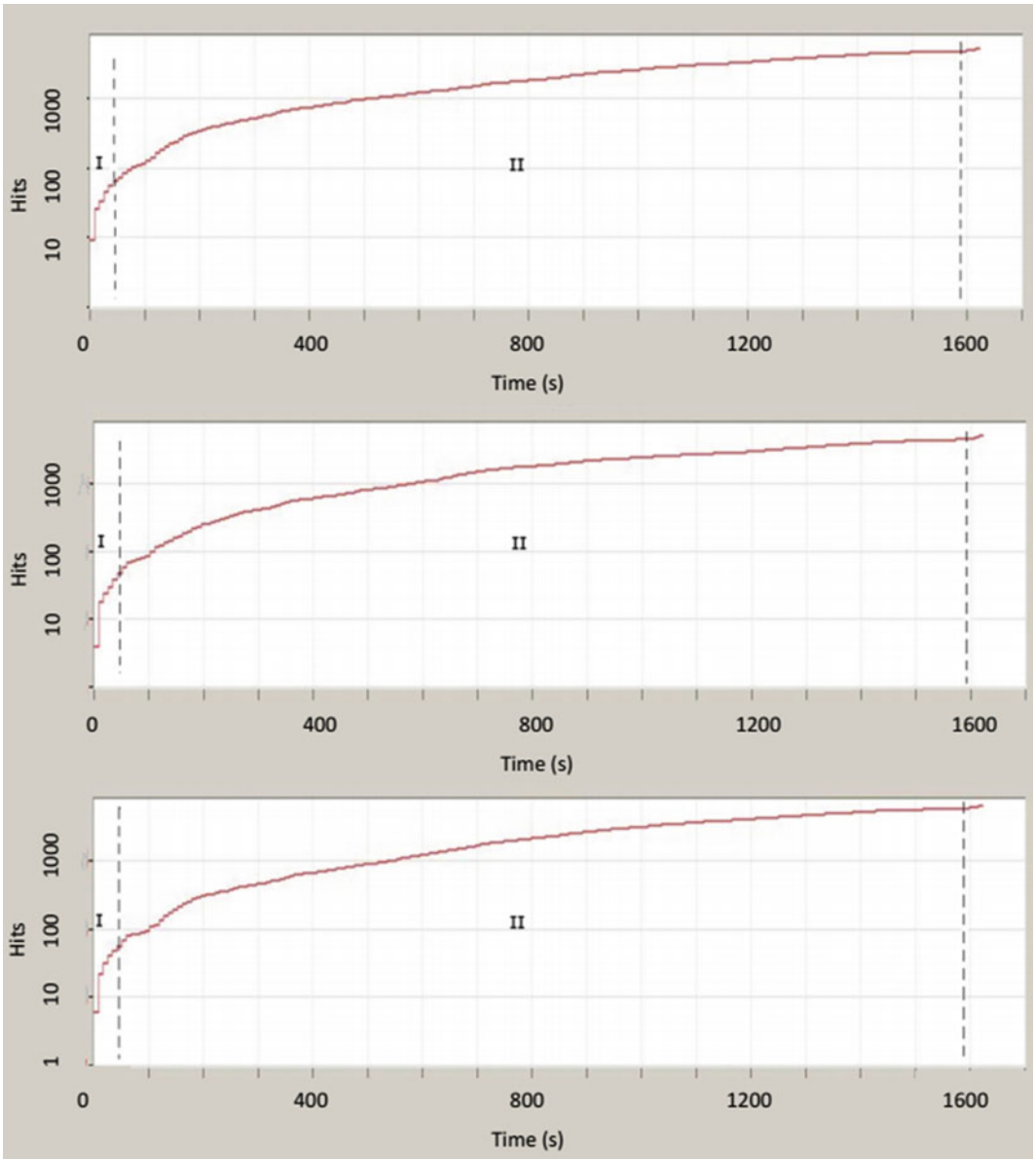

Fig. 32.2 AE graph of three sensors on specimen A: Hits vs. Test time

Temperature level on the whole specimen was a result of thermo-elastic effect. In the area closest to the notch the temperature was a combination of thermo-elastic effect and the notch growth. Curves in Fig. 32.4 represent the temperature in correspondence of the notch curtailed of the thermo-elastic effect.

AE data can also provide another important information regarding the total life of specimen. Plotting the events of AE as function of the time is possible to detect an increment in the number of recorded events with a certain advance with respect to the final fracture of the specimen (Fig. 32.5).

Data up to 800 s show a regular and low acoustic activity, these events can be related to background noise. Over 800 s the numbers of events deeply increase between sensor 1 and 2 but in particular tend to be concentrated close to the sensor 2 up to 1,600 s when the fracture occurs. This result lead us to conclude that the AE technique should be reliable and able to estimate both the lifetime of the specimen and the direction of the crack [13].

Three dimensional plot of AE (Fig. 32.6) technique shows cumulative hits recorded as function of localization in unit time. As can be seen the highest number of hits stay in the neighborhood of the crack at the position of 100–105 mm.

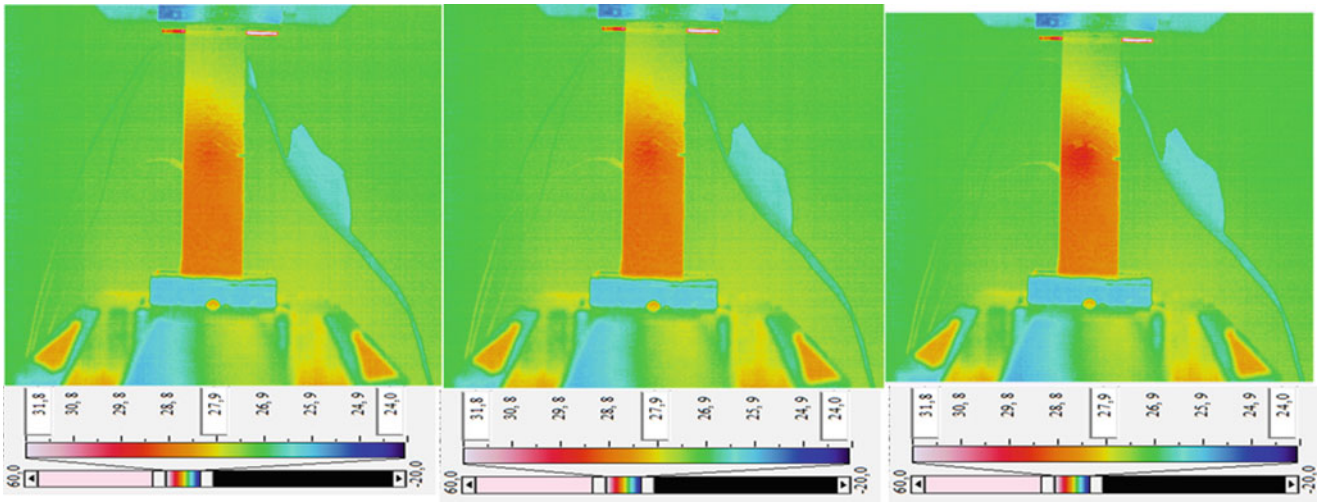

Fig. 32.3 Sequence of acquired thermo graphic images (specimen A)

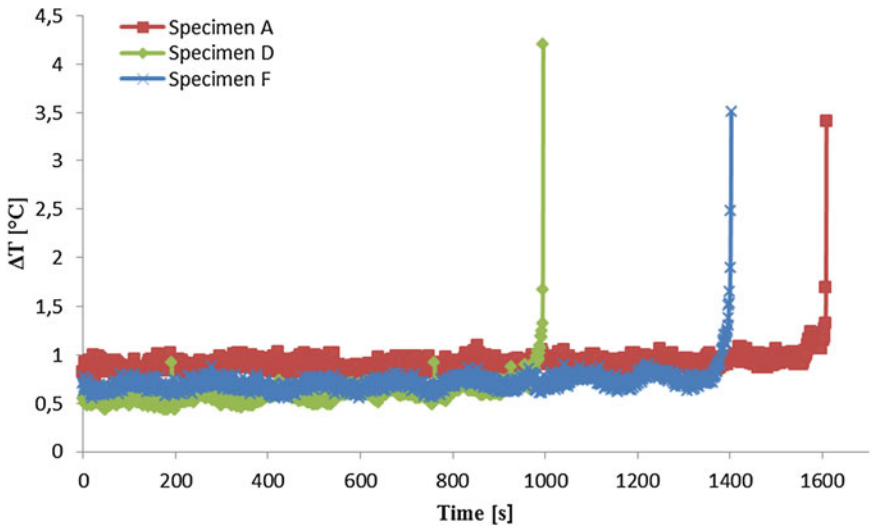

Fig. 32.4 Thermo graphic curve: ΔT vs. test time. The plot reports the increment of temperature recorded in an area close to the notch for three specimens

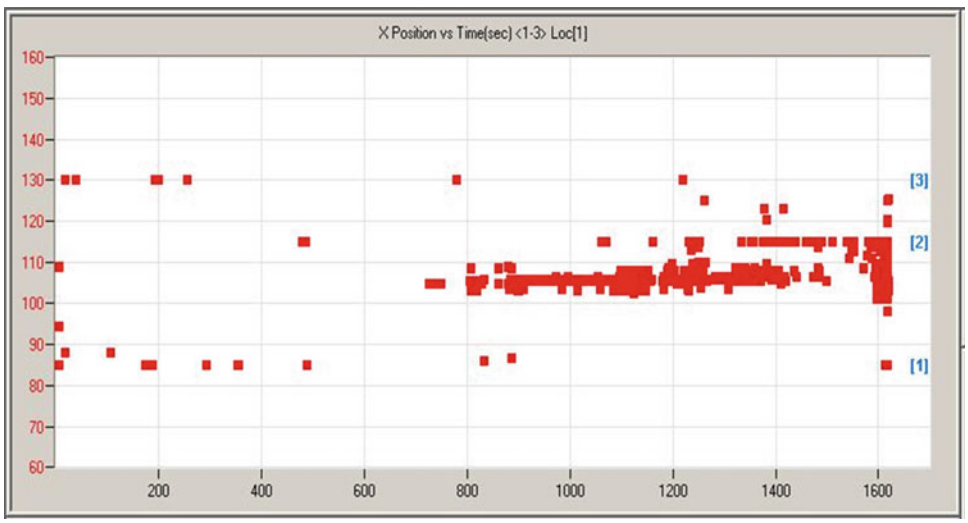

Fig. 32.5 Plot of the acoustic events recorded on specimen A. Location of the acoustic event is reported also in relationship with the location of the three acoustic emission sensors (in blue between square bracket)

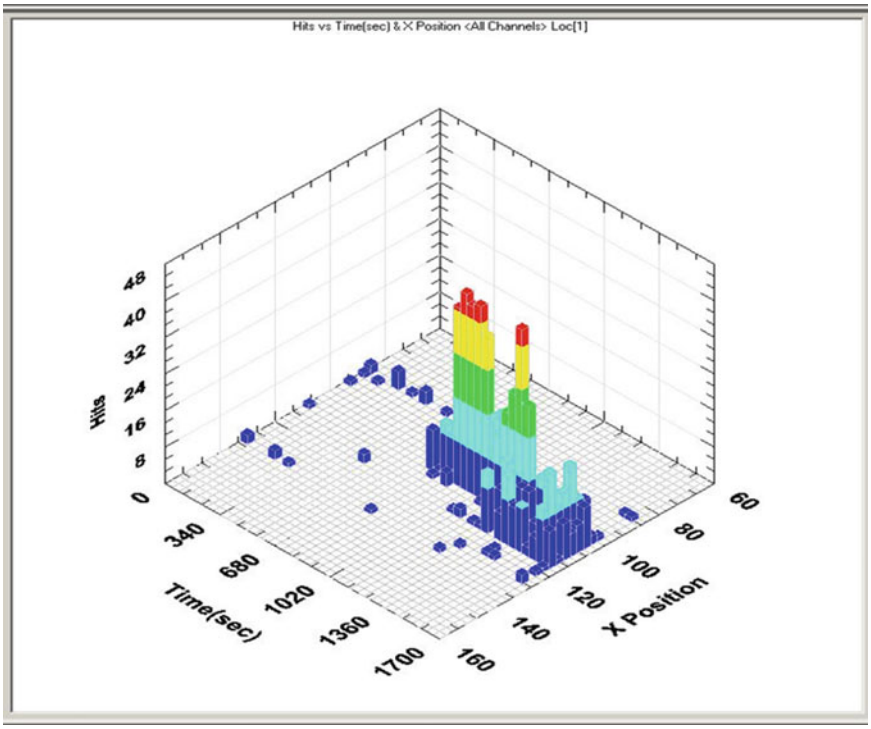

Fig. 32.6 3D histogram plot Hits vs. Test Time vs X position (specimen A)

32.4 Conclusions

In this paper crack propagation during fatigue tests was analyzed. This phenomenon was analyzed and described by combining two non-destructive techniques: acoustic emission and thermography. Data recorded on three specimens by both approaches were analyzed. It was found that precise information about the crack localization, the direction of propagation could be obtained by both acoustic emission and thermography, but acoustic emission seems to be more accurate in providing indications about the oncoming fracture of the specimen.

References

1. Barile C, Casavola C, Pappalettera G, Pappalettere C (2013) Feasibility of local stress relaxation by laser annealing and x-ray measurement. Strain 49:393–398
2. Barile C, Casavola C, Pappalettera G, Pappalettere C (2012) Preliminary analysis for a new approach to relieve residual stresses by laser heating. In: Conference proceedings of eleventh YSESM youth symposium experimental solid mechanics, Brasov, Romania, 30 May–2 June 2012
3. Casavola C, Campanelli SL, Pappalettere C (2008) Experimental analysis of residual stresses in the selective laser melting process. In: Society for Experimental Mechanics—eleventh international congress and exhibition on experimental and applied mechanics 2008, Orlando, vol 3, pp 1479–1486
4. Barile C, Casavola C, Pappalettera G, Pappalettere C (2013) Discussion on the thermal field produced by laser annealing for the residual stress relaxation. In: Conference proceedings of new trends in fatigue and fracture, Moscow, Russia, 13–16 May 2013, pp 22–30
5. Miller RK, McIntire P (1987) Nondestructive testing handbook, vol 5, 2nd edn, Acoustic emission testing. American Society for Nondestructive Testing, Columbus, pp 275–310
6. Drouillard TF, Glenn TG (1985) Production acoustic emission testing of braze joint. J Acoust Emiss 1(2):81–85
7. Barile C, Casavola C, Pappalettera G, Pappalettere C. Acoustic emission analysis of aluminum specimen subjected to laser annealing (2014) Conference Proceedings of the Society for Experimental Mechanics Series, vol 8, pp 309–315
8. Pao YH (1978) Theory of acoustic emission. In: Elastic waves and non-destructive testing of materials, AMD20. American Society of Mechanical Engineers, New York, pp 107–128
9. Enoki M, Kishi T, Kohara S (1983) Determination of microcracking moment tensor of quasi-cleavage facet by AE source characterization. In: Progress in acoustic emission III, proceedings of the eighth international acoustic emission symposium, The Japanese Society for Non-Destructive Inspection, Tokyo, pp 763–770

10. www.mistrasgroup.com
11. Ono K (1994) Trends of recent acoustic emission literature. J Acoust Emiss 12:177–198
12. Dornfeld D (1992) Application of acoustic emission techniques in manufacturing. NDT Int 25:259–269
13. Calì M, La Rosa G, Lo Savio F, Maiolino L (2002) Valutazione della propagazione di cricche in provini saldati con tecniche di emissione acustica e termografica. da Atti del XVI Convegno Nazionale “Gruppo italiano frattura”, Catania, 20–22 Giugno 2002